THE
PHYSICAL REVIEW

A journal of experimental and theoretical physics established by E. L. Nichols in 1893

SECOND SERIES, VOL. 73, No. 9 MAY 1, 1948

Excitation Function for Proton-Neutron Reaction in Lithium ($Li^7(p,n)$)*

J. E. HILL AND W. E. SHOUPP
Westinghouse Electric Corporation, Pittsburgh, Pennsylvania
(Received January 12, 1948)

The excitation function of the (p,n) reaction in lithium ($Li^7(p,n)$) has been studied in the region from the threshold (1.85 Mev) to 3.20 Mev. Neutron groups have been found to be emitted at proton energies of 1.92, 2.28, and 3.06 Mev, suggesting the existence of energy levels in Be^8 at 19.8, 19.1, 18.8 Mev in addition to the other well-known states.

I. INTRODUCTION

REACTIONS of the (p,n) type in Li^7 were first observed by DuBridge, Barnes, and Buck[1] who showed that the excitation function possessed a definite threshold, and a rough measurement of it was made by using the radioactivity induced in silver foils by the neutrons. Since then the threshold was measured more accurately by detecting the neutron emission with a BF_3 ionization chamber.[2] The neutrons are copiously emitted from this source, and the apparent sharpness and easy reproducibility of the threshold has since been used in many laboratories as a convenient voltage calibration point. Furthermore the $Li^7(p,n)Be^7$ reaction provides a convenient source of fast neutrons, the maximum energy of which may be varied in a determinable manner by controlling the energy of the incident protons. The presence of resonance levels demonstrated here requires that this technique be used with some caution. These neutrons have been used to investigate the energy threshold of certain neutron-induced endoenergetic nuclear reactions.[3-5] In the work reported here, the yield of neutrons from thin films of lithium was measured as a function of energy of the bombarding protons. This investigation resulted in the discovery of two rather sharp maxima and possibly a third.

II. EXPERIMENTAL PROCEDURE

The Westinghouse pressure electrostatic generator[6] was used as a source of high energy protons. The magnetically deflected mass one (H^+) spot was used to avoid any possible deuterium contamination. A boron tri-fluoride ionization chamber surrounded by 12 cm of paraffin and placed in the direct line of the proton beam beyond the lithium target was used as the neutron detector[2] (Fig. 1). The output pulses from the ionization chamber were amplified and fed into a scale of 16 circuit that was

* This work was completed in 1940 and was voluntarily withheld from publication.
[1] DuBridge, Barnes, and Buck, Phys. Rev. 51, 995 (1937).
[2] Haxby, Shoupp, Stephens, and Wells, Phys. Rev. 58, 1035 (1940).
[3] Haxby, Shoupp, Stephens, and Wells, Phys. Rev. 57, 1088(A) (1940).
[4] Haxby, Shoupp, Stephens, and Wells, Phys. Rev. 58, 199(A) (1940).
[5] Haxby, Shoupp, Stephens, and Wells, Phys. Rev. 59, 57 (1940).
[6] Haxby, Shoupp, Stephens, and Wells, Phys. Rev. 58, 162 (1940).

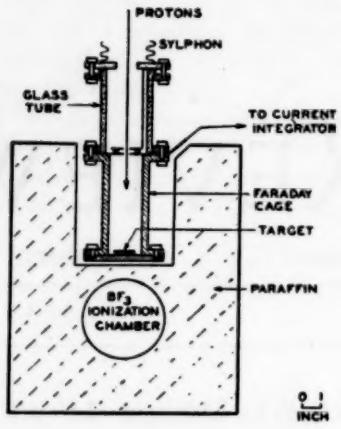

FIG. 1. Target arrangement.

used to drive a mechanical recorder. The neutron yield from a lithium target of about 140-kilovolts equivalent half-width was measured as a function of proton energy. The thin lithium targets were evaporated in vacuum onto a tantalum sheet which could be turned from evaporating position to a position under the proton beam. As a final cleaning measure, the tantalum sheet was bombarded by protons prior to the evaporation. Without the lithium film in the bombarding position no neutron background was observed. The equivalent thickness of the lithium films was observed by measuring the half-width of the $Li^7(p,\gamma)$ resonance which occurs for 440-kilovolt protons. The neutron excitation function obtained when the same lithium films were bombarded by protons of varying energy is plotted in Fig. 2.

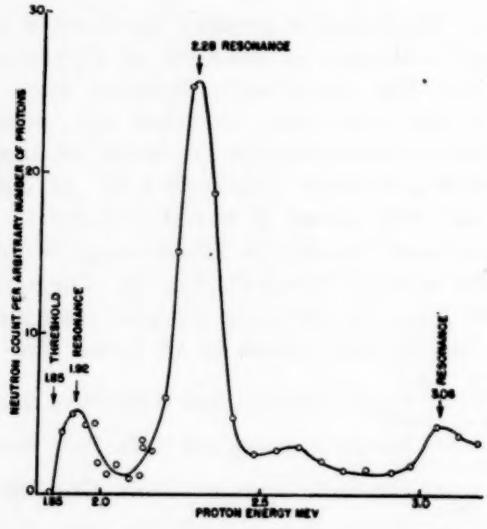

FIG. 2.

III. RESULTS

It is apparent from (Fig. 2) that the neutron emission from the $Li^7(p,n)$ reaction possesses definite maxima at proton energies of 1.92, 2.28 Mev and possibly another at 3.06 Mev. The calculated statistical deviation is not indicated, but at all points taken it is less than the diameters of the circles used in the drawings.

Using a thick LiH crystal as a target, it was found that the γ-ray intensity also started to increase at the (p,n) threshold and increases further with increasing proton energy. This agrees with the observations of Hudson, Herb, and Plain,[7] who also observed the increase in the hard component of γ-rays at the bombarding proton energy of 1.83 Mev. The intensity of γ-rays seems to flatten out and give a maximum at about 1.9 Mev.

The composite nucleus $_4Be^{8*}$ may be assumed to form first when a proton enters a $_3Li^7$ nucleus. This nucleus is highly excited since 17.5-Mev γ-ray is emitted for a bombarding proton energy of only 0.440 Mev. The excited $_4Be^{8*}$ nucleus, assuming it was formed with zero proton energy, may decompose in several ways as follows:

$$_4Be^{8*} \rightarrow {}_2He^4 + {}_2He^4 + 17.28 \text{ Mev.} \quad (1)$$

$$_4Be^{8*} \rightarrow {}_4Be^8 + \gamma + 17.5 \text{ Mev.} \quad (2)$$

$$_4Be^{8*} \rightarrow {}_4Be^7 + {}_0n^1 - 1.62 \text{ Mev.} \quad (3)$$

$$_4Be^{8*} \rightarrow {}_3Li^7 + {}_1H^1 + 0 \text{ Mev.} \quad (4)$$

$$_4Be^{8*} \rightarrow {}_3Li^6 + {}_1H^2 - 4.96 \text{ Mev.} \quad (5)$$

Reactions (3) and (5) will not proceed unless the bombarding proton beam possesses enough kinetic energy to supply the necessary reaction energy. In this particular case ($Li^7(p,n)$), the proton energy should be about 8/7 of the reaction energy. In the range of proton energy used in this experiment, 1.85 to 3.2 Mev, all the reactions with the exception of reaction (5) have a probability of occurring. However, it is unlikely that the variation of neutron yield, as indicated in Fig. 2, is due to the result of competition of these various processes because the natural

[7] Hudson, Herb, and Plain, Phys. Rev. 57, 587 (1940).

energy spread of the maxima is very small, as indicated by their half-widths, which are about the same order as the target thickness. It is possible that these maxima actually indicate resonance levels of certain nuclear mechanism. The neutrons are probably due to the excited energy levels in the composite $_4Be^{8*}$ nucleus from which decomposition by emission of a neutron is highly possible. If this is the case, the energy levels of the $_4Be^{8*}$ will have a value given by $17.5-(7/8)\times 0.440+(7/8)E$, where E is the bombarding proton energy at the neutron maxima. For the three maxima observed, these levels correspond to 18.8, 19.1, and 19.8 Mev, respectively. It should be noted that decomposition in other fashions is not impossible, since our quantitative detection only covered the emitted neutrons. Since the reaction energy Q of $_3Li^7(p,n)_4Be^7$ is -1.62 Mev, the excess energies possessed by the Be^{8*} composite nucleus at the resonances are 0.06, 0.38, and 1.06 Mev, and will be distributed between the neutron and the residual nucleus $_3Be^7$, as kinetic energy. Since the Be^7 nucleus has a much greater mass than the neutron, most of the energy will be carried away by the neutrons. In the forward direction of the laboratory coordinate system, the neutrons also carry a part of bombarding proton energy lost through the kinetic energy transfer during collision. The maximum energy of the neutrons in the forward direction in the laboratory system at these resonance levels is then 0.16, 0.58, and 1.4 Mev, respectively. It is probable that the excited nucleus $_4Be^{8*}$ may at the same time also emit hard γ-rays which accounts for the experimental indication of Hudson, Herb, and Plain[7] (as well as ours), even though the (p,γ) process is, in general, not as significant as the (p,n) process.[8] It is interesting to note that, in the study of proton bombardment of thin beryllium targets, Hushley[9] also found a sharp resonance maximum after the threshold both for neutrons and γ-rays.

An alternative explanation may be made by assuming the existence of several excited states of the product nucleus $_4Be^7$ from which it decays to the ground state by emitting γ-rays. The excess energy supplied by the proton above the threshold will be distributed among the neutrons and $_4Be^7$ until the optimum energy is reached which corresponds to the excited levels of $_4Be^{7*}$. At this point all the neutrons will assume zero energy (in the center of gravity system). According to the $1/v$ law, the BF_3 chamber should respond much more efficiently to these slow neutrons. The maxima, then, would not represent a real increase in neutrons, but would be characteristic of the method of detection. If this hypothesis were true, one would expect to be able to observe γ-rays associated with the excited states of Be^{7*}, and definite energy groups would be observable. Observations have not been made on this point. A careful study of the thin target (p,γ) excitation function and the neutron and γ-ray energy above the (p,n) threshold would be most interesting.

---

[8] H. A. Bethe, *Elementary Nuclear Theory* (John Wiley and Sons, Inc., New York, 1947), p. 115.
[9] W. J. Hushley, Phys. Rev. 67, 34 (1945).

Note on Second Born Approximation and Proton-Neutron and Proton-Proton Scattering

TA-YOU WU
Department of Physics, Columbia University, New York

(Received January 19, 1948)

The scattered amplitude $f(\vartheta)$ is regarded as a series in powers of the interaction potential V, and the second Born approximation consists in calculating the scattered intensity up to the fourth power of V. The calculation can be carried out analytically for a Gaussian potential, leading to a simple way of calculating the second approximation for the phases. The result is applied to the proton-neutron and proton-proton scattering at 100 Mev, on the basis of the three forms of nucleon interaction suggested by Rarita and Schwinger, with a Gaussian $V(r)$ and without tensor forces. The result for the symmetrical theory is: $\sigma_{p-n}=0.96\times10^{-25}$ cm², $\sigma_{p-p}=0.22\times10^{-25}$ cm², as compared with the first approximation values 1.40×10^{-25} and 0.28×10^{-25} cm², respectively. These give for $(\sigma_{p-n}+\sigma_{p-p})$ the value 1.18, in much closer agreement with the observed value 1.17 for σ_{p-d} than the other two forms of interaction potential.

I. INTRODUCTION

FOR the scattering by a central field, the scattered amplitude is given by the Faxen-Holtzmark formula, namely,

$$f(\vartheta)=\frac{1}{2ik}\sum(2l+1)(e^{2i\delta_l}-1)P_l(\cos\vartheta)$$

$$=\frac{1}{k}\sum(2l+1)[\delta_l-\tfrac{2}{3}\delta_l{}^3+\cdots$$

$$+i(\delta_l{}^2-\tfrac{1}{3}\delta_l{}^4\cdots)]P_l(\cos\vartheta). \quad (1)$$

The usual first Born approximation consists in (i) dropping off all terms except δ_l, and (ii) replacing δ_l by its first approximation

$$\delta_l{}^{(1)}=-\frac{\pi M}{2\hbar^2}\int_0^\infty V(r)J_{l+\frac{1}{2}}{}^2(kr)rdr, \quad (2)$$

where M is the proton or neutron mass for proton-neutron collisions.

Recent calculations on the cross section of proton-neutron scattering at high energies show that the first Born approximation is unsatisfactory at 100 Mev.[1] As the exact calculation of the phases δ_l by numerical integration of the wave equation is lengthy for any potential other than the rectangular hole one, it is of some interest to have better approximate methods than the usual Born approximation.

One usual method of improving on the Born approximation is to use $\delta_l{}^{(1)}$ in (1), so as to take into account the higher powers of δ_l. This procedure will be justified if the difference $\delta_l{}^{\text{exact}}-\delta_l{}^{(1)}$ is very small compared with $(\delta_l{}^{(1)})^2$. This is, however, in general not the case for low values of l, so that this procedure does not form any consistent approximation in the sense of the perturbation theory.

It has been shown[2] that the phase δ_l can be developed as a series in powers of the interaction potential $V(r)$, namely,

$$\delta_l=\delta_l{}^{(1)}+\delta_l{}^{(2)}+\cdots, \quad (3)$$

where $\delta_l{}^{(1)}$ is given by (2) and

$$\delta_l{}^{(2)}=(-1)^l\left(\frac{M}{2\pi\hbar^2}\right)^2\int_0^\infty V(r)J_{l+\frac{1}{2}}{}^2(kr)rdr$$

$$\times\int_0^\infty V(r)J_{l+\frac{1}{2}}(kr)J_{-l-\frac{1}{2}}(kr)rdr$$

$$+(-1)^{l+1}\left(\frac{M}{2\pi\hbar^2}\right)^2\int_0^\infty V(r)J_{l+\frac{1}{2}}(kr)rdr$$

$$\times\int_0^r[J_{l+\frac{1}{2}}(kr)J_{-l-\frac{1}{2}}(k\xi)-J_{-l-\frac{1}{2}}(kr)$$

$$\times J_{l+\frac{1}{2}}(k\xi)]J_{-l-\frac{1}{2}}(k\xi)\,V(\xi)\xi d\xi. \quad (4)$$

Calculation of $\delta_l{}^{(2)}$ by means of this expression is very lengthy, if not difficult.

[1] J. Ashkin and T. Y. Wu, Phys. Rev. **73**, 973 (1948); M. Camac and H. A. Bethe, Phys. Rev. **73**, 191 (1948).

[2] E. J. Hellund, Phys. Rev. **59**, 395 (1941).

Another approximate formula for δ_l has been found by Pais[3] by the variational method. The expression is

$$\frac{2l+1-(2\delta_l/\pi)}{2l+1-(4\delta_l/\pi)}\delta_l = -\frac{\pi M}{2\hbar^2}\int_0^\infty V(r)J^2_{l+\frac{1}{2}-(2\delta_l/\pi)}(kr)rdr. \quad (5)$$

If δ_l is small, this can be put in the form (3), with $\delta_l^{(1)}$ given by (2) and

$$\delta_l^{(2)} = \frac{2}{\pi}\left(a_l - \frac{\delta_l^{(1)}}{2l+1}\right)\delta_l^{(1)}, \quad (6)$$

where

$$a_l = -\left(\frac{\partial\delta_p^{(1)}}{\partial p}\right)_{p=l+\frac{1}{2}}. \quad (6a)$$

When δ_l is small, calculation of $\delta_l^{(2)}$ according to (6) is easy. Unfortunately, Pais' method is not valid for low values of l, and $l=0$ in particular, and recourse must be made to numerical solution of the wave equation.

In the present note, we shall obtain the second Born approximation and apply the result to proton-neutron and proton-proton scatterings at 100 Mev.

II. SECOND BORN APPROXIMATION

We shall regard $f(\vartheta)$ as a series in powers of the interaction potential $V(r)$. The scattered intensity $I(\vartheta)$ is, up to the fourth power of $V(r)$,

$$I(\vartheta) = |f^{(1)}(\vartheta)|^2 + |f^{(2)}(\vartheta)|^2 + 2f^{(1)}(\vartheta)f^{(3)}(\vartheta), \quad (7)$$

where

$$f^{(1)}(\vartheta) = \frac{1}{k}\sum(2l+1)\delta_l P_l(\cos\vartheta), \quad (8a)$$

$$f^{(2)}(\vartheta) = \frac{i}{k}\sum(2l+1)\delta_l^2 P_l(\cos\vartheta), \quad (8b)$$

$$f^{(3)}(\vartheta) = -\frac{2}{3k}\sum(2l+1)\delta_l^3 P_l(\cos\vartheta). \quad (8c)$$

In the second and the third term in (7), it is sufficient to employ $\delta_l^{(1)}$ in (8), but in the first term it is necessary to employ[4]

$$\delta_l = \delta_l^{(1)} + \delta_l^{(2)}. \quad (9)$$

Instead of summing (8a) with $\delta_l = \delta_l^{(1)} + \delta_l^{(2)}$ and $\delta_l^{(2)}$ given by (4) or a similar expression obtained by the perturbation method, it is found convenient to calculate the first two terms in (7) together, namely,

$$|f^{(1)}(\vartheta)|^2 + |f^{(2)}(\vartheta)|^2 = |f^{(1)}(\vartheta) + f^{(2)}(\vartheta)|^2.$$

Let ψ be the solution of

$$\Delta\psi + \left[k^2 - \frac{M}{\hbar^2}V(r)\right]\psi = 0,$$

and let

$$\psi = \psi_{(0)} + \psi_{(1)} + \psi_{(2)} + \cdots,$$

where $\psi_{(0)}$ is the solution of the equation

$$\Delta\psi + k^2\psi = 0$$

and represents the incident wave. By successive approximation, one obtains

$$[\Delta + k^2]\psi_{(1)} = \frac{M}{\hbar^2}V(r)\psi_{(0)},$$

$$[\Delta + k^2]\psi_{(2)} = \frac{M}{\hbar^2}V(r)\psi_{(1)},$$

and their solutions

$$\psi_{(1)}(\mathbf{r}'') = -\frac{1}{4\pi}\int e^{ik|\mathbf{r}''-\mathbf{r}'|}\frac{1}{|\mathbf{r}''-\mathbf{r}'|}\cdot\frac{M}{\hbar^2} \times V(r')e^{ik\cdot\mathbf{r}'}d\mathbf{r}',$$

$$\psi_{(2)}(\mathbf{r}) = -\frac{1}{4\pi}\int e^{ik|\mathbf{r}-\mathbf{r}''|}\frac{1}{|\mathbf{r}-\mathbf{r}''|}\cdot\frac{M}{\hbar^2} \times V(r'')\psi_{(1)}(\mathbf{r}'')d\mathbf{r}''.$$

From the asymptotic solutions $\psi_{(1)}(r)$, $\psi_{(2)}(r)$ for large r, one obtains the scattered amplitude up

[3] A. Pais, Proc. Camb. Phil. Soc. **42**, 45 (1946).

[4] Strictly, one should have included in (9) the next $\delta_l^{(3)}$ which is cubic in V. Including it, however, makes any calculation too difficult. We shall therefore neglect it by assuming the condition (18) below to be valid.

to the second power of V,

$$f(\vartheta)=f_{(1)}(\vartheta)+f_{(2)}(\vartheta)$$
$$=-\frac{M}{4\pi\hbar^2}\int e^{-i\mathbf{k}'\cdot\mathbf{r}'}V(\mathbf{r}')e^{i\mathbf{k}\cdot\mathbf{r}'}d\mathbf{r}'$$
$$+\left(\frac{M}{4\pi\hbar^2}\right)^2\int\int e^{-i\mathbf{k}'\cdot\mathbf{r}''}V(r'')\frac{e^{ik|\mathbf{r}''-\mathbf{r}'|}}{|\mathbf{r}''-\mathbf{r}'|}$$
$$\times V(r')e^{i\mathbf{k}\cdot\mathbf{r}'}d\mathbf{r}'d\mathbf{r}''. \quad (10)$$

Now it is seen that

$$f_{(1)}(\vartheta)+f_{(2)}(\vartheta)=f^{(1)}(\vartheta)+f^{(2)}(\vartheta). \quad (11)$$

Since $f_{(1)}(\vartheta)$, the first term in (10), is known to be the sum (8a) with δ_l replaced by $\delta_l^{(1)}$, it follows from (11) that the real and the imaginary part of $f_{(2)}(\vartheta)$ in (10) must be, respectively,

real part of

$$f_{(2)}(\vartheta)=\frac{1}{k}\sum(2l+1)\delta_l^{(2)}P_l(\cos\vartheta), \quad (12a)$$

imag. part of

$$f_{(2)}(\vartheta)=\frac{i}{k}\sum(2l+1)(\delta_l^{(1)})^2P_l(\cos\vartheta). \quad (12b)$$

To calculate the last term $f^{(1)}(\vartheta)f^{(3)}(\vartheta)$ in (7), one would have to sum (8c) with δ_l replaced by $\delta_l^{(1)}$. This series cannot be summed in a simple manner as (12b). However, as the δ_0, δ_1, δ_2, $\cdots$ must converge, we may approximate $f^{(3)}(\vartheta)$ by taking the first few terms, say three, in (8c). Up to the approximation desired, the $f^{(1)}(\vartheta)$ in the last term in (7) is given by the usual Born's expression.

To enable $f_{(2)}(\vartheta)$ to be evaluated in analytical form and incidentally to demonstrate the relation (12b), we shall take a Gaussian potential

$$V(r)=V_0\exp(-\alpha^2r^2). \quad (13)$$

The integration in (10) can be effected by a transformation from $\mathbf{r}'$, $\mathbf{r}''$ to $\boldsymbol{\xi}=\mathbf{r}''-\mathbf{r}'$ and $\boldsymbol{\eta}=\mathbf{r}''+\mathbf{r}'$. It can be shown that

$$f_{(2)}(\vartheta)=\frac{(\pi)^{\frac{1}{2}}}{\alpha}\left(\frac{MV_0}{4\alpha^2\hbar^2}\right)^2\left(\frac{k}{\alpha}\cos\frac{\vartheta}{2}\right)^{-1}$$
$$\times\exp\left(-\frac{k^2}{2\alpha^2}\sin^2\frac{\vartheta}{2}\right)$$
$$\times\Big[x\exp(-x^2)\,{}_1F_1(\tfrac{1}{2};\tfrac{3}{2};x^2)$$
$$-y\exp(-y^2)\,{}_1F_1(\tfrac{1}{2};\tfrac{3}{2};y^2)$$
$$+\frac{i(\pi)^{\frac{1}{2}}}{2}(\exp(-y^2)-\exp(-x^2))\Big], \quad (14)$$

where

$$x^2=\frac{2k^2}{\alpha^2}\cos^4\frac{\vartheta}{4}, \quad y^2=\frac{2k^2}{\alpha^2}\sin^4\frac{\vartheta}{4},$$

and ${}_1F_1$ is the usual confluent hypergeometric function which for numerical work can be more conveniently expressed in the form

$$x\,{}_1F_1(\tfrac{1}{2};\tfrac{3}{2};x^2)=\int_0^x\exp(t^2)dt.$$

The relation (12b) in this case can then be proved by means of Weber's second exponential integral, together with the addition theorem of Bessel functions.[5]

For Gaussian potential,

$$f_{(1)}(\vartheta)=\frac{(\pi)^{\frac{1}{2}}}{2^{\frac{1}{2}}}\left(\frac{MV_0}{4\alpha^2\hbar^2}\right)\times\exp\begin{bmatrix}-\frac{k^2}{\alpha^2}\sin^2\frac{\vartheta}{2}\\ -\frac{k^2}{\alpha^2}\cos^2\frac{\vartheta}{2}\end{bmatrix} \quad (15)$$

for ordinary and Majorana exchange force, respectively. For ordinary force, one readily finds

$$2\pi\int_0^\pi 2f^{(1)}(\vartheta)f^{(3)}(\vartheta)\sin\vartheta d\vartheta$$
$$=-\frac{16\pi^{\frac{1}{2}}}{3\alpha^2}\left(\frac{\alpha}{k}\right)^3\left(\frac{MV_0}{4\alpha^2\hbar^2}\right)\Big[\left(\delta_0{}^3-\frac{5}{2}\delta_2{}^3\cdots\right)\left(1-\exp\left(-\frac{k^2}{\alpha^2}\right)\right)$$
$$+3(\delta_1{}^3\cdots)\left\{1-\frac{2\alpha^2}{k^2}+\left(1+\frac{2\alpha^2}{k^2}\right)\exp\left(-\frac{k^2}{\alpha^2}\right)\right\}+\frac{15}{2}(\delta_2{}^3\cdots)$$
$$\times\left\{1-\frac{4\alpha^2}{k^2}+\frac{8\alpha^4}{k^4}-\left(1+\frac{4\alpha^2}{k^2}+\frac{8\alpha^4}{k^4}\right)\exp\left(-\frac{k^2}{\alpha^2}\right)\right\}+\cdots\Big]. \quad (16)$$

[5] G. N. Watson, *Theory of Bessel Functions* (The Macmillan Company, New York, 1944), §§13.31, 11.41.

TABLE I. Phases in proton-neutron and proton-proton scattering. The $\delta_l^{(1)}$ and $\delta_l^{(2)}$ in the table are, for 100 Mev, those given in (22).

	Neutral		Charged		Symmetrical		
	$\delta_l^{(1)}$	$\delta_l^{(2)}$	$\delta_l^{(1)}$	$\delta_l^{(2)}$	$\delta_l^{(1)}$	$\delta_l^{(2)}$	
p-n, triplet	$\delta_l^{(1)}$	$\delta_l^{(2)}$	$(-1)^l\delta_l^{(1)}$	$\delta_l^{(2)}$	$\delta_l^{(1)}$ $-\frac{1}{3}\delta_l^{(1)}$	$\delta_l^{(2)}$ $1/9\delta_l^{(2)}$	for l even for l odd
singlet	$(1-2g)\delta_l^{(1)}$	$(1-2g)^2\delta_l^{(2)}$	$(-1)^l(1-2g)\delta_l^{(1)}$	$(1-2g)^2\delta_l^{(2)}$	$(1-2g)\delta_l^{(1)}$ $-3(1-2g)\delta_l^{(1)}$	$(1-2g)^2\delta_l^{(2)}$ $9(1-2g)^2\delta_l^{(2)}$	for l even for l odd
p-p, triplet odd	$2\delta_l^{(1)}$	$4\delta_l^{(2)}$	$-2\delta_l^{(1)}$	$4\delta_l^{(2)}$	$-\frac{2}{3}\delta_l^{(1)}$	$4/9\delta_l^{(2)}$	
singlet even	$2(1-2g)\delta_l^{(1)}$	$4(1-2g)^2\delta_l^{(2)}$	$2(1-2g)\delta_l^{(1)}$	$4(1-2g)^2\delta_l^{(2)}$	$2(1-2g)\delta_l^{(1)}$	$4(1-2g)^2\delta_l^{(2)}$	

For the case of exchange force, one employs the lower expression in (15) and remembers that the $\delta_l^{(1)}$ with odd l change their sign. Hence

$$|f^{(1)}(\vartheta)f^{(2)}(\vartheta)|_{\text{exchange}} = |f^{(1)}(\pi-\vartheta)f^{(2)}(\pi-\vartheta)|_{\text{ordinary}}, \quad (17)$$

and the contribution to the total cross section from the last term in (7) is again given by (16).

For interaction potentials which are mixtures of the ordinary and exchange force, the $f^{(1)}(\vartheta)$, $f^{(2)}(\vartheta)$, $f^{(3)}(\vartheta)$ can be found in a similar manner, as will be illustrated below in III.

A better approximation than the second can be obtained by substituting (9), namely, $\delta_l=\delta_l^{(1)}+\delta_l^{(2)}$, into (1) so as to include the contribution of all powers of δ_l higher than the fourth. While this procedure again does not form any definite approximation in the sense of the perturbation theory, it may be justified and expected to be very good if

$$\delta_l^{\text{exact}}-(\delta_l^{(1)}+\delta_l^{(2)})\ll(\delta_l^{(1)})^2. \quad (18)$$

To obtain the $\delta_l^{(2)}$, one may either calculate them by the perturbation theory, by (4), by (6), or, in the case of the Gaussian potential, make use of the following procedure which is very much shorter. From (12a) and (14), one has

$$\sum(2l+1)\delta_l^{(2)}P_l(\cos\vartheta) = (\pi)^{\frac{1}{2}}\left(\frac{MV_0}{4\alpha^2\hbar^2}\right)^2\frac{1}{\cos(\vartheta/2)}\exp\left(-\frac{k^2}{2\alpha^2}\sin^2\frac{\vartheta}{2}\right) \times[x\exp(-x^2)\,{}_1F_1(\tfrac{1}{2};\tfrac{3}{2};x^2) - y\exp(-y^2)\,{}_1F_1(\tfrac{1}{2};\tfrac{3}{2};y^2)].$$

By taking n different values of ϑ, one can calculate the first n $\delta_l^{(2)}$'s which are not negligible.

III. PROTON-NEUTRON AND PROTON-PROTON SCATTERING

We shall apply the above result to the problem of proton-neutron and proton-proton scattering at 100 Mev on the basis of the three forms of nucleon interaction suggested by Rarita and Schwinger[6] with Gaussian dependence on r and without tensor force, namely,

"Neutral"

$$V(r)=-[1-g+\tfrac{1}{2}g(1+\sigma_1\cdot\sigma_2)]V_0\exp(-\alpha^2r^2),$$

"Charged" (19)

$$V(r)=\tfrac{1}{2}(1+\tau_1\cdot\tau_2)[1-g+\tfrac{1}{2}g(1+\sigma_1\cdot\sigma_2)]V_0\exp(-\alpha^2r^2),$$

"Symmetrical"

$$V(r)=\tfrac{1}{3}\tau_1\cdot\tau_2[1-g+\tfrac{1}{2}g(1+\sigma_1\cdot\sigma_2)]V_0\exp(-\alpha^2r^2).$$

We have chosen the following constants

$$V_0=45\text{ Mev},\quad (1-2g)V_0=26\text{ Mev},\quad \alpha^2=0.266\times10^{26}\text{ cm}^{-2} \quad (20)$$

to fit the data on the ground state of the deuteron and the proton-proton scattering at low energies.

The scattered amplitudes $f^{(1)}(\vartheta)$, $f^{(2)}(\vartheta)$, $f^{(3)}(\vartheta)$ in the case of the "N" and the "C" theory can be readily obtained as explained in II. For the symmetrical theory, it can be shown that for the triplet state scattering,

$$\begin{aligned} {}^3V(r)&=-\tfrac{1}{3}(1+2P_{12})V_0\exp(-\alpha^2r^2),\\ f_{(1)}{}^t(\vartheta)&=\tfrac{1}{3}[f_{(1)}(\vartheta)+2f_{(1)}(\pi-\vartheta)],\\ f_{(2)}{}^t(\vartheta)&=\tfrac{1}{9}[5f_{(2)}(\vartheta)+4f_{(2)}(\pi-\vartheta)], \end{aligned} \quad (21a)$$

[6] W. Rarita and J. Schwinger, Phys. Rev. 59, 557 (1941).

and for the singlet state scattering,

$$^1V(r) = -(1-2g)(-1+2P_{12})V_0 \exp(-\alpha^2 r^2),$$
$$f_{(1)}{}^s(\vartheta) = (1-2g)[-f_{(1)}(\vartheta)+2f_{(1)}(\pi-\vartheta)], \quad (21b)$$
$$f_{(2)}{}^s(\vartheta) = (1-2g)^2[5f_{(2)}(\vartheta)-4f_{(2)}(\pi-\vartheta)],$$

where $f_{(2)}(\vartheta)$ is given by (14), and $f_{(1)}(\vartheta)$, $f_{(1)}(\pi-\vartheta)$ are given by the upper and lower expression in (15), respectively. For $f^{(3)}(\vartheta)$, the appropriate phases δ_l are given in Table I.

For the potential (13) with constants as given in (20), we obtain[7]

TABLE II. Differential cross section $2\pi I(\vartheta)$ in 10^{-25} cm² of proton-neutron scattering at 100 Mev.

	Neutral		Charged		Symmetrical	
ϑ	1st Born	2nd Born	1st Born	2nd Born	1st Born	2nd Born
0	6.41	6.45	0.00064	1.066	1.280	1.234
15	5.46	5.51	0.00071	1.035	1.085	1.072
30	3.46	3.41	0.0012	0.849	0.692	0.759
45	1.61	1.58	0.0024	0.614	0.303	0.438
60	0.641	0.530	0.0061	0.388	0.135	0.263
90	0.064	0.052	0.064	0.054	0.062	0.057
120	0.0061	0.018	0.641	0.020	0.51	0.117
135	0.0024	0.0140	1.61	0.51	1.28	0.515
150	0.0012	0.0137	3.46	1.66	2.78	1.40
165	0.00077	0.0094	5.46	3.28	4.38	2.53
180	0.00064	0.0044	6.41	4.12	5.12	3.27

TABLE III. Total cross section in 10^{-25} cm² of proton-neutron scattering at 100 Mev.

	Neutral	Charged	Symmetrical		
	Gaussian	Gaussian	Gauss.	Yukawa	Rect. hole
1st Born	1.40	1.40	1.40	1.39	1.40
Using $\delta_l^{(1)}$ in (7)	1.33	1.25	1.15		
Using $\delta_l^{(1)}$ in (1)	1.22	1.22	1.14		1.20
2nd Born	1.34	1.02	0.83		
Using $\delta_l^{(1)}+\delta_l^{(2)}$ in (1)	1.35	1.07	0.966	(exact)	0.94

TABLE IV. Twice the total cross section in 10^{-25} cm² of proton-proton scattering at 100 Mev.

	Neutral	Charged	Symmetrical		
	Gaussian	Gaussian	Gauss.	Yukawa	Rect. hole
1st Born	2.69	2.69	0.56	0.57	0.56
Using $\delta_l^{(1)}$ in (1)	1.83	1.83	0.47		
2nd Born	3.08	0.72	0.41		
Using $\delta_l^{(1)}+\delta_l^{(2)}$ in (1)	2.39	1.24	0.43		

[7] It is of interest to compare the phases (22) with those calculated by the method of Pais. They are as follows: from (5), $\delta_1=0.534$, $\delta_2=0.221$; from (6), $\delta_1^{(2)}=0.063$, $\delta_2^{(2)}=0.026$. For $l=0$, Pais' method is not valid, but calculation with (6) gives $\delta_0^{(2)}=-0.28$, with the sign correct.

l	0	1	2	3	4
$\delta_l^{(1)}$	0.833	0.487	0.197	0.0605	0.0127
$\delta_l^{(2)}$	−0.0793	0.068	0.0325	0.00477	0.00211.

(22)

Remembering that to the approximation (3), the $\delta_l^{(1)}$ are linear and the $\delta_l^{(2)}$ quadratic in $V(r)$, one readily obtains the phases for the triplet and singlet state scatterings for the three potentials in (19), as shown in Table I.

The result of the calculation is given in Tables II, III, and IV. Table II gives the differential cross section $2\pi I(\vartheta)$ in the first and the second Born approximation. An important feature of the second approximation is the appearance of a maximum in the forward direction in the case of the exchange force, recently noted by Ashkin and Wu.[1]

Table III gives the total proton-neutron cross section obtained in the first Born approximation, by using $\delta_l^{(1)}$ in (7), and in (1), in the Second Born approximation, and by using $\delta_l^{(1)}+\delta_l^{(2)}$ in (1). Table IV gives the corresponding values for proton-proton scattering.

As the exact values of the cross sections cannot be obtained without lengthy numerical integration of the wave equation, it is not possible to make a comparison between these approximate and the exact σ's. From the values of the $\delta_l^{(1)}$ and $\delta_l^{(2)}$ in (22), one may perhaps expect the $\delta_l^{(3)}$ to be small so that (18) is satisfied. If this is the case, the value obtained by using $\delta_l^{(1)}+\delta_l^{(2)}$ in (1) should be rather close to the exact values. One can then see the improvement achieved by the Second Born approximation.

The above calculation cannot be carried out so simply for potentials other than the Gaussian one. It seems, however, that with other forms of $V(r)$ one may still estimate the correction to the first Born approximation by replacing the field $V(r)$ by an appropriate Gaussian one. The angular distribution of the scattered intensity certainly depends on the shape of the potential $V(r)$; but it seems that the total cross section is, for a given proportion of ordinary and exchange force, rather insensitive to the exact form of $V(r)$. To illustrate this, we have calculated the cross sections for the potential on the Møller-Rosenfeld meson theory, with constants deter-

mined by the variational method,[8] namely,

$$
\begin{aligned}
{}^3V^{\text{even}} &= -3(A+B)V_0\frac{e^{-\lambda r}}{r},\\
{}^3V^{\text{odd}} &= (A+B)V_0\frac{e^{-\lambda r}}{r},\\
{}^1V^{\text{even}} &= (A-B)V_0\frac{e^{-\lambda r}}{r},\\
{}^1V^{\text{odd}} &= -3(A-B)V_0\frac{e^{-\lambda r}}{r},
\end{aligned}
\tag{23}
$$

where

$$
\begin{aligned}
&A=-1.303, \qquad B=4.606,\\
&V=0.977\times10^{-13}, \quad \lambda=5.655\times10^{12}.
\end{aligned}
$$

We have also calculated the cross sections on the symmetrical theory in (19), replacing the Gaussian potential by a rectanglar hole with the following constants

$$
\begin{aligned}
&\text{range } \rho=2.80\times10^{-13}\text{ cm}, \quad V_0=21\text{ Mev},\\
&\qquad (1-2g)V_0=11.7\text{ Mev}.
\end{aligned}
\tag{24}
$$

For this potential we have also calculated the exact σ for proton-neutron scattering. The result is given in Tables III and IV. A comparison of the values obtained for the Yukawa potential in (23) and the rectangular hole potential (24) with those obtained for the Gaussian potential leads one to think that a higher approximation for these potentials probably gives approximately the same values as for the Gaussian potential.

In view of the strong dependence of the total cross section on the proportion of ordinary and exchange force and comparatively weak dependence on the exact form of the radial $V(r)$, it seems of significance to compare the total cross section calculated with Gaussian potential for various mixtures of ordinary and exchange force with the experimental values. Recently Cook *et al.*[9] reported the following total cross sections for 90 Mev:

$$
\begin{aligned}
\sigma_{p-n}&=0.83\times10^{-25}\text{ cm}^2,\\
\sigma_{p-d}&=1.17\times10^{-25}\text{ cm}^2.
\end{aligned}
\tag{25}
$$

It is seen that the calculated σ_{p-n} on the symmetrical theory agrees better with the observed value than the other two theories. On regarding the proton-deuteron cross section as approximately the sum of the proton-neutron and proton-proton cross sections,[10] one finds for the ratio $\sigma_{p-n}/\sigma_{p-d}$ the values 0.36, 0.51, 0.69 for the neutral, charged, and the symmetrical theory, respectively, as compared with the observed value 1.17.

This agreement, however, does not establish the symmetrical theory in the form (19). The great difference between the observed value for the ratio $\sigma(\pi)/\sigma(\pi/2)\simeq3$ for proton-neutron and the calculated value shown in Table I seems to indicate the presence of tensor force, whose effect is to increase the scattered intensity in directions $\vartheta\simeq\pi/2$ (in the center of mass system).[1] But an exact calculation on the symmetrical theory, including tensor force, still leads to a much larger value for the ratio than the observed one.[1] It seems that both the range of the force and the proportion of central and tensor forces have to be readjusted in order to agree with the meagre data now available at 90 Mev.

The writer wishes to express his indebtedness to Professor G. E. Uhlenbeck for helpful discussions.

[8] Frohlich, Huang, and Snedden, Proc. Roy. Soc. A191, 61 (1947).

[9] Cook, McMillan, Peterson, and Sewell, Phys. Rev. 72, 1264 (1947).

[10] T. Y. Wu and J. Ashkin, Phys. Rev. 73, 986 (1948).

Nuclear Properties of 93^{237} *

ARTHUR C. WAHL** AND GLENN T. SEABORG
Department of Chemistry and Radiation Laboratory, University of California, Berkeley, California

(Received January 19, 1948)

The isotope Np^{237}, produced as the decay product of the previously known 6.8-day U^{237}, has been isolated with carrier material and some of its nuclear properties measured. The U^{237} was formed by means of the reaction $U^{238}(n, 2n)U^{237}$. Np^{237} decays with the emission of alpha-particles with a half-life of about 3×10^6 years. It has been shown that the upper limit for the cross section for the fission of Np^{237} with slow neutrons is less than 1 percent of that of U^{235}.

THE bombardment of uranium with fast neutrons produces[1,2] the beta-emitting 6.8-day U^{237}, formed in the reaction $U^{238}(n,2n)U^{237}$. We have investigated 93^{237}, the daughter of U^{237}, the primary purpose of our investigation being to measure the fission properties of this isotope. Our measurements, performed upon a sample weighing about 0.6 microgram, show that 93^{237} does not undergo appreciable fission with slow neutrons. The experiments also show that 93^{237} is an alpha-emitting isotope with a half-life of about 3×10^6 years.

For the preparation of the sample of 93^{237} about 1200 grams of uranyl nitrate hexahydrate, $UO_2(NO_3)_2\cdot6H_2O$, were placed directly behind the beryllium target of the 60-inch Berkeley cyclotron and exposed to the fast neutrons produced in a 15,000-microampere hour bombardment of the beryllium with deuterons. After the lapse of several months, so that substantially all of the U^{237} had decayed to 93^{237}, a chemical separation was performed on this bombarded uranyl nitrate in order to isolate the 93^{237} into a thin rare earth fluoride precipitate (approximately 0.3 mg/cm^2), special care being exercised to remove all of the 94, uranium, protactinium, and thorium. This procedure has been described in principle in another report.[3]

The chemical procedure, in outline, is as follows. The uranyl nitrate hexahydrate is subjected to an ether extraction process in order to remove the bulk of the uranium, and rare earth fluoride is precipitated from the water phase. This rare earth fluoride contains the 94, 93, and thorium, the uranium and the protactinium (when zirconium carrier is present) remaining in solution. This rare earth fluoride is dissolved in sulfuric acid, and from a cold potassium bromate ($KBrO_3$) solution the rare earth fluoride is again precipitated. In this step the 94, in its reduced form, and the thorium and the rare earth fission products are precipitated as insoluble fluorides, and the 93 remains in solution in its oxidized form. After reduction with sulfur dioxide, the 93 in the solution is precipitated with a small amount of rare earth fluoride. Of course, it is necessary that a number of cycles be performed in order to remove completely from the final sample the 94, uranium, protactinium, and thorium, and in our procedure there were three separations from 94, six separations from uranium, five separations from protactinium, and five separations from thorium. The last 94-containing rare earth precipitate was mounted for alpha-counting and was found to contain practically no 94 (<30 counts per minute) while the final sample containing the 93^{237} had a counting rate of about 300 alphas per minute. In order to keep track of the yield of 93 through this rather lengthy chemical procedure there was added at the beginning some 2.3-day 93^{239} as tracer for the 93, and it was found that the yield of 93 in the final sample amounted to about 50 percent of that originally added to the bombarded uranium nitrate.

In order to prove that in this chemical pro-

* This article was mailed, as a secret report, from Berkeley, California to the Uranium Committee in Washington, D. C. on April 14, 1942. The experimental work was done during 1941 and the early part of 1942. The original article is published here essentially without change. The abstract was written at the time of publication since the original report contained no summary.

** Now at Department of Chemistry, Washington University, St. Louis, Missouri.

[1] E. M. McMillan, Phys. Rev. 58, 178 (1940).

[2] Y. Nishina, T. Yasaki, H. Ezoe, K. Kimura, and M. Ikawa, Phys. Rev. 57, 1182 (1940).

[3] G. T. Seaborg and A. C. Wahl, J. Am. Chem. Soc. (March, 1948).

cedure no uranium, protactinium, or thorium remained in the final sample, a chemical separation, of a similar type, was performed on non-irradiated uranyl nitrate using U^{233} as tracer for uranium, Pa^{233} as tracer for protactinium, and UX_1 as tracer for thorium. This "blank experiment" proved that in our chemical procedure there remains in the final sample much less than a microgram of each of these elements.

In order to know how much 93^{237} was formed in the bombardment described above, it was necessary, of course, to determine the yield of U^{237} in the bombardment of uranyl nitrate hexahydrate under similar conditions. A sample of 700 grams of $UO_2(NO_3)_2 \cdot 6H_2O$ was placed directly behind the beryllium target and subjected to a 500-microampere hour bombardment. This sample was carefully purified from all of the fission products and from element 93 by the ether extraction method; the ether phase, containing the bulk of the uranyl nitrate and the U^{237}, was washed 8 or 10 times with water in order to insure a very thorough purification. Aliquot amounts, determined by weighing the uranyl nitrate containing the 6.8-day U^{237}, were taken from the ether phase and the intensity of the activities was measured with a Lauritsen quartz fiber electroscope calibrated in an absolute manner for the radiation from the 6.8-day U^{237}. This calibration was accomplished by preparing thin electrolytically deposited aliquots of the uranium and counting the beta-particles from the 6.8-day U^{237} with a thin-window Geiger-Müller counter of calibrated efficiency; the weight of uranium in these small aliquots was determined by counting its natural alpha-particles with an ionization chamber of calibrated efficiency. (Correction for the self-absorption in the samples and absorption in the Geiger-Müller counter window of the 6.8-day U^{237} beta-particles was made by using the value for the half thickness of the absorption of these beta-particles, which we have determined as 6 mg Al/cm^2.) From the measurements on the calibrated Lauritsen electroscope of the chemically purified aliquots from the 500-microampere hour bombardment, we found that the yield of 6.8-day U^{237} was 0.0054 microcurie per gram of

$$UO_2(NO_3)_2 \cdot 6H_2O$$

per microampere hour of deuterons on beryllium.

From this yield it follows that there was formed in the 15,000-microampere hour bombardment of 1200 grams of $UO_2(NO_3)_2 \cdot 6H_2O$ about 97 millicuries of U^{237}, which corresponds to about 1.2 microgram. Since substantially all of this decayed to 93^{237} before the chemical separation was performed and since the yield in the chemical procedure for the isolation of 93 was about 50 percent, as mentioned above, this means that there was present in our final sample about 0.6 microgram of 93^{237}. We consider this estimate of the amount to be accurate to within a factor of about 2. The alpha-counting rate of this sample, as mentioned above, was about 300 counts per minute, and, from this value, together with the calibrated efficiency (45 percent) of the ionization chamber, it is calculated that the half-life of alpha-emitting 93^{237} is about 3×10^6 years.

This sample was placed on one electrode of an ionization chamber connected to a linear amplifier and recording system which was adjusted so as to record the pulses due to fissions. As a neutron source we used 300 milligrams of radium mixed with beryllium powder. The ionization chamber and the 300-mg radium-beryllium neutron source were completely surrounded by paraffin. Under these conditions the 0.6 microgram 93^{237} sample gave four fission counts in about 56 hours of counting time. When the ionization chamber was surrounded by cadmium, there were recorded two counts in 56 hours of counting time. Thus, the counting rate due to slow neutrons was two counts in 56 hours or 0.035 fission counts per hour. For a calibration experiment the 0.6-microgram sample of 93^{237} was replaced by 200 micrograms of electrolytically deposited uranium, whose weight was determined by counting its alpha-particles with an ionization chamber of calibrated efficiency. The easily measurable fission rate of this uranium sample, containing 1.4 micrograms of U^{235}, when compared to that for 93^{237} showed that the slow neutron fission cross section of 93^{237} is less than one percent[4] of that for U^{235}.

[4] Note added at time of publication. More recent work by A. Ghiorso, D. W. Osborne, and L. B. Magnusson has demonstrated that Np^{237} undergoes slow neutron fission with a cross section a few thousandths of a percent of that of U^{235}. (Science **104**, 386 (1946).)

Shapes of Nuclear Induction Signals*

BORIS A. JACOBSOHN AND ROALD K. WANGSNESS
Stanford University, Stanford, California

(Received January 19, 1948)

The various shapes of nuclear induction signals are discussed for small values of the r-f field. In the case of a linear variation with time of the strong magnetic field, numerical results are given for various values of the sweep rate and the total relaxation time.

1. INTRODUCTION

THE equations of motion of the total nuclear magnetic moment in the nuclear induction experiment have been given by Bloch.[1] He discusses the solution for the adiabatic case, i.e., when the rate of change of the strong magnetic field is sufficiently small. However, for rapid variations of the strong field, oscillations are experimentally observed in the tails of the curves. These were first explained by Purcell,[2] who pointed out that when the magnetic moment does not have time to follow the adiabatic solution through resonance, the moment will be found pointing in a non-equilibrium direction when the strong field is so far beyond resonance that the effect of the rotating field can be neglected. From this point on the moment will precess about the direction of the strong field, with a damping determined by the relaxation time and with the instantaneous Larmor frequency. The beats between this varying frequency and that of the r-f field will appear as damped oscillations on an oscilloscope screen. In the course of our detailed discussion of these oscillations it will be shown that in certain cases they can be used for a relatively accurate determination of the total relaxation time.

We shall consider the case where the r-f field is weak enough to be treated as a small perturbation. The equations can then be solved for arbitrary dependence of the sweep field on the time. The use of a weak r-f field can be of advantage, since it enables one to obtain the sharpest possible lines. A detailed analysis of the signal shape for this case is of considerable importance since, as long as there remain essential features in the line shape which are unexplained,[3] a resonance value can hardly be known with a limit of error less than the line width.

2. SYMMETRY PROPERTIES OF THE EQUATIONS

The equations of motion of the magnetic moment of a collection of nuclei in a homogeneous magnetic field $H_0(t)$ in the z direction, acted upon by a rotating magnetic field of amplitude H_1 and angular frequency ω, are:[1]

$$(du/dt)+(u/T_2)+(\Delta\omega)v=0, \tag{1a}$$

$$(dv/dt)+(v/T_2)-(\Delta\omega)u=-|\gamma|H_1M_z, \tag{1b}$$

$$(dM_z/dt)+(M_z/T_1)-|\gamma|H_1v=M_0/T_1. \tag{1c}$$

u and v are components of the magnetic moment in- and out-of-phase, respectively, with the rotating field H_1; $|\gamma|$ is the absolute value of the gyromagnetic ratio; $\Delta\omega=|\gamma|H_0(t)-\omega$; and $M_0=\chi H_0$ is the equilibrium polarization. In practice, the percentage variation in H_0 is very small, and M_0 will be treated as a constant. Finally, T_1 is the longitudinal relaxation time which governs the approach to thermal equilibrium, and T_2 is the "transverse relaxation time" which contributes only to the broadening of the resonance line.

Equations (1) possess a symmetry property of considerable practical interest. Suppose that $\Delta\omega(t)$ is a periodic function of the time with period τ, and further that $\Delta\omega(t+\tau/2)=-\Delta\omega(t)$ for all times t. Then, if $u(t)$, $v(t)$ and $M_z(t)$ are a solution of Eqs. (1), the functions $-u(t+\tau/2)$, $v(t+\tau/2)$, and $M_z(t+\tau/2)$ are likewise solutions. This can be seen from direct substitution into the equations provided that the very small variation in M_0 is neglected. The most general

* Work supported by grants from the Office of Naval Research.

[1] F. Bloch, Phys. Rev. **70**, 460 (1946).

[2] To be published soon; previous verbal communication to Professor Bloch.

[3] A. Roberts, Phys. Rev. **72**, 979 (1947).

solutions of (1) consist of a superposition of a damped homogeneous solution and an inhomogeneous solution. It will be only the latter which is left after initial transients have damped out and it must, therefore, possess the above property of even periodicity in a half-cycle $\tau/2$ for v and M_z, and "odd" periodicity for u. Seen on the screen of an oscilloscope, the horizontal sweep of which has the same periodicity as $\Delta\omega$, the v traces will thus appear symmetrical about the resonance point at the center of the screen while the u trace will be antisymmetrical, once stationary conditions have established themselves. Either phase can, of course, be observed by proper phase adjustment in the receiver circuit.

This property, since it is independent of the magnitudes of H_1, T_1, T_2 or the rate of sweep, is quite useful in practice. For example, one may wish to compare the resonance frequencies of two different nuclei simultaneously in the same magnetic field.[4] It is not always practicable to adjust the parameters so that simple line shapes are seen. A sinusoidal sweep, however, has the property that $\Delta\omega(t+\tau/2)=-\Delta\omega(t)$, provided that one sweeps equally on either side of resonance. If one, therefore, uses the v mode and adjusts the r-f frequencies so that the two sets of traces are completely symmetrical about a common symmetry point, one has a very sensitive method of ascertaining that the two resonances occur at the same value of H_0. In this way, the proton-deuteron magnetic moment ratio has been determined[5,6] with a precision much better than that given by the line widths.

3. SOLUTION OF THE EQUATIONS

Equations (1a) and (1b) can be rewritten in terms of a complex function $F=v+iu$ as follows:

$$(dF/dt)+[(1/T_2)+i\Delta\omega(t)]F=-|\gamma|H_1M_z, \quad (2)$$

which has the solution

$$F=-|\gamma|H_1\int_{-\infty}^{t}dt'M_z(t')\times\exp\left[-(t-t'/T_2)-i\int_{t'}^{t}[\Delta\omega(t'')dt''\right]. \quad (3)$$

In our case, H_1 is small enough so that the effect of the rotating field can be treated as a small perturbation. We see from (3) and (1c) that, to terms proportional to $(H_1)^2$, one can take for M_z the approximately constant value M_0, so that in this approximation

$$v+iu=-|\gamma|H_1M_0\int_{-\infty}^{t}dt'\times\exp\left[-(t-t'/T_2)-i\int_{t'}^{t}\Delta\omega(t'')dt''\right]. \quad (4)$$

Experimental conditions for which this approximate solution is valid can be obtained by decreasing the r-f power until the shape of the signal remains unchanged and its magnitude varies proportional to H_1.

It is interesting to see that the solution (4) can be found from a slightly different viewpoint. Following Bloch,[1] one can think of the transverse relaxation time effects as due to an effective inhomogeneity in H_z. If $N(H')dH'$ is the fraction of nuclei for which H_z lies between $H_0(t)+H'$ and $H_0(t)+H'+dH'$, and also, if $u(t,H')dH'$, for example, is the in-phase component of the total moment of such nuclei, then Eqs. (1) can be replaced by

$$\frac{du(H')}{dt}+\frac{u(H')}{T_1}+(\Delta\omega+|\gamma|H')v(H')=0, \quad (5a)$$

$$\frac{dv(H')}{dt}+\frac{v(H')}{T_1}-(\Delta\omega+|\gamma|H')u(H')=-|\gamma|H_1M_z(H'), \quad (5b)$$

$$\frac{dM_z(H')}{dt}+\frac{M_z(H')}{T_1}-|\gamma|H_1v(H')=(M_0/T_1)N(H'). \quad (5c)$$

Rewriting (5a) and (5b) in a form corresponding to (3), we find for the total v and u

$$v+iu=\int_{H'}[v(H')+iu(H')]dH'=-|\gamma|H_1\int_{-\infty}^{t}dt'\exp\left[-\frac{t-t'}{T_1}-i\int_{t'}^{t}\Delta\omega(t'')dt''\right]\int_{H'}M_z(t',H')\times\exp[-i(t-t')|\gamma|H']dH'.$$

[4] F. Bloch, A. C. Graves, M. Packard, and R. W. Spence, Phys. Rev. 71, 551 (1947).
[5] F. Bloch, E. C. Levinthal, and M. E. Packard, Phys. Rev. 72, 1125 (1947).
[6] F. Bitter, Alpert, Nagle, and Poss, Phys. Rev. 72, 1271 (1947).

For strong r-f fields the above expression is not equivalent to (3) for any plausible choice of $N(H')$, and Eqs. (1) are not, in general, mathematically equivalent to an effective inhomogeneity in H_s. However, for very small H_1 we have $M_s(H')\cong M_0N(H')$. If one assumes a broadening of the simple form

$$N(H')dH'=1/\pi[\Gamma dH'/(H')^2+\Gamma^2],$$

one again obtains Eq. (4) with neglect of terms proportional to $(H_1)^3$; T_2 is now given by $1/T_2=(1/T_1)+|\gamma|\Gamma$.

4. ASYMPTOTIC BEHAVIOR

The general characteristics of the solution far from resonance can be seen immediately by performing an integration by parts on (4) which yields

$$v+iu=-\frac{|\gamma|H_1T_2M_0(1-i\Delta\omega T_2)}{1+(\Delta\omega T_2)^2}-i|\gamma|H_1M_0$$
$$\times\exp\left[-\frac{t}{T_2}-i\int_b^t\Delta\omega''dt''\right]\int_{-\infty}^t dt'$$
$$\exp\left[\frac{t'}{T_2}+i\int_b^{t'}\Delta\omega''dt''\right]\frac{d\Delta\omega'/dt'}{[(1/T_2)+i\Delta\omega']^2}. \quad (6)$$

If two times τ_1 and τ_2 exist, so that

$$\frac{d\Delta\omega'/dt'}{(1/T_2)^2+(\Delta\omega')^2}\ll 1 \quad (7)$$

for $\tau_1<t'<\tau_2$, then the integral in (6) is roughly constant for times t between τ_1 and τ_2, and

$$v(t)+iu(t)\approx-\frac{|\gamma|H_1T_2M_0(1-i\Delta\omega T_2)}{1+(\Delta\omega T_2)^2}$$
$$-B\exp\left[-\frac{t}{T_2}-i\int_b^t\Delta\omega''dt''\right],$$
$$\tau_1<t<\tau_2; \quad (8)$$

$$B=i|\gamma|H_1M_0\int_{-\infty}^{\tau_1}dt'$$
$$\times\exp\left[\frac{t'}{T_2}+i\int_b^{t'}\Delta\omega''dt''\right]\frac{d\Delta\omega'/dt'}{[(1/T_2)+i\Delta\omega']^2}.$$

The first term of this solution represents the familiar contribution obtained from slow passage, and is seen to depend only on the instantaneous value of $\Delta\omega(t)$. Upon this contribution is superimposed a damped free oscillation which is excited by the passage through resonance. The amplitude and phase of this oscillation will of course depend on the explicit time dependence of $\Delta\omega$. In the case that T_2 is shorter than about $\frac{1}{4}$ cycle of the sweep, the oscillations will have been damped out before $\Delta\omega(t)$ becomes so small that (7) is no longer valid, and the signals will be seen to have oscillations immediately after resonance and none before resonance. The occurrence of the damping factor in (8) provides a method for measuring T_2 in favorable cases.

In the limiting case where $(d\Delta\omega/dt)(T_2)^2$ is at all times negligible one has the situation of slow passage without the excitation of transient oscillations.

5. LINEAR SWEEP

In practice, the strong magnetic field may be swept sinusoidally back and forth about resonance. If the total relaxation time T_2 is less than about one-tenth of the sweep period, the periodicity and the variation of $d\Delta\omega/dt$ can be neglected, and the sweep can be approximated by a linear function of the time.

We shall let $\Delta\omega=at$ where

$$a=|\gamma|(dH_0/dt)_{\text{resonance}}$$

and consider only positive values of a; for a negative, the only change is in the sign of u. If we introduce the dimensionless quantities

$$x=a^{\frac{1}{2}}t, \quad A=1/(a^{\frac{1}{2}}T_2), \quad (9)$$

and express all components of the magnetic moment in units of M_0, (4) becomes

$$v+iu=-(|\gamma|H_1/a^{\frac{1}{2}})\exp[-Ax-i(x^2/2)]$$
$$\times\int_{-\infty}^x\exp[Ax'+i(x'^2/2)]dx'$$
$$=-(|\gamma|H_1/a^{\frac{1}{2}})2^{\frac{1}{2}}\exp[-i\pi/4-z_0^2]$$
$$\times\int_{(\infty)\exp[-3\pi i/4]}^{z_0}\exp[z^2]dz; \quad (10)$$

$$z_0=(1/2^{\frac{1}{2}})(xe^{i\pi/4}+Ae^{-i\pi/4}). \quad (11)$$

Thus, the solution is expressed in terms of the error function of complex argument.

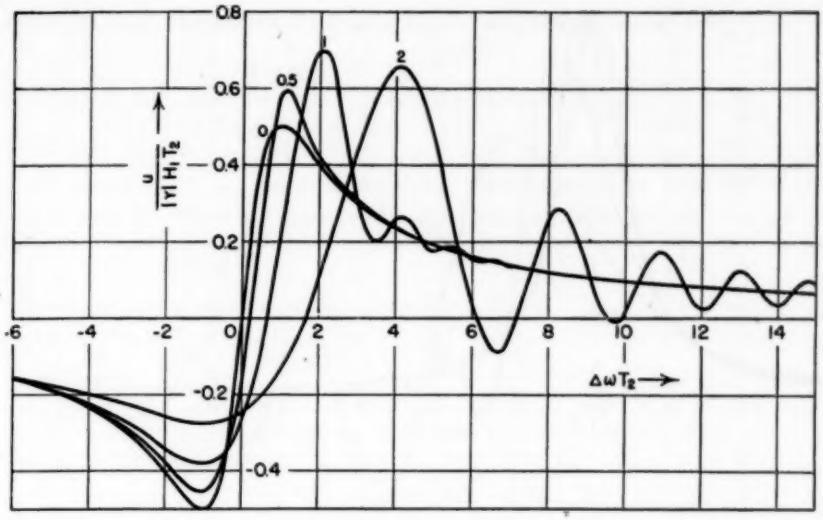

FIG. 1. In-phase resonance shapes (small r-f field and linear sweep) for various values of $a^{\frac{1}{2}}T_2$ given by the numbers near the first maximum. u = in-phase component; T_2 = total relaxation time; $\Delta\omega = at$ = deviation from resonance angular frequency; H_1 = amplitude of rotating r-f field; and $|\gamma|$ = absolute value of gyromagnetic ratio.

For $A=0(T_2=\infty)$, v and u can be expressed in terms of the Fresnel integrals.[7] Values at the points $x=\pm A$ and 0 can likewise be expressed in terms of tabulated functions:

$$u(-A)=v(-A)=-(|\gamma|H_1/a^{\frac{1}{2}})(\pi^{\frac{1}{2}}/2)\times[\exp A^2][1-\mathrm{erf}(A)];\quad (du/dx)_{-A}=0. \quad (12)$$

$$\left.\begin{matrix}u(0)\\v(0)\end{matrix}\right\}=-(|\gamma|H_1/a^{\frac{1}{2}})\times\pi^{\frac{1}{2}}\left[\left\{\begin{matrix}\cos(A^2/2)\\-\sin(A^2/2)\end{matrix}\right\}(\tfrac{1}{2}-C(A^2/2))+\left\{\begin{matrix}\sin(A^2/2)\\\cos(A^2/2)\end{matrix}\right\}(\tfrac{1}{2}-S(A^2/2))\right]. \quad (13)$$

$$\left.\begin{matrix}u(A)\\v(A)\end{matrix}\right\}=-(|\gamma|H_1/a^{\frac{1}{2}})\times[\exp -A^2]\left[(\pi^{\frac{1}{2}}/2)\mp\int_0^A \exp z^2 dz\right]. \quad (14)$$

C and S are the Fresnel integrals.[8]

By performing successive integrations by parts on (10), one finds the following asymptotic expressions, valid when $A^2+x^2\gg 1$:

$$u=\left\{\begin{matrix}1\\0\end{matrix}\right\}\frac{|\gamma|H_1}{a^{\frac{1}{2}}}(2\pi)^{\frac{1}{2}}\exp[-t/T_2]\times\sin\left(\frac{x^2-A^2}{2}-\frac{\pi}{4}\right)+\frac{|\gamma|H_1T_2(\Delta\omega T_2)}{1+(\Delta\omega T_2)^2}+\frac{|\gamma|H_1}{a^{\frac{1}{2}}}\left\{\frac{\sin 3\theta}{(A^2+x^2)^{\frac{1}{2}}}-\cdots\right\},$$

$$v=\left\{\begin{matrix}1\\0\end{matrix}\right\}\frac{|\gamma|H_1}{a^{\frac{1}{2}}}(2\pi)^{\frac{1}{2}}\exp[-t/T_2]\times\cos\left(\frac{x^2-A^2}{2}-\frac{\pi}{4}\right)-\frac{|\gamma|H_1T_2}{1+(\Delta\omega T_2)^2}+\frac{|\gamma|H_1}{a^{\frac{1}{2}}}\left\{\frac{\cos 3\theta}{(A^2+x^2)^{\frac{1}{2}}}+\cdots\right\},\quad 0\leqslant\theta=\arctan(A/x)\leqslant\pi. \quad (15)$$

TABLE I. In-phase component u.

$a^{\frac{1}{2}}T_2$	First maximum $x=\Delta\omega/a^{\frac{1}{2}}$	First maximum $(a^{\frac{1}{2}}/\|\gamma\|H_1)u$	First minimum x	First minimum $(a^{\frac{1}{2}}/\|\gamma\|H_1)u$
0.5	2.32	0.296	...	...
1.0	2.06	0.697	3.45	0.202
2.0	2.08	1.303	3.35	−0.178
∞	2.14	2.93	3.32	−2.22

TABLE II. Out-of-phase component v.

$a^{\frac{1}{2}}T_2$	First maximum $x=\Delta\omega/a^{\frac{1}{2}}$	First maximum $-(a^{\frac{1}{2}}/\|\gamma\|H_1)v$	First minimum x	First minimum $-(a^{\frac{1}{2}}/\|\gamma\|H_1)v$
0.5	0.60	0.49	...	...
1.0	1.00	0.866	2.92	−0.058
2.0	1.09	1.323	2.78	−0.590
∞	1.32	2.33	2.80	−2.54

[7] F. Bitter *et al.*, M.I.T. Research Laboratory of Electronics, Quarterly Progress Report, July 15, 1947, p. 26.
[8] Jahnke and Emde, *Tables of Functions* (Dover Publications, New York, 1945), pp. 35–36.

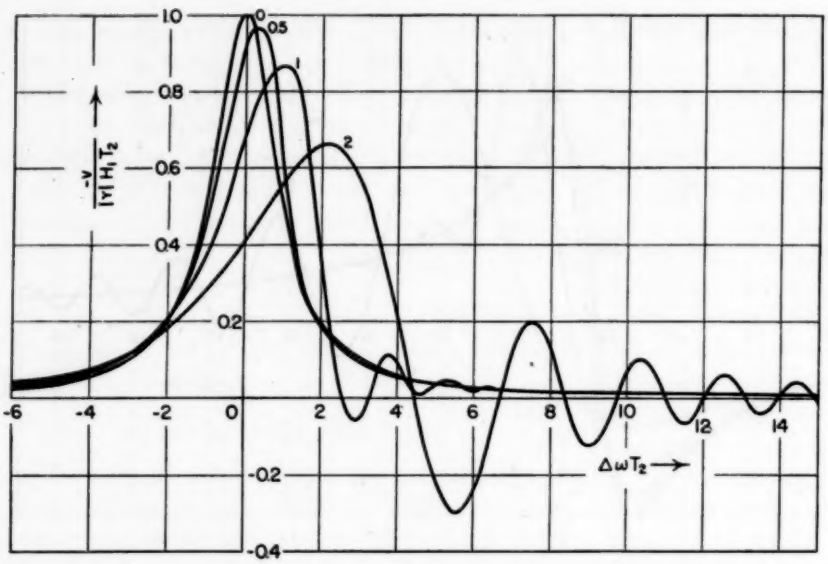

FIG. 2. Out-of-phase resonance shapes (small r-f field and linear sweep) for various values of $a^{\frac{1}{2}}T_2$ given by the numbers near the first maximum. v=out-of-phase component. Other symbols same as for Fig. 1.

The coefficient of the damped oscillation is 1 for $x>A$, while the term is absent for $x<A$. At $x=A$, the discontinuity in Eq. (15) is of the same order as the error in the semiconvergent sums.

Equations (12) through (15) are sufficient to cover most of the range of values of x, except for the first maximum and minimum beyond resonance. In these cases, the integrals (10) were found by following an integration path through the origin and making an angle of $+45°$ with the real axis (Fresnel integrals), and then from an appropriate point integrating numerically along a $-45°$ angle path to the point z_0.

6. RESULTS

The curves for u and $-v$ for various values of $a^{\frac{1}{2}}T_2$ are shown in Figs. 1 and 2, plotted against $\Delta\omega T_2=x/A$. The free oscillations are completely damped out for $a^{\frac{1}{2}}T_2\leqslant\frac{1}{2}$.

For $a^{\frac{1}{2}}T_2\sim1$, the ratio of the first maximum of u and $-v$ to the first minimum serves as a fairly sensitive measurement of the total relaxation time. These values are given in Tables I and II.

For values of $a^{\frac{1}{2}}T_2\geqslant\sim2$, the free oscillations about the slow passage tail appear far enough out so that the total relaxation time can be measured from their damping rate.

The curves shown in Figs. 1 and 2 were in existence when measurements on the proton-deuteron magnetic moment ratio were made at Stanford.[5] It was realized that, because of their smaller gyromagnetic ratio, the relaxation time due to the presence of paramagnetic ions had to be appreciably longer for the deuterons than for the protons in the same sample. The agreement between the aspect of the theoretical curves and that of the signals which were observed lent confidence to the precision attached to the experimental results.

We wish to thank Professor F. Bloch for suggesting this problem and for many valuable discussions concerning it.

A Photographic Study of the Neutron Spectra from Al(αn) and Si(dn)*

R. A. PECK, JR.
Sloane Physics Laboratory, Yale University,† New Haven, Connecticut
(Received January 15, 1948)

The two neutron spectra named have been studied by the photographic method, using the new Eastman NTB nuclear particle emulsion. Details of the experimental method are discussed, with reference also to some features of the histogram representation employed here. The following mass differences are obtained:

$P^{30}-Al^{27}=2.998\ 06\pm0.24\times10^{-3}$ mass units,
$P^{29}-Si^{28}=1.006\ 64\pm0.14\times10^{-3}$,
$P^{30}-Si^{29}=1.002\ 15\pm0.21\times10^{-3}$,
$P^{31}-Si^{30}=1.000\ 88\pm0.18\times10^{-3}$.

A level in P^{30} at 1.02 ± 0.12 Mev above ground is found and confirmed, and three levels in P^{31} established. Group widths and intensities are listed.

1. INTRODUCTION

SINCE a given atomic nucleus may be formed as the end product of any of several cyclotron-induced reactions, the study with a single bombarding instrument of such series of reactions may be expected to yield internally consistent mass values for, and possibly selection rules in the formation of, the several product nuclei involved. This paper deals with four neutron-yielding reactions studied by the photographic-microscopic method of observation of recoil hydrogen nuclei originating within the photographic emulsion. These protons, elastically scattered by the incident neutrons, produce columnar ionization and, consequently, microscopically observable tracks in the emulsion, which thus assumes the character of an extremely large, continuously sensitive, hydrogenous cloud chamber. Measurements on the range distribution of the recoil protons allow the determinations of their energy distribution and, in turn, the energy distribution of the neutrons impinging on the emulsion. A comprehensive examination of the present characteristics of photographic detection has recently been given by Lattes, Fowler, and Cuer.[1]

The reactions here studied are:

$$Al^{27}+He^4=P^{30}+n^1+Q_1, \quad (1)$$

$$Si^{28}+D^2=P^{29}+n^1+Q_2, \quad (2)$$

$$Si^{29}+D^2=P^{30}+n^1+Q_3, \quad (3)$$

$$Si^{30}+D^2=P^{31}+n^1+Q_4. \quad (4)$$

Neutrons from (1) have been observed by several investigators, though no complete energy spectrum appears to have been published. However, the excitation curve for the reaction has been obtained by Waring and Chang,[2] Pollard, Schultz, and Brubaker,[3] and Fünfer;[4] the favored value for the threshold excitation seems to be approximately 2.0 ± 0.2 cm for the alpha-particle range. No data were found in the literature pertaining to reactions (2) to (4), other than the predicted[5] Q-values, $+3.9$ and $+4.3$ Mev for (3) and (4), respectively.

2. EXPERIMENTAL DETAILS

Exposure

Bombarding particles were in all cases accelerated in the cyclotron, which provided approximately 0.03 microampere of 7.6-Mev alpha-particles or 1 microampere of 3.7-Mev deuterons.

* Part of a dissertation presented to the Faculty of the Graduate School of Yale University in candidacy for the degree of Doctor of Philosophy.

† Assisted by the O.N.R. under Contract No. N6ori-44.

[1] C. M. G. Lattes, P. H. Fowler, and P. Cuer, Proc. Phys. Soc. London 59, 883 (1947).

[2] J. R. S. Waring and W. Y. Chang, Proc. Roy. Soc. 157, 652 (1936).

[3] E. C. Pollard, H. L. Schultz, and G. Brubaker, Phys. Rev. 53, 351 (1938).

[4] E. Fünfer, Ann. d. Physik 32, 313 (1938).

[5] M. S. Livingston and H. A. Bethe, Rev. Mod. Phys. 9, 245 (1937).

An ultimate limit on the practicable exposure of photographic plates is set by the gamma-ray background from the cyclotron chamber. That limit is reached when the random grains, which develop in the emulsion in response to the background gamma-rays, are so frequent as to render uncertain the identification of the beginning of a proton track. The limiting exposure is considerably increased by the use of thick lead shielding for the plates. The arrangement used provided a minimum of 10 cm of lead on all sides, except in the direct path of neutrons from the target.

The plates were held in a small box made of lead to minimize protons knocked on from the holder material. They were arranged to intercept neutrons emitted at 90° (in the laboratory system) to the direction of projectile incidence, and, with their emulsions in the horizontal plane, subtended angles not greater than ±3° about the 90° position. This fore-and-aft spread can be completely eliminated by rotating the plates into a vertical plane.

The effect of collimation of neutrons from the target is achieved by keeping the plates at least a certain distance from the target. The same solid angle limitation which thus affords collimation also reduces yield, effecting an upper limitation on the plate-to-target separation. In the present work all plates were kept between 18 and 19 cm from the bombarded sample, providing adequate yield and good geometry.[6]

Photography

The new Eastman NTB emulsions were used, batch number 347,126, coated on 1×3 inch microscope slides. The emulsion contained 85 percent AgBr by weight and was 51±7 microns thick when exposed, shrinking to 20–25 microns when processed. The batch was calibrated with a standard group of protons at successively reduced values of energy.[7] Since appreciable fading of the image was noted when development was delayed two days after exposure, it has been the practice to process plates within a few hours of their use.

Satisfactory tracks were obtained by developing for 3 to 4 minutes in Eastman D8. Development was followed by a 2 minute rinse in the stopping solution SB 1-a, and fixing in acid hardening solution F5. All processing was done at room temperature, the normal variation in which did not appear to alter the track quality appreciably. The plates were then washed in a slow current for approximately 30 minutes, and allowed to dry (emulsion up) on blotting paper, covered with an inverted glass dish. The dried emulsions were covered with No. 0 microscope slide cover glasses, using as adhesive a suspension in xylene of the resin damar. In addition to protecting the emulsion surface, this procedure has the advantages that (a) dust particles floating in the gum aid in locating (microscopically) the emulsion surface, and (b) mechanical scratches in the surface are filled in and largely rendered invisible by the damar suspension.

Microscopy

A Bausch & Lomb binocular microscope (Model CT) fitted with a mechanical stage was used. Verniers on the stage, with least count 0.1 mm, allowed easy resetting on a track at low magnification. Two pairs of eyepieces, compensated for use with apochromatic objectives and having magnifications 10× and 25×, were used with the following objectives: apochromat, 10×, 16 mm, 0.30 NA, dry; apochromat, 20×, 8.3 mm, 0.65 NA, dry; apochromat, 90×, 2 mm, 1.30 NA, oil; achromat, 45×, 4 mm, 0.85 NA, dry, with iris diaphragm.

When the limited abundance of tracks necessitated searching the plates at the lowest available magnification (100× over-all), a system of oblique illumination was used. True dark field illumination was not obtainable at this magnification, though quasi-dark field was advantageous, to minimize eyestrain. One of the first conditions to be applied in selecting tracks for close scrutiny is that all acceptable ones must be traveling in approximately the same direction. But the oblique system illuminates preferentially tracks having a particular orientation and, consequently, effects automatically a rough preselection of tracks with respect to direction. In effect, scanning is made easier with oblique illumination by the apparent elimination of irrelevant, off-angle tracks. Measurements were, in the main, made at 450× magnification. A

[6] Reference 5. Here, a/b was approximately 0.05 in all cases, while $\cos\theta_0$ ranged from 0.1 to 0.4.
[7] R. A. Peck, Jr., Phys. Rev. 72, 1121(L) (1947).

considerable advantage was gained from an iris in the high dry objective. This allowed a variability in focal depth with the 450× system, so that track measurements were made with ease and at the same time many tracks could definitely be established as originating and terminating within the emulsion by observing grains in focus above and below the ends. For those tracks requiring an even shallower focus for the latter discrimination, the immersion objective (900× over-all) was used. An alternative system which has been found convenient in the case of somewhat higher yields employs the 25× eyepieces, scanning at 250× over-all with oblique illumination, measuring and discriminating at 1125× (high dry), at which excellent dark field is obtainable.

In addition to the obvious necessity that a track begin and end within the emulsion, an acceptable track was required to lie within the square cone $\pm 11°$ about the direction of neutron incidence, in both the plane of the emulsion and that normal to it. Two criteria thus appear, with separate techniques for their application. The horizontal angle test is easily applied, for any angle in the emulsion plane can be pre-set by the use of a diametrical hairline in each of the paired oculars. The maximum allowable angular divergence in the vertical plane is related, in terms of the focal depth of the system, to a minimum length of track which is required to be in focus at a single setting. The vertical criterion applies to the emulsion when exposed, and must be corrected in application for the shrinkage of the emulsion which occurs during processing.

This pair of criteria effectively selects for measurement those tracks moving in a particular direction, that of the incident neutrons. A considerable simplification in the handling of data derives from the consequence that all tracks measured correspond directly to neutron energies, unreduced.[8]

Track measurements were accomplished by the use of an eyepiece scale, calibrated by reference to a stage micrometer. When track scattering occurred, a conventional[1] procedure was adopted. Direction changes in the plane of the emulsion were followed by re-orienting the eyepiece scale, while changes in the angle of dip (in the plane normal to the emulsion) were ignored, unless they took the track at any point outside of the maximum obliquity acceptable in that plane. The small inaccuracies thus introduced into some length measurements is the price of the considerable increase in operational facility.

3. TREATMENT OF THE DATA

Each set of data is represented graphically in the form of a histogram, in which are plotted successive values of the number of tracks with length between certain values. The numbers of tracks are plotted as a function of some length characteristic of the interval used, and the interval is moved uniformly along the scale of range or energy. It seems proper that the constant interval of the histogram should be constant in terms of energy rather than range. On the other hand, the use of extrapolated range as a defining property necessitates plotting on a linear range (not energy) scale, which indeed is the most convenient procedure. Therefore, the histogram interval used has been made to increase with range in such a manner as to preserve the magnitude of the equivalent interval in energy. This is easily accomplished in a calibrated emulsion, for the air range-energy curve[5] and the stopping power-energy function[7] render equivalent the quantities emulsion range, air range, and energy. As abscissae in the histograms, the median value of the tracks in each interval has been used so long as the number of those tracks remained high. When the number of those tracks dropped below 10 (arbitrary), the median was replaced by the mean length of the tracks involved. This procedure has the advantage of giving some indication of the distribution of tracks within the interval, but the disadvantage that low yield regions of short extent tend to appear as depopulated areas on the graph, rather than areas with small ordinates typically spaced. The prime advantage to the use of the median, of course, is the time saved in plotting.

For the fuller expression of the significance of each set of data, the histograms plotted have been of an "overlapping" type. For example, the spectra in this paper represent tracks per

[8] H. T. Richards, Phys. Rev. **59**, 796 (1941).

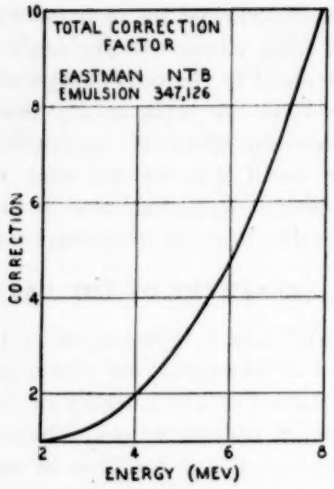

FIG. 1. Product of geometrical and cross-section correction functions for Eastman NTB emulsion 347,126. Thickness 51 microns.

200-kev interval calculated and plotted every 100 kev. Each datum, in general, is thus represented twice on the graph, and the area beneath the curve corresponds approximately to twice the number of tracks observed.

A strong observer bias has been noted in the recording of the last significant (estimated) figure of range values. This bias offers an absolute limit to the significant resolution possible with a given eyepiece scale and optical system. It is further to be expected that the bias may lead to spurious structure in a given histogram, revealed as a falsely high or low yield at a particular locus due to the accidental location of a boundary between successive intervals. This structure was partly rejected by the use of overlapping histograms as just described, and also by plotting, on the same graph, two or more point sets representing histograms with their starting points shifted by arbitrary amounts. Whatever characteristics survive such replotting are assumed to be associated with the data set itself.

Corrections

The histograms must next be altered to compensate for a recording efficiency which is energy dependent on two counts. The "geometrical correction" recognizes that the event of an acceptable track passing out of the emulsion and consequently being rejected is more frequent for high energy recoil protons than for slow ones. This is corrected by the application of a calculated weighting function[8] dependent on the emulsion thickness and the maximum acceptable obliquity in the vertical plane.

The "cross-section correction" is a direct compensation for the energy dependence of the neutron-proton scattering cross section (on which neutron recording depends), and is accomplished by the use of a weighting function given by the reciprocal of the cross section as a function of energy. For the cross-section function, a smooth curve was drawn through various experimental determinations.[9] The total correction, the product of the two functions, is shown in Fig. 1 for the Eastman NTB emulsion (No. 347,126) used in the present experiments. In the region below 1 Mev the cross-section correction function drops very rapidly, so that normalization at 0 Mev is not practical. Both corrections were, therefore, normalized to unity at 2 Mev, where both functions were varying fairly slowly. The 2-Mev point happens also to represent the lower limit of reliable observation with the photographic and microscopic systems employed.

In practice, the correction function was applied to the histogram points before a curve was drawn. The apparent best fitting, smooth curve was then drawn through the corrected points, and the location of groups decided on the basis of it. The procedure outlined here was then followed to describe the groups quantitatively. The high energy side of the most energetic group was assumed to represent the true shape of its low energy side as well, the latter being distorted by the presence of the next less energetic group. The high side was, therefore, reflected about the estimated last peak, and subtracted from the curve. It was assumed that this revealed the true form of the high energy side of the next group, and the process was repeated. It is from the symmetrical group forms thus deduced from the observed curve that extrapolated ranges, widths, and intensities were taken. It was felt that this procedure was necessary, even when a complex spectrum afforded relatively little indi-

[9] R. Sherr, Phys. Rev. **68**, 240 (1945); E. O. Salant and N. F. Ramsey, Phys. Rev. **57**, 1075 (1940); M. Bunge, Nature **156**, 301 (1945); C. L. Bailey, W. E. Bennett, T. Bergstrahl, R. G. Nuckolls, H. T. Richards, and J. H. Williams, Phys. Rev. **70**, 583 (1946).

vidual group structure on which to base the deduced shapes.

The extrapolated ranges were corrected and reduced to mean ranges, following Bethe.[5] The corresponding mean energies were employed in the computation of Q-values.

4. THE ENERGY DISTRIBUTION CURVES

Al(αn)

A thick target of aluminum foil was bombarded with alpha-particles from the cyclotron, mean energy 7.64±0.14 Mev, the width (at half-value) 0.3 Mev. The distribution of 775 satisfactory tracks is displayed in Figs. 2 and 3. The data there represented were taken in two parts, so that the curve from 3.2 Mev up is based on about one third of the total number of tracks observed. This higher energy portion of the aluminum spectrum is shown in Fig. 3. The true yield of acceptable tracks per mm² per microampere-minute was distributed as follows: 2.0 to 4.0 Mev, 8.6×10^{-2}; 4.0 to 6.5 Mev, 4.3×10^{-4}; over 6.5 Mev, 4.3×10^{-5}; employing a 51-micron thick emulsion at grazing incidence, 19 cm from the target.

Two groups are indicated in Fig. 2; their poor definition is attributed to the use of a thick target (necessary for adequate yield) and the considerable energy spread of the alpha-particle beam. That they are separate groups, suggested by the curve form, is confirmed by their widths (0.6 Mev each) which individually are greater than that of the beam. The extrapolated ranges of these groups correspond to 3.58±0.05 and 2.63±0.07 Mev. They are attributed to the reaction (1) and give values $Q_1=-2.93\pm0.17$ and $Q_1'=-3.91\pm0.19$ Mev.

The rare tracks above 3.9 and extending as high as 10.7 Mev may well be caused by the reaction

$$Al^{27}+D^2=Si^{28}+n^1+Q_5, \qquad (5)$$

excited by the residual deuteron beam in the cyclotron. A maximum neutron energy of 11.7 Mev is expected for this reaction. Another possible origin of the occasional high energy tracks is the primary cosmic radiation. This hypothesis will be discussed at the end of the paper. In considering the possibility of two sources of the high energy particles, the marked decrease in yield which occurs around 6.5 Mev may be of interest. For, while cosmic radiation seems a reasonable cause for the rare tracks above 6.5 Mev, those from 4.0 to 6.5 Mev seem too abundant to be so explained.

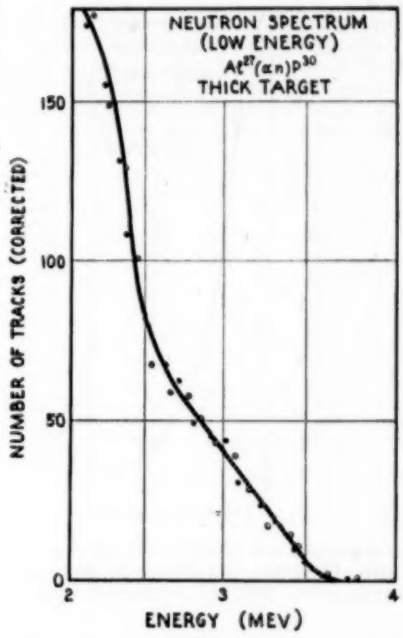

FIG. 2. Neutrons from $Al^{27}+He^4$. 500 tracks, from 4.3 cm² of plate area. Ordinates corrected for geometrical and cross-section effects (correction factor plotted in Fig. 1). Each set of points represents number of tracks in 200-kev interval taken every 100 kev. The two point sets are displaced approximately 50 kev. Re abscissae, see text.

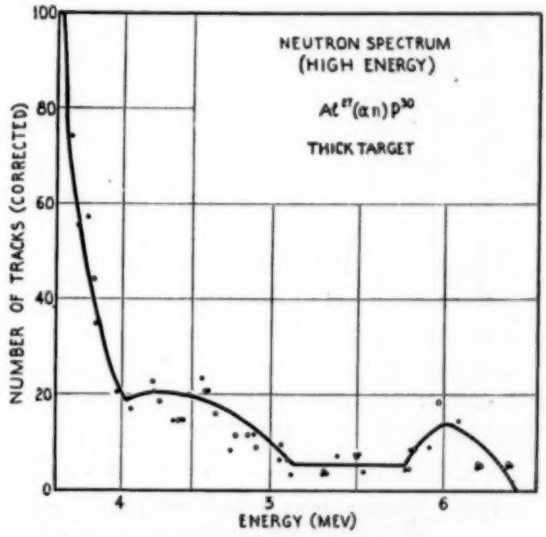

FIG. 3. Neutrons from $Al^{27}+He^4$. 275 tracks from 85 cm² of plate area. Additional tracks (not plotted): 7.16–7.54–8.70–10.57–10.73 Mev. Otherwise as Fig. 2.

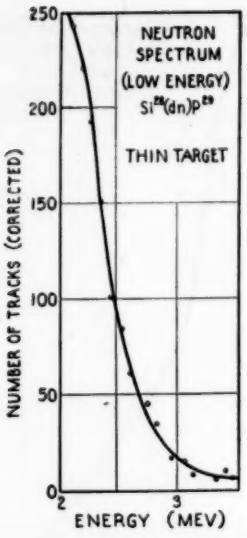

FIG. 4. Neutrons from Si(*dn*)P. 600 tracks, from 1.1 cm² of plate area. Ordinate is number of tracks in 200-kev interval taken every 100 kev, corrected (Fig. 1). This is group X.

Si(*dn*)

The silicon target used was a thin film of the pure element[10] (1 mg/cm², equivalent to 6 mm of air) deposited by evaporation on a thick gold foil. It was bombarded with deuterons of mean energy 3.72±0.07 Mev and width 0.17 Mev. Approximately 1500 tracks are represented in the distribution of Figs. 4 and 5. As with the aluminum spectrum, certain regions were emphasized, when the data were taken, to gain definition. The distribution of the 1500 tracks is therefore roughly as follows: 2.0 to 3.75 Mev, 45 percent; 3.75 to 4.65 Mev, 20 percent; above 4.65 Mev, 35 percent. The peak height of the most energetic group in Fig. 5 represents 1.53 $\times 10^{-4}$ acceptable tracks per mm² per microampere-minute of exposure, in a 51-micron thick emulsion at glancing incidence, 18 cm from the target.

This silicon spectrum is the composite of separate spectra from the reactions on the three constituent isotopes Si^{28}, Si^{29} and Si^{30} of abundances, respectively, 89.6, 6.2, and 4.2 percent. The groups which appear are listed in Table I.

5. RESULTS AND INTERPRETATION

Aluminum

The group from the ground-state transition in reaction (1) yielded the value $Q_1 = -2.93 \pm 0.17$ Mev. The observed threshold for (1), as indi-

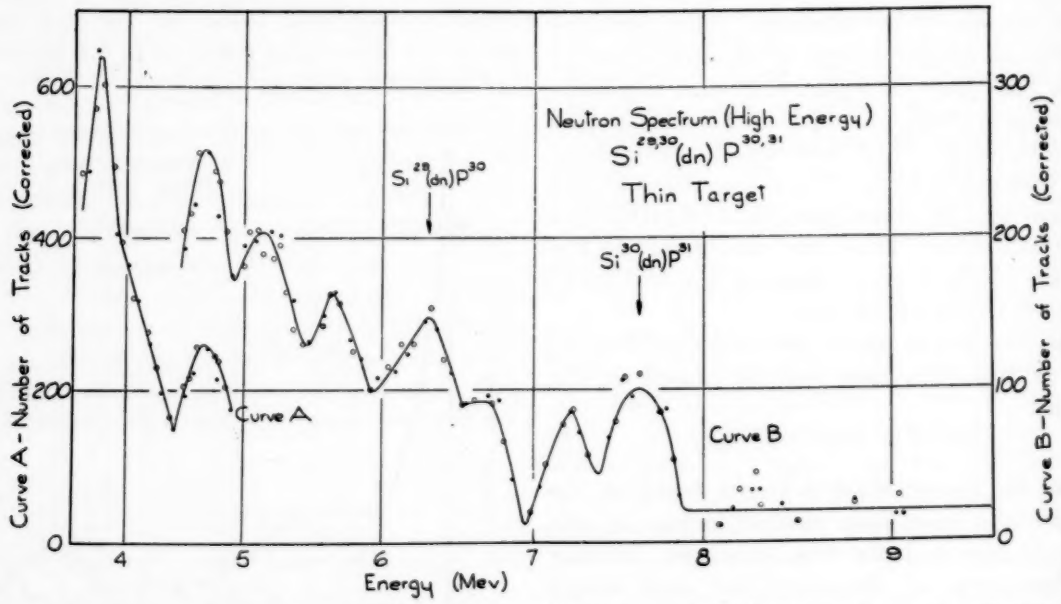

FIG. 5. Neutrons from Si(*dn*)P. 900 tracks, from 62 cm² of plate area. Additional tracks (not plotted): 9.92–10.38–10.46 Mev. Otherwise as Fig. 2. Groups are called I to IX, from right to left.

[10] Impurities not over a few thousandths of a percent. I am indebted to the Bell Telephone Laboratories for the pure silicon from which this target was prepared.

cated in the Introduction, is about 2.0±0.2 cm alpha-particle range, corresponding to 3.4±0.4 Mev in energy, and $Q_1 = -2.9 \pm 0.3$ Mev; Bethe's prediction[5] is $Q_1 = -3.3$ Mev.

The value of Q_1 here observed leads to the mass difference

$$P^{30} - Al^{27} = 2.998\ 06 \pm 0.24 \times 10^{-3} \text{ mass units,}$$

and, with Mattauch's listing[11] for aluminum, to

$$P^{30} = 29.988\ 75 \pm 0.67 \times 10^{-3} \text{ mass units.}$$

This is consistent with 29.988 5 which was derived[11] from the beta-ray upper limit of P^{30}.

The lower energy group here observed in the aluminum spectrum, $Q_1' = -3.91 \pm 0.19$ Mev, corresponds to a transition to an excited level in P^{30}, 1.02±0.12 Mev above ground.

Silicon 28

Group X of Table I may be identified immediately with the reaction (2) by virtue of its yield, Si^{28} being 89.6 percent abundant. The observed energy change, $Q_2 = -0.80 \pm 0.10$ Mev, gives the mass difference

$$P^{29} - Si^{28} = 1.006\ 64 \pm 0.14 \times 10^{-3} \text{ mass units}$$

and, with Mattauch's listing[11] for Si^{28},

$$P^{29} = 28.993\ 87 \pm 0.59 \times 10^{-3} \text{ mass units.}$$

No comparison value for Q_2 has been located, but a P^{29} mass can be calculated[11] on the basis of the beta-spectrum of that nucleus.[12] It is $P^{29} = 28.991\ 51$ mass units. The discrepancy between this and the above value is considerable, but the present identification of group X seems unambiguous.

Silicon 29

The group from the ground-state transition in reaction (3) may be located in terms of the mass of P^{30}, determined from the present investigation of reaction (1). The value thus predicted is $Q_3 = 3.30 \pm 1.23$ Mev, which indicates strongly that IV of Table I is the group arising from the ground-state transition in the reaction (3). Bethe's prediction[5] of 3.9 Mev may be compared.

[11] S. Flügge and J. Mattauch, Physik. Zeits. 42, 1 (1941); also, J. Mattauch, *Nuclear Physics Tables* (Interscience Publishers, Inc., New York, 1946), Table IV.

[12] M. G. White, E. C. Creutz, L. A. Delsasso, and R. R. Wilson, Phys. Rev. 59, 63 (1941).

TABLE I. Neutron groups in the composite spectrum Si(*dn*)P. Reliability is based on comparison of group elevation (peak over valley preceding) with the square root of the peak yield. *A*: elevation is greater than $N^{\frac{1}{2}}$, *B*+: elevation is approximately equal to $N^{\frac{1}{2}}$, *B*: elevation is less than $N^{\frac{1}{2}}$, *C*: no peak appears (group deduced from break in the slope of the curve).

Group	Extrapolated range (Mev)	Half-value width (Mev)	Relative intensity	Reliability	*Q* (Mev)
X	2.62±0.02	0.64	~140.	*A*	−0.80±0.10
IX	4.12±0.06	0.38	5.5	*A*	0.71±0.13
VIII	4.43±0.04	0.28	2.5	*C*	1.03±0.11
VII	4.92±0.08	0.30	2.2	*A*	1.52±0.15
VI	5.49±0.23	0.54	1.8	*B*	2.11±0.31
V	6.15±0.09	0.50	1.6	*A*	2.78±0.16
IV	6.76±0.10	0.44	1.5	*A*	3.38±0.17
III	6.93±0.08	0.20	0.8	*B*	3.57±0.15
II	7.47±0.09	0.26	0.8	*B*+	4.12±0.16
I	7.90±0.06	0.36	1.0	*A*	4.56±0.13

This Q_3 value provides a determination of the Si^{29} mass, thus:

$$P^{30} - Si^{29} = 1.002\ 15 \pm 0.21 \times 10^{-3} \text{ mass units}$$

and, with the mass of P^{30} determined from the Al(*αn*) reaction,

$$Si^{29} = 28.986\ 60 \pm 0.88 \times 10^{-3} \text{ mass units.}$$

The corresponding value listed[11] is 28.986 51. An internal consistency check is possible between reactions (1) and (3), in terms of the equation derived by eliminating the unknown P^{30} mass from the *Q*-value expressions, *viz.*,

$$Q_3 - Q_1 = Si^{29} - Al^{27} + D^2 - He^4. \qquad (6)$$

The right-hand member of (6), dependent only on masses of stable nuclei, has the value 6.23 Mev, while the left-hand member, as observed here, is $+3.38 - (-2.93) = 6.31$ Mev, in good agreement.

Silicon 30

The remaining groups (I, II and III) of Table I are assigned to the remaining isotope, in reaction (4). The most energetic group (I) corresponds to $Q_4 = 4.56 \pm 0.13$ Mev, for which Bethe's prediction[5] is 4.3 Mev. This observation determines the mass difference

$$P^{31} - Si^{30} = 1.000\ 88 \pm 0.18 \times 10^{-3} \text{ mass units.}$$

For this reaction, both involved nuclei are stable. The mass of P^{31} is better known than

TABLE II. Interpretation of the neutron groups in Table I. Means of identification are amplified in text, under "Results and Interpretation."

Means of identification	Group	Reaction	Final nucleus	Q (Mev)	Excitation (Mev)	Comparison excitation (Mev)	Comparison reference
Sole isotope	I	(4)	P^{31}_{gnd}	4.56±0.13	0.00		
Sole isotope	II	(4)	P^{31*}	4.12±0.16	0.44±0.29		
Sole isotope	III	(4)	P^{31**}	3.57±0.15	0.99±0.28	1.05	Haxel,† Bethe††
Q predicted	IV	(3)	P^{30}_{gnd}	3.38±0.17	0.00		Reaction (1)
Sole isotope, and level predicted	V	(4)	P^{31***}	2.78±0.16	1.78±0.29	1.7	Haxel,† Bethe††
Level predicted	VI	(3)	P^{30*}	2.11±0.31	1.27±0.48	1.02±0.12	Reaction (1)
Ambiguous	VII	(3), (4)	$P^{30,31}$	1.52±0.15			
Ambiguous	VIII	(3), (4)	$P^{30,31}$	1.03±0.11			
Ambiguous	IX	(3), (4)	$P^{30,31}$	0.71±0.13			
Abundance	X	(2)	P^{29}_{gnd}	−0.80±0.10	0.00		

† See reference 14.
†† See reference 5.

Si^{30}, however, so Mattauch's value[11] for the former is used, with the above mass difference, to find

$$Si^{30} = 29.983\,53 \pm 0.45 \times 10^{-3} \text{ mass units.}$$

The corresponding listing[11] is $29.983\,99 \pm 0.50 \times 10^{-3}$ units. An internal consistency checking equation may be derived by considering, in addition to (3) and (4), the activity (positron) of P^{30}, decaying into Si^{30}. The reported upper limit for the positron spectrum[12] is alternatively 3.0 or 3.5 Mev, corresponding to $Q_7 = 4.26 \pm 0.25$ Mev, if Q_7 is used to denote the energy release in the activity mentioned. The checking relation is

$$Q_3 + Q_4 = 2D^2 - 2n^1 + Si^{29} - P^{31} - Q_7. \qquad (7)$$

The right-hand member of (7), depending only on stable masses and Q_7 just mentioned, has the value 8.4±1.1 Mev. The left-hand member as here observed is 3.38+4.56=7.94±0.30 Mev, in adequate agreement.

Energy Levels

No excited state transitions in reaction (2) were observed, because of its low Q-value. The remaining groups of Table I may to some extent be distributed between the remaining reactions (3) and (4), as in Table II. The identification of groups I, II, III, IV, and X has already been discussed. Group VI is associated with reaction (3) and the formation of P^{30} in its 1-Mev excited state, that state having been established in reaction (1). Then, since no lower level intervened in (1), it is assumed that the intervening group V is not associated with P^{30}, and, consequently, derives from reaction (4) and a third excitation level in P^{31}. This identification is confirmed by an independent observation of the same level by Haxel,[14] in studying the reaction

$$Si^{28} + He^4 = P^{31} + H^1 + Q_8. \qquad (8)$$

Groups VII, VIII, and IX remain ambiguous, identified either with reaction (3) or (4).

Intensity Ratios

The ratio of the yield from the ground-state transition in reaction (3) to that from the ground-state transition in (4) is given by the ratio of group intensities IV:I and is equal to 1.5. The ratio of the target isotope abundances (Si^{29}:Si^{30}) is 6.2:4.2=1.5. This indicates that the cross section for the ground-state transition in (3) and that in (4) are equal at the bombarding energy employed.

The yield ratio P^{29}_{gnd}:(mean of P^{30}_{gnd} and P^{31}_{gnd}) is given by the group intensities X:(mean of I and IV), and is equal to 110. The corresponding target isotope abundance ratio is 89.6:5.2, only 17. The cross section for the ground-state transition in reaction (2), therefore, seems to be greater than that for the same transition in (3) and (4) by a factor about 6.5.

In reaction (8), Haxel[14] found intensity ratios 1.0:1.8:2.4 for transitions to the ground, first excited, and second excited states of P^{31}, respec-

[12] G. T. Seaborg, Rev. Mod. Phys. 16, 4 (1944).

[14] O. Haxel, Physik. Zeits. 36, 804 (1935).

tively. The intensities of the corresponding neutron groups are 1.0:0.8:1.6 for I:III:V. However no group observed by Haxel corresponds to the present II. If the intensity of this group is added to that of III, the ratios are I:(II+III):V =1.0:1.6:1.6 and the remaining discrepancy, amounting to less than a factor 2, is in the third excited level transition. In any event, two different reactions—(4) and (8)—are involved, and a selection rule may be indicated.

A similar comparison is possible for yields from the ground and first excited state transitions to P^{30} as revealed, on the one hand, in reaction (1), on the other, in (3). For (3), the ratio is given by ground:first excited = IV:VI = 1.5:1.8 =1.0:1.2. For reaction (1), the corresponding ratio is not definitely determinate from Fig. 2, but is certainly greater than 2.8, in distinct disagreement with 1.2, above. Again, a selection rule may be involved.

High Energy Background Tracks

The silicon spectrum was terminated with group I on the basis of yield, for a distinct reduction in intensity characterizes the tracks following. Additional data taken in the range above 8 Mev show no organization into groups, but only a scattered background extending as far as 10.5 Mev. It is unlikely that these tracks derive from a reaction on the target, since the latter is believed to have been very pure and any appreciable contamination of the deuteron beam is very unlikely. It is believed that the high energy background observed in both the silicon and aluminum reactions is attributable to cosmic rays. The qualitative features supporting this idea follow.

The background seems independent of the exposure and of the reaction recorded, appearing on all plates. For example, the background intensity in the presence of reaction (1) was of order 1 track per plate, the cyclotron exposure having been 12.5 microampere-minutes. The background intensity accompanying the silicon reactions was only of order 4 per plate, however, though the exposure in that case was 330 microampere-minutes.

Observations[15] have shown approximately 0.1 track per cm^2 per day accumulating in photographic emulsions due to cosmic rays, corresponding to 1.5 tracks per plate per day, for 1×3 inch plates. The present data show roughly 3 tracks per plate after five months, entirely consistent (300 per plate) when corrected for the angular discrimination practiced in recording track data. Further, these 300 (deduced) single tracks per plate are accompanied by between 0.1 and 1.0 cosmic-ray "star" per plate, a frequency which is consistent with the expectation[15] of roughly 200 single tracks per star.

Finally, the cosmic-ray track distribution previously recorded[15] has its peak at about 13 Mev and a width of 8 Mev (at half-intensity), which distribution is expected to be degraded in energy at sea level. It has, therefore, the right location to account for the background observed around 10 Mev without providing an equal or greater disturbance at the lower energies.

The assistance of Professor R. F. Humphreys throughout this project is gratefully acknowledged.

[15] Edited by W. Heisenberg, *Cosmic Radiation* (Dover Publications, New York, 1946), Chapter 13.

PHYSICAL REVIEW VOLUME 73, NUMBER 9 MAY 1, 1948

Search for a Resonance Absorption of Neutrons in Graphite

S. BERNSTEIN
Clinton National Laboratory, Oak Ridge, Tennessee
(Received January 14, 1948)

The purpose of the experiment was to determine whether or not an appreciable absorption of neutrons takes place in graphite during the slowing down process. A simplified description of the experiment is as follows: A Ra-Be photo-neutron source was surrounded by a solid sphere of graphite of 11-inch radius. The graphite sphere was immersed in an essentially infinite mass of paraffin. The activities of thin indium foils due to thermal neutrons were measured as a function of distance from the source for the following two cases: (a) with the graphite sphere in place, (b) with the graphite sphere removed. From these distributions and the relative thermal neutron capture cross sections of graphite and paraffin, the relative numbers of neutrons captured as thermal neutrons in the two cases were calculated. The difference between these two numbers is a measure of the number of neutrons absorbed by the graphite sphere during the slowing down process. The results indicate that if a resonance absorption exists in graphite, then, at most, 5 percent of all neutrons passing through such a level would be absorbed by the 11-inch radius graphite sphere.

1. INTRODUCTION

THE work described in this report was done at the Metallurgical Laboratory of the University of Chicago during the summer preceding the achievement of the graphite-moderated, self-sustaining chain reaction on December 2, 1942. A pertinent pile problem at that time was to what extent the fast neutrons arising from fission in the uranium lumps would be absorbed by the graphite moderator during the slowing down process. Such neutrons would be lost to the chain reaction since their absorption in the graphite would prevent them from reaching the thermal energy region where they could effectively cause fission in the uranium and again give birth to a new generation of fission neutrons. The purpose of this experiment was to determine in the limited time available the magnitude of such "resonance absorption" in graphite. The work is presented here essentially in the same form as it appeared in 1942 as a project report of the Metallurgical Laboratory.[1]

If the capture of a neutron by normal carbon led to an easily detectable activity, a measure of the amount of resonance capture could be obtained merely by placing a cadmium-surrounded sample in a beam of slow neutrons. The activity under these conditions would be due to neutrons having energies above the energy of the Cd "cut-off." However, since the 99 percent abundant C^{12} leads to stable C^{13} on neutron capture and the 1 percent abundant C^{13} leads to the soft β-emitter C^{14}, this method appeared to be infeasible. Consequently, the more devious method described here was used.

The principle of the experiment can be described by use of the following illustration. Consider a source of fast neutrons at the center of a spherical cavity in a mass of paraffin large enough to absorb all the neutrons. The neutrons will be slowed down to thermal energies by collisions with the protons in the paraffin. Essentially, all of them will then be captured as thermal neutrons by the hydrogen nuclei. In the steady state, the strength of the source or the rate of production of neutrons, Q_1, is equal to the rate at which they are captured, or

$$Q_1 = \int (nv)_t \sigma_H dv,$$

where $(nv)_t$ is the flux of thermal neutrons at any point in the paraffin, σ_H is the capture cross section per unit volume of paraffin for thermal neutrons, and the volume integral is taken over the paraffin. Suppose now that the cavity is filled with a solid sphere of graphite. If the graphite captures only thermal neutrons, the strength of the source is now given by

$$Q_2 = \int (nv)_t \sigma_G dv + \int (nv)_t \sigma_H dv,$$

[1] A report of this work will appear in the Manhattan Project Technical Series.

where σ_G is the macroscopic thermal neutron capture cross section of graphite and the integrals are taken over the respective volumes of graphite and paraffin. If neutrons are absorbed by the graphite during the slowing down process, then Q_2 will be less than Q_1, by the number of neutrons so absorbed.

Since the saturated activity of a thin detector due to thermal neutrons is proportional to the thermal neutron flux, the saturated activity (A) can be inserted into the above expressions instead of $(nv)_t$.

2. EXPERIMENTAL ARRANGEMENT

The actual experimental arrangement used is as shown in the drawing of Fig. 1 and in the accompanying photograph (Fig. 1A). It consisted of a graphite sphere, 11 inches in radius surrounded by a spherical graphite shell 4 inches thick. The original plan for the experiment was to take measurements for two cases: (1) sphere, shell and paraffin in place; (2) sphere removed, shell and paraffin in place. It was the function of the graphite shell, to furnish the same graphite-paraffin interface boundary conditions in the two cases, so that the angular distribution of the neutrons striking a detector foil immersed in the paraffin would remain unchanged. Actually, a limited number of measurements were taken with both sphere and shell removed. Both the sphere and shell were machined from pieces of AGX graphite of 4-in. by 4-in. cross section. The sphere and its surrounding shell fit snugly into a 30-inch diameter spherical cavity in a 40-in. ×40-in. cube of paraffin. The cube of paraffin was cast in eight separate pieces, each wieghing approximately 85 kilograms. Along the outside surfaces of the paraffin cube was placed one course of 8-in.×8-in.×12-in. paraffin bricks, bringing the over-all length of the side of the cube to 56 inches. The graphite sphere weighed 146 kilograms, the graphite shell weighed 232 kilograms. The entire mass of paraffin weighed 2200 kilograms.

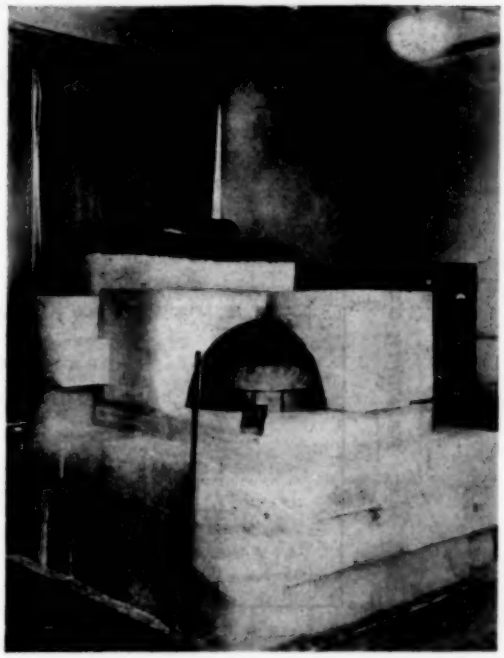

FIG. 1A.

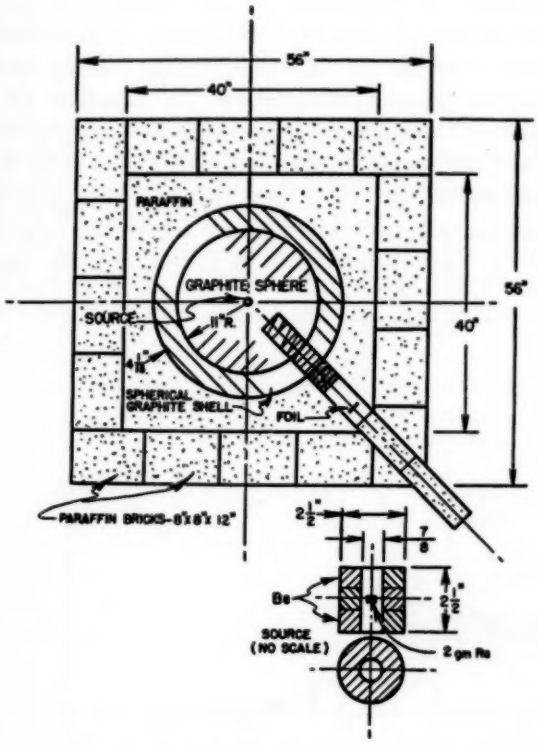

FIG. 1. Equator plane cross section. Scale: 1 in. = 1. in.

A Ra-Be photo-neutron source rather than the usual Ra-Be mixture was used because the lower average energy of the photoneutrons should make the intensity fall off more quickly in the paraffin and thus reduce the number of measurements needed. A cross section of the photo source is shown in Fig. 1. It consisted of 2 g of Ra

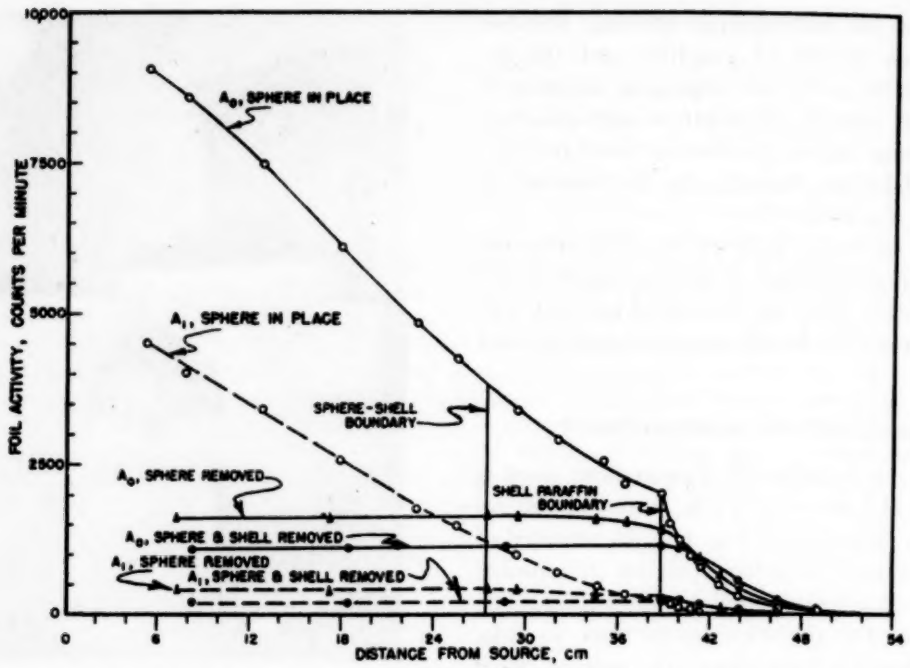

FIG. 2. Foil activity with and without Cd *vs.* position. A_0=foil activity without Cd. A_1=foil activity with Cd.

surrounded by 319 g of Be in the form of a cylindrical shell.

3. MEASUREMENTS

Indium foils were placed at various positions in the rectangular slot shown in the drawing, between rectangular plugs of graphite or paraffin, depending upon which of the two media surrounded the plugs. The plane of each foil was perpendicular to the "equator plane," with the foil centers in this plane. The axis of the cylinder of beryllium of the source was perpendicular to the equator plane. Thin indium foils of 10 mg per square cm, and 150 mg total weight, were used wherever the intensity permitted, in order to obtain as closely as possible the true neutron density. Thicker foils of 80 mg per square cm were used at large distances in the paraffin beyond the point where the ratio of thick foil activity to thin foil activity had

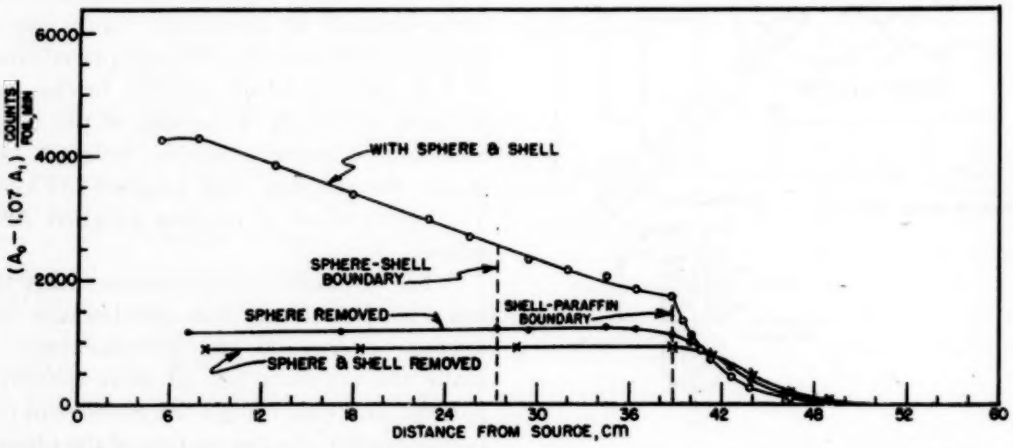

FIG. 3. Foil activity due to thermal neutrons *vs.* r. A_0=foil activity without Cd. A_1=foil activity with Cd.

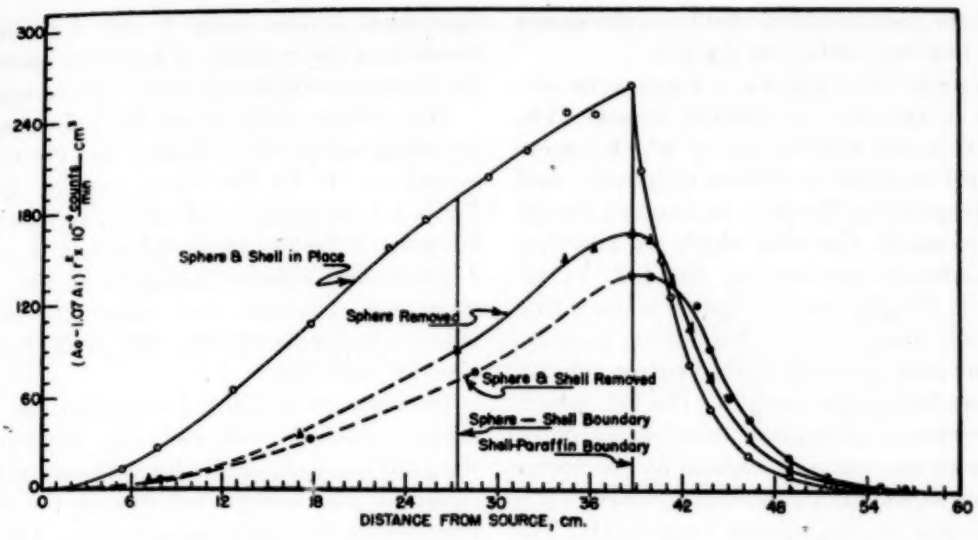

FIG. 4. Foil activity due to thermal neutrons $\times r^2$ *vs.* distance. A_0 = foil activity without Cd. A_1 = foil activity with Cd surrounding foil.

become constant. This constant ratio of thick foil activity to thin foil activity was then used to calculate what the thin foil activities would be at points where there was more than a 4-inch thickness of paraffin between the foil and the source. Exposures lasted about thirty minutes. Only one foil was exposed at a time in order to eliminate any possible interaction between foils. Foil activities were measured with Geiger tube and scaling circuit. The consistency of the counting apparatus was checked by taking a uranium oxide standard count before and after every foil count.

Foil activities were measured with and without 0.020-inch thick cadmium surrounding the foil, for the following arrangements:

Case 1. In the sphere, shell and paraffin.
Case 2. In the shell and in the paraffin, with the graphite sphere removed.
Case 3. In the paraffin, with the sphere and shell both removed.

The foil activity *vs.* position curves are shown in Figs. 2 and 3. The (foil activity $\times r^2$) *vs.* position curves are shown in Fig. 4. As can be seen in Fig. 4, the number of thermal neutrons in a spherical-shell volume element falls off quite slowly in the graphite and very abruptly in the paraffin. The thermal neutron and resonance neutron foil activities are quite constant in the cavity for Cases 2 and 3. The curves seem to show a slight decrease toward the center of the cavity, which might be due to absorption of neutrons by the materials of the source. The r^2 curves become exponential in the paraffin as can be seen from the semilog plot of Fig. 5. The relaxation distance for both of these curves is 2.84 cm. This value was used in extrapolating the r^2 curves beyond the largest distance at which the intensity was great enough for measurements to be taken. The small contribution to the volume integral of the foil activity for this region was then computed analytically.

If there is no resonance absorption in graphite, then the total number of neutrons emitted by the source is proportional to:

$$4\pi\sigma_G\int_{\text{graphite}}(A_0-1.07A_1)\bar{r}^2dr + 4\pi\sigma_H\int_{\text{paraffin}}(A_0-1.07A_1)\bar{r}^2dr, \quad (1)$$

where $A_1 \equiv$ saturated activity of the foil after having been irradiated with Cd foil completely surrounding it ("with cadmium foil activity"); $A_0 \equiv$ saturated activity of the foil after having been exposed without the Cd jacket around it ("no Cd foil activity"); $\sigma_G \equiv$ capture cross section per unit volume of graphite for thermal neutrons; $\sigma_H \equiv$ capture cross section per unit volume of paraffin for thermal neutrons; $\bar{r}^2 \equiv$ the

square of the distance of the foil from the source averaged over the surface of the foil.

The quantity $(A_0-1.07A_1)$ is taken to be proportional to the thermal neutron density. The factor 1.07 is an empirical factor which applies to the 0.020-inch thick cadmium commonly used on the Metallurgical Project. It accounts for the indium resonance neutrons which are absorbed by the cadmium surrounding the foil. In expression (1) the implicit assumption is made that the capture cross sections of graphite, paraffin, and indium vary inversely as the neutron velocity for energies below the energy of the Cd cut-off.

If a resonance absorption exists in graphite, then some of the neutrons emitted by the source do not live to become thermal, and consequently do not appear in the volume integral (1). The result would then be that the value of expression (1) would be greater for case 2 than for case 1, because of the greater volume of graphite present in case 1. The difference between the values of expression (1) for cases 1 and 2 would be a measure of the number of neutrons absorbed in the resonance region by the graphite sphere.

The volume integrals of the foil activity, or the areas under the r^2 curves, and the values of expression (1) for the three cases are given in Table I. Column 2 of the table gives the volume integrals of the no-cadmium foil activity, column 3 gives the volume integrals of the indium resonance activities, and column 5 gives the volume integrals of the foil activity due to thermal neutrons.

In column 6 of Table I are given the thermal capture cross sections per cubic centimeter for the graphite and paraffin for neutrons of velocity equal to the average velocity of the Maxwell distribution at room temperature. The values given in column 6 are based on 5.92×10^{-27} cm^2 per atom for the AGX graphite (density = 1.6 g per cm^3) and 0.29×10^{-24} cm^2 per atom of hydrogen. (The use of these values for the cross

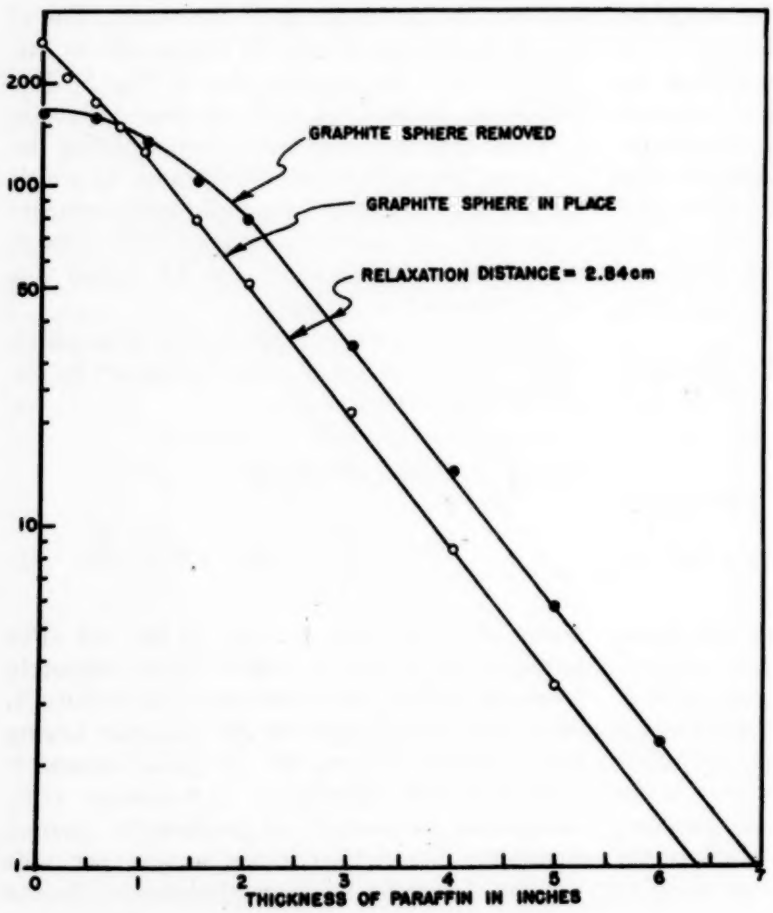

FIG. 5. Semilog plots of foil activity $\times r^2$ vs. position. A_0 = foil activity without Cd. A_1 = foil activity with Cd.

TABLE I. Areas under "r^2" curves.

(1)	(2) $4\pi\int A_0 r^2 dr$ counts/foil min. cm³	(3) $4\pi\int 1.07A_1\bar{r}^2 dr$ counts/foil min. cm³	(4) % passing through indium resonance level	(5) $4\pi\int(A_0-1.07A_1)\bar{r}^2 dr$ counts/foil min. cm³	(6) cm²/cm³	(7) $\sigma_a[\int 4\pi(A_0-1.07A_1)\bar{r}^2 dr]$ counts/foil min. cm³	(8) % of neutrons captured as thermals
Case 1: Sphere	4648×10^5	1960×10^5	42.2	2688×10^5	4.78×10^{-4}	12.8×10^4	5.5
shell paraffin	3716	878	18.8	2838	4.78	13.6	5.8
	1071	75.3	39.0	996	208.0	207.2	88.7
						$Q_1=233.6\times10^4$	
Case 2: Shell	2138×10^5	480×10^5	10.3	1658×10^5	4.78×10^{-4}	7.9×10^4	3.4
paraffin	1257	173×10^5	89.7	1084	208.0	225.5	96.6
						$Q_2=233.4\times10^4$	
Case 3: Paraffin			100.0	1176×10^5	208.0×10^{-4}	$Q_3=238\text{–}244\times10^4$	100.0

sections was suggested by E. Fermi at the time of the experiment. Actually it is the ratio of these two cross sections which is significant here.) The density of the paraffin was 0.83 g per cm³. A chemical analysis showed that the paraffin consisted of 14.2 percent hydrogen.

In column 4 of Table I are given the fractions of the total number of neutrons emitted by the source which are passing through the indium resonance level in the graphite and paraffin. These percentages were obtained by means of the following considerations:

The resonance activity of a thin foil is given by the following expression, in which the integral is taken over the resonance line:

$$\nu=(q\lambda/\Delta)\int\sigma(dE/E). \tag{2}$$

In (2) $q\equiv$slowing down density, or the number of neutrons per cm³ per sec. passing through the resonance level, $\lambda\equiv$mean free path in the medium surrounding the foil for neutrons of the resonance energy, $\Delta\equiv$average loss in the logarithm of the energy per collision[1] ($\Delta=1$ for hydrogen, and is equal to 0.158 for carbon).

From (2) it follows that the ratio of the slowing down densities in paraffin and carbon is given by:

$$\frac{q_p}{q_c}=\left(\frac{1}{0.158}\frac{\lambda_c}{\lambda_p}\right)\frac{\nu_p}{\nu_c}\equiv A\left(\frac{\nu_p}{\nu_c}\right), \tag{3}$$

where

$$A=(1/0.158)(\lambda_c/\lambda_p). \tag{4}$$

The constant A, may be determined from the volume integrals of the foil activities due to resonance neutrons, given in Table I. Since $Q=\int q dv$, then

$$1960+878+A(75)=480+A(173), \tag{5}$$

$$A=24.1. \tag{6}$$

This value for A agrees quite well with the value $A=23.6$ obtained by substituting in (4), the values $\lambda_c=2.6$ cm and $\lambda_p=0.7$ cm for the mean free paths of indium resonance neutrons in graphite and paraffin, respectively. The entries in column 4 of Table I were calculated using $A=24.1$.

In column 7 of Table I are given the values for the product of the areas under the r^2 curves and the respective capture cross sections. These values are proportional to the numbers of thermal neutrons captured in the various portions of the assembly. The sums Q_1, Q_2, and Q_3 are proportional to the total number of neutrons captured as thermals for the three cases.

[1] H. L. Anderson, E. Fermi, A. Wattenberg, G. L. Weil, W. H. Zinn, Phys. Rev. 72, 16 (1947).

The measurements were standardized by using manganese foils of known cross section. The calibration can be expressed in terms of the thin indium foils and the Geiger tube used in measuring their activities by:

$$nv = 0.92(A_0 - 1.07A_1), \tag{7}$$

where nv is given in neutrons per cm² per sec. and $(A_0 - 1.07A_1)$ is the standard foil activity due to thermal neutrons in counts per foil per minute. Using (7) the total number of neutrons emitted by the source is 2.2×10^6 per sec.

4. DISCUSSION OF RESULTS

The agreement between the values $Q_1 = 233.6 \times 10^4$ and $Q_2 = 233.4 \times 10^4$ is perhaps better than could be expected from the data. Usually two to four foils were measured for each position. The difference between the greatest and the least of the saturation activities for foils of the same position was about 2 percent for all measurements in the graphite and for measurements in the paraffin up to positions well beyond the point where the r^2 curves become exponential in the paraffin. The average of the activities for foils of the same position should be determined to within 1 percent.

The reproducibility of the complete process of assembling the paraffin-graphite structure, procuring a complete set of data, and then computing the area under the r^2 curve can be judged from the following results. Two complete sets of measurements in the paraffin were obtained with the thick foils for cases 1 and 2. In the interval between these two sets of measurements the entire structure had been completely dismantled and set up again. Let I_1 = area under the r^2 curve for the paraffin only with the sphere in place, I_2 = area under the r^2 curve for the paraffin only with the sphere removed. The value of $(I_2 - I_1)/I_1$ was found to be 10.6 percent for one set of measurements, and 10.7 percent for the second set.

After having completed the measurements for cases 1 and 2 there was a short time available before the space being used for the experiment was needed for other work. This short period was devoted to case 3. The number of foils measured for case 3 was about $\frac{1}{3}$ the number for case 1 or 2. Unlike the first two cases, the points for case 3 showed quite a spread. The maximum and minimum values that could be obtained for Q_3 from the r^2 curve were 238×10^4 and 244×10^4. The mean of these two values is about 3 percent higher than for cases 1 and 2.

The more reliable data of cases 1 and 2 show, then, that the fraction of neutrons absorbed by the graphite during the slowing down process is less than experimental error, which might have been about one to two percent. The less reliable data of case 3 indicates that this fraction might be about 3 percent. Even if these two upper limits are given equal weight, then the average results can be expressed by the statement that at most $2\frac{1}{2}$ percent of all the neutrons emitted by the source are absorbed while passing through the resonance region in the graphite. Since roughly half of all the neutrons pass through the resonance region in the graphite, at most 5 percent of all those neutrons passing through the resonance region in the 11-inch graphite sphere would be absorbed.

The author is very grateful to J. H. Manley, L. Szilard, and E. Fermi for many helpful discussions.

Slow Neutron Velocity Spectrometer Studies of Cu, Ni, Bi, Fe, Sn, and Calcite*

W. W. Havens, Jr., L. J. Rainwater, C. S. Wu, and J. R. Dunning
Pupin Physics Laboratories, Columbia University, New York, New York

(Received January 15, 1948)

The thermal cross section of Cu is well matched by the curve $\sigma=(7.8+0.54E^{-\frac{1}{2}})$. Microcrystalline interference is observed in the low energy region. The cross section decreases slowly from 8 to 7.3 between 2 and 100 ev, then decreases more rapidly until at zero timing it is 5.3. A small dip is observed near 3000 ev. The thermal cross section of Ni is well matched by the curve $\sigma=(17.0+0.77E^{-\frac{1}{2}})$. Microcrystalline interference effects are observed at low energies. The Ni cross section is approximately constant at 17.2 from 3 to 50 ev. A small dip is observed with a minimum near 100 ev. Above 100 ev the cross section drops rapidly to 8 at zero time of flight. Bismuth shows no $1/v$ slope in the thermal region because of microcrystalline interference effects. The free cross section of Bi is (9.0 ± 0.2) and is constant over the energy region investigated. The thermal cross section of Fe is well matched by the curve $\sigma=(11.0+0.35E^{-\frac{1}{2}})$. Microcrystalline interference effects are observed in the low energy region. The cross section of Fe remains approximately constant at 11 from 3 to 300 ev, then decreases to 4.8 at zero time of flight. The cross section of Sn in the thermal region rises because of microcrystalline interference effects which mask any $1/v$ slope. The free cross section is (4.9 ± 0.1). There is a slight dip in the transmission curve of tin around 6 ev which may or may not be real. Other small dips near 50 and 100 ev are probably real. The cross section increases near zero time of flight indicating that there are probably resonances above 1000 ev. The cross section of a large Nicol Prism decreases from the additive $CaCO_3$ cross section of 20 at short wave-lengths to about 3.5 at 0.005 ev. The residual cross section cannot be explained by theory.

I. INTRODUCTION

In several previous papers[1-3] the results of investigations of the slow neutron cross section as a function of the neutron energy have been presented for a large number of materials. In order to make available in published form as complete information as possible on slow neutron cross sections the results acquired over the past few years have been re-examined and the data which were considered to be in publishable form are presented in two papers, of which this is the second.

The results presented here were taken with the new system[2] which has been somewhat improved to obtain better resolution, as will be described in detail in a forthcoming paper in the regular series.[2] All of these materials will be investigated more thoroughly in the future, although complete results will probably not be obtained soon. In presenting the results on Cu, Ni, Bi, Fe, Sn and calcite the conventions previously adopted are used,[1,2] in particular:

1. All cross section values are given in units of 10^{-24} cm²/atom.
2. The resolution function is roughly triangular in shape having a width at its base between 2 and 3 times the timing spacing of adjacent experimental points. The resolution function is usually not shown explicitly on each curve.
3. When a sufficiently strong slow neutron resonance is present in one of the isotopes of the material studied a dip will be observed in the transmission *vs.* slow neutron time of flight at the timing corresponding to the energy of the level. Because of the resolution width of the apparatus, this dip will generally be very much wider and shallower than the "true" transmission dip (infinitely sharp resolution). Thus, in general, the true cross section at exact resonance will be many times larger than the value of σ_{max} corresponding to the bottom of the observed dip in the transmission curve. The position of the dip will give an indication of the position of the resonance if single, but resonances which are closely spaced relative to the resolution width will appear as a single dip. The "area" of a transmission dip, that is, the area between the experimental transmission curve and the transmission of the sample due to the scattering cross section, if the "true" transmission drops to zero, will depend on the sample thickness, the energy E_0, of the resonance and the product $\sigma_0\Gamma^2$, σ_0 being the cross section at exact resonance and Γ the full width of the level at half the maximum cross section.

* Publication assisted by the Ernest Kempton Adams Fund for physical research at Columbia University.

[1] L. J. Rainwater and W. W. Havens, Jr., Phys. Rev. 70, 136–153 (1946); W. W. Havens, Jr. and L. J. Rainwater, Phys. Rev. 70, 154–173 (1946).

[2] L. J. Rainwater, W. W. Havens, Jr., C. S. Wu, and J. R. Dunning, Phys. Rev. 71, 65–79 (1947); W. W. Havens, Jr., C. S. Wu, L. J. Rainwater, and C. L. Meaker, Phys. Rev. 71, 165–173 (1947); C. S. Wu, L. J. Rainwater, and W. W. Havens, Jr., Phys. Rev. 71, 174–181 (1947).

[3] L. J. Rainwater, W. W. Havens, Jr., J. R. Dunning, and C. S. Wu, Phys. Rev. 73, 733 (1948).

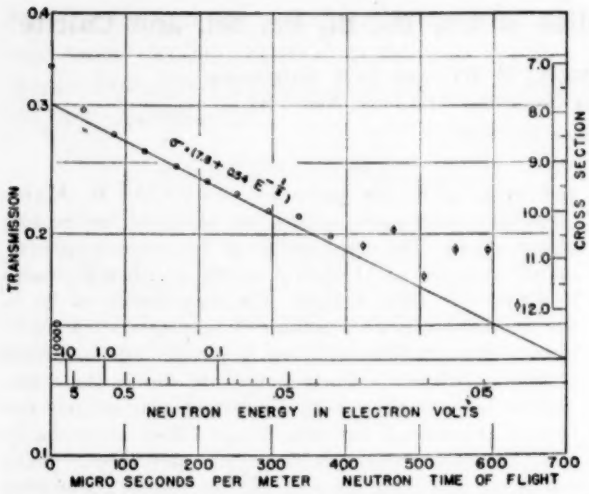

FIG. 1. The slow neutron transmission of 16.3 g/cm² of copper. The best $1/v$ line (0.05 ev to 3 ev) is $\sigma=(7.8+0.54E^{-\frac{1}{2}})$. Crystal interference effects cause the points below 0.05 ev to deviate above the $1/v$ line.

4. The time of flight scale is a $1/v$ scale. When the transmission is plotted on a logarithmic scale the cross section scale is linear and thus a cross sectional dependence linear in $1/v$ will give a straight line on this plot.

II. COPPER

The slow neutron transmission of Cu has been studied using three plates of commercial Cu, each 4.6 mm thick, to give a total sample thickness of 16.3 g/cm². The results of these measurements are presented in Figs. 1 and 2. The results shown in Fig. 1 were obtained when the region above 0.013 ev was investigated using broad resolution and those in Fig. 2 when the region above 3 ev was investigated using higher resolution.

The points in Fig. 1 between 0.06 ev and 1.0 ev are well matched by the $1/v$ relation $\sigma=(7.8+0.54E^{-\frac{1}{2}})$. This relation probably indicates the magnitudes of the free copper scattering cross section (7.8) and the $1/v$ absorption cross section ($0.54E^{-\frac{1}{2}}$) in the thermal region. The points below 0.05 ev are above the $1/v$ line and do not follow a smooth curve. This is to be expected as a result of slow neutron interference effects caused by the microcrystalline nature of the sample. The positions of the discontinuities in the transmission curve at low energies are for neutron wave-lengths which are multiples of the characteristic spacings between crystal lattice planes.

In Fig. 2 the transmission increases gradually with decreasing time of flight to the point corresponding to about 100 ev. For smaller timings (higher energies) there is a more rapid increase in transmission which continues to zero time except for the small dip near 3000 ev. This dip probably represents the lowest resonance level in one of the copper isotopes.

For a proper interpretation of Figs. 1 and 2 it is necessary to consider other information which has been obtained on the interaction of slow neutrons with copper.

Normal Cu consists[4] of 70.13 percent Cu^{63} and 29.87 percent Cu^{65}. Capture of a neutron by Cu^{63} produces Cu^{64} which has a 12.8-hour half-life and decays[4] by β^--emission (0.58 Mev max.), β^+-emission (0.66 Mev max.), or by K capture. Capture of a neutron by Cu^{65} produces β^--active (2.9 Mev max.) Cu^{66} of 5-minute half-life. The partial Cu cross sections due to these separate capture processes have been studied by activation measurements using thermal neutrons. Rasetti[5] obtained $\sigma_{capt.}=1.8$ due to Cu^{63} and 1.2 due to Cu^{65} giving $\sigma_{capt.}=3.0$ total. Sinma and Yamasaki[6] found $\sigma_{capt.}=1.3$ due to Cu^{63} and 1.5 due to Cu^{65} giving $\sigma_{capt.}=2.8$ total. Goldhaber and O'Neal[7] gave $\sigma_{capt.}=0.8$ due to Cu^{65}. Total absorption measurements have also been made using thermal neutrons. Coltman[8] obtained $\sigma_{abs.}=(4.3\pm0.3)$ and Coltman and Goldhaber[9] found $\sigma_{abs.}=(3.4\pm0.3)$. Volz[10] gave $\sigma_{capt.}=2.2$ to 2.6. Lichtenberger, Nobles, Monk, Kubetschek, and Dancoff[11] obtained $E_0=570$ ev for the Cu^{65} resonance using the boron method.[12] They also give values for the "activation integrals." These previous results for the absorption cross section are in good agreement with $\sigma_{abs.}=2.7$ at 0.4 ev from the $1/v$ line in Fig. 1. Previous studies[1, 3, 13] have indicated that the "effective energy" of previous "thermal neutron"

[4] G. T. Seaborg, Rev. Mod. Phys. 16, 1 (1944).
[5] Franco Rasetti, Phys. Rev. 58, 869 (1940).
[6] K. Sinma and F. Yamasaki, Phys. Rev. 59, 402 (1941).
[7] M. Goldhaber and R. D. O'Neal, Phys. Rev. 59, 109 (1941).
[8] J. W. Coltman, Phys. Rev. 59, 917 (1941).
[9] J. W. Coltman and M. Goldhaber, Phys. Rev. 69, 411 (1946).
[10] H. Volz, Zeits. f. Physik 121, 201 (1943).
[11] H. V. Lichtenberger, R. G. Nobles, G. O. Monk, H. Kubetschek, and S. M. Dancoff, Phys. Rev. 72, 164 (1947).
[12] H. A. Bethe, Rev. Mod. Phys. 9, 69 (1937).
[13] R. F. Bacher, C. P. Baker, and B. D. McDaniel, Phys. Rev. 69, 443 (1946).

measurements was ~0.04 ev rather than 0.025 ev corresponding to kT for room temperature.

The slow neutron cross section values obtained using resonance neutrons (energies above 1 ev) should give the free copper cross section since binding and interference effects should be unimportant in this region. Measurements using thermal neutrons will be markedly influenced by the microcrystalline state of the sample due to interference effects. The following values for the different cross section have been obtained using thermal neutrons: (a) Dunning *et al.*,[14] $\sigma_{tot.}=7.5$; (b) Mitchell, Murphy, and Whitaker,[15] $\sigma_{scatt.}=8.3$; (c) Goldhaber and Briggs,[16] $\sigma_{tot.}=11.9$, $\sigma_{scatt.}=8.6$; (d) Whitaker and Beyer,[17,18] $\sigma_{tot.}=(10.5\pm0.4)$; (e) Whitaker and Bright,[19] $\sigma_{tot.}=10.3$ and $\sigma_{scatt.}=5.5$. Nix and Clement[20] made a careful study of the effect of microcrystalline structure on the thermal cross section. They obtained $\sigma=(10.84\pm0.03)$ for cold-worked Cu (0.005-mm grain size) and $\sigma=(7.04\pm0.3)$ for a highly annealed (2.4 mm-grain size) sample, with several intermediate values for intermediate grain sizes. They were thus able to obtain a curve of "thermal cross section" *vs.* sample grain size. The value 10.84 is in good agreement with Fig. 1. Hanstein[21] obtained $\sigma_{tot.}=(8.3\pm0.3)$ using In resonance neutrons (1.44 ev).[1,2] This is in good agreement with the value for this energy in Fig. 1.

According to the theory of Feshbach, Peaslee, and Weisskopf[22] the scattering cross section should be very nearly equal to the value $4\pi R^2$ due to potential scattering (where R is the nuclear radius) when the neutron energy differs from that of the nearest resonance level by an amount which is not small compared to the spacing between levels. Since Cu may be considered a relatively light element, the spacing between neutron resonance levels would be expected[12] to be of the order of hundreds to thousands of ev. Therefore, the energy region below ~10 ev can be considered narrow compared to the average level spacing. Using the value $R=6.75\times10^{-13}$ cm for Cu given by Amaldi and Cacciapuoti[23] gives $4\pi R^2=5.7$ for the expected Cu cross section due to potential scattering. This is somewhat larger than the value $4\pi R^2=4.5$ given by Feshbach, Peaslee, and Weisskopf.[22] The observed value $\sigma=7.8$ in Figs. 1 and 2 probably indicates that the scattering cross section of one of the Cu isotopes is larger than $4\pi R^2$ as a result of the interference between potential and resonance scattering. Weisskopf's[22] theory predicts this effect when the neutron energy is near and just above the energy of the nearest resonance. On this basis the shape of the curve in Fig. 2 should be explained as due to the presence of a virtual level[1,12] with a resonance energy near zero neutron kinetic energy. The decrease in cross section above 100 ev would be interpreted as a return to the "potential" scattering cross section value at larger distances from the resonance. The shape of the increase also suggests that the virtual level is near −500 ev energy. Since there are two isotopes, each with non-zero spin, the level near 3000 ev in Fig. 2

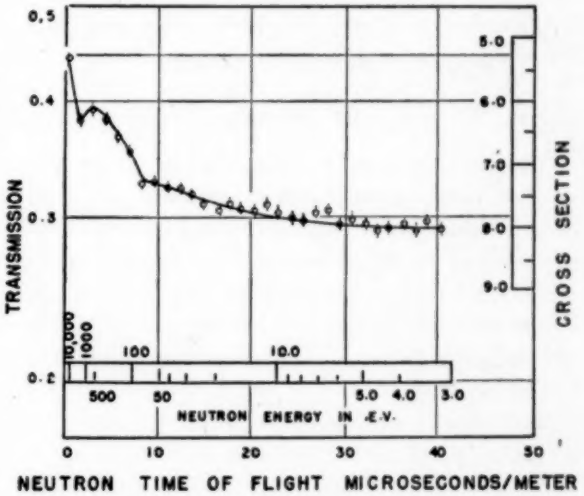

FIG. 2. The slow neutron transmission of 16.3 g/cm² of copper. This curve shows the small dip in transmission at 1.5 μsec./meter which indicates the presence of one or more resonance levels near 3000 ev.

[14] J. R. Dunning, G. B. Pegram, G. A. Fink, and D. P. Mitchell, Phys. Rev. **48**, 265 (1935).
[15] A. C. G. Mitchell, E. J. Murphy, and M. D. Whitaker, Phys. Rev. **50**, 133 (1936).
[16] M. Goldhaber and G. M. Briggs, Roy. Soc. Proc. **162A**, 127 (1937).
[17] M. D. Whitaker and H. G. Beyer, Phys. Rev. **55**, 1101 and 1124 (1939).
[18] H. G. Beyer and M. D. Whitaker, Phys. Rev. **57**, 976 (1940).
[19] M. D. Whitaker and W. C. Bright, Phys. Rev. **60**, 155 (1941).
[20] F. C. Nix and G. F. Clement, Phys. Rev. **68**, 159 (1945).
[21] Henry B. Hanstein, Phys. Rev. **59**, 489 (1941).
[22] H. Feshbach, D. C. Peaslee, and V. F. Weisskopf, Phys. Rev. **71**, 145 (1947).
[23] E. Amaldi and B. N. Cacciapuoti, Phys. Rev. **71**, 739 (1947).

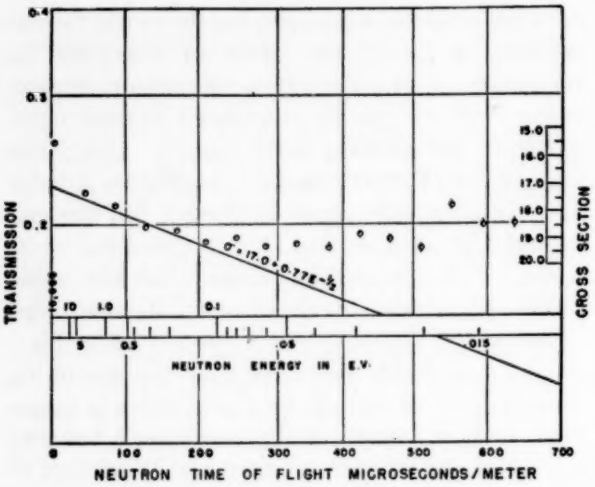

FIG. 3. The slow neutron transmission of 8.47 g/cm² of nickel. The best $1/v$ line (0.1−5 ev) is $\sigma=(17.0+0.77E^{-\frac{1}{2}})$. Crystal interference effects cause the points below 0.1 ev to deviate above the $1/v$ line.

may not correspond to the same compound nucleus which is responsible for the large scattering.

Measurements by Fields, Russell, Sachs, and Wattenberg[24] using photo-neutrons indicate that the cross section averages nearer $4\pi R^2$ at higher energies. They obtained $\sigma=8.0$, 6.2, 5.9, 5.3, and 3.8 at 24, 130, 140, 220, and 830 kev. Since the measurements in Fig. 2 were not taken with the highest resolution of the spectrometer, it is planned to study the resonance region above 50 ev again using much better resolution.

III. NICKEL

The slow neutron transmission of Ni has been studied using three plates of commercial Ni each 3.3 mm thick for a total sample thickness of 8.47 g/cm². The results shown in Fig. 3 were obtained when the region above 0.013 ev was studied using broad resolution and those in Fig. 4 when the region above 3 ev was investigated using better resolution.

The points in Fig. 3 between 0.1 and 3 ev may be used to locate the $1/v$ slope in the thermal region although it is less well defined than the similar region for Cu in Fig. 1. The "best straight line" indicated in Fig. 3 corresponds to $\sigma=(17.0+0.77E^{-\frac{1}{2}})$ in which the two terms may be interpreted as giving, respectively, the scattering and absorption cross sections. The points for energies below 0.1 ev lie above the $1/v$ line due to the microcrystalline interference effects as discussed for Cu. The points in Fig. 4 indicate that the cross section is relatively constant below 50 ev since the points lie close to the $1/v$ line of Fig. 3 in this region. The dip at 7μ sec./meter indicates that one or more unresolved resonance levels are present near 100 ev. For still higher energies the cross section decreases with the first point shown approaching the value of $4\pi R^2=5.7$ as discussed for Cu.

Normal Ni consists[4] of 67.4 percent Ni^{58}, 26.7 percent Ni^{60}, 1.2 percent Ni^{61}, and 3.8 percent Ni^{62}. Capture of a neutron by Ni^{62} produces β-active Ni^{63} of 2.6-hr. half-life. Capture of a neutron by the principal isotope Ni^{58} produces Ni^{59} which is β^+-active with a 15-year half-life,[25] while absorption by Ni^{60} and Ni^{61} produces stable isotopes. The total absorption cross section of Ni and the partial cross section for the production of the Ni^{63} activity have been measured using thermal neutrons. Sinma and Yamasaki[6] obtained $\sigma_{capt.}=0.35$ for the production of the Ni^{63} activity. Goldhaber and O'Neal[7] found $\sigma_{capt.}$

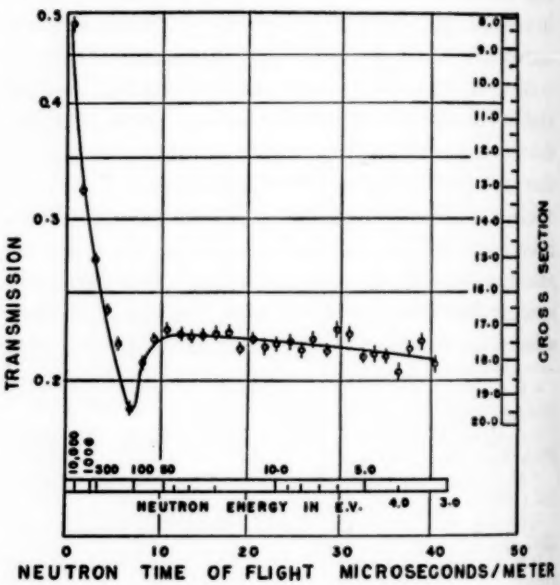

FIG. 4. The slow neutron transmission of 8.47 g/cm² of nickel. This curve shows the dip in transmission at 7 μsec./meter which indicates the presence of one or more resonance levels near 100 ev.

[24] R. Fields, B. Russell, D. Sachs, and A. Wattenberg, Phys. Rev. 71, 508 (1947).

[25] Isotope Committee, Science 103, 697 (1946).

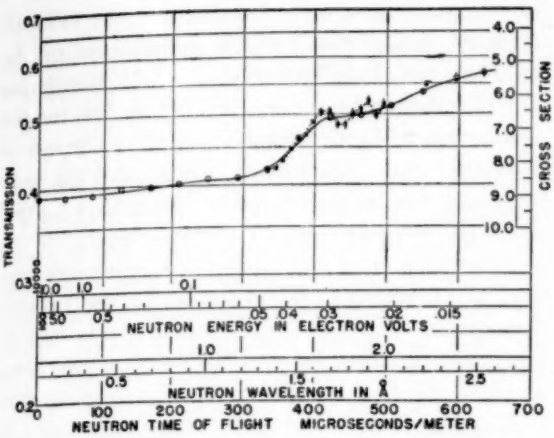

FIG. 5. The slow neutron transmission of 36.72 g/cm² of bismuth. The presence of the crystal interference effects makes the determination of the $1/v$ line impossible.

<0.03 for the same process. Coltman[8] gave $\sigma_{abs.}=(6.2\pm0.5)$. Coltmann and Goldhaber[9] obtained $\sigma_{abs.}=(5.6\pm0.5)$. Volz[10] gave $\sigma_{abs.}=3.6$. The $1/v$ line in Fig. 3 corresponds to $\sigma_{capt.}=3.8$ at 0.04 ev which is in agreement with the results of Volz[10] but is lower than those of Coltman and Goldhaber.[8,9]

The results given in Figs. 3 and 4 may be compared with previously measured values of $\sigma_{tot.}$ and $\sigma_{scatt.}$ using thermal and resonance neutrons. It should be remembered that the value of the "thermal" cross section depends on the microcrystalline structure of the sample as discussed under Cu. The following values of the different cross sections have been obtained using thermal neutrons: (a) Dunning *et al.*,[14] $\sigma_{tot.}=15.4$; (b) Mitchell, Murphy, and Whitaker,[15] $\sigma_{scatt.}=18$; (c) Goldhaber and Briggs,[16] $\sigma_{tot.}=19.7$ and $\sigma_{scatt.}=12.4$; (d) Whitaker and Beyer,[19] $\sigma_{tot.}=(19.8\pm0.5)$ for polycrystalline nickel and $\sigma_{tot.}=(14.1\pm1.2)$ for a single crystal of Ni (both 4.4 g/cm²): (e) Whitaker and Bright, $\sigma_{tot.}=21.2$ and $\sigma_{scatt.}=13.9$. Laslett[26] found no change in the Ni cross section when Ni was heated to above the Curie point. (This measurement was to test the possibility that the high scattering cross section is partly of ferromagnetic origin.) Mitchell and Varney[27] obtained $\sigma_{scatt.}=19.2$ for thermal neutrons, 11.9 for In resonance neutrons (1.44 ev), 13.5 for Ag resonance neutrons[2] (~5 ev) and 12 for I resonance neutrons[2] (~40 ev). Kimura[28] obtained $\sigma_{scatt.}=19$ for In resonance neutrons and 20 for thermal neutrons. Hanstein[21] obtained $\sigma_{tot.}=(16.1\pm0.8)$ using In resonance neutrons. The results of Figs. 3 and 4 are in agreement with the previous results for Ni to the extent that they indicate a definite value.

The value of scattering cross section as indicated in Fig. 4 is very large compared to the value $4\pi R^2=5.7$ for potential scattering. According to the theory of Feshbach, Peaslee, and Weisskopf[22] this would indicate the presence of a virtual level near zero energy (near relative to the level spacing) and the cross section should drop to $4\pi R^2$ for most of the region to the next level. In Fig. 4 the high value of the scattering cross section continues up to, and perhaps above, the level near 100 ev. Although this at first seems to contradict the theory, the fact that there are several isotopes probably means that one isotope is responsible for this level, while another (probably the principal Ni^{58} isotope) is responsible for the large scattering cross section. The extent of the region over which the scattering is large indicates an average level spacing of about 50,000 ev. which is not unreasonable for such a light nucleus. It is planned to investigate the region above 50 ev with much higher resolution to study this matter more carefully. The above conclusions are in agreement with the results of Fields, Russell, Sachs, and Wattenberg[24] using photo-neutrons. They obtained $\sigma=23$, 6.2, 4.2, 5.8, 3.7, and 3.5 at 24, 130, 140, 220, 620, and

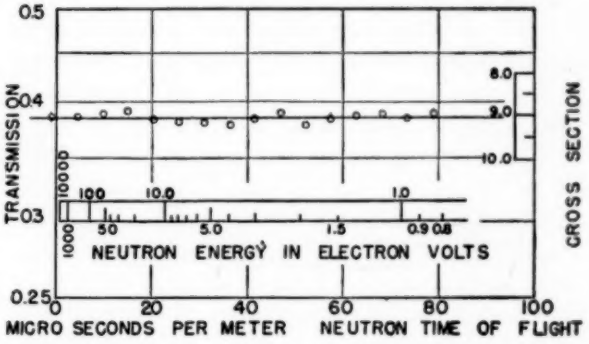

FIG. 6. The slow neutron transmission of 36.72 g/cm² of bismuth. The cross section is constant where crystal interference effects are not important to within the accuracy of the results.

[26] L. Jackson Laslett, Phys. Rev. **51**, 72 (1937).
[27] A. C. G. Mitchell and R. N. Varney, Phys. Rev. **52**, 282 (1937).
[28] N. Kimura, Phys. and Math. Soc. Japan, Proc. **22**, 391 (1940).

830 kev. This indicates that there is a strong resonance near 24 kev and shows that the cross section is close to the potential scattering value at the other energies.

IV. BISMUTH

The slow neutron transmission of Bi has been studied using a sample of 36.72 g/cm² thickness cast from C.P. Bi metal. The results of the transmission measurements are shown in Figs. 5 and 6. The results shown in Fig. 5 were obtained when the region above 0.013 ev was studied using broad resolution and those in Fig. 6 when the region above 0.8 ev was studied with higher resolution. There is no evidence of a 1/v slope in Fig. 5 since the curve rises after the first three points due to microcrystalline interference effects. In Fig. 6 the cross section is constant over the entire region to within the accuracy of the measurements and is equal to (9.0±0.2). This may be interpreted as the free Bi scattering cross section in the region studied. There is no evidence of any resonance dips although an investigation using higher resolution is planned and may indicate the presence of weak resonances.

Normal Bi consists[4] entirely of the 100 percent Bi^{209} isotope of spin 9/2. Capture of a neutron produces β^--active Bi^{210} (RaE) of 5 days half-life. Several measurements have been made of the absorption and activation capture cross sections

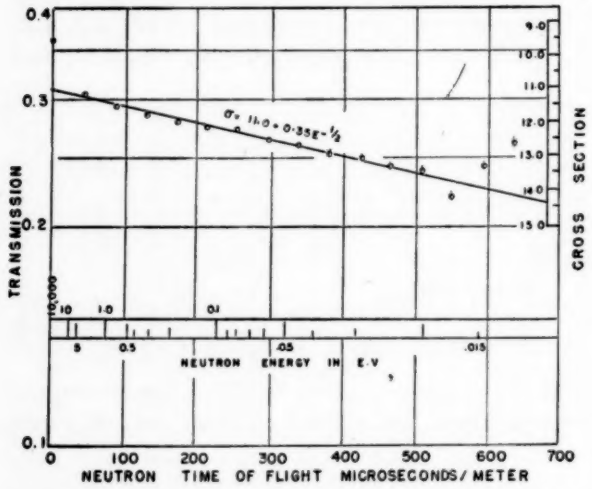

FIG. 7. The slow neutron transmission of 9.93 g/cm² of iron. The best 1/v line is $\sigma=(11.0+0.35E^{-\frac{1}{2}})$. The last three points deviate from the straight line because of the neutron interference due to the microcrystalline structure of the sample.

for thermal neutrons. Goldhaber and O'Neal[7] obtained $\sigma_{capt.}<0.1$ for the production of the RaD activity. Volz[10] found $\sigma_{abs.}=0.33$, Meulhause and Goldhaber[29] gave $\sigma_{abs.}\sim10^{-2}$ or less for the production of RaE. Considering all of the results it seems that the higher value of Volz may represent the effect of impurities in his sample since the capture should result entirely in the production of RaE. It is therefore not surprising that no 1/v slope was observed in the present measurements. Lead and bismuth are known to have abnormally low radiative capture cross sections for fast neutrons[22, 30] relative to neighboring elements, thus indicating that there is an anomalous level pattern for these nuclei probaby due to the relatively small binding energy of the captured neutron. The total cross section and the scattering cross sections should thus be essentially equal over a wide range of energies.

The following values of the different cross sections have been obtained using thermal neutrons: (a) Dunning *et al.*,[14] $\sigma_{tot.}=8.2$; (b) Mitchell, Murphy, and Whitaker,[15] $\sigma_{scatt.}=10.2$; (c) Goldhaber and Briggs,[16] $\sigma_{tot.}=8.9$ and $\sigma_{scatt.}=8.9$; (d) Rasetti,[31] $\sigma=6.6$ for a single crystal and $\sigma=8.3$ for the liquid. He subsequently obtained $\sigma=6.39$ for a single crystal using a room temperature source and 5.94 using a source at 80°K. Kimura[28] obtained $\sigma_{scatt.}=7.5$ for thermal neutrons and 8.3 for In resonance neutrons. Hanstein[21] obtained $\sigma=(8.7\pm0.5)$ using In resonance neutrons. Anderson, Fermi, and Marshall[32] obtained $\sigma=6.68$ using thermal neutrons and only 1.03 using the very low energy neutrons (~0.0015 ev or 7.15A wave-length) obtained by filtering pile neutrons through graphite. Fields, Russell, Sachs, and Wattenberg[24] obtained $\sigma=12.1$, 10.2, 9.7, 8.0, and 5.9 using 24, 130, 140, 220, and 830 kev photoneutrons.

The above values are in essential agreement with the results shown in Figs. 5 and 6 considering that the thermal values are structure dependent. The value $\sigma=9.0$ obtained from Fig. 6

[29] C. O. Muehlhause and M. Goldhaber, Phys. Rev. **57**, 976 (1940).
[30] D. J. Hughes, Phys. Rev. **70**, 106 (1946).
[31] Franco Rasetti, Phys. Rev. **58**, 321 (1940).
[32] H. L. Anderson, E. Fermi, and L. Marshall, Phys. Rev. **70**, 815 (1946).

is close to the value of $4\pi R^2=10$ for potential scattering.

V. IRON

The slow neutron transmission of iron has been measured using a 9.93 g/cm² thick sample of ordinary cold-rolled iron sheet. A spectrographic analysis of the sample by the Bureau of Standards indicated 0.01 to 1 percent Cr, Cu, and Mn and less than 0.01 percent of Ca, Co, Ge, Mg, Ni, Si, and Sn. The results of the transmission measurements above 0.013 ev using broad resolution are shown in Fig. 7. The experimental results between 0.02 ev and 2 ev are well matched by the straight line $1/v$ relation

$$\sigma=[11.0+0.35E^{-\frac{1}{2}}].$$

This indicates that the iron scattering cross section in this energy region is (11.0 ± 0.2) and the capture cross section is $0.35E^{-\frac{1}{2}}$. The deviation of the last three points in Fig. 7 from the straight line is due to microcrystalline interference effects.

The results of the transmission measurements above 3 ev using better resolution are shown in Fig. 8. The points for energies below about 200 ev closely follow the 1/v line of Fig. 7. For higher energies the cross section decreases rapidly to about 4. The scattering cross section for Fe is considerably higher than the value[22,23] $4\pi R^2=5.5$ for pure potential scattering. The explaination in this case is probably the same as for Cu and Ni. Normal Fe contains[4] mainly the 91.57 percent Fe^{56} plus 6.04 percent Fe^{54}, 2.11 percent Fe^{57}, and 0.28 percent Fe^{58}. On the basis of the theory of Feshbach, Peaslee, and Weisskopf[22] the large scattering cross section is probably the result of the interference between potential and resonance scattering due to a relatively near virtual level in Fe^{56}. The decrease in cross section above 200 ev is then due to the increased distance from the virtual level indicating that it is probably several thousand ev. below zero neutron energy. The level spacing[22] on this basis would be greater than 10,000 ev. This next resonance cannot be observed in Fig. 8. Further investigation of this sample above 50 ev. is planned using much better resolution.

The value of the capture cross section indicated from the 1/v slope in Fig. 7 may be compared with the results of absorption measurements using thermal neutrons. Coltman[8] obtained $\sigma_{abs.}=(2.1\pm0.2)$, Coltman and Goldhaber[9] found $\sigma_{abs.}=(2.05\pm0.15)$, and Volz[10] gave $\sigma_{abs.}=1.6$. These values are in good agreement with the result $\sigma_{abs.}=1.8$ at 0.04 ev from Fig. 7.

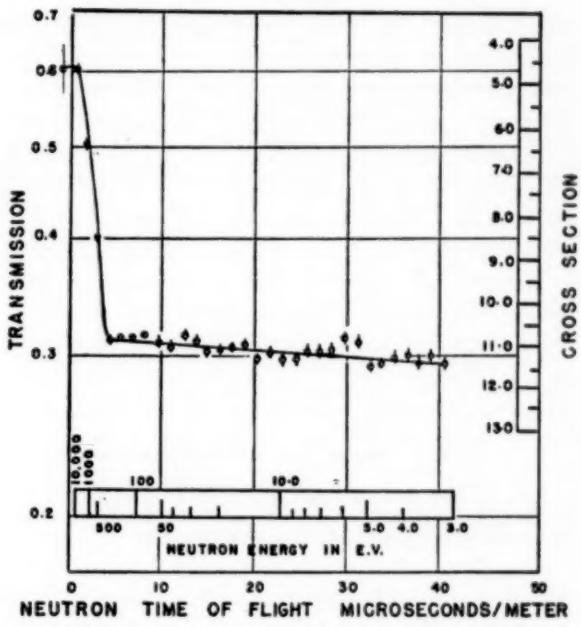

FIG. 8. The slow neutron transmission of 9.93 g/cm² of iron. The points for energies below 200 ev closely follow the $1/v$ line obtained from the results in Fig. 7.

It is also of interest to compare the results of Figs. 7 and 8 with previous measurements of $\sigma_{tot.}$ and $\sigma_{scatt.}$ cross sections using thermal and resonance neutrons, remembering that the resonance neutron cross sections should be directly comparable and the thermal values are structure sensitive. Dunning *et al.*[14] obtained $\sigma_{tot.}=12.0$ using thermal neutrons. Mitchell, Murphy, and Whitaker[15] found $\sigma_{scatt.}=10.6$ using thermal neutrons. Goldhaber and Briggs[16] gave $\sigma_{tot.}=13.6$ and $\sigma_{scatt.}=10.3$ using thermal neutrons. Whitaker and Beyer[17,18] obtained $\sigma=(12.0\pm0.2)$ for a 1.6 g/cm² thick sample of polycrystalline iron, (7.0 ± 0.1) for a 1.6 g/cm² single crystal of iron and (6.1 ± 1) for an 8.8 g/cm² single crystal of iron. Powers, Goldsmith, Beyer, and Dunning[33] obtained $\sigma=(12.0\pm0.4)$ using "room temperature" neutrons and (12.0 ± 1.0) using "liquid air" temperature neutrons. Whitaker and Bright[19]

[33] P. N. Powers, H. H. Goldsmith, H. G. Beyer, and J. R. Dunning, Phys. Rev. **53**, 947 (1938).

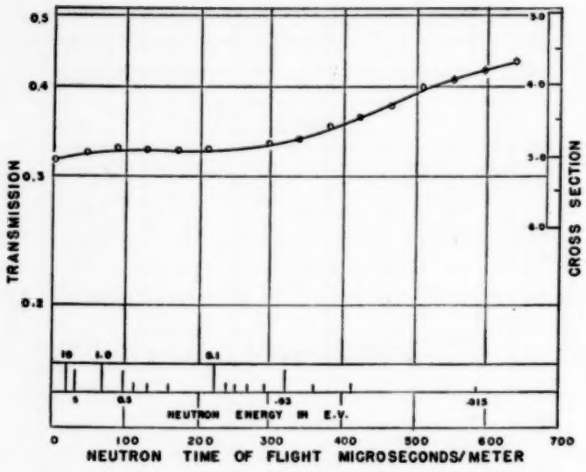

FIG. 9. The slow neutron transmission of 45.15 g/cm² of tin. The presence of crystal interference effects makes the determination of the $1/v$ line impossible.

found $\sigma_{tot.}=12.8$ and $\sigma_{scatt.}=9.5$ using thermal neutrons. Nix and Clement[20] investigated the effect of sample grain size on the thermal cross section and obtained $\sigma=(13.06\pm0.4)$ for cold-worked Fe (0.077-mm grain size), and (11.39 ±0.3) for annealed Fe (0.127-mm grain size). Laslett[26] observed no change in the thermal neutron cross section when a sample was heated above the Curie point during an investigation to see if the large cross sections of Fe and Ni are due to their ferromagnetic properties. Mitchell and Varney[27] obtained $\sigma_{scatt.}=9.8$ using thermal neutrons, 10.0 using Rh resonance neutrons, 11.6 using Ag resonance neutrons, and 10.8 using I resonance neutrons. Kimura[28] found $\sigma_{scatt.}=9.7$ using thermal neutrons, and 8.5 using In resonance neutrons. Hanstein[21] obtained $\sigma=(11.1$ $\pm0.3)$ using In resonance neutrons. Using photo-neutrons Field, Russell, Sachs, and Wattenberg[24] obtained $\sigma=2.2$, 4.1, 3.9, 3.3, and 2.7 using 24, 130, 140, 220, and 830 kev neutrons. These results suggest that there is a resonance above 24 kev and show that the cross section is nearer the potential scattering value at higher energies.

VI. TIN

The slow neutron transmission of tin has been measured using a sample of 45.15g/cm² thickness which was made by melting mossy C.P. tin and molding to the desired shape. A quantitative spectrographic analysis of the sample showed an indium impurity of (0.03 ± 0.01) percent. A qualitative spectrographic analysis showed a Pb impurity of the order of 0.05 percent; Sb impurities of the order of 0.005 percent. For all other metals the prominent lines were not apparent. Therefore, the impurity was probably less than 0.05 percent for arc insensitive materials and less than 10^{-5} percent for arc sensitive materials. The results of the measurements above 0.013 ev using broad resolution are shown in Fig. 9. The rise in transmission for larger timings is due to microcrystalline interference effects and probably masks any $1/v$ type slope[34] that may be present. The points between 0.09 and 1 ev all have essentially constant cross section values equal to (4.9 ± 0.1). A "thermal" neutron absorption cross section of (0.53 ± 0.05) has been observed by Coltman and Goldhaber[3] and a value $\sigma_{abs.}=0.4$ was obtained by Volz.[10] On the basis of these values for the thermal absorption cross section an increase of 0.2 in σ should be observed between 1 ev and 0.09 ev in Fig. 9.

The results of the measurements above 0.8 ev using higher resolution are shown in Fig. 10. The dip near 1.4 ev is probably due to a slight In impurity in the sample. From the size of the dip an In impurity of about 0.05 percent is indicated which is in agreement with the spectroscopic measurements. The small dip near 6 ev may be

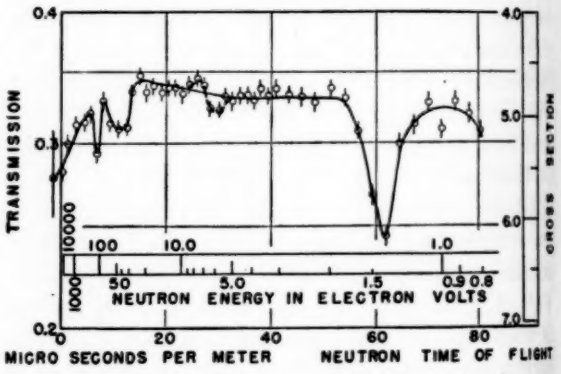

FIG. 10. The slow neutron transmission of 45.15 g/cm² of tin. The transmission dip at 1.44 ev is caused by a 0.03 percent indium impurity in the sample. The small dip at 6 ev may be spurious. The dips near 50 ev and 100 ev are probably real, although exact location of the resonances is difficult with these data.

[34] M. E. Nahmías, Comptes rendus **202**, 1050 (1936); R. Naidu, Nature **137**, 578 (1936); G. T. Livingood and J. J. Seaborg, Phys. Rev. **55**, 667(1939); H. Volz, Zeits. f. Physik **121**, 201 (1943).

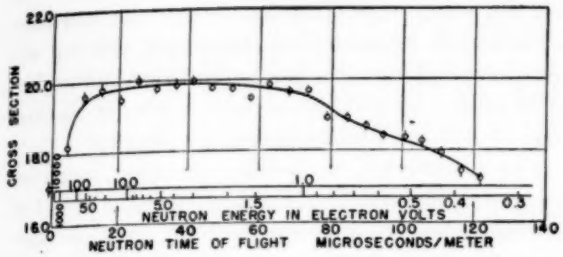

FIG. 11. The slow neutron cross section of calcite. The cross section begins to decrease just below 1.0 ev because of the crystal structure of the sample.

spurious or may represent a weak resonance level for one of the ten stable isotopes of Sn. The dips near 50 and 100 ev are probably real although the exact location of the resonance or resonances is difficult with the present data. Higher resolution will be used to determine more accurately the position and magnitude of these dips. The fact that the cross section increases near zero time of flight is also of interest as it indicates that there are probably levels above 1000 ev.

The results of Figs. 9 and 10 may be compared with values previously obtained for the total and scattering cross sections. Dunning *et al.*[14] obtained $\sigma_{tot.}=4.0$ using thermal neutrons. Mitchell, Murphy, and Whitaker[15] found $\sigma_{scatt.}=4.1$, and Goldhaber and Briggs[16] gave $\sigma_{scatt.}=4.9$ using thermal neutrons. Hanstein[21] obtained $\sigma_{tot.}=(5.7\pm0.3)$ using In resonance neutrons. Fields, Russell, Sachs, and Wattenberg[24] obtained $\sigma=5.9$, 6.4, 6.4, 6.3, 6.8, and 6.7 using 24, 130, 140, 220, 620, and 830 kev photoneutrons. The value of $4\pi R^2$ for potential scattering of 6.6 given by Feshbach, Peaslee, and Weisskopf[22] is in better agreement with the above experimental results than the value 9 obtained using the value of Amaldi and Cacciapuoti[23] for the Sn nuclear radius.

VII. CALCITE

The slow neutron transmission of a calcite crystal has been measured using the Tyndall Nicol Prism of Columbia University which has a sample thickness of 24.53 g/cm². The results of these transmission measurements using broad resolution are presented in Figs. 11 and 12. The effective $CaCO_3$ cross section decreases from about 20 in the energy region where the nuclei should scatter independently to about 3.5 in the lowest energy region studied.

Using the values $\sigma=3.7$ and 4.8, respectively, for the free oxygen and carbon cross sections, a value of 4.1 is indicated for the free Ca cross section. This is in good agreement with Rassetti's value[31] of (4.4 ± 0.2) using thermal neutrons. The values $\sigma_{tot.}=11.0$ obtained by Dunning *et al.*[14] and $\sigma_{scatt.}=9.5$ obtained by Goldhaber and Briggs[16] for Ca were probably due to hydrogenous impurities in the samples.

Carbon and oxygen each have only one important stable isotope, each with zero spin. They both have very small capture cross sections as is indicated by their use as moderator materials in graphite and heavy water piles. Thus, for example, Anderson, Fermi, Wattenberg, Weil, and Zinn[35] obtained $\sigma_{abs.}=0.0049$ for graphite using thermal neutrons and Muehlhouse and Goldhaber[29] obtained $\sigma_{abs.}\sim10^{-2}$ or less for

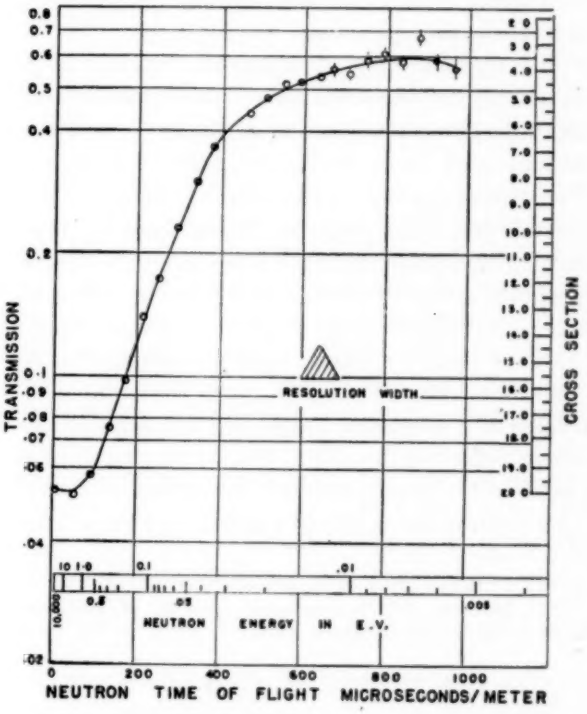

FIG. 12. The slow neutron transmission of calcite. The effective cross section of calcite decreases from 20 where the nuclei should scatter independently to about 3.5 at 0.008 ev. The principle charge occurring between 1.0 ev and 0.02 ev.

[35] H. L. Anderson, E. Fermi, A. Wattenberg, G. L. Weil, and W. H. Zinn, Phys. Rev. **72**, 16 (1947).

oxygen. Although there are seven stable Ca isotopes,[4] normal Ca consists mainly of the 96.96 percent Ca^{40} isotope which forms radioactive Ca^{41} of 8.5-day half-life on neutron capture. Measurements of the absorption cross section for Ca for thermal neutrons show that it is small compared to the residual $CaCo_3$ cross section of 3.5. Coltman[8] obtained $\sigma_{abs.}=(0.50\pm0.04)$ and Coltman and Goldhaber[9] obtained (0.37 ± 0.04). Volz[10] gave $\sigma_{abs.}=0.28$. Subtracting the value $\sigma_{abs.}\sim0.3$ to 0.4 from Rassetti's value $\sigma_{tot.}=(4.4\pm0.2)$ gives a result in good agreement with the value 4.1 from Fig. 11 obtained as described above.

The most extensive previous investigation of the effective $CaCo_3$ cross section for calcite at low energies was made by Rasetti[31] who obtained $\sigma=6.6$ for a 10.0 g/cm² thick sample of optical grade iceland spar using thermal neutrons. He showed that $\sigma_{eff.}$ increases with decreasing crystal size in ground crystals and showed that the thermal neutrons transmitted through calcite have their average energy lowered.

The transparency of crystalline materials to low energy neutrons has been investigated experimentally using the thermal neutrons from RaBe sources and using monochromatic neutrons.[32] The theory of the scattering of neutrons by crystals has been given by Wick[36] and by Halpern, Hammermesh, and Johnson.[37] A simple qualitative explanation can be given in terms of wave scattering usually applied to x-rays. When the slow neutron wave-length is comparable to the crystal lattice spacing there is strong scattering only when the conditions are satisfied for Bragg reflection by the different sets of crystal planes. This gives complete scattering of certain very narrow wave-length regions and very little for the other wave-lengths. When the neutron wave-length is more than twice the spacing of the crystal planes the Bragg condition cannot be satisfied so the total cross section should be due only to capture and incoherent scattering.

The incoherent scattering at long neutron wave-lengths must be ~2.5 after a value of ~1.0 is subtracted for the Ca capture cross section (note the $1/v$ factor increase from the "thermal" value). This measurement was made at the request of Professor Otto Halpern and the cross section was found to be unexpectedly large and difficult to explain on the basis of present theories. The residual cross section can, perhaps, be accounted for by the following causes of incoherent scattering.

1. Isotope effects: The elements all have only one main isotope each and these each have zero spin, so this effect should not be important.
2. Temperature effects: The temperature of the sample is not small compared to its Debye temperature.
3. Crystal imperfections: This should not be important for the Tyndall Nicol.

The exact manner in which the effective cross section decreases in Fig. 12 is of interest. It is seen that the main change in cross section occurs between about 1 ev and 0.02 ev with the half-value point near 0.1 ev. It is evident from Fig. 11 that a calcite crystal filter will lower the energy of a transmitted beam of thermal spectrum neutrons as observed by Rasetti.[31]

ACKNOWLEDGMENTS

We wish to thank Miss Miriam Levin, who assisted with the numerous calculations involved in this paper, Mr. Royal Schweiger, and other members of the cyclotron staff who aided with these measurements. This document is based on work performed under Contract AT-30-1-Gen-72 for the Atomic Energy Commission at Columbia University.

[36] G. C. Wick, Phys. Zeits. 38, 403, 689 (1937).
[37] O. Halpern, M. Hammermesh, and M. H. Johnson, Phys. Rev. 59, 981 (1941).

Neutron-Proton and Proton-Proton Scattering at High Energies*

JULIUS ASHKIN
*University of Rochester, Rochester, New York**

AND

TA-YOU WU**
University of Michigan, Ann Arbor, Michigan

(Received December 26, 1947)

The tensor force has been taken into account in calculating the neutron-proton and proton-proton scattering at energies in the range from 100 to 200 Mev. Most of the calculations are performed in the Born approximation using a square well potential and the exchange models of Rarita and Schwinger. The rigorous scattering theory has also been applied to the neutron-proton scattering with the symmetrical force model at 100 and 200 Mev. The results show that the Born approximation is inaccurate at 100 Mev but not bad at 200 Mev. Comparison with the experimental neutron-protron scattering at 90 Mev shows that the theoretical cross section for symmetrical forces is too large by a factor of about 1.6.

THE scattering of neutrons by protons at energies up to 80 Mev has recently been calculated by Camac and Bethe.[1] Throughout this work central forces alone were used, the tensor force being consistently neglected. The primary object was to investigate the scattering under different assumptions concerning the exchange character of the forces and their range.

In the present article the scattering has been calculated in the higher energy range from 100 to 200 Mev, taking account of the tensor forces. For this we have used the square well potential adjusted by Rarita and Schwinger[2] to fit the ground state of the deuteron and the low energy neutron-proton scattering. Calculations were made for three types of forces:[2] ordinary forces, Majorana (spatial) exchange forces, and "symmetric" exchange forces. The work may therefore be regarded as an extrapolation of the results of Rarita and Schwinger to the high energy range.

Preliminary measurements at Berkeley of the neutron-proton scattering at 90 Mev indicate important qualitative differences from all three of the above exchange models. The experiment is consistent with a force containing equal amounts of ordinary interaction and spatial exchange.[3] We feel, nevertheless, that the present calculations are worth reporting. The lack of agreement with experiment is in itself interesting. Further, the exact calculations at 100 and 200 Mev, which were made with the symmetrical forces, should serve as a valuable check on any approximate method for obtaining the cross section.

In Section I the neutron-proton and the proton-proton scattering has been calculated in the Born approximation for energies 100, 150, and 200 Mev. In IA we obtain the amplitude scattered by the tensor force alone in the Born approximation, and in IB and C the amplitudes are combined according to the three exchange models to give the differential cross section. Section II contains an *exact* calculation of the neutron-proton scattering for the symmetric force model. Comparison with I shows that the Born approximation is fairly good at 200 Mev but is untrustworthy at 100 Mev.

I. SCATTERING IN THE BORN APPROXIMATION

A. Effect of the Tensor Forces

Since the operator representing the tensor force between neutron and proton gives zero when applied to any singlet spin function, we need consider only the triplet scattering in this section. Separating out the motion of the center of mass, the wave function in the relative coor-

* This work was supported in part by the Office of Naval Research Contract N6ori-126 T. O. II.

** At present at Columbia University, New York, New York.

[1] M. Camac and H. A. Bethe, Phys. Rev. **73**, 191 (1948).

[2] W. Rarita and J. Schwinger, Phys. Rev. **59**, 436 (1941); Phys. Rev. **59**, 556 (1941).

[3] R. Serber, private communication.

dinate system representing the initial incident wave will be of the form

$$\psi_{\text{inc}}=\exp(ik\mathbf{n}_0\cdot\mathbf{r})\sum_{m_s=-1}^{1}a_{m_s}\chi_{m_s}. \quad (1)$$

Here $\mathbf{r}$ is the vector from proton to neutron, $\mathbf{n}_0$ is a unit vector in the direction of the initial relative motion, and $\hbar k\mathbf{n}_0$ is the momentum of the incident neutron in the center of mass coordinate system. The χ_{m_s} ($m_s=1, 0, -1$) are the three triplet spin functions taken for convenience with respect to $\mathbf{n}_0$ as axis of quantization, and the a_{m_s} are three arbitrary constants.

Under the influence of the tensor force the spin function will, in general, change upon scattering, giving rise to a scattered wave of asymptotic form

$$\psi_{\text{scatt}}\sim(1/r)e^{ikr}\sum_{m_s'=-1}^{1}\chi_{m_s'}\times\sum_{m_s=-1}^{1}\mathcal{S}_{m_s'm_s}(\theta,\varphi)a_{m_s}. \quad (2)$$

The amplitude of the scattered wave in the direction θ, φ with respect to $\mathbf{n}_0$ depends on the azimuthal angle φ as well as on the polar angle θ, since the tensor force is non-central. The angular dependence of the matrix of coefficients $\mathcal{S}_{m_s'm_s}(\theta,\varphi)$ gives a complete description of the scattering of any wave with definite initial spin state. In this section we shall calculate this matrix in the Born approximation. In II we shall use the rigorous scattering theory.

In most experiments the neutrons in the incident beam will be unpolarized with respect to spin. To find the triplet scattering cross section per unit solid angle in this case we must, therefore, average the square modulus of the scattered amplitude in (2) over the phases of the three amplitudes a_{m_s} of the triplet spin functions. Since the χ_{m_s} are orthogonal and normalized to unity, and since $a_{m_s}^*a_{m_s''}$ averages to zero if $m_s\neq m_s''$ and to $\frac{1}{3}$ if $m_s=m_s''$, we find

$$\sigma_{\text{trip}}=\text{Average}\Big(\sum_{m_s}\sum_{m_s'}\sum_{m_s''}\mathcal{S}^*_{m_s'm_s}\mathcal{S}_{m_s'm_s''}a^*_{m_s}a_{m_s''}\Big)=\tfrac{1}{3}\sum_{m_s'}\sum_{m_s''}|\mathcal{S}_{m_s'm_s''}|^2. \quad (3)$$

The Born approximation for scattering problems[4] gives a simple explicit expression for the asymptotic scattered wave in terms of the interaction potential V between the neutron and proton.

$$\psi_{\text{scatt}}\sim-(1/r)e^{ikr}(M/4\pi\hbar^2)\times\int\exp(-ik\mathbf{n}\cdot\mathbf{r})V\psi_{\text{inc}}d\mathbf{r}, \quad (4)$$

M is the neutron or proton mass and $\mathbf{n}$ is the unit vector in the direction of scattering. If we define a set of matrix elements $V_{m_s'm_s}(r)$ by the equation

$$V\chi_{m_s}=\sum_{m_s'=-1}^{1}V_{m_s'm_s}(r)\chi_{m_s'}, \quad (5)$$

we find, from (1) and (4)

$$\mathcal{S}_{m_s'm_s}(\theta,\varphi)=-(M/4\pi\hbar^2)\int\exp(-ik\mathbf{n}\cdot\mathbf{r})\times V_{m_s'm_s}(r)\exp(ik\mathbf{n}_0\cdot\mathbf{r})d\mathbf{r}. \quad (6)$$

In the case of exchange forces, $V_{m_s'm_s}(r)$ will in general contain an operator which exchanges proton and neutron, i.e., changes $\mathbf{r}$ to $-\mathbf{r}$. It is therefore essential to keep the order of the factors in (6) as it is instead of combining the exponentials as is usually done in atomic scattering problems.

The linearity of the scattered amplitude in the interaction potential V allows us to calculate separately the amplitude scattered by the tensor force and by the central forces, and then to combine the two at the end according to whatever model of the forces one wishes to consider. Apart from a possible Majorana (spatial) exchange operator whose effect will be discussed later, the term in the potential containing the tensor force will be of the form $-S_{12}J(r)$, where $-J(r)$ gives the shape of the potential and

$$S_{12}=3\frac{(\boldsymbol{\sigma}_1\cdot\mathbf{r})(\boldsymbol{\sigma}_2\cdot\mathbf{r})}{r^2}-\boldsymbol{\sigma}_1\cdot\boldsymbol{\sigma}_2. \quad (7)$$

$\boldsymbol{\sigma}_1$ and $\boldsymbol{\sigma}_2$ are the spin operators of neutron and proton, respectively.

In calculating the amplitude scattered by the tensor force, however, we shall not expand $S_{12}\chi_{m_s}$ as in (5), but rather perform the integral

[4] Mott and Massey, *Theory of Atomic Collisions* (The Clarendon Press, Oxford, 1933), p. 88.

in (4) directly treating the spin operators simply as constant vectors in the spatial integration. The result is:

$$(M/4\pi\hbar^2)\int \exp(ik(\mathbf{n}_0-\mathbf{n})\cdot\mathbf{r})J(r) \times\{(3/r^2)(\boldsymbol{\sigma}_1\cdot\mathbf{r})(\boldsymbol{\sigma}_2\cdot\mathbf{r})-\boldsymbol{\sigma}_1\cdot\boldsymbol{\sigma}_2\}d\mathbf{r} = C(\theta)\mathcal{T}(\theta,\varphi), \quad (8)$$

where

$$C(\theta)=-(M/\hbar^2)\int_0^\infty r^2J(r) \times\left(\frac{\sin Kr}{Kr}-3\frac{\sin Kr-Kr\cos Kr}{(Kr)^3}\right)dr,$$

$$K=k|\mathbf{n}_0-\mathbf{n}|=2k\sin\tfrac{1}{2}\theta, \quad (8a)$$

and

$$\mathcal{T}(\theta,\varphi)=\boldsymbol{\sigma}_1\cdot\boldsymbol{\sigma}_2-3\sigma_{1,\,\mathbf{n}_0-\mathbf{n}}\sigma_{2,\,\mathbf{n}_0-\mathbf{n}}. \quad (8b)$$

$\mathcal{T}$ is an angular average of the tensor operator weighted by $\exp[ik(\mathbf{n}_0-\mathbf{n})\cdot\mathbf{r}]$. $\sigma_{1,\,\mathbf{n}_0-\mathbf{n}}$ and $\sigma_{2,\,\mathbf{n}_0-\mathbf{n}}$ are the components of $\boldsymbol{\sigma}_1$ and $\boldsymbol{\sigma}_2$ in the direction of $\mathbf{n}_0-\mathbf{n}$, i.e., in the direction of the momentum transfer.

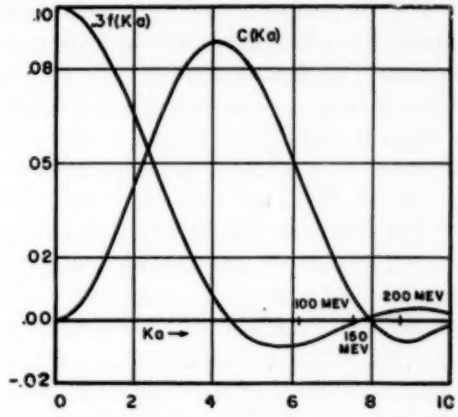

FIG. 1. The amplitude $c(Ka)$ scattered by the tensor force for a square well potential. The central force amplitude $f(Ka)$ (multipled by 0.3) is given for comparison.

To find the contribution to the matrix $\mathcal{S}$ of (6) we need to know the result of applying the operator $\mathcal{T}$ to the triplet spin functions. Defining the matrix elements of $\mathcal{T}$ by the equation

$$\mathcal{T}\chi_{m_s}=\sum_{m_s'=-1}^{1}\mathcal{T}_{m_s'm_s}(\theta,\varphi)\chi_{m_s'},$$

we find, after a simple calculation,

$$\{\mathcal{T}_{m_s'm_s}(\theta,\varphi)\}=\begin{array}{c|ccc} m_s'\backslash m_s & 1 & 0 & -1 \\ \hline 1 & -\frac{1}{2}(1-3\cos\theta) & (3/\sqrt{2})\sin\theta e^{-i\varphi} & -3\cos^2(\theta/2)e^{-2i\varphi} \\ 0 & (3/\sqrt{2})\sin\theta e^{i\varphi} & 1-3\cos\theta & -(3/\sqrt{2})\sin\theta e^{-i\varphi} \\ -1 & -3\cos^2(\theta/2)e^{2i\varphi} & -(3/\sqrt{2})\sin\theta e^{i\varphi} & -\frac{1}{2}(1-3\cos\theta) \end{array} \quad (9)$$

The azimuthal angle φ of the direction of scattering enters only in the off-diagonal elements where it enters in terms of unit modulus. Since the remaining central interaction in V contributes only additional diagonal terms to the matrix $\mathcal{S}$ of (6), we see that in the averaging process (3) for the cross section there is no dependence on φ. For an unpolarized incident beam the scattering is axially symmetric.

It is also evident from (9) that the sum of the diagonal elements of $\mathcal{T}$ vanishes. This is important since it leads to the result that in the Born approximation the cross section (3) is composed additively of a contribution from the tensor forces and one from the central forces. The central forces give the same contribution to each diagonal element of $\mathcal{S}$ since they do not mix the triplet spin functions. In the calculation of the triplet cross section (3) the sum of the squares of the diagonal elements of $\mathcal{S}$ will contain cross terms between tensor force and central force amplitudes of the form: central force amplitude multiplied by the sum of the diagonal elements of $\mathcal{T}$. Since this vanishes, the above-mentioned additivity follows.

If the function $J(r)$, giving the shape of the nuclear potential, is taken as a square well of range a and depth V, evaluation of the function $C(\theta)$ of (8a) is simple:

$$C(\theta)=a\frac{MVa^2}{\hbar^2}\frac{1}{(Ka)^3}\left\{3\int_0^{Ka}\frac{\sin t}{t}dt -4\sin Ka+Ka\cos Ka\right\}. \quad (10)$$

Thus, $C(\theta)$ is proportional to a dimensionless function of Ka which may be calculated once for all energies. This function, which we call $c(Ka)$, is plotted in Fig. 1. For any given energy, Ka varies from 0 to $2ka$ as the angle of scattering in the center of mass system varies from 0 to π. On the graph there are indicated the values of $2ka$ for 100, 150, and 200 Mev calculated for the range $a=2.80\times10^{-13}$ cm. In this energy range $C(\theta)$ has its maximum value somewhere between 50° and 80° as we can see readily from the graph. This has the effect of bolstering up the triplet scattering cross section for intermediate angles. The vanishing of $C(\theta)$ for $\theta=0$ is not a special property of the square well, but holds for any potential $J(r)$ which does not have too bad a singularity at $r=0$. In particular it holds for the Yukawa-type potential.

B. Neutron-Proton Cross Sections Corresponding to Various Types of Exchange

In this section we shall calculate the neutron-proton scattering cross section using the nuclear force models of Rarita and Schwinger.[2] For states of even parity all the models must give the same potential since they are adjusted to fit the ground state of the deuteron, and the low energy neutron-proton scattering. The former gives the potential for triplet spin states and the latter for singlet. These have the form

$$\begin{aligned} {}^3V_{\text{even}} &= -(1+\gamma S_{12})J(r), \\ {}^1V_{\text{even}} &= -(1-2g)J(r). \end{aligned} \tag{11}$$

$J(r)$ is taken as a square well of depth 13.89 Mev and range $a=2.80\times10^{-13}$ cm, $\gamma=0.775$ and $1-2g=0.857$. S_{12} is the tensor operator (7).

The differences between the models arise in the states of odd parity which play an increasingly important role as the energy increases. Three cases are chosen. (i) *Ordinary forces* in which the potential is the same for odd as it is for even parity, (ii) *Majorana exchange forces* in which the potential changes sign in going from even to odd parity, and (iii) "*Symmetric*" *exchange forces* described by

$${}^3V_{\text{odd}} = -\tfrac{1}{3}\,{}^3V_{\text{even}}, \quad {}^1V_{\text{odd}} = -3\,{}^1V_{\text{even}}.$$

This dependence of the potential on the parity of the wave function may be described alternatively in terms of the Majorana exchange operator, P_M, which interchanges the spatial coordinates of the two particles.[5] Thus, since P_M does not affect wave functions of even parity but changes the sign of a wave function of odd parity, we have

exchange forces:

$${}^3V_{\text{exch}} = P_M\,{}^3V_{\text{even}}, \quad {}^1V_{\text{exch}} = P_M\,{}^1V_{\text{even}}; \tag{12a}$$

symmetric forces:[6]

$$\begin{aligned} {}^3V_{\text{sym}} &= \tfrac{1}{3}(1+2P_M)\,{}^3V_{\text{even}}, \\ {}^1V_{\text{sym}} &= -(1-2P_M)\,{}^1V_{\text{even}}. \end{aligned} \tag{12b}$$

The effect of the P_M operator on the scattered amplitude is strikingly demonstrated in the exchange force case (12a). Insertion of this potential into (4) produces a change[7] in ψ_{inc} from $\exp[ik\mathbf{n}_0\cdot\mathbf{r}]$ to $\exp[-ik\mathbf{n}_0\cdot\mathbf{r}]$. This has the same effect, however, as changing $\mathbf{n}$ to $-\mathbf{n}$ in $\exp[-ik\mathbf{n}\cdot\mathbf{r}]$ and leaving ψ_{inc} alone. As a result, the amplitude scattered in the direction $-\mathbf{n}$ with exchange forces is identical in the Born approximation with the amplitude in the direction $\mathbf{n}$ with ordinary forces. The exchange forces produce a simple exchange of identity between the interacting particles. Thus, if a beam of high energy neutrons is incident on a material containing protons in the laboratory system, the pattern of scattered particles will contain a large fraction of energetic protons peaked in the forward direction. Recent experiments at Berkeley[3] show such an effect but indicate an exchange interaction more complicated than the simple exchange model (12a). The possibility of such a phenomenon was first pointed out by Wick and Bhabha soon after the exchange forces were introduced into nuclear physics.

With this observation on the effect of the operator P_M we may write down immediately the scattered amplitudes for each model. Denoting by

$$F(\theta) = (M/4\pi\hbar^2)\int \exp[ik(\mathbf{n}_0-\mathbf{n})\cdot\mathbf{r}]J(r)d\mathbf{r}$$

$$= (M/\hbar^2)\int_0^\infty (\sin Kr/Kr)J(r)r^2dr, \tag{13}$$

[5] H. A. Bethe, *Elementary Nuclear Theory* (John Wiley and Sons, Inc., New York, 1947), pp. 80–84.

[6] In the isotopic spin notation the potential for symmetric forces may be written $-\tfrac{1}{3}\tau_1\cdot\tau_2\sigma_1\cdot\sigma_2 V_{\text{even}}$.

[7] ψ_{inc} is now considered to include the singlet as well as the triplet part of the incident wave.

the amplitude scattered in the direction $\mathbf{n}$ by a central force of potential $-J(r)$, we have for the triplet amplitudes (6), according to (11), (12), and (8):

ordinary:

$$S_{m_s'm_s}(\theta,\varphi)=F(\theta)\delta_{m_s'm_s}+\gamma C(\theta)\mathcal{T}_{m_s'm_s}(\theta,\varphi),$$

exchange:

$$S_{m_s'm_s}(\theta,\varphi)=F(\pi-\theta)\delta_{m_s'm_s}+\gamma C(\pi-\theta)\mathcal{T}_{m_s'm_s}(\pi-\theta,\pi+\varphi),$$

symmetric:

$$S_{m_s'm_s}(\theta,\varphi)=\tfrac{1}{3}\{F(\theta)+2F(\pi-\theta)\}\delta_{m_s'm_s}+\tfrac{1}{3}\gamma\{C(\theta)\mathcal{T}_{m_s'm_s}(\theta,\varphi)+2C(\pi-\theta)\mathcal{T}_{m_s'm_s}(\pi-\theta,\pi+\varphi)\}. \quad (14)$$

$\pi-\theta$ and $\pi+\varphi$ are the polar and azimuthal angles of $-\mathbf{n}$ with respect to the incident direction $\mathbf{n}_0$. $\delta_{m_s'm_s}$ is unity or zero according as m_s' and m_s are equal or unequal.

For the singlet amplitudes we have, according to (11), (12), and (13):

$$\begin{aligned}&\text{ordinary:} && (1-2g)F(\theta),\\ &\text{exchange:} && (1-2g)F(\pi-\theta),\\ &\text{symmetric:} && -(1-2g)\{F(\theta)-2F(\pi-\theta)\}.\end{aligned} \quad (15)$$

The complete cross section for the neutron-proton scattering is obtained from the singlet and triplet cross sections by

$$\sigma(\theta)=\tfrac{1}{4}\sigma_{\text{sing}}(\theta)+\tfrac{3}{4}\sigma_{\text{trip}}(\theta).$$

Squaring the amplitudes (15) for the singlet cross section and performing the sum in (3) we find:

ordinary:

$$\sigma(\theta)=\tfrac{1}{4}(3+(1-2g)^2)F^2(\theta)+6\gamma^2C^2(\theta),$$

exchange:

$$\sigma(\theta)=\tfrac{1}{4}(3+(1-2g)^2)F^2(\pi-\theta)+6\gamma^2C^2(\pi-\theta),$$

symmetric:

$$\begin{aligned}\sigma(\theta)=&(\tfrac{1}{3}+(1-2g)^2)(\tfrac{1}{4}F^2(\theta)+F^2(\pi-\theta))\\&+(\tfrac{1}{3}-(1-2g)^2)F(\theta)F(\pi-\theta)\\&+(8/3)\gamma^2(\tfrac{1}{4}C^2(\theta)+C^2(\pi-\theta))\\&-(4/3)\gamma^2C(\theta)C(\pi-\theta).\end{aligned} \quad (16)$$

Tensor forces and central forces contribute separately to the cross section, as has been noted earlier.

For a square well potential $F(\theta)$ is proportional to a dimensionless function, $f(Ka)$, of the variable Ka.

$$F(\theta)=a\frac{MVa^2}{\hbar^2}\frac{\sin Ka-Ka\cos Ka}{(Ka)^3}. \quad (17)$$

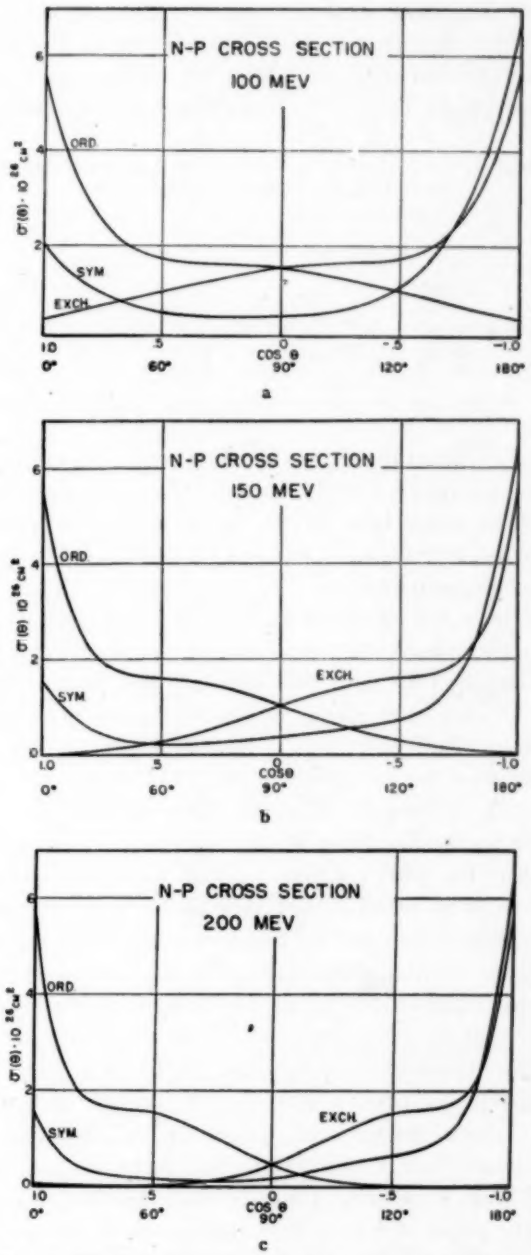

FIG. 2. Neutron-proton scattering cross section (center of mass system) in the Born approximation for a square well potential including the tensor forces. (a) 100 Mev, (b) 150 Mev, (c) 200 Mev.

This is plotted in Fig. 1 (multiplied by 0.3 for convenience) to show the contrast between the central and tensor force amplitudes. The cross sections based on these functions $f(Ka)$ and $c(Ka)$ are shown in Fig. 2a, b, c for the energies 100, 150, and 200 Mev. The general qualitative features are evident from (16) and Fig. 1. Thus the exchange curve is the reflection of the ordinary cross section about the 90° position. It is clear also, that as the energy increases the differences between the different models become sharper. In Table I we have summarized some of

TABLE I. Neutron-proton scattering in the Born approximation for different exchange models.

Neutron energy (lab.) Mev	Total cross section (10^{-24} cm²) Ord.	Exch.	Symm.	$\sigma(180°)/\sigma(90°)$ Ord.	Exch.	Symm.
100	0.205	0.205	0.167	0.31	3.69	13.1
150	0.143	0.143	0.114	0.011	5.43	17.6
200	0.108	0.108	0.090	0.030	12.1	35.5

the information to be obtained from the curves. The comparison with the Berkeley experiments will be made later in Section II where the cross section is computed more accurately than in the Born approximation.

Table I shows that for the exchange and symmetric forces the ratio of the scattered intensities at 180° and 90° is a rapidly increasing function of the energy as expected. For ordinary forces, however, this ratio shows an erratic behavior which is clarified by the graphs in Fig. 1. Thus the low value 0.011 at 150 Mev is due to the accidentally low values of $f(Ka)$ and $c(Ka)$ for 180° relative to 90°. The subsequent *increase* to 0.030 at 200 Mev seems at first sight surprising, but can be readily explained in terms of the oscillatory behavior of $f(Ka)$ and may, be attributed, therefore, to the special nature of the square well potential. This effect was first pointed out by Camac and Bethe[1] who investigated the ratio $\sigma(180°)/\sigma(90°)$ in the absence of tensor forces and found an extraordinary increase from 1.1 to 93 in going from 40 Mev to 80 Mev. From Fig. 1 we see that this may occur if the value of Ka for 90° at some energy happens to be near the node of $f(Ka)$. In the Born approximation the node occurs at the 90° angle for 106 Mev. With tensor forces the effect is not so pronounced since $f(Ka)$ and $c(Ka)$ do not have a node for a common value of Ka, in general.

As we shall see in Section II, the Born approximation is a poor one at 100 Mev. Apart from numerical disagreements, however, it is possible at this point to notice an important *qualitative* deficiency in the approximation which may be of importance in making comparisons with experiment. Thus for exchange forces the curves in Fig. 2 are the reflections of the ordinary curves about 90°, the behavior near 0° being identical with the behavior of the ordinary cross section near 180°. In actual fact the exact cross section for exchange forces shows a pronounced maximum at 0° which is entirely lacking in the Born approximation.

The explanation for this is given most directly if we restrict the consideration to ordinary and exchange central forces leaving out the tensor forces and the spin dependence. In the Born approximation the phase shift for the partial wave of angular momentum l is given in terms of the potential V by[8]

$$\delta_l = -(\pi M/2h^2)\int_0^\infty V(r)J_{l+\frac{1}{2}}^2(kr)rdr. \quad (18)$$

Due to the change of sign of V for odd l in the case of exchange forces, the phase shifts are alternately the same and opposite to the phase shifts for ordinary forces as l goes through the sequence 0, 1, 2, 3, $\cdots$. If the energy is high enough and the potential V is not too large, the approximate phase shifts (18) will not be very different from the exact values. In terms of the δ_l the scattered amplitude in the direction θ is given rigorously by

$$f(\theta) = (1/2ik)\sum_{l=0}^{\infty}(2l+1)(e^{2i\delta_l}-1)P_l(\cos\theta).$$

If we take an energy like 200 Mev and V approximately 20 Mev, the phase shifts are comparatively small, of the order 0.4 radians, and are appreciable up to $l=5$. It is therefore legitimate to expand $\exp(2i\delta_l)-1$. Taking the exchange force amplitude at $\theta=0$,

$$f(0) = (1/2ik)\sum_{l=0}^{\infty}(2l+1)(2i\delta_l - 2\delta_l^2 + \cdots).$$

[8] Reference 4, p. 28.

As is well known,[9] the Born approximation results if only the terms $2i\delta_l$ are kept in the expansion, with δ_l given by (18). Since these terms alternate in sign like $(-1)^l$ they contribute very little to the sum. They give the same contribution at $\theta=0$ as the similar terms at $\theta=180°$ for ordinary forces where the Legendre polynomials $P_l(-1)$ contribute the alternation of sign instead of the δ_l. However, the δ_l^2 terms all contribute with the same sign to $f(\theta)$ and give maximum effect at $\theta=0$ where the Legendre polynomials give the strongest constructive interference. Some idea of the size of the effect can be seen from Fig. 3 where the energy 200 Mev and a square well of depth 20 Mev and range $a=e^2/mc^2$ were chosen. With tensor forces the same phenomenon should manifest itself. As a result the angular dependence of the neutron-proton cross section for exchange forces and for symmetric forces should be qualitatively the same, contrary to the Born approximation.

C. Neutron-Neutron or Proton-Proton Cross Section

If it is assumed that the forces between neutron and neutron and between neutron and proton are the same if the pairs of particles are in the same state, we may use the same set of scattered amplitudes (14) and (15), appropriately modified by the Pauli exclusion principle, to calculate the $n-n$ or the $p-p$ scattering. For singlet scattering the spatial part of the wave function must be symmetric and all three of the models give the amplitude:

singlet: $\quad(1-2g)(F(\theta)+F(\pi-\theta))$.

For the triplet case the spatial wave function must be antisymmetric giving:

triplet: $\mathcal{S}_{m_s'm_s}(\theta,\varphi)-\mathcal{S}_{m_s'm_s}(\pi-\theta,\pi+\varphi)$.

The cross sections resulting from these amplitudes are:

ordinary:

$$\sigma(\theta)=\tfrac{1}{4}(3+(1-2g)^2)(F^2(\theta)+F^2(\pi-\theta))+6\gamma^2(C^2(\theta)+C^2(\pi-\theta))-\tfrac{1}{2}(3-(1-2g)^2)F(\theta)F(\pi-\theta)+6\gamma^2C(\theta)C(\pi-\theta);$$

[9] Reference 4, p. 90.

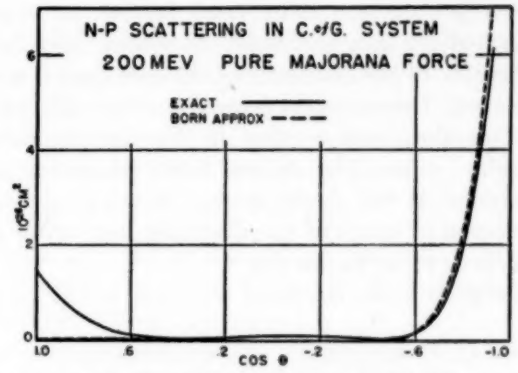

FIG. 3. Existence of a forward maximum in the scattered intensity for exchange forces. Spin dependence and tensor forces are neglected in this illustration.

exchange: same as ordinary;

symmetric: (19)

$$\sigma(\theta)=(\tfrac{1}{12}+\tfrac{1}{4}(1-2g)^2)(F^2(\theta)+F^2(\pi-\theta))+(\tfrac{1}{2}(1-2g)^2-\tfrac{1}{6})F(\theta)F(\pi-\theta)+\tfrac{2}{3}\gamma^2(C^2(\theta)+C^2(\pi-\theta)+C(\theta)C(\pi-\theta)).$$

From the curves in Fig. 4 we see that the cross section in the symmetrical force theory is much smaller than the one corresponding to ordinary forces or exchange forces. This is due to the fact that for symmetric forces in the odd triplet states the interaction is one third as large as for ordinary or exchange forces. Since the even triplet states are excluded for identical particles, the triplet cross section with symmetrical forces is reduced by a factor 9. The admixture of the singlet cross section, which is the same in all three models, makes the ratio somewhat less than 9 but still large. An absolute measurement of the

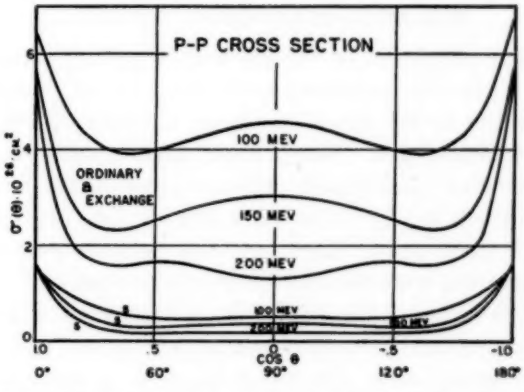

FIG. 4. Proton-proton cross section in the Born approximation for the same potentials as Fig. 2. Coulomb scattering is neglected.

proton-proton scattering cross section at some intermediate angle should, therefore, give an indication of the character of the exchange forces involved. Tensor forces have the effect of bringing up the cross section in the intermediate angular range. The change from maximum to minimum at 90° as the energy increases can be explained in terms of the slope and curvature of the curve for $c(Ka)$ in Fig. 1.

Table II gives the total $p-p$ (or $n-n$) cross section and its comparison with the $n-p$ cross section. A simple estimate of the ratio of cross sections $\sigma_{n-p}/\sigma_{p-p}$ can be made if the energy is large enough so that angular integrals of the type $\int F(\theta)F(\pi-\theta)d\omega$ or $\int C(\theta)C(\pi-\theta)d\omega$ may be neglected. Comparison of (16) and (19) shows that the ratio should be approximately 1.0 for ordinary or exchange forces and 5.0 for symmetric forces. It should be noted that the total proton-proton cross section is obtained from (19) by integrating over all solid angles and then dividing by two, since in each scattering event two protons are ejected with no means for distinguishing the initial particle from the target particle.

TABLE II. Proton-proton and neutron-proton scattering compared in the Born approximation.

Energy (lab.) Mev	σ_{p-p} (10^{-24} cm^2) Ord.	Exch.	Symm.	$\sigma_{n-p}/\sigma_{p-p}$ Ord.	Exch.	Symm.
100	0.278	0.278	0.0414	0.738	0.738	4.04
150	0.182	0.182	0.0289	0.788	0.788	3.96
200	0.115	0.115	0.0208	0.944	0.944	4.34

II. NEUTRON-PROTON CROSS SECTION IN THE RIGOROUS SCATTERING THEORY

The extension of the method of partial waves to scattering problems with non-central forces, like the tensor force, has been made by Rarita and Schwinger.[9] Since their final results are somewhat condensed, however, we shall first put them in a form more suitable for computation and then apply them to the neutron-proton scattering with the symmetric force model.

We consider the triplet $n-p$ scattering under a non-central force of potential $V(\mathbf{r}, \boldsymbol{\sigma}_1, \boldsymbol{\sigma}_2)$ which commutes with the total angular momentum $\mathbf{J}=\mathbf{L}+\mathbf{S}$, with the magnitude of the spin S^2, and with the space exchange operator P_M. V will, in general, not commute with any of the components of the orbital angular momentum $\mathbf{L}$, or of the spin angular momentum $\mathbf{S}$. These are the commutation properties of the tensor force. To facilitate the phase shift analysis, which is the basis of the method of partial waves, it is convenient to transform to the $SLJm$ representation in which states are labeled according to the value of total spin S, total orbital angular momentum L, total angular momentum J, and z-component of J equal to m. In this representation we define a set of functions $F_L{}^{Jm}$, the "normalized spherical harmonics with spin," which are eigenfunctions of the operators S^2, L^2, J^2, J_z, and P_M. The total spin $S=1$ and the eigenvalue of the exchange operator, P_M, is the parity $(-1)^L$.

These functions, $F_L{}^{Jm}$, may be obtained by a unitary transformation applied to the orthogonal functions $Y_{Lm_L}(\theta,\varphi)\chi_{m_s}$, which are appropriate for the SLm_Lm_s representation, where the Y_{Lm_L} are the ordinary spherical harmonics and the χ_{m_s} are the triplet spin functions ($m_s=1, 0, -1$).

$$F_L{}^{Jm}=\sum_{m_s=-1}^{1} Y_{L,m-m_s}\chi_{m_s} \times(SLm-m_sm_s|SLJm), \tag{20}$$

$$Y_{Lm_L}\chi_{m_s}=\sum_{J=L-1}^{L+1} F_L{}^{Jm_L+m_s} \times(SLJm_L+m_s|SLm_Lm_s).$$

For a given value of J we must have $|m|\leqq J$ and L one of the values $J-1$, J, $J+1$ as is shown by the vector model. Condon and Shortley[10] give a table for the transformation coefficients which is reproduced in (21) for the special case of $m_L=0$.

$(SL0m_s|SLJm_s)$

J \ m_s	±1	0
$J=L+1$	$\left(\frac{L+2}{2(2L+1)}\right)^{\frac{1}{2}}$	$\left(\frac{L+1}{2L+1}\right)^{\frac{1}{2}}$
$J=L$	$-1/\sqrt{2}$	0
$J=L-1$	$\left(\frac{L-1}{2(2L+1)}\right)^{\frac{1}{2}}$	$-\left(\frac{L}{2L+1}\right)^{\frac{1}{2}}$

(21)

[10] Condon and Shortley, *Theory of Atomic Spectra* (The Macmillan Company, New York, 1935), p. 76, Table 2[3].

Taking the z axis as the direction of propagation of the incident triplet wave and using this same direction as axis of quantization for the angular momentum, we make the usual expansion:

$$e^{ikz}\sum_{m_s=-1}^{1} a_{m_s}\chi_{m_s}=\sum_{L=0}^{\infty}\sum_{m_s=-1}^{1}(2L+1)i^L \times[g_L(kr)/kr][4\pi/(2L+1)]^{\frac{1}{2}} \times Y_{L0}(\theta)\chi_{m_s}a_{m_s}, \tag{22}$$

where

$$g_L(kr)=(\pi kr/2)^{\frac{1}{2}}J_{L+\frac{1}{2}}(kr)\sim\sin(kr-\tfrac{1}{2}L\pi)$$

is the Lth radial wave function in the absence of interaction. The complete wave function for the scattering problem is obtained by first writing the incident plane wave as a sum of partial waves in the $SLJm$ representation and then replacing the radial function $g_L(kr)$ by

$$\exp(i\delta_L{}^{Jm})u_L{}^{Jm}(r),$$

where $u_L{}^{Jm}(r)$ is the radial function with the non-central interaction and $\delta_L{}^{Jm}$ is the phase shift for this partial wave:

$$u_L{}^{Jm}(r)\sim\sin(kr-\tfrac{1}{2}L\pi+\delta_L{}^{Jm}).$$

Subtracting the incident wave gives for the asymptotic form of the scattered wave, in the customary way,

$$\psi_{\text{scatt}}\sim\frac{e^{ikr}}{2ikr}\sum_{m_s=-1}^{1}\sum_{L=0}^{\infty}\sum_{J=L-1}^{L+1}[4\pi(2L+1)]^{\frac{1}{2}}\{\exp(2i\delta_L{}^{Jm_s})-1\}(SLJm_s|SL0m_s)F_L{}^{Jm_s}a_{m_s}$$

$$=\frac{e^{ikr}}{2ikr}\sum_{m_s,m_s'}\sum_{L,J}[4\pi(2L+1)]^{\frac{1}{2}}\{\exp(2i\delta_L{}^{Jm_s})-1\}(SLm_s-m_s'm_s'|SLJm_s) \times(SLJm_s|SL0m_s)Y_{L,m_s-m_s'}(\theta,\varphi)\chi_{m_s'}a_{m_s}.$$

The coefficient of a_{m_s} in this formula is the matrix element $s_{m_s'm_s}(\theta,\varphi)$ of (2) given in the Born approximation by (6).

Application of the table of Condon and Shortley gives:

$$m_s=1\begin{cases} s_{11}=\dfrac{1}{2ik}\displaystyle\sum_{L=0}^{\infty}[4\pi(2L+1)]^{\frac{1}{2}}Y_{L0}(\theta)\left\{\frac{L-1}{2(2L+1)}[\exp(2i\delta_L{}^{L-1,1})-1]+\tfrac{1}{2}[\exp(2i\delta_L{}^{L,1})-1]\right. \\ \qquad\left.+\dfrac{L+2}{2(2L+1)}[\exp(2i\delta_L{}^{L+1,1})-1]\right\}, \\ s_{01}=\dfrac{1}{2ik}\displaystyle\sum_{L=1}^{\infty}[4\pi(2L+1)]^{\frac{1}{2}}\frac{Y_{L1}(\theta,\varphi)}{[2L(L+1)]^{\frac{1}{2}}}\left\{-\frac{L^2-1}{2L+1}[\exp(2i\delta_L{}^{L-1,1})-1]\right. \\ \qquad\left.-[\exp(2i\delta_L{}^{L,1})-1]+\dfrac{L(L+2)}{2L+1}[\exp(2i\delta_L{}^{L+1,1})-1]\right\}, \\ s_{-11}=\dfrac{1}{2ik}\displaystyle\sum_{L=2}^{\infty}[4\pi(2L+1)]^{\frac{1}{2}}Y_{L2}(\theta,\varphi)[(L-1)L(L+1)(L+2)]^{\frac{1}{2}} \\ \qquad\times\left\{\frac{\exp(2i\delta_L{}^{L-1,1})-1}{2L(2L+1)}-\frac{\exp(2i\delta_L{}^{L,1})-1}{2L(L+1)}+\frac{\exp(2i\delta_L{}^{L+1,1})-1}{(2L+1)(2L+2)}\right\}; \end{cases} \tag{23}$$

$$m_s=0\begin{cases} s_{10}=\dfrac{1}{2ik}\displaystyle\sum_{L=1}^{\infty}[4\pi(2L+1)]^{\frac{1}{2}}Y_{L-1}(\theta,\varphi)\left[\frac{L(L+1)}{2}\right]^{\frac{1}{2}}\left\{-\frac{\exp(2i\delta_L{}^{L-1,0})-1}{2L+1}+\frac{\exp(2i\delta_L{}^{L+1,0})-1}{2L+1}\right\}, \\ s_{00}=\dfrac{1}{2ik}\displaystyle\sum_{L=0}^{\infty}[4\pi(2L+1)]^{\frac{1}{2}}Y_{L0}(\theta)\left\{\frac{L}{2L+1}[\exp(2i\delta_L{}^{L-1,0})-1]+\frac{L+1}{2L+1}[\exp(2i\delta_L{}^{L+1,0})-1]\right\}, \\ s_{-10}=\dfrac{1}{2ik}\displaystyle\sum_{L=1}^{\infty}[4\pi(2L+1)]^{\frac{1}{2}}Y_{L1}(\theta,\varphi)\left[\frac{L(L+1)}{2}\right]^{\frac{1}{2}}\left\{-\frac{\exp(2i\delta_L{}^{L-1,0})-1}{2L+1}+\frac{\exp(2i\delta_L{}^{L+1,0})-1}{2L+1}\right\}; \end{cases}$$

Equation (23) continued on next page)

$m_s=-1$ {
- $\mathcal{S}_{1-1}$: change Y_{L2} in $\mathcal{S}_{-11}$ to Y_{L-2} and replace the phase shifts by those for $m_s=-1$;
- $\mathcal{S}_{0-1}$: change Y_{L1} in $\mathcal{S}_{01}$ to Y_{L-1} and replace the phase shifts;
- $\mathcal{S}_{-1-1}$: replace the phase shifts in $\mathcal{S}_{11}$ by those for $m_s=-1$.

Actually, for interactions of the symmetry of the tensor force the phase shifts for $m_s=1$ and for $m_s=-1$ are the same. In the averaging process (3) the amplitudes with $m_s=1$ and -1 give the same contribution to the sum. It is also understood in the formulas that the phase shifts $\delta_{L^{Jm_s}}$ which appear formally must obey the conditions $|m_s|\leqq J$ and $0\leqq J$; otherwise they are to be replaced by zero.

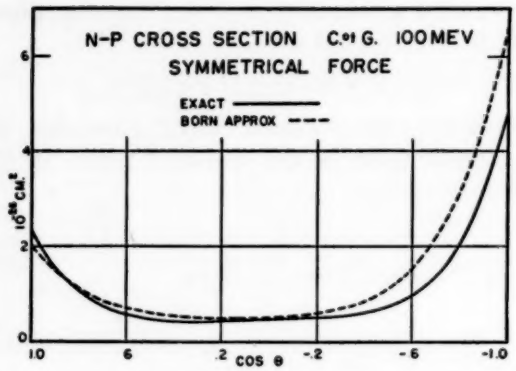

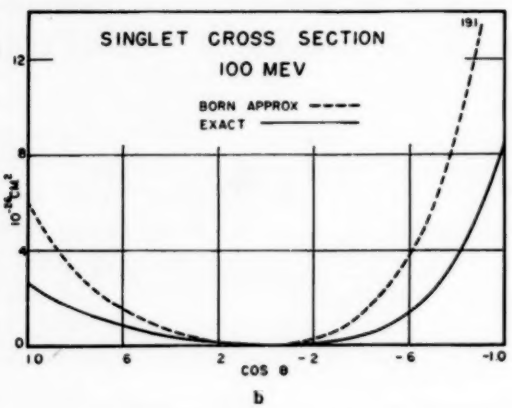

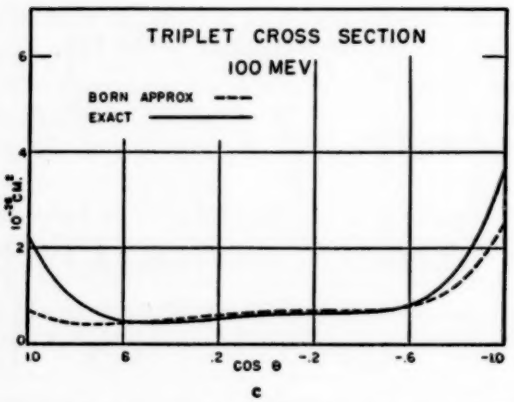

FIG. 5. The rigorous scattering theory and the Born approximation compared at 100 Mev for the neutron-proton scattering with symmetrical forces. (a) the complete differential cross section; (b) the singlet cross section; (c) the triplet cross section.

To obtain numerical values for the phase shifts it is necessary to integrate the radial wave equations for the functions $u_{L^{Jm}}(r)$. These equations are obtained from the Schrödinger equation

$$(\nabla^2+k^2)\psi-(M/\hbar^2)\,V(\mathbf{r},\boldsymbol{\sigma}_1,\boldsymbol{\sigma}_2)\psi=0 \tag{24}$$

by expanding ψ in the form

$$\psi=\sum_{J=0}^{\infty}\sum_{m=-J}^{J}\sum_{L=J-1}^{J+1}(1/r)u_{L^{Jm}}(r)F_{L^{Jm}}.$$

Using the orthogonality of the spin angular functions $F_{L^{Jm}}$ and the fact that V commutes with J, we find for each Jm three coupled equations for $u_{L^{Jm}}$ with $L=J-1,\ J,\ J+1$:

$$\frac{d^2u_{L^{Jm}}}{dr^2}+\left(k^2-\frac{L(L+1)}{r^2}\right)u_{L^{Jm}}-\frac{M}{\hbar^2}\sum_{L'=J-1}^{J+1}V_{LL'^J}(r)u_{L'^{Jm}}(r)=0. \tag{25}$$

$V_{LL'^J}(r)$ is the matrix element $(F_{L^{Jm}},\ VF_{L'^{Jm}})$. These matrix elements are easily shown to be independent of m and are given for the tensor force S_{12} in the appendix of Rarita's and Schwinger's paper:

$$S_{LL'^J}=\begin{array}{c|ccc} L\backslash L' & J-1 & J & J+1 \\ \hline J-1 & -2\dfrac{(J-1)}{2J+1} & 0 & \dfrac{6[J(J+1)]^{\frac{1}{2}}}{2J+1} \\ J & 0 & 2 & 0 \\ J+1 & \dfrac{6[J(J+1)]^{\frac{1}{2}}}{2J+1} & 0 & -\dfrac{2(J+2)}{2J+1} \end{array} \tag{26}$$

Actually the three Eqs. (25) split into two

coupled equations for $u_{J-1}{}^{Jm}$ and $u_{J+1}{}^{Jm}$ and one equation for $u_J{}^{Jm}$ alone. This is an immediate consequence of the fact that V commutes with the spatial exchange operator and hence cannot couple states of different parity.

Integration of the equations is greatly simplified for the case of a square well potential. Following the procedure of Rarita and Schwinger, one can express the solutions inside the well for $u_{J-1}{}^{Jm}$ and $u_{J+1}{}^{Jm}$ by power series[11] involving two arbitrary constants which must be adjusted to give continuity of the functions and their derivatives at the boundary. The solution outside will be a linear combination of the regular solution $g_L(kr)$ and the irregular solution $g_{-L-1}(kr)$ which has asymptotic form

$$\sin(kr-\tfrac{1}{2}L\pi+\delta_L{}^{Jm}).$$

Since

$$g_{-L-1}(kr)=[\pi kr/2]^{\frac{1}{2}}J_{-L-\frac{1}{2}}(kr) \sim(-1)^L\cos(kr-\tfrac{1}{2}L\pi),$$

the outside solutions are:

$$u_L{}^{Jm}=A_L{}^{Jm}\{\cos\delta_L{}^{Jm}g_L(kr) +(-1)^L\sin\delta_L{}^{Jm}g_{-L-1}(kr)\}. \quad (27)$$

This solution must represent the incident wave plus an outgoing spherical wave. From (22), (20), (21), and (24) the incident wave is represented by

$$(u_L{}^{Jm})_{\text{inc}}=C_L{}^{Jm}g_L(kr), \quad (28)$$

where

$$C_L{}^{Jm}=\frac{[4\pi(2L+1)]^{\frac{1}{2}}}{k}i^L(SLJm|SL0m). \quad (28a)$$

If the difference between (27) and (28) is to be an outgoing wave proportional to $\exp(ikr)$, the constant $A_L{}^{Jm}$ must be chosen so that

$$u_L{}^{Jm}=C_L{}^{Jm}\exp(i\delta_L{}^{Jm})\{\cos\delta_L{}^{Jm}g_L(kr) +(-1)^L\sin\delta_L{}^{Jm}g_{-L-1}(kr)\}. \quad (29)$$

In this formula the index m is identical with m_s, the projection of the spin in the incident direction, since the orbital angular momentum of the incident wave with respect to this direction is zero. Equating the values and derivatives on both sides of the boundary gives the pair of

[11] W. Rarita and J. Schwinger, Phys. Rev. **59**, 436 (1941), Eqs. (10) and (11).

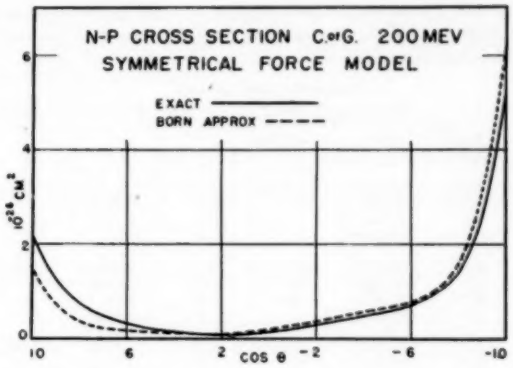

FIG. 6. Neutron-proton cross section at 200 Mev for symmetrical forces. Comparison of the rigorous theory with the Born approximation.

phase shifts $\delta_{J-1}{}^{Jm_s}$ and $\delta_{J+1}{}^{Jm_s}$ for each J and $m_s=\pm1$, 0. The phase shifts[12] $\delta_J{}^{Jm_s}$ and the singlet phase shifts are obtained in the usual way.

The method given above has been applied to the neutron-proton scattering with the symmetrical force model and calculations performed for 100 and 200 Mev. Figure 5a, b, c and Fig. 6 give the results in graphical form. For the total scattering cross section one finds:

Symm. forces:

$$\sigma_{n-p}=0.129\times10^{-24}\text{ cm}^2,\quad 100\text{ Mev},$$
$$\sigma_{n-p}=0.090\times10^{-24}\text{ cm}^2,\quad 200\text{ Mev}. \quad (30)$$

Experiments by E. M. McMillan and coworkers[13] with 90-Mev neutrons give

$$(0.083\pm0.004)\times10^{-24}\text{ cm}^2$$

for the total cross section, in serious disagreement with the theory. Judging from the Born approximation, the discrepancy should be even larger for the pure exchange forces. Furthermore, the measured angular distribution is qualitatively very much in disagreement with the symmetrical theory. Experimentally the ratio

$$\sigma(180°)/\sigma(90°)$$

is about 3, whereas the curve of Fig. 5a shows about 10. Although the angular distribution has not been measured to very small angles in the center of mass system for the neutrons (angles near 90° in the laboratory for the recoil protons)

[12] Only the phases $\delta_J{}^{J\pm1}$ enter. This is because $(SL=JJm|SJ0m)$ vanishes for $m=0$ as can be seen from (21).

[13] L. J. Cook, E. M. McMillan, J. M. Peterson, and D. C. Sewell, Phys. Rev. **72**, 1264 (1947).

TABLE III. Phase shifts (in radians) for the neutron-proton scattering at 100 Mev with the symmetrical force model.

		Coupled triplet phases				
		Exact	Born		Exact	Born
$J=0$	K_1^{10}	0.3022	0.2920			
	ζ_1^{10}	0	0			
$J=1$	K_0^{11}	0.4191	0.1976	K_0^{11}	0.5743	0.9137
	ζ_0^{11}	0.0498	0	ζ_0^{11}	−0.0771	0
	K_2^{11}	−0.2602	−0.5624	K_2^{11}	0.1047	0.1538
	ζ_2^{11}	−0.0773	0	ζ_2^{11}	0.0500	0
$J=2$	K_1^{21}	−0.0064	−0.0358	K_1^{21}	−0.1553	−0.1860
	ζ_1^{21}	0.0059	0	ζ_1^{21}	−0.0087	0
	K_3^{21}	0.0911	0.0923	K_3^{21}	−0.0578	−0.0578
	ζ_3^{21}	−0.0087	0	ζ_3^{21}	0.0059	0
$J=3$	K_2^{31}	0.1292	0.0443	K_2^{31}	0.2413	0.1416
	ζ_2^{31}	0.0095	0	ζ_2^{31}	−0.0122	0
	K_4^{31}	−0.0610	−0.0559	K_4^{31}	0.0515	0.0413
	ζ_4^{31}	−0.0122	0	ζ_4^{31}	0.0095	0
$J=4$	K_3^{41}	−0.0016	−0.0029	K_3^{41}	−0.0055	−0.0068
	ζ_3^{41}	0	0	ζ_3^{41}	0	0
	K_5^{41}	0.0022	0.0022	K_5^{41}	−0.0017	−0.0018
	ζ_5^{41}	0	0	ζ_5^{41}	0	0
$J=5$	K_4^{51}	0.0016	0.0010	K_4^{51}	0.0026	0.0018
	ζ_4^{51}	0	0	ζ_4^{51}	0	0
	K_6^{51}	−0.0006	−0.0004	K_6^{51}	0.0004	0.0003
	ζ_6^{51}	0	0	ζ_6^{51}	0	0

Uncoupled triplet phases				Singlet phases		
J	$\delta_J{}^{J1}$	Exact	Born	L	Exact	Born
1	$\delta_1{}^{11}$	−0.3214	−0.3546	0	0.3193	0.3740
2	$\delta_2{}^{21}$	0.6777	0.3937	1	−0.7438	−1.0724
3	$\delta_3{}^{31}$	−0.0219	−0.0241	2	0.1577	0.1323
4	$\delta_4{}^{41}$	0.0096	0.0079	3	−0.0562	−0.0730
5	$\delta_5{}^{51}$	−0.0002	−0.0002	4	0.0028	0.0027
				5	−0.0007	−0.0006

the indication is that the cross section is symmetrical about 90°. This would imply a potential of the type

$$V=\tfrac{1}{2}(1+P_M)J(r, \sigma_1, \sigma_2),$$

in which ordinary and exchange forces enter with equal weight. Investigation of the cross section with such a potential, taking $(1/r)\exp(-r/a)$ for the spatial dependence, is being carried on by Serber.

Relativistic corrections to the cross section would be expected to play a role at energies comparable with the rest energy of the meson. Since it is the energy in the center of mass system which is important for this consideration it is unlikely that at 100 Mev in the laboratory any relativistic effects could account for the discrepancy between the theory and the experiment. An estimate of the corrections to the total cross section can be obtained from the formulas of Snyder and Marshak[14] which are valid in the Born approximation. At 100 Mev the differences are only 5–10 percent but they increase rapidly with increasing energy

From the curves of Fig. 5 and Fig. 6 we can estimate the reliability of the Born approximation used in Section I. The weakness of the approximation is especially evident from Fig. 5b, showing the singlet scattering cross section at 100 Mev. In the Born approximation, the total singlet cross section is 0.39×10^{-24} cm², while the exact calculation gives 0.17×10^{-24} cm². Such large differences have already been noticed by Camac and Bethe.[1] The primary reason for the discrepancy is the failure of the approximation for the $L=1$ phase shift. Comparison of the exact phase shifts and the Born phase shifts as given in Table III shows that this is the only serious difference for the singlet scattering. This may be attributed to the fact that for odd singlet states with the symmetrical model the potential is especially large, $-3\,{}^1V_{\text{even}}$. For the triplet phases the differences between the exact calculation and the Born approximation are much more erratic but the resulting cross sections, as shown in Fig. 5c, agree somewhat better than for the singlet case. Presumably, this is due to accidental cancellation of errors. We must conclude that the Born approximation is untrustworthy for energies as low as 100 Mev. At 200 Mev, however, the situation is much improved as is shown by the curves in Fig. 6. Both the singlet and triplet parts of the cross section are also in much better agreement with the approximation.

The triplet phases in the Born approximation are obtained from a generalization of the well-known formula (18) valid for central forces. Since this formula may be of some value for estimating phases at energies high enough where the Born approximation is valid it is included in the Appendix. Table III gives the real and imaginary parts of the phases using the notation

$$\delta_L{}^{Jm_s}=K_L{}^{Jm_s}+i\zeta_L{}^{Jm_s}.$$

A check on the calculations can be made by seeing if the real and imaginary parts of the phases obey the relations (42), (43), and (44) of Rarita and Schwinger:[15]

$$K_{J-1}{}^{J0}-K_{J+1}{}^{J0}=K_{J-1}{}^{J1}-K_{J+1}{}^{J1},$$

$$\zeta_{J-1}{}^{J0}=\zeta_{J+1}{}^{J1},\quad \zeta_{J-1}{}^{J1}=\zeta_{J+1}{}^{J0},$$

$$\exp(2i\delta_{J-1}{}^{J0})-\exp(2i\delta_{J+1}{}^{J0})=\exp(2i\delta_{J-1}{}^{J1})-\exp(2i\delta_{J+1}{}^{J1}).$$

[14] H. Snyder and R. E. Marshak, Phys. Rev. **72**, 1253 (1947).

[15] W. Rarita and J. Schwinger, Phys. Rev. **59**, 436 (1941), especially page 445.

In conclusion we should like to thank Professor R. E. Marshak and Professor G. E. Uhlenbeck for interesting discussions.

APPENDIX

For central forces the phase shifts for different angular momenta L are given in the Born approximation by the formula (18) as obtained in Mott and Massey, page 28. Applying the same method to the Eqs. (25), starting from the unperturbed solution

$$u_L{}^{Jm_s}=C_L{}^{Jm_s}g_L(kr),$$

given by (28), we find an expression for the phase shift, correct to the first order in the potential:

$$\delta_L{}^{Jm_s}=-\frac{M}{k\hbar^2}\frac{\sum_{L'=J-1}^{J+1}[2(2L'+1)]^{\frac{1}{2}}i^{L'-L}(SL'Jm_s|SL'0m_s)\int_0^\infty g_L(kr)g_{L'}(kr)\,V_{LL'}{}^J(r)dr}{[2(2L+1)]^{\frac{1}{2}}(SLJm_s|SL0m_s)}.$$

In spite of the factor $i^{L'-L}$ in the summation, these phase shifts are real since this factor is real for $L'-L$ equal to 0 or 2 and $V_{LL'}{}^J$ is equal to zero if L and L' differ by unity. In the higher approximation the phase shifts are in general complex. It is not very difficult to show that if in the rigorous expressions (23) for the $S_{m_s'm_s}(\theta,\varphi)$ one replaces $\exp(2i\delta_L{}^{Jm_s})-1$ by $2i\delta_L{}^{Jm_s}$ with $\delta_L{}^{Jm_s}$ given by the approximate formula above, the Born approximation of Section I results. This is completely analogous to the results for central forces.

As an example, for the symmetrical force model we find, using (26), (11), (12b), and (21):

Triplet phases

L even:

$$\delta_L{}^{L-1,1}=\frac{M}{k\hbar^2}\left[\left(1-\gamma\frac{2L+2}{2L-1}\right)\int_0^\infty g_L{}^2J(r)dr-\gamma\frac{6L}{2L-1}\int_0^\infty g_Lg_{L-2}J(r)dr\right],$$

$$\delta_L{}^{L,1}=\frac{M}{k\hbar^2}\left[(1+2\gamma)\int_0^\infty g_L{}^2J(r)dr\right],$$

$$\delta_L{}^{L+1,1}=\frac{M}{k\hbar^2}\left[\left(1-\gamma\frac{2L}{2L+3}\right)\int_0^\infty g_L{}^2J(r)dr-\gamma\frac{6(L+1)}{2L+3}\int_0^\infty g_Lg_{L+2}J(r)dr\right],$$

$$\delta_L{}^{L-1,0}=\frac{M}{k\hbar^2}\left[\left(1-\gamma\frac{2L+2}{2L-1}\right)\int_0^\infty g_L{}^2J(r)dr+\gamma\frac{6(L-1)}{2L-1}\int_0^\infty g_Lg_{L-2}J(r)dr\right],$$

$$\delta_L{}^{L+1,0}=\frac{M}{k\hbar^2}\left[\left(1-\gamma\frac{2L}{2L+3}\right)\int_0^\infty g_L{}^2J(r)dr+\gamma\frac{6(L+2)}{2L+3}\int_0^\infty g_Lg_{L+2}J(r)dr\right].$$

L odd: Phases are $-\frac{1}{3}$ times those for even L.

Singlet phases

L even:

$$\delta_L=\frac{M}{k\hbar^2}(1-2g)\int_0^\infty g_L{}^2J(r)dr,$$

L odd: Phases are -3 times those for even L.

Elastic and Inelastic Scattering of 100- to 200-Mev Protons or Neutrons by Deuterons

TA-YOU WU*
Randall Laboratory of Physics, University of Michigan, Ann Arbor, Michigan

AND

JULIUS ASHKIN**
Department of Physics, University of Rochester, Rochester, New York

(Received January 12, 1948)

Expressions have been obtained, on the Born approximation, for the elastic and the total scattering cross section of protons or neutrons by deuterons, on the basis of the three forms of nucleon potentials suggested by Rarita and Schwinger, including tensor forces but with a Gaussian function for the radial part $V(r)$. Numerical calculations have, however, been carried through without tensor forces for (i) the angular distribution and total cross section of elastic scattering at 100, 150, and 200 Mev, (ii) the energy spectrum of protons scattered (elastically plus inelastically) in different directions from that of the incident protons and total cross section, and (iii) the energy spectra of neutrons ejected in directions making angles 0° and 30° with the direction of the incident protons, for 200 Mev. The three potentials predict considerable differences in both the differential and the total cross sections for both elastic and total scattering. The proton-deuteron total cross sections for 100 Mev is 0.424, 0.212, 0.089×10^{-24} cm^2 according to the ordinary, exchange, and symmetrical force, respectively, as compared with the observed value 0.117×10^{-24} recently reported from Berkeley for 90 Mev. The calculations show that the interference of the amplitudes scattered by the two particles of the deuteron plays an important role in the determination of the total cross section for proton-deuteron scattering. It is therefore not a good approximation to set the total *p-d* cross section equal to the sum of the *p-n* and *p-p* cross sections for free particle collisions.

I. INTRODUCTION

THERE has been a number of calculations of the cross section of the elastic scattering of a proton or neutron by a deuteron, with the view of testing the various forms of nucleon interactions by comparison with experimental data. Motz and Schwinger and Buckingham and Massey have calculated the cross sections on the basis of nucleon interaction potentials which are linear combinations of the Heisenberg, Majorana, Bartlett, and Wigner types.[1] All these calculations are made for incident protons or neutrons of energy of the order 15 Mev. For such energies, the calculation is usually very lengthy and the difference between the various forms of potentials is rather small so that a definite choice of the interaction potential by comparison with the experimental data on the angular distribution of the scattered intensities is difficult.

For higher energies of 100 to 200 Mev the calculation can be considerably simplified by the use of Born's approximation. Recent calculations[2] of the cross sections of proton-neutron collisions at these energies show that the angular distribution of the scattered intensities is quite different for the three forms of the interaction potential suggested by Rarita and Schwinger.[3] As high energy protons and neutrons (100 Mev) are now available, it seems desirable to carry out similar calculations, i.e., to Born's approximation, for the elastic and inelastic collisions between a deuteron and a proton or neutron. In the following, with some simplifying assumptions about the radial dependence of the potentials and the wave function of the ground state of the deuteron, expressions have been obtained for the cross sections of both elastic and total (elastic plus inelastic) scattering of a proton or neutron by a deuteron on the basis of the

* At present at Columbia University, New York.

** The work was supported in part by the Office of Naval Research Contract N60ri-126 T. O. II.

[1] L. Motz and J. Schwinger, Phys. Rev. **58**, 26 (1940); R. A. Buckingham and H. S. W. Massey, Proc. Roy. Soc. **A179**, 121 (1941); Phys. Rev. **71**, 558 (1947); H. Höcker, Physik. Zeits. **43**, 236 (1942).

[2] J. Ashkin and T. Y. Wu, Phys. Rev. **73**, 973 (1948).

[3] William Rarita and Julian Schwinger, Phys. Rev. **59**, 557 (1941).

three potentials of Rarita and Schwinger. As these expressions entail considerable amounts of computational labor, the actual numerical calculations have been carried out by omitting the tensor forces from the general formulae obtained. The result of the present calculation and that of the proton-neutron scattering, which includes the tensor forces, show that the difference among the three potentials is quite pronounced at these high energies.

II. FORMULATION OF THE PROBLEM

A. Wave Function for the Scattering Problem

Let 1 denote the incoming proton, 2 and 3 the proton and the neutron originally forming the deuteron.[4] Let us introduce the relative coordinates

$$\mathbf{r}=\mathbf{r}_1-\tfrac{1}{2}(\mathbf{r}_2+\mathbf{r}_3), \quad \boldsymbol{\rho}=\mathbf{r}_3-\mathbf{r}_2. \tag{1}$$

The wave equation, after separating off the motion of the system as a whole, is

$$\left[\frac{3\hbar^2}{4M}\Delta_r+\frac{\hbar^2}{M}\Delta_\rho+E-V_{12}(|\mathbf{r}+(\boldsymbol{\rho}/2)|)\right.$$
$$\left.-V_{13}(|\mathbf{r}-(\boldsymbol{\rho}/2)|)-V_{23}(|\boldsymbol{\rho}|)\right]\Psi(1,2,3)=0, \tag{2}$$

where M is the proton or neutron mass. The interaction potential V depends on the symmetry property of the state of the pair of nucleons with respect to spin and space exchange. For convenience, we tabulate below the potentials for a pair of unequal nucleons in various states according to the three models of Rarita and Schwinger:

State	Ordinary	Exchange	Symmetrical
${}^3V^{\text{even}}$	$-(1+\gamma S)U(r)$	$-(1+\gamma S)U(r)$	$-(1+\gamma S)U(r)$
${}^3V^{\text{odd}}$	$-(1+\gamma S)U(r)$	$+(1+\gamma S)U(r)$	$\frac{1}{3}(1+\gamma S)U(r)$
${}^1V^{\text{even}}$	$-(1-2g)U(r)$	$-(1-2g)U(r)$	$-(1-2g)U(r)$
${}^1V^{\text{odd}}$	$-(1-2g)U(r)$	$+(1-2g)U(r)$	$3(1-2g)U(r)$

(3)

For two equal nucleons, only the ${}^3V^{\text{odd}}$ and ${}^1V^{\text{even}}$ states are allowed by the Pauli principle. Here ${}^3V^{\text{even}}$ refers to a state which is symmetrical in the spins and even in the space coordinates of the two particles, etc. S is the tensor interaction,

$$S_{ij}=\frac{3(\boldsymbol{\sigma}_i\cdot\mathbf{r})(\boldsymbol{\sigma}_j\cdot\mathbf{r})}{r^2}-(\boldsymbol{\sigma}_i\cdot\boldsymbol{\sigma}_j), \tag{4}$$

$U(r)$ is a central force potential. g and γ are constants. The potential for ${}^3V^{\text{even}}$ has been chosen to be the same in the three theories to fit the data on the ground state of the deuteron. The potential for ${}^1V^{\text{even}}$ has also been given the same value in the three theories to fit the data on proton-proton scattering at low energies.

The wave function $\Psi(1,2,3)$ of the system may be developed in a series of products of a spin wave function and a space wave function. There are eight linearly independent and orthogonal spin wave functions. Of these there are four which are totally symmetrical in the three particles. These may be put in the form

$$\begin{aligned}
\chi_1&=\alpha_1\alpha_2\alpha_3,\\
\chi_2&=\beta_1\beta_2\beta_3,\\
\chi_3&=(1/\sqrt{3})(\alpha_1\beta_2\alpha_3+\beta_1\alpha_2\alpha_3+\alpha_1\alpha_2\beta_3),\\
\chi_4&=(1/\sqrt{3})(\beta_1\alpha_2\beta_3+\alpha_1\beta_2\beta_3+\beta_1\beta_2\alpha_3).
\end{aligned} \tag{5}$$

For the other four, we shall construct

$$\begin{aligned}
\chi_5&=(1/\sqrt{6})(\alpha_1\alpha_2\beta_3+\alpha_1\beta_2\alpha_3-2\beta_1\alpha_2\alpha_3),\\
\chi_6&=(1/\sqrt{6})(\beta_1\beta_2\alpha_3+\beta_1\alpha_2\beta_3-2\alpha_1\beta_2\beta_3),
\end{aligned} \tag{6}$$

which are symmetric in 2, 3, and

$$\begin{aligned}
\chi_7&=(1/\sqrt{2})\alpha_1(\alpha_2\beta_3-\beta_2\alpha_3),\\
\chi_8&=(1/\sqrt{2})\beta_1(\beta_2\alpha_3-\alpha_2\beta_3),
\end{aligned} \tag{7}$$

which are antisymmetric in 2, 3. These eight spin wave functions are appropriate for the description of the scattering processes treated below.

The wave function $\Psi(1,2,3)$ can be expanded

[4] To avoid the awkwardness of expression, we consider the scattering of protons by deuterons in the following. As the Coulomb interaction is neglected throughout, the whole calculation holds also for the case of the scattering of neutrons by deuterons. We then only have to interchange the names of proton and neutron throughout the present paper.

in the form

$$\Psi(1,2,3)=\sum_{i=1}^{6}\chi_i f^{(i)}(\mathbf{r})\psi_0(\boldsymbol{\rho})+\sum_{i=1}^{6}\chi_i\int F_{k''}^{(i)}(\mathbf{r})\psi_{k''}^{\,t}(\boldsymbol{\rho})d\mathbf{k}''+\sum_{j=7}^{8}\chi_j\int F_{k''}^{(j)}(\mathbf{r})\psi_{k''}^{\,s}(\boldsymbol{\rho})d\mathbf{k}'', \quad (8)$$

where $\psi_0(\rho)$ is the wave function of the ground state of the deuteron, $\psi_{k''}^{\,t}(\boldsymbol{\rho})$, $\psi_{k''}^{\,s}(\boldsymbol{\rho})$ are the continuum triplet and singlet state wave function of the deuteron, respectively. These satisfy the equations

$$\begin{aligned}
&\left[-\frac{\hbar^2}{M}\Delta_\rho+{}^3V_{23}+\epsilon\right]\chi_i\psi_0(\boldsymbol{\rho})=0, && i=1,\cdots,6,\\
&\left[-\frac{\hbar^2}{M}\Delta_\rho+{}^3V_{23}-\frac{\hbar^2}{M}k''^2\right]\chi_i\psi_{k''}^{\,t}(\boldsymbol{\rho})=0, && i=1,\cdots,6,\\
&\left[-\frac{\hbar^2}{M}\Delta_\rho+{}^1V_{23}-\frac{\hbar^2}{M}k''^2\right]\chi_j\psi_{k''}^{\,s}(\boldsymbol{\rho})=0, && j=7,8,
\end{aligned} \quad (9)$$

where ϵ is the binding energy of the deuteron. The functions $f^{(i)}(\mathbf{r})$, $F_{k''}^{(i)}(\mathbf{r})$, $F_{k''}^{(j)}(\mathbf{r})$ satisfy the following equations obtained by substituting (8) into (2) and making use of the above equations,

$$\begin{aligned}
&\left[\frac{3\hbar^2}{4M}\Delta_r+E+\epsilon\right]f^{(i)}(\mathbf{r})=\sum_{\text{spin}}\int\chi_i^*\psi_0^*(\boldsymbol{\rho})(V_{12}+V_{13})\Psi(1,2,3)d\boldsymbol{\rho}, && i=1,\cdots,6,\\
&\left[\frac{3\hbar^2}{4M}\Delta_r+E-\frac{\hbar^2}{M}k''^2\right]F^{(i)}(\mathbf{r})=\sum\int\chi_i^*\psi_{k''}^{*\,t}(\boldsymbol{\rho})(V_{12}+V_{13})\Psi(1,2,3)d\boldsymbol{\rho}, && i=1,\cdots,6,\\
&\left[\frac{3\hbar^2}{4M}\Delta_r+E-\frac{\hbar^2}{M}k''^2\right]F^{(j)}(\mathbf{r})=\sum\int\chi_j^*\psi_{k''}^{*\,s}(\boldsymbol{\rho})(V_{12}+V_{13})\Psi(1,2,3)d\boldsymbol{\rho}, && j=7,8.
\end{aligned} \quad (10)$$

To satisfy Pauli's principle, we must employ a wave function which is antisymmetric in the two identical particles 1 and 2. To this end, we construct

$$\Psi_a(1,2,3)=\Psi(1,2,3)-P_{12}\Psi(1,2,3), \quad (11)$$

where P_{12} is the operator permuting both the spin and the space coordinates of 1 and 2. Now $P_{12}\Psi(1,2,3)$ can also be expanded in a series

$$P_{12}\Psi(1,2,3)=\sum_{i=1}^{6}\chi_i g^{(i)}(\mathbf{r})\psi_0(\boldsymbol{\rho})+\sum_{i=1}^{6}\chi_i\int G_{k''}^{(i)}(\mathbf{r})\psi_{k''}^{\,t}(\boldsymbol{\rho})d\mathbf{k}''+\sum_{j=7}^{8}\chi_j\int G_{k''}^{(j)}(\mathbf{r})\psi_{k''}^{\,s}(\boldsymbol{\rho})d\mathbf{k}'', \quad (12)$$

where the functions $g^{(i)}(\mathbf{r})$, $G_{k''}^{(i)}(\mathbf{r})$, $G_{k''}^{(j)}(\mathbf{r})$ satisfy equations similar to (10), with $\Psi(1,2,3)$ in the integrand replaced by $P_{12}\Psi(1,2,3)$. For the wave function $\Psi_a(1,2,3)$ we have, on subtracting the corresponding equations for the $f^{(i)}(\mathbf{r})$, $g^{(i)}(\mathbf{r})$, $F_{k''}^{(i)}(\mathbf{r})$, $G_{k''}^{(i)}(\mathbf{r})$, etc., and denoting by

$$\begin{aligned}
&\phi^{(i)}\equiv f^{(i)}(\mathbf{r})-g^{(i)}(\mathbf{r}), \quad \Phi^{(i)}\equiv F^{(i)}(\mathbf{r})-G^{(i)}(\mathbf{r}),\\
&\Phi^{(j)}\equiv F^{(j)}(\mathbf{r})-G^{(j)}(\mathbf{r}),\\
&i=1,\cdots,6, \quad j=7,8,
\end{aligned} \quad (13)$$

$$\begin{aligned}
&\left[\frac{3\hbar^2}{4M}\Delta_r+E+\epsilon\right]\phi^{(i)}=\sum_{\text{spin}}\int\chi_i^*\psi_0^*(\boldsymbol{\rho})(V_{12}+V_{13})\times(1-P_{12})\Psi(1,2,3)d\boldsymbol{\rho},\\
&\left[\frac{3\hbar^2}{4M}\Delta_r+E-\frac{\hbar^2}{M}k''^2\right]\Phi^{(i)}=\sum\int\chi_i^*\psi_{k''}^{*\,t}(\boldsymbol{\rho})\times(1-P_{12})\Psi(1,2,3)d\rho,\\
&\left[\frac{3\hbar^2}{4M}\Delta_r+E-\frac{\hbar^2}{M}k''^2\right]\Phi^{(j)}=\sum\int\chi_j^*\psi_{k''}^{*\,s}(\boldsymbol{\rho})(V_{12}+V_{13})\times(1-P_{12})\Psi(1,2,3)d\boldsymbol{\rho}.
\end{aligned} \quad (14)$$

The functions $\phi^{(i)}$, $\Phi^{(i)}$, $\Phi^{(j)}$ in (13) are the correctly symmetrized wave functions. $\phi^{(i)}$ describes the elastically scattered wave with spin wave function χ_i, together with the incoming wave. The $\Phi^{(i)}(\mathbf{r})$ describe those inelastically scattered waves with spin wave functions which are symmetric in 2 and 3, while $\Phi^{(i)}(\mathbf{r})$ describe those inelastically scattered waves which are antisymmetric in the spins of 2 and 3.

B. Elastic Scattering Cross Section

To obtain the amplitude of the elastically scattered wave of spin wave function χ_i, one calculates as usual the amplitude of the asymptotic solution of $\phi^{(i)}(r)$ for large r and obtains

$$f(\vartheta, \varphi) = -\frac{1}{4\pi}\left(\frac{4M}{3\hbar^2}\right)\Sigma\int\int \exp[-i\mathbf{k}'\cdot\mathbf{r}] \times\chi_i^*\psi_0^*(\boldsymbol{\rho})(V_{12}+V_{13}) \times(1-P_{12})\Psi(1,2,3)d\boldsymbol{\rho}d\mathbf{r}, \quad (15)$$

where ϑ, φ are the polar angles of the direction $\mathbf{k}'$ of the scattered wave. To calculate $f(\vartheta, \varphi)$ one replaces, in an approximation, the function $\Psi(1,2,3)$ in the integrand by the initial wave function

$$\chi_l f^{(l)}(\mathbf{r})\psi_0(\boldsymbol{\rho}), \quad (16)$$

where χ_l may be one of the six $\chi_1, \cdots\chi_6$. For a given initial spin state χ_l, the amplitude of the scattered wave with spin function χ_i is then given by the matrix element

$$(i|f(\vartheta, \varphi)|l) = -\frac{M}{3\pi\hbar^2}\Sigma\int\int \exp[-i\mathbf{k}'\cdot\mathbf{r}] \times\chi_i^*\psi_0^*(\rho)(V_{12}+V_{13})(1-P_{12}) \times\chi_l f^{(l)}(\mathbf{r})\psi_0(\boldsymbol{\rho})d\boldsymbol{\rho}d\mathbf{r}. \quad (17)$$

The intensity of the scattered waves of all spin states is the sum

$$\sum_{i=1}^{6}|(i|f(\vartheta, \varphi)|l)|^2.$$

For $l=1, 2, 3, 4$, one has the "quartet" state scattering, while for $l=5, 6$, one has the "doublet" state scattering. The intensity to be compared with the observed scattered waves of an unpolarized incident beam is the weighted average

$$I(\vartheta, \varphi) = \tfrac{2}{3}\cdot\tfrac{1}{4}\sum_{l=1}^{4}\sum_{i=1}^{6}|(i|f(\vartheta, \varphi)|l)|^2 + \tfrac{1}{3}\cdot\tfrac{1}{2}\sum_{l=5}^{6}\sum_{i=1}^{6}|(i|f(\vartheta, \varphi)|l)|^2. \quad (18)$$

For central force, all non-diagonal matrix elements $i\neq l$ in (17) vanish.

The differential cross section of a proton being scattered into the solid angle $d\omega = 2\pi\sin\vartheta d\vartheta$ (the polar axis being the direction of the incoming beam) is, since $I(\vartheta, \varphi)$ actually does not depend on φ,

$$\sigma_{el}(E_0, \vartheta)d\omega = 2\pi I(\vartheta, \varphi)\sin\vartheta d\vartheta = 2\pi I(\vartheta)\sin\vartheta d\vartheta, \quad (19)$$

where E_0 denotes the energy of the incident proton.

It is desirable to transform the above expression to the laboratory coordinate system. Let Θ be the angle between the direction of the scattered proton (as seen in the laboratory system) and the direction of the incident beam. It can be shown that

$$\tan\Theta = 2\sin\vartheta/(1+2\cos\vartheta). \quad (20)$$

The differential cross section of a proton being scattered into directions between Θ and $\Theta+d\Theta$ is then given by

$$2\pi\sigma_{el}(E_0, \Theta)\sin\Theta d\Theta = 2\pi g I(\Theta)\sin\Theta d\Theta, \quad (19a)$$

where $I(\Theta)$ is obtained from $I(\vartheta)$ in (19) by means of (20), and where

$$g = (1+2\cos\vartheta)^3/4(2+\cos\vartheta)\cos^3\Theta.$$

C. Inelastic Scattering Cross Section

For inelastic scattering, let us introduce the wave vectors $\mathbf{k}'$ and $\mathbf{k}''$ corresponding to $\mathbf{r}$ and $\boldsymbol{\rho}$, respectively, in (1), namely,

$$E' = \frac{3\hbar^2k'^2}{4M}, \quad E'' = \frac{\hbar^2k''^2}{M}, \quad (21)$$

where E' is the energy of the scattered proton relative to the center of gravity of the other two particles, and E'' is the energy of relative motion of the other two particles. If E_0 denotes the energy of the incident proton in the laboratory

system and ϵ the binding energy of the deuteron, the energy relation is

$$\tfrac{3}{2}E_0=E'+E''+\epsilon. \quad (22)$$

Simple energy and momentum considerations show that while the magnitudes of $\mathbf{k}'$ and $\mathbf{k}''$ are restricted by (22), their directions are entirely arbitrary so that the differential cross section must be specified by five variables, such as the directions of both $\mathbf{k}'$ and $\mathbf{k}''$ and the magnitude of either $\mathbf{k}'$ or $\mathbf{k}''$. The differential cross section of a proton being scattered into the solid angle $d\Omega'$ (in the center of gravity system) and $\mathbf{k}''$ lying in the volume element $d\mathbf{k}''=k''^2dk''d\Omega''$ is

$$\sigma(E_0, k'', \Omega')d\Omega'k''^2dk''d\Omega''$$
$$=(k'/k)I(\Omega', \Omega'')d\Omega'k''^2dk''d\Omega'', \quad (23)$$

where $I(\Omega', \Omega'')$ is given by the weighted average of the "quartet" and the "doublet" scattered intensity

$$I(\Omega', \Omega'')=\tfrac{2}{3}\cdot\tfrac{1}{4}\sum_{l=1}^{4}\sum_{i=1}^{8}|(i|f(\Omega', \Omega'')|l)|^2$$
$$+\tfrac{1}{3}\cdot\tfrac{1}{2}\sum_{l=5}^{6}\sum_{i=1}^{8}|(i|f(\Omega', \Omega'')|l)|^2, \quad (24)$$

where $(i|f(\Omega', \Omega'')|l)$ is given by

$$(i|f(\Omega', \Omega'')|l)$$
$$=-\frac{1}{4\pi}\left(\frac{4M}{3\hbar^2}\right)\Sigma\int\int \exp[-i\mathbf{k}'\cdot\mathbf{r}]$$
$$\times\chi_i^*\psi_{k''}^*(\rho)(V_{12}+V_{13})(1-P_{12})$$
$$\times\chi_l f^{(l)}(\mathbf{r})\psi_0(\rho)d\rho d\mathbf{r}. \quad (25)$$

Here $\psi_{k''}(\rho)$ is $\psi_{k''}{}^{i}(\rho)$ for $i=1, \cdots 6$, and is $\psi_{k''}{}^{*}(\rho)$ for $i=7, 8$, as shown in (8) and (12).

The calculation of $I(\Omega', \Omega'')$ and the transformation to the laboratory system will be given in Section IVB.

III. ELASTIC SCATTERING

For the energy range $E_0=100-200$ Mev, we shall employ Born's approximation by replacing the $\Psi(1, 2, 3)$ in the integrand in (15) by the initial wave function (16) in which $f^{(l)}(r)$ is represented by a plane wave, namely,

$$\Psi(1, 2, 3)\equiv\chi_i\psi(1, 2, 3)=\chi_i\exp[i\mathbf{k}\cdot\mathbf{r}]\psi_0(\rho). \quad (26)$$

In integrating over $\mathbf{r}$ and ρ in (17), since the operators V_{12}, V_{13} depend on the symmetry of the wave function of the state with respect to the interchange of the two particles, it is expedient, in dealing with the term V_{13}, to express the wave function $(1-P_{12})\psi(1, 2, 3)$ as a combination of terms which are either symmetric or antisymmetric with respect to 1 and 3 so that for each term the appropriate potential can be immediately picked out from Eqs. (3). Let X_1, X_2, $\cdots X_6$ be the following linearly independent combinations of the basic functions ψ, $P_{12}\psi$, $P_{13}\psi$, $P_{23}\psi$, $P_{12}P_{23}\psi$, $P_{12}P_{13}\psi$:

	ψ	$P_{12}\psi$	$P_{13}\psi$	$P_{23}\psi$	$P_{12}P_{23}\psi$	$P_{12}P_{13}\psi$
X_1	1	1	1	1	1	1
X_2	1	−1	1	1	−1	1
X_3	1	1	1	−1	1	−1
X_4	1	1	−1	1	−1	−1
X_5	1	−1	−1	1	1	−1
X_6	1	−1	−1	−1	1	1

Thus X_1 is totally symmetric, X_6 totally antisymmetric, in 1, 2, 3, X_2, X_3 are symmetric and X_4, X_5 are antisymmetric in 1, 3. Then one finds

$$\psi=\tfrac{1}{4}(X_2+X_3+X_4+X_6),$$
$$P_{12}\psi=\tfrac{1}{4}(X_1-X_2+X_4-X_5).$$

With (26), it can be shown that

$$\psi=P_{23}\psi=\exp[i\mathbf{k}\cdot\mathbf{r}]\psi_0(\rho),$$
$$P_{12}\psi=P_{12}P_{23}\psi=\exp[-i\mathbf{k}\cdot(\tfrac{1}{2}\mathbf{r}+\tfrac{3}{4}\rho)]\psi_0(|\mathbf{r}-\tfrac{1}{2}\rho|),$$
$$P_{13}\psi=P_{12}P_{13}\psi=\exp[-i\mathbf{k}\cdot(\tfrac{1}{2}\mathbf{r}-\tfrac{3}{4}\rho)]\psi_0(|\mathbf{r}+\tfrac{1}{2}\rho|).$$

In the present paper, the scattered intensity $I(\vartheta, \varphi)$ in (18) has been calculated with the potentials (3) which include the tensor force. But since the actual numerical calculation has been performed after omitting the tensor force on account of the excessive amount of computational work that would be involved, we shall only give the formulas without tensor force in the following and give the complete formulas including tensor force in Appendix I.

Without tensor force, there are only diagonal matrix elements in (17) and the summation over the spin coordinates can be immediately carried out. All integrals in (17) can be shown to reduce to the following three:

$$L_1=\int\int \exp[-i\mathbf{k}'\cdot\mathbf{r}]\psi_0^*(\rho)\,U(|\mathbf{r}+\tfrac{1}{2}\boldsymbol{\rho}|)\times\exp[i\mathbf{k}\cdot\mathbf{r}]\psi_0(\rho)\,d\boldsymbol{\rho}\,d\mathbf{r}, \quad (27a)$$

$$L_2=\int\int \exp[-i\mathbf{k}'\cdot\mathbf{r}]\psi_0^*(\rho)\,U(|\mathbf{r}+\tfrac{1}{2}\boldsymbol{\rho}|)\times\exp[-i\mathbf{k}\cdot(\tfrac{1}{2}\mathbf{r}+\tfrac{3}{4}\boldsymbol{\rho})]\times\psi_0(|\mathbf{r}-\tfrac{1}{2}\boldsymbol{\rho}|)\,d\boldsymbol{\rho}\,d\mathbf{r}, \quad (27b)$$

$$L_3=\int\int \exp[-i\mathbf{k}',\mathbf{r}]\psi_0^*(\rho)\,U(|\mathbf{r}-\tfrac{1}{2}\boldsymbol{\rho}|)\times\exp[-i\mathbf{k}\cdot(\tfrac{1}{2}\mathbf{r}+\tfrac{3}{4}\rho)]\times\psi_0(|\mathbf{r}-\tfrac{1}{2}\boldsymbol{\rho}|)\,d\boldsymbol{\rho}\,d\mathbf{r}. \quad (27c)$$

In order to be able to carry out the integrations in (27) analytically, we shall represent the radial wave function of the ground state of the deuteron by a Gaussian function

$$\psi_0(\rho)=A\exp[-\lambda^2\rho^2]. \quad (28a)$$

For the radial part of the potential $U(|\xi|)$, we shall assume a Gaussian function

$$U(|\xi|)=V_0\exp[-\alpha^2\xi^2]. \quad (28b)$$

Carrying out the integration, we find

$$L_1=B_1\exp\left[-\frac{\alpha^2+8\lambda^2}{8\lambda^2}x^2\right],\qquad x^2=\left(\frac{k}{\alpha}\right)^2\sin^2\frac{\vartheta}{2},$$

$$L_2=B_2\exp\left[-\frac{\alpha^2}{8\lambda^2}x^2-y^2\right],\qquad y^2=\frac{9k^2}{32(\alpha^2+\frac{1}{2}\lambda^2)}(1+\cos\vartheta), \quad (29)$$

$$L_3=B_3\exp\left[-\frac{k^2}{16\lambda^2}(5+4\cos\vartheta)-z^2\right],\qquad z^2=\frac{k^2}{16(\alpha^2+\lambda^2)}(5+4\cos\vartheta),$$

where

$$B_1=\frac{A^2V_0\pi^3}{2^{\frac{1}{2}}\alpha^3\lambda^3},\quad B_2=\frac{A^2V_0\pi^3}{2^{\frac{1}{2}}\lambda^3(\alpha^2+\frac{1}{2}\lambda^2)^{\frac{1}{2}}},\quad B_3=\frac{A^2V_0\pi^3}{\lambda^3(\alpha^2+\frac{1}{2}\lambda^2)^{\frac{1}{2}}}.$$

After some calculation whose details we shall omit here, it is found that $I(\vartheta,\varphi)$ in (18), which is independent of φ and is hereafter denoted by $I(\vartheta)$, is given, on the three theories of nucleon interaction, by the following expressions.

Ordinary force:

$$(3\pi\hbar^2/M)^2I(\vartheta)=4(1-g+\tfrac{3}{4}g^2)L_1^2+\tfrac{3}{4}(1-\tfrac{2}{3}g+g^2)L_2^2+\tfrac{3}{4}L_3^2-2(1+\tfrac{2}{3}g-\tfrac{3}{2}g^2)L_1L_2-2(1+\tfrac{1}{2}g)L_1L_3+\tfrac{3}{2}(1-\tfrac{1}{3}g)L_2L_3. \quad (30a)$$

Exchange force:

$$(3\pi\hbar^2/M)^2I(\vartheta)=\text{the expression above, with 1, 2 interchanged.} \quad (30b)$$

Symmetrical force:

$$(3\pi\hbar^2/M)^2I(\vartheta)=\tfrac{1}{4}(11-30g+27g^2)L_2^2+\tfrac{3}{4}L_3^2-\tfrac{1}{2}(1+3g)L_2L_3. \quad (30c)$$

It is to be noticed that of the three integrals L_1, L_2, L_3, L_1 is by far the most important one. It has a strong maximum in the forward direction $\vartheta=0$. The integrals L_2, L_3 contain the exchange operators P_{12} or P_{13} and give but small contributions, L_3 only in the backward direction $\vartheta\simeq\pi$, as is seen from (29). That the scattered intensity $I(\vartheta)$ on the symmetrical theory does not depend on L_1 is a consequence of the potential (3). This can perhaps be brought out more clearly as follows. We may write (3) in the form

$$V_{12}=\boldsymbol{\sigma}_1\cdot\boldsymbol{\sigma}_2(1+2P_{12})\,V_{12}^{\text{even}}.$$

According to (17), the scattered amplitudes are proportional to the matrix elements of the operator:

$$\begin{aligned}&(V_{12}+V_{13})(1-P_{12})\\&=\boldsymbol{\sigma}_1\cdot\boldsymbol{\sigma}_2V_{12}^{\text{even}}(1+2P_{12})(1-P_{12})+\boldsymbol{\sigma}_1\cdot\boldsymbol{\sigma}_3V_{13}^{\text{even}}(1+2P_{13})(1-P_{12})\\&=\boldsymbol{\sigma}_1\cdot\boldsymbol{\sigma}_2V_{12}^{\text{even}}(-1+P_{12})+\boldsymbol{\sigma}_1\cdot\boldsymbol{\sigma}_3V_{13}^{\text{even}}(1+2P_{13}-P_{12}-2P_{13}P_{12}).\end{aligned}$$

The terms containing the exchange operators give the L_2 and L_3 of (30c). The remaining terms $-\boldsymbol{\sigma}_1\cdot\boldsymbol{\sigma}_2V_{12}$ and $\boldsymbol{\sigma}_1\cdot\boldsymbol{\sigma}_3V_{13}$ give exactly equal and opposite matrix elements since the ground state of the deuteron is symmetrical in the particles 2 and 3. This cancellation for the symmetrical theory accounts for the very small cross sections shown in Tables I and II.

TABLE I. Differential cross section $\sigma_{el}(E_0,\Theta)$ in 10^{-25} cm², defined in (19a), for elastic proton-deuteron scattering.

Θ	Ordinary	Exchange	Symmetrical
100 Mev			
0	100.5	20.2	0.010,2
10	67.7	13.6	0.010,0
20	19.6	3.82	0.009,9
30	2.79	.506	0.009,9
41	.208	.037,2	0.009,5
63	.002,9	.017,7	0.008,3
90	.003,1	.012,0	0.005,5
106	.006,6	.006,2	0.003,8
126	.025,8	.008,6	0.014,0
150	.086,9	.047,9	0.061,7
180	.129	.082,4	0.099,5
150 Mev			
0	101.2	20.8	0.000,184
10	56.3	11.55	0.000,184
20	9.09	1.86	0.000,184
30	.498	.098	0.000,190
41	.011,4	.001,93	0.000,183
63	.000,07	.000,38	0.000,172
90	.000,06	.000,29	0.000,127
106	.000,02	.000,17	0.000,108
126	.000,80	.000,28	0.000,48
150	.006,23	.004,30	0.004,53
180	.012,0	.009,67	0.010,6
200 Mev			
0	101.0	20.9	0.000,004
10	46.3	9.56	0.000,004
20	4.12	.85	0.000,004
30	.093	.019	0.000,004
41	.000,633	.000,112	0.000,004
63	.000,002	.000,009	0.000,004
90	.000,001	.000,006	0.000,003
106	.000,002	.000,005	0.000,003
126	.000,025	.000,007	0.000,015
150	.000,45	.000,43	0.000,40
180	.001,17	.001,08	0.001,11

TABLE II. Total cross section σ_{el} in 10^{-24} cm² for elastic proton-deuteron scattering.

	Ordinary	Exchange	Symmetrical
100 Mev	0.384	0.077	0.003,8
150 Mev	0.255	0.051	0.000,2
200 Mev	0.185	0.037	0.000,01

IV. TOTAL (ELASTIC PLUS INELASTIC) SCATTERING

A. Total Scattering

We shall again relegate the complete formula including tensor force to Appendix II and confine ourselves to the case of central force in the following.

It is important to notice that since two protons of indeterminate origin are emitted in each inelastic scattering event, we must divide the integral of expression (23) by two to obtain the total inelastic cross section. Representing the incident wave by the plane wave (26), one can express all the matrix elements $(i|f(\Omega',\Omega'')|l)$ in terms of integrals $\mathfrak{L}_1$, $\mathfrak{L}_2$, $\mathfrak{L}_3$ which are obtained from those for L_1, L_2, L_3 in (27) by replacing $\psi_0^*(\rho)$ by $\psi_{k''}^{*t}(\rho)$ or $\psi_{k''}^{*s}(\rho)$ according as $i=1,2,\cdots 6$ or $i=7,8$, and $\mathfrak{L}_1^*$, $\mathfrak{L}_2^*$, $\mathfrak{L}_3^*$ such that $\mathfrak{L}_1^*=\mathfrak{L}_1$ with $\mathbf{k}''$ replaced by $-\mathbf{k}''$. Thus for $i=1,\cdots 6$, we have

$$\mathfrak{L}_1^t=\int\int \exp[-i\mathbf{k}'\cdot\mathbf{r}]\psi_{k''}^{*t}(\rho) \times U(|\mathbf{r}+\tfrac{1}{2}\rho|)\exp[i\mathbf{k}\cdot\mathbf{r}]\psi_0(\rho)d\rho d\mathbf{r}, \quad (31a)$$

and for $i=7, 8$,

$$\mathfrak{L}_1^s=\int\int \exp[-i\mathbf{k}'\cdot\mathbf{r}]\psi_{k''}^{*s}(\rho) U(|\mathbf{r}+\tfrac{1}{2}\rho|)\exp[i\mathbf{k}\cdot\mathbf{r}]\psi_0(\rho)d\rho d\mathbf{r}. \quad (31b)$$

The actual evaluation of these integrals requires a knowledge of the continuum wave functions $\psi_{k''}^t(\rho)$ and $\psi_{k''}^s(\rho)$ of the deuteron. This is essential for any detailed investigation of the energy spectrum or angular distribution of the particles resulting from collisions in which the deuteron disintegrates. For the gross information provided by the total cross section, however, only the following general properties of the continuum wave functions are important, namely, the functions $\{\psi_{k''}^t(\rho),\ \psi_0(\rho)\}$ and $\psi_{k''}(\rho)$ form two complete orthonormal sets, and for large k'', $\psi_{k''}^t(\rho)$ and $\psi_{k''}^s(\rho)$ approach the plane wave $1/(2\pi)^{\frac{3}{2}}\exp[i\mathbf{k}''\cdot\rho]$.

If one makes the plane wave approximation

$$\psi_{k''}^t(\rho)=\psi_{k''}^s(\rho)=\frac{1}{(2\pi)^{\frac{3}{2}}}\exp[i\mathbf{k}''\cdot\rho], \quad (32)$$

one finds readily

$$\begin{aligned}&\mathfrak{L}_1^t=\mathfrak{L}_1^s=\mathfrak{L}_1=D\exp[-q^2-x^2],\\ &\qquad 16\lambda^2q^2=|\mathbf{k}-\mathbf{k}'+2\mathbf{k}''|^2,\\ &\qquad 4\alpha^2x^2=|\mathbf{k}-\mathbf{k}'|^2,\\ &\mathfrak{L}_2^t=\mathfrak{L}_2^s=\mathfrak{L}_2=D\exp[-q^2-y^2],\\ &\qquad 4\alpha^2y^2=|\mathbf{k}+\tfrac{1}{2}\mathbf{k}'+\mathbf{k}''|^2,\\ &\mathfrak{L}_1^*=\mathfrak{L}_1 \text{ with } \mathbf{k}'' \text{ replaced by } -\mathbf{k}'', \text{ etc.},\end{aligned} \quad (33)$$

$$D=\frac{A\,V_0\pi^3}{\alpha^3\lambda^3}.$$

The integrals $\mathfrak{L}_3$, $\mathfrak{L}_3^*$ corresponding to L_3 in (27) can be shown to contain a δ-function and contribute nothing to the scattered intensity. They have therefore been left out in the following.

To the approximation (32), the intensity $I(\Omega', \Omega'')$ in (24) is given by the following expressions.

Ordinary force:

$$(2\pi)^3(3\pi\hbar^2/M)^2 I(\Omega', \Omega'') = (1-g+g^2)(\mathfrak{L}_1^2+\mathfrak{L}_2^2+\mathfrak{L}_1^{*2}) - (1+2g-2g^2)\mathfrak{L}_1\mathfrak{L}_2 + (2-2g+g^2)\mathfrak{L}_1\mathfrak{L}_1^* - (1+g-g^2)\mathfrak{L}_2\mathfrak{L}_1^*. \quad (34a)$$

Exchange force:

$$(2\pi)^3(3\pi\hbar^2/M)^2 I(\Omega', \Omega'') = \text{the expression above, with 1, 2 interchanged.} \quad (34b)$$

Symmetrical force:

$$(2\pi)^3(3\pi\hbar^2/M)^2 I(\Omega', \Omega'') = (\tfrac{1}{3}-g+g^2)(\mathfrak{L}_1^2+\mathfrak{L}_2^2+\mathfrak{L}_1^{*2}+4\mathfrak{L}_2^{*2}) + (\tfrac{1}{3}-2g+2g^2)(\mathfrak{L}_1\mathfrak{L}_2-2\mathfrak{L}_1^*\mathfrak{L}_2^*) - (2/9)(1-3g+(9/2)g^2)\mathfrak{L}_1\mathfrak{L}_1^* + (\tfrac{1}{9}-g+g^2)(2\mathfrak{L}_1\mathfrak{L}_2^*-\mathfrak{L}_1^*\mathfrak{L}_2) + (2/9)(5-4g+9g^2)\mathfrak{L}_2\mathfrak{L}_2^*. \quad (34c)$$

It appears that (23), with $I(\Omega', \Omega'')$ given by (34) and (33), gives the cross section for inelastic scattering. The approximation (32), however, has the consequence that the cross section given by (23) and (34) also contains contributions of the elastic scattering, since the plane waves $\psi_{k''}{}^{t}(\varrho)$ are not orthogonal to the wave function of the ground state of the deuteron and hence contains components of $\psi_0(\rho)$. It will be shown below that (23), (33), and (34) actually form a closer approximation to the total scattering (elastic plus inelastic) than to the inelastic.[5]

To simplify the presentation of the argument, let us first consider that part of $I(\Omega', \Omega'')$ that comes from $\mathfrak{L}_1^2$, in the case of ordinary force (34a). Without making the approximation (32,) one would have obtained instead of $(1-g+g^2)\mathfrak{L}_1^2$ the expression

$$(1-g+\tfrac{3}{4}g^2)(\mathfrak{L}_1{}^t)^2+\tfrac{1}{4}g^2(\mathfrak{L}_1{}^s)^2.$$

Let us define

$$\mathbf{K}=\mathbf{k}-\mathbf{k}', \quad \xi=\mathbf{r}+\tfrac{1}{2}\varrho. \quad (35)$$

From (31a), one finds

$$\mathfrak{L}_1{}^t = C_{0k''}(\mathbf{K}, \mathbf{k}'')F(K), \quad (36)$$

where

$$C_{0k''}(\mathbf{K}, \mathbf{k}'') = \int \exp[-(i/2)\mathbf{K}\cdot\varrho] \times \psi_{k''}{}^{*t}(\varrho)\psi_0(\rho)d\varrho, \quad (37)$$

$$F(K) = \int \exp[i\mathbf{K}\cdot\xi]U(|\xi|)d\xi.$$

$F(K)$ is seen to be a function of the magnitude K of $\mathbf{K}$ alone. Also

$$|C_{0k''}(K)|^2 \equiv \int |C_{0k''}(\mathbf{K}, \mathbf{k}'')|^2 d\Omega'' \quad (37a)$$

can be seen to be a function of the magnitude K of $\mathbf{K}$ alone. On transforming from the variables k', Ω' in (23) to the variable K by means of (35), namely,

$$KdK = kk' \sin\vartheta' d\vartheta' = (1/2\pi)kk'd\Omega',$$

one obtains from (23) that part of the inelastic scattering cross section that comes from $(\mathfrak{L}_1{}^t)^2$

$$2\{\sigma_{\text{ine}}\} = (1-g+\tfrac{3}{4}g^2)(M/3\pi\hbar^2)^2 \times\frac{1}{k}\int\int k'(\mathfrak{L}_1{}^t)^2 d\Omega' d\mathbf{k}'' = (1-g+\tfrac{3}{4}g^2)(M/3\pi\hbar^2)^2 \times\frac{2\pi}{k^2}\int |F(K)|^2 KdK \times\int |C_{0k''}(K)|^2 k''^2 dk''. \quad (38)$$

Now since the ground state of the deuteron is a triplet state, it is clear from (33), (27), (18), and (24) that every inelastic triplet amplitude $\mathfrak{L}^t$ has a corresponding elastically scattered amplitude L differing from $\mathfrak{L}^t$ in having $\psi_0(\rho)$ in place of $\psi_{k''}{}^{t}(\rho)$. On adding to (38) the contribution of elastic scattering $(1-g+3/4g^2)L_1$ from (30a), one obtains as a typical contribution to the elastic plus twice the inelastic cross section the

[5] Cf. N. F. Mott and H. S. W. Massey, *Theory of Atomic Collisions* (Oxford University Press, New York, 1933), p. 172.

expression

$$\sigma_{el}+2\sigma_{ine}=(1-g+\tfrac{3}{4}g^2)(M/3\pi\hbar^2)^2 \times\frac{2\pi}{k^2}\int|F(K)|^2KdK\Big\{|C_{00}(K)|^2 +\int|C_{0k''}(K)|^2k''^2dk''\Big\}, \quad (39)$$

where, analogous to (37),

$$C_{00}(K)=\int\exp\Big[-\frac{i}{2}\mathbf{K}\cdot\boldsymbol{\rho}\Big]\psi_0^*(\rho)\psi_0(\rho)d\boldsymbol{\rho}. \quad (40)$$

In (39), for any fixed value K of the magnitude of $\mathbf{K}$, the range of integration of k'' is from 0 to the maximum value k_m'' given by the energy equation (22), or, in view of (35),

$$k_m''^2=\tfrac{3}{4}k^2-(M/\hbar^2)\epsilon-\tfrac{3}{4}(k-K)^2. \quad (41)$$

The range of integration of K is from $k-[k^2-(4M/3\hbar^2)\epsilon]^{\frac{1}{2}}$ to $k+[k^2-(4M/3\hbar^2)\epsilon]^{\frac{1}{2}}$.

As $\psi_0(\rho)$ and the $\psi_{k''}{}^{(+)}(\boldsymbol{\rho})$ form a complete orthonormal set of functions, one can expand in (37)

$$\exp[-(i/2)\mathbf{K}\cdot\boldsymbol{\rho}]\psi_0(\rho)=C_{00}(K)\psi_0(\rho) +\int C_{0k''}(\mathbf{K},\mathbf{k}'')\psi_{k''}{}^{(+)}(\boldsymbol{\rho})d\mathbf{k}''.$$

From this and

$$\int|\exp[-(i/2)\mathbf{K}\cdot\boldsymbol{\rho}]\psi_0(\rho)|^2d\boldsymbol{\rho}=1$$

one obtains the relation

$$|C_{00}(K)|^2+\int_0^\infty|C_{0k''}(K)|^2k''^2dk''=1. \quad (42)$$

In view of (42), we can write in (39)

$$|C_{00}(K)|^2+\int_0^{k_m''}|C_{0k''}(K)|^2k''^2dk'' =1-\int_{k_m''}^\infty|C_{0k''}(K)|^2k''^2dk''. \quad (43)$$

Now if one makes the plane wave approximation (32) in (37), then, instead of (37) and (37a), one has

$$D_{0k''}(\mathbf{K},\mathbf{k}'')=\frac{1}{(2\pi)^{\frac{1}{2}}}\int\exp[-(i/2)\mathbf{K}\cdot\boldsymbol{\rho}] \times\exp[-i\mathbf{k}''\cdot\boldsymbol{\rho}]\psi_0(\rho)d\boldsymbol{\rho} \quad (44)$$

and

$$|D_{0k''}(K)|^2=\int|D_{0k''}(\mathbf{K},\mathbf{k}'')|^2d\Omega''. \quad (44a)$$

From (44), it follows that

$$\int_0^\infty|D_{0k''}(K)|^2k''^2dk''=1.$$

The second integral in (38) for the inelastic cross section will be replaced by

$$\int_0^{k_m''}|D_{0k''}(K)|^2k''^2dk'' =1-\int_{k_m''}^\infty|D_{0k''}(K)|^2k''^2dk''. \quad (45)$$

But on comparing (45) with (43), it is seen that to the approximation (32), the use of plane waves in (38) leads to (39).

An entirely similar argument holds for the singlet part $\mathfrak{L}_1{}^s$. It cannot be applied to terms containing $\mathfrak{L}_2$ or $\mathfrak{L}_2{}^*$ in (34). Calculations show, however, that $\mathfrak{L}_2$ gives some contribution only for large values of k''. This is expected since it arises from the effect of exchange. For large k'', the plane wave approximation would be valid. Now, for elastic scattering, the contribution from L_2 in (30) is negligibly small. Hence $\mathfrak{L}_2$ in (34), while giving the inelastic scattering, also gives approximately the total scattering. The other terms in (34) are either negligibly small, or give some small contributions only for large values of k''.

Finally let us consider the validity of the approximation (32) which replaces (43) by (45). In (39), the important region in K is when $|F(K)|^2K$ is near its maximum. With the Gaussian potential (28b), this maximum occurs at $K=\alpha$. With the value $\alpha=0.515\times10^{13}$ cm^{-1} in (57), one finds for an incident proton of 100 Mev the corresponding $k_m''(\alpha)$ at 37 Mev. For 200-Mev protons, this $k_m''(\alpha)$ corresponds to 56 Mev. For these k_m'', the approximation of replacing (43) by (45) is justified. For the region of small K in (39), however, the corresponding $k_m''(K)$ is smaller and the plane wave approximation will be bad. Actual calculation shows that the contribution to the total cross section from the region of small k'' is rather small in the case of the symmetrical theory. Hence the error committed

by the plane wave approximation in this case is presumably not very great. The situation is less favorable with the ordinary and the exchange force, especially the former.

B. Angular Distribution and Energy Spectrum of Scattered Protons

For comparison with experimental results, it is desirable to transform to the laboratory coordinate system. Let $\mathbf{p}$ be the wave vector corresponding to the momentum of the scattered proton referred to the laboratory system. It can be shown that

$$\mathbf{p}=\tfrac{1}{2}\mathbf{k}+\mathbf{k}'. \tag{46}$$

Let E_p be the energy, in the lab system, of the scattered proton. Then $E_p=\hbar^2p^2/2M$. From (21) and (22), one has $k''dk''=\frac{3}{4}k'dk'$. Hence

$$k'k''^2dk''d\Omega'd\Omega''=\tfrac{3}{4}k''k'^2dk'd\Omega'd\Omega''=\tfrac{3}{4}k''d\mathbf{p}d\Omega''$$
$$=(3M/4\hbar^2)pk''dE_pd\Omega d\Omega'',$$

where $d\Omega$ is the solid angle into which $\mathbf{p}$ is directed. Hence the differential cross section of a proton being scattered into the solid angle $d\Omega=2\pi\sin\vartheta d\vartheta$ is given by

$$2\pi\sigma(E_0,E_p,\vartheta)dE_p\sin\vartheta d\vartheta$$
$$=\frac{3M}{4\hbar^2}\frac{k''}{k}pdE_p2\pi\sin\vartheta d\vartheta\int I(\Omega,\Omega'')d\Omega'', \tag{47}$$

where $I(\Omega,\Omega'')$ is obtained from $I(\Omega',\Omega'')$ in (34) by means of the transformation (46).

The evaluation of $\int I(\Omega,\Omega'')d\Omega''$ involves a large amount of work on account of the complicated manner in which the directions of $\mathbf{k}'$ and $\mathbf{k}''$ appear in the expressions (33). In the following, we have carried out a preliminary calculation without the tensor forces. The integral $I(\Omega)\equiv\int I(\Omega,\Omega'')d\Omega''$ is given by the following expressions for the three theories of nucleon interaction.

Ordinary:

$$(2\pi)^3(3\pi\hbar^2/M)^2I(\Omega)$$
$$=(1-g+g^2)(2\Lambda_1^2+\Lambda_2^2)$$
$$-(1+2g-2g^2)\Lambda_1\Lambda_2$$
$$+2(1-g+\tfrac{1}{2}g^2)\Lambda_1\Lambda_1^*$$
$$-(1+g-g^2)\Lambda_1^*\Lambda_2.$$

Exchange:

$$(2\pi)^3(3\pi\hbar^2/M)^2I(\Omega)=\text{expression above with 1, 2 interchanged.} \tag{48}$$

Symmetrical:

$$(2\pi)^3(3\pi\hbar^2/M)^2I(\Omega)$$
$$=(\tfrac{1}{3}-g+g^2)(2\Lambda_1^2+5\Lambda_2^2)$$
$$-(\tfrac{1}{3}-2g+2g^2)\Lambda_1\Lambda_2$$
$$-(2/9)(1-3g+(9/2)g^2)\Lambda_1\Lambda_1^*$$
$$+(\tfrac{1}{9}-g+g^2)\Lambda_1^*\Lambda_2$$
$$+((10/9)-(8/3)g+2g^2)\Lambda_2\Lambda_2^*,$$

where

$$\Lambda_1^2=4\pi D^2\frac{\lambda^2}{xk''}\exp\left[-\frac{x^2}{2\alpha^2}-\frac{(x-2k'')^2}{8\lambda^2}\right]$$
$$\times\left(1-\exp\left[-\frac{xk''}{\lambda^2}\right]\right),\quad \mathbf{x}=\tfrac{3}{2}\mathbf{k}-\mathbf{p}$$

$$\Lambda_1\Lambda_1^*=4\pi D^2\exp\left[-\frac{k''^2}{2\lambda^2}-\frac{\alpha^2+4\lambda^2}{8\alpha^2\lambda^2}x^2\right],$$

$$\Lambda_2\Lambda_2^*=4\pi D^2\exp\left[-\frac{\alpha^2+\lambda^2}{2\alpha^2\lambda^2}k''^2-\frac{x^2}{8\lambda^2}-\frac{y^2}{2\alpha^2}\right],$$
$$\mathbf{y}=\tfrac{3}{4}\mathbf{k}+\tfrac{1}{2}\mathbf{p}$$

$$\Lambda_1\Lambda_2^*=\Lambda_1^*\Lambda_2=4\pi D^2\frac{\alpha^2}{yk''}$$
$$\times\exp\left[-\frac{k''^2}{2\lambda^2}-\frac{\alpha^2+2\lambda^2}{8\alpha^2\lambda^2}x^2\right.$$
$$\left.-\frac{(y-k'')^2}{4\alpha^2}\right](1-\exp[-yk''/\alpha^2]),$$

$$\Lambda_1\Lambda_2=4\pi D^2\frac{\sinh z}{z}\exp\left[-\frac{9}{64}\left(\frac{2\alpha^2+5\lambda^2}{\alpha^2\lambda^2}\right)k^2\right.$$
$$-\frac{2\alpha^2+5\lambda^2}{16\alpha^2\lambda^2}p^2-\frac{2\alpha^2+\lambda^2}{4\alpha^2\lambda^2}k''^2$$
$$\left.+\frac{3}{16}\cdot\frac{2\alpha^2+3\lambda^2}{\alpha^2\lambda^2}kp\cos\vartheta\right], \tag{49}$$

$$z^2=\xi^2+\eta^2,\quad \xi=\frac{2\alpha^2-\lambda^2}{4\alpha^2\lambda^2}pk''\sin\vartheta,$$

$$\eta=\frac{3(2\alpha^2+\lambda^2)}{8\alpha^2\lambda^2}kk''-\frac{2\alpha^2-\lambda^2}{4\alpha^2\lambda^2}pk''\cos\vartheta,$$

$$\Lambda_2^2=4\pi D^2\frac{\sinh t}{t}\exp\left[-\frac{9}{32}\frac{\alpha^2+\lambda^2}{\alpha^2\lambda^2}k^2\right.$$
$$\left.-\frac{\alpha^2+\lambda^2}{8\alpha^2\lambda^2}(p^2+4k''^2)+\frac{3}{8}\frac{\alpha^2-\lambda^2}{\alpha^2\lambda^2}kp\cos\vartheta\right],$$

$$t=\mu^2+\nu^2, \quad \mu=\frac{\alpha^2-\lambda^2}{2\alpha^2\lambda^2}pk''\sin\vartheta,$$

$$\nu=\frac{3(\alpha^2+\lambda^2)}{4\alpha^2\lambda^2}kk''-\frac{\alpha^2-\lambda^2}{2\alpha^2\lambda^2}pk''\cos\vartheta.$$

The numerical values of the total cross section given in Table III were obtained by integrating

TABLE III. Cross sections σ_t for total (elastic plus inelastic) proton-deuteron scattering, in 10^{-24} cm^2.

		Ordinary	Exchange	Symmetrical
100 Mev	σ_{p-n}	0.140	0.140	0.140
	σ_{p-p}	0.130	0.130	0.028
	$\sigma_{p-n}+\sigma_{p-p}$	0.270	0.270	0.168
	$\sigma_{t(p-d)}$	0.424	0.213	0.089
200 Mev	σ_{p-n}	0.070	0.070	0.070
	σ_{p-p}	0.070	0.070	0.014
	$\sigma_{p-n}+\sigma_{p-p}$	0.140	0.140	0.084
	$\sigma_{t(p-d)}$	0.214	0.119	0.043

(47) over the energy and angular distribution of the emerging proton to give $\sigma_{\text{el}}+2\sigma_{\text{ine}}$.

C. Angular Distribution and Energy Spectrum of Neutrons Ejected in Proton-Deuteron Collisions

Experimentally one may have a beam of high energy neutrons impinging on a deuterium target and is interested in the angular distribution of the protons ejected and their spectrum for a given direction. When the Coulomb interaction is neglected, this situation is the same as studying the neutrons ejected in a proton-deuteron collision. To find the differential cross section of a neutron being scattered with energy E_n (in the laboratory system) into the solid angle $d\Omega_n$, one proceeds as follows. It can be shown that the wave vector of the neutron in the laboratory system is given by

$$\mathbf{p}_n=\tfrac{1}{2}\mathbf{k}-\tfrac{1}{2}\mathbf{k}'+\mathbf{k}''. \tag{50}$$

Let us define the vector $\mathbf{s}$,

$$\mathbf{s}=\mathbf{k}''-\tfrac{1}{2}\mathbf{k}' \tag{51}$$

so that $d\mathbf{p}_n=d\mathbf{s}$. Now the volume element in (23) can be written, on introducing a δ-function,

$$d\mathbf{k}''d\Omega'=d\mathbf{k}''d\Omega'dk'\delta(k'-g(k''))$$
$$=d\mathbf{k}''\frac{1}{k'^2}d\mathbf{k}'\delta(k'-g(k'')),$$

where the pole of the δ-function is at the value of k' related to k'' by the energy equation (22), namely,

$$k'=g(k'')\equiv\left(\frac{4M}{3\hbar^2}\right)^{\frac{1}{2}}\left(\frac{2}{3}E_0-\epsilon-\frac{\hbar^2k''^2}{M}\right)^{\frac{1}{2}}. \tag{52}$$

On changing the variables $\mathbf{k}'$, $\mathbf{k}''$ into $\mathbf{k}'$, $\mathbf{s}$, the differential cross section for $\mathbf{k}'$, $\mathbf{s}$ being directed into $d\mathbf{k}'$ and $d\mathbf{s}$, respectively, is

$$\sigma(E_0,\mathbf{s},\mathbf{k}')d\mathbf{s}d\mathbf{k}'=(k'/kk''^2)I(\Omega_s,\Omega')$$
$$\times\delta(k'-g(|\mathbf{s}+\tfrac{1}{2}\mathbf{k}'|))d\mathbf{s}d\mathbf{k}', \tag{53}$$

where $I(\Omega_s,\Omega')$ is obtained from (34) by means of (51). Writing

$$\mu=\cos\mathbf{k}'\mathbf{s}, \quad \kappa^2=(M/\hbar^2)(\tfrac{2}{3}E_0-\epsilon)=\tfrac{3}{4}k^2-(M\epsilon/\hbar^2),$$

and inserting (51) into (52), one obtains

$$2k'=-s\mu\pm(s^2\mu^2-4s^2+4\kappa^2)^{\frac{1}{2}}. \tag{54}$$

The condition that at least one of the two roots k_1', k_2' be real and positive imposes a restriction on the values that s and μ may assume. A little consideration shows that for $0\leq s^2\leq\kappa^2$, the root k_1' corresponding to the positive sign in (54) is real and positive for all values of μ between -1 and 1. For $\kappa^2\leq s^2\leq 4/3\kappa^2$, and positive values of μ, both roots are negative and must be excluded. For negative values of μ between -1 and $-2[1-(\kappa^2/s^2)]^{\frac{1}{2}}$, both roots are real and positive. s^2 cannot exceed $(4/3)\kappa^2$ since in that case the roots become complex.

Let us denote by $v(k')$

$$v(k')\equiv k'-g(|\mathbf{s}+\tfrac{1}{2}\mathbf{k}'|).$$

To transform the δ-function $\delta(v(k')-0)$ so that the variable is the same as that of integration k', we have

$$\delta(v-0)=\sum_i(dk'/dv)_{v=0}\delta(k'-k_i')$$

where k_i' is a positive real root of (54), or, $v(k')=0$. For the two ranges of s^2 discussed above, we have

(i) $0\leq s^2\leq\kappa^2$, $-1\leq\mu\leq 1$,

$$\delta(v-0)=\tfrac{3}{2}k_1'W\delta(k'-k_1'),$$

(ii) $\kappa^2\leq s^2\leq(4/3)\kappa^2$, $-1\leq\mu\leq-2\left(1-\frac{\kappa^2}{s^2}\right)^{\frac{1}{2}}$,

$$\delta(v-0)=\tfrac{3}{2}k_1'W\delta(k'-k_1')+\tfrac{3}{2}k_2'W\delta(k'-k_2'),$$

where

$$W\equiv(4\kappa^2-4s^2+s^2\mu^2)^{-\frac{1}{2}}.$$

Putting these into (53), one finds, for the differential cross section for a neutron being ejected with energy $E_n=\hbar^2p_n^2/2M$ (in the lab system) into the solid angle $d\Omega_n$,

$$\sigma(E_0, E_n, \Omega_n)dE_nd\Omega_n=\frac{Mp_n}{\hbar^2k}I(\Omega_n)dE_nd\Omega_n. \quad (55)$$

Here $I(\Omega_n)$ is obtained from $I(\Omega_s)$ by means of (50) and (51), and $I(\Omega_s)$ is given, in the two ranges of values for s^2 above, by

$$\text{(i)}\quad I(\Omega_s)=\frac{3}{2}\int_0^{2\pi}\int_{-1}^{1}k_1'^2WI(\Omega_s, \Omega')d\mu d\varphi',$$

$$\text{(ii)}\quad I(\Omega_s)=\frac{3}{2}\int_0^{2\pi}\int_{-1}^{-\nu}k_1'^2WI(\Omega_s, \Omega')d\mu d\varphi' \quad (56)$$

$$+\frac{3}{2}\int_0^{2\pi}\int_{-1}^{-\nu}k_2'^2WI(\Omega_s, \Omega')d\mu d\varphi',$$

where

$$\nu=2\left(1-\frac{\kappa^2}{s^2}\right)^{\frac{1}{2}}.$$

Calculations show that the important contribution to $I(\Omega)$ comes from those terms in (34) which are significant only for large values of k''. For large k'', the plane wave approximation (32) may not be seriously in error. Hence (55) may be expected to give the cross section for inelastic scattering only.

V. CALCULATION AND RESULT

A. Elastic Scattering

While the cross sections of elastic scattering on the basis of the three theories of nucleon interaction can be calculated from (19), (29), and (30), it is seen that the amount of numerical work is very great. In the present preliminary calculation, we have neglected the tensor force and so chosen the constants g, V_0, α^2 as to fit the data on the proton-proton scattering and the ground state of the deuteron. For the singlet even state, the potential is, according to (3) and (28b),

$$^1V^{\text{even}}=-(1-2g)V_0\exp[-\alpha^2r^2].$$

The analysis of Breit *et al.*[6] gives

$$(1-2g)V_0=26 \text{ Mev}, \quad \alpha^2=0.266\times10^{26} \text{ cm}^{-2}. \quad (57)$$

[6] L. E. Hoisington, S. S. Share, and G. Breit, Phys. Rev. 56, 88 (1939).

For this value of α^2, the binding energy of the deuteron gives the depth V_0:[7]

$$V_0=45 \text{ Mev}. \quad (58)$$

For the constants of the approximate wave function (28b) of the ground state of the deuteron, we take the variational wave function of Gerjuoy and Schwinger,[8]

$$A=0.312\times10^{13}, \quad \lambda^2=0.0716\times10^{26} \text{ cm}^{-2}. \quad (59)$$

With these constants, the cross sections for incident protons of 100, 150, and 200 Mev (in the lab system) have been calculated from (19a), (29), and (30). Table I gives the differential cross section $\sigma_{el}(E_0, \Theta)$ defined by (19a). Table II gives the total elastic scattering cross section.

$$\sigma_{el}(E_0)=2\pi\int\sigma_{el}(E_0, \Theta)\sin\Theta d\Theta.$$

It is seen that the difference predicted by the three theories of nucleon interaction is rather

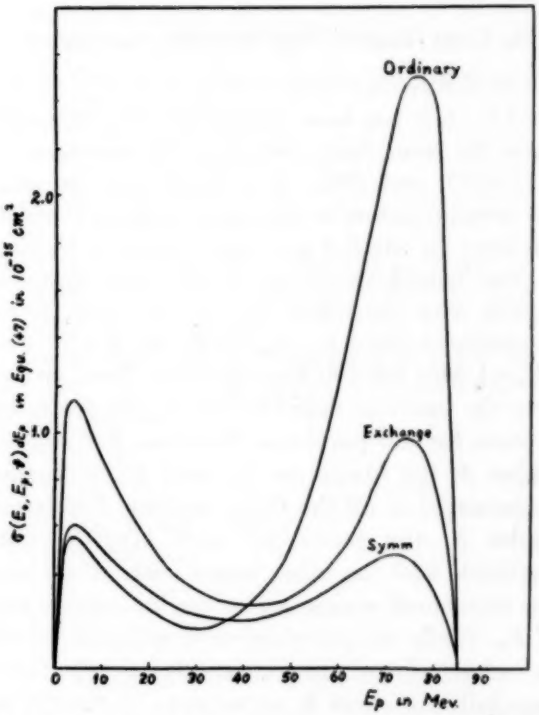

FIG. 1. Differential cross section $\sigma(E_0, E_p, \vartheta)dE_p$ defined in Eq. (47) of proton-deuteron total scattering. $E_0=100$ Mev, $\vartheta=30°$, and $dE_p=1$ Mev.

[7] H. A. Bethe and R. F. Bacher, Rev. Mod. Phys. 8, 111 (1936).

[8] E. Gerjuoy and J. Schwinger, Phys. Rev. 61, 138 (1942).

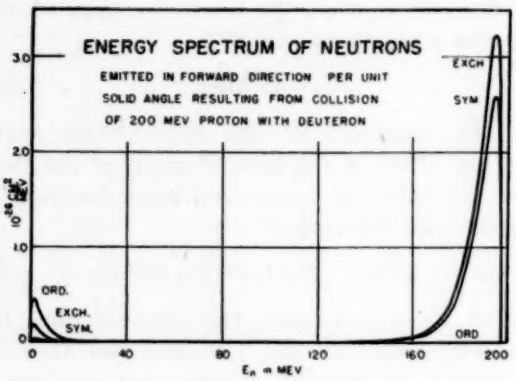

FIG. 2. Energy spectrum of ejected neutrons in the forward direction $\vartheta=0$ in proton-deuteron scattering at 200 Mev.

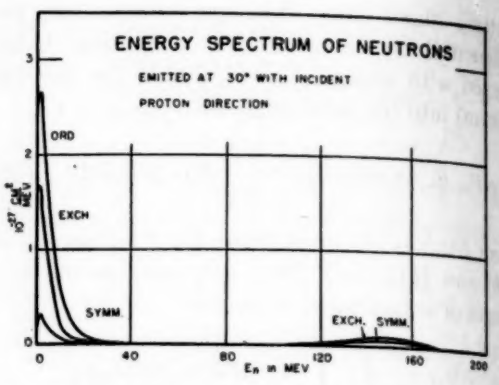

FIG. 3. Energy spectrum of neutrons ejected in directions $\vartheta=30°$ in proton-deuteron scattering at 200 Mev.

large. The very much smaller values of σ_{el} on the symmetrical theory have been discussed at the end of III. The sharp contrast from the two other models lends some interest to an experimental investigation of the elastic scattering at high energies.

B. Total (Elastic Plus Inelastic) Scattering

The differential cross section $\sigma(E_0, E_p, \vartheta)$ defined by (47) has been calculated without tensor forces by using (48), (49) and the constants in (57), (58), and (59). It is found that in (48), the most important terms are Λ_1^2 and $\Lambda_1\Lambda_1^*$ which are large for small ϑ and large values of E_p, i.e., in the neighborhood of $E_0-\epsilon$, and decrease rapidly with decreasing E_p. In Fig. 1 are given as examples the $\sigma(E_0, E_p, \vartheta)dE_p$ for $\vartheta=30°$ and $dE_p=1$ Mev for 100-Mev protons. These curves give the spectral distributions of the scattered protons for this particular direction. For smaller angles ϑ, the maximum at large E_p is further accentuated in all the three theories. For larger angles ϑ, the terms Λ_1^2 and $\Lambda_1\Lambda_1^*$ become negligible and the other terms such as Λ_2^2 give rise to a small maximum at the low energy end of E_p. While no quantitative significance should be attached to these spectral distributions, especially for small ϑ, on account of the failure of the plane wave approximation (32) for large E_p and hence small k'', as discussed in §IVA, the qualitative differences among the three potentials is believed to be of significance for comparison with experimental observations.

In Table III are given the integrated total scattering (elastic plus inelastic) cross sections for 100- and 200-Mev protons on the basis of the three potentials. In the same table are also given for comparison the total cross sections for proton-neutron and proton-proton scatterings calculated with the same potential constants in (57) and (58). The total proton-deuteron cross section σ_t is to be compared with the sum $\sigma_{p-n}+\sigma_{p-p}$ of the proton-neutron and the proton-proton cross sections. It is evident that the effect of interference of the scattered waves in the proton-deuteron scattering plays a large role in determining the final value of the total cross section.

It is of interest to compare the relative importance of elastic and dissociating collisions on the basis of the three theories of nucleon interaction. From σ_{el} in Table II for elastic scattering and σ_t in Table III for total scattering, one finds for the ratio σ_{el}/σ_t the values 0.83, 0.22, and 0.022 for 100 Mev and 0.40, 0.106, and 0.000,06 for 200 Mev, according to the ordinary, the exchange, and the symmetrical potential, respectively.

It is also of interest to make the following indirect comparison with the observed cross sections now available.[9] Recent calculations have shown that in the case of proton-neutron and proton-proton scatterings, the usual Born approximation is quite unsatisfactory for 100 Mev.[1,10] As the above calculation was made in this approximation, we do not expect the numerical values for the σ's to be very accurate at 100

[9] L. J. Cook, E. M. McMillan, J. M. Peterson, and D. C. Sewell, Phys. Rev. **72**, 1264 (1947).
[10] M. Camac and H. A. Bethe, Phys. Rev. **73**, 191 (1948).

Mev. The ratio $\sigma_{p-n}/\sigma_{t(p-d)}$, however, may not be in as serious error as the individual σ's. This ratio for 100 Mev is, for the three potentials,

0.33 (ordinary); 0.66 (exchange); 1.6 (symmetrical).

The observed values are $\sigma_{p-n}=0.083\times10^{-24}$ cm^2 and $\sigma_{t(p-d)}=0.117\times10^{-24}$ cm^2, giving for the ratio $\sigma_{p-n}/\sigma_{t(p-d)}$ the value 0.71. It is seen that the ordinary and symmetrical theories are in definite disagreement with the observed data.

C. Energy Spectrum of Neutrons Ejected in Proton-Deuteron Collisions

By means of (55) and (56) the energy spectra of the neutrons for the forward direction and for directions making an angle of 30° with that of the incident protons have been calculated. The result for 200-Mev incident protons is given in Figs. 2 and 3. As expected, the exchange and the symmetrical potential give neutrons with a well defined narrow energy peak near 200 Mev in the forward direction. These neutrons are the result of a direct exchange between the incident proton and the neutron in the deuteron. That this is essentially a two-body collision is made evident by the fact that the area under the high energy peak for either theory is very nearly equal to the proton-neutron cross section at zero degrees. The low energy peak may be regarded as due to the proton-proton collision in which the outgoing proton pulls the neutron along with it.

At 30°, the high energy peak is very much reduced in intensity and becomes very much wider. The maximum occurs at 150 Mev, corresponding to the conservation of energy and momentum in a two-body collision in which the neutron goes off at 30°, but the spectrum extends all the way to 173 Mev. This upper limit comes from collisions in which both protons come off with the same momentum. All collisions therefore involve the interactions between the three particles in an essential way. The low energy peaks are practically the same as at 0°, as should be expected from their physical interpretation.

The writers wish to thank Professor G. E. Uhlenbeck for suggesting the problem and Professor H. A. Bethe for helpful discussions.

APPENDIX I.†

Elastic Scattering with Tensor Force

When the potentials (3) including tensor force are employed, in summing over the spin coordinates in (17), it is necessary to evaluate the matrix elements $(i|S_{12}|l)$, $(i|S_{13}|l)$ of the operators S_{ij} in (4). These are readily obtained. We shall not give all these except the following few as examples.

$$(1|S_{12}|1)=(1|S_{13}|1)=3\cos^2\mu-1,$$
$$(1|S_{12}|2)=(1|S_{13}|2)=0,$$
$$(3|S_{12}|1)=(3|S_{13}|1)=2\sqrt{3}\sin\mu\cos\mu e^{i\nu},$$

where μ, ν are the polar angles of the line joining the two particles with respect to the direction of quantization of the spin.

The integrals in (17) that arise from the terms S_{12} and S_{13} can be shown to reduce to the following nine:

$$\left.\begin{matrix}I_1\\J_1\\K_1\end{matrix}\right\}=\gamma\int\int\exp[-i\mathbf{k}'\cdot\mathbf{r}]\psi_0^*(\rho)U(|\mathbf{r}+\tfrac{1}{2}\boldsymbol{\varrho}|)\begin{pmatrix}3\cos^2\mu-1\\\sin\mu\cos\mu e^{i\nu}\\\sin^2\mu e^{2i\nu}\end{pmatrix}\exp[i\mathbf{k}\cdot\mathbf{r}]\psi_0(\rho)d\boldsymbol{\varrho}d\mathbf{r},\tag{27A}$$

$$\left.\begin{matrix}I_2\\J_2\\K_2\end{matrix}\right\}=\gamma\int\int\exp[-i\mathbf{k}'\cdot\mathbf{r}]\psi_0^*(\rho)U(|\mathbf{r}+\tfrac{1}{2}\boldsymbol{\varrho}|)\begin{pmatrix}3\cos^2\mu-1\\\sin\mu\cos\mu e^{i\nu}\\\sin^2\mu e^{2i\nu}\end{pmatrix}\exp[-i\mathbf{k}\cdot(\tfrac{1}{2}\mathbf{r}+\tfrac{3}{4}\boldsymbol{\varrho})]\psi_0(|\mathbf{r}-\tfrac{1}{2}\boldsymbol{\varrho}|)d\boldsymbol{\varrho}d\mathbf{r},\tag{27B}$$

$$\left.\begin{matrix}I_3\\J_3\\K_3\end{matrix}\right\}=\gamma\int\int\exp[-i\mathbf{k}'\cdot\mathbf{r}]\psi_0^*(\rho)U(|\mathbf{r}-\tfrac{1}{2}\boldsymbol{\varrho}|)\begin{pmatrix}3\cos^2\mu-1\\\sin\mu\cos\mu e^{i\nu}\\\sin^2\mu e^{2i\nu}\end{pmatrix}\exp[-i\mathbf{k}\cdot(\tfrac{1}{2}\mathbf{r}+\tfrac{3}{4}\boldsymbol{\varrho})]\psi_0(|\mathbf{r}-\tfrac{1}{2}\boldsymbol{\varrho}|)d\boldsymbol{\varrho}d\mathbf{r}.\tag{27C}$$

† This appendix refers to Section III.

The angles μ, ν are again the polar angles of the vector $\mathbf{r}+\frac{1}{2}\boldsymbol{\rho}$ or $\mathbf{r}-\frac{1}{2}\boldsymbol{\rho}$ in the argument of the potential U with respect to the direction of quantization.

It can be shown that these integrals are given by

$$I_1=\frac{2}{5}\gamma L_1 x^2\left(1-3\sin^2\frac{\vartheta}{2}\right){}_1F_1(1;7/2;x^2),$$

$$I_2=-\frac{1}{5}\gamma L_2 y^2(1+3\cos^2\vartheta)\,{}_1F_1(1;7/2;y^2),$$

$$I_3=\frac{2}{5}\gamma L_3\left[z^2-\frac{3}{16}\frac{k^2}{\alpha^2+\lambda^2}(1+2\cos\vartheta)^2\right]\times{}_1F_1(1;7/2;z^2),$$

$$J_1=\frac{1}{5}\gamma L_1 x^2\sin\vartheta\,{}_1F_1(1;7/2;x^2),$$

$$J_2=\frac{1}{10}\gamma L_2\left(\frac{3k}{4}\right)^2\frac{1}{\alpha^2+\frac{1}{2}\lambda^2}\sin\vartheta(1+\cos\vartheta)\times{}_1F_1(1;7/2;y^2), \quad (29A)$$

$$J_3=\frac{1}{20}\gamma L_3\frac{k^2}{\alpha^2+\lambda^2}\sin\vartheta(1+2\cos\vartheta)\times{}_1F_1(1;7/2;z^2),$$

$$K_1=\frac{2}{5}\gamma L_1 x^2\cos^2\frac{\vartheta}{2}\,{}_1F_1(1;7/2;x^2),$$

$$K_2=\frac{1}{40}\gamma L_2 x^2\frac{\alpha^2}{\alpha^2+\frac{1}{2}\lambda^2}\cos^2\frac{\vartheta}{2}\,{}_1F_1(1;7/2;y^2),$$

$$K_3=\frac{2}{5}\gamma L_3 x^2\frac{\alpha^2}{\alpha^2+\lambda^2}\cos^2\frac{\vartheta}{2}\,{}_1F_1(1;7/2;z^2),$$

where the x, y, z are given in (29). For the convenience of calculation, the confluent hypergeometric functions can be expressed in terms of the error integral as follows.

$$\frac{4}{15}x^2\,{}_1F_1(1;7/2;x^2)=\frac{1}{x^3}\exp[x^2]\int_0^x\exp[-t^2]dt-\frac{1}{x^2}-\frac{2}{3}.$$

The scattered intensity is given, in the three theories, by the following expressions.

Ordinary force:

$$(3\pi\hbar^2/M)^2I(\vartheta)=\text{expression (30a)}+(2I_1-I_2)^2-(2I_1-I_2)I_3+\tfrac{3}{2}I_3^2+12\{(2J_1-J_2)^2-(2J_1-J_2)J_3+\tfrac{3}{2}J_3^2\}+3\{(2K_1-K_2)^2-(2K_1-K_2)K_3+\tfrac{3}{2}K_3^2\}. \quad (30A)$$

Exchange force:

$$(3\pi\hbar^2/M)^2I(\vartheta)=\text{expression above, with 1, 2 interchanged.} \quad (30B)$$

Symmetrical force:

$$(3\pi\hbar^2/M)^2I(\vartheta)=\text{expression (30c)}+(I_2^2-I_2I_3+I_3^2)+12(J_2^2-J_2J_3+J_3^2)+3(K_2^2-K_2K_3+K_3^2). \quad (30C)$$

That the central force and the tensor force in (3) contribute additively to the scattered intensity is due to the fact that the spur of the tensor interaction S_{ij} is zero.

APPENDIX II.††

Total Scattering with Tensor Force

The integrals arising from the terms S_{12} and S_{13} in (25) can be shown to reduce to nine which are obtainable from (27A), (27B), (27C) above by replacing $\psi_0^*(\rho)$ by the continuum functions $\psi_{k''}{}^{*1}(\rho)$ or $\psi_{k''}{}^{*2}(\rho)$, and the nine others obtained from these by replacing $\mathbf{k}''$ by $-\mathbf{k}''$. Of these eighteen, the six integrals $\mathcal{I}_3$, $\mathcal{J}_3$, $\mathcal{K}_3$, $\mathcal{I}_3^*$, $\mathcal{J}_3^*$, $\mathcal{K}_3^*$, can be shown to contain a δ-function and contribute nothing to the scattered intensity. They have therefore been omitted in the following. To the approximation (32), these 12 integrals are as follows.

$$\mathcal{I}_1=\frac{2}{5}\gamma\mathfrak{L}_1\left[x^2-\frac{3}{4\alpha^2}(k-k'\cos\vartheta')^2\right]\times{}_1F_1(1;7/2;x^2),$$

$$\mathcal{I}_2=\frac{2}{5}\gamma\mathfrak{L}_2\left[y^2-\frac{3}{4\alpha^2}(k+K\cos\widehat{\mathbf{kK}})^2\right]\times{}_1F_1(1;7/2;y^2),\quad \mathbf{K}=\tfrac{1}{2}\mathbf{k}'+\mathbf{k}'',$$

†† This appendix refers to Section IV.

$$\mathcal{J}_1=\frac{1}{10}\gamma\mathfrak{L}_1\cdot\frac{1}{\alpha^2}k'\sin\vartheta'(k-k'\cos\vartheta')$$
$$\times{}_1F_1(1;7/2;x^2),$$
$$\mathcal{J}_2=\frac{1}{10}\gamma\mathfrak{L}_2\cdot\frac{1}{\alpha^2}K\sin\widehat{\mathbf{kK}}(k+K\cos\widehat{\mathbf{kK}})$$
$$\times{}_1F_1(1;7/2;y^2),$$
$$\mathcal{K}_1=-\frac{1}{10}\gamma\mathfrak{L}_1\left(\frac{k'}{\alpha}\right)^2\sin^2\vartheta'\,{}_1F_1(1;7/2;x^2),$$
$$\mathcal{K}_2=-\frac{1}{10}\gamma\mathfrak{L}_2\left(\frac{K}{\alpha}\right)^2\sin^2\widehat{\mathbf{kK}}\,{}_1F_1(1;7/2;y^2),$$

(33A)

$\mathcal{J}_1^*=\mathcal{J}_1$ with $\mathbf{k}''$ replaced by $-\mathbf{k}''$, etc.,

where x, y, D are those expressions given in (33).

The scattered intensity in the three theories is given below.

Ordinary force:

$$(2\pi)^3(3\pi\hbar^2/M)^2I(\Omega',\Omega'')$$
$$=\text{expression (34a)}+\tfrac{3}{2}(\mathcal{J}_1-\mathcal{J}_2)^2$$
$$+(\mathcal{J}_1-\mathcal{J}_2+\tfrac{3}{2}\mathcal{J}_1^*)\mathcal{J}_1^*+18(\mathcal{J}_1-\mathcal{J}_2)^2$$
$$+12(\mathcal{J}_1-\mathcal{J}_2+\tfrac{3}{2}\mathcal{J}_1^*)\mathcal{J}_1^*$$
$$+(9/2)(\mathcal{K}_1-\mathcal{K}_2)^2$$
$$+3(\mathcal{K}_1-\mathcal{K}_2+\tfrac{3}{2}\mathcal{K}_1^*)\mathcal{K}_1^*. \quad (34A)$$

Exchange force:

$$(2\pi)^3(3\pi\hbar^2/M)^2I(\Omega',\Omega'')=\text{expression}$$
above, with 1, 2 interchanged. (34B)

Symmetrical force:

$$(2\pi)^3(3\pi\hbar^2/M)^2I(\Omega',\Omega'')$$
$$=\text{expression (34c)}+\tfrac{1}{6}(\mathcal{J}_1-\mathcal{J}_2)^2$$
$$-\tfrac{1}{3}(\mathcal{J}_1-\mathcal{J}_2)(\mathcal{J}_1^*+2\mathcal{J}_2^*)$$
$$+\tfrac{1}{6}(\mathcal{J}_1^*+2\mathcal{J}_2^*)^2+2(\mathcal{J}_1-\mathcal{J}_2)^2$$
$$-(4/3)(\mathcal{J}_1-\mathcal{J}_2)(\mathcal{J}_1^*+2\mathcal{J}_2^*)$$
$$+2(\mathcal{J}_1^*+2\mathcal{J}_1^*)^2+\tfrac{1}{2}(\mathcal{K}_1-\mathcal{K}_2)^2$$
$$-\tfrac{1}{2}(\mathcal{K}_1-\mathcal{K}_2)(\mathcal{K}_1^*+2\mathcal{K}_2^*)$$
$$+\tfrac{1}{2}(\mathcal{K}_1^*+2\mathcal{K}_2^*)^2. \quad (34C)$$

On the Behavior of Cross Sections Near Thresholds

EUGENE P. WIGNER
Palmer Physical Laboratory, Princeton University, Princeton, New Jersey
(Received January 16, 1948)

The energy dependence of the cross section for the formation of a product, near the threshold energy for that formation, is considered. It is shown that the cross section is, apart from a constant, in the neighborhood of the threshold the same function of energy, no matter what the reaction mechanism is, as long as the long-range interaction of the product particles is the same. The same must hold, because of the principle of detailed balance, for the back reaction, i.e., the reaction between particles with very low relative velocities. In this case, the cross section, as function of the energy, depends only on the long-range interaction of the reacting particles. The energy dependence of the cross section is determined for three types of interactions, *viz.* no interaction, Coulomb repulsion and Coulomb attraction. The rule for a $1/r^n$ interaction can be obtained from the first case. Reasons are adduced to show that two interactions, the difference of which goes to zero at least as fast as $r^{-2-\epsilon}$ with $(\epsilon>0)$, give the same energy dependence of the cross section. Hence, long-range interaction in the above connection should mean an interaction which, at large distances of the particles, does not go to zero faster than r^{-2}. The effect of small perturbations in the long-range interaction is discussed in general.

SECTION I

THE results of the present article are probably well known to a great many readers: they are concerned with the behavior of the various cross sections in the neighborhood of the threshold of a new mode of reaction. Examples for the rules to be derived can be found in almost every article which is concerned with reaction cross sections.[1] It is believed, however, that the generality of these rules has not been emphasized before, nor have they been derived with the same claim for universal validity as will be done in the present paper. The principal interest in such an investigation arises from the experimental difficulty in measuring threshold energies without the knowledge of how the yield of the product approaches zero with decreasing energy. From this point of view, it would be desirable to obtain also an expression for the yield of reactions in which the number of end products is three or more (e.g., an $(n, 2n)$ reaction). This, however, will not be attempted in the present article which deals only with processes in which only pairs of particles are formed.

The mathematical formalism will be that adopted in a previous article of L. Eisenbud and the present writer.[2] In fact, this formalism will be used in the simplest possible form (*viz.* Eq. (1), reference 2):

$$\varphi=\sum_\lambda \frac{\int X_\lambda(\mathrm{grad}\varphi)_n dS}{E_\lambda-E} X_\lambda. \qquad (1)$$

In this, φ is an arbitrary wave function with energy E, the E being part of the continuous spectrum; $\mathrm{grad}\varphi$ is the vector with components $(\hbar^2/2M)\partial\varphi/\partial x$, $\cdots$, etc. Only φ and $\mathrm{grad}\varphi$ in (1) depend on E. The X_λ and E_λ are the characteristic functions and characteristic values of the Hamiltonian, with the boundary condition that the normal derivative in the above sense of X_λ vanish on a surface S. This S is the boundary between the internal and the external region of the configuration space. The integration in (1) is over this surface. The external region of the configuration space is defined by the requirement that, at the energy E, in the external region (i.e., outside of S) single alternative wave functions

$$F_{sl}(r_s)P_l(\Omega_s)\psi_s=F_{sl}(r_s)\psi_{sl} \qquad (2)$$

form a complete set of solutions of the Schrö-

[1] It would be idle to attempt to give a full list of the pertinent papers. Suffice it to say, therefore, that, if there is no long-range interaction between the colliding particles, Born's approximation already gives the correct asymptotic behavior even in cases in which it is quite inaccurate as far as absolute magnitude is concerned. The importance of the potential type of interaction (cf. Eq. (5)) of the colliding particles at large distances was probably first recognized by P. M. Morse and E. C. G. Stueckelberg (Ann. d. Physik 9, 579 (1931)). Their method, if properly carried out, should give the asymptotic behavior correctly in all cases, even if the method itself is quite inaccurate for the calculation of the magnitude of the cross section.

[2] L. Eisenbud and E. P. Wigner, Phys. Rev. 72, 29 (1947).

dinger equation. The ψ_s in (2) is the product of the wave functions of a pair s of particles which may be formed by the reaction, r_s and Ω_s are the length and direction of the line connecting their centers of mass. P_l can be assumed to be a spherical harmonic of degree l, giving an angular momentum $l\hbar$ to the two particles of the pair s about their common center of mass. The $\psi_{sl}=P_l(\Omega_s)\psi_s$ are orthogonal to each other on the surface S, the letter s specifying not only the nature of the particles which form the pair s but also their state of excitation, the resultant of their spin angular momenta, and the projection of this into a given direction. The ψ_{sl} will be further assumed to be normalized if integrated over S

$$\int \psi_{sl}\psi_{s'l'}dS=\delta_{ss'}\delta_{ll'}. \tag{2a}$$

Let us assume that φ and $(\mathrm{grad}\varphi)_n$, the component of $\mathrm{grad}\varphi$ perpendicular to S, can be expanded on S in terms of the ψ_{sl}

$$\varphi=\sum_{sl} V_{sl}\psi_{sl}, \tag{3a}$$

$$(\mathrm{grad}\varphi)_n=\sum_{sl} hD_{sl}\psi_{sl}. \tag{3b}$$

Equation (1) then becomes

$$V_{sl}=\sum_{s'l'} R_{sl;s'l'}D_{s'l'}, \tag{4}$$

with

$$R_{sl;s'l'}=\sum_{\lambda}\frac{\gamma_{\lambda sl}\gamma_{\lambda s'l'}}{E_\lambda-E}, \tag{4a}$$

where

$$\gamma_{\lambda sl}=h^{\frac{1}{2}}\int X_\lambda\psi_{sl}dS. \tag{4b}$$

The above is a repetition of the line of argument of reference 2 with the difference that the boundary conditions on S are assumed in the simplest possible form, no attempt being made to make the E_λ, $\gamma_{\lambda sl}$, etc., independent of the position of S. The above equations are almost identical with Eqs. (13), (23), and (17) of the above reference, but the derivation is, of course, much simpler. All that will be used in the following is that the expansion coefficients of φ on S (as φ itself), are linear functions of the expansion coefficients of $(\mathrm{grad}\varphi)_n$ on S (or of $(\mathrm{grad}\varphi)_n$ itself) which has no singularity at the threshold to be investigated as none of the E_λ can be expected to coincide with that threshold.

SECTION II

The $F_{sl}(r_s)$ satisfy, in the external region, the differential equation

$$-\frac{\hbar^2}{2M_s}\left(\frac{d^2}{dr_s^2}+\frac{2}{r_s}\frac{d}{dr_s}-\frac{l(l+1)}{r_s^2}\right)F_{sl}+V_sF_{sl}=(E-\epsilon_s)F_{sl}. \tag{5}$$

The M_s, V_s, and ϵ_s are the reduced mass, potential energy in the external region, and proper energy of the pair s. We shall be particularly concerned with that solution E_{sl} of (5) which corresponds to an outgoing wave and which we shall assume to be normalized in such a way that $\mathrm{E}_{sl}\psi_{sl}$ correspond to unit flux. Assuming that, in the direction of configuration space which corresponds to separation into the pair s, the surface S lies at $r_s=a_s$, the condition of unit flux is that at $r_s=a_s$

$$\frac{\hbar}{2iM_s}\left(\mathrm{E}_{sl}\frac{d\mathrm{E}_{sl}}{dr_s}-\mathrm{E}_{sl}\frac{d\mathrm{E}_{sl}^*}{dr_s}\right)=1 \quad (\text{at } r_s=a_s). \tag{6}$$

Since it follows from (5) that the expression in the bracket of (6) is r^{-2} times a constant, the normalization adopted implies

$$i(\mathrm{E}_{sl}e_{sl}^*-\mathrm{E}_{sl}^*e_{sl})=a_s^2/r_s^2, \tag{6a}$$

where

$$e_{sl}=(\hbar/2M_s)d\mathrm{E}_{sl}/dr_s. \tag{6b}$$

If, for large r_s, the potential V goes to zero sufficiently fast, (6a) should mean that $(r_s/a_s)\mathrm{E}_{sl}$ is asymptotically equal to $(M_s/k\hbar)^{\frac{1}{2}}\exp ikr_s$.

The above definition of E_{sl} applies if the pair s is energetically possible at the energy considered. However, particularly just below a threshold, the expansion (3) requires also such ψ_{sl} which are energetically impossible. In this case, E_{sl} shall be that solution of (5) which goes to zero exponentially at $r_s=\infty$. The E_{sl}^* which is in this case not the conjugate complex of E_{sl} is any other linearly independent solution of (5). E_{sl}^* goes, of course, to infinity for large r_s. It is not necessary to specify E_{sl} and E_{sl}^* more closely in this case.

It is convenient to introduce a symbol for the reciprocal logarithmic derivative of E_{sl}:

$$\mathrm{E}_{sl}=q_{sl}e_{sl}, \tag{7}$$

which permits (6a) to be written in the form

$$i(q_{sl}-q_{sl}^*)\,|e_{sl}|^2=a_s^2/r_s^2. \tag{7a}$$

This shows that the imaginary part of q_{sl}^* is positive for every r_s and permits one to introduce

$$j_{sl}^2=i(q_{sl}-q_{sl}^*)=a_s^2/r_s^2 e_{sl}e_{sl}^*. \tag{7b}$$

Actually, q_{sl} satisfies a Ricatti-type differential equation which follows from (5). The q_{sl} as defined by (7) is real for s which are energetically impossible and (7a) and (7b) will not be used for such s.

Equations (3) and (4) permit the determination of half of the coefficients of the most general solution

$$\varphi=\sum_{sl}\psi_{sl}(\alpha_{sl}\mathrm{E}_{sl}+\beta_{sl}\mathrm{E}_{sl}^*) \tag{8}$$

of the Schrödinger equation in the external region. The coefficient of ψ_{sl} in φ is

$$V_{sl}=\alpha_{sl}q_{sl}e_{sl}+\beta_{sl}q_{sl}^*e_{sl}^* \quad (r_s=a_s), \tag{9a}$$

while its coefficient in $(\mathrm{grad}\varphi)_n$ becomes

$$D_{sl}=\alpha_{sl}e_{sl}+\beta_{sl}e_{sl}^*, \quad (r_s=a_s). \tag{9b}$$

If φ is to be a permissible solution, the β_{sl} whose s is energetically impossible must vanish. It is, therefore, immaterial that the coefficients of these β_{sl} are not defined.

One can write (4) by means of (9) in terms of the α and β

$$q_{sl}e_{sl}\alpha_{sl}+q_{sl}^*e_{sl}^*\beta_{sl}=\sum_{s'l'}R_{sl;s'l'}(e_{s'l'}\alpha_{s'l'}+e_{s'l'}^*\beta_{s'l'}). \tag{10}$$

From this the collision matrix U, which gives the outgoing wave coefficients in terms of the incoming wave coefficients, can be obtained:

$$\alpha_{sl}=-\sum_{s'l'}U_{sl;s'l'}\beta_{s'l'}, \tag{11}$$

where

$$U=e^{-1}(q-R)^{-1}(q^*-R)e^*$$
$$=e^{-1}e^*+e^{-1}(q-R)^{-1}(q^*-q)e^*. \tag{11a}$$

The e and q are diagonal matrices with diagonal elements $e_{sl}(a_s)$ and $q_{sl}(a_s)$, respectively. The summation over s', l' must be extended in (11) only over the energetically possible s'. This makes it possible to use the relation (7a) to give

$$U=e^{-1}e^*+ie^{-1}(q-R)^{-1}e^{-1}. \tag{12}$$

The simple form of (12) could be obtained by the use of the relation (7a) because the columns of U, which refer to energetically impossible states, are without significance. Since, on the other hand, the rows of U which refer to such states are without much interest—they give only the coefficients of the exponentially decaying solutions in the external region—it is permissible to make use of (7b) to eliminate $|e|$ from (12). For this purpose we define

$$e=|e|\omega^*, \tag{13a}$$

where ω is a unitary diagonal matrix defined by (13a). We obtain

$$U=\omega(1+ij(q-R)^{-1}j)\omega. \tag{13}$$

In this, j_{sl}^2 can be considered to be the imaginary part of $2q_{sl}^*$, which is zero if s is energetically impossible. For these s, the e_{sl} can be assumed to be real, $\omega_{sl}=1$. As a result, U will assume the form

$$U=\begin{Vmatrix}\bar{U} & 0\\ 0 & 1\end{Vmatrix}. \tag{13b}$$

$\bar{U}$, the reduced U, occupies the rows and columns which correspond to energetically possible pairs s, the 1 to the energetically impossible pairs. This form of U gives automatically zero cross section to those transitions which are energetically impossible. The unitary symmetric nature of (13b) can be easily proved directly by means of the relation (7b) $j=(i(q-q^*))^{\frac{1}{2}}$. Even though (12) and (13) are not fundamentally different from (38), reference 2, their form is not the same and they are more general by permitting the surface S to be drawn in close even just below a threshold (compare footnote 9, reference 2).

From (12) and (13) one obtains for the reaction cross sections (either $s\neq s'$ or $l\neq l'$)

$$\sigma_{sl;s'l'}=\pi k_s^{-2}(2l+1)\,|U_{sl;s'l'}|^2$$
$$=\pi k_s^{-2}(2l+1)\,|e_{sl}e_{s'l'}|^{-2}\,|((q-R)^{-1})_{sl;s'l'}|^2$$
$$=\pi k_s^{-2}(2l+1)\,|j_{sl}j_{s'l'}|^2$$
$$\times|((q-R)^{-1})_{sl;s'l'}|^2. \tag{14}$$

TABLE I. No interaction in external region. Asymptotic values of E, q, j, ω for small $k_s a_s$.

	$E_{sl}(r_s)$	$q_{sl}(a_s)$	$j_{sl}(a_s)$	$1+i\omega_{sl}(a_s)$
$l=0$	$[(M/\hbar k)^{\frac{1}{2}}]a/r$	$-2Ma/\hbar$	$2ka(M/\hbar k)^{\frac{1}{2}}$	$[i(ka)^2]/3$
$l=1$	$[i(M/\hbar k)^{\frac{1}{2}}]a/kr^2$	$-Ma/\hbar$	$[(ka)^2/3](M/\hbar k)^{\frac{1}{2}}$	$-[i(ka)^2]/6$
$l\geq 1$	$\dfrac{i^l 1.3.\cdots(2l-1)}{(\hbar k/M)^{\frac{1}{2}}(r/a)(kr)^l}$	$-\dfrac{2Ma}{(l+1)\hbar}$	$\dfrac{2(ka)^{l+1}(M/\hbar k)^{\frac{1}{2}}}{(l+1)1.3.\cdots(2l-1)}$	$\dfrac{-il(ka)^{2l+1}}{(l+1)(2l+1)(1.3.\cdots(2l-1))^2}$

TABLE II. $V=Ze^2/r>0$. Asymptotic values of E, q, j for small kr or ka.

	$E(r)$	$q(a)$	$j(a)$
$l=0$	$\dfrac{-\exp(\pi\alpha+i\alpha\ \ln 2kR)H_1(i\beta)}{(\hbar r/\pi Ma^2)^{\frac{1}{2}}\arg}$	$\dfrac{(4Ma/\hbar)H_1(i\beta)}{i\beta H_0(i\beta)-2H_1(i\beta)}$	$\dfrac{4(Ma/\pi\hbar)^{\frac{1}{2}}\exp(-\pi\alpha)}{i\beta H_0(i\beta)-2H_1(i\beta)}$
general	$\dfrac{(-)^{l+1}\exp(\pi\alpha+i\alpha\ \ln 2kR)H_{2l+1}(i\beta)}{(\hbar r/\pi Ma^2)^{\frac{1}{2}}\arg}$	$\dfrac{(4Ma/\hbar)H_{2l+1}(i\beta)}{i\beta H_{2l}(i\beta)-(2l+2)H_{2l+1}(i\beta)}$	$\dfrac{4(Ma/\pi\hbar)^{\frac{1}{2}}\exp(-\pi\alpha)}{\lvert i\beta H_{2l}(i\beta)-(2l+2)H_{2l+1}(i\beta)\rvert}$

The scattering cross sections become

$$\sigma_{sl;sl}=\pi k_s^{-2}(2l+1)\,|1-(-)^l U_{sl;sl}|^2$$
$$=\pi k_s^{-2}(2l+1)\,|1-(-)^l\omega_{sl}{}^2$$
$$-(-)^l i\omega_{sl}{}^2 j_{sl}{}^2((q-R)^{-1})_{sl;sl}|^2. \quad (15)$$

SECTION III

Table I gives E_{sl}, q_{sl}, j_{sl}, ω_{sl} for a free particle ($V_s=0$ in (5)) in terms of $k_s=(2M_s(E-\epsilon_s))^{\frac{1}{2}}/\hbar$, assuming that $k_s a_s$ is very small.

These are the quantities to be used in Eqs. (12) to (15) in case of neutral particles. It will be noted that the j_{sl} cannot be obtained from the q_{sl} of Table I by means of (7b) because the q_{sl} are real in the approximation used in this table. It is necessary, rather, to calculate the q_{sl} to the first imaginary term or, alternately, to obtain its imaginary part by means of (7b) and the e_{sl}. Table II contains the same quantities for Coulomb wave functions if both charges have the same sign. In this and Table III

$$\eta=2MZe^2/\hbar^2,$$
$$\alpha=\tfrac{1}{2}\eta/k=MZe^2/\hbar^2 k=Ze^2/\hbar v, \quad (16a)$$

$\beta=2(\eta r)^{\frac{1}{2}}=(8MZe^2 r)^{\frac{1}{2}}/\hbar$ in the expression for E and $\beta=2(\eta a)^{\frac{1}{2}}$ in the expressions for q and j. The Z is the product of the charges on the reaction products to which the E, q, and j apply. The ηa is not assumed to be small in the derivation of the above formulae, while the ka is. On the other hand, $\alpha=\eta a/2ka$ is a large number. R is the distance outside of which the electrostatic potential ceases to act. It is well known that, because of the complicated asymptotic behavior of the Coulomb wave functions at large distances, the introduction of such a range for the Coulomb force is necessary in order to obtain a definite phase shift, etc., $\arg=\Pi(i\alpha)/|\Pi(i\alpha)|$ is the phase factor of $\Pi(i\alpha)=(i\alpha)!$ The H_{2l} and H_{2l+1} are defined as these quantities with the upper index 1 are defined by Jahnke-Emde. Watson's $K_n(z)=i^{n-1}(2/\pi)H_n(iz)$. The above formulae were calculated on the basis of the outgoing Coulomb wave function[3]

$$E(r)=-(M/\hbar k)^{\frac{1}{2}}\eta a(\eta r)^l\exp(i\alpha\ \ln(2kR))$$
$$\times(\exp(\tfrac{1}{2}\pi\alpha)/\Pi(i\alpha))(1-\exp(-2\pi\alpha))$$
$$\times\int(y^2+k^2r^2)^{-l-1}$$
$$\exp[-y+i\alpha\ \ln((y+ikr)/(y-ikr))]dy, \quad (16)$$

where the path of integration runs from $y=\infty$ (where the value of the ln is zero) counter-clock-

[3] W. Gordon, Zeits. f. Physik **48**, 180 (1928). See also A. Sommerfeld and G. Schur, Ann. d. Physik **4**, 409 (1930); M. Stobbe, *ibid.* **7**, 661 (1930). H. Bethe, *Geiger-Scheel's Handbuch der Physik* (Berlin, 1933), 2nd edition, Volume XXIV/1, p. 289 ff. and N. F. Mott and H. S. W. Massey, *The Theory of Atomic Collisions* (Oxford University Press, London, 1933). The remark that the Coulomb wave functions of the continuous spectrum reduce to Bessel functions for low values of the energy is due to J. G. Beckerley, Phys. Rev. **67**, 11 (1945). I could find no reference for the numerical coefficient of the Bessel function at a given asymptotic behavior of the wave function for large r, i.e., the essential part of Tables II and III. See, however, L. W. Nordheim, Proc. Roy. Soc. **A121**, 628 (1928), and Th. Sexl, Zeits. f. Physik **56**, 72 (1929).

TABLE III. $V=Ze^2/r<0$. Asymptotic values of E, q, j for small $k_s a_s$ or kr.

	$E_{sl}(r)$	$q_{sl}(a_s)$	$j_{sl}(a_s)$
$l=0$	$\dfrac{\exp[i\alpha\ln(2kR)]iH_1(\bar\beta)}{(\hbar r/\pi Ma^2)^{\frac{1}{2}}\arg}$	$\dfrac{(4Ma/\hbar)H_1(\bar\beta)}{\bar\beta H_0(\bar\beta)-2H_1(\bar\beta)}$	$\dfrac{4(Ma/\pi\hbar)^{\frac{1}{2}}}{\lvert\bar\beta H_0(\bar\beta)-2H_1(\bar\beta)\rvert}$
general	$\dfrac{(-)^l\exp[i\alpha\ln(2kR)]iH_{2l+1}(\bar\beta)}{(\hbar r/\pi Ma^2)^{\frac{1}{2}}\arg}$	$\dfrac{(4Ma/\hbar)H_{2l+1}(\bar\beta)}{\bar\beta H_{2l}(\bar\beta)-(2l+2)H_{2l+1}(\bar\beta)}$	$\dfrac{4(Ma/\pi\hbar)^{\frac{1}{2}}}{\lvert\bar\beta H_{2l}(\bar\beta)-(2l+2)H_{2l+1}(\bar\beta)\rvert}$

wise around the singularity at $y=-ikr$ back to $y=\infty$ (where the value of the ln is $2\pi i$ now).

Table III, which applies if the potential is attractive, is calculated on the basis of the same formula. The η and $\alpha=\eta/2k$ are negative in this case, and $\bar\beta=2(-\eta r)^{\frac{1}{2}}$ is real and positive. The most essential difference between these formulae and those of Table II is the absence of the factor $\exp(\pi\alpha)$ or $\exp(-\pi\alpha)$. It is to be remembered that $\alpha=Ze^2/\hbar v$ goes to infinity near the threshold. This factor is the most important part of the "penetration factor" and its absence in the case of the attractive potential of Table III is quite natural. Mathematically, the difference can be said to arise from the $1-\exp(-2\pi\alpha)$ factor in (16): the 1 is dominant if $\alpha>0$; the exponential term, which cancels a similar factor which always occurs at small kr is dominant if $\alpha<0$. This also accounts for the differences in sign. In addition, the $H=J+iN$ has a real argument in case of the attractive potential of Table III, an imaginary argument in case of the repulsive potential of Table II. In the latter case, it goes to zero exponentially for large $\beta=2(\eta a)^{\frac{1}{2}}$. This partly compensates for the $\exp(\pi\alpha)$ factor and is particularly important for large a in accord with the fact that only the part of the barrier outside a has to be penetrated. Strictly speaking, however, this factor is irrelevant from the point of view of the present paper since it is independent of energy. It is clear, however, that it influences the absolute magnitude of the cross section even if it leaves its energy dependence unaffected.

The important point to be noted is that $q-R$ is, in first approximation, independent of energy. This means that $q-R$ assumes a definite value for the threshold energy ϵ_n and that its derivative is finite at that point. The same will be true of the matrix $(q-R)^{-1}$. It then follows from (14) that the factors $|e_{sl}e_{s'l'}|^{-2}$ or $|j_{sl}j_{s'l'}|^2$ will determine the behavior of the reaction cross section near ϵ_n. Even these factors will be independent of E in first approximation if ϵ_n is not a threshold for the formation of the pair s or s'. They will contain the relevant dependence on k if it is. It should be noted that only the dependence on k is meaningful in Tables I, II, III because R or $(q-R)^{-1}$ will depend on the a_s in such a way as to compensate for the dependence of e_{sl} or j_{sl} on these quantities.

The rules which follow can be best described by using, instead of s, the letters p or n for pairs which are or are not energetically possible below the threshold. These will also be denoted as old or new type of particles, respectively. The e_{pl}, j_{pl} will be considered as independent of E.

A. Reaction Cross Sections

1. *Production of new type of particles with angular momentum l from old type.* The behavior of the cross section depends in this and all other cases on whether the new type of particles, in the present case the reaction products, are charged or uncharged. We have to distinguish, therefore, three cases:

Neutral particles: $\sigma\sim k_n^{2l+1}$;
Coulomb repulsion:
$$\sigma\sim\exp(-2\pi M_n Z_n e^2/\hbar^2 k_n);$$
Coulomb attraction: $\sigma\sim 1$.

In the last case, the cross section sets in with a finite value right at the threshold, even for higher angular momenta.

2. *Reaction of new type of particles with angular momentum l to form old type of particles.* This is the typical case of the reaction of particles with very low kinetic energy. Again, three cases have to be distinguished, depending on the charged or uncharged character of the reacting particles.

Neutral particles: $\sigma\sim k_n^{2l-1}$;
Equal charges:
$$\sigma\sim k_n^{-2}\exp(-2\pi M_n Z_n e^2/\hbar^2 k_n);$$
Opposite charges: $\sigma\sim k_n^{-2}$.

These rules can be obtained, of course, from the above ones by the principle of detailed balance. According to this principle, the ratio of the cross sections of forward and back reaction is equal to the ratio of the square of the relative momenta of the particles in the final state. Since the relative momentum of an old type of pair is considered to be constant near the threshold, the quantities just enumerated are just k_n^{-2} times the quantities enumerated above.

The best known example for the above rule is the $1/v$ law of the absorption of slow neutrons. The angular momentum l can always be assumed to be zero in this case since any excess angular momentum can be carried off, if necessary, by the emitted light quantum. In fact, the above consideration is a more rigorous derivation of this law in the case of reactions like $B^{10}+n\rightarrow Li^7+He^4$ or $Li^6+n\rightarrow He^4+He^3$ than the one originally given.[4]

A greater variety of examples can be found, e.g., in the article of Schwinger and Teller or of Hamermesh and Schwinger.[5] Even these examples show, however, that the total cross section almost always follows the behavior given above for $l=0$. The reason for this is that an excess angular momentum can always be supplied or carried away by the l of the "old type" of particles.

3. *Reaction of new type to new type (depolarization at low energies) $n, l\rightarrow n, l'$.*

Neutral particles: $\sigma\sim k_n^{2l+2l'}$;
Equal charges:
$$\sigma\sim k_n^{-2}\exp(-4\pi M_n Z_n e^2/\hbar^2 k_n);$$
Opposite charges: $\sigma\sim k_n^{-2}$.

Naturally, all these reactions have finite cross sections only if they are consistent with the conservation rules for angular momentum and for parity.

B. Scattering Cross Sections

The only important case here is the scattering of a new type of particles $n, l\rightarrow n, l$.

Neutral particles: $\sigma\sim k_n^{4l}$;
Coulomb repulsion: $\sigma\sim k_n^{-2}$;
Coulomb attraction: $\sigma\sim k_n^{-2}$.

Even in the case of neutral particles the cross section is finite for $l=0$ at very low energy. In this case, the $\omega^2 j^2(q-R)^{-1}$ term of (15) is the dominant one. On the other hand, in the case of charged particles, the first two terms within the absolute sign do not compensate and most of the scattering is due to these. In this case, the potential scattering is of the order of the maximum possible scattering and this situation is not altered by the nuclear scattering, and our rules become rather meaningless. All these rules are valid, of course, only if $k_n a_n \ll 1$ where a_n is a distance outside of which (5) can be expected to be valid. This condition assures, at the same time, the accuracy of the asymptotic expressions of Tables I and II. In addition to this, it is necessary that $(q-R)^{-1}$ or $q-R$ do not change substantially in the energy interval considered. For q, this condition amounts to $\Delta(k^2a^2)\ll 1$ but although this has to be valid for all s (rather than only for the particular s the formation or reaction of which we are considering) it will hardly limit the validity of the above rules. On the other hand, the condition that $\Delta E(dR/dE)\ll R$ effectively limits the validity of the above rules for the behavior of the cross sections to an energy interval which is small compared with the distance of the next resonance. It is clear, of course, that such a limitation must exist. The inclusion of the formulae for higher l into the tables can be of value only if the angular distribution of the reaction products can be investigated. The total cross section will be proportional to the expression given for the lowest l which can be formed.

SECTION IV

The above tabulations which form the essential result of the present note, give the energy dependence of the dominant term for the various cross sections just above the threshold. They give, of course, the cross section only up to a factor the determination of which cannot be carried out by the methods used in this article. It may be worth while to remark, however, that the next term in all cross sections is proportional

[4] G. Beck and H. L. Horsley, Phys. Rev. **47**, 510 (1935); H. A. Bethe, Phys. Rev. **47**, 747 (1935); F. Perrin and W. Elsasser, Comptes Rendus **200**, 450 (1935).
[5] J. Schwinger and E. Teller, Phys. Rev. **52**, 286 (1937); M. Hamermesh and J. Schwinger, Phys. Rev. **69**, 145 (1946); compare, in particular, Figs. 1 and 2 of the former article.

to $|k_n|$ and that there is such a term in all cross sections, even in those which do not involve the new mode of reaction. Furthermore, a term of this nature is present both above and also below the threshold. As a result, for example, all reaction and scattering cross sections, which are possible below the threshold energy of the new mode, show a cusp at the threshold energy for the new mode, i.e., have a functional dependence on E both for $E<\epsilon_n$ and for $E>\epsilon_n$ like $a+b|E-\epsilon_n|^{\frac{1}{2}}$ +higher order terms in $E-\epsilon_n$. In fact, the coefficients b can be determined if the R matrix (i.e., essentially the coefficients of the dominant term) is known at $E=\epsilon_n$. However, it does not seem that these cusps are particularly important and they will not be discussed further.[6]

It may be more important to consider small deviations from the potentials considered above. Indeed, it can hardly be expected that it is possible to choose the surface S so far out that the interaction outside of it be represented accurately by Ze^2/r (Z positive, negative, or zero). One can approximate such a condition by choosing the a_s very large but one thereby increases the internal region and thus also the fluctuations of R in a given energy range. It seems more natural, therefore, to investigate directly how a small potential outside S will affect the quantities of Table I. Such an investigation shows that if the small potential is twice integrable to infinity, i.e., if it drops as fast as r^{-n} with $n>2$, the asymptotic behavior will not be affected. This shows then that the centrifugal potential, which causes the differences between the different rows of Table I, is just about the weakest potential to change the asymptotic behavior. Indeed, a comparison with Tables II and III shows that the much stronger electrostatic potential completely washes out the effect of the centrifugal potential. On the other hand, while a potential which is small in the above sense does not alter the asymptotic behavior of the cross sections, it can substantially influence both the absolute magnitude of it and also the range within which the asymptotic behavior is valid.

As is well known, the emerging wave function, $\bar{\mathrm{E}}$, for a potential $V+\hbar^2P/2M$ can be obtained from the emerging wave function E for the potential V by means of the formula

$$\bar{\mathrm{E}}(r)=\mathrm{E}(r)+\mathrm{E}(r)\int_r^\infty (r'\mathrm{E}(r'))^{-2}dr' \times\int_{r'}^\infty r''\mathrm{E}(r'')r''\bar{\mathrm{E}}(r'')P(r'')dr''. \quad (17)$$

This can be rewritten as

$$\frac{\bar{\mathrm{E}}(r)}{\mathrm{E}(r)}=1+\int_r^\infty \frac{dr'}{r'^2\mathrm{E}(r')^2}\int_{r'}^\infty (r''\mathrm{E}(r''))^2 \times\bar{P}(r'')dr'', \quad (17a)$$

where $\bar{P}=P(\bar{\mathrm{E}}/\mathrm{E})$. Now a changed asymptotic behavior would entail a change of j^2, or of $|e|^2$, at $k=0$, by an infinitely large or infinitely small factor. The same would then hold for E. It thus appears that the asymptotic behavior of the cross section can change only if the perturbation P is such that the integral on the right side of (17a) diverges at $k=0$. Since however, $r\mathrm{E}(r)$ is, at large r, proportional to $\exp(ikr)$ this condition is equivalent with the condition that the second integral of $\bar{P}$ diverge. This certainly will be true if the second integral of P diverges. On the other hand, if the second integral of P converges, and goes to zero for large r, then $\bar{\mathrm{E}}/\mathrm{E}$ goes to 1 at large r and $\bar{P}$ becomes equal to P under the same condition. Hence, $\bar{P}$'s second integral will converge or diverge if P's second integral converges or diverges. It appears to follow that the asymptotic behavior of the cross section near a resonance remains unaltered by the addition of a "small" potential P whose second integral to infinity converges. Although this derivation of the insensitivity of the asymptotic behavior of the cross sections is certainly not rigorous (it can be made rigorous easily if P drops to zero exponentially or faster), the writer feels convinced that its result is correct.

Even if the above surmise should prove to be correct, there remains the question of the restriction of the region of validity of the limiting laws above derived for the cross sections. This region is determined, in the absence of the additional potential $\hbar^2P/2M$, by the more rigorous of the two conditions enumerated before: (a) The region must be small as compared with the distance of resonances E_λ of (4a) from each other.

[6] It may be mentioned, though, that these cusps are not given by either of the two methods of reference 1.

(This is the condition which apparently limits the validity of the $1/v$ law for slow neutron absorption.) (b) In the case of uncharged particles $k_n a_n \ll 1$, and in the case of charged particles also $\alpha = Ze^2/\hbar v \gg 1$.

It is clear, however, that the additional potential can further reduce the region in which the asymptotic behavior is followed. An obvious example for this is a low but extended repulsive potential of constant magnitude of say $\hbar^2 k_0^2/2M$. The $|e|^2$ for a potential of this height and of extension l outside a is

$$|e|^2 = (\hbar/4Mka^2)[(\mathrm{Ch}\kappa l + \kappa a\ \mathrm{Sh}\kappa l)^2 + (k^2/\kappa^2)(\mathrm{Sh}\kappa l + \kappa a\ \mathrm{Ch}\kappa l)^2] \quad (18)$$

$$\kappa = (k_0^2 - k^2)^{\frac{1}{2}}.$$

Hence, for small k,

$$j(a)^2 = |e(a)|^{-2} \approx (4Mka^2/\hbar) \times (\mathrm{Ch}k_0 l + k_0 a\ \mathrm{Sh}k_0 l)^{-2} \quad (18a)$$

+terms proportional to k^2 and higher powers of k. The dependence of the j on k is, according to (18a), the same as given in the first row of Table I. This illustrates the point that a potential which goes at $r = \infty$ sufficiently fast to zero does not affect the asymptotic behavior of the cross sections. However, even for $k = k_0$ the j is equal to $[1 + k_0^2(l+a)^2]^{-\frac{1}{2}}$ which is already very different from (18a) and shows that the asymptotic behavior does not extend to $k = k_0$. This was, of course, to be expected, since the potential $\hbar^2 k_0^2/2M$ for $a < r < a + l$, which is important for $k = 0$, becomes insignificant for $k \gg k_0$. The condition that the potentials be insignificant for all k, and therefore do not affect the region of validity of the asymptotic law for the cross section, is that the integral of (17a) with P instead $\bar{P}$, be not only finite but also small compared to 1. This is equivalent with the condition that the second integral P_2 of P from a to infinity be small compared with 1. In practice this is equivalent with the condition that the *WKB* integral be small.

As an example, the magnetic interaction of a neutron with a nucleus may be considered. The P is in this case

$$P \approx \frac{2M}{\hbar^2}\left(\frac{e\hbar}{2Mc}\right)^2 \frac{\mu_1\mu_2}{r^3},$$

and the second integral of this is

$$P_2 \approx \frac{e^2\mu_1\mu_2}{4Mc^2 r}.$$

For $r = a \sim e^2/mc^2$ this is of the order of 10^{-3}, and shows that the magnetic interaction should be without appreciable effect on slow neutron processes.

For $k \gg k_0$ the κ of (18) becomes imaginary and $|e|^2$ fluctuates with a small amplitude around the value of Table I. If the other conditions of the asymptotic behavior of the cross section remain valid, there will then be at $k \gg k_0$ a second region in which the reaction cross section is proportional to k but the constant of proportionality will be different from the constant of proportionality at $k \ll k_0$. A similar second region at somewhat larger k, in which the asymptotic behavior is followed, may exist even if P goes so slowly to zero at $r = \infty$ that it changes the asymptotic behavior at very low k. Its existence depends more on the maximum of P than on its behavior at large r, and its appearance can be judged from the decrease of the integral in (17a) to a very low value at such a low k that the other conditions for the validity of the asymptotic behavior still hold.

The Production of Nucleons by the Cosmic Radiation. II.

S. A. KORFF
New York University, University Heights, New York, New York
AND
A. COBAS
University of Puerto Rico, Rio Piedras, Puerto Rico
(Received January 15, 1948)

A series of experiments at high elevations is described. Balloon flights reaching altitudes corresponding to a pressure of 2-cm Hg were carried out. No maximum in the neutron counting rate was found. The effect produced by surrounding by water a counter near the ground was found to be small, indicating that most of the neutrons were already slow. No diurnal effect as large as ten percent in the neutrons was found at a level of 6 meters of water equivalent.

1. INTRODUCTION

IN a series of experiments reported previously,[1] we have studied the various processes by which neutrons and protons are produced in the atmosphere by cosmic radiation. In connection with the interpretation of the experiments, a number of points seemed to us to require clarification, and the experiments described in the present paper were made for this purpose. The questions which we sought to answer experimentally in the present tests were: 1. At what elevation is the maximum neutron intensity? (There must be a maximum somewhere, because the neutrons cannot be considered primary particles on account of their radioactivity.) 2. Can we evaluate the number of neutrons at various elevations? 3. Can we obtain further information about the effects produced by surrounding matter, such as water and lead, on the number and energy distribution of the neutrons? 4. Can we further evaluate and explain the background counting rates of proportional counters at high elevations? 5. Is there any evidence for neutrons reaching us from the sun, i.e., is there any diurnal effect in the neutrons? The experiments described below were designed to throw light on these questions.

Because of the different limitations on various experimental techniques, two sets of experiments were performed. One was carried out by comparatively light instruments lifted to a high elevation by free balloons for a short period, and the other by heavier apparatus operated at moderate elevations for longer times. The mountain experiments were performed at the Inter-University High Altitude Laboratory on Mt. Evans, Colorado.[2]

2. BALLOON EXPERIMENTS

A. Apparatus

In order to measure the number of neutrons at high elevations, a series of balloon flights was carried out. Each flight instrument consisted of a pair of identical proportional counters, an electronic circuit to amplify and prolong the counts, a barograph and an arrangement for recording photographically the counts and the pressure determined by the barograph. Each pair of counters was filled on a manifold to the same pressure of BF_3. One counter in each flight was surrounded by a shield of powdered boron carbide about 7 mm thick, while the other was left unshielded. A small electric motor drove a switch which connected the two counters alternately to the recording circuit for a two-minute period. The purpose of switching, instead of using two amplifiers and recording the counts for both counters separately and simultaneously, was to insure that the amplifier gain, and hence the recorded pulse size, was always the same for each counter. The record, therefore, showed the number of counts occurring every two minutes with shielded and unshielded counters in succession. We shall designate the difference in counting the rate of the shielded and unshielded

[1] S. A. Korff and B. Hamermesh, Phys. Rev. 71, 842 (1947).

[2] Altitude 14,156 feet, or about 6 meters of water equivalent below the top of the atmosphere.

counters as the "boron difference," and we shall assume this quantity to be a measure of the number of neutrons. The counters were placed end to end and as far apart as the frame permitted, so as to minimize the solid angle of the shield as presented to the unshielded counter. In order to obtain further information about the number and cause of the background counts, a different pressure of BF_3 was used in each pair of otherwise identical counters. Four flights of this type were made and recovered, but one camera was lost, so that three records were obtained.

B. Observations

First we shall present the data regarding the maximum in the neutron intensity as a function of elevation. One flight reached an altitude of 82,000 feet, corresponding to a pressure of a trifle less than 2-cm Hg, or to a depth of about $\frac{1}{4}$-meter of water equivalent below the top of the atmosphere. The other flights went to 72,000 and 55,000 feet, respectively. In no case was any maximum of the neutron counting rate or boron difference observed. Unfortunately, the statistical accuracy of the counting rate at the highest elevation is not especially good, whereas at 55,000 feet several thousand counts were recorded. In the highest flight, the counting rate rose from 14 per minute at the level corresponding to one meter of water equivalent below the top of the atmosphere to 14.4 at half a meter of water. This altitude is well above the level at which the maximum in the soft component is observed.

The observed counting rates are set forth in Table I.

TABLE I. Counts per minute at various elevations. PV is pressure of BF_3 in atmospheres times volume of counter in liters. The counts are the boron difference, the difference in counting rates between shielded and unshielded counters.

Flight No.	PV	c.p.min. at 20	10	5	2-cm Hg
30	0.193	1.6	3		
32	0.262	2	4	9	
33	0.391	3	10	14	14.4

The background on the highest flight was fairly large, especially near the top, and was of the same order as the neutron difference. In other words, the unshielded counter counted about twice as fast as the shielded one. Except at the highest altitude, the background counting rate did not increase rapidly with elevation.

C. Discussion of the Flight Experiments

Consider first the question about the maximum of the neutron intensity. It appears quite probable that such a maximum exists and that its elevation will be found in due course. The number of neutrons increases with elevation. Because of their presumed radioactivity, however, neutrons are not thought of as primary particles; therefore, the neutron intensity at great altitudes must be zero. Since neutrons do not travel great distances because of the capture probability in nitrogen, the neutrons must have been produced and slowed down near where they are observed. Therefore, knowledge of the altitude of the maximum in the neutron intensity curve will presumably throw light on the processes by which the neutrons are formed. Thus for example, if the maximum in the neutrons intensity occurred at the same altitude as the maximum in the soft component, it might suggest a connection between the neutrons and the soft component. The altitude of the maximum is therefore an extremely important quantity to be determined.

In the present experiments, no maximum was found. This conclusion, however, rests on an insufficient amount of data and steps to augment it are under way.

These experiments indicate that the maximum of the neutron intensity does not occur at the same elevation as the maximum in the soft component. This situation strongly suggests that the soft component is not the chief source of the neutrons at the higher elevations, but that most of them are produced by some other mechanism at still higher elevations. Such a mechanism might well be closely connected with the formation of mesotrons by the primary radiation. As the experiments of Schein and his colleagues[3] have shown, mesotron production must have a large cross section, and takes place at very high elevations. Such elevations are still above those reached in our flights, for 2-cm pressure corre-

[3] M. Schein, W. P. Jesse, and E. O. Wollan, Phys. Rev. 59, 615 (1941).

sponds to around four radiation lengths. Possibly, several fast neutrons are produced in each mesotron process, and these, in turn, produce more slower neutrons lower down.

Consider next the background counting rate, i.e., the counting rate of the shielded counter. The background counting rate in these counters is produced by (a) natural contamination alpha-particles, which do not show an increase with elevation, and (b) large ionizing events such as nuclear disintegrations and giant showers, which do increase with altitude. In these experiments, factor (a) was predominant up to elevations between one and two meters of water equivalent. At higher levels (b) began to be increasingly important, and higher up it overshadowed (a) by a factor of five or ten. As a further check, the counters were filled to various pressures of BF_3. The contamination background will presumably not be a function of filling gas, but will chiefly depend on the inside areas of the counters, which were all the same. Giant showers, on the other hand, will produce more ionization (larger pulses) in the counters containing more gas. Hence it is not surprising that the high pressure counters also had the highest background.

In these experiments, the bias on the amplifier was set at a high value to insure that electrical noise, spurious effects, and the numerous smaller ionizing events do not record. This procedure results in missing some of the neutrons. Hence, only relative increases with elevation can be inferred from the data. Further, exact proportionality of the neutron counting rate and BF_3 pressure is not to be expected because of minor differences in amplifier bias settings between flights.

The authors wish to emphasize that these experiments and discussions are preliminary. Additional flights will be made in the near future to secure further data.

3. THE MOUNTAIN EXPERIMENTS

A. Apparatus

Two proportional counters were operated at the Mount Evans Laboratory[2] in this test. One was 15 cm in diameter, 150 cm long, and filled to 30-cm pressure with BF_3, while the other was 8 cm in diameter, 100 cm long, and filled to 18 cm with BF_3. Hence, the PV of counter A was 10.6 liters at 1 atmos., and for counter B it was 1.19. Ordinary commercial BF_3 was used. The counts were amplified by a circuit whose gain could be adjusted, and counting rates as a function of voltage for constant gain were observed. A cadmium shield about 0.8 mm thick could be slipped over the counters; forty 5-gallon water cans were stacked about the counter in most of the tests, so that in these cases, the counters were surrounded by a water barrier of irregular outline, but mostly between 30 and 80 cm thick. A mass of lead weighing about 200 kg could be placed directly above the counters and inside the water surroundings. The difference in counting rate with and without cadmium will be called the "cadmium difference." This quantity was measured under various conditions, with and without water and/or lead. The counting rate was usually observed as a function of voltage and the highest values were used. In order not to miss any neutrons, the voltage was increased until the counters started counting beta-particles and the lower (most ionizing) end of the beta-spectrum was explored.

B. Observations

The counting rates, with and without cadmium, for both counters were determined, and curves similar to those already published were obtained. Cadmium differences of 100 and 15 counts per minute were obtained for the two counters, respectively.

Next, the effect of removing the water was sought. A slight decrease in the cadmium difference was noted; in one case, the neutron counting rate fell from 55 to 40 with the removal of the water. Then the lead was removed. No difference as large as the experimental error was observed in the number of neutrons. The bottom half of the cadmium shield was found to cause a reduction of about half in the total cadmium difference.

The cadmium difference, for a constant geometry, was next measured at various times of day, from 5 A.M. to midnight, at four-hour intervals. No difference as large as the reproducible accuracy of the counting rates was observed. Since such tests presuppose that the voltage and amplifier gain do not vary over a long period, accuracy is controlled not by the number of

counts, which is large, but by voltage stability. A test was always made of the ability of the circuit to reproduce counting rates the next day for the same setting. This test showed that reproducibility limited the accuracy to around 10 percent, regardless of the number of counts, which was always much larger than required for ten percent statistically.

C. Discussion of the Mountain Experiments

The rate of production of neutrons has been estimated in previous papers. A counting rate of about 10 per minute per liter of ordinary BF_3 at S.T.P. (corresponding to a PV of unity) was found, which agrees with previous estimates. The main purpose of these experiments, however, was to test for the effect of the surrounding matter. In most theoretical analyses, uniform conditions are assumed which are seldom attained in experiment. Hence, the effects of water and lead were studied by determining the cadmium difference for various arrangements.

It is interesting to note that the presence or absence of a substantial amount of lead does not materially affect the neutron counting rate. We may, therefore, conclude that most of the neutrons are not produced in the lead, nor are they dependent on the presence of large nuclei for their production.

The effect produced by the presence of the water was studied next. It was found that the removal of the water reduced the cadmium difference slightly. Removal of water will have two effects in removing a number of oxygen nuclei from which the neutrons could have been produced and also removing the slowing-down agent. It will be noted that the effect of the water is not large because most of the neutrons are already slow. They have presumably been produced in the vicinity, and many have been slowed down by diffusing into the ground and back out. The small difference made by the presence of the water had been noted at sea level in previous tests.[4] It indicates that conditions near the surface of the ground are importantly influenced by the presence of the nearby ground, and that the energy distribution of the neutrons is mostly determined by the nearby ground. The result of the concentrated matter and moisture in the ground is that most of the neutrons near the ground are slow. This energy distribution is quite different from that found in the free atmosphere,[5] where most of the neutrons are captured before having become thermal.

The test with the bottom half of the cadmium shield supports the view that the neutrons reach the counter more or less isotropically. About half the neutrons reaching the counter come from below. This does not mean that these have necessarily diffused back up from the ground, but merely that large-angle scattering is common and that the directional isotropy characteristic of a diffusion equilibrium exists.

The absence of any pronounced diurnal effect also rules out the sun as the predominant source of the neutrons at the six-meter level. Since, however, neutrons are not affected by the earth's magnetic field, the possibility remains that neutrons from the sun may reach the upper parts of the atmosphere at any latitude. Such neutrons are evidently not energetic enough to penetrate the atmosphere to a depth of six meters of water equivalent, in any appreciable quantity. Radioactivity of the neutron will not necessarily rule out solar origin since the sun is only eight minutes away for velocities comparable to that of light.

Rates of production of neutrons may be computed by the use of an equation previously derived,[6] which we repeat for convenience:

$$q=(n/PV)(\sigma_w/\sigma_B)(2.24\times10^4/W), \quad (1)$$

where q is the rate of production of neutrons per gram per second, n is the number of counts per second, PV is the pressure in atmospheres of the BF_3 in the counter times the volume of the counter in cc, σ_w is the capture cross section of the surrounding material, σ_B is the capture cross section of boron, and W the atomic weight of the surrounding substance. In this case, for a surrounding of water, we take σ_w as 0.5×10^{-24}, and σ_B as 550×10^{-24} sq cm, and W as 18. Then, for a counter whose PV is 10.6×10^3, an observed n of 2 per second yields a q of 2×10^{-4} neutrons

[4] M. Kupferberg and S. A. Korff, Phys. Rev. **65**, 253A (1944).

[5] S. A. Korff and B. Hamermesh, Phys. Rev. **69**, 155 (1946).

[6] H. A. Bethe, S. A. Korff, and G. Placzek, Phys. Rev. **57**, 573 (1940).

per gram per sec. produced in the surrounding water by the cosmic radiation.

It will be noted that this figure is slightly higher than that estimated from the balloon data. The reason for this, as has already been pointed out, is that in the balloon flights the bias is set at a sufficiently high value so that only the larger pulses are detected, and, hence, some neutrons are missed. This procedure is necessary in unmanned flights to preclude the inclusion of spurious counts and electrical noise. Hence, our estimates of the number of neutrons should be based on the mountain data and not on the flights carried on to date. For example the number of neutrons estimated by Libby[7] from our data should be somewhat more than doubled.

[7] F. W. Libby, Phys. Rev. 69, 671 (1946).

ACKNOWLEDGMENTS

The authors wish to acknowledge assistance rendered in connection with this work by Lt. Col. M. S. George, Capt. J. W. Kerr, Lt. George Alexander, and M. Swetnick of the New York University cosmic-ray group. The instruments were built by L. G. Collyer. The work was financed by a grant from the Research Corporation. To Professors Byron Cohn and Mario Iona go our especial thanks for cordial cooperation and assistance with every phase of both the balloon work and observations on Mt. Evans. Our thanks are also due the Colorado State Patrol for assistance in the recovery of flight instruments, as well as to station KOA for assisting in establishing a balloon-theodolite station, and to many other individual for incidental assistance.

PHYSICAL REVIEW VOLUME 73, NUMBER 9 MAY 1, 1948

Gamma-Rays from Alpha-Particle Reactions*

DAVID E. ALBURGER
*Sloane Physics Laboratory, Yale University,** New Haven, Connecticut*
(Received January 21, 1948)

Gamma-rays from sodium, magnesium, aluminum, silicon, phosphorus, and sulfur targets under cyclotron bombardment by 7-Mev alpha-particles have been observed. Energies were obtained by measuring the maximum range of Compton-recoil electrons in aluminum, using two beta-ray counters in coincidence. The following gamma-ray energies were found: sodium, 1.85 ± 0.15 Mev and 2.80 ± 0.25 Mev, with an intensity ratio of 6 to 1; magnesium, 1.8 ± 0.2 Mev and 4.3 ± 0.3 Mev, with an intensity ratio of 3 to 1; aluminum, 3.5 ± 0.3 Mev; silicon, 2.3 ± 0.3 Mev; phosphorus, 2.55 ± 0.25 Mev and 4.1 ± 0.4 Mev, with an intensity ratio of 8 to 1; sulfur, 2.4 ± 0.3 Mev. In cases where correlation can be made with energy levels given by the corresponding αp reactions the transition from the second excited state to ground in the product nucleus seems to be favored.

I. INTRODUCTION

THE presence of gamma-radiation in nuclear reactions gives the most direct evidence for the existence of excited states in the product nucleus. In the case of alpha-particle bombardment of the light elements gamma-radiation has been reported,[1] but few reliable energy measurements have been made. This is in contrast to the relatively large amount of consistent data on αp reactions from which energy levels in the final nucleus can be inferred from proton groups. Another approach to the problem is the association of gamma-radiation with particle groups resulting from a nuclear reaction. This has been studied in only a few cases, most recently by Benson who performed[2] proton-gamma coincidence experiments on the $Al^{27}(\alpha p)Si^{30}$ reaction at specific values of proton energy but without

* Part of a dissertation to be presented to the graduate school of Yale University in partial fulfillment of requirements for the degree of Doctor of Philosophy.

** Assisted by the Office of Naval Research under Contract N6ori-44.

[1] M. Stanley Livingston and H. A. Bethe, Rev. Mod. Phys. 9, 298 (1937).

[2] Bruce B. Benson, Phys. Rev. 73, 7 (1948).

regard to gamma-ray energy. Coincidences were obtained for protons to the excited states of the Si^{30} nucleus but none were observed for protons to the ground state.

The gamma-ray energy spectrum gives further useful information. If this has been determined, the level separations obtained from proton groups may be compared with independent measurements on quantum transitions in the final nucleus. In addition, the relative gamma-ray intensities may be used to determine transition probabilities and selection rules according to which the product nucleus drops to the ground state. Some work along this line has recently been done.[3] Absorption in lead of gamma-radiation from Na, Mg, Al, Si, P, and S targets under alpha-particle bombardment has been studied and absorption coefficients obtained. The predominant radiations were found to be in a 1.5–5-Mev energy range. Because of the minimum in the lead-absorption curve at 3 Mev, a determination of the energies present in all cases was not possible. However, since the energies were considerably greater than the level separations from other evidence, it seemed that direct transitions were preferred to cascade.

Another gamma-ray measurement technique consists in observing the maximum range of Compton-recoil electrons in aluminum. This method was first described[4] by Bothe and Kolhörster and later applied[5] by Becker and Bothe to the gamma-rays excited in B and Be by alpha-particles. Curran, Dee, and Petržílka used[6] the scheme to measure the gamma-rays resulting from proton capture by Be, B, C, and F. More recently Deutsch has measured[7] the gamma-rays of La^{140}. The method consists in placing two thin-window beta-ray counters on a line with the source so that gamma-rays falling on the end wall of the first counter produce recoil electrons in the forward direction which traverse both counters giving coincidences. By inserting aluminum between the counters the number of coincidences decreases in a roughly logarithmic fashion from a single gamma-ray energy. The thickness of absorber at which counts are reduced to the random coincidence rate gives the maximum range of the electrons. Applying the modified Feather relation[8] for the maximum range of beta-rays in aluminum,

$$\text{range (g/cm}^2\text{ Al)} = 0.571E\text{ (Mev)} - 0.161,$$

the electron energy may be calculated. Addition of the back-scattered quantum energy gives the incident gamma-ray energy. The method is good to 5–10 percent accuracy for a single gamma-ray. If two gamma-rays are present it is difficult to single out the softer component unless well separated in energy and three or more times the intensity of the harder component. In such a case a break in the curve will appear at an absorption corresponding to the lower energy gamma-ray.

In the present work this coincidence method has been applied to the gamma-rays resulting from the alpha-particle bombardment of Na, Mg, Al, Si, P, and S and an attempt has been made to correlate the energies obtained with levels of excitation observed in αp studies.

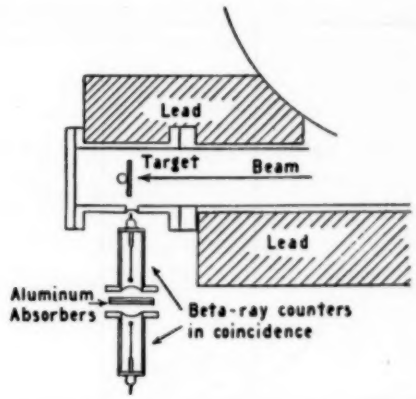

FIG. 1. Experimental arrangement for measuring the maximum range in aluminum of Compton-recoil electrons produced by gamma-rays from targets under cyclotron bombardment.

II. EXPERIMENTAL

Figure 1 shows the experimental arrangement. A 7-Mev alpha-particle beam is brought out from the main cyclotron chamber into an external

[3] Ernest Pollard and D. E. Alburger, Phys. Rev. 72, 1196 (1947).
[4] W. Bothe and W. Kolhörster, Zeits. f. Physik 56, 751 (1929).
[5] H. Becker and W. Bothe, Zeits. f. Physik 76, 421 (1932).
[6] S. C. Curran, P. I. Dee, and V. Petržílka, Proc. Roy. Soc. 169, 269 (1938).
[7] M. Deutsch, Manhattan Engineer District, LAMS Report 142, Series c; MDDC Report 237, October, 1944.
[8] E. Bleuler and W. Zünti, Helv. Phys. Acta 19, 137 (1946).

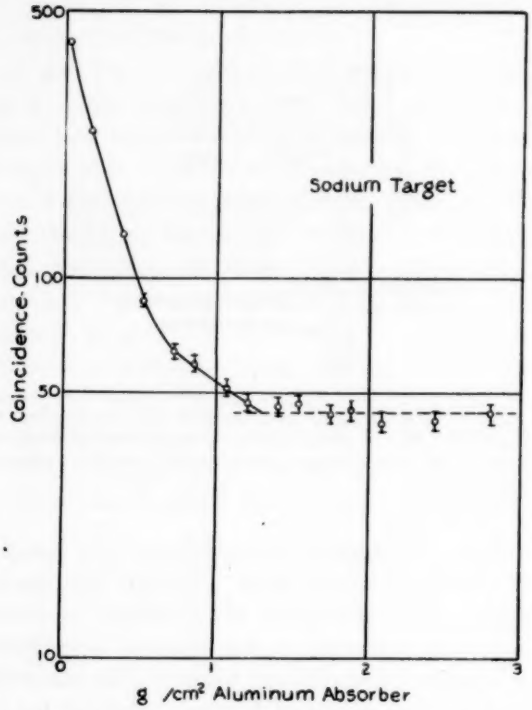

FIG. 2. Absorption of Compton-recoil electrons produced by gamma-rays from a sodium target under alpha-particle bombardment, indicating the presence of two gamma-ray energies.

bombardment chamber. Targets are attached to a tin holder and consist of Na, Mg, and Al metals, fused silicon, red phosphorus, and sulfur fused with gold dust for beam current conduction. To minimize absorption of gamma-radiation from the target by the wall of the bombardment chamber a foil window has been provided. Two thin-window beta-ray counters are placed outside the bombardment chamber on a line with the target. These are shielded by lead blocks located so as to reduce stray radiation from the main cyclotron chamber. As previously described, Compton-recoil electrons are produced by gamma-rays from the target falling on the brass end and side walls of the first counter. Some of these pass through both counters, resulting in time-coincident pulses. Separate inputs connect the two counters to a double-coincidence recording circuit. The first counter input circuit also operates a scaling and recording circuit. The number of counts registered by this circuit is independent of the absorber placed between the counters and may therefore be used to integrate

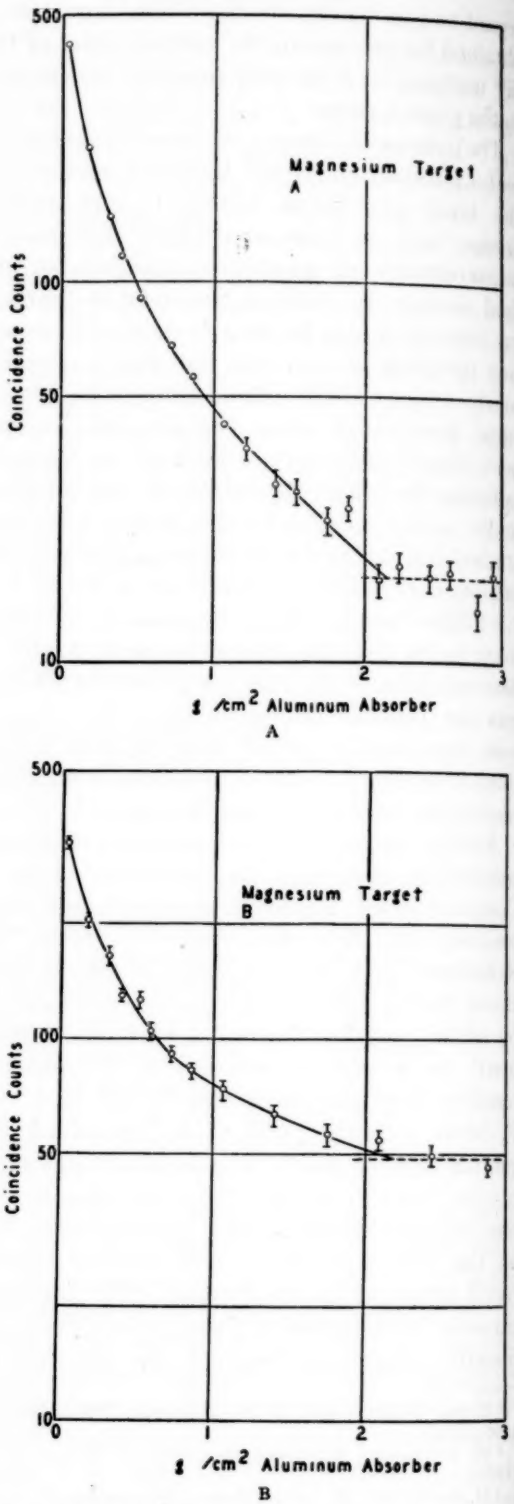

FIG. 3. Absorption curves for a magnesium target: A—counter bases ¾ inch apart; B—improved geometry with counter bases 2 inches apart, showing more clearly the presence of a second gamma-ray.

the beam. Thus, at each value of absorption coincidences are observed for a fixed number recorded by the first counter.

As a check on the method for the particular geometry and absorbers used, runs were made with sodium (24) and thorium active deposit sources. In each case the maximum range obtained corresponded to the known highest energy gamma-ray within the experimental limits of error.

III. EXPERIMENTAL RESULTS

Sodium

Figure 2 shows one of two careful runs on sodium targets made after a series of preliminary experiments. Coincidence counts per 8000 registered by the first counter have been plotted logarithmically against aluminum-absorber thickness expressed in grams per square centimeter. The value at each absorber thickness is the average of a number of points taken so as to smooth out non-random as well as statistical variations. Expected deviations were calculated from total numbers of counts and are indicated by vertical lines. Two ranges at 0.76 g/cm² and 1.29 g/cm² can be resolved from the curve. Application of the Feather relation as previously described shows that the observed end points correspond to 1.85±0.15-Mev and 2.80±0.25-Mev gamma-rays. Extrapolating the higher energy component portion of the curve back to zero absorption and deducting the background gives a soft-to-hard component yield ratio of approximately 6 to 1. No correction has been made for the variation of counter efficiency with gamma-ray energy. There is slight evidence for a gamma-ray of even higher energy.

Magnesium

Curve *A* of Fig. 3 was obtained with the counter bases separated by a ¾-inch spacer ordinarily used. This shows an end point at 2.15 g/cm² produced by a gamma-ray of 4.3±0.3-Mev energy and considerable curvature below 1 g/cm². An improvement in geometry by increasing the counter separation to 2 inches resulted in curve *B* of Fig. 3. A more definite break has appeared at 0.75 g/cm² corresponding to a 1.8±0.2-Mev gamma-ray. A ratio of soft-to-hard gamma-ray intensities of approximately 3 to 1 is obtained from either curve.

Aluminum

A single electron group with an end point at 1.72 g/cm² was obtained, as shown in Fig. 4. This corresponds to a 3.5±0.3-Mev gamma-ray. Slight indication of a curvature near the observed end point suggests a second gamma-ray of lower energy.

Silicon

Figure 5 shows one of several runs made on silicon yielding a maximum electron range of 1.02 g/cm² with slight evidence for a higher energy component. The gamma-ray observed has an energy of 2.3±0.3 Mev.

Phosphorus

The curve in Fig. 6 was obtained with the usual ¾-inch counter separation. The two end points have the values 1.17 g/cm² and 2.05 g/cm² and correspond to 2.55±0.25-Mev and

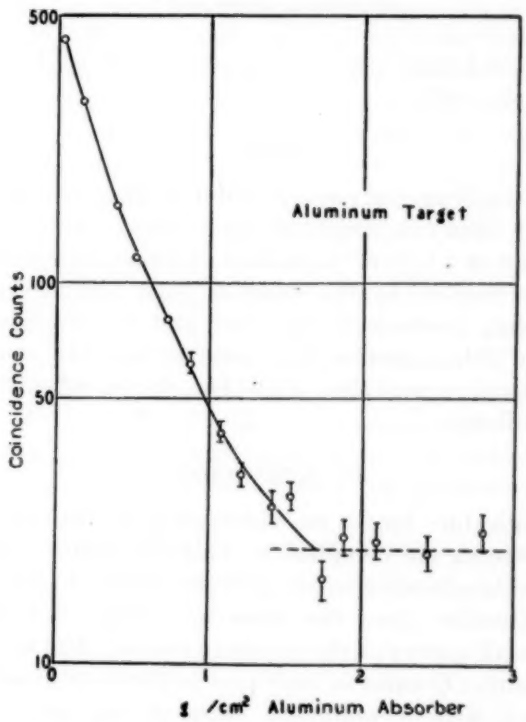

FIG. 4. Aluminum target absorption curve indicating a single gamma-ray energy.

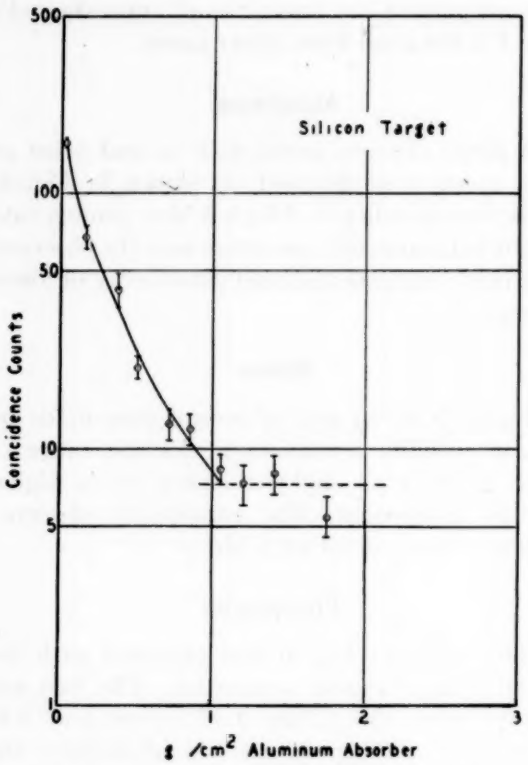

FIG. 5. Absorption of recoil electrons produced by gamma-rays from a silicon target.

4.1±0.4-Mev gamma-rays with an 8 to 1 intensity ratio.

Sulfur

One of several runs on sulfur is given in Fig. 7 and shows a single electron group. The end point at 1.1 g/cm² is produced by a 2.4±0.3-Mev gamma-ray. In the cases of both silicon and sulfur, yields were very low and resolution of any other gamma-rays present was not considered practicable with the beam intensity available.

IV. DISCUSSION

Q-values for αp reactions with the six target elements are compiled in Table I. Addition of the bombarding alpha-particle energy to these quantities gives the observed values of total kinetic energy of the product particles. The most positive Q-value in each case is therefore associated with a minimum mass of the product nucleus and corresponds to the ground state Q_0. More negative values represent successive ex-

TABLE I.

Reaction	Q_0	Q_1	Q_2	Q^3		Gamma-rays (Mev)	Relative intensity
$Na^{23}(\alpha p)Mg^{26}$	1.44	1.12	−0.30	−1.35	a	1.85	6
						2.80	1
$Mg^{24\ 25\ 26}(\alpha p)Al^{27\ 28\ 29}$	−1.2	−2.0	−2.9		b	1.8	3
						4.3	1
$Al^{27}(\alpha p)Si^{30}$	2.26	−0.02	−1.32	−2.49	c	3.5	
$Si^{28\ 29\ 30}(\alpha p)P^{31,32,33}$	−2.4	−3.2	−4.0		b	2.3	
$P^{31}(\alpha p)S^{34}$	0.00	−1.2	−2.6	−4.6	d	2.55	8
						4.1	1
$S^{32}(\alpha p)Cl^{35}$	−2.35	−2.85	−3.6		e	2.4	

[a] Data recently taken in this laboratory and to be published by R. F. Humphreys and H. T. Motz. Values are tentative pending analysis of proton range corrections.
[b] O. Haxel, Zeits. f. tech. Physik 16, 410 (1935).
[c] W. E. Duncanson and H. Miller, Proc. Roy. Soc. 146, 396 (1934) (corrected by Livingston and Bethe).
[d] E. Pollard and C. J. Brasefield, Phys. Rev. 50, 890 (1936).
[e] C. J. Brasefield and E. Pollard, Phys. Rev. 50, 296 (1936).

cited states Q_1, Q_2, etc., and by subtracting these from Q_0 the levels of excitation in Mev are obtained.

The last two columns in Table I summarize the gamma-ray energies and relative intensities found in the present work. The sodium target values correspond quite well to Q_2 to Q_0 and Q_1 to Q_0 transitions, the former yielding the higher intensity. The lower energy of the two gamma-rays observed from the magnesium target and

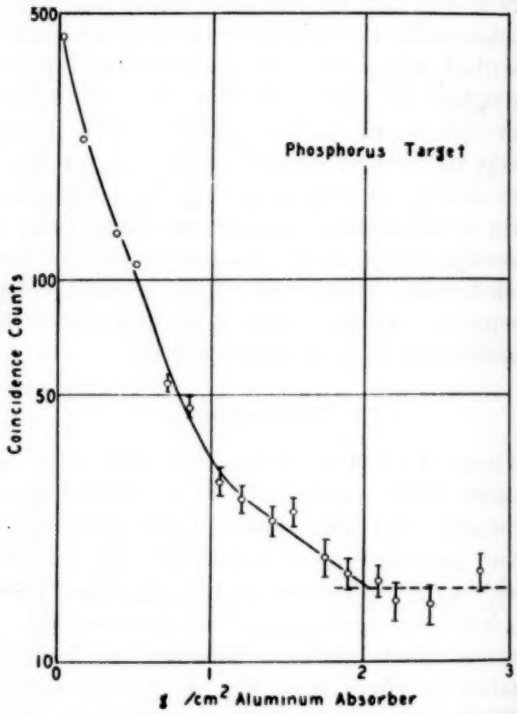

FIG. 6. Absorption curve for a phosphorus target giving clear indication of two gamma-ray energies.

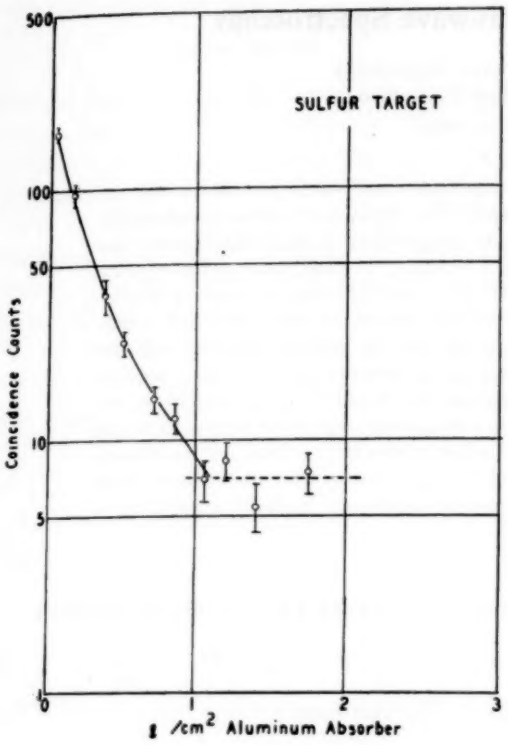

FIG. 7. Absorption of recoil electrons produced by gamma-rays from a sulfur target.

the single gamma-ray from the aluminum target both find correlation with Q_2 to Q_0 transitions. The gamma-rays from both silicon and sulfur targets exceed the highest excitation level observed with proton groups. In the case of phosphorus, good agreement is obtained for the lower energy and more intense gamma-ray with the Q_2 to Q_0 separation while the higher energy component is in fair agreement with the Q_3 to Q_0 transition.

Of the nine gamma-rays observed, six seem to compare favorably with energy level schemes derived from αp reactions. In no case is the lowest energy observed less than the Q_2 to Q_0 separation, although lower energy gamma-rays are undoubtedly present.

A general feature of αp reactions is the more prolific yield of lower energy proton groups. Since these are associated with higher levels of excitation, then such states may be said to be more heavily populated. Thus, more nuclei are left after proton emission in the Q_3 level than in Q_2, while relatively few will be found in the Q_1 and Q_0 levels. Assuming that the gamma-rays observed in the cases of sodium and phosphorus targets are truly produced as a result of αp reactions according to the correlations made above, then the relative intensities and state populations indicate a definite preference for the Q_2 to Q_0 transition. This implies that the more numerous nuclei in the Q_3 state prefer to drop to the ground state by a cascade process of successive Q_3 to Q_2 and Q_2 to Q_0 steps, although some direct transitions do occur. The predominance of Q_2-Q_0 radiation in these cases, as well as from the magnesium and aluminum targets, indicates that the nuclei in the Q_2 level drop directly to the ground state rather than cascade via Q_1.

The remaining gamma-rays from magnesium, silicon, and sulfur targets are due to either higher states of αp excitation or to competing processes. Energy calculations show that the 4.3-Mev and 4.1-Mev components from magnesium and phosphorus targets could well be the result of αn reactions. Other possibilities are inelastic scattering and simple capture. The former is unlikely because of the high potential barrier for emergence of an alpha-particle, while the latter would lead to excited states of more than 10 Mev and might be expected to yield gamma-rays more energetic than those observed. Yields from both silicon and sulfur targets were very low, and it is quite possible that breaks in these curves are being masked by statistical fluctuations. If this were the case the principal yield at zero absorption could be due to gamma-rays corresponding to known level separations while the observed maximum ranges are caused by gamma-rays from competing processes.

It is a pleasure to acknowledge the guidance given in this research by Professor Ernest Pollard.

A Note on Saturation in Microwave Spectroscopy

ROBERT KARPLUS* AND JULIAN SCHWINGER
Harvard University, Cambridge, Massachusetts

(Received January 9, 1948)

The investigation of Van Vleck and Weisskopf, on the shape of collision-broadened absorption lines, is extended to high power levels of the exciting radiation. Transitions among the molecular states are then induced at a rate that is not negligible compared with the collision rate, thus invalidating the assumption of thermal equilibrium. The theory is based on a quantum transcription of the previous semiclassical treatment, the essential tool being the density matrix. When the resonant frequencies of the molecule are widely spaced, an absorption line is ultimately broadened as the power level increases. Correspondingly, the peak absorption coefficient decreases, the power absorbed per unit volume approaching saturation with increasing incident power. It is shown that the broadening of an absorption line is not to be attributed to any intrinsic modification of the line shape, but rather to a frequency dependent alteration of the energy level populations. A molecule for which all resonant frequencies coincide, a one-dimensional harmonic oscillator, is treated in Appendix II. No saturation effect occurs here, since the absorption is independent of the molecular distribution among the oscillator energy levels.

THE shape of collision-broadened absorption lines has been investigated by Van Vleck and Weisskopf[1] for weak monochromatic radiation. Their results are of importance for the interpretation of the extensive data recently acquired on microwave absorption spectra. However, the investigation of Van Vleck and Weisskopf does not include a discussion of two aspects of these experimental studies—saturation and frequency modulation. At high power levels of the exciting radiation, transitions among the molecular states are induced at a rate that is not negligible compared with the collision rate, thus invalidating the assumption of thermal equilibrium. This note contains a theoretical analysis of the resultant modification of the absorption coefficient. A discussion of frequency modulation is given in a companion note by R. Karplus.

To facilitate the extension of the theory, we shall first derive the results of Van Vleck and Weisskopf, replacing their semiclassical treatment by a suitable quantum transcription. The linear absorption coefficient for radiation of angular frequency ω, in a gas of molecular density N, is

$$\alpha=4\pi(\omega/c)NIm\chi, \tag{1}$$

where χ is the molecular susceptibility. The latter is determined by the dipole moment

$$\mathbf{p}(t)=Re(\chi\mathbf{F}e^{-i\omega t}), \tag{2}$$

induced by the field

$$\mathbf{F}(t)=\mathbf{F}\cos\omega t=Re(\mathbf{F}e^{-i\omega t}), \tag{3}$$

which may be either electric or magnetic. The assumptions of Van Vleck and Weisskopf are most compactly expressed in quantum language with the aid of the density matrix.[2] Thus, to calculate the dipole moment at time t, we suppose that a strong collision has occurred at a previous time $t_0=t-\vartheta$. This assumption of complete thermal equilibrium, immediately following the collision, is described by

$$\rho_0(t_0)=Ce^{-H(t_0)/kT}, \quad 1/C=Spe^{-H(t_0)/kT}, \tag{4}$$

where $H(t)$ is the Hamiltonian of the molecule, including the energy in the external field,

$$H(t)=H_0-\mathbf{p}\cdot\mathbf{F}(t)=H_0+V\cos\omega t. \tag{5}$$

In the latter formula, H_0 is the Hamiltonian of the isolated molecule and $\mathbf{p}$ is the dipole moment operator. The subsequent development of the density matrix in time is determined by

$$i\hbar(\partial/\partial t)\rho=H\rho-\rho H. \tag{6}$$

The final task of the theory lies in the calculation

* U. S. Rubber Company, Predoctoral Fellow.

[1] J. H. Van Vleck and V. F. Weisskopf, Rev. Mod. Physics 17, 227 (1945).

[2] Cf. R. C. Tolman, *Principles of Statistical Mechanics* (Oxford University Press, New York, 1930), Chapter IX.

of the average dipole moment at time t,

$$\mathbf{p}(t)=Sp\mathbf{p}\bar{\rho}(t), \tag{7}$$

where the bar indicates that one must eventually average over t_0, the time of the last collision, in accordance with the assumption of random collisions spaced by an average time interval τ.

This program is greatly simplified by first performing the average over the time of the last collision, using the fact that the probability that the last collision occurs in the time interval $t-\vartheta$, $t-\vartheta-d\vartheta$ is $e^{-\vartheta/\tau}d\vartheta/\tau$. The density matrix may be considered to depend parametrically upon the initial time t_0, say $\rho(t,t_0)$, and is subject to the equation of motion (6) together with the initial condition (Cf. Eq. (4))

$$\rho(t_0,t_0)=\rho_0(t_0). \tag{8}$$

Now

$$\bar{\rho}(t)=\int_0^\infty \rho(t,\,t-\vartheta)e^{-\vartheta/\tau}d\vartheta/\tau, \tag{9}$$

and

$$(\partial/\partial t)\bar{\rho}(t)=\int_0^\infty [(\partial/\partial t)\rho(t,t_0)]_{t_0=t-\vartheta}e^{-\vartheta/\tau}d\vartheta/\tau$$

$$-\int_0^\infty [(\partial/\partial\vartheta)\rho(t,\,t-\vartheta)]e^{-\vartheta/\tau}d\vartheta/\tau, \tag{10}$$

whence

$$(\partial/\partial t)\bar{\rho}(t)=-(i/\hbar)[H(t)\bar{\rho}(t)-\bar{\rho}(t)H(t)]$$
$$-(1/\tau)[\bar{\rho}(t)-\rho_0(t)]. \tag{11}$$

We have thus succeeded in constructing an equation of motion for the averaged density matrix $\bar{\rho}(t)$, which is the quantity directly concerned in the evaluation of the average dipole moment. However, it is somewhat more convenient to introduce

$$D(t)=\bar{\rho}(t)-\rho_0(t) \tag{12}$$

which obeys the equation of motion

$$(\partial/\partial t)D(t)=-(i/\hbar)[H(t)D(t)-D(t)H(t)]$$
$$-(1/\tau)D(t)-(\partial/\partial t)\rho_0(t) \tag{13}$$

and measures the deviation of the density matrix $\bar{\rho}(t)$ from instantaneous thermal equilibrium.

We shall first solve this equation of motion under the conditions of Van Vleck and Weisskopf, namely, a weak monochromatic radiation field. On employing a matrix scheme in which the unperturbed Hamiltonian, H_0, is diagonal, the equation of motion (13) becomes

$$(\partial/\partial t+i\omega_{mn}+1/\tau)D_{mn}(t)=-(\partial/\partial t)[\rho_0(t)]_{mn}$$
$$-(i/\hbar)\textstyle\sum_k(V_{mk}D_{kn}(t)-D_{mk}(t)V_{kn})\cos\omega t, \tag{14}$$

where

$$\omega_{mn}=(E_m-E_n)/\hbar \tag{15}$$

designates the angular frequency associated with the transition from state m to state n of the unperturbed molecule. The assumption of a weak radiation field implies that the density matrix differs little from that of the isolated molecule at temperature T:

$$\rho^{(0)}=C^{(0)}e^{-H_0/kT},\quad 1/C^{(0)}=Spe^{-H_0/kT}. \tag{16}$$

The latter operator is represented by the diagonal matrix

$$\rho_{mn}{}^{(0)}=\rho_m{}^{(0)}\delta_{mn},\ \rho_m{}^{(0)}=e^{-E_m/kT}/\textstyle\sum_n e^{-E_n/kT}. \tag{17}$$

Thus, we may neglect the terms in Eq. (14) in which D is multiplied by the magnitude of the field. In addition, the matrix $\rho_0(t)$ may be simplified since the energy of the molecule in the external radiation field will always be small compared to kT. It is shown in Appendix I that, to a sufficient approximation,

$$[\rho_0(t)]_{mn}=\rho_m{}^{(0)}\delta_{mn}$$
$$+(\rho_m{}^{(0)}-\rho_n{}^{(0)})(V_{mn}/h\omega_{mn})\cos\omega t. \tag{18}$$

With these simplifications, Eq. (14) becomes

$$(\partial/\partial t+i\omega_{mn}+1/\tau)D_{mn}(t)$$
$$=\omega(\rho_m{}^{(0)}-\rho_n{}^{(0)})(V_{mn}/h\omega_{mn})\sin\omega t. \tag{19}$$

The steady-state solution of the latter equation is

$$D_{mn}(t)=\frac{\omega}{\omega-\omega_{mn}+i/\tau}(\rho_n{}^{(0)}-\rho_m{}^{(0)})$$
$$\times(V_{mn}/2h\omega_{mn})e^{-i\omega t}$$
$$+\frac{\omega}{\omega-\omega_{mn}-i/\tau}(\rho_n{}^{(0)}-\rho_m{}^{(0)})$$
$$\times(V_{mn}/2h\omega_{mn})e^{i\omega t}, \tag{20}$$

whence

$$\tilde{\rho}_{mn}(t)=\rho_m^{(0)}\delta_{mn}+\left(\frac{\omega}{\omega-\omega_{mn}+i/\tau}-1\right)\times(\rho_n^{(0)}-\rho_m^{(0)})(V_{mn}/2\hbar\omega_{mn})e^{-i\omega t}+\left(\frac{\omega}{\omega-\omega_{mn}-i/\tau}-1\right)\times(\rho_n^{(0)}-\rho_m^{(0)})(V_{mn}/2\hbar\omega_{mn})e^{i\omega t}, \quad (21)$$

and, finally,

$$\begin{aligned}\mathbf{p}(t)&=\sum_{m,n}\mathbf{p}_{nm}\tilde{\rho}_{mn}(t)\\&=\sum_{m,n}\mathbf{p}_{nm}\mathbf{p}_{mn}\cdot\mathbf{F}e^{-i\omega t}\times\left(1-\frac{\omega}{\omega-\omega_{mn}+i/\tau}\right)\frac{\rho_n^{(0)}-\rho_m^{(0)}}{2\hbar\omega_{mn}}\\&\quad+\sum_{m,n}\mathbf{p}_{mn}\mathbf{p}_{nm}\cdot\mathbf{F}e^{i\omega t}\times\left(1-\frac{\omega}{\omega-\omega_{mn}-i/\tau}\right)\frac{\rho_n^{(0)}-\rho_m^{(0)}}{2\hbar\omega_{mn}}\end{aligned} \quad (22)$$

in which the indices m and n have been interchanged in the second term. In virtue of the spherical symmetry of an isolated molecule, it is possible to replace $\mathbf{p}_{nm}\mathbf{p}_{mn}\cdot\mathbf{F}$ with $(1/3)\mathbf{p}_{nm}\cdot\mathbf{p}_{mn}\mathbf{F}$, or $(1/3)|\mathbf{p}_{mn}|^2\mathbf{F}$. We therefore obtain a formula for $\mathbf{p}(t)$ of the form (2), with

$$\begin{aligned}\chi&=\sum_{m,n}\tfrac{1}{3}|\mathbf{p}_{mn}|^2\left(1-\frac{\omega}{\omega-\omega_{mn}+i/\tau}\right)\frac{\rho_n^{(0)}-\rho_m^{(0)}}{\hbar\omega_{mn}}\\&=\sum_{m,n}\tfrac{1}{6}|\mathbf{p}_{mn}|^2\left(2-\frac{\omega}{\omega-\omega_{mn}+i/\tau}-\frac{\omega}{\omega+\omega_{mn}+i/\tau}\right)\frac{\rho_n^{(0)}-\rho_m^{(0)}}{\hbar\omega_{mn}}.\end{aligned} \quad (23)$$

In particular,

$$Im\chi=\sum_{m,n}\frac{1}{6\hbar}|\mathbf{p}_{mn}|^2\frac{\omega}{\omega_{mn}}\left[\frac{1/\tau}{(\omega-\omega_{mn})^2+1/\tau^2}+\frac{1/\tau}{(\omega+\omega_{mn})^2+1/\tau^2}\right](\rho_n^{(0)}-\rho_m^{(0)}), \quad (24)$$

and

$$\alpha=\frac{2\pi}{3}\frac{\omega^2}{c}\frac{N}{kT}\sum_{m,n}|\mathbf{p}_{mn}|^2\left[\frac{1/\tau}{(\omega-\omega_{mn})^2+1/\tau^2}+\frac{1/\tau}{(\omega+\omega_{mn})^2+1/\tau^2}\right]\frac{1-e^{-\hbar\omega_{mn}/kT}}{\hbar\omega_{mn}/kT}\rho_n^{(0)}, \quad (25)$$

which is essentially the final result of Van Vleck and Weisskopf.

An important specialization of this formula refers to the situation in which the resonant frequencies of the molecule are widely spaced, in comparison with the resonance width $\Delta\omega=1/\tau$. If the applied frequency lies in the vicinity of a particular resonance frequency, $\omega_0=(E_a-E_b)/\hbar$, only terms involving $\omega-\omega_0$ will appreciably contribute to the summation in Eq. (25). However, the energy levels E_a and E_b will be degenerate, in general, and we must further specify the states contributing to (25) by a degeneracy index, say κ and λ, respectively. Thus

$$\alpha=\frac{4\pi}{3}\frac{\omega^2}{c}\frac{N}{kT}\left[\sum_{\kappa,\lambda}|\mathbf{p}_{a\kappa,b\lambda}|^2\right]\frac{1/\tau}{(\omega-\omega_0)^2+1/\tau^2}\times\frac{1-e^{-\hbar\omega_0/kT}}{\hbar\omega_0/kT}\frac{e^{-E_b/kT}}{\sum_m e^{-E_m/kT}}. \quad (26)$$

SATURATION

We shall now extend our treatment to include the effects of a strong monochromatic radiation field. The discussion will, however, be limited to the situation embodied in Eq. (26), that is, where $\omega-\omega_0$ is comparable with $1/\tau$, but all other such differences, $\omega-\omega_{mn}$, are large compared to $1/\tau$. In addition, we shall impose an inocuous restriction on the field strength that amounts to requiring that the external radiation field be small compared to the internal molecular field; we ignore any time variation of $\mathbf{p}(t)$ that involves harmonics of the fundamental frequency ω. This restriction is expressed by the assumption

$$D_{mn}(t)=R_{mn}+P_{mn}^{(+)}e^{-i\omega t}+P_{mn}^{(-)}e^{i\omega t}, \quad (27)$$

which is to be inserted in the equation of motion

(14). The resultant set of equations are:

$$P_{mn}^{(+)}=\frac{1}{2\hbar(\omega_{mn}-\omega-i/\tau)}\left[\frac{\omega}{\omega_{mn}}V_{mn}(\rho_m^{(0)}-\rho_n^{(0)})-\sum_k(V_{mk}R_{kn}-R_{mk}V_{kn})\right],$$

$$P_{mn}^{(-)}=-\frac{1}{2\hbar(\omega_{mn}+\omega-i/\tau)}\left[\frac{\omega}{\omega_{mn}}V_{mn}(\rho_m^{(0)}-\rho_n^{(0)})+\sum_k(V_{mk}R_{kn}-R_{mk}V_{kn})\right], \quad (28)$$

$$R_{mn}=-\frac{1}{2\hbar(\omega_{mn}-i/\tau)}\sum_k[V_{mk}(P_{kn}^{(+)}+P_{kn}^{(-)})-(P_{mk}^{(+)}+P_{mk}^{(-)})V_{kn}].$$

With the impressed frequency in approximate resonance with the transition frequency $\omega_0=(E_a-E_b)/\hbar$, only the matrix elements $P_{ab}^{(+)}$, $P_{ba}^{(-)}$, R_{aa}, and R_{bb} are of significance, if we suppose the energy levels a and b to be non-degenerate. This statement is accurate to the extent that $\Delta\omega=1/\tau\ll\omega_{mn}$. The simultaneous equations (28) then reduce to

$$P_{ab}^{(+)}=-\frac{V_{ab}}{2\hbar(\omega-\omega_0+i/\tau)}\left[\frac{\omega}{\omega_0}(\rho_a^{(0)}-\rho_b^{(0)})+(R_{aa}-R_{bb})\right],$$

$$P_{ba}^{(-)}=-\frac{V_{ba}}{2\hbar(\omega-\omega_0-i/\tau)}\left[\frac{\omega}{\omega_0}(\rho_a^{(0)}-\rho_b^{(0)})+(R_{aa}-R_{bb})\right], \quad (29)$$

$$R_{aa}-R_{bb}=-i(\tau/\hbar)[V_{ab}P_{ba}^{(-)}-P_{ab}^{(+)}V_{ba}],$$

$$R_{aa}+R_{bb}=0.$$

The solution of these equations is

$$R_{aa}-R_{bb}=-\frac{\omega}{\omega_0}\frac{|V_{ab}|^2/\hbar^2}{(\omega-\omega_0)^2+1/\tau^2+|V_{ab}|^2/\hbar^2}\times(\rho_a^{(0)}-\rho_b^{(0)}),$$

$$P_{ab}^{(+)}=P_{ba}^{(-)*}=-\frac{V_{ab}}{2\hbar}\frac{\omega}{\omega_0}\frac{\omega-\omega_0-i/\tau}{(\omega-\omega_0)^2+1/\tau^2+|V_{ab}|^2/\hbar^2}\times(\rho_a^{(0)}-\rho_b^{(0)}). \quad (30)$$

In computing the average dipole moment,

$$\mathbf{p}(t)=Sp\mathbf{p}\bar{\rho}(t)=Sp\mathbf{p}\rho_0(t)+Sp\mathbf{p}D(t), \quad (31)$$

we may ignore the time-dependent contribution of ρ_0, for this is neither resonant nor contributes to the absorption. Hence

$$\mathbf{p}(t)=Sp\mathbf{p}D(t)=2Re\mathbf{p}_{ba}P_{ab}^{(+)}e^{-i\omega t}=Re\frac{1}{\hbar}\mathbf{p}_{ba}\mathbf{p}_{ab}\cdot\mathbf{F}e^{-i\omega t}\times\frac{\omega}{\omega_0}\frac{\omega-\omega_0-i/\tau}{(\omega-\omega_0)^2+1/\tau^2+|V_{ab}|^2/\hbar^2}\times(\rho_a^{(0)}-\rho_b^{(0)}). \quad (32)$$

The assumption of non-degeneracy must be relinquished at this point, for orientation degeneracy, at least, is necessarily present. However, our theory is easily extended if the component of the dipole moment in the direction of the field has vanishing matrix elements between different degenerate states. This is indeed realized in the most important situation of orientation degeneracy since the magnetic quantum number relative to the direction of the field is unaltered in any transition induced by the radiation. Under these circumstances the appropriate generalization of Eq. (32) is

$$\mathbf{p}(t)=Re\frac{1}{\hbar}\sum\kappa|p_{ab}{}^{\kappa}|^2\mathbf{F}e^{-i\omega t}\times\frac{\omega}{\omega_0}\frac{\omega-\omega_0-i/\tau}{(\omega-\omega_0)^2+1/\tau^2+|p_{ab}{}^{\kappa}|^2F^2/\hbar^2}\times(\rho_a^{(0)}-\rho_b^{(0)}), \quad (33)$$

where $p_{ab}{}^{\kappa}$ designates a non-vanishing matrix element of the component of the dipole moment in the field direction, and κ is a degeneracy index. This is of the desired form (2), with

$$Im\chi=\frac{1}{\hbar}\sum_{\kappa}|p_{ab}{}^{\kappa}|^2\times\frac{\omega}{\omega_0}\frac{1/\tau}{(\omega-\omega_0)^2+1/\tau^2+|p_{ab}{}^{\kappa}|^2F^2/\hbar^2}\times(\rho_b^{(0)}-\rho_a^{(0)}), \quad (34)$$

whence, finally

$$\alpha=4\pi\frac{\omega^2}{c}\frac{N}{kT}\sum_\kappa|p_{ab}{}^\kappa|^2 \times\frac{1/\tau}{(\omega-\omega_0)^2+1/\tau^2+|p_{ab}{}^\kappa|^2F^2/\hbar^2} \times\frac{1-e^{-\hbar\omega_0/kT}}{\hbar\omega_0/kT}\frac{e^{-E_b/kT}}{\sum_m e^{-E_m/kT}}. \quad (35)$$

In the weak field limit, this result reduces to Eq. (26), as it must, since

$$\tfrac{1}{3}\sum_{\kappa,\lambda}|\mathbf{p}_{a\kappa,b\lambda}|^2=\sum_\kappa|p_{ab}{}^\kappa|^2. \quad (36)$$

When, however, $|p_{ab}{}^\kappa|F$ becomes comparable with $\hbar/\tau$, the absorption line begins to widen, and the peak absorption coefficient correspondingly decreases. Indeed, in the limit $|p_{ab}{}^\kappa|F\gg\hbar/\tau$ and $\hbar(\omega-\omega_0)$, but $|p_{ab}{}^\kappa|F\ll\hbar(\omega-\omega_{mn})$, the power absorbed per unit volume exhibits a saturation phenomenon, approaching a value independent of the field strength, namely,

$$P=\alpha cF^2/8\pi \rightarrow\frac{(\hbar\omega)^2}{2\tau}\frac{N}{kT}\frac{g}{\hbar\omega_0/kT}\frac{1-e^{-\hbar\omega_0/kT}}{\sum_m e^{-E_m/kT}}e^{-E_b/kT}. \quad (37)$$

In this formula, g denotes the total number of degenerate transitions contributing to the absorption line.

It is well to note, finally, that our essential results, Eqs. (29) and (30), permit an elementary interpretation. In the immediate vicinity of resonance, ω/ω_0 may be replaced by unity, and the first of Eq. (29) can be written

$$P_{ab}{}^{(+)}=-\frac{V_{ab}}{2\hbar(\omega-\omega_0+i/\tau)}[\bar\rho_{aa}-\bar\rho_{bb}]. \quad (38)$$

It is apparent from this form that the broadening of the absorption line at high power levels is not to be attributed to any intrinsic modification of the line shape, but rather to a frequency dependent alteration of the populations of the two levels. The net rate of absorption is the difference between the rates of true absorption and stimulated emission, with the common transition probability for the two processes possessing the characteristic frequency dependence $1/[(\omega-\omega_0)^2+1/\tau^2]$. The frequency dependence of the population difference is contained in the first of Eq. (30), which may be written

$$\bar\rho_{aa}-\bar\rho_{bb}=\frac{1/\tau}{1/\tau+w}(\rho_a{}^{(0)}-\rho_b{}^{(0)}), \quad (39)$$

where

$$w=\frac{1}{\hbar^2}\frac{|V_{ab}|^2/\tau}{(\omega-\omega_0)^2+1/\tau^2}. \quad (40)$$

To interpret this result, we note that $1/\tau$ is the rate at which the population difference tends toward its thermal equilibrium value, as induced by collisions, whence w may be considered the rate at which radiative transitions tend to produce equality in population. That this is a self-consistent interpretation may be seen on computing the power absorbed per unit volume in accordance with the detailed radiative processes:

$$P=\tfrac{1}{2}w\hbar\omega(\bar\rho_{aa}-\bar\rho_{bb})N =\tfrac{1}{2}\hbar\omega\frac{w(1/\tau)}{w+1/\tau}(\rho_a{}^{(0)}-\rho_b{}^{(0)})N \quad (41)$$

which, with appropriate modifications for degeneracy, agrees precisely with Eq. (35). In writing the last equation, the transition probability for absorption or stimulated emission has been placed equal to $\frac{1}{2}w$, since both processes contribute equally to the rate at which radiative transitions tend to decrease the population difference.

We have enjoyed several conversations on this subject with J. H. Van Vleck.

APPENDIX I

To simplify the density matrix $\rho_0(t)$, in accordance with the smallness of $\mathbf{p}\cdot\mathbf{F}/kT$, we consider the problem of expanding the operator $\exp(A+B)$ in powers of B. We shall be content with the first two terms of the expansion. It is convenient to introduce

$$F(\lambda)=e^{\lambda(A+B)} \quad (I.1)$$

which satisfies the differential equation

$$d/d\lambda F(\lambda)=(A+B)F(\lambda) \quad (I.2)$$

and the initial condition

$$F(0)=1. \tag{I.3}$$

On performing the transformation

$$F(\lambda)=e^{\lambda A}G(\lambda), \quad G(0)=1, \tag{I.4}$$

we encounter the differential equation

$$d/d\lambda G(\lambda)=e^{-\lambda A}Be^{\lambda A}G(\lambda) \tag{I.5}$$

which is equivalent to the integral equation

$$G(\lambda)=1+\int_0^\lambda e^{-\lambda' A}Be^{\lambda' A}G(\lambda')d\lambda'. \tag{I.6}$$

The latter may be solved by successive substitution, which generates a series of which the first two terms are

$$G(\lambda)=1+\int_0^\lambda e^{-\lambda' A}Be^{\lambda' A}d\lambda'+\cdots. \tag{I.7}$$

Hence

$$e^{(A+B)}=F(1)=e^A+\int_0^1 e^{(1-\lambda)A}Be^{\lambda A}d\lambda+\cdots. \tag{I.8}$$

The matrix elements of $\exp(A+B)$, in a scheme with A diagonal, are

$$[e^{(A+B)}]_{a'a''}=e^{a'}\delta_{a'a''}+\frac{e^{a'}-e^{a''}}{a'-a''}B_{a'a''}+\cdots. \tag{I.9}$$

Thus, with $A=-H_0/kT$, $B=-(V/kT)\cos\omega t$,

$$[e^{-H(t)/kT}]_{mn}=e^{-E_m/kT}\delta_{mn}+\frac{e^{-E_m/kT}-e^{-E_n/kT}}{E_m-E_n}V_{mn}\cos\omega t, \tag{I.10}$$

and

$$1/C=Spe^{-H(t)/kT}=Spe^{-H_0/kT}+\frac{1}{kT}Spe^{-H_0/kT}\mathbf{p}\cdot\mathbf{F}\cos\omega t \tag{I.11}$$
$$=1/C^{(0)}.$$

The latter statement is valid since the average dipole moment of the molecule vanishes, in the absence of an external field. We finally obtain

$$[\rho_0(t)]_{mn}=\rho_m{}^{(0)}\delta_{mn}+(\rho_m{}^{(0)}-\rho_n{}^{(0)})(V_{mn}/\hbar\omega_{mn})\cos\omega t, \tag{I.12}$$

which is Eq. (18) of the text.

APPENDIX II

The situation treated in the text is that of a molecule with widely spaced resonant frequencies. We now treat the opposite extreme, a one-dimensional harmonic oscillator, and we shall show that no saturation effect occurs. The electric dipole moment of a charged particle confined to the x axis, $p=ex$, has the following non-vanishing matrix elements:

$$p_{n,n-1}=p_{n-1,n}=e\left[\frac{n\hbar}{2m\omega_0}\right]^{\frac{1}{2}}, \quad n=1,2,3,\cdots, \tag{II.1}$$

where m and ω_0 are the mass and natural frequency of the particle. According to the third equation of the set (28), only the diagonal elements, R_{nn}, are significant if $\omega_0\gg 1/\tau$. The properties of the dipole moment matrix then restrict the other non-vanishing matrix elements of $D(t)$ to

$$P^{(+)}_{n,n-1}=P^{(-)}_{n-1,n}{}^*=\frac{V_{n,n-1}}{2\hbar(\omega_0-\omega-i/\tau)}\left[\frac{\omega}{\omega_0}(\rho_n{}^{(0)}-\rho_{n-1}{}^{(0)})+R_{n,n}-R_{n-1,n-1}\right],$$
$$P^{(+)}_{n-1,n}=P^{(-)}_{n,n-1}{}^*=-\frac{V_{n-1,n}}{2\hbar(\omega_0+\omega+i/\tau)}\times\left[\frac{\omega}{\omega_0}(\rho_n{}^{(0)}-\rho_{n-1}{}^{(0)})-R_{n,n}+R_{n-1,n-1}\right]. \tag{II.2}$$

The average dipole moment may now be computed as

$$\begin{aligned}p(t)&=2Re\sum_{n=1}^{\infty}(p_{n-1,n}P^{(+)}_{n,n-1}+p_{n,n-1}P^{(+)}_{n-1,n})e^{-i\omega t}\\&=Re\sum_{n=1}^{\infty}\frac{|p_{n,n-1}|^2}{\hbar(\omega_0-\omega-i/\tau)}Ee^{-i\omega t}\times\left[\frac{\omega}{\omega_0}(\rho_{n-1}{}^{(0)}-\rho_n{}^{(0)})+R_{n-1,n-1}-R_{n,n}\right]\\&\quad-Re\sum_{n=1}^{\infty}\frac{|p_{n,n-1}|^2}{\hbar(\omega_0+\omega+i/\tau)}Ee^{-i\omega t}\times\left[\frac{\omega}{\omega_0}(\rho_{n-1}{}^{(0)}-\rho_n{}^{(0)})-R_{n-1,n-1}+R_{n,n}\right],\end{aligned} \tag{II.3}$$

whence

$$Im\chi=\frac{e^2}{2m\omega_0}\frac{1/\tau}{(\omega-\omega_0)^2+1/\tau^2}\times\sum_{n=1}^{\infty}n\left[\frac{\omega}{\omega_0}(\rho_{n-1}{}^{(0)}-\rho_n{}^{(0)})+R_{n-1,n-1}-R_{n,n}\right]+\frac{e^2}{2m\omega_0}\frac{1/\tau}{(\omega+\omega_0)^2+1/\tau^2}\times\sum_{n=1}^{\infty}n\left[\frac{\omega}{\omega_0}(\rho_{n-1}{}^{(0)}-\rho_n{}^{(0)})-R_{n-1,n-1}+R_{n,n}\right]. \quad \text{(II.4)}$$

However

$$\sum_{n=1}^{\infty}n(\rho_{n-1}{}^{(0)}-\rho_n{}^{(0)})=\sum_{n=0}^{\infty}\rho_n{}^{(0)}=Sp\rho^{(0)}=1, \quad \text{(II.5)}$$

and

$$\sum_{n=1}^{\infty}n(R_{n-1,n-1}-R_{n,n})=SpD=Sp\tilde{\rho}-Sp\rho_0=0. \quad \text{(II.6)}$$

We thus obtain

$$Im\chi=\frac{e^2}{2m\omega_0}\frac{\omega}{\omega_0}\left[\frac{1/\tau}{(\omega-\omega_0)^2+1/\tau^2}+\frac{1/\tau}{(\omega+\omega_0)^2+1/\tau^2}\right], \quad \text{(II.7)}$$

which leads, finally, to

$$\alpha=2\pi\frac{e^2}{mc}\left(\frac{\omega}{\omega_0}\right)^2N\left[\frac{1/\tau}{(\omega-\omega_0)^2+1/\tau^2}+\frac{1/\tau}{(\omega+\omega_0)^2+1/\tau^2}\right] \quad \text{(II.8)}$$

in complete agreement with Eq. (17) of reference (1). It is evident that the absorption coefficient of an oscillator is independent of the distribution of molecules among the states of the system and is therefore unaffected by the redistribution induced by the radiation field.

Frequency Modulation in Microwave Spectroscopy

ROBERT KARPLUS*
Mallinckrodt Chemical Laboratory, Harvard University, Cambridge, Massachusetts
(Received December 24, 1947)

The absorption coefficient of a gas is related to the density matrix of that gas. The density matrix is obtained formally from its equation of motion, which takes into account a possible time-dependence of the resonant frequency of the molecule and of the frequency of the exciting radiation. The shape of the absorption line is calculated explicitly in a variety of cases. For low frequency modulation, it reduces to Lorentz's expression with a time-dependent frequency difference. For high frequency sinusoidal modulation, resolved sidebands to the resonant frequency are obtained. Finally, for square wave modulation, the line shape is again given by Lorentz's expression with a varying frequency difference, except that damped oscillations are superimposed on the expected square wave time-dependence. In this case, the deviations from the Lorentz expression are no greater than about ten percent for the zero frequency and fundamental frequency components, if the modulation frequency is less than one-half of the half-width of the absorption line.

I. GENERAL TREATMENT

MODIFICATIONS of the theory of collision-broadened lines of Van Vleck and Weisskopf[1] have been discussed in the paper preceding this.[2] There the theory has been extended to include the effects of the induced transitions on the Boltzmann distribution. In this paper, effects of a time-dependent radiation frequency or resonance frequency will be discussed. Since almost all microwave spectroscopes described in the literature use some such modulation,[3] it seemed worth while to examine the conditions under which easily interpretable results might be obtained. The notation of reference (2) will be adopted. The radiation will be considered sufficiently weak so as not to affect the Boltzmann distribution appreciably, and frequency modulation effects will be of the order of the line width, which in turn is much smaller than the resonant frequency.

The argument in *I* leading to Eq. (14) can now be repeated, provided the Hamiltonian is modified so as to include frequency modulation of both molecule and radiation:

$$\mathbf{H}(t)=\mathbf{H}_0(t)-\mathbf{p}\cdot F\cos\left[\int_0^t\omega(t')dt'\right]$$

$$=\bar{\mathbf{H}}_0+[\mathbf{H}_0(t)-\bar{\mathbf{H}}_0]+\mathbf{V}\cos\left[\int_0^t\omega(t')dt'\right]. \quad (1)$$

$\bar{\mathbf{H}}_0$ is written for some value of the operator $\mathbf{H}_0(t)$. The matrix elements will be calculated in the representation based on the eigenfunctions of $\bar{\mathbf{H}}_0$. Equation (14) of *I* then becomes

$$\left[\frac{\partial}{\partial t}+i\omega_{mn}(t)+1/\tau\right]D_{mn}(t)=-\frac{\partial}{\partial t}[\rho_0(t)]_{mn}, \quad (2)$$

where

$$\hbar\omega_{mn}(t)=[\mathbf{H}_0(t)]_{mm}-[\mathbf{H}_0(t)]_{nn}$$

and the terms in which $\mathbf{D}$ is multiplied by the magnitude of the field have been neglected. After multiplication by

$$\exp\left[i\int_0^t\omega_{mn}(t')dt'+t/\tau\right],$$

Eq. (2) above may be integrated to give

$$D_{mn}(t)=-[\rho_0(t)]_{mn}+\int_0^t dt'[\rho_0(t')]_{mn}[i\omega_{mn}(t)+1/\tau]\times\exp\left[i\int_t^{t'}\omega_{mn}(t'')dt''-(t-t')/\tau\right], \quad (3)$$

the right side of this equation has been integrated

---

* United States Rubber Company predoctoral fellow.

[1] J. H. Van Vleck and V. F. Weisskopf, Rev. Mod. Phys. **17**, 227 (1945).

[2] Robert Karplus and Julian Schwinger (henceforth referred to as I), Phys. Rev. **73**, 1020 (1948).

[3] See, for example, (a) W. E. Good, Phys. Rev. **70**, 213; (b) C. H. Townes, Phys. Rev. **70**, 665 (1946); (c) R. H. Hughes and E. B. Wilson, Jr., Phys. Rev. **71**, 562 (1947); (d) B. P. Dailey, Phys. Rev. **72**, 84 (1947); (e) R. J. Watts and Dudley Williams, Phys. Rev. **72**, 1122 (1947); (f) W. D. Herschberger (to be published).

by parts, and it is assumed that a long time has elapsed, $t \gg \tau$.

As is shown in I, the matrix $\varrho_0(t)$ may be approximated by

$$[\rho_0(t')]_{mn} = \rho_m{}^0\delta_{mn} + (\rho_m{}^0 - \rho_n{}^0)\, V_{mn} \times \cos\left[\int_0^{t'} \omega(t'')dt''\right]/\hbar\tilde{\omega}_{mn} + (\rho_m{}^0 - \rho_n{}^0)(H_0(t') - \bar{H}_0)_{mn}/\hbar\tilde{\omega}_{mn}, \quad (4)$$

where $\hbar\tilde{\omega}_{mn} = (\bar{H}_0)_{mn} - (\bar{H}_0)_{nn}$, and ρ^0 is the equilibrium density matrix associated with the Hamiltonian $\bar{\mathbf{H}}_0$,

$$\varrho^0 = \exp[-\bar{\mathbf{H}}_0/kT]/Sp\{\exp[-\bar{\mathbf{H}}_0/kT]\}.$$

Now it has to be assumed that $[H_0(t) - \bar{H}_0]_{mn}$ contains no terms that oscillate at a frequency close to ω_{mn} and are comparable to V_{mn} in magnitude. This means that an alternating electric field, which may be used to introduce a time dependence into $\mathbf{H}_0(t)$ *via* the Stark effect, has no appreciable Fourier components near the resonance frequency of the molecule. If only resonant contributions to the density matrix are considered, therefore, the last term in Eq. (4) as well as the non-resonant term in the cosine may be neglected, so that the equivalent of I, Eq. (21), is

$$\tilde{\rho}_{mn}(t) = [\rho_0(t)]_{mn} + D_{mn}(t) = \rho_m{}^0\delta_{mn} + (i/2\hbar)(\rho_m{}^0 - \rho_n{}^0)\, V_{mn} \times \exp\left[-i\int_0^t \omega(t')dt'\right] \times \int_0^t [(\omega_{mn}(t') - i/\tau)/\tilde{\omega}_{mn}] \times \exp\left[i\int_t^{t'} [\omega_{mn}(t'') - \omega(t'')]dt'' - (t-t')/\tau\right]dt'. \quad (5)$$

All other off-diagonal elements of $\varrho(t)$ except $\rho_{nm}(t)$ will make negligible contributions to absorption at the frequency ω if the resonances are widely spaced and non-degenerate. Hence the average dipole moment responsible for this absorption is

$$p(t) = Sp\{\mathbf{p}\bar{\varrho}(t)\} = 2Re\{p_{nm}\tilde{\rho}_{mn}(t)\} = Re\left\{(1/\hbar)p_{nm}p_{mn}\cdot F\exp\left[-i\int_0^t \omega(t')dt'\right] \times (\rho_n{}^0 - \rho_m{}^0) f(\omega_{mn},\omega;t)\right\}, \quad (6)$$

where the function $f(\omega_{mn},\omega;t)$ has been written for the integral

$$f(\omega_{mn},\omega;t) = \int_0^\infty idT \times \exp\left[-i\int_{t-T}^t [\omega_{mn}(t'') - \omega(t'')]dt'' - T/\tau\right], \quad (7)$$

which is obtained from the integral in Eq. (5) by setting $T = t - t'$ and by approximating $(\omega_{mn}(t') - i/\tau)/\tilde{\omega}_{mn}$ by unity, again with $t \gg \tau$.

Since the transitions occur independently of each other in the absence of saturation, Eq. (6) may readily be extended to include degenerate or approximately degenerate resonances:

$$p(t) = Re\left\{(1/\hbar)\sum_{\kappa,\lambda} |p_{mn}{}^{\kappa\lambda}|^2 F\exp\left[-i\int_0^t \omega(t')dt'\right] \times (\rho_{n\lambda}{}^0 - \rho_{m\kappa}{}^0) f(\omega_{mn}{}^{\kappa\lambda},\omega;t)\right\}; \quad (8)$$

here all p's refer to the component of the dipole moment along the field F and κ and λ are degeneracy indices. Finally, the absorption coefficient is

$$\alpha(t) = 4\pi(\omega/\hbar c)\sum_{\kappa,\lambda} |p_{mn}{}^{\kappa\lambda}|^2 (\rho_{n\lambda}{}^0 - \rho_{m\kappa}{}^0) \times Imf(\omega_{mn}{}^{\kappa\lambda},\omega;t). \quad (9)$$

Transitions induced by the modulating fields may somewhat alter the populations of the initial and final states, but they will not affect the function $f(\omega_{mn}{}^{\kappa\lambda},\omega;t)$, which alone determines the shape of the absorption line. Since all essential information is obtained from the study of a simple transition, the degeneracy indices will hereafter be omitted.

The remainder of the paper will be devoted to the evaluation of $Imf(\omega_{mn},\omega;t)$ in various special cases. Periodic modulation alone is of interest in

microwave spectroscopy, because only in this case is a quasi-steady state reached eventually. The frequency difference appearing in the function $f(\omega_{mn},\omega;t)$ may then be expressed

$$\omega_{mn}(t)-\omega(t)=\omega' g(\nu t)+\tilde{\omega},^{**} \tag{10}$$

with

$$g(x+2\pi)=g(x)\sim\text{unity} \tag{11}$$

and

$$\int_0^{2\pi} g(x)dx=0,$$

so that

$$f(\omega_{mn},\omega;t)=i\int_0^\infty dT \times\exp\left[-i\omega'\int_{t-T}^{t} g(\nu t')dt'-(i\tilde{\omega}+1/\tau)T\right]. \tag{12}$$

It may be noticed that most of the integral comes from values of $T\lesssim\tau$ because of the exponential decrease of the integrand. It should further be pointed out that ω' will be the same for all members of a group of coincident absorption lines if the exciting radiation is frequency modulated, but that ω' will, in general, vary from component to component if the resonance frequency is modulated.

II. SLOW MODULATION

If ν is small compared to $1/\tau$, the function $g(\nu t)$ will change only slightly in a time interval of the order of $1/\tau$. The exponent of the integrand may therefore be replaced by

$$-[i\omega' g(\nu t)+\tilde{\omega}+1/\tau]T =-i[\omega_{mn}(t)-\omega(t)]T-T/\tau. \tag{13}$$

Hence

$$Imf(\omega_{mn},\omega;t)=Im\frac{i}{i[\omega_{mn}(t)-\omega(t)]+1/\tau} =\frac{1/\tau}{[\omega_{mn}(t)-\omega(t)]^2+1/\tau^2}. \tag{14}$$

Physically, the line has the same shape as in the absence of modulation; the absorption peak is merely shifted in a straightforward manner, according to the modulation.

This kind of modulation has found most use in microwave set-ups. A low frequency saw-tooth modulation, for instance, is almost universally employed to display the absorption coefficient as a function of frequency (3); the problem of low frequency sinusoidal modulation has recently been discussed by Herschberger (3f); square wave modulation of the resonance frequency by an external electric field has been used to aid detection of absorption lines as well as to study their Stark effect (3d).

III. WEAK MODULATION††

If the amplitude of the modulation is small compared to the modulation frequency, $\omega'\ll\nu$, the exponential can be expanded to give ($x=\nu t'$)

$$f(\omega_{mn},\omega;t)=\int_0^\infty idT\left[1-i(\omega'/\nu)\int_{\nu(t-T)}^{\nu t} g(x)dx\right] \times\exp[-(i\tilde{\omega}+1/\tau)T], \tag{15}$$

so that

$$Imf(\omega_{mn},\omega;t)=\frac{1/\tau}{\tilde{\omega}^2+1/\tau^2}+(\omega'/\nu)Im\int_0^\infty dT \times\exp[-(i\tilde{\omega}+1/\tau)T]\int_{\nu(t-T)}^{\nu t} g(x)dx. \tag{16}$$

Because it is periodic, $g(x)$ can be expanded in a Fourier series

$$g(x)=\sum_{k=1}^{\infty}[g_{ck}\cos kx+g_{sk}\sin kx]. \tag{17}$$

By carrying out the indicated operations, the shape for any modulation can be obtained (cf. Appendix A). A typical result is that for simple harmonic time dependence, $g(x)=\cos x$. Then

$$Imf(\omega_{mn},\omega;t) =\frac{1/\tau}{\tilde{\omega}^2+1/\tau^2}+\frac{\tau^3\tilde{\omega}\omega'}{[(\tilde{\omega}^2-\nu^2)\tau^2-1]^2+4\tilde{\omega}^2\tau^2} \times\left[\nu\tau\frac{[\tilde{\omega}^2-\nu^2]\tau^2-3}{\tilde{\omega}^2\tau^2+1}\sin\nu t-2\cos\nu t\right]. \tag{18}$$

At low modulation frequency, $\nu\ll 1/\tau$, this is seen to represent an effective differentiation of the absorption line shape obtained in II above. At high modulation frequency, the time de-

** Observe that ν is an angular frequency.

†† The experimental use of such modulation was suggested by Dr. W. D. Hershberger.

pendent term decreases as (ω'/ν) near the line center $\bar{\omega}=0$.

IV. SINUSOIDAL MODULATION

If the modulation is simply harmonic, $g(\nu t)=\cos\nu t$, the exponential in the integrand may be expanded in the Fourier series

$$\exp[-i\beta\sin x]=\sum_{l=-\infty}^{\infty}J_l(\beta)\exp[-ilx],^{5} \quad (19)$$

so that

$$f(\omega_{mn},\omega;t)=\int_0^\infty idT\exp\left[-i\omega'\int_{t-T}^{t}\cos\nu t'dt'-i\bar{\omega}T-T/\tau\right], \quad (20)$$

$$f(\omega_{mn},\omega;t)=\int_0^\infty idT\exp[-i(\omega'/\nu)\sin\nu t]\exp[-i(\omega'/\nu)\sin(\nu T-\nu t)]\exp[-(i\bar{\omega}+1/\tau)T]$$

$$=i\sum_{l=-\infty}^{\infty}J_l(\omega'/\nu)\exp[-il\nu t]\int_0^\infty dT\sum_{s=-\infty}^{\infty}J_s(\omega'/\nu)\exp[-is(\nu T-\nu t)-(i\bar{\omega}+1/\tau)T]$$

$$=\sum_{s=-\infty}^{\infty}\sum_{l=-\infty}^{\infty}J_s(\omega'/\nu)J_l(\omega'/\nu)\exp[i(s-l)\nu t]\frac{(s\nu+\bar{\omega})+i/\tau}{(s\nu+\bar{\omega})^2+1/\tau^2}. \quad (21)$$

$$Imf(\omega_{mn},\omega;t)=(1/\tau)\sum_{s,\ k=-\infty}^{\infty}J_s(\omega'/\nu)J_{s+k}(\omega'/\nu)\frac{\cos k\nu t-(s\nu+\bar{\omega})\tau\sin k\nu t}{(s\nu+\bar{\omega})^2+1/\tau^2}. \quad (22)$$

This expression is convenient only for relatively high modulation frequencies ($\nu\sim1/\tau$), since otherwise it converges slowly.

The average value of the shape factor is relatively simple ($k=0$):

$$\langle Imf(\omega_{mn},\omega;t)\rangle_{Av}$$

$$=\sum_{s=-\infty}^{\infty}[J_s(\omega'/\nu)]^2\frac{1/\tau}{(s\nu+\bar{\omega})^2+1/\tau^2}. \quad (23)$$

This predicts a series of absorption lines separated by a frequency ν and resolved if $\nu\sim1/\tau$; their intensity varies as $[J_s(\omega'/\nu)]^2$. This phenomenon has been observed and accounted for.[6,7]

Also of interest is that component of the line shape that oscillates at the modulation frequency. It is (see Appendix B)

$$\sum_{s=-\infty}^{\infty}\frac{1/\tau}{(s\nu+\bar{\omega})^2+1/\tau^2}a_s\cos(\nu t+\varphi_s). \quad (24)$$

The coefficients a_s depend to some extent on the frequency $\bar{\omega}$. This results in removing the central line ($s=0$) and in distorting the side-band lines.

Similar results will be obtained for the higher harmonics.

V. SQUARE WAVE MODULATION

As already pointed out, square wave modulation has been applied particularly successfully. This has been made possible by the fact that a low frequency square wave modulation of the molecular resonance together with a still slower saw-tooth sweep of the exciting frequency permits the simultaneous observation of two absorption lines, corresponding to the two values of the resonance frequency in the two half-cycles. If these two resonance frequencies are sufficiently different, a Lorentz shape will be obtained at each one. The detection of weak lines can be facilitated by using a filter circuit tuned to the square wave frequency or to any of its harmonics, because all Fourier components of the absorption coefficient reproduce the true line shape. Furthermore, the Stark effect pattern of a degenerate transition as well as the unperturbed line are obtained if the modulation is brought about by a square wave electric field based on zero voltage (3d); measurement of the splitting and square

[5] E. T. Whittaker and C. N. Watson, *Modern Analysis* (Cambridge University Press, Teddington, England, 1927), p. 358.
[6] C. H. Townes and F. R. Merritt, Phys. Rev. **72**, 1266 (1947).
[7] D. Blochinzew, Phys. Zeit. USSR, **4**, 501 (1933).

wave amplitude then give the Stark effect coefficient directly.††

Square wave modulation will be obtained if

$$g(x)=+\tfrac{1}{2}, \quad 0<x-2r\pi<\pi, \qquad g(x)=-\tfrac{1}{2}, \quad \pi<x-2r\pi<2\pi. \tag{25}$$

It is convenient to rename the frequencies

$$\bar{\omega}+\tfrac{1}{2}\omega'=\omega_1, \quad \bar{\omega}-\tfrac{1}{2}\omega'=\omega_2.$$

As is shown in Appendix C, the function determining the line shape then has the following time dependence:

$$f(\omega_{mn},\omega;t)=\frac{\omega_1+i/\tau}{\omega_1^2+1/\tau^2}\{1-A_1\exp[-(i\omega_1+1/\tau)(t-2\pi r/\nu)]\}, \quad 0<\nu t-2\pi r<\pi, \tag{26a}$$

$$f(\omega_{mn},\omega;t)=\frac{\omega_2+i/\tau}{\omega_{12}+1/\tau^2}\{1-A_2\exp[-(i\omega_2+1/\tau)(t-(2r+1)\pi/\nu)]\}, \quad \pi<\nu t-2r\pi<2\pi, \tag{26b}$$

where A_1 and A_2 are complex functions of ω_1, ω_2, ν, and τ. These equations show that the square wave shape that would be predicted from the treatment of slow modulation has superimposed damped oscillations. The damping decreases with an increase in modulation frequency. In the case of slow modulation, of course, the fundamental frequency component reproduces the true shape of the line.

It is of interest to calculate at what modulation frequency the line shape becomes distorted by the modulation. As long as the frequency ν is still smaller than the line width ($\nu\tau\lesssim\frac{1}{2}$), the coefficients A_1 and A_2 are practically unity. Experimentally, also, the line is usually swept from near resonance ($\omega_1\sim 1/\tau$) to non-resonance, ($\omega_2\gg 1/\tau$), so that terms with ω_2 in the denominator may be neglected. The average value of $Imf(\omega_{mn},\omega;t)$ and the fundamental frequency component of this function are then, to about 1 percent accuracy,

$$\langle Imf(\omega_{mn},\omega;t)\rangle_{Av}=\frac{1}{2}\frac{1/\tau}{\omega_1^2+1/\tau^2+(\nu/\pi\tau)(1-\omega_1^2\tau^2)}, \tag{27a}$$

and

$$\langle Imf(\omega_{mn},\omega;t)\rangle_{\text{fund}}=(2/\pi)\frac{1/\tau}{\omega_1^2+1/\tau^2+(1/8)\nu^2(3-\omega_1^2\tau^2)}. \tag{27b}$$

Inspection of these equations shows that the distortion is largest at the line center. Quantitatively, the peak intensity is changed as follows:

$$\langle\alpha_{\nu\sim 1/\tau}\rangle_{Av}/\langle\alpha_{\nu\ll 1/\tau}\rangle_{Av}\cong 1-\nu\tau/\pi, \tag{28a}$$

and

$$\langle\alpha_{\nu\sim 1/\tau}\rangle_{\text{fund}}/\langle\alpha_{\nu\ll 1/\tau}\rangle_{\text{fund}}\cong 1-(3/8)\nu^2\tau^2. \tag{28b}$$

Thus the corrections are indeed small up to $\nu\tau\sim\frac{1}{2}$. Another interesting parameter is the half-width $\Delta\omega$ of the absorption line. This may also be estimated from Eq. (27) and (28):

$$\langle\Delta\omega_{\nu\sim 1/\tau}\rangle_{Av}/\langle\Delta\omega_{\nu\ll 1/\tau}\rangle_{Av}\cong 1+\nu\tau/\pi, \tag{29a}$$

and

$$\langle\Delta\omega_{\nu\sim 1/\tau}\rangle_{\text{fund}}/\langle\Delta\omega_{\nu\ll 1/\tau}\rangle_{\text{fund}}\cong 1+(1/4)\nu^2\tau^2. \tag{29b}$$

The effects here are of the same order of magnitude as the effects on the peak intensity. It may be noticed that the fundamental frequency component is affected much less than the average value.

VI. CONCLUSION

A general equation has been derived for the shape of a collision-broadened absorption line. When the transition frequency and the exciting frequency depend on time, only their difference enters into the final result. Hence, modulation of the exciting radiation and modulation of the molecular resonances are equivalent.

The author wishes to express his appreciation to Professor Julian Schwinger and to Professor J. H. Van Vleck for many clarifying discussions.

†† This observation prompted the author last March to suggest the replacement of the sinusoidal modulation used by Hughes and Wilson (Phys. Rev. 71, 562 (1947)) by square wave modulation (B. P. Dailey, Phys. Rev. 72, 84 (1947)) to permit better interpretation of experimental results.

APPENDIX

A. Weak Modulation

Following Eq. (17),

$$\int_{\nu(t-T)}^{\nu t} g(x)dx=\sum_{n=1}^{\infty}(1/n)\{g_{cn}[\sin n\nu t+\sin n\nu(T-t)]+g_{sn}[-\cos n\nu t+\cos n\nu(T-t)]\}$$

$$=\sum_{n=1}^{\infty}(1/n)\{\sin n\nu t[g_{cn}-g_n\cos n\nu T-g_{sn}\sin n\nu T]$$

$$+\cos n\nu t[-g_{sn}+g_{cn}\sin n\nu T+g_{sn}\cos n\nu T]\}. \quad \text{(A1)}$$

Using the fact that

$$\int_0^{\infty} dt\,\sin n\nu t\exp[-(i\tilde{\omega}+1/\tau)t]=n\nu/[n^2\nu^2+(i\tilde{\omega}+1/\tau)^2],$$

$$\int_0^{\infty} dt\,\cos n\nu t\exp[-(i\tilde{\omega}+1/\tau)t]=(i\tilde{\omega}+1/\tau)/[n^2\nu^2+(i\tilde{\omega}+1/\tau)^2], \quad \text{(A2)}$$

gives

$$Im\int_0^{\infty} dT\exp[-(i\tilde{\omega}+1/\tau)T]\int_{\nu(t-T)}^{\nu t} g(x)dx$$

$$=\sum_{n=1}^{\infty}(\tau/n)\left\{\sin n\nu t\left[-\frac{\tilde{\omega}\tau}{\tilde{\omega}^2\tau^2+1}g_{cn}+\frac{[\tilde{\omega}\tau(\tilde{\omega}^2-n^2\nu^2)\tau^2+1]g_{cn}-2n\nu\tilde{\omega}\tau^2g_{sn}}{[(\tilde{\omega}^2-n^2\nu^2)\tau^2-1]^2+4\tilde{\omega}^2\tau^2}\right]\right.$$

$$\left.+\cos n\nu t\left[\frac{\tilde{\omega}\tau}{\tilde{\omega}^2\tau^2+1}g_{sn}-\frac{\tilde{\omega}\tau[(\tilde{\omega}^2-n^2\nu^2)\tau^2+1]g_{sn}-2n\nu\tilde{\omega}\tau^2g_{cn}}{[(\tilde{\omega}^2-n^2\nu^2)\tau^2-1]^2+4\tilde{\omega}^2\tau^2}\right]\right\}$$

$$=\frac{\tilde{\omega}\nu\tau^3}{\tilde{\omega}^2\tau^2+1}\sum_{n=1}^{\infty}\left\{\frac{n\nu\tau[(\tilde{\omega}^2-n^2\nu^2)\tau^2-3]g_{cn}-2(\tilde{\omega}^2\tau^2+1)g_{sn}}{[\tilde{\omega}^2-n^2\nu^2)\tau^2-1]^2+4\tilde{\omega}^2\tau^2}\sin n\nu t\right.$$

$$\left.-\frac{n\nu\tau[(\tilde{\omega}^2-n^2\nu^2)\tau^2-3]g_{sn}-2(\tilde{\omega}^2\tau^2+1)g_{cn}}{[(\tilde{\omega}^2-n^2\nu^2)\tau^2-1]^2+4\tilde{\omega}^2\tau^2}\cos n\nu t\right\}. \quad \text{(A3)}$$

B. Sinusoidal Modulation

The imaginary part of the fundamental frequency term of the shape-determining function is, from Eq. (21),

$$(1/\tau)\sum_{s=-\infty}^{\infty}\frac{J_s(\omega'/\nu)[J_{s+1}(\omega'/\nu)+J_{s-1}(\omega'/\nu)]\cos\nu t-J_s(\omega'/\nu)[J_{s+1}(\omega'/\nu)-J_{s-1}(\omega'/\nu)]\tau(s\nu+\tilde{\omega})\sin\nu t}{(s\nu+\tilde{\omega})^2+1/\tau^2}$$

$$=(1/\tau)\sum_{s=-\infty}^{\infty}\frac{a_s\cos(\nu t+\varphi_s)}{(s\nu+\tilde{\omega})^2+1/\tau^2}, \quad \text{(B1)}$$

where

$$\varphi_s=\tan^{-1}\left[\tau(s\nu+\tilde{\omega})\frac{J_{s+1}(\omega'/\nu)-J_{s-1}(\omega'/\nu)}{J_{s+1}(\omega'/\nu)+J_{s-1}(\omega'/\nu)}\right] \quad -\pi/2<\varphi_s<\pi/2, \quad \text{(B2)}$$

$$a_s=J_s(\omega'/\nu)\{[J_{s+1}(\omega'/\nu)+J_{s-1}(\omega'/\nu)]^2+\tau^2(s\nu+\tilde{\omega})^2[J_{s+1}(\omega'/\nu)-J_{s-1}(\omega'/\nu)]^2\}^{\frac{1}{2}}. \quad \text{(B3)}$$

Note that

$$a_0 = 2J_0(\omega'/\nu)J_1(\omega'/\nu)\tau\tilde{\omega} = 0 \text{ if } \tilde{\omega} = 0.$$

C. Square Wave Modulation

$$f(\omega_{mn}, \omega; t) = \int_0^\infty i dT \exp\left[-i\int_{t-T}^{t}(\omega_{mn}-\omega)dt' - T/\tau\right], \tag{C1}$$

where

$$\left.\begin{aligned}\omega_{mn}-\omega &= \omega_1 \quad 0<\nu t-2r\pi<\pi\\ \omega_{mn}-\omega &= \omega_2 \quad \pi<\nu t-2r\pi<2\pi\end{aligned}\right\} r=0, \pm1, \pm2, \cdots. \tag{C2}$$

To simplify the manipulations, it is convenient to use

$$\varphi = \int_{t-T}^{t}(\omega_{mn}-\omega)dt'; \tag{C3}$$

$$\nu t_k \begin{cases} = \nu t - 2r\pi + (k-1)\pi \text{ and } t_0 = 0 & (0<\nu t-2r\pi<\pi)\\ = \nu t - 2r\pi + (k-1)\pi - \pi, \quad t_0 = 0 & (\pi<\nu t-2r\pi<2\pi); \end{cases} \tag{C4}$$

and

$$A_k = \int_{t_k}^{t_{k+1}} dT \exp[-i\varphi - T/\tau]. \tag{C5}$$

Comparing (C.5) and (C.1), one can see that

$$f(\omega_{mn},\omega;t) = i\sum_{k=0}^{\infty} A_k. \tag{C6}$$

The calculation of the A_k will now be divided into four cases ($s=0, 1, 2, \cdots$):

I

$$\left.\begin{aligned}&0<\nu t-2r\pi<\pi\\ &0<\nu(t-T)-2(r-s)\pi<\pi\end{aligned}\right\} t_{2s}<T<t_{2s+1}, \tag{C7}$$

$$\varphi^{\mathrm{I}} = (\omega_1+\omega_2)(s\pi/\nu)+\omega_1(T-2s\pi/\nu), \tag{C8}$$

$$A_0{}^{\mathrm{I}} = (i\omega_1+1/\tau)^{-1}\{1-\exp[-(i\omega_1+1/\tau)(t-2r\pi/\nu)]\}, \tag{C9}$$

$$A_{2s}{}^{\mathrm{I}} = (i\omega_1+1/\tau)^{-1}\exp[-(i(\omega_1+\omega_2)+2/\tau)s\pi/\nu]\exp[-(i\omega_1+1/\tau)(t-2r\pi/\nu)] \times\{\exp[(i\omega_1+1/\tau)\pi/\nu]-1\}. \tag{C10}$$

II

$$\left.\begin{aligned}&0<\nu t-2r\pi<\pi\\ &-\pi<\nu(t-T)-2(r-s)\pi<0\end{aligned}\right\} t_{2s+1}<T<t_{2s+2}, \tag{C11}$$

$$\varphi^{\mathrm{II}} = (\omega_1+\omega_2)(s\pi/\nu)+(\omega_1-\omega_2)(t-2r\pi/\nu)+\omega_2(T-2s\pi/\nu), \tag{C12}$$

$$A_{2s+1}{}^{\mathrm{II}} = (i\omega_2+1/\tau)^{-1}\exp[-(i(\omega_1+\omega_2)+2/\tau)s\pi/\nu]\exp[-(i\omega_1+1/\tau)(t-2r\pi/\nu)] \times\{1-\exp[-(i\omega_2+1/\tau)\pi/\nu]\}. \tag{C13}$$

III

$$\left.\begin{aligned}&\pi<\nu t-2r\pi<2\pi\\ &\pi<\nu(t-T)-2(r-s)\pi<2\pi\end{aligned}\right\} t_{2s}<T<t_{2s+1}, \tag{C14}$$

$$\varphi^{III}=(\omega_1+\omega_2)(s\pi/\nu)+\omega_2(T-2s\pi/\nu), \tag{C15}$$

$$A_0{}^{III}=(i\omega_2+1/\tau)^{-1}\{1-\exp[-(i\omega_2+1/\tau)(t-(2r+1)\pi/\nu)], \tag{C16}$$

$$A_{2s}{}^{III}=(i\omega_2+1/\tau)^{-1}\exp[-(i(\omega_1+\omega_2)+2/\tau)s\pi/\nu]\exp[-(i\omega_2+1/\tau)(t-(2r+1)\pi/\nu)]$$
$$\times\{\exp[(i\omega_2+1/\tau)\pi/\nu]-1\}. \tag{C17}$$

IV

$$\left.\begin{aligned}&\pi<\nu t-2r\pi<2\pi\\&0<\nu(t-T)-2(r-s)\pi<2\pi\end{aligned}\right\}t_{2s+1}<T<t_{2s+2}, \tag{C18}$$

$$\varphi^{IV}=(\omega_1+\omega_2)(s\pi/\nu)-(\omega_1-\omega_2)(t-(2r+1)\pi/\nu)+\omega_1(T-2s\pi/\nu), \tag{C19}$$

$$A_{2s+1}{}^{IV}=(i\omega_1+1/\tau)^{-1}\exp[-(i(\omega_1+\omega_2)+2/\tau)s\pi/\nu]\exp[-(i\omega_2+1/\tau)(t-(2r+1)\pi/\nu)]$$
$$\times\{1-\exp[-(i\omega_1+1/\tau)\pi/\nu]\}. \tag{C20}$$

These results may now be substituted into Eq. (C6). The sums are geometric series that are easily evaluated. Inspection of (C10), (C13), (C16), and (C20) shows that

$$f(\omega_{mn},\omega;t)=i\sum_{s=1}^{\infty}(A_{2s}{}^{I}+A_{2s+1}{}^{II})\qquad(0<\nu t-2r\pi<\pi), \tag{C21}$$

$$f(\omega_{mn},\omega;t)=i\sum_{s=0}^{\infty}(A_{2s}{}^{III}+A_{2s+1}{}^{IV})\quad(\pi<\nu t-2r\pi<2\pi). \tag{C22}$$

The result can be written most conveniently with the aid of two constants:

$$A_1=\frac{1-\exp[-(i\omega_2+1/\tau)\pi/\nu]}{1-\exp[-(i(\omega_1+\omega_2)+2/\tau)\pi/\nu]}\left\{1-\frac{i\omega_1+1/\tau}{i\omega_2+1/\tau}\exp[-(i(\omega_1+\omega_2)+2/\tau)\pi/\nu]\right\}, \tag{C23}$$

$$A_2=\frac{1-\exp[-(i\omega_1+1/\tau)\pi/\nu]}{1-\exp[-(i(\omega_1+\omega_2)+2/\tau)\pi/\nu]}\left\{1-\frac{i\omega_2+1/\tau}{i\omega_1+1/\tau}\exp[-(i(\omega_1+\omega_2)+2/\tau)\pi/\nu]\right\}. \tag{C24}$$

It is

$$f(\omega_{mn},\omega;t)=(\omega_1-i/\tau)^{-1}\{1-A_1\exp[-(i\omega_1+1/\tau)(t-2r\pi/\nu)]\}\qquad(0<\nu t-2r\pi<\pi), \tag{C25}$$

$$f(\omega_{mn},\omega;t)=(\omega_2-i/\tau)^{-1}\{1-A_2\exp[-(i\omega_2+1/\tau)(t-(2r+1)\pi/\nu)]\}\quad(\pi<\nu t-2r\pi<2\pi). \tag{C26}$$

It may be observed that the deviation of A_1 and A_2 from unity depends on the exponential $\exp[-\pi/\nu\tau]$. If $\nu\tau\gtrsim\frac{1}{2}$, as considered in the body of the paper, $\exp[-\pi/\nu\tau]\gtrsim\exp[-6]\sim2\times10^{-3}$, certainly a negligible quantity as far as comparison with experiment is concerned.

With the assumption, moreover, that $\omega_2\gg1/\tau$, the function $f(\omega_{mn},\omega;t)$ becomes effectively zero during one-half of the cycle. Hence

$$\begin{aligned}\langle f(\omega_{mn},\omega;t)\rangle_{Av}&=(\omega_1-i/\tau)^{-1}\left\{1/2-A_1(\nu/2\pi)\int_0^{\pi/\nu}dt\exp[-(i\omega_1+1/\tau)t]\right\}\\&=\{i/2(i\omega_1+1/\tau)\}\{1+\nu/\pi(i\omega_1+1/\tau)\}\\&=i/2(i\omega_1+1/\tau+\nu/\pi).\end{aligned} \tag{C27}$$

Taking the imaginary part then leads to Eq. (27a). Equation (27b) is derived in a similar way.

Radioactive Cerium and Praseodymium

M. L. POOL AND N. L. KRISBERG*
Mendenhall Laboratory, Ohio State University, Columbus, Ohio
(Received January 21, 1948)

A 140±1-day half-life is assigned Ce^{139}. It decays by K-electron capture to La^{139}. Two γ-rays of 0.184 and 0.8 Mev are associated with Ce^{139}. The 0.184-Mev γ-ray is found to be partially internally converted, giving electrons of approximately 0.145 and 0.178 Mev. A 30.6±0.7-day half-life is assigned to Ce^{141} which is found to decay by the emission of a 0.66-Mev β^--particle and a γ-ray of approximately 0.2 Mev to stable Pr^{141}. A 1.4±0.1-day half-life is assigned to Ce^{143} which decays by the emission of a 1.3-Mev β^--particle and a 0.6-Mev γ-ray to Pr^{143}. A 13.5±0.1 half-life is assigned Pr^{143} which decays to stable Nd^{143} by emission of a 0.83-Mev β^--particle. The saturation intensity ratio of the $Ce^{142}(d,n)Pr^{143}$ reaction to the $Ce^{142}(d,2n)Pr^{142}$ reaction is found to be 2.9.

1. INTRODUCTION

FIRST attempts to produce radioactive cerium by neutrons from a radium-berryllium source were ineffective.[1] The first attempts at using the greater neutron flux made possible by cyclotron bombardments gave activities of low intensity.[2] Cerium and praseodymium activities produced by alpha-particle, deuteron, and proton bombardments have been investigated at this laboratory for a number of years.[3] It is the purpose of this paper to summarize the results obtained to date.

All bombardments were done in the 42-inch cyclotron at Ohio State University, giving 20-Mev alpha-particles, 10-Mev deuterons and 5-Mev protons. Activity measurements and absorption measurements, unless otherwise indicated, were made by means of a Wulf unifilar electrometer with an ionization chamber kept at 20 lb./in.^{2} pressure of freon. The stopping power of this electrometer window has been included in determining β-particle energies. All β-particle energies were computed by means of the Sargent formula.[4] Hilger material was used throughout.

Ce^{139} Data

A strong activity in the cerium fraction was obtained when lanthanum was bombarded with deuterons. The chemical separation** was accomplished by oxidizing the cerium from Ce^{+3} to Ce^{+4} while in a solution of concentrated HNO_3. In this condition cerium is precipitated when the pH is brought to 3.1 while the lanthanum remains in solution. The decay curve of the chemically separated cerium is shown in Fig. 1. This activity was observed for 1100 days during which time the intensity passed through approximately eight half-lives until no measurable activity remained. From this curve the half-life was determined as 140±1 days.

The 140-day activity was also produced in the cerium fraction by the bombardment of alpha-particles on barium, protons on lanthanum, and fast neutrons on cerium. The fast neutron bombardment was obtained by completely intercepting the cyclotron beam with a layer of lithium sufficiently thick to prevent any deuterons from passing through the lithium. The cerium sample was placed so as to be exposed only to the neutron flux produced by the reaction $Li^7(d,n)Be^8$.

While the sample was decaying with this 140-day half-life, x-rays in the neighborhood of 0.36 angstrom were found by aluminum absorption measurements. When the sample was used as a source for a Cauchois[5] camera the lanthanum K_α x-ray line was photographed. In order to determine that the lanthanum K_α x-ray line was emitted, the camera was first calibrated with cerium fluorescent x-rays. During this calibration only the lower half of the film was exposed to

* Lt. Col. U. S. Air Forces, research done under auspices of Air University, Maxwell Field, Alabama.
[1] E. Amaldi, O. D'Agostino, E. Fermi, P. Pontecorvo, F. Rasatti, and E. Segrè, Proc. Roy. Soc. **49**, 522 (1935).
[2] M. L. Pool, J. M. Cork, and R. L. Thornton, Phys. Rev. **52**, 239 (1937).
[3] M. L. Pool and J. D. Kurbatov, Phys. Rev. **63**, 463 (1943); J. D. Kurbatov and M. L. Pool, Phys. Rev. **65**, 61 (1944).
[4] B. W. Sargent, Can. J. Research **17A**, 82 (1934).
** The chemistry was kindly done by Ruth M. Steelman.
[5] Y. Cauchois, J. de Phys. **3**, 320 (1932).

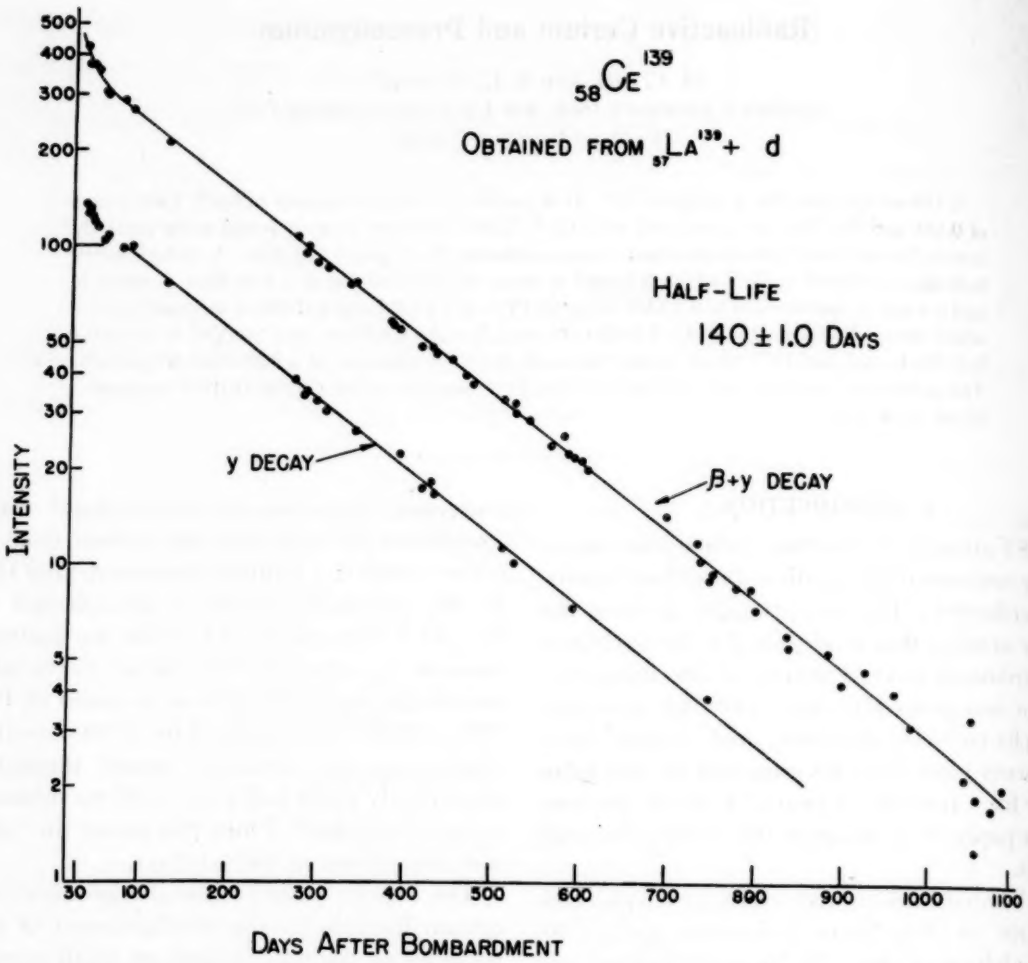

FIG. 1. Decay curves for the Ce fraction of a deuteron bombardment of lanthanum. A 140±1.0-day half-life was observed for both β- and γ-decay.

the cerium x-rays. Thereafter the upper half of the film was exposed to the x-rays produced by the active cerium decaying with the 140-day half-life. A vertical line was obtained on the upper half of the film which was horizontally displaced from the calibration line on the lower half by a distance corresponding in displacement and direction to the wave-length difference between the cerium and lanthanum K_α x-ray line.

By using an electrometer with an ionization chamber open to the atmosphere and a number of aluminum foils of 0.0023 g/cm² each, electrons of approximately 0.150 Mev were found. The shape of this absorption curve indicated that these electrons were monoergic. The fact that monoergic electrons were present was confimed by obtaining exposures on a β-ray spectrograph of the 180° focusing type. The β-ray spectrograph exposures gave lines for monoergic electrons of 0.135 and 0.165 Mev, with the former more intense.

A portion of the lead absorption curve obtained while the sample was in the 140-day period is shown in Fig. 2. Two gamma-rays, one of 0.184-Mev and one of approximately 0.8 Mev, were observed, the former being more intense. The gamma-ray decay of this cerium activity is also shown in Fig. 1. The half-life again is found to be 140 days.

Ce^{139} Interpretation

Obtaining the 140-day activity in the cerium fraction of an alpha-particle bombardment of barium and a deuteron bombardment of lanthanum permits assignment of this period to either Ce^{140} as an isomeric activity of stable Ce^{140} or to

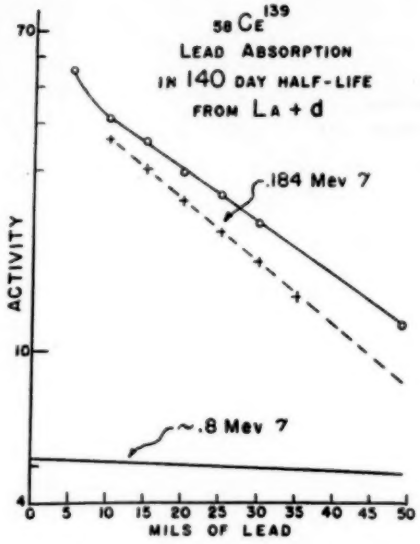

FIG. 2. Portion of a lead-absorption curve of cerium while in the 140-day activity. The dashed line was obtained by subtraction of the 0.8-Mev γ-ray curve from the total γ-ray curve.

Ce^{139}. Assignment of this period to Ce^{140} is eliminated by the fact that the lanthanum K_α x-ray line is emitted during the decay of this activity. The 140-day half-life is therefore assigned to Ce^{139}. The monoergic electrons indicated by aluminum absorption and obtained as 0.135 and 0.165 Mev by the β-ray spectrograph are attributed to a partial internal conversion of the observed 0.184-Mev gamma-ray. The two energies expected by conversion of the 0.184-Mev gamma based on the known binding energies of the K and L shells of lanthanum are 0.145 and 0.178 Mev. These values are within experimental error of the β-ray spectrograph values, 0.135 and 0.165 Mev. Since no electrons with energies greater than approximately 0.165 Mev were observed, it is concluded that the 0.8-Mev gamma-ray is essentially not internally converted.

It is therefore concluded that Ce^{139} decays by K-electron capture to La^{139}. The La^{139} nucleus obtained after the decay of the Ce^{139} by K-electron capture has two excited levels and decays either by the emission of a 0.184-Mev gamma-ray or a 0.8-Mev gamma-ray to the ground state of stable La^{139}.

Ce^{141}

An activity with 30.6-day half-life in the chemically separated cerium was produced by the bombardment of barium with alpha-particles, cerium with deuterons, and cerium with fast neutrons. This activity was not produced by the bombardment of deuterons on lanthanum. A plot of this activity produced by the bombardment of deuterons on cerium is shown as Fig. 3. The half-life, 30.6 ± 0.7 days, was determined by following the activity over a period of 300 days during which time it decayed through approxi-

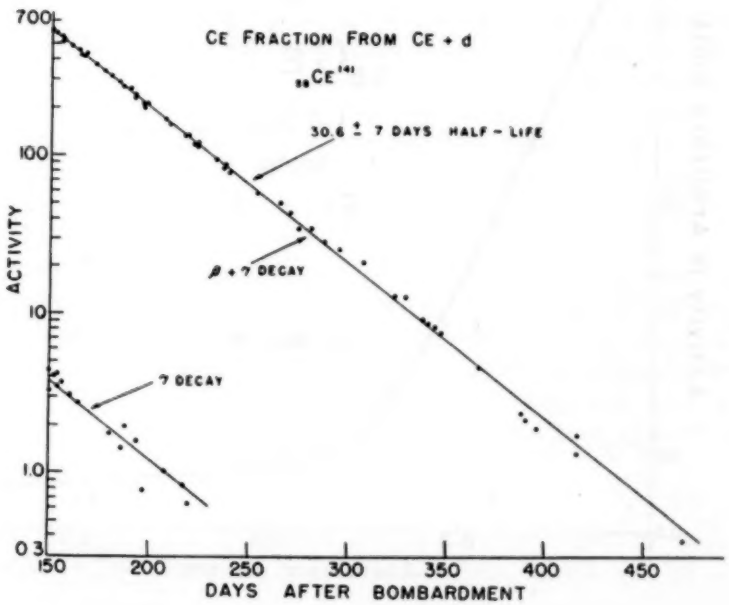

FIG. 3. Decay curves for the Ce fraction of a deuteron bombardment of cerium. A 30.6 $\pm$0.7-day half-life was observed for both β- and γ-decay.

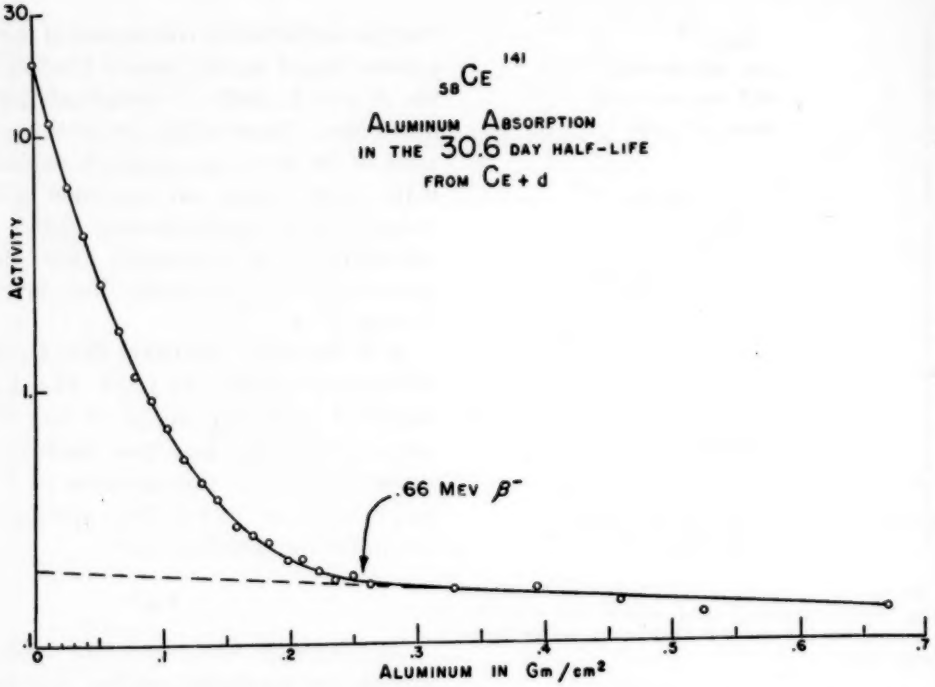

FIG. 4. Aluminum-absorption curve of the 30.6-day activity showing a β-end point of 0.66 Mev.

mately ten half-lives until no measurable activity remained. As shown by the decay curve, a gamma-ray of low intensity was found to be associated with this period. By means of lead-absorption measurements the energy of this gamma-ray was found to be 0.2 Mev. Cloud-chamber observations showed that this 30.6-day activity decayed with the emission of a negative

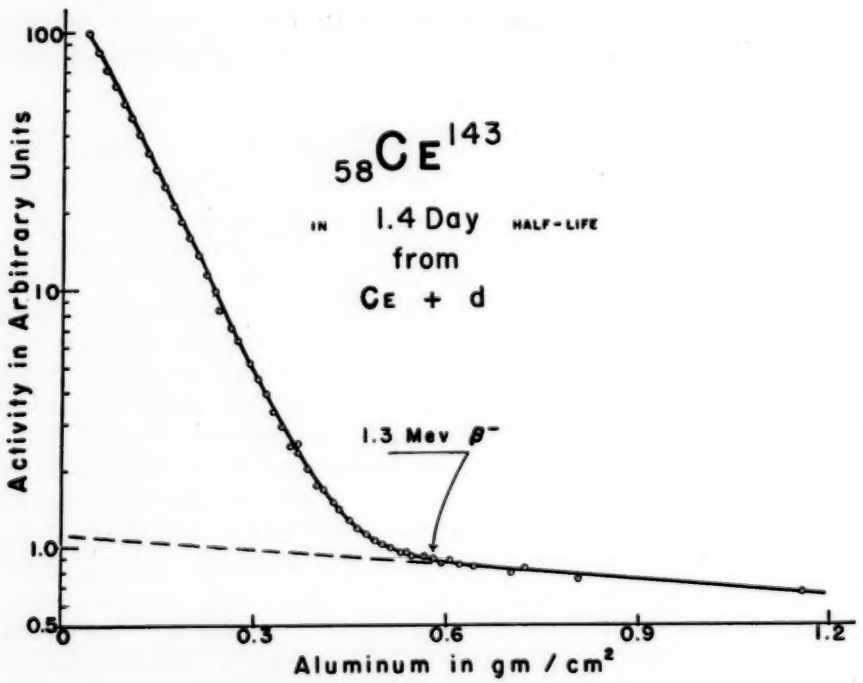

FIG. 5. Aluminum-absorption curve of the 1.4-day activity showing a β end point of 1.3 Mev.

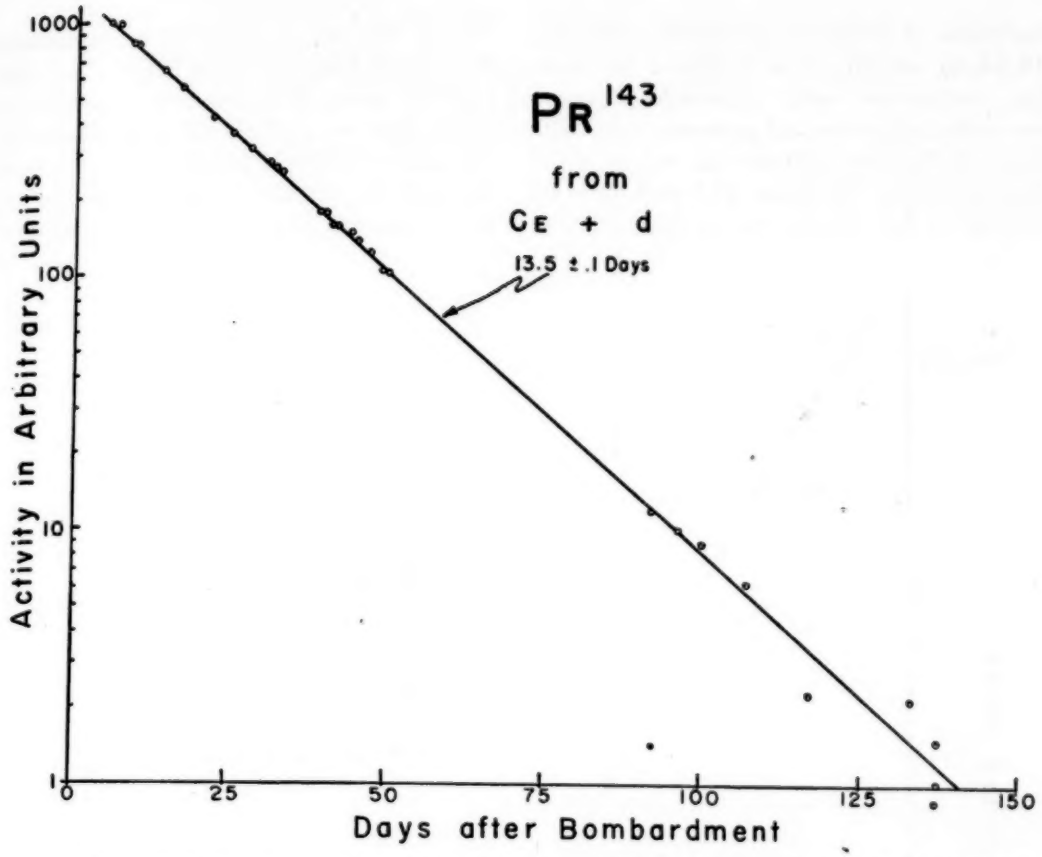

FIG. 6. Decay curve for the Pr fraction of a deuteron bombardment of cerium. A 13.5±0.1-day half-life was observed.

β-particle. The energy of the β-particle was determined as 0.66 Mev by aluminum-absorption measurements, as shown by Fig. 4.

The bombardment of barium with α-particles by which this 30.6-day period was produced would permit assignment of the activity to either Ce^{140} as an isomer or Ce^{141}. However, the fact that the activity was not obtained from the bombardment of lanthanum with deuterons removes the possibility of assignment to Ce^{140}. The 30.6-day activity is therefore assigned Ce^{141} and decays to stable Pr^{141} by emission of a 0.66-Mev β-particle and a gamma-ray of approximately 0.2 Mev.

Ce^{143}

A cerium activity emitting negative β-particles with a half-life of approximately 1.4±0.1 days was produced by bombarding cerium with deuterons or neutrons. An aluminum-absorption curve showing the energy of the β-particle to be 1.3 Mev is shown in Fig. 5. This activity was not produced by the bombardment of barium with alpha-particles. The value of the half-life was obtained by subtraction of the 30.6-day activity from the total activity in cerium. A gamma-ray was found to be associated with this decay and the energy determined as approximately 0.6 Mev by means of lead-absorption measurements.

Since the 1.4-day activity in cerium could be produced by a deuteron bombardment of cerium but not by an alpha-particle bombardment of barium, it is assigned to Ce^{143} which decays by the emission of a 1.3-Mev β-particle and a gamma-ray of approximately 0.6 Mev to Pr^{143}.

Pr^{143}

A 19.3-hour and a 13.5-day half-life were produced in the praseodymium fraction of a

bombardment of cerium by deuterons. Although the 19.3-hour activity was produced by bombarding lanthanum with α-particles, praseodymium with deuterons, and praseodymium with neutrons, the 13.5-day activity was not produced by these reactions. The value 13.5 ± 0.1 days for the half-life of this activity was determined from Fig. 6, covering a period of approximately 135 days or 10 half-lives. The activity was followed until no measurable intensity remained. It was found that no gamma-ray was associated with this activity. Cloud-chamber observations showed the 13.5-day activity to decay with the emission of a negative β-particle. The energy of this

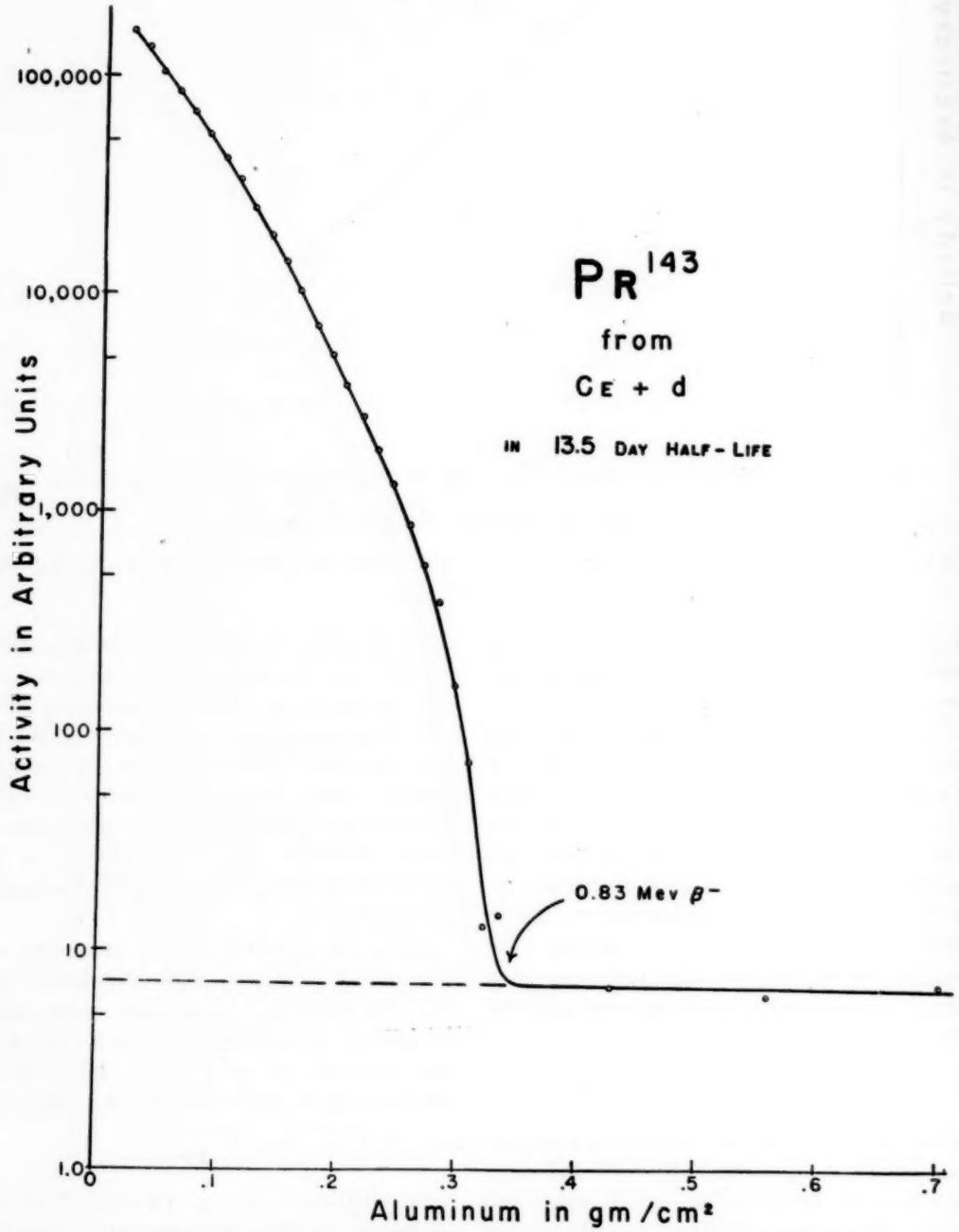

FIG. 7. Aluminum-absorption curve of the 13.5-day activity showing a β-end point of 0.83 Mev.

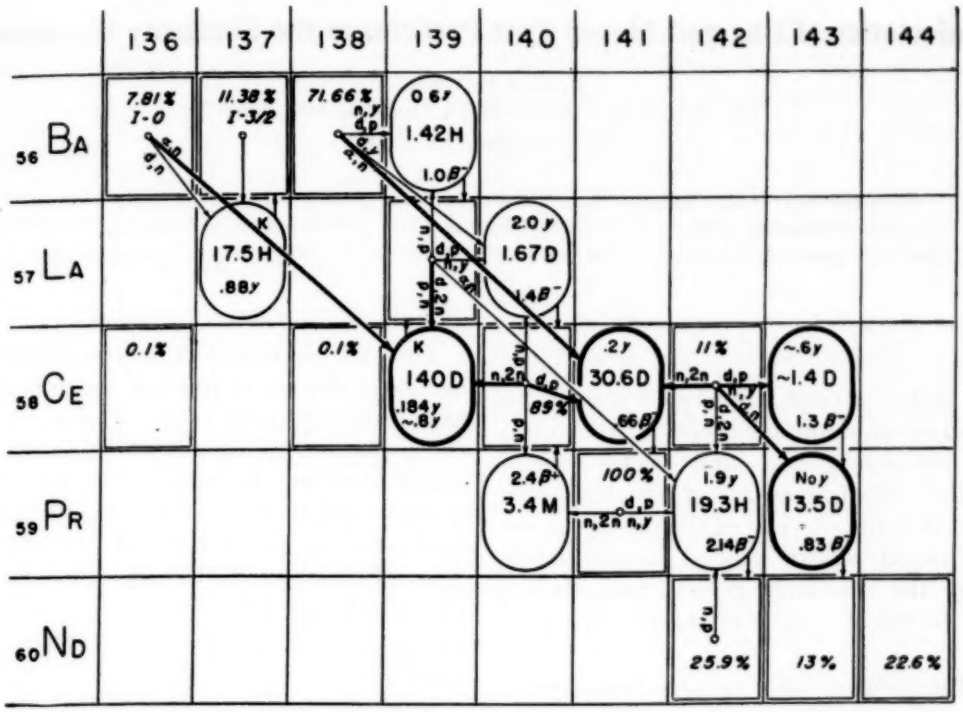

FIG. 8. Cerium region of an isotopic chart. Activities assigned by this paper are heavily outlined and reactions obtained which produced these activities are indicated by heavy arrows.

β-particle was determined to be 0.83 Mev, as shown in Fig. 7.

In accordance with the reactions given above, the 13.5-day period of praseodymium is assigned Pr^{143} which decays with the emission of a 0.83-Mev β-particle to stable Nd^{143}.

II. DISCUSSION

A portion of the isotopic chart is reproduced in Fig. 8. The activities with which this paper deals are accentuated by heavy outline. It will be noted that the above assignments require a genetic relationship to exist between Ce^{143} and Pr^{143}. This relationship reported in previous abstracts[3] was established by successive chemical separations of praseodymium from a cerium sample decaying with a 1.4-day half-life. This relationship is in agreement with the results of others.[6]

Certain data were obtained during these experiments which permit computing the ratio of saturation intensities of the (d,n) and $(d,2n)$ reactions of Ce^{142}. The praseodymium fraction from a $Ce(d,n)Pr$ reaction gave the 19.3-hour half-life of Pr^{142} and the 13.5-day half-life of Pr^{143}. The ratio of the saturation intensity of the 13.5-day period to that of the 19.3-hour period was found to be 2.9.

III. ACKNOWLEDGMENTS

The authors are grateful for support received from The Ohio State University Development Fund, The Ohio State University Research Foundation, and The Graduate School.

[6] Plutonium Project, "Nuclei Formed in Fission," Rev. Mod. Phys. 18, 535 (1946).

Trajectories of Charged Meson Test Particles in the Similarity Geometry

BANESH HOFFMANN
*The Institute for Advanced Study, Princeton, New Jersey**

(Received January 19, 1948)

Using the ideas of the similarity theory, it is shown that there is a close relationship between the hitherto distinct theories of Weyl and Kaluza. Also, simple equations belonging to the similarity geometry are found to give the correct trajectories for charged mesonic test particles.

I.

IN two recent papers[1] it was shown that one can formulate a unitary theory of the gravitational, electromagnetic, and vector meson fields within the framework of the similarity geometry. It is the purpose of the present paper to put forward certain general considerations concerning the similarity theory, and also to carry the technical aspects of the theory a step farther.

From the point of view of pure field theory, the idea of a metric is extraneous. If, though, we permit consideration of the physical trajectories of test particles, the concept of a metric becomes less remote. For the null geodesics define a light cone at every point of space-time, and thus at once define a metrical tensor g_{ab} to within an arbitrary (non-zero) multiplying factor $\rho^2(x)$. We may express this by saying that the null geodesics determine a conformal metric.

It is well known that the null geodesics are invariant under conformal transformations

$$g_{ab}(x)\rightarrow\bar{g}_{ab}(x)=\rho^2(x)g_{ab}(x). \tag{1}$$

The non-null geodesics, however, are not invariant under the general conformal group. If we seek the subgroup of the general conformal group which leaves all geodesics invariant, we come to precisely the group characterized by

$$g_{ab}(x)\rightarrow\bar{g}_{ab}(x)=k^2g_{ab}(x), \tag{2}$$

which yields what I have called the similarity geometry. Thus, even from the point of view of the gravitational trajectories of uncharged test particles, it appears reasonable that the similarity geometry should play a fundamental role.

That the similarity geometry should involve two extra degrees of freedom can be understood from this particular point of view as follows: the projective geometry, which leaves all geodesics invariant, introduces one new degree of freedom which finds expression in some such device as the use of homogeneous coordinates. The other degree of freedom then pertains to the transformations (2), these transformations taking place irrespective of coordinate transformations.[2]

Reference was made in V.M.P.R. to the work of Lubański and Rosenfeld. It is significant that, starting from the commutation properties of the β-matrices of meson theory, and working purely algebraically, they found that meson fields are fundamentally related to the group of rotations in space of six dimensions, and thus to the group of a four-dimensional quadric surface in a projective space of five dimensions. For it is just such a geometrical picture which underlies the similarity and the general conformal geometries.

Reference was also made, in S.G., to the relationship of spinors to the same underlying geometrical picture. It may not be out of place to state briefly the nature of this relationship. If,[3] φ_A, ψ_B are two four-component spinors (where the indices A, B have the range 1, 2, 3, 4, referring not to space-time but to spin space), a parametric representation of space-time in terms of four-component spinors is achieved, through the Plücker-Klein correspondence, by first writing

$$X^{AB}\equiv\tfrac{1}{2}(\psi^A\varphi^B-\psi^B\varphi^A), \tag{3}$$

and then relabeling the six independent non-zero

* Now at Queens College, Flushing, New York.

[1] Banesh Hoffmann, Phys. Rev. **72**, 458 (1947), and **73**, 30 (1948). These papers will be referred to, respectively, as V.M.P.R. and S.G.

[2] Note that $\bar{g}_{ab}$ in (2) is a function of x, not of new coordinates $\bar{x}$.

[3] See O. Veblen, Proc. Nat. Acad. Sci. **19**, 503 (1933).

components of the antisymmetric quantity X^{AB} according to the scheme

$$\begin{aligned} X^{12}&=\tfrac{1}{2}(X^5+iX^0), & X^{34}&=\tfrac{1}{2}(X^5-iX^0),\\ X^{13}&=\tfrac{1}{2}(X^3+X^4), & X^{42}&=\tfrac{1}{2}(X^3-X^4),\\ X^{14}&=\tfrac{1}{2}(X^1+iX^2), & X^{23}&=\tfrac{1}{2}(X^1-iX^2). \end{aligned} \tag{4}$$

The quantities X^{AB} satisfy the identity

$$X^{12}X^{34}+X^{13}X^{24}+X^{14}X^{23}=0. \tag{5}$$

In terms of the six quantities X^σ defined in (4), this becomes

$$(X^0)^2+(X^1)^2+(X^2)^2+(X^3)^2 -(X^4)^2+(X^5)^2=0. \tag{6}$$

The spinor representation of the Lorentz group is then obtained by considering the real points of the quadric (6) and setting, say,

$$X^0=0, \quad X^5=0. \tag{7}$$

Thus the spinor representation of the Lorentz group is here obtained only after specialization of a formalism which basically involves six variables, X^σ, and is concerned with an invariant four-dimensional quadric surface (6) in a projective space of five dimensions.

II.

Hitherto it has seemed that the unitary theories of Weyl and Kaluza were quite distinct, if not actually rivals. In the light of the present ideas, though, one finds a close relationship between them.

Weyl developed his conformal theory without the aid of extra degrees of freedom. Consequently, unification was incomplete, in the sense that the Lagrangian for the total field had to be formed by the arbitrary addition of partial Lagrangians for the gravitational and electromagnetic parts of the field, respectively.[4] Also the gravitational part of the Lagrangian could not be formed from $R(g)^{\frac{1}{2}}$, since this was not gauge invariant, the only available gauge invariant densities formed from g_{ab} being $R^2(g)^{\frac{1}{2}}$, $R^{ab}R_{ab}(g)^{\frac{1}{2}}$, and so on.

The modern form of the general conformal geometry, with its conformal tensors having $(n+2)^k$ components, does not seem to have been applied to the Weyl theory. Yet it is a natural step to employ in a basically conformal physical theory the full resources of the general conformal geometry, and a generalization along these lines would undoubtedly qualify as a modern version of the original Weyl theory. Such a generalized theory might avoid the difficulty regarding the gravitational part of the Lagrangian since there would be available in it quantities analogous to G_{00} of V.M.P.R. and S_{00}, etc., of S.G. which could be used, as in those papers, to form a simpler gauge invariant Lagrangian than was possible in the original Weyl theory. Such a theory could also achieve a closer unification of the different parts of the total Lagrangian. It might also meet the grave objections to Weyl's theory made by Einstein,[5] since a normalized, affine g_{ab} could be defined in it much as an affine g_{ab} is defined in the projective theory of relativity. Whether this modernized version of Weyl's theory would yield results physically preferable to those of the present similarity theory, which is a restricted form of it, is hard to say without detailed investigation, and, unfortunately, the necessary calculations appear formidable. Nevertheless, we may reasonably say that, from the present point of view, Weyl's idea does imply a transition from entities having 4^k components to entities having 6^k components. And the initial step from 4^k to 5^k components was just that taken by Kaluza. The relationship between the ideas of Kaluza and Weyl is seen to be even closer when one notes that the general conformal geometry is essentially projective in character, and that Kaluza's theory has been interpreted as a projective theory. That the relationship between the two ideas extends even to details is indicated by the fact that both in the Weyl and the Eddington theories terms appear in the curvature scalar analogous to the terms involving N and N^2 in the curvature scalar in V.M.P.R.

Since the present similarity theory is a special case of the above-mentioned modernized form of the Weyl theory, and since it is so closely related, too, to the Kaluza-Klein and projective theories, one sees that it is not only a unitary theory of certain physical fields but also, to some extent, a unitary theory of unitary theories.

[4] Eddington, in his generalization of Weyl's theory, was able to make this addition more plausible.

[5] A. Einstein, Physik. Zeits. 21, 651 (1920).

III.

In S.G., the basic similarity tensor $S_{\sigma\tau}$ was subjected, for simplicity, to the arbitrary invariant restrictions

$$S_{05}=0, \tag{8}$$

$$S_{55}/S_{00} \text{ independent of } x^a. \tag{9}$$

We retain these restrictions in the present paper.

In setting up the field equations for the gravitational, electromagnetic, and vector meson fields in S.G., certain physical identifications had to be made. If the equations of the trajectories we are about to discuss are to have any relevance to the work of S.G., they must involve the same physical identifications as those of that paper. From Eqs. (22) to (28) of S.G., and Eqs. (5), (6) of V.M.P.R., we may summarize these physical identifications as follows:

Let $g_{\sigma\tau}$ be such that

$$g_{\sigma 5}=g_{\sigma 0}=0; \tag{10}$$

let ψ_σ be such that

$$\psi_0=0,\ \psi_5 \text{ independent of } x^a; \tag{11}$$

and let φ_σ be such that

$$\varphi_0=1, \quad \varphi_5=0. \tag{12}$$

Then

$$s_{\sigma\tau}\equiv S_{\sigma\tau}/S_{00}, \tag{13}$$

and

$$s_{\sigma\tau}\equiv g_{\sigma\tau}+\varphi_\sigma\varphi_\tau+\psi_\sigma\psi_\tau, \tag{14}$$

where

g_{ab} is the gravitational metric,

ψ_a is the electromagnetic potential,

and

φ_a is the vector meson field quantity.

In the general theory of relativity the gravitational trajectories of test particles are the geodesics, given by the variational principle

$$\delta\int\left\{g_{ab}\frac{dx^a}{dt}\frac{dx^b}{dt}\right\}^{\frac{1}{2}}dt=0, \tag{15}$$

where t is a parameter.

To obtain equations of physical trajectories of test particles in the present case, we set up an analogous variational principle. Since the field equations of the present theory are obtained from a variational principle which does not contain $\exp(Nx^0)$ as a factor, the $\exp(Nx^0)$ being cancelled by a suitable power of S_{00}, we write here for the trajectories not

$$\delta\int\left\{S_{\sigma\tau}\frac{dx^\sigma}{dt}\frac{dx^\tau}{dt}\right\}^{\frac{1}{2}}dt=0, \tag{16}$$

but

$$\delta\int\left\{S_{\sigma\tau}\frac{dx^\sigma}{dt}\frac{dx^\tau}{dt}\Big/S_{00}\right\}^{\frac{1}{2}}dt=0, \tag{17}$$

in which too the $\exp(Nx^0)$ factor is cancelled by a suitable power of S_{00}. By (13), this is the same as

$$\delta\int\left\{s_{\sigma\tau}\frac{dx^\sigma}{dt}\frac{dx^\tau}{dt}\right\}^{\frac{1}{2}}dt=0. \tag{18}$$

It is well known that the trajectories defined by (18) are given by

$$\frac{d^2x^\sigma}{du^2}+A_{\tau\pi}{}^\sigma\frac{dx^\tau}{du}\frac{dx^\pi}{du}=0, \tag{19}$$

where $A_{\tau\pi}{}^\sigma$ are the Christoffel symbols of the second kind formed from $s_{\sigma\tau}$, and $du^2=s_{\sigma\tau}dx^\sigma dx^\tau$. To investigate the physical significance of these equations it is convenient to go over to their covariant form. Multiplying by $s_{\sigma\rho}$ and summing over σ, we obtain

$$s_{\sigma\rho}\frac{d^2x^\sigma}{du^2}+A_{\tau\pi,\rho}\frac{dx^\tau}{du}\frac{dx^\pi}{du}=0, \tag{20}$$

where $A_{\tau\pi,\rho}$ are the Christoffel symbols of the first kind formed from $s_{\sigma\tau}$.

Inserting the explicit form of $A_{\tau\pi,\rho}$, we have, owing to the symmetry of $(dx^\tau/du)(dx^\pi/du)$,

$$s_{\sigma\rho}\frac{d^2x^\sigma}{du^2}+\frac{\partial s_{\tau\rho}}{\partial x^\pi}\frac{dx^\tau}{du}\frac{dx^\pi}{du}-\frac{1}{2}\frac{\partial s_{\tau\pi}}{\partial x^\rho}\frac{dx^\tau}{du}\frac{dx^\pi}{du}=0, \tag{21}$$

or

$$\frac{d}{du}\left\{s_{\sigma\rho}\frac{dx^\sigma}{du}\right\}-\frac{1}{2}\frac{\partial s_{\tau\pi}}{\partial x^\rho}\frac{dx^\tau}{du}\frac{dx^\pi}{du}=0. \tag{22}$$

There are six component equations in (22). Consider first the two equations given by $\rho=0$ and $\rho=5$, respectively. Since $s_{\tau\pi}$ does not contain x^0 or x^5, the last term vanishes in each of these cases and the equations admit of the first

integrals

$$S_{\sigma 0}\frac{dx^\sigma}{du}=\epsilon_0, \tag{23}$$

$$S_{\sigma b}\frac{dx^\sigma}{du}=\epsilon_b, \tag{24}$$

where ϵ_0, ϵ_b are independent of the coordinates. From invariance considerations, ϵ_0 is a scalar, but ϵ_b becomes multiplied by k^{-2} under the transformations of x^b given by Eq. (14) of S.G.

Using (10)–(12), and (14), we may write these as

$$\varphi_\sigma\frac{dx^\sigma}{du}=\epsilon_0, \tag{25}$$

$$\psi_\sigma\frac{dx^\sigma}{du}=\epsilon_b/\psi_b, \tag{26}$$

where ϵ_0 and ϵ_b/ψ_b are now both scalars. They are thus constants of the motion.

Consider now the remaining four equations in (22), corresponding to $\rho=a$. They are, by (10)–(12), (14),

$$\frac{d}{du}\left\{g_{ab}\frac{dx^b}{du}+\left(\varphi_\sigma\frac{dx^\sigma}{du}\right)\varphi_a+\left(\psi_\sigma\frac{dx^\sigma}{du}\right)\psi_a\right\}$$
$$-\frac{1}{2}\frac{\partial g_{bc}}{\partial x^a}\frac{dx^b}{du}\frac{dx^c}{du}-\left(\varphi_\sigma\frac{dx^\sigma}{du}\right)\frac{\partial\varphi_\tau}{\partial x^a}\frac{dx^\tau}{du}$$
$$-\left(\psi_\sigma\frac{dx^\sigma}{du}\right)\frac{\partial\psi_\tau}{\partial x^a}\frac{dx^\tau}{du}=0, \tag{27}$$

or, using (25) and (26), and also (11) and (12),

$$\left\{\frac{d}{du}\left(g_{ab}\frac{dx^b}{du}\right)-\frac{1}{2}\frac{\partial g_{bc}}{\partial x^a}\frac{dx^b}{du}\frac{dx^c}{du}\right\}$$
$$+\epsilon_0\left(\frac{\partial\varphi_a}{\partial x^b}-\frac{\partial\varphi_b}{\partial x^a}\right)\frac{dx^b}{du}$$
$$+\left(\frac{\epsilon_b}{\psi_b}\right)\left(\frac{\partial\psi_a}{\partial x^b}-\frac{\partial\psi_b}{\partial x^a}\right)\frac{dx^b}{du}=0. \tag{28}$$

Multiplying by g^{ae} and summing over a, we may write these as

$$\frac{d^2x^e}{du^2}+\left\{\begin{matrix}e\\b\ c\end{matrix}\right\}\frac{dx^b}{du}\frac{dx^c}{du}+2\epsilon_0\varphi^e{}_b\frac{dx^b}{du}$$
$$+2\left(\frac{\epsilon_b}{\psi_b}\right)\psi^e{}_b\frac{dx^b}{du}=0, \tag{29}$$

where, as in S.G.,

$$\varphi^e{}_b=g^{ec}\varphi_{bc}=\tfrac{1}{2}g^{ec}\left(\frac{\partial\varphi_b}{\partial x^c}-\frac{\partial\varphi_c}{\partial x^b}\right), \tag{30}$$

with a similar definition for $\psi^e{}_b$. Interpreting the constants of the motion ϵ_0, ϵ_b/ψ_b as being proportional to g/μ, e/μ, respectively, where g is the mesonic charge of the test particle, e its electric charge, and μ its mass, we see that these equations give the correct trajectories of charged meson test particles in a combined gravitational, electromagnetic, and vector meson field.

IV.

Removing the restrictions (8), (9) on the fundamental similarity tensor $S_{\sigma\tau}$ presents some problems. These may in part be due to incomplete guidance from invariance considerations owing to the use of a specialized[6] transformation matrix $U_\tau{}^\sigma$ in S.G.

In tentative attempts to remove the restrictions on $S_{\sigma\tau}$, I have been able to dissect a general $S_{\sigma\tau}$ in such a way that the field equations contain a scalar meson field alongside the gravitational, electromagnetic, and vector meson fields, together with another scalar field whose physical significance is unclear. The two meson fields have the same value for the mass. However, the presence of certain interaction terms in the field equations, and the form taken by the corresponding equations of the trajectories indicate that the particular dissection and physical identification of the general $S_{\sigma\tau}$ in these calculations may not be the appropriate one. There are some indications that with a different dissection the second scalar field might absorb the $20N^2$ term which was subtracted from the Lagrangian in S.G.[7] and take on the character of a Stueckelberg field.

From the point of view of meson theory, the field quantities should, in general, be complex. Now, it is known that two-component spinors suffice to give a representation of the Lorentz group. Since, despite this, four-component spinors are required in the Dirac equations, it is

[6] The specialization is actually present in the original conformal transformation matrix of Veblen, from which the transformation matrix of S.G. was derived. It is manifest here in the arbitrary linking of the x^0 and x^4 transformations to a single parameter k.

[7] See S.G., Eq. (51).

reasonable to consider the physical potentialities of more extended groups, having the Lorentz group as a subgroup, which the four-component spinors are able to represent. Because of the close relationship of the conformal and similarity geometries to the geometry of four-component spinors, it would be of interest to investigate a theory analogous to the present theory but based on spinors rather than tensors. Complex field quantities would enter such a theory automatically. And if the detailed computations bore a sufficient resemblance to those of the present tensorial theory, as is not unlikely, one would expect to find field equations containing not only the fields already obtained but, in addition, pseudovector and pseudoscalar fields, as well as fields pertaining to half-integral values of the spin.

PHYSICAL REVIEW VOLUME 73, NUMBER 9 MAY 1, 1948

The Breakdown of Gases in High Frequency Electrical Fields*

DONALD H. HALE**
Northwestern University, Evanston, Illinois
(Received May 19, 1947)

A theory is proposed to explain the mechanism of breakdown of gases in high frequency electrical fields. It is assumed that breakdown occurs when the electrical field and the frequency are such that an electron acquires the ionizing energy at the end of one mean free path. The field for breakdown is thus a function of the frequency of the applied potential and the ionization potential and pressure of the gas. The fields for breakdown of argon and xenon are calculated and expressed as functions of the frequency and the gas pressure. The calculated potentials are compared with experimental data, and good agreement is found for frequencies greater than 10×10^6 c.p.s.

1. INTRODUCTION

THE breakdown of gases in high frequency electrical fields has been studied by a number of workers.[1] In general, the procedure followed has been to measure the minimum potential for breakdown of the gas as a function of the gas, gas pressure, electrode separation, and frequency of the applied field. The potential for breakdown, V_s, was plotted as a function of the gas pressure, p, for one frequency and gap width. The data, when plotted in this manner, gave V_s-p curves which have the general appearance of the Paschen curves for breakdown in d.c. fields.

Thomson's[2] work was typical. He studied the breakdown of hydrogen in this manner. He used a number of frequencies of the applied potential and experimentally determined a series of V_s-p curves, each of which corresponded to one frequency. As he increased the frequency, from about 2×10^6 to about 40×10^6 c.p.s., V_s took on lower and lower values. However, as the frequency was increased above about 40×10^6 c.p.s., V_s began to increase with increasing frequency. The present paper reports a somewhat different approach to the problem. It is assumed that the breakdown potential for high frequency fields is determined by those electrons in the gas which succeed in acquiring the ionizing energy in one mean free path. Thus, the breakdown potential should be a function of the gas, gas pressure, electrode separation, and frequency of the applied field. Thomson's experimental work showed that for hydrogen V_s was a function of the gas pressure and the frequency of the applied field.

Under this assumption the solution of the equation of motion of the electron which moves in the gas and the high frequency field is not

* This work was sponsored by the U. S. Navy Bureau of Ships.
** Now at the Army Chemical Center, Maryland.
[1] L. B. Loeb, *Fundamental Processes of Electrical Discharge in Gases* (John Wiley and Sons, Inc., New York, 1939), p. 550.
[2] J. Thomson, Phil. Mag. **23**, 1 (1937).

difficult since before the gas breaks down the electric field is not distorted by space charge. The motion of the electron under such conditions is given by

$$\ddot{x} = (e/m)E \sin 2\pi ft. \quad (1)$$

The electron is assumed to be at rest when the instantaneous value of the applied field is zero and all collisions which do not result in the formation of an ion pair are disregarded since such collisions cannot lead to the breakdown of the gas. Also it is only those electrons which are at rest when the instantaneous value of the field is zero which will acquire the ionizing potential at the end of one mean free path under the conditions to be imposed. These simplifying assumptions should not greatly alter the results since it is assumed that the electrons which acquire the ionizing energy in one mean free path are those which cause the initial breakdown.

Integration of the equation of motion gives,

$$\dot{x} = v = (e/m)E/2\pi f(1 - \cos 2\pi ft), \quad (2)$$

$$x = d = (e/m)E/4\pi^2 f^2(2\pi ft - \sin 2\pi ft). \quad (3)$$

It is assumed that the gas will break down when the values of E and f are such that d will be one electron free path, L_e, for the gas and gas pressure considered, and that the electron will have the ionizing energy at the end of the mean free path. Thus v will be determined by $\frac{1}{2}mv^2 = eV_i$, where V_i is the ionization potential of the gas under consideration. Some value must be assigned to t. This can be done by assuming that the electron is to acquire the ionizing energy and move one mean free path in a time t which is some fractional part of one period of the applied electrical field. Thus, t is expressed in terms of f, and E and f computed for this value of t. This amounts to determining, for the gas and gas pressure considered, the proper values for E and f so that an electron will acquire the ionizing energy, after acceleration during a fraction of a period of the applied field, and be displaced one mean free path. Under such conditions the probability of ionizing collisions should be a maximum. Further, by calculating E and f for several values of t it is possible to plot a curve showing E, the peak value of the field for breakdown in volts per centimeter, as a function of the frequency of the applied field.

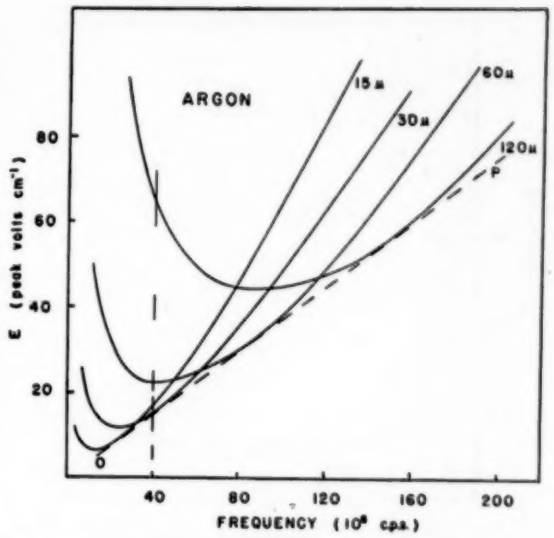

FIG. 1. Calculated values of E, the field for breakdown of A at several pressures, plotted against the frequency.

This has been done. Figure 1 shows calculated values of E, the peak value of the field for breakdown, plotted as a function of frequency for argon at several pressures from 15 to 120 microns of mercury. For any of the curves, the values of E corresponding to values of t less than about $t = 1/4f$ lie to the left of the minimum. This shows that if the electron is to have a high probability of ionizing after being accelerated during a small part of a period of the applied high frequency, E must be large and the frequency comparatively low. If the electron is accelerated over a large portion of one period, t equal to about $1/f$, E is large and the frequency is high for high probability of ionization. The minimum value of E is given by t about equal to $3/8f$. The curves of Fig. 1 show that when the pressure of the gas is increased the minimum value of E increases and lies at greater frequencies. Also the minimum becomes less pronounced for the higher pressures.

Figure 2 shows curves of calculated values of V_s, the peak value of the breakdown potential for a 5-cm gap, for xenon, argon, krypton, and hydrogen, all at a pressure of 30 microns of mercury. These curves show the dependence of E and the frequency, for breakdown, upon the ionization potentials and the electron mean free paths for these gases. The values of E corresponding to $t = 1/4f$ and $t = 3/8f$ are indicated for hydrogen.

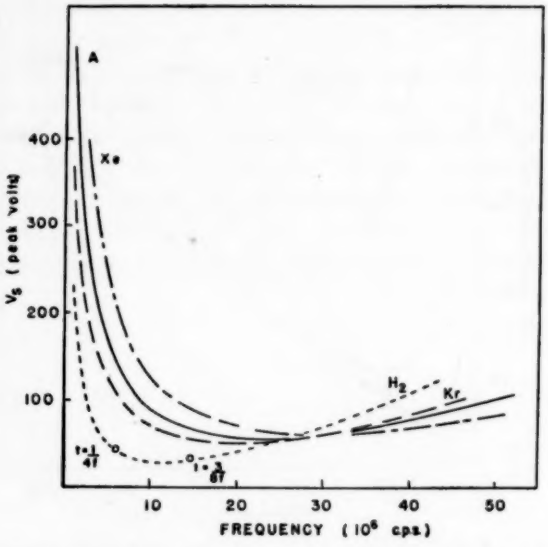

FIG. 2. Theoretical variation of V_s with frequency for a 5-cm gap in A, H_2, Kr, and Xe all at 30μ pressure.

Each of the curves of Fig. 1 is tangent to the line OP at one point. The value of E, for each curve, at the point of tangency is given approximately by $t=7/16f$.

It is possible, using the data of Fig. 1, to derive a set of theoretical V_s-p curves such as Thomson measured experimentally. This is done by reading off, from Fig. 1, the values of E corresponding to the various pressures shown and for one frequency. As an example the following data were taken from Fig. 1 for a frequency of 40×10^6 c.p.s.

p (microns)	V_s (peak volts)
15	17.6
30	15
60	22
120	65

These data were plotted in Fig. 3 as the $E-p$ curve for 40 megacycles. The data, as plotted in Fig. 3, give the peak value of the field for breakdown for a gap in argon as a function of the pressure. Figure 3 also shows similar curves for the breakdown potential at other frequencies. These theoretical curves all have the same general shape as do the Thomson curves for low pressures and high frequencies. That is, both Thomson's experimental curves and the curves of Fig. 3 show E_s minimum decreasing with decreasing frequencies and falling at lower values of the pressure. Thomson's curves for hydrogen do not show E_s increasing as rapidly, to the right of the minimum, as do the curves of Fig. 3. However, the shape of the curves for hydrogen might be expected to be quite different from those for argon. This is shown by a comparison of the curves for hydrogen and argon in Fig. 2.

The minimum value of E_s for any one of the $E-p$ curves of Fig. 3 will be nearly equal to the value of E given by $t=7/16f$ for one of the curves of Fig. 1. This is so because no matter what frequency is chosen in deriving an $E-p$ curve, from a set of the type shown in Fig. 1, the lowest value of E_s for that frequency will always be given by the curve which is tangent to OP at the intersection of OP and the line of constant frequency. Thus it is possible to calculate the minimum value of E_s for any $E-p$ curve and for any gas and frequency. All that need be known is V_i and the frequency applied. A study of Eq. (2) indicates the method. If the velocity and frequency are known and t is set equal to $7/16f$, this equation can be solved for E and this value of E, multiplied by the electrode separation, gives V_s minimum, for the V_s-p curve at the frequency chosen.

It is also possible to estimate the pressure at which the minimum value of V_s will fall for curves of the type shown in Fig. 3. Equation (3) is used in this calculation. The value of E, as calculated above, the frequency under consideration and $t=7/16f$ are substituted in the equation and d is calculated. This gives the electron mean free path in the gas considered and at the pressure for which V_s is a minimum. It is thus possible to estimate the gas pressure.

2. EXPERIMENTAL PROCEDURE

Breakdown potentials were measured for xenon and argon at constant pressure and in the range of frequencies from 5×10^6 to 50×10^6 c.p.s. Two xenon-filled tubes were used. The gas pressure in each was 20 microns of mercury. Two argon tubes were used with gas pressures of 30 and 49 microns of mercury. The pressures were measured at 22°C. The tubes were of Pyrex and were either 22 or 41 mm in diameter. External electrodes were used so that the purity of the gas might be of a high order. The length of all tubes was 22 cm. The external electrodes were made from strips of copper 1 cm wide fitted

about the tubes. Electrode separations of 5 and 10 cm were used.

Considerable care was used in filling the tubes. They were attached to the vacuum system and baked out at 400°C over night. The vacuum system had a side bulb in which was fitted a tungsten filament. This filament supported a pellet of barium or calcium. After the gas was admitted the pellet was flashed to act as a getter for contaminating gases. This flashing formed a freshly deposited surface of the getter on the walls of the containing bulb and the gases were allowed to stand in contact with this surface for some time before the discharge tubes were sealed off. After sealing off, the spectra of the gases were examined and showed no trace of contamination. However, this is only a rough check since many discharge phenomena in gases at low pressures can be altered by traces of impurities which cannot be detected by a study of the spectrum of the gas.

Most of the work was done with two oscillators and a few values of V_s, at the lower frequencies, checked with a third oscillator. The two oscillators most used were of the same type but covered different frequency ranges. They were of a modified Hartley type and employed 100 TH tubes rated at 200 watts. The electrodes of the discharge tubes were connected directly across a few turns of the oscillator plate coil. The potential applied to the electrodes was varied by varying the oscillator plate potential. This arrangement made it possible to change the potential on the electrodes continuously and smoothly from about 100 to 1000 volts. A few values of V_s were taken as a check with a Navy type TDE transmitter oscillator. This oscillator had a buffer stage and it was assumed, therefore, that the potential applied to the discharge tubes was nearly free of harmonics. Potentials were measured by a vacuum tube voltmeter. This indicated potentials in peak volts and all values of potential and field mentioned are so expressed.

The procedure followed in determining the breakdown potential was to start with a low value for the applied high frequency potential and then to slowly increase it until the gas broke down. Breakdown was indicated by the appearance of a glow in the body of the gas and also by a slight kick of the voltmeter needle. All

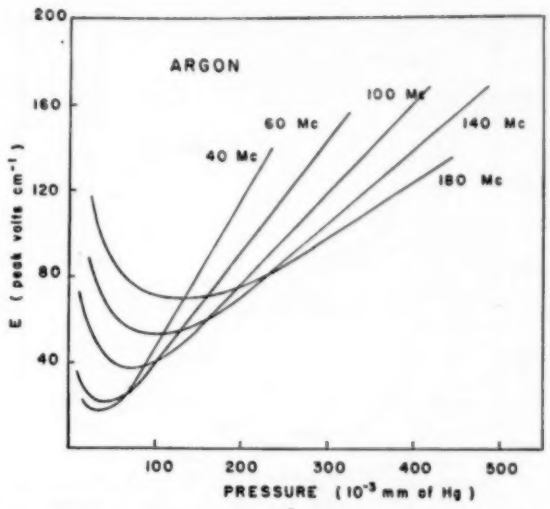

FIG. 3. Calculated E-p curves for breakdown of A at several frequencies.

points were checked a number of times. The breakdown potentials were readily reproducible within the limit of error of reading the voltmeter with the exception of those for the lowest frequencies. For these frequencies there was considerable spread among the readings taken at any one frequency.

3. EXPERIMENTAL RESULTS

The measured values of V_s for argon plotted as a function of frequency are shown in Fig. 4. The values of V_s indicated by circles were taken with the Harley oscillators and those indicated by triangles were taken with the Navy type TDE oscillator. The smooth curves represent the average of the experimental data. The two curves at lower values of V_s were taken using a tube 41 mm in diameter and filled to a pressure of 30 microns of mercury. Electrode separations of 5 and 10 cm were used for the two curves. The values of V_s for the upper curve of Fig. 4 were measured using a tube filled to a pressure of 49 microns of mercury and with a 10-cm electrode separation. This tube was also 41 mm in diameter.

The dotted lines of Fig. 4 are calculated values of V_s for the gap widths and pressures shown. In making such calculations it is necessary to assume some value for the potential drop in the wall of the discharge tube. However, the data of the two lower curves make it possible to do this

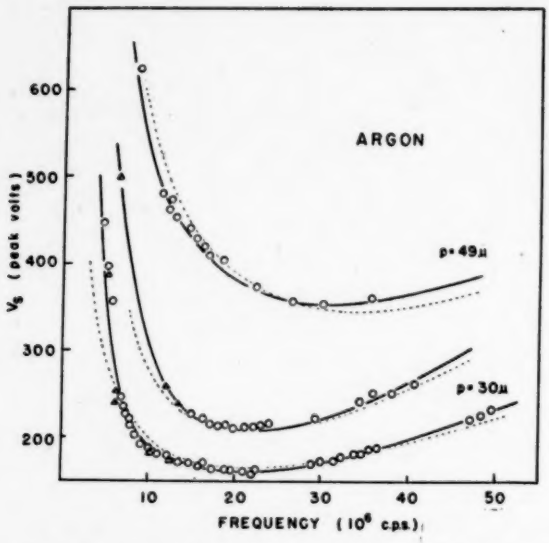

FIG. 4. Measured values of V_s, for breakdown of A, plotted against the frequency. The electrode separation was 5 cm for the bottom curve, and 10 cm for the other two. The dotted curves indicate calculated values.

since it may be assumed that each of the two values of V_s, for any one frequency, is equal to the potential drop in the gas plus the drop in the tube wall, and that the drop in the wall is the same for each. Thus, for any frequency, two equations may be set up and the solution will give the drop in glass and also the field in the gas for breakdown. This calculation was made for several frequencies and gave an average value of 120 v for the potential drop in the tube wall. This value was used in calculating the data shown by the dotted lines.

The experimental data shown in Fig. 4 are in good agreement with the calculated values except at frequencies less than about 10×10^6 c.p.s. The shape of the experimental curves is about that predicted and for the higher frequencies the measured values of V_s differ from the calculated values by no more than the experimental error.

The V_s-f curves of Fig. 5 are for xenon at a pressure of 20 microns. Two discharge tubes were used. The data of the upper curve were taken with a tube 22 cm in diameter and with a 10-cm electrode separation. The data of the lower curve were taken using a tube 41 mm in diameter and with 5-cm electrode separation. The dotted line shows the calculated values of V_s for the larger tube. Here also it was assumed that the potential drop in the tube wall was 120 v. Since measurements were taken for only one electrode separation for the smaller tube it was not possible to calculate the potential drop in the tube wall. Therefore, the calculated value of E was assumed for a frequency of 30×10^6 c.p.s. and the potential drop in the tube wall was calculated upon this assumption. This gave 150 v for the potential drop in the tube wall for this frequency. This value was used in calculating the values of V_s shown by the dotted curve for the smaller tube.

The data of Fig. 5 are not in as good agreement with the calculated values as is the case for argon. In xenon, at this pressure, the minimum value of E should fall at a frequency of about 22×10^6 c.p.s. and should be about 10 v cm^{-1}. However, the discrepancy may be due, in part, to the fact that two tubes of different diameters were used in taking the data. Under such conditions the non-uniformity of the fields in the gas, due to the external electrodes, will be different for the two cases.

The few data taken with the Navy TDE oscillator were used as a check on the data taken with the Hartley type oscillators since these oscillators would be expected to have a considerable harmonic component. Such harmonics would be particularly troublesome in taking values of V_s which lie along the steeply rising part of the V_s-f curve. However, the values of V_s measured with the essentially harmonic free oscillator do not differ greatly from those taken with the Hartley oscillators.

4. DISCUSSION

It was mentioned above that it is possible, on the basis of the proposed theory, to calculate the minimum value of V_s for the V_s-p curves as measured by Thomson and others and also the gas pressure at which the minimum occurs. This can be done for any gas, gap width, and frequency of the applied field.

TABLE I.

Frequency (10^6 c.p.s.)	$(V_s)_{min}$ Calculated	$(V_s)_{min}$ Thomson	Pressure Calculated	Pressure Thomson
99.0	112.2 volts	138 volts	177 microns	360 microns
77.1	87.4	104	135	340
65.4	78.8	99	117	300
49.5	56.1	100	70	340
15.6	23.0	112	64	400

This calculation has been made for hydrogen and several frequencies of the applied field. Table I gives the calculated values of V_s, minimum, for a gap width of 2.58 cm as was used by Thomson. Also the table shows the experimentally determined values of Thomson. The agreement is fairly good for the higher frequencies. Thomson also measured the minimum value of V_s for a number of frequencies which were lower than any shown in Table I. For those cases the calculated values of V_s are much lower than the measured values. This may mean that some mechanism, other than the one considered here, determines breakdown at the lower frequencies.

The gas pressure at which V_s is a minimum for the Thomson V_s-p curves has been calculated for hydrogen and for the frequencies used by Thomson. These results, with Thomson's measured values, are shown in Table I. In making the calculations it was assumed that the molecular free path for hydrogen was 18.3×10^{-6} cm at 760 mm of mercury and 0°C. The agreement is poor for all frequencies used by Thomson. However, as shown by Fig. 3, the minima in the V_s-p curves are broad and it would be difficult, experimentally, to determine the pressure at the minimum.

Brasefield[3] measured the conductivity of hydrogen for one frequency and after breakdown, as a function of the pressure. He found that for any one frequency there was a pressure for which the conductivity was a maximum. It has been remarked that the observed maxima, in the values of the conductivity, should occur for those pressures which give the minima in the V_s-p curves for the same gas and frequency.[3,4] It is observed that, for values of the applied potential slightly greater than V_s, discharges in argon, krypton, and xenon are brightest when the pressure is about that corresponding to the minimum breakdown potential for the frequency used. If it is assumed that the maximum conductivity and the minimum in the V_s-p curves fall at the same gas pressure for any one frequency of the applied potential, the pressures for maximum conductivity in hydrogen at the frequencies used by Brasefield can be calculated by the method used above in calculating the pressures at minimum breakdown potentials. Table II shows the calculated values and Brasefield's experimental results. Here the agreement is fair for the higher frequencies and is poor for frequencies below about 15×10^6 c.p.s. However, the agreement here is better than was the case for Thomson's data.

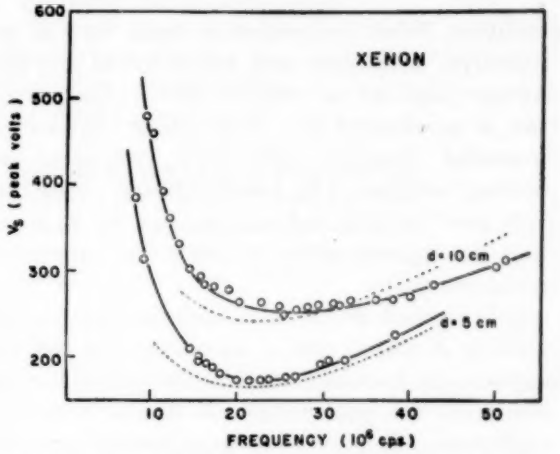

FIG. 5. Measured values of V_s, for breakdown of Xe at 20μ pressure, plotted against the frequency. Electrode separations of 5 and 10 cm were used. The dotted curves indicate calculated values.

The value of the electron mean free path used in calculating E and f was that given by the kinetic theory. This can hardly be correct and the good agreement between the calculated and experimental values, as shown in Figs. 4 and 5, is most likely fortuitous. The kinetic theory yields a value for the mean free path which is independent of the electron energy. The Ramsauer type experiments indicate that the electron mean free path is a function of the electron energy.[5] In the case considered here the electron energy varies from zero to the ionizing energy. It is difficult to estimate the mean free path for this

TABLE II.

Frequency (10^6 c.p.s.)	Pressure	
	Calculated	Brasefield
20	28.6 microns	20 microns
15	21.0	15
12	15.9	30
10	14.0	35
5	7.2	10

[3] C. J. Brasefield, Phys. Rev. **35**, 1073 (1930).
[4] H. Steinhauser, Zeits. f. Physik **54**, 788 (1929).
[5] Reference 1, p. 649.

condition. What is needed is some sort of an "effective" mean free path which would give the average path for an electron which starts from rest, is accelerated in a field which varies in a sinusoidal manner, and then undergoes an ionizing collision. The kinetic theory mean free path used in these calculations can be no more than an approximation to such an "effective" mean free path.

It is implied, in the assumptions made in calculating E and f, that if an electron in the gas acquires the ionizing energy at the end of a mean free path the probability of its ionizing is a maximum. This is also questionable. Smith[6] found that the efficiency of ionization, for electrons in argon, increased with increasing electron energies up to electron energies of several times the ionizing energy. Thus, for argon, the probability of ionization increases quite rapidly with increasing electron energies for energies slightly above the ionizing energy of 15.69 v. This would also be expected in xenon. Thus it may be, for breakdown in high frequency fields, that the large increase in electron density which breakdown demands comes when the electron acquires energy at the end of a mean free path somewhat above that given by the expression $\frac{1}{2}mv^2=eV_i$. This would mean that the calculated values of E and f, as given here, are too small.

It is assumed, in comparing the calculated and experimental values of V_s, that the electrical field in the gas is uniform under the conditions of this experiment. That is, it is assumed that the field is given by dividing the applied potential by the distance between the electrodes. However, with external electrodes, such as used here, the field cannot be uniform and a distortion of the field along the discharge tube axis must be expected. Thus at some point along the axis the field should be greater than estimated. The breakdown of the gas would then be expected to start at the point where the field is the greatest. Once breakdown starts at any point in the tube, space charge would be expected to cause the rapid propagation of the breakdown throughout the tube.

This assumption of a uniform field makes the measured value of V_s too small. It is likely, since no space charge would be expected before breakdown, that the measured value of V_s is correct to a first-order approximation. Thus it appears that the assumptions that the field is uniform and that breakdown occurs for electron energies given by $\frac{1}{2}mv^2=eV_i$ may be only approximations, and that the two approximations tend to offset each other and thus make the calculations appear better than they actually are.

The author wishes to acknowledge that the discharge tubes used were filled by Mr. Charles Hendee, and that the Hartley type oscillators were designed and built by Mr. John Frank. Also many helpful discussions were held with Dr. Richard Nelson and Professor Walter S. Huxford during the course of the experiments.

[6] P. T. Smith, Phys. Rev. **36**, 1293 (1930).

Saturation Effect in Microwave Absorption of Ammonia*

ROBERT L. CARTER AND WILLIAM V. SMITH
Department of Physics, Duke University, Durham, North Carolina

(Received January 12, 1948)

Attenuation and line width for the NH_3 3,3 line are measured as a function of the intensity of radiation incident on the gas for several different pressures. The saturation effects are found to be proportional to the power and inversely proportional to the square of the line width, in agreement with theory. An estimate of the collision cross section given by saturation data is in agreement with that deduced from collision broadening data.

I. INTRODUCTION

THE use of vacuum tube oscillators as high intensity monochromatic sources for certain types of spectra has initiated investigations of "saturation" phenomena in which absorption or induced emission varies with intensity of the incident radiation, since the latter can be made sufficiently intense to disturb the thermal equilibrium of the irradiated material. While the earliest experiments of this sort are in the field of nuclear induction in the solid state,[1] recent experiments by Townes[2] have shown that similar effects exist in molecular absorption in the microwave region. The only molecule quantitatively studied so far is ammonia, and, more specifically, the 3,3 member of the inversion spectrum at 23,870 megacycles, as this line, with an absorption for plane waves of about 8×10^{-4} cm^{-1} is the strongest yet discovered in the microwave region.[2,3] In spite of this high absorption, experimental results of different investigators are in marked disagreement as to the amount of broadening accompanying saturation.[2,4-6] In our own investigations we find that an underestimation of certain systematic errors masked a broadening which we now find to be observable, but still somewhat less than quoted by Townes. Our present observations taken before the publication of Pond and Cannon's letter[6] agree with their data, and extend the data to higher pressures. A quantitative agreement with theory is now found.**

II. THEORY

Of the several possible mechanisms proposed by Townes, which might lead to saturation, the only one now believed to be operative is the disturbance of the distribution of molecules between the ground and excited states.[7] This arises when the rate of absorption of energy per molecule in the ground state becomes comparable with the collision rate between molecules. The resulting modification of Van Vleck and Weisskopf's relation[8] for the absorption of pressure broadened lines under conditions where the line width is small compared to the frequency can be shown to be

$$\gamma(\nu)=\frac{\gamma_0}{\left(\frac{\nu-\nu_0}{\Delta\nu_0}\right)^2+1+\frac{AP}{(\Delta\nu_0)^2}} \tag{1}$$

with the line width at half-power

$$2\Delta\nu=2\Delta\nu_0\left(1+\frac{AP}{(\Delta\nu_0)^2}\right)^{\frac{1}{2}}, \tag{2}$$

where

γ_0 = peak unsaturated attenuation = attenuation at resonant frequency, ν_0, for low input power

$$=\frac{8\pi^2\nu^2 n_0}{3ckT\Delta\nu_0}|\mu_{jk}|^2 \text{ in cm}^{-1},$$

* The research described in this report was supported by Contract No. W-28-099-ac125 with the Army Air Forces, Watson Laboratories, Air Materiel Command.

[1] F. Bloch, Phys. Rev. **70**, 460 (1946); F. Bloch, W. W. Hansen, and M. Packard, Phys. Rev. **70**, 474 (1946); Purcell, Torrey, and Pound, Phys. Rev. **69**, 37 (1946).

[2] H. Townes, Phys. Rev. **70**, 665 (1946).

[3] B. Bleaney and R. P. Penrose, Proc. Roy. Soc. **189**, 358 (1947).

[4] W. Gordy and M. Kessler, Phys. Rev. **71**, 640 (1947).

[5] W. V. Smith and R. L. Carter, Phys. Rev. **72**, 638 (1947).

[6] T. A. Pond and W. F. Cannon, Phys. Rev. **72**, 1121 (1947).

** Subsequent to submission of this manuscript a very thorough paper on saturation in ammonia by Bleaney and Penrose, Proc. Phys. Soc. **60**, 83 (1948), has appeared. Their results are in substantial agreement with ours.

[7] J. Schwinger and R. Karplus, private communication.

[8] J. H. Van Vleck and V. F. Weisskopf, Rev. Mod. Phys. **17**, 227 (1945).

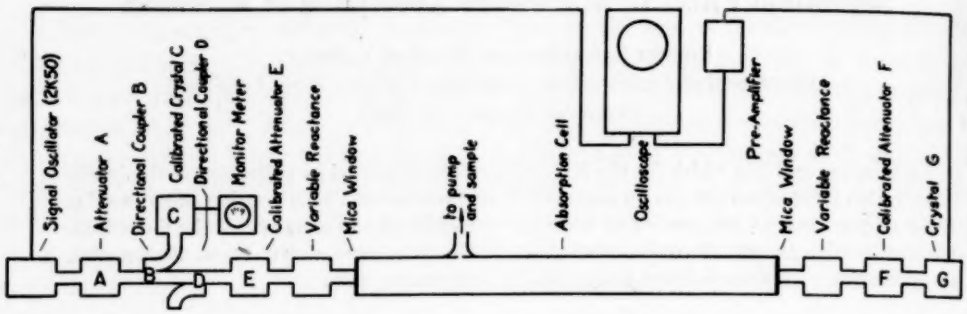

FIG. 1. Block diagram of apparatus.

$2\Delta\nu_0$ = half-power line width at low input power,
n_0 = number of molecules in the 3,3 ground state for thermal equilibrium,
P = input power in ergs/cm² sec.,

$$|\mu_{ij}|^2=\frac{K^2}{J(J+1)}\mu^2 \text{ where } K=J=3,$$

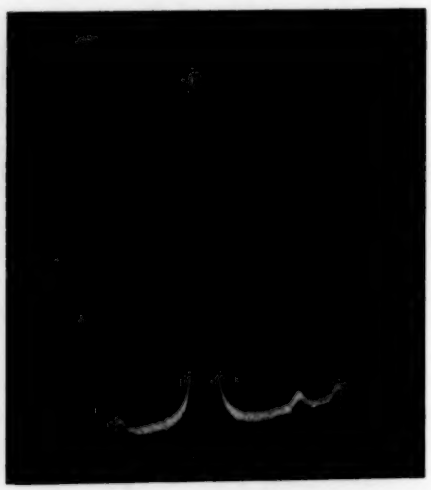

(a)

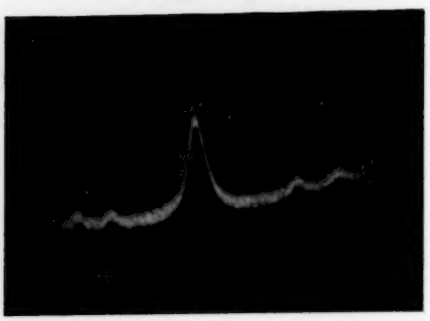

(b)

FIG. 2. Ammonia 3,3 line with input to crystal 0.15×10^{-6} watt $2\Delta\nu_0 \leqq 300$ kc. (a) Input to cell $=1.5\times10^{-6}$ watt; (b) input to cell $=150\times10^{-6}$ watt.

μ = dipole moment $=1.45\times10^{-18}$ e.s.u.,

$$A=\frac{8\pi|\mu_{ij}|^2}{3ch^2}=1.02\times10^{7},^{***}$$

h, c, k, T = Planck's constant, velocity of light, Boltzmann constant, and absolute temperature, respectively.

Expressions (1) and (2) assume a non-degenerate line with pressure broadening and saturation the sole causes for line width. Constant power along the guide and over the cross section is also assumed. The first condition is approximately attained experimentally, but not the second.

Averaging over the guide cross section and replacing the unsaturated absorption at ν_0 by $(\lambda_g\gamma_0/\lambda)$ replaces Eqs. (1) and (2) by

$$\langle\gamma(\nu)\rangle_{Av}=\frac{\gamma_0}{\alpha}\left\{1-1\Big/\left(1+\frac{2\alpha}{((\nu-\nu_0)/\Delta\nu_0)^2+1}\right)^{\frac{1}{2}}\right\}\frac{\lambda g}{\lambda}, \quad (3)$$

and

$$\langle 2\Delta\nu\rangle_{Av}=2\Delta\nu_0\left(\frac{2\alpha^2-\alpha-1+(1+2\alpha)^{\frac{1}{2}}(1+2\alpha)}{1+3\alpha-(1+2\alpha)^{\frac{1}{2}}}\right)^{\frac{1}{2}}, \quad (4)$$

where $\alpha=[A\bar{P}/(\Delta\nu_0)^2](\lambda g/\lambda)$ and $\bar{P}$ is the average power density over the guide cross sections.

Despite the complicated forms of Eqs. (3) and (4), they differ only to a minor extent from the unaveraged expressions, as is evident from

*** This value neglects averaging over the Zeeman components of the line. Proper averaging yields more complicated expressions than those used here,[7] and, to a first approximation, gives a value of $A=1.75\times10^{7}$.

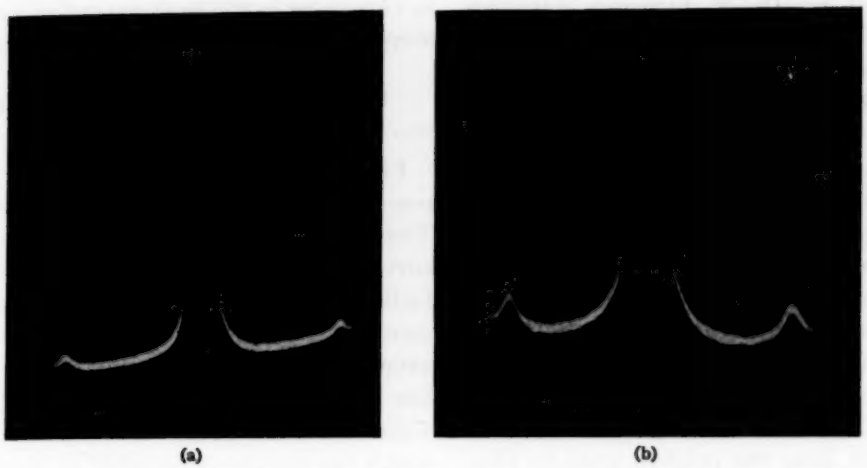

(a) (b)

FIG. 3. Ammonia 3,3 line with gain adjusted for approximately constant height; $2\Delta\nu_0 \cong 300$ kc. (a) Input to cell $= 1.5 \times 10^{-6}$ watt; (b) input to cell $= 150 \times 10^{-6}$ watt.

Figs. 4 and 5. If the average power density is used in Eqs. (1) and (2), the ratio of (1) to (3) is unity at both low and high powers, while the ratio of (2) to (4) is unity at low powers and $(\frac{3}{2})^{\frac{1}{2}}$ at high powers. This small variation is reasonable, since in the average the low power regions of the guide cross section contribute little to the power absorbed per unit length. It should be noted that variation in power over the guide length is a more serious factor, as it is the relative power absorbed per unit length that counts in the total observed attenuation. Indeed, this power variation along the guide length probably accounts for one of the failures to observe saturation.[4] The cell length of 2 meters used in the present work is short enough to avoid this difficulty, as its attenuation in the absence of ammonia is only 1 decibel.

III. EXPERIMENTAL METHOD

The apparatus used is shown schematically in Fig. 1. The signal oscillator was a Western Electric 2K50 reflex klystron. A saw-tooth voltage derived from a DuMont oscilloscope was applied to the reflector of the tube. The voltage used was sufficient to sweep the tube about 10 megacycles, over which range the variation in output power was very small, as the 2K50 reflector modes are about 100 megacycles wide. Attenuator A was adjusted to maintain a constant reading on crystal C, which was calibrated against a thermistor. The small reflections set up by the mica windows of the cell were balanced out by variable reactances. The quality of match was checked both by minimizing reflections observed at directional coupler D, and by obtaining a smooth mode presentation on the scope which was connected to a crystal G through a preamplifier. The crystal also was tuned to eliminate reflections. In general, calibrated attenuators E and F were varied together to vary power input to the cell while maintaining the input to crystal G at a constant level in the region where the crystal response was proportional to power, thus eliminating any possibility that variation in line shape might result from crystal saturation. An additional result of the use of constant crystal input was a constant noise level and constant (small) curvature of the base line.

The preamplifier and oscilloscope have a flat response from 10 to 100,000 cycles. As a sweep frequency of 120 cycles was used, in general, no distortion was present in reproducing absorption lines covering from 1 percent to 10 percent of the sweep length. Variation in sweep speed checked the flatness of the response.

We have made no direct pressure measurements, preferring to present our data as a function of the unsaturated line width $2\Delta\nu_0$, which was accurately measured by photographing both the main line and the fine structure, the latter establishing the frequency scale.[9]

Both the 2K50 and the preamplifier were battery operated to minimize hum and fluctua-

tions. The cell length of 2 meters gave an attenuation in the absence of ammonia of only one decibel, so that the power could be considered sensibly constant over the cell length. The cell cross section was 10.7×4.3 mm.

The data were obtained as 35-mm photographs of a five-inch oscilloscope screen; they were examined in enlarged projection. Typical pictures are shown in Figs. 2 and 3. The crystal input power was the same for Figs. 2a and 2b, while the power through the cell was 100 times as large for 2b as 2a. The factor of difference in peak attenuation is clearly seen, while the factor of differences in line width can only be measured by enlargement from the original film. In Figs. 3a and 3b, attenuator F is maintained constant while the oscilloscope gain is varied to maintain constant line height. There is the same factor of 100 in input power to the cell, and here the change in line width is evident although changes in curvature in the background make the measurements uncertain by about 20 percent.

IV. EXPERIMENTAL RESULTS AND COMPARISON WITH THEORY

Figure 4 shows a plot of $\gamma(\nu_0)$ *versus* input power P to the cell for three different pressures. The vertical scale is arbitrary, the different curves being displaced relative to one another to facilitate comparison. Each curve approaches a constant asymptote at low input powers. (The asymptotes for the different curves differ by a few percent from the theoretically constant value.) For curve C, the highest pressure at which the fine structure could be clearly resolved, the asymptote is taken as 7.7×10^{-4} cm^{-1}, less by 10 percent than the value of 8.6×10^{-4} cm^{-1} which we measured independently at higher pressures with an 8-meter cell. The departure of absorbed power from linearity with γ, while

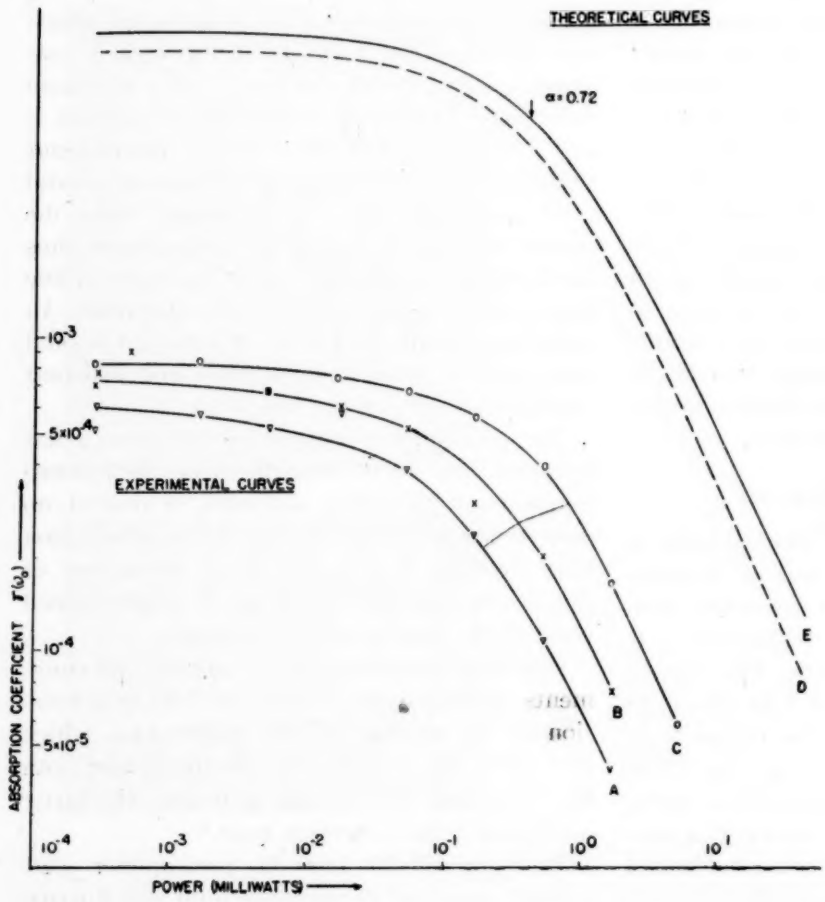

FIG. 4. Peak attenuation of $N^{14}H_3$ 3,3 line as function of power. Experimental curves (A, B, and C) taken at successively higher pressures. Theoretical curves were fitted to C at $\gamma/\gamma_0=0.5$ and displaced vertically. Curves D and E were obtained from unaveraged theory (Eq. (1)) and averaged theory (Eq. (3)), respectively.

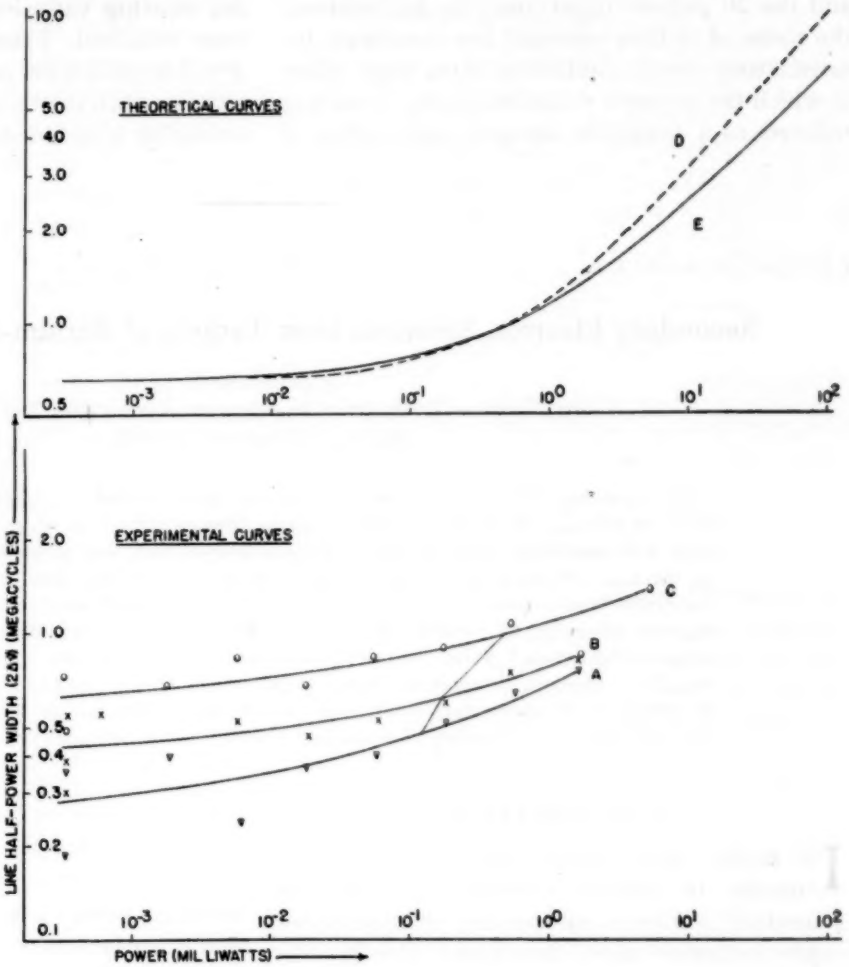

FIG. 5. Line width of the $N^{15}H_3$ 3,3 line as a function of power. Experimental curves *A*, *B*, and *C* correspond to curves *A*, *B*, and *C* of Fig. 4. Theoretical curves were fitted to *C* at $\gamma/\gamma_0=0.5$. Curves *D* and *E* were obtained from unaveraged theory (Eq. (2)) and averaged theory (Eq. (4)), respectively.

small for these values of γ, has been corrected for in the data. Also plotted on the graph are theoretical curves *D* and *E*, fitted to curve *C* at the observed half-power point, and displaced vertically to facilitate comparison.

It is clear that a combination of vertical and horizontal displacements of the curves *A* and *B* will superpose both on *C* within the 20 percent error estimated in our observations. To this accuracy, the data can also be fitted to either theoretical curve, although the averaged curve *E* will be taken as correct.

Since the theoretical curves are functions of the ratio $[P/(\Delta\nu_0)^2]$, it is clear that the horizontal displacements of 4*db* and 6*db* (2.5 and 4 in power ratios) necessary to superpose *A* and *B* on *C* should correspond to ratios of line width of 1.6 and 2, respectively. Examining Fig. 5, in which a similar comparison of experiment with theory is made for the line widths, the respective ratios are found to be 1.6 and 2.2. Since the line widths are estimated to be accurate to only 20 percent, the agreement with theory is more than satisfactory. That the observed scatter in the data at the low input power end of the graph is more than this 20 percent estimate is due to the fact that the data were taken with the system sealed off from the pumps, and ammonia absorbed on the walls was released during the run, which was taken from low to high powers and back to low in interlocking steps; an average of the data thus represents a run at constant pressure.

Finally, the constant *A* was calculated from the data of Fig. 4 and the corresponding half-power line width at low powers obtained from Fig. 5. The value of *A* is very sensitive to $\Delta\nu_0$,

and the 20 percent uncertainty in $\Delta\nu_0$ rendered the value of A thus obtained too inaccurate for satisfactory check. Additional data were taken in which the pressure variation during a run was reduced to a negligible amount, and values of $\Delta\nu_0$ showing variations of less than 10 percent were obtained. From these data a value of $A=(1.6\pm0.3)\times10^7$ cm²/erg sec. was calculated, agreeing with the theoretical value when Zeeman averaging is included.

PHYSICAL REVIEW VOLUME 73, NUMBER 9 MAY 1, 1948

Secondary Electron Emission from Targets of Barium-Strontium Oxide

J. B. JOHNSON
Bell Telephone Laboratories, Incorporated, Murray Hill, New Jersey
(Received December 22, 1947)

The secondary electron yield of (BaSr)O has been studied, as induced by microsecond pulses of primary electrons with energy up to 2000 ev. The δ *vs.* V_p curves have the usual form, with maximum δ near 1200 ev. At room temperature, and before surface charges build up, the δ_{max} is of the order 12, but it may be reduced to 6 by less than 0.1 atomic layer of Ba evaporated from a nearby thermionic cathode. With increasing temperature δ decreases to an apparent minimum at ~600°C. With the onset of d.c. thermionic emission the total yield increases during each pulse, in rough proportion to the thermionic current. The increase is thought to represent a transient change in thermionic activity caused by the bombardment. No change with temperature is observed for the energy distribution of the true secondaries. The possibility of field-enhanced secondary emission at low temperatures is considered.

I. INTRODUCTION

IN earlier short notes and abstracts some results of pulsed measurements on the secondary emission properties of thermionic oxide cathodes were described.[1] Briefly, the results were these: The yield δ of secondary electrons from oxide cathodes is relatively high, from 4 to 10 at the optimum voltage, depending on various conditions. Near room temperature the δ tends to be high, decreasing slowly with temperature up to 600°C. In the temperature region where thermionic emission is appreciable, an increase in the thermionic emission occurs during and shortly after the bombardment with primary electrons and this emission is superimposed on the secondary current.

These measurements have now been amplified and extended and will be described more fully in this paper. The earlier conclusions are supported in all essentials, particularly as regards the presence of the bombardment-enhanced thermionic emission. The principal results of the measurements on secondary emission are given in Section 4.0 of the paper, which deals with the influence of the various parameters such as primary energy, temperature, current density, and other factors on the secondary emission ratio of the oxide target. The test circuit and the general characteristics of the experimental tubes are dealt with in Section 2.0. In Section 3.0 are described the specific characteristics of a particular tube and target from which the typical results in Section 4.0 were derived, involving the determination of temperature, thermionic activity, and the possible limitations imposed on the measurements by space charge in the tube. Matters which do not bear directly on the main results of Section 4.0 but which are still of considerable interest are dealt with in the last four sections. These include the effects of barium poisoning, the primary energy at which $\delta=1$, the energy of the secondary electrons, and the possible effects of high internal field in the target.

Two other reports on the secondary yield of oxide cathodes have appeared in recent years. The first, by Morgulis and Nagorsky,[2] presents

[1] J. B. Johnson, Phys. Rev. 66, 352 (1944); Phys. Rev. 69, 693 (1946); Phys. Rev. 69, 702 (1946).

evidence obtained by a d.c. method that the secondary yield from the oxide cathode increases exponentially with temperature from its room temperature value to the point where the secondary emission is eventually swamped by the thermionic emission. Later work by Pomerantz,[3] using in part a technique of microsecond pulsing very similar to that of the present work, supports the conclusions of Morgulis and Nagorsky. Extrapolation to higher temperatures indicated that a very high secondary yield should be reached. In the work to be reported on here the results and interpretations differ in several respects from those of the other authors, and are therefore presented in considerable detail.

II. APPARATUS

2.1 Tube Structure

In order to have a set of consistent data, nearly all of the experiments reported here have been made on a single tube, MN-74. All of the phenomena have been observed on other tubes, so that they are not peculiar to this one specimen of tube or target, but in the present tube the target is even closer to the collector electrode than in previous tubes, in order to reduce the effect of space charge. Figure 1 shows a scale drawing of part of the tube, with electron gun, the two perforated copper disks serving as anode and collector, and the oxide-coated nickel cup serving as the target. The gun has a cathode with a standard oxide coating on grade A nickel, indirect heater, and a cap serving as grid for turning the electron beam on and off. The gun was designed by Dr. A. L. Samuel for another purpose, on the basis that the electron beam would have a cross-over near the gap between the copper disks independent of voltage between cathode and anode over a wide range. The target is a cup of grade A nickel $\frac{1}{4}$-inch in diameter. It is coated on the flat face with the standard "double carbonate"[4] coating of $(BaSr)CO_3$ about 0.001 in. thick. In pumping, the tube was baked at about 500°C, the electrodes were well outgassed with high frequency, the cathodes activated, the KIC getter fired, and the tube sealed off.

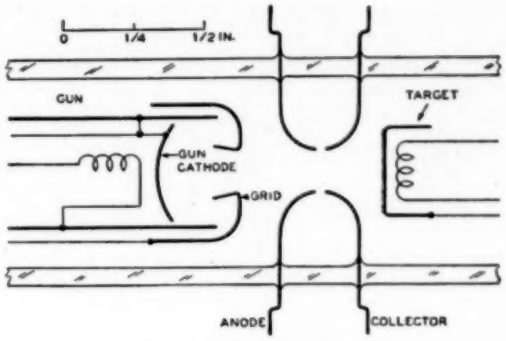

FIG. 1. Tube structure.

2.2 The Circuit

The testing circuit for pulsed operation is shown schematically in Fig. 2. The gun cathode is run at a potential V_p negative to ground in the range 0–2000 volts. Normally the gun is biased beyond cut-off, but is turned on by pulses of positive voltage from the pulser P, smoothly adjustable in voltage, and variable in duration from about 0.2 to 30 microseconds with a repetition rate to 500 to 4000 pulses per second. The collector is at the potential V_c, the gun anode is at +22 volts with respect to the collector to keep secondaries from the anode out of the collector space. For measuring the primary electron current, i_p, the target is made 22 volts more positive than the collector as shown in the diagram. The primary electrons then strike the target with energy which exceeds V_p by V_c+22 volts. This increase in energy does not alter the primary current appreciably and therefore makes no essential difference in the measurements. The effect of high energy secondaries which escape

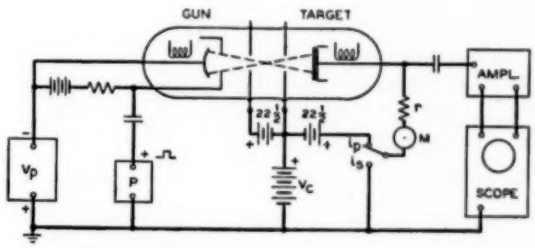

FIG. 2. Secondary emission circuit.

[3] N. Morgulis and A. Nagorsky, J. Tech. Phys. U.S.S.R. 5, 848 (1938).
[3] M. A. Pomerantz, J. Frank. Inst. **241**, 414 (1946); *ibid.* **242**, 41 (1946); Phys. Rev. **70**, 33 (1946).
[4] 45 percent $BaCO_3$, 55 percent $SrCO_3$, by weight, suspended in amyl acetate with a nitrocellulose binder.

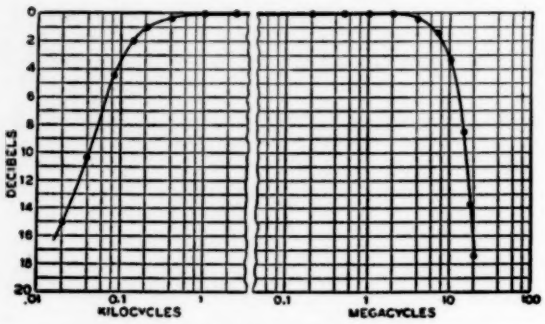

FIG. 3. Amplifier characteristic.

the target against the retarding potential of 22 volts, and so affect the measurement of the primary current, will be discussed later. When with the key in the position i_s the target is connected effectively to ground, the a.c. circuit measures the excess secondary current $i_s - i_p$, while the average d.c. current including any thermionic current i_{th} is measured by the d.c. meter. The electrons then strike the target with energy V_p, and the collector is positive by the amount V_c to draw the secondary electrons from the target. The target connection includes the load resistance r of 240 ohms, and a meter so that direct current in the target circuit can be measured. By-pass condensers are provided wherever needed in the circuit, but are not individually shown in the drawing.

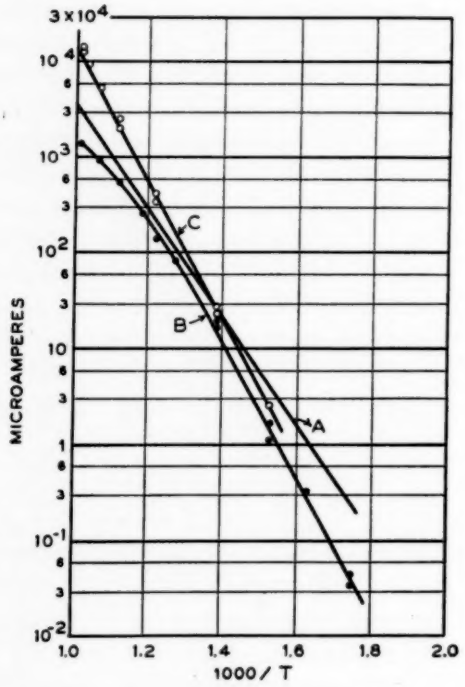

FIG. 4. Richardson plots of target: *A*—early, average, $V_c = 39$; *B*—late, $V_c = 6$; *C*—late, pulsed, $V_c = 36$.

The pulsed component of the target current is amplified and displayed on the oscilloscope. The amplifier has a flat characteristic that is down 3 db at a few hundred cycles and at 10 megacycles, about as shown in Fig. 3. It terminates in a balanced 829B tube that is resistance-capacity coupled to the plates of the 5LP1 cathode-ray tube. Its gain is such that 21μa in the target circuit gives 1.0-in. deflection on the scope at the highest gain. The gain is variable in six steps of 2.0:1.0.

The linear sweep circuit is coupled to the horizontal plates of the CR tube. The pulser, sweep, and intensity control are triggered by a synchronizer having adjustable repetition rate and phase.

III. CHARACTERISTICS OF TUBE MN-74

3.1 Temperature Calibration

For calibrating the temperature of the target a second tube was used containing only a target with as nearly as possible the same structure as that in MN-74. This target had welded to the center of its face a thermocouple of 0.003-in. Pt-PtRh wires for measurements in the low temperature range. The couple was calibrated against a mercury thermometer with the whole tube in an oven. For the high temperature range, the temperature of the target was measured by an accurate optical pyrometer, correcting for spectral emissivity of the target (taken as 0.40) and for the measured transmission of the slightly darkened glass wall (0.56). The heater power was the variable parameter in these calibrations, and the same calibrations were then assumed to hold for the target of MN-74 on the basis of equal heater power. The heater of this target was then calibrated in terms of a high resistance a.c. voltmeter which served as the indicating instrument during the tests. The temperature is probably not in error by as much as 20° in any part of the curve.

3.2 Thermionic Activity

The variation of thermionic emission of the target with temperature is shown by the Richardson plots of Fig. 4. The thermionic current

emitted from the 0.317 cm² of target area is plotted on a log scale, against 1000/T°K on a linear scale. Three experimental curves are shown: (*A*) an extensive set of readings made early in the life of the tube, with $V_c = 39$ volts; (*B*) a set made toward the end of the present tests, with V_c at 6 volts; and (*C*) a set made at the same period as *B* but with the initial current read on the 'scope as V_c of 36 volts was applied by the tap of a key. In *B*, as contrasted with *C*, the effect of decaying emission with time after applying V_c is clearly shown, especially at the higher temperatures. When δ-measurements are made the V_c has always been on for several seconds so that the lower lying curves should then more nearly apply. The thermionic currents were not extrapolated to the values for zero field by means of the log i *vs.* $E^{\frac{1}{2}}$ plot as is sometimes done. The curves show that there was a change of thermionic constants toward lower activity during the course of the tests.

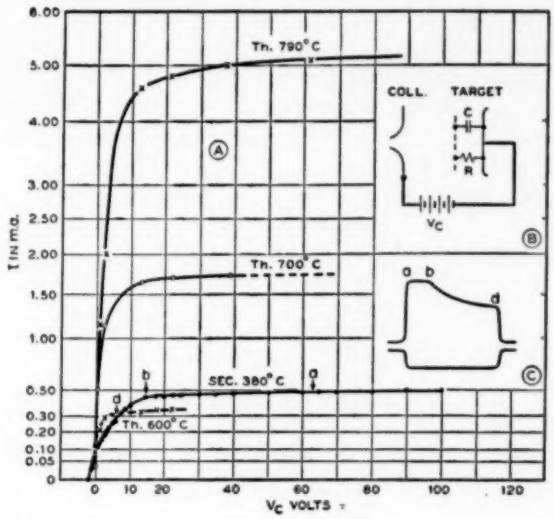

FIG. 5. Current-voltage curves, and effect of surface charge. Currents on $\frac{2}{3}$-power scale. *A*—thermionic current at 600°, 700°, 790°C. Secondary current at 380°C. Space charge limitation at lower values of collector potential V_c. *B* and *C*, discussed in text.

3.3 Space Charge Conditions

In Fig. 5A are shown curves for electron emission from the target as a function of collector voltage V_c. The currents are plotted on a $\frac{2}{3}$-power scale. The steep parts of the curves define regions where the current is limited by space charge. A log i *vs.* $E^{\frac{1}{2}}$ plot of the more nearly horizontal parts of the curves yields nearly straight lines, showing that here space charge limitation is not significant. The curves marked Th correspond to d.c. thermionic emission at the temperatures 600°, 700°, and 790°C. In the subsequent tests the thermionic emission was never larger than the highest of these, and the collector potential was usually 63 volts. The curve marked Sec. was made with pulsed secondary emission current at the temperature 380°C where the thermionic current was negligible and the secondary pulse was flat-topped. This current of 0.5 ma is larger than ever used in the δ-tests. With the aid of these curves it was arranged that space charge was never a serious limitation upon either thermionic or secondary measurements.

IV. SECONDARY EMISSION MEASUREMENTS

4.1 Procedure

The measurements of secondary yields will be described with the aid of Fig. 8, which is a series of photographs* of the patterns on the 'scope, made at various target temperatures. The pattern for 400°C may be selected. The lower trace represents a pulse of primary current set to read 0.40 in. on the screen, which corresponds to 8.5-μa beam current. The collector is 22-volts negative. Time passes from left to right and the pulse is 4.0μsec. long. The upper trace, with the axis shifted upward slightly to prevent overlap in the photograph, is the corresponding secondary current, the collector being here 63-volts positive. The gain of the amplifier is reduced by a factor 4.0 for this trace in order to keep the two traces at nearly the same size. The pulse rate was 1000 per second, with each photograph exposed here 3 seconds.

Normally the readings were made directly on the 'scope by means of an accurate reticle in front of the screen, rather than from photographs The primary pulse was set usually to give the primary deflection $D_p = 0.40$ in. by adjusting the pulser output, at some selected amplifier gain. The gain was then decreased by a factor 4.0 and the height of the secondary pulse D_s was

* In the original negatives of these oscillograms the steep side-traces are clearly visible but are too faint to reproduce in the printing. These parts have therefore been intensified without any of their features being altered.

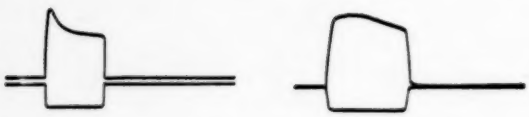

a b

FIG. 6. Charging of target surface. $V_p=1250$; $V_c=63$; $T=30°C$; $i_p=34$ μa; *a*, $t=10$ μsec.; *b*, $t=2$ μsec.

observed, giving the yield almost directly:

$$\delta=\frac{4D_s+D_p}{D_p}=\frac{4D_s}{D_p}+1=\frac{4D_s}{0.4}+1=10D_s+1.$$

In the figure just considered δ is thus 8.2. The remaining photographs of Fig. 8 were made with the target at different temperatures but otherwise under constant conditions.

The δ so measured is subject to the limitations that not all the secondaries are stopped by the retarding potential of 22 volts, and that the secondary current does not saturate sharply but varies somewhat with collector voltage as is shown later in Figs. 21–22. These conditions form part of the definition of the present δ.

4.2 δ at Low Temperatures, and the Charging Effect

At room temperature, Fig. 8, the secondary pulse is seen to reach a maximum value quickly and then to decrease with time. This is shown more clearly in Fig. 6, where the curves were made with larger beam current and with two different pulse lengths. In Fig. 6a the pulse length is 10 μsec. and a slow sweep is used, while in 6b details of the early part of the pulse are shown using a faster sweep and a 2 μsec. pulse under otherwise identical conditions. This shape of the secondary pulse arises from the fact that the coating is at this temperature a fair insulator and its surface charges positive under the bombardment when δ is greater than one.

The effect is illustrated by the curves of Fig. 5. In Fig. 5B the oxide coating is drawn as having resistance R and capacity C per unit area, between the outer surface and the base, with the potential V_c between base and collector. Initially the surface is at the same potential as the base and conditions are as indicated at *a* in Fig. 5A and 5C. As now an excess of electrons flows from the surface to the collector the capacity becomes charged, reducing the effective collector voltage until it can no longer support the full secondary current. The surface potential is then within a few volts of the collector potential and the current breaks as at *b* in Fig. 5A and 5C. The current finally decreases to an equilibrium value where it is limited chiefly by the iR drop in the coating as at *d* in the figures. The time from the beginning of the pulse to the point where the decrease begins, about 0.8 μsec. in Fig. 6b, is nearly proportional to V_c, and varies in not quite the inverse proportion with the beam current.

In this temperature range, then, the measure of δ is taken from the peak height of the secondary pulse. The curves of Fig. 8 show that the charging effect disappears rapidly as the temperature, and with it the conductivity, of the target increases. At the same time the peak height of the pulse decreases so that δ becomes less with increasing temperature.

The charging effect and the high values of δ at low temperatures could not have been observed in the d.c. method of Morgulis and Nagorsky, and were not found by Pomerantz. Possibly in the latter case the resistance of the coating was for some reason never as high as here, or the bombarded area was larger. It is not known whether the accumulation of charge and the high δ are related, but it seems quite possible either on the basis that secondary electron escape more readily from an insulator than from a better conductor[5] or that in the insulator internal fields are set up which direct the secondaries toward the outside.[6] Of the reality of the charging effect there is no question.

4.3 The Bombarded Area

The size of the target area bombarded by the beam of primary electrons needs to be known for some of the results which are to be cited. It cannot be seen directly by the fluorescence of the coating, but the charging effect gives a

[5] H. Bruining and H. J. deBoer, Physica **6**, 823 (1939); G. Maurer, Zeits. f. Physik **118**, 122 (1941); H. Bethe, Phys. Rev. **59**, 940 (1941).

[6] H. Hintenberger, Zeits. f. Physik **114**, 98 (1939); H. Bruining and H. J. deBoer, Physica **6**, 823 (1939); P. V. Timofeef and R. M. Aranovich, J. Tech. Phys. U.S.S.R. **10**, 32 (1940); D. V. Zernov, Bull. Acad. Sc. U.S.S.R. **8**, 352 (1944).

method of estimating this area. At the point of break, as at b in Fig. 5A and 5C, the total charge on the bombarded area σ_s is

$$q=(i_s-i_p)t_b=C\sigma_s(V_a-V_b),$$

where (i_s-i_p) is the excess of secondary over primary current, t_b the time at break, V_a the initial value of collector voltage, and V_b the effective collector potential at break, usually estimated at a few volts, and C is the capacitance per cm² of the coating. (The resistance R plays only a minor role up to this stage of the process.)

For determining C, the target from another tube, similarly activated, was removed and the capacity between the base and a plate pressed lightly against the oxide was measured, with suitable precautions. It was 51 $\mu\mu$f, the capacitance C of the coating[7] being then 160 $\mu\mu$f per cm². The extent of the bombarded area σ_s was computed from a series of measurements with varied i_p and V_c, for a fixed V_p of 1250. The results are shown in Fig. 7, where σ_s is given as a function of i_p. The curve covers the whole range of beam currents used, and σ_s is always small compared to the total area of the target. The area ought not to vary in any major way with V_p.

Another method of estimating the area is furnished by the current-voltage curves of Fig. 5A, where saturation of the curve of secondary current may be compared with that for the nearly equal thermionic current at 600°C. The secondary current requires higher V_c for saturation than thermionic current of the same magnitude. This is because only a small part of the target area is bombarded by the primary electrons whereas the thermionic current comes from the whole area. A comparison of the secondary curve and the lowest thermionic curve gives a rough estimate of the area on which the primary beam impinges. Neglecting initial velocities and assuming the $\frac{3}{2}$-power law to hold, we have

$$\frac{\sigma_s}{\sigma_t}=\frac{i_s}{i_t}\left(\frac{V_t}{V_s}\right)^{\frac{3}{2}},$$

where t refers to thermionic and s to secondary

[7] The measured thickness of the coating was 0.0008 in., density 1.27, dielectric constant 3.5 at the frequency of one megacycle.

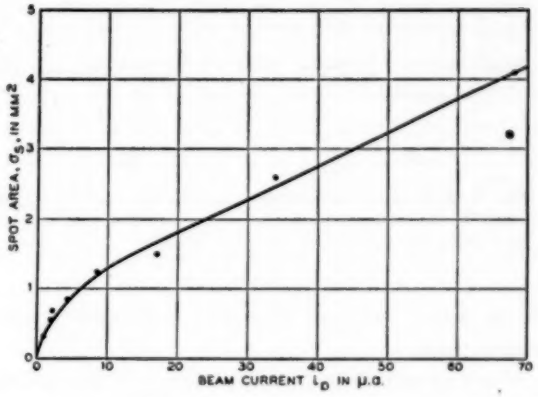

FIG. 7. Variation of spot area with beam current. $V_p=1250$. Total target area, 31.7 mm².

currents and the V's refer to saturation voltages. The total area is $\sigma_t=0.317$ cm². Values may be taken from the curves as follows: $V_t=2.5$, $V_s=15$ volts; $i_t=0.30$ ma, $i_s=0.45$ ma. This gives for the bombarded area $\sigma_s=0.032$ cm², when the primary beam current was 68 μa at 1250 volts. The large point in Fig. 7 represents this value, and it is not much out of line with the other points of the figure.

4.4 δ at Higher Temperatures, and the Bombardment-Enhanced Thermionic Emission

Returning to Fig. 8, we see that above 650°C the shape of the secondary pulse departs in a different way from that of the primary one. The charging effect has ceased, D_s rises during the pulse, and a tail remains at the end of the pulse. At the same time, thermionic current is emitted by the target and is measured separately by the d.c. meter but it does not directly appear in the

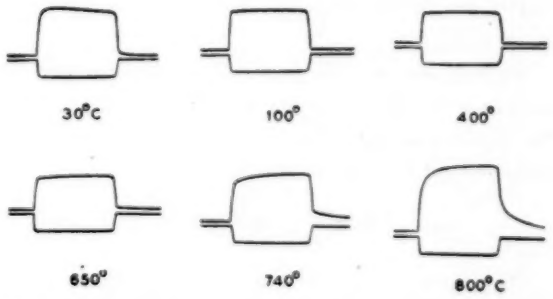

FIG. 8. Variation of yield with temperature. Lower trace, primary current; upper trace, secondary current on ½-scale. Base lines separated by vertical shift on 'scope. Pulse time $t=4$ μsec., from left to right. $i_p=8.5$ μa; $V_p=1250$.

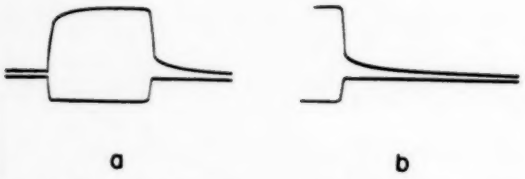

FIG. 9. Enhanced thermionic emission curves. $V_p=1250$; $T=800°C$; $i_p=17$ μa; $t=4$ μsec. Curves *b* are the same as *a*, but shifted to left to show more of tail.

D_s. In Fig. 9 the tail of a pulse is followed for a longer time.

The current that produces the tail flows after the primary pulse is over and cannot be secondary current.[8] It must be a temporary increase in the thermionic current, and presumably the increase in current *during* the pulse must be of the same origin. The emission is not caused by local heating at the surface of the target, for calculations show conclusively that heating by the bombardment must be quite negligible. Some part of the secondary emission process, rather, must change temporarily the thermionic constants of the target. An increase in the number of conduction electrons under the bombarded surface could raise the thermionic emission, though the validity of this mechanism could not be urged without careful study.

At low temperatures the δ is seen, as in Fig. 8, to decrease with increasing temperature. In the higher temperature range it becomes difficult to select by inspection the boundary between secondary emission and the added thermionic emission and to say how much each contributes to the final pulse height. Attempts were made to find the boundary by making semilog plots of the top or tail of pulses on the basis that they might be exponential with a definite intercept at zero time.

Such plots are shown in Fig. 10 for the top and tail of the pulse in Fig. 9 as measured on the photographic film. If the pulse top can be represented by the time function

$$D_s=D_0+D_1(1-e^{-\alpha t})$$

or

$$D_0+D_1-D_s=D_1e^{-\alpha t}=y,$$

then y should have an intercept D_0 when the curve is extrapolated to $t=0$. Curve *A* of Fig. 10 is such a plot for the head of the pulse. At long times the curve represents an exponential with a time constant of about 0.67 μsec. and an intercept at 0.35 in. below the top at 1.13 in. as measured on the 'scope. This suggests that the true secondary emission is given by

$$\delta_0=10(1.13-0.35)+1=8.8.$$

On the other hand, the point at 0.1 μsec. is definitely out of line and points to a higher intercept and lower δ_0. This is at the limit of resolution of the system so that one cannot say with certainty where the intercept actually is. A similar graph for the tail of the pulse is given by *B* of Fig. 10. Here the curve may represent two exponentials, one certainly with a longer time constant. The intercept may again be at 0.35 in., but the 0.1-μsec. point suggests a higher one. A number of such curves plotted for different conditions have failed to make a clear separation and thus to show how the true δ varies with temperature in the region of the enhanced thermionic emission. It may be that the curves are not truly exponential, or that higher time resolution is needed.

For the purpose of the next figure, in view of this difficulty, the highest yield during a pulse

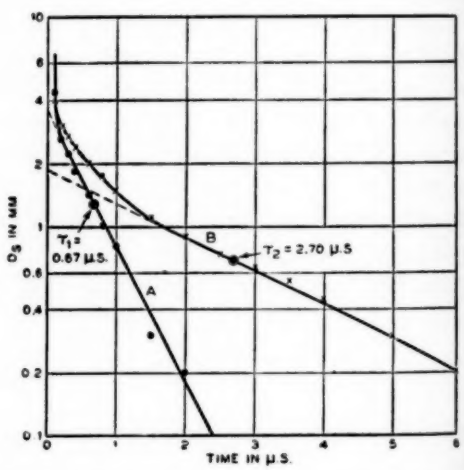

FIG. 10. Time constants and intercepts of head (*A*) and tail (*B*) of enhanced emission. Plotted from photograph. $V_p=1250$; $T=800°C$.

[8] The interval between the arrival of a primary electron and the emission of the secondaries has been estimated as follows: (4×10^{-10} sec.), F. Kirchner, Ann. d. Physik **78**, 277 (1925). Less than 2×10^{-9} sec., L. Malter, Proc. I.R.E. **29**, 578 (1941); for at least some electrons less than 5×10^{-11} sec., M. H. Greenblatt and R. H. Miller, Jr., Phys. Rev. **72**, 160 (1947).

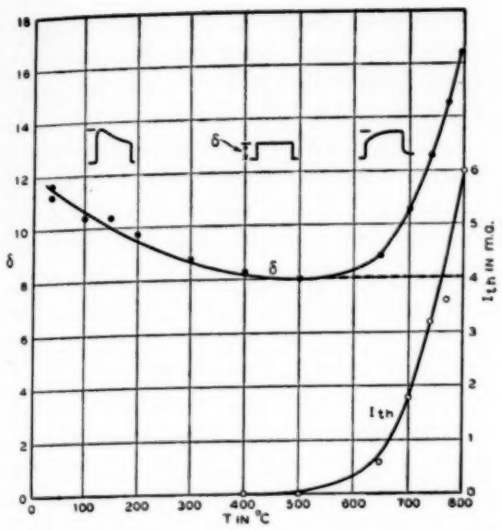

FIG. 11. Variation of yield δ with temperature. Inserts show shape of secondary current pulse for the various regions, for defining δ. $\delta_{min}=8.0$; $V_p=1250$; $i_p=8.5$ μa. D.c. thermionic current shown as I_{th}.

will be called δ. In Fig. 11 are plotted the yields given by the series of photographs from which those of Fig. 8 were selected, against target temperature. Many such runs have been made. They differ slightly one from the other but the general features are the same. The yield definitely decreases with increasing temperature until appreciable d.c. thermionic emission sets in, and then it increases rapidly. The curve I_{th} of Fig. 11 gives the thermionic current read at each time the corresponding photograph was made.

For a measure of the enhanced emission one needs to know how much of the yield is of true secondary origin. Figure 11 suggests that the true δ could continue to decrease with temperature, and the intercept extrapolations discussed above point rather to a slow increase. One expedient is to assume that δ remains constant at its minimum value, as suggested by the dashed line of Fig. 11, and to measure the increase from this value. A similar procedure was followed both by Morgulis and Nagorsky and by Pomerantz, with the minimum δ at room temperature, and they concluded that the increase in δ depends on temperature in the same way as does thermionic emission.

Data of this kind are plotted in Fig. 12. The independent variable is the current density of d.c. thermionic emission from the whole of the target, in ma/cm². The ordinates are the values of enhanced current density determined as in Fig. 11 by the difference between dashed and solid curves, with the bombarded area obtained in each case from Fig. 7. The bombarding primary current density is given by the circled points. Four different runs are included. While the points scatter somewhat, they lie along a band with 45° slope on the logarithmic scales, indicating proportionality between enhanced and steady-state thermionic emission. Over most of the range the density of bombarding current is small compared to either the steady or the enhanced emission, and for these particular conditions of primary voltage and current density the enhanced emission has about one-third the density of the steady thermionic emission.

4.5 Enhanced *vs.* Primary Current

The variation of enhanced thermionic emission with bombarding current is illustrated in Fig. 13. The four photographs were made with successively doubled beam current, reducing at the same time the gain in steps of 2.0. The curves superimpose with almost perfect fit, indicating that the enhanced emission is proportional to the bombarding current. Inspection of Fig. 7 shows that changing the current by the factor 8 changes the bombarded area by the factor 4 and therefore the current density by the factor 2.

4.6 Enhanced Current *vs.* Primary Voltage

The bombarding voltage is shown in Fig. 14 to have little effect on the enhanced emission

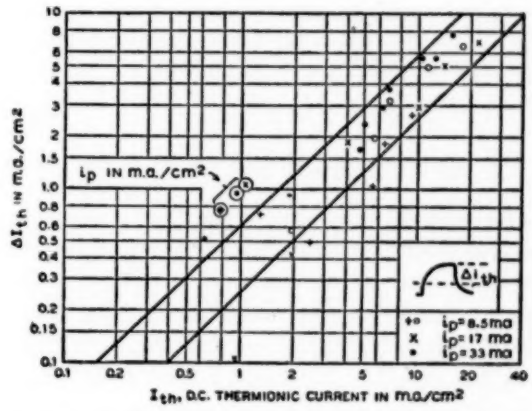

FIG. 12. Relation between normal and enhanced thermionic emission. ΔI_{th} is determined as $\delta-\delta_{min}$, as in Fig. 11. $V_p=1250$.

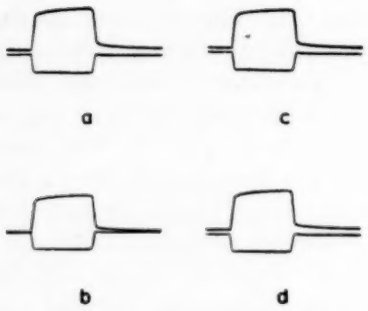

FIG. 13. Variation of enhanced emission with primary current. $V_p = 1250$; $T = 750°C$; $t = 3$ μsec.; $i_p = a$, 8.5 μa; b, 17 μa; c, 34 μa; d, 68 μa.

over a considerable range, in agreement with the conclusion of Morgulis and Nagorsky. The photographs cover the range of V_p from 2000 volts down to 50 volts. Above 200 volts the tops of the secondary pulses are surprisingly alike, although the total heights of the pulses change considerably. This suggests strongly that in this region the true secondary yield increases rapidly with V_p while the enhanced thermionic emission remains constant, and that the two yields are fundamentally different. Below 200 volts the tops of the pulses become somewhat flatter and at 50 volts the enhanced emission appears rather small.

These findings are somewhat different from those of the earlier notes[1] where the enhanced emission seemed to vary somewhat less rapidly than the first power of the voltage and as the square root of the beam current. The characteristics of both the pulse and the amplifier were then such as to introduce an apparent, sharper but false boundary between secondary and thermionic yield. The present results with the improved system are thought to be in closer accord with the true facts.

4.7 Comparison with Pomerantz

The view taken here is that true secondary emission does not increase with temperature, but that the increased current is caused by a temporary change in the thermionic constants of the oxide cathode. Pomerantz, on the other hand, finds the steeply rising yield with temperature without evidence of the delayed rise and fall of the pulse at high temperatures, and his increased yield is evident even at temperatures too low for thermionic emission. In special cases he observed the rising head and falling tail, but he supposed them to be the spurious result of space charge or other neglected factors. Assuming that in both studies the space charge problem has been adequately considered, one must conclude that the targets of the two series of measurements were somehow different although they were intended to represent about the same kind of thermionic cathode. If in the targets of Pomerantz the large yield at high temperatures is caused by enhanced thermionic emission, then this enhancement must rise and fall in a time usually too short for the time resolution of his system. If, on the other hand, in the present work there is a rise of true secondary emission in the higher temperature range, it is not large enough to be distinguished clearly from the undoubted enhanced thermionic emission. The solution to the difference is not now clear.

4.8 δ *vs.* Beam Current

It is well established that for metals the secondary current is proportional to the bombarding current over a wide range. With semiconductors and insulators the proportionality has sometimes been in question. With the targets studied here there has never been any serious departure from constancy of δ with varied beam current. Figure 15 reproduces one such run, where δ was constant within experimental errors over a range of more than 100:1 in beam current. The target was here at an intermediate temperature where the charging effect was small even at the larger currents.

4.9 δ *vs.* Primary Voltage

The maximum yield per primary electron comes at V_p about 1200 volts. In Fig. 16 are

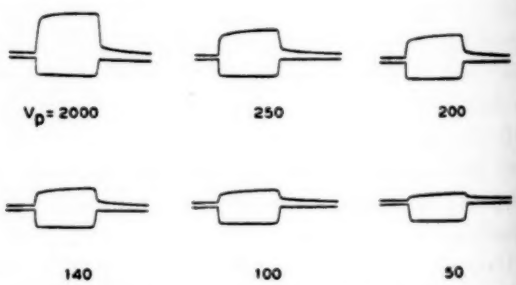

FIG. 14. Variation of enhanced emission with primary voltage. $i_p = 17$ μa; $T = 750°C$; $t = 3$ μsec.

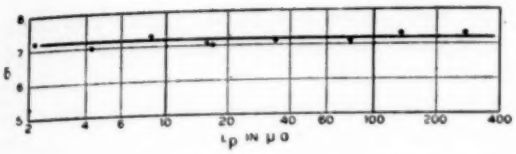

FIG. 15. Dependence of δ on beam current i_p. $V_p=1250$; $T=500°C$.

given curves A, B, and C of δ *vs.* V_p for three different temperatures, the one at 710°C being in the range where the thermionic contribution is considerable. The temperature variation is, in general, in accord with the data of Fig. 11.

It would be of interest to follow the curves beyond 2000 volts where Pomerantz finds a rapid decrease of δ, but this has not yet been done for reasons of insulation.

V. BARIUM POISONING

It is well known that the secondary emission of insulating or composite layers decreases with time when they are exposed in line-of-sight to a hot oxide cathode. Jonker and Overbeck,[9] for instance, discussed the effect in connection with targets of MgO. They assumed that deposition of metallic barium which evaporated from the oxide cathode[10] is responsible and took steps to avoid it by geometrical means.

The effect is very evident in the present tubes and has been given some consideration. When the target is heated for a short while to 700–800°C and cooled again to room temperature, curves of the form of curve A in Fig. 16 are obtained. All of the room temperature data shown so far have been obtained with the target thus relatively freshly cleaned. If now the target is exposed to the hot gun cathode for some hours the secondary yield decreases continuously. Curve D in Fig. 17 gives the secondary yield from the cold oxide target in the "poisoned" state. During the poisoning process there is no bombardment of the target and all but the gun heater voltage is turned off. The poisoning and cleaning processes seem not to depend on the presence of electric fields. When the entire system is turned off at any time during the poisoning cycle, the value of δ remains the same for a period of at least many days.

The variation of δ as the poisoning proceeds is shown by the series of photographs in Fig. 17. Here the gun cathode was continuously at operating temperature but the rest of the system was turned on only for a few minutes at a time to make the exposures. The secondary pulses look very much like the earlier ones in Fig. 8 where the target temperature was varied. Obviously δ decreases with time, and here, as in Fig. 8, the changing shape of the pulse indicates successively decreased resistivity of the oxide coating. In these respects the effects of barium poisoning are very similar to those of increasing temperature of the target.

The data of Fig. 18 show the time variation more clearly for three separate runs, where δ is plotted against time on a logarithmic scale. The target was started in the clean condition. At the end of the first run certain operations to be described were done, and the target was cleaned off for the second run. A single point marks the end of a third run of 6 hours after another clean-off. It is seen that in a period of 6 hours δ changed from about 12 to about 5 and would doubtless have reached a final value somewhat lower than this.

With this large change in δ one might expect also a change in work function of the oxide target. A number of attempts have been made to measure the change in work function, but they have been not entirely conclusive. The following is one of the best. The target was heated at 800°C for an hour and then let come to room temperature overnight. Then the target heater

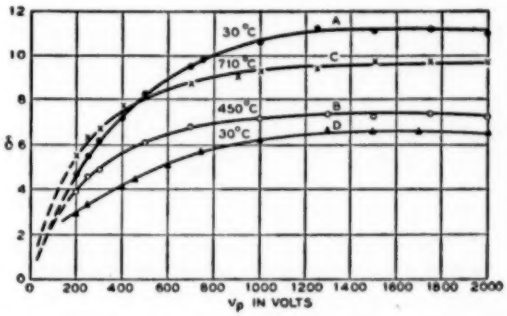

FIG. 16. Variation of δ with temperature, primary voltage, and poisoning. $i_p=8.5$ μa. A, B, C—clean target at 30°, 450°, and 710°C. D—poisoned target at 30°C.

[9] J. L. H. Jonker and A. J. W. M. v. Overbeck, W. Eng. 15, 150 (1938).
[10] J. A. Becker, Phys. Rev. 34, 1323 (1929).

was turned on and set to arrive at a final temperature of 305°C. The thermionic emission was measured once per minute, and after 15 minutes had reached the equilibrium current of 0.050 μa, representing the emission of the clean target. Now, after room temperature had again been reached, the second run of Fig. 18 was made ending at $\delta=6$. With the target in the poisoned state a second thermionic run was made in the same way, with the final emission 0.044 μa. At the end of this run with the target at 305° for half an hour the δ was measured again at room temperature. It had increased to 8.8 from 6.0 as a result of this low temperature heating, to the point of about 1-hr. poisoning. If it is assumed that the change of emission from 0.050 μa to 0.044 μa is caused by a change of work function of the target, then this change is given by

$$\Delta\varphi=\frac{2.3}{11600}T\log_{10}\frac{i_1}{i_2}=+0.005 \text{ ev.}$$

The same change of emission could also have been caused by the target temperature being lower in the second run by 1.5°. It is doubtful that the target heater could be set closer than this. Certainly no radical change in work function accompanies the change in δ from 12 to 8.8.

Secondary yield from metallic targets is known to vary with work function,[11] according to theoretical expectations,[12] but the variation is not rapid. Here the converse situation exists: large change in secondary emission and inappreciable change in work function. Some other factor than work function must here be responsible for the change in secondary yield.

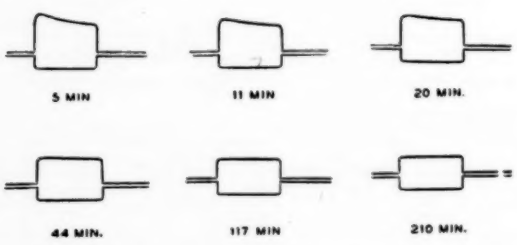

FIG. 17. Poisoning cycle. Exposure to gun cathode for various times. $t=10$ μsec.; $i_p=8.5$ μa; $V_p=1250$.

[11] K. Sixtus, Ann. d. Physik **3**, 1017 (1929); K. G. McKay, Phys. Rev. **61**, 708 (1942).
[12] D. E. Wooldridge, Phys. Rev. **56**, 562 (1939); J. H. deBoer and H. Bruining, Physica **6**, 941 (1939).

The most obvious explanation for the change in δ is that material evaporates from the gun cathode and settles on the target. Data in the files of these Laboratories indicate that the evaporated material is predominantly metallic Ba, and that at normal thermionic operating temperature and before long aging the evaporation rate is a maximum of the order 0.1 μg/cm^2 hr. The gun cathode, with the same type of coating material and base as the cathodes used in these evaporation tests, is run at a low temperature and can be assumed to have no greater evaporation rate than the figure quoted. The amount of Ba deposited on our target in a run will be estimated on the basis of this figure.

Examination of the tube structure, Fig. 1, shows that practically all of the emitting surface of the gun cathode "sees" a part of the target and all of the target "sees" the emitter through the disk apertures. Therefore, all of the evaporated material that reaches the apertures falls more or less uniformly on the target. Let S be the area of the emitter (0.80 cm^2), s the area of the target (0.317 cm^2), σ the area of the aperture (0.057 cm^2), and r the distance from emitter to aperture (1.46 cm). Let E be the rate of evaporation from the emitter (1×10^{-7} g/cm^2 hr.). Then, if the evaporation is uniform in all directions, the rate of arrival of material at the aperture from an element dS of the emitter is approximately

$$dW=E(\sigma/2\pi r^2)dS,$$

where $2\pi r^2$ is the area of the hemisphere about dS with radius r. From the whole emitter the rate is very nearly, per unit target area,

$$\frac{W}{s}=E\frac{\sigma S}{2\pi r^2 s}=1.08\times10^{-9} \text{ g/cm}^2 \text{ hr.}$$

The mass of the Ba atom is 2.3×10^{-22} g. The rate of deposit is therefore

$$W/s=0.47\times10^{13} \text{ atoms/cm}^2 \text{ hr.}$$

BaO crystallizes in the rocksalt structure with lattice spacing 5.5×10^{-8} cm. If we assume that the mixed oxide has the same lattice spacing and presents a smooth (100) plane, then the density of O atoms in this plane is

$$3.3\times10^{14} \text{ O atoms/cm}^2.$$

If each of these oxygen atoms were to adsorb one Ba atom for a monatomic layer of Ba, then the deposition of one layer would require 70 hrs. The actual surface of the target is, of course, much greater than 0.317 cm² and the density of adsorbed atoms correspondingly less. In the 6 hrs. of the longest poisoning run certainly much less than 0.1 monatomic layer was thus deposited on the target, and yet δ changed from 12 to 5.

It may be that the Ba does not remain on the surface but is absorbed into the lattice of the oxide, even at room temperature. The density of massive (BaSr)O should be 5.4. On the target is a layer 0.002 cm thick of density 1.27, so that the corresponding thickness of massive oxide would be

$$\tau = 4.7 \times 10^{-4} \text{ cm}.$$

After 6 hrs. of evaporation a cm² of this layer would have 2.85×10^{13} Ba atoms absorbed, or

$$0.6 \times 10^{17} \text{ Ba atoms/cm}^3.$$

This concentration of barium atoms, though not high, would affect the conductivity of the coating in the observed direction, and would be more likely to influence the secondary yield than the corresponding surface layer.

Evaporated metal atoms are known to have some mobility when condensed on a surface, tending to aggregate into small crystals. Yet it does not seem plausible that the Ba atoms can diffuse throughout the whole thickness of the coating at room temperature. If they migrate into a layer a few atoms deep, or the depth to which the primary electrons penetrate, then a considerable conductivity would be developed in this layer on top of the major insulating part of the coating. The surface charge could then spread to occupy a much larger area than the bombarded spot, affecting the induced surface potential in the same way as a larger body conductivity. This would delay or prevent the approach of the surface potential to that of the collector and so reduce the charging effect. At the same time the secondary emission would come largely from this more conducting part of the coating and could well be smaller than that of the more insulating oxide, in accordance with the variation of δ with temperature in the low temperature range.

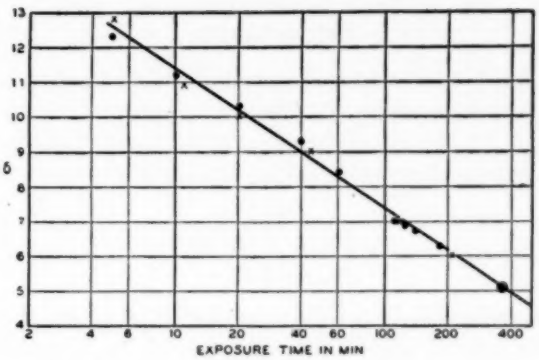

FIG. 18. Effect of exposure to gun cathode. $V_p = 1250$; Room temperature; three runs.

VI. THE POINT OF UNITY YIELD

At low values of bombarding voltage the yield as observed on the 'scope is illustrated by Fig. 19. The target is clean and at room temperature, and the curve should join curve A of Fig. 16. It is seen that δ passes through unity at about 27 volts, reaches a minimum at 7 volts, and then increases toward unity again as V_p is lowered. The values of δ are probably not very accurate over most of this range because the primary and secondary currents are not measured under nearly identical conditions in this region where V_c may be larger than V_p. Indeed, the observed δ varies considerably with V_c at low V_p.

At one point, however, where $\delta = 1.0$, the value of V_{p1} can be determined quite accurately. This is the value of V_p where the secondary deflection D_s is neither positive nor negative and the trace on the CR screen is straight with only slight kinks to mark the beginning and end of the pulse. V_{p1} can be set well within 0.1 volt for this condition with constant V_c. (Increasing V_c decreases V_{p1} because of incomplete saturation of i_s.) In this case D_p need not be measured separately, eliminating one source of error. Furthermore, there is then no net current through the coating and therefore no iR drop to consider; the face of the coating is at the same potential as the base plate.

In Fig. 20 is shown a series of values of V_{p1} for the clean target over a range of temperatures. At high temperatures the value is surprisingly low. With the "poisoned" target the values go to 35–40 volts at room temperature.

VII. ENERGY DISTRIBUTION OF THE SECONDARIES

In a gas with Maxwellian distribution of velocities of the molecules, the fraction of molecules having energy greater than a given amount E independent of direction of travel is given by[13]

$$f_e = \left(1+\frac{E}{kT}\right)e^{-(E/kT)}.$$

For thermionic electrons, a distribution curve of this type is obtained if the electrons come from a small central electrode surrounded by a large concentric sphere as collector, on which is applied the retarding potential E. The curve has a point of inflection where its derivative is highest, indicating the most probable energy of emission which in this case is greater than zero.

The central field method of retarding potential measurements has been much used because of its simplicity. The derivative of the curve gives the energy distribution even if the distribution is not Maxwellian. If, on the other hand, the electrodes have a planar structure, the retarding potential method does not give the total energy but only the energy corresponding to one of the three components of velocity. The equation is, for Maxwellian distribution,

$$f_x = e^{-(E_x/kT)}.$$

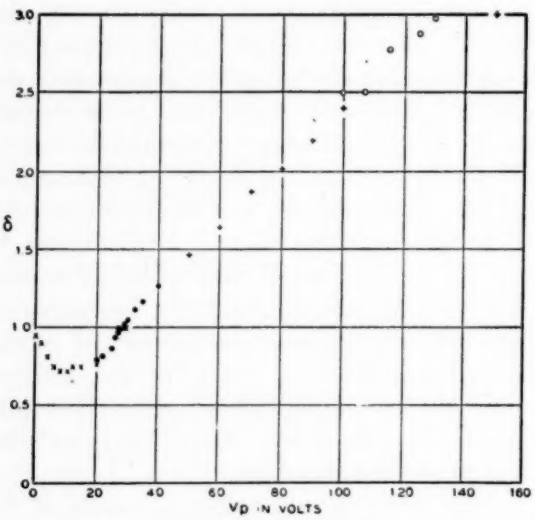

FIG. 19. Yield at low V_p—clean target, room temperature, four runs.

[13] J. H. Jeans, *Dynamical Theory of Gases* (The Cambridge University Press, New York, 1925), Section 28.

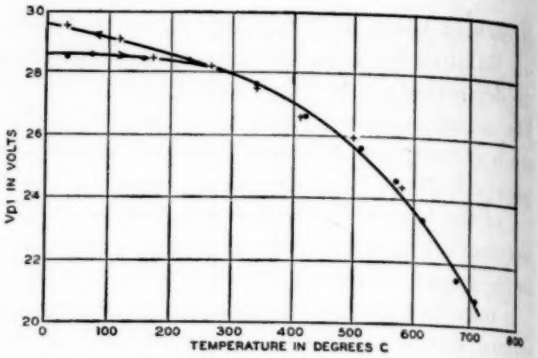

FIG. 20. Variation of V_{p1} with target temperature. Potential at which $\delta = 1.0$, with rising and falling temperature.

It has no point of inflection and its derivative is a maximum when the velocity component is zero. Retarding potential measurements on the planar structure are therefore ill-suited for giving information on the total energy distribution of electrons.

The structure of target and collector in the present tube is far from either of these simple systems. On the other hand, both Pomerantz and Morgulis and Nagorsky have published curves obtained with structures no more suitable, and concluded from these that the average energy of the secondaries decreases with increasing temperatures. For a comparison, some retarding potential curves have therefore been run on our tube.

In these measurements the target was bombarded with electrons at 1250 volts, the beam current being made so small that the secondary current was only a fraction of a microampere in order to keep down space charge and iR drop. The beam current was steady and the secondary current was measured by a sensitive d.c. meter. Potential in the range of -25 to $+25$ volts was applied to the collector. Figure 21 shows a set of results, the secondary current being plotted against collector voltage. The change of voltage scale at -5 and $+5$ volts is to be noted. For curve a the target was at room temperature, while for curve b it was at 305°C. In the latter case there was a slight thermionic emission, observed separately in the absence of bombarding current and plotted as curve c. This curve gives the contact potential difference, the collector being obout 0.8-volt negative with respect to

the target. The difference between curves *b* and *c* is plotted as curve *b'*, representing the secondary current alone at the higher temperature. In the region to the left of +0.8 volt there is no significant difference between curves *a* and *b'* for the two temperatures. The curves are not differentiated in the usual way, for reasons already discussed, but their close coincidence suggests that there is here no appreciable change in energy distribution between room temperature and 305°C.

A similar set of curves is shown in Fig. 22 for the higher temperature 380°C. Here the thermionic emission is large instead of small compared with the secondary emission. Curve *a* is for room temperature as before, curves *d* and *e* are the total and thermionic emissions, plotted on a compacted current scale, and curve *d'* is the secondary current given by the difference between *d* and *e*, plotted on the original scale. To the left of the origin there is again no significant difference between curves *a* and *d'*. Any difference caused by a change in energy distribution must lie to the right in the region where a comparatively large thermionic current flows from which the secondary current cannot accurately be separated.

Finally, for comparison with the oxide target, an uncoated Ni target was used in a tube of similar structure, MN-1. A set of δ *vs.* V_p measurements for this target is shown in Fig. 23 for room temperature and an estimated 800°C. There is no appreciable change in δ over this temperature range, and the maximum δ occurs at about 500 v, in conformity with the usual results for metallic targets. That the target is not a clean metal surface is indicated by the value of $\delta=2.2$, which is too high for a clean

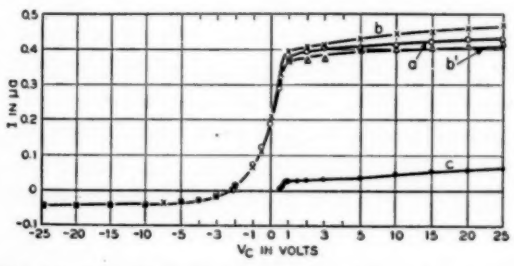

FIG. 21. Retarding potential curves. Thermionic current smaller than secondary current. $V_p=1250$; *a*, $T=30$°C; *b*, $T=305$°C; *c*, Thermionic, $T=305$°C; $b'=b-c$. Change of scale at −5 and +5 volts.

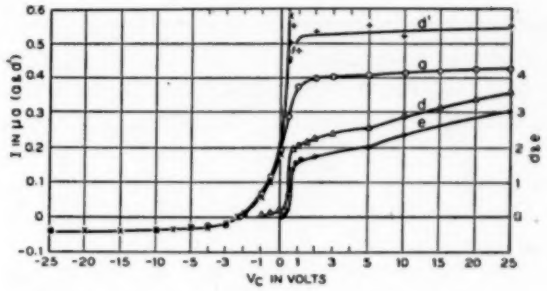

FIG. 22. Retarding potential curves. Thermionic current larger than secondary current. $V_p=1250$; *a*, $T=30$°C; *d*, 380°C; *e*, thermionic, $T=380$°C; $d'=d-e$.

metal. The best available information is that nickel has a δ_{max} of 1.3 at 550 volts.

The retarding-potential curve for this target is shown in Fig. 24, curve *II*, in comparison with curve *I* for the oxide target. The thermionic curve *III* for the nickel target indicates a contact potential of about 1 volt. While neither of the secondary curves gives a true energy distribution, the difference between the curves is very striking. Evidently the secondary electrons from the oxide have on the average a much lower energy of emission than those from the metallic target. Among the former only a small fraction is not stopped by −5 volts, while among the latter a larger fraction is not stopped by −25 volts. (This would make the observed δ for Ni too large, by indicating too small a primary current.) We can conclude, then, that while we do not know the exact energy distribution of the secondary electrons from the present oxide coating, their average energy is considerably below that for the metal, and that this distribution does not here change much in the temperature range where the secondary current is not swamped by thermionic current.

The assumption that the pulsed yield is all true secondary emission even at high temperatures here meets difficulties. The yield has been extrapolated by Pomerantz from values measured below 600°C to the thermionic operating temperature of 850°C, where it may be 100 secondary electrons per 1000-volt primary electron. This means that an incredibly large part of the primary energy goes into energy of the secondary electrons unless the energy of the latter is unusually small at the higher temperatures. Pomerantz considers the difficulty resolved in his finding (and that of Morgulis and Nagorsky)

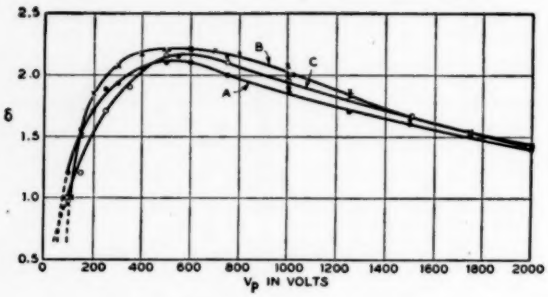

FIG. 23. Tube MN-1, Ni target, $i_p = 10.6\ \mu a$. *A*—room temperature; *B*—~800°C; *C*—room temperature.

that the secondary energy does decrease fairly rapidly with increasing temperature. This conclusion rests on the shape of energy distribution curves obtained by differentiating rather crude retarding-potential curves obtained with apparatus not suitable, as discussed above, for determining total energy distribution.

Other literature on the energy distribution of secondary electrons from insulators is also quite confusing. In some cases the experimental procedure has been faulty, leading to contradictory results. Treloar[14] working with composite CsO layers *predicted* for these a lower energy of secondary electrons than for metals. For NaCl Vudinsky[15] concluded that the energy distribution curves are similar to those for metals with a peak at possibly 3 to 6 volts. Kalckhoff[16] found for glass and mica the secondary energy peak at 15–20 volts and seemed not surprised. Malter[17]

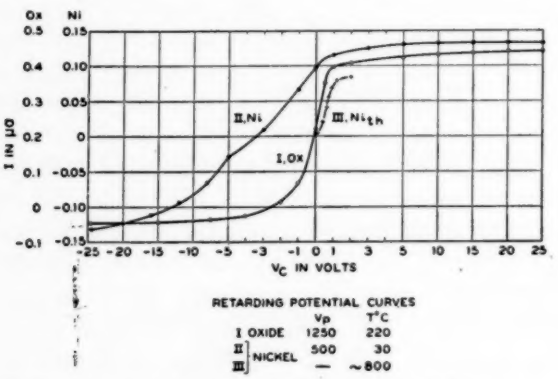

FIG. 24. Retarding potential curves. Nickel target compared with oxide target.

obtained for Mg-Ag alloy (presumably oxidized) the most probable energy of emission of secondary electrons at 2–6 volts. For MgF_2 in thin layers Geyer[18] gives a distribution curve with the peak energy below his curve for Ni (2 volts), and similar layers of NaCl are not much different from the Ni curves. His insulator curves, however, show signs of an iR drop in the coating ("negative energy").

VIII. EFFECT OF HIGH FIELD ON SECONDARY EMISSION

In some instances when the target is poorly conducting there is seen a rising initial top portion of the secondary pulse. In Fig. 6b, for instance, there is a distinct rise during the first quarter-microsecond. A ready explanation is that as the surface becomes positively charged the internal field aids electrons in getting out and so increases the yield.[5] One might propose this as a major factor in making the δ of insulators high at low temperatures.

Some simple computations make this explanation less plausible. In the present targets the surface potential may reach at most that of the collector, say 60 volts. If this is distributed as a uniform field through the target, it would amount to about one millivolt per atomic layer of the oxide. It seems hardly reasonable that this small field could appreciably affect the motion of an internal secondary electron with energy of several electron volts. On the other hand, a field might be concentrated in a thin layer near the surface, say over the depth which the primary electrons reach, caused by the primaries being trapped at this depth while secondaries leave the surface. In order to get a significant field strength, say 0.1 volt per atomic layer, the charge delivered by the beam in the first quarter-microsecond in Fig. 6b should have been about 500 times what it actually was. It seems difficult to explain the initial rising top of the secondary pulse for the cold target on the basis of internal fields with the simple distribution assumed here. More needs to be known about the effect of field on the motion of internal electrons.

[14] L. R. G. Treloar, Proc. Lond. Phys. Soc. **49**, 392 (1937).
[15] M. Vudinsky, J. Tech. Phys. U.S.S.R. **9**, 1583 (1939).
[16] G. Kalckhoff, Zeits. f. Physik **80**, 305 (1932).
[17] L. Malter, Proc. I.R.E. **29**, 587 (1941).
[18] H. K. Geyer, Ann. d. Physik **41**, 117 (1942).

IX. ACCURACY OF THE δ-MEASUREMENTS

The question was raised near the beginning of the article whether a retarding potential of 22 volts is sufficient to prevent all the secondaries from leaving the target so that an accurate measure can be made of the primary current. The retarding-potential curves, such as that of Fig. 21, seem to answer in the affirmative, having a very flat tail at the left in the retarding potential region. On the other hand, it is well recognized that secondary electrons have energies distributed all the way up to the primary energy. If in Fig. 21, 20 percent of the secondary electrons had energy near the primary energy the curve could still be as flat as it is now at -25 volts. The high speed secondaries would then in part strike the collector and there give rise to tertiary electrons which would be drawn to the target and measured as primary current. Similar errors, but not quite so large, apply to measurement of the secondary current. This confusion applies to practically all δ-measurements made by retarding-potential methods and makes the values of δ somewhat uncertain. It is never possible to draw unassailable conclusions about the origin of the various currents measured. This is why the retarding potential was specified in the definition of δ for the present measurements. A study of the few published reports on the ratio of high speed to low speed secondaries for various materials, and measurement in a few cases of currents to all the electrodes in the present work, suggests that 20 percent may be an upper limit to the errors in δ in the present measurements, introduced largely by the uncertainty in the measurement of primary current.

X. ACKNOWLEDGMENT

The author wishes to express his gratitude to many of his colleagues for valuable discussions during the progress of this work, in particular to Dr. K. G. McKay and Dr. Conyers Herring.

Mechanical Properties of Long Chain Molecule Liquids at Ultrasonic Frequencies

W. P. MASON, W. O. BAKER, H. J. MCSKIMIN, AND J. H. HEISS
Bell Telephone Laboratories, Murray Hill, New Jersey

(Received October 3, 1947)

Measurements have been made of the mechanical properties of long chain molecule liquids of the polyisobutylene type by means of shear and longitudinal waves in the ultrasonic frequency range. The shear waves show that these liquids behave as Maxwell relaxing liquids. The viscosity measurements in the range around 14 kilocycles check the viscosities measured by falling ball measurements within the experimental error. As the temperature decreases or the frequency increases, the reaction of the liquid shows that a shear elasticity of the Maxwell type comes into play with a shear elastic constant of from 5×10^6 dynes/cm^2 to 5×10^7. This elasticity increases with decreasing temperature and increases with chain length, and represents an intermediate type to the "frozen" type of elasticity or the "kinetic theory" type in that it has the high compliance of the "kinetic theory" type but the temperature variation of the "frozen" type of elasticity. It is suggested that this type of elasticity may be due to a composite motion of the chains, including hindered rotation within chains, as well as interaction of segments between chains. At very high frequencies this composite motion disappears and the shear stiffness becomes very high.

Above about 30 kilocycles for these liquids, some shear viscosity is relaxed by the shear elasticity. Measurements with longitudinal ultrasonic waves show, however, a dispersion of velocity and an associated attenuation curve. From very low frequencies to very high frequencies the velocity increases by about 25 percent, while the attenuation has the high value of 0.7 neper per wave-length at a frequency for which the velocity is a mean between the two extremes. These measurements show that a relaxation occurs in either the shear elasticity, μ, or the Lame constant, λ. Current investigations show this to be in the shear constant, μ. However, the measured attenuation frequency curve is broader than that of a single relaxation frequency and moreover indicates that the attenuation reaches a constant value per wave-length at high frequencies. A simple explanation of this is that the rearrangement compliance has a hysteresis component. Calculations of the velocity and attenuation on this basis agree very well with the measured curves.

I. INTRODUCTION

VELOCITY dispersion and associated sound absorption caused by molecular process are very hard to locate and measure in ordinary liquids because they come at frequencies higher than can be utilized with present day ultrasonic equipment. If, however, we use liquids containing long chain molecules, the frequencies of the relaxing effects are low enough to be measurable by ordinary ultrasonic equipment. This is because the shear and compressional viscosities are high enough to lower the relaxation frequencies to easily measurable ranges.

In order to study these effects, shear and longitudinal measurements have been made for a number of samples of polyisobutylene of viscosity average molecular weight ranging from 900 to 5600. This is a molecule composed of chains of $\left[\begin{array}{c}CH_3\\|\\(-C-CH_2-)\\|\\CH_3\end{array}\right]$ groups without cross linkages. At least as observed when crystallized, this chain occurs in a spiraled zigzag form, as shown in Fig. 1. It turns all the way around in the direction of its length probably once in every 9 pairs of CH_3 groups. In the liquid state some less regular twisted form is likely. The different average chain lengths used result in a range of viscosities from 0.3 to 1700 poises at 25°C. By measuring the shear properties of these liquids with a torsionally vibrating crystal, it is shown that they act as a Maxwellian relaxing liquid with a shear elasticity as well as a shear viscosity. The shear elasticity depends on the chain length, and if one plots the logarithm of the elasticity against the inverse of the temperature, one obtains a straight line having less than half the slope of the logarithm of the viscosity *versus* inverse temperature curve. Although the different chain length liquids have different elasticities, it is found that all of their elasticities for different temperatures and chain lengths can be represented by a single curve when plotted against density.

At frequencies so high that the shear viscosity is relaxed, the shear viscosity cannot be contributing to the loss of a longitudinal wave.

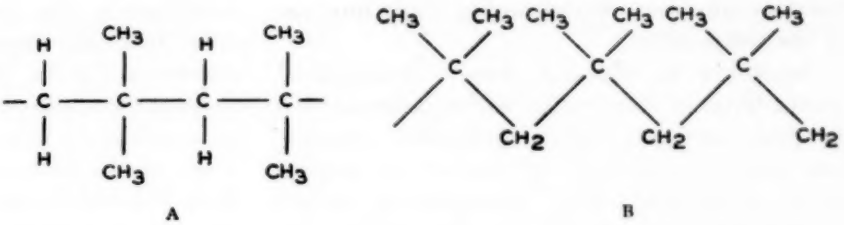

FIG. 1. Molecular structure and chain form for polyisobutylene.

Torsional crystal measurements show that the first marked relaxation frequencies for all of these liquids are less than 30 kilocycles. Measurements by a pulsing technique show however that there are other components of the shear elasticity that are not relaxed until the high megacycle region, and these are the most likely cause of the relaxation phenomenon so far observed for longitudinal waves. By measuring the initial slope of attenuation-frequency curves, these secondary components of the shear viscosity can be determined.

The logarithm of this second component of the shear viscosity for all chain lengths was directly proportional to the inverse absolute temperature with a slope about $\frac{3}{4}$ as large as that for the lower frequency or "primary" shear viscosity. All the different molecular weight liquids had the same slope, indicating that the element that was rearranged was a segment of the molecule rather than the whole molecule. As with the low frequency shear viscosity, an increase in molecular weight of the chain causes a marked increase in viscosity.[1] Measurements over a wide frequency range show that the attenuation increases to a maximum and falls off at higher frequencies. At the same time the velocity increases with frequency and then levels off for higher frequencies. This agrees with the prediction of a relaxation theory. However, when plotted on a logarithmic scale the attenuation is not symmetrical about the frequency of highest attenuation, but indicates that the loss comes down to a constant value per wave-length independent of the frequency. This deviation from the relaxation theory can be explained if the molecular rearrangement compliance has a hysteresis[2] component. When calculated, attenuation and velocity curves fit the measured values very well. Since the hysteresis component appears only at high frequencies for which the secondary shear viscosity is relaxed, it appears to be due to a twisting up of chain segments which cannot quite jump from one stable potential well to a neighboring one by untwisting.

II. MEASUREMENTS OF SHEAR VISCOSITY AND SHEAR ELASTICITY FOR POLYISOBUTYLENE

Polyisobutylene is a polymer molecule that occurs in a long chain. It has the formula shown by Fig. 1A and the (non-planar) zigzag form shown by Fig. 1B. This chain in an ordered, stretched state appears to rotate about the direction of its length once in every 9 pairs of CH_3 groups. Accordingly, non-planar zigzag segments can be expected in the liquid state. The specimens used were designated *A*, *B*, *C*, and *D*, which had, respectively, average molecular weights of 903, 3520, 4550, and 5590.

Measurements of the viscosity of these four samples were made by the falling ball method (b) over a range of temperatures and are shown plotted as the logarithm of the viscosity *versus* the inverse temperature by Fig. 2. All of these liquids have the same slope, which indicates according to Eyring's theory[3] that the element which moves from one potential well to an adjacent one is a segment of the chain of 20 submolecules or so, whose length is essentially independent of the total chain length. The large decrease in viscosity for any one temperature as a function of chain length has been explained as the increased probability that the chain as a whole will jump to a new position as the chain length gets shorter. Measurements have also been made of the density of these liquids, and

[1] (a) P. J. Flory, J. Am. Chem. Soc. **62**, 1057 (1940); (b) W. O. Baker, C. S. Fuller and J. H. Heiss, *Ibid.* **63**, 2142 (1941). The molecular weight-melt viscosity relation seems to be linear in a log-log plot rather than in the simpler forms in the references.

[2] By elastic hysteresis we mean a stress-strain loop (usually nearly an ellipse) that does not vary with frequency. For elastic hysteresis for small strains, the area of the loop is proportional to the square of the maximum strain.

[3] Walter Kauzmann and Henry Eyring, J. Am. Chem. Soc. **62**, 3113, 3125 (1940).

the data are shown plotted on Fig. 3 as a function of the temperature.

According to classical theory, longitudinal waves have an attenuation which is determined by both the shear and compressional viscosity, but recent experiments by one of the writers[4] have shown that shear viscosities of viscous liquids are often relaxed at relatively low frequencies by the shear elasticities of the liquids, and the low frequency shear viscosities do not contribute to the attenuation of a longitudinal wave. Both the shear elasticities and the shear viscosities can be measured by means of the resistance and reactance loading that the liquids impress upon a torsionally vibrating crystal. In order to demonstrate that the low frequency shear viscosities were relaxed at frequencies well below the frequencies used for longitudinal measurements, torsional crystals were used to measure the shear viscosities and shear elasticities.

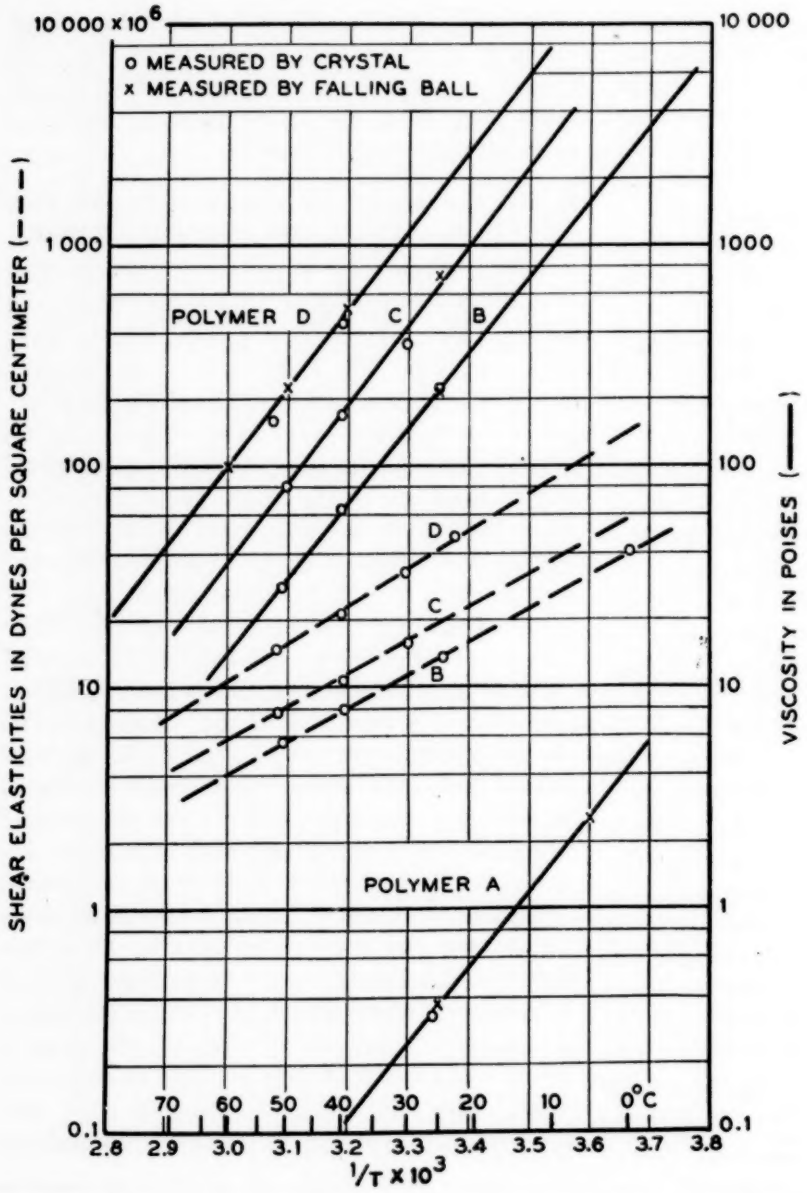

FIG. 2. Shear viscosity and shear elasticity of polyisobutylene liquids.

[4] W. P. Mason, Measurement of the viscosity and shear elasticity of liquids by means of a torsionally vibrating crystal, Proc. A.S.M.E. (May 1947).

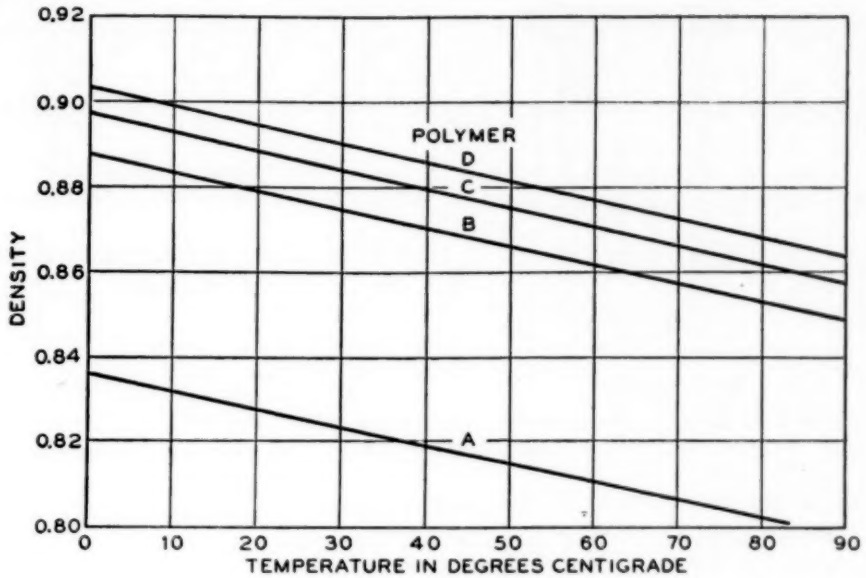

FIG. 3. Density of polyisobutylene liquids as a function of the temperature.

The experimental arrangement is shown by Fig. 4. A torsional crystal of ADP (ammonium dihydrogen phosphate) was gold-plated by the evaporation process and suspended from its nodal plane by three wires glued to the surface by Bakelite cement. The resonant frequency, the antiresonant frequency, the resistance at resonance, and the capacity at 1000 cycles were all measured, and the results are shown by Eq. (1)

$$\text{Crystal length} = 5.0 \text{ cm}; \text{O.D.} = 2R = 0.472 \text{ cm}; \text{I.D.} = 2R_0 = 0.30 \text{ cm}; \rho = 1.804; f_R = 19615 \text{ cycles}; f_A = 19835; C_0 = 100 \ \mu\mu\text{f}; R = 500 \text{ ohms}. \tag{1}$$

From these data the ratios between the shear resistance and reactance and the increase in electrical resistance and decrease in resonant frequency can be calculated by formulae developed in the previous paper. These are given by the equations

$$\Delta R_E = K_1 R_M; \quad \Delta f = -K_2 X_M, \tag{2}$$

where ΔR_E is the increase in electrical resistance, Δf the decrease in resonant frequency, R_M the mechanical resistance loading of the shear wave per square centimeter, X_M the mechanical reactance loading of the crystal per square centimeter, and K_1 and K_2 are constants of the crystal. These are related to the above measurements by the formulae

$$K_1 = \frac{1}{2\pi^2 f_R (\Delta f_R) C_0 \rho}\left[\frac{R^3+R_0^3}{R^4-R_0^4}+\frac{1}{l}\right]; \qquad K_2 = \frac{1}{\pi\rho}\left[\frac{R^3+R_0^3}{R^4-R_0^4}+\frac{1}{l}\right], \tag{3}$$

where Δf_R is the separation $f_A - f_R$. With the above values, at 25°C

$$K_1 = 425, \quad K_2 = 1.15. \tag{4}$$

The value of K_1 changes slightly with temperature and at 50°C was evaluated as 455.

It was found that the resistance values at resonance gave the most reliable results since it was difficult to locate accurately the resonant frequency of the crystal in a viscous liquid. The measurements were made in a balanced electrical bridge and data similar to Fig. 7 of the previous paper[4] were used to evaluate the resistance loading. Measurements were made at the first, third, and fifth harmonic of the crystal. For the harmonics, the same value of K_1 holds as for the fundamental. Typical data for the resistance loading per square centimeter in terms of the frequency and temperature are shown for the polymer "B" liquid by Fig. 5. To interpret this data in terms of shear viscosity use is made of a calculation of the resistance and reactance loading of a liquid having shear viscosity and

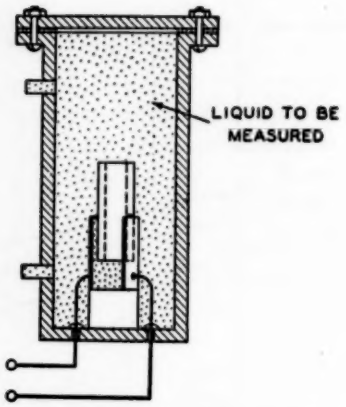

FIG. 4. Torsional crystal and container, used for measuring shear viscosity and shear elasticity of liquids.

shear elasticity given in the previous paper.[4] This is reproduced in Fig. 6 of this paper. Comparing this with the data of Fig. 5, we see, for example, that at 0°C, the loading is nearly independent of frequency, which means that the relaxation frequency is considerably below the lowest measuring frequency of 17.5 kilocycles. The curves for 24°, 40°, and 50°, however, show enough bending with frequency to allow one to fit them to the theoretical curve. From this data, one can find that the ratio of the lowest frequency (about 17.5 kc) to the relaxation frequency is given by the second column of Table I, while the asymptotic value of the loading resistance at very high frequencies is given by the third column. Since the shear elasticity is related

TABLE I. Polyisobutylene "B."

Temperature	f/f_c	R at high frequency mech. ohms	μ dynes cm^2	Relaxation frequency f_c cycles	Value of shear viscosity in poises
0°C	—	6100	42×10^8	—	—
24°C	1.8	3500	14×10^8	9700	230.0
40°C	0.9	2650	8×10^8	19400	65.8
50°C	0.6	2200	5.6×10^8	29200	30.5

to the resistance loading at high frequencies by the formula

$$(\rho\mu)^{\frac{1}{2}}=R \quad \text{or} \quad \mu=R^2/\rho, \tag{5}$$

the shear elasticity μ is shown by the fourth column. The fifth column shows the calculated relaxation frequency, while the sixth column shows the shear viscosity η which can be calculated from the formula

$$\eta=\mu/(2\pi f_c). \tag{6}$$

The values of viscosity measured by the crystal are shown plotted by the circles of Fig. 2 for all three liquids and, as is evident, they agree with the values measured by the falling ball method within 5 percent, which is probably the accuracy of measurement by the present method.

The values of shear elasticity measured for the three polymer liquids, *B*, *C*, and *D* are shown plotted by the dashed lines of Fig. 2. They lie nearly on straight lines of uniform slope when plotted as logμ *versus* $1/T$, at least within the temperature range shown. If we plot all of these

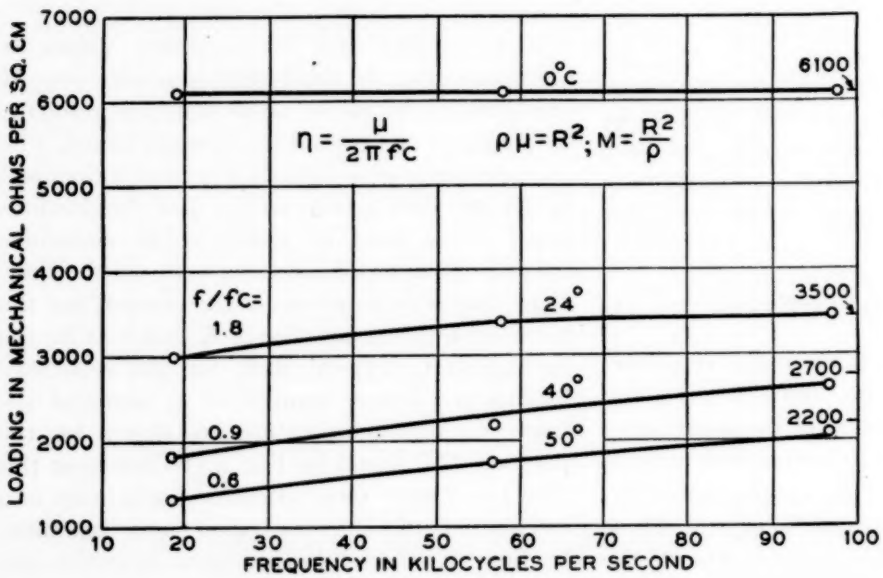

FIG. 5. Resistance loading of torsional crystal for polymer *B* plotted as a function of frequency and temperature.

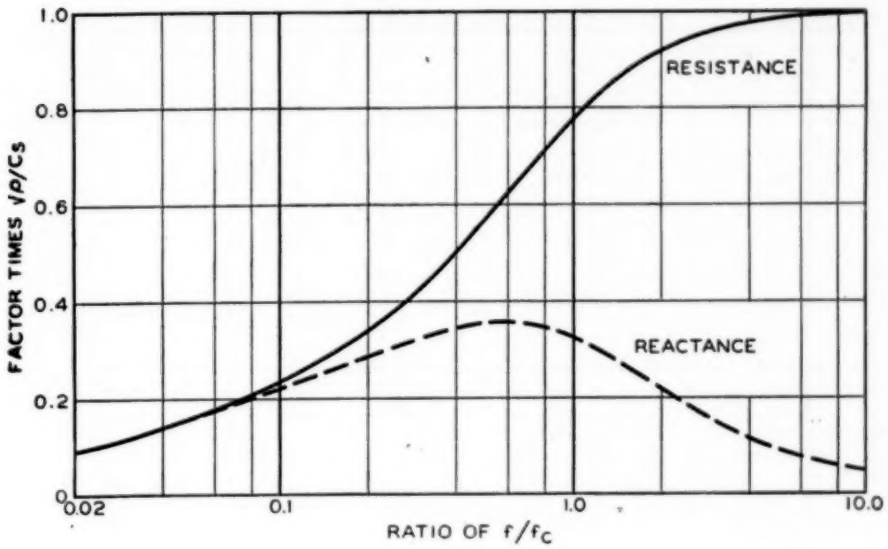

FIG. 6. Resistance and reactance values for a Maxwellian relaxing liquid plotted as a function of the frequency to the relaxation frequency.

shear elasticities as a function of density alone, which can be done using the data of Fig. 2 and Fig. 3, the points of Fig. 7 result. It appears likely, within the experimental error, that all of these points can be represented by a single curve.

III. VELOCITY AND ATTENUATION FOR LONGITUDINAL WAVES

In the last section it was shown that the first components of shear viscosities of these polyisobutylene liquids were relaxed at frequencies from several kilocycles to 30 kilocycles. Measurements made by terminating a rod of fused quartz, which is carrying shear wave pulses, by a layer of these liquids have shown that there are other components of the shear viscosity which are the causes of the dispersion measured with longitudinal waves. These measurements will be discussed in another paper. The losses in these materials run as high as 300 db per centimeter in the eight megacycle region and have necessitated new experimental means for measuring the attenuation and velocity. The experimental method chosen is a combination of pulsing and steady-state methods and is shown schematically by Fig. 8. Here a source of high frequency is fed to an amplifier-rectifier through two parallel paths. One is through an amplifier that is gated by a direct-current pulse. The pulse of a.c. current is impressed on a transmitting crystal which sends a pulse of alternating longitudinal waves into the liquid. This wave is picked up by a second crystal accurately parallel to the sending crystal which is placed at a variable distance from the sending crystal. The voltage generated by the receiving crystal is sent through a wide band amplifier, is rectified, and actuates the vertical set of electrodes of the oscilloscope. The sweep circuit of the horizontal set is controlled by the same synchronizing oscillator that controls the d.c. pulse generator so that the pulse received always occurs in the same position on the fluorescent screen. The second path from the high frequency oscillator is a steady state one through an attenuation box to the amplifier rectifier and oscilloscope. The attenuation box has carbon film resistors that are stable in value up to a frequency of 10 megacycles. Attenuation measurements are made by comparing the output of the receiving crystal with the output of the attenuator (connection shown by dotted line). If the loss in the liquid is 15 db or more, the pulse length does not make any difference and comparisons can be made by steady-state methods. However, if the loss between the two crystals is small, trouble is experienced with standing waves. To get around this difficulty a very short pulse length is used, and the first received pulse, which is free from standing wave complications, is used. Figure 9 shows a typical measurement of attenuation *versus* change in path length for polymer *D*. A change of 38 db occurs in a path difference of 0.1465 cm, indicating an attenuation of

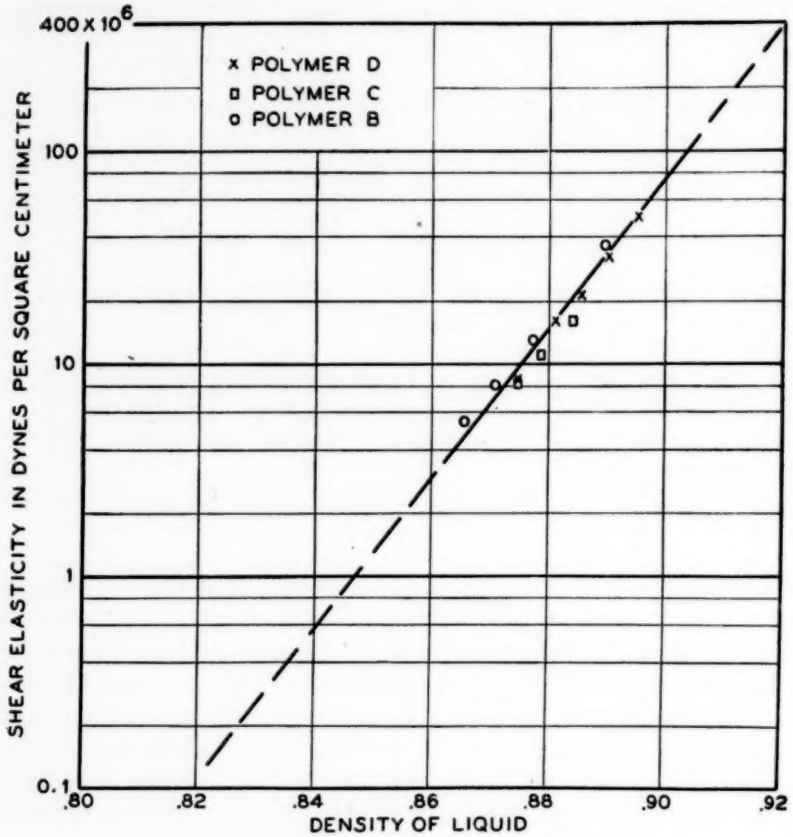

FIG. 7. Shear elasticity of polyisobutylene liquids plotted as a function of the density.

259 db per cm for a frequency of 8 megacycles and a temperature of 31°C. From the straightness of the attenuation-distance line it appears likely that the attenuation can be measured within ±2 percent for a high loss material and ±5 percent for a low loss material.

A measurement of the velocity for such a high loss material is more difficult by conventional methods. The path length is so short that a comparison of the position of received pulse with transmitted pulse does not give an accurate measurement of the velocity. On the other hand, the attenuation is too high to utilize the standing wave properties of the liquid as is done with the acoustic interferometer. The method adopted was to compare the phase of the received pulse with the phase of the steady-state transmission. For this purpose both paths were connected simultaneously to the amplifier-rectifier, and the attenuation in the db box was adjusted to be approximately equal to that through the liquid. As the path length was changed, the output from the pulse alternately added and subtracted from that through the box. By plotting the positions of the maxima, the wave-length in the liquid can be obtained. Figure 10 shows a typical measurement for the same liquid polymer *D*, plotting the number of wave-lengths change against the separation in centimeters. A very good straight line can be drawn through these points, and it is estimated that the velocity can be measured about ±1 percent. By this method velocities can

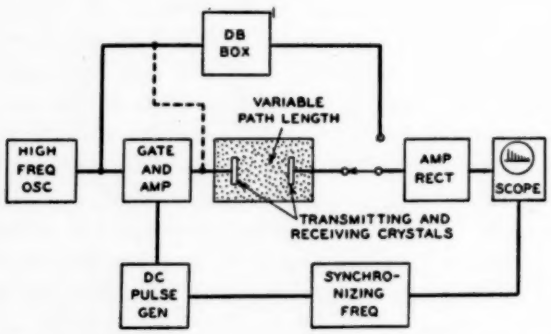

FIG. 8. Experimental arrangement for measuring the velocity and attenuation of a liquid at ultrasonic frequencies.

be measured even though the liquid path has 50 db or more attenuation.

Employing these methods a series of measurements were made for these three liquids at the frequencies 2 mc, 5 mc, and 8 mc and over a wide temperature range. The data on the attenuation for polymer *D* is shown plotted by Fig. 11, while the velocities for the same conditions are plotted on Fig. 12. The attenuation is plotted in terms of nepers (1 neper equals 8.68 db) per wavelength, since the theoretical attenuation is most easily calculated for that quantity. It is obvious from the data that an attenuation and associated velocity dispersion is occurring for this liquid.

In order to classify the measured results and to obtain parameters in terms of which they can be expressed, use is made of the calculated value of the attenuation and phase shift due to a relaxation theory. The effect can be represented by the equivalent circuit of Fig. 13, in which the series arm is the density times the length of the section dx considered, and the shunt arm consists of a stiffness κ_1/dx in parallel with a second shear viscosity divided by dx and the two in series with a second stiffness κ_0/dx. At very low frequencies this will reduce to the impedance of the stiffness κ_0, so that κ_0 represents the compressibility of the liquid measured by static methods. At very high frequencies, the impedance of the shunt arm reduces to that of the two stiffnesses in series. Hence, κ_0 = low frequency compressibility; κ_1 = difference between high frequency

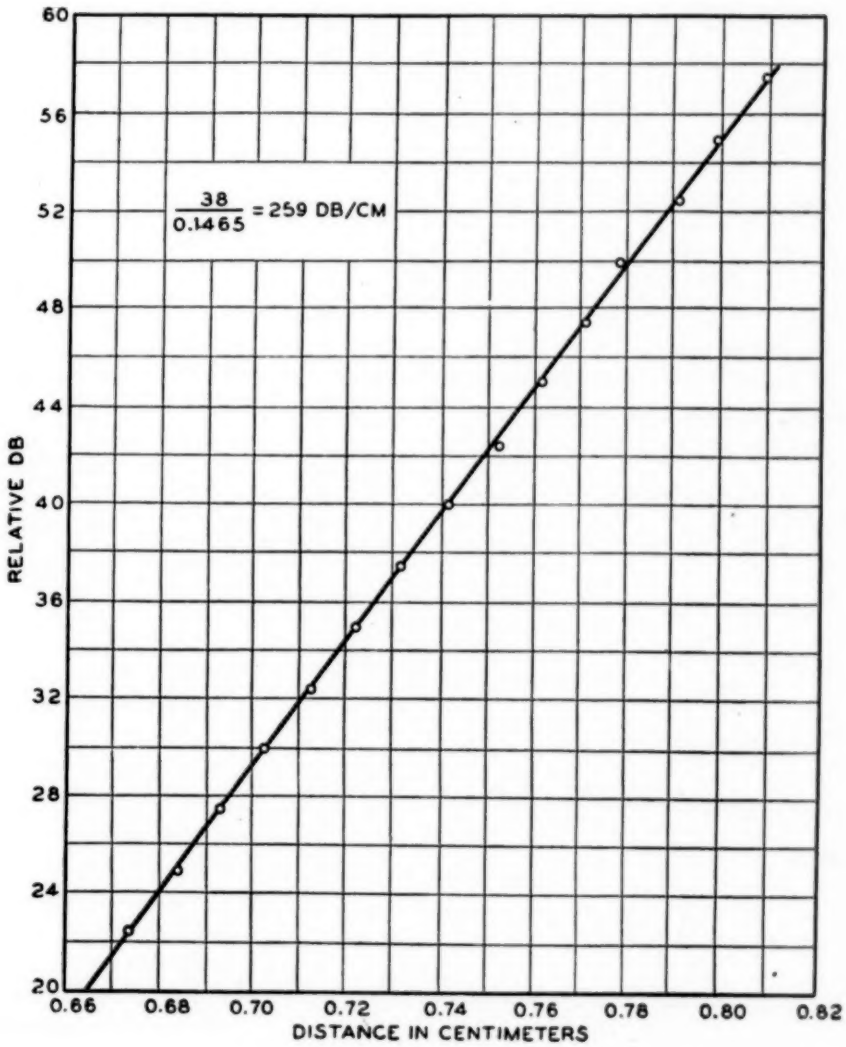

FIG. 9. *DB* attenuation plotted as a function of crystal separation for polymer *D*. Temperature 31°C, frequency 8 megacycles.

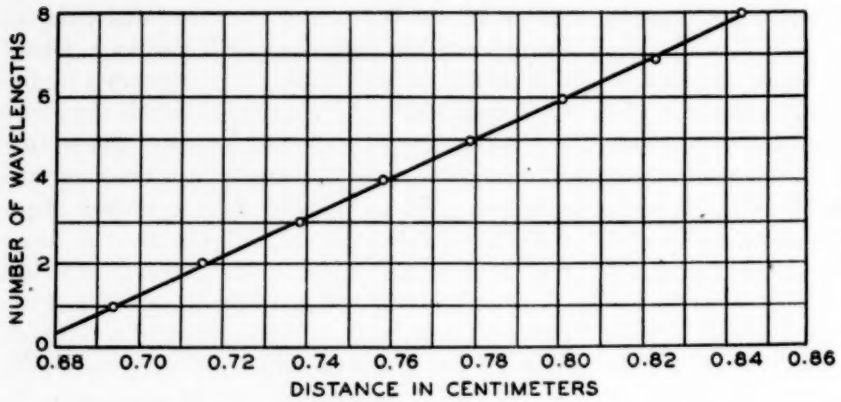

FIG. 10. Number of wavelengths plotted as a function of crystal separation for polymer *D*. Temperature 31°C, frequency 8 megacycles.

and low frequency compressibility. The resistance λ represents the viscosity. The attenuation and velocity can be calculated from the formula

$$Pdx=(A+jB)dx$$

$$=\left(\frac{Z_1}{Z_2}\right)^{\frac{1}{2}}=\left[\frac{j\omega\rho(dx)^2}{\dfrac{-j\kappa_0}{\omega}+\dfrac{\lambda(-j\kappa_1/\omega)}{\lambda-j\kappa_1/\omega}}\right]^{\frac{1}{2}}, \quad (7)$$

where $Z_1=j\omega\rho dx$ is the series arm and

$$Z_2=\left[\frac{-j\kappa_0}{\omega}+\frac{\lambda(-j\kappa_1/\omega)}{\lambda-j\kappa_1/\omega}\right]\times\frac{1}{dx}$$

is the shunt arm.

If we solve for the attenuation A (expressed in nepers per cm) and B the phase shift (expressed in radians per cm), we have

$$B=\omega\left(\frac{\rho}{\kappa^0}\right)^{\frac{1}{2}}\left(\frac{1+\lambda^2\omega^2(\kappa_0+\kappa_1/\kappa_0\kappa_1^2)}{1+\lambda^2\omega^2(\kappa_0+\kappa_1/\kappa_0\kappa_1)^2}\right)^{\frac{1}{2}}$$

$$=\frac{\omega}{\left(\dfrac{k^2v_0^2+\omega^2v_\infty^2}{k^2+\omega^2}\right)^{\frac{1}{2}}}. \quad (8)$$

$$\frac{A}{B}=\frac{1}{2}\frac{\omega\lambda/\kappa_0}{1+\lambda^2\omega^2\left(\dfrac{\kappa_0+\kappa_1}{\kappa_0\kappa_1^2}\right)}=\frac{1}{2}\left(\frac{v_\infty^2-v_0^2}{v_0v_\infty}\right)\frac{k\omega}{k^2+\omega^2},$$

where

$$v_0=\left(\frac{\kappa_0}{\rho}\right)^{\frac{1}{2}};\quad v_\infty=\left(\frac{\kappa_0+\kappa_1}{\rho}\right)^{\frac{1}{2}};$$

$$k=\frac{1}{\lambda(\kappa_0+\kappa_1/\kappa_0\kappa_1^2)^{\frac{1}{2}}}=\frac{(v_\infty^2-v_0^2)\rho v_0}{v_\infty}.$$

v_0 is the velocity at low frequencies, v_∞, the velocity at high frequencies, and $k/2\pi$ is the relaxation frequency f_0. If we multiply the ratio A/B by 2π, we obtain the attenuation A_w in nepers per wave-length, which is the quantity measured and expressed in Fig. 11. This becomes

$$A_w=\frac{\pi\omega\lambda}{\rho v_0^2}\times\frac{1}{1+\lambda^2\omega^2\left[\dfrac{v_\infty^2}{\rho^2v_0^2(v_\infty^2-v_0^2)^2}\right]}. \quad (9)$$

For very low frequencies this reduces to

$$A_w=2\pi^2f\lambda/(\rho v_0^2), \quad (10)$$

and the attenuation should initially be proportional to the frequency. This agrees with the measurements of Fig. 11 for high temperatures where the initial slopes of the attenuation frequency curves can be obtained. Equation (8) gives a method for determining the second component of the shear viscosity for

$$\lambda=A_w\rho v_0^2/(2\pi^2f). \quad (11)$$

Since all these quantities are known, λ can be determined and for poymer *D* is shown plotted as logλ *versus* $1/T$ by Fig. 14. The points lie on a straight line having a slope of $\frac{3}{4}$ that for the first component of the shear vicosity. The initial slopes have been determined for the other three liquids and are shown by Fig. 14. All the curves are parallel, indicating, as for the first component of shear viscosity, that the temperature dependent jump occurs by chain sections that are the same for all average molecular weights. The viscosity increases with molecular weight,

although the spread is not nearly as large as that for the low frequency shear viscosity.

To correlate all the measurements of Fig. 11, over temperature and frequency ranges we plot the product

$$A_w \rho v_0^2/(\rho v_0^2)_S \qquad (12)$$

against the product of frequency times second shear viscosity, where $(\rho v_0^2)_S$ is the product of density times v_0^2 for polymer D at 20°C. All these viscosities are determined by the curves of Fig. 14, while the zero frequency velocities can be obtained by extrapolating the data of Fig. 12 and are shown by Fig. 15. Within the experimental error all these points lie on one curve shown by Fig. 16. Also the measured attenuation per wave-length of the polymer C liquid and the polymer B liquid can be plotted on the same curve. From the equation for the phase shift (6) since $B=\omega/v$, we see that the ratio of v/v_0 should also be a function of the product of the frequency by the secondary shear viscosity. From the data of Fig. 12, showing the measured velocity, the data of Fig. 14, showing the viscosity, and the data of Fig. 15 for the zero frequency velocity, the ratio of v/v_0 can be evaluated and is shown plotted by Fig. 17 as a function of the product frequency times

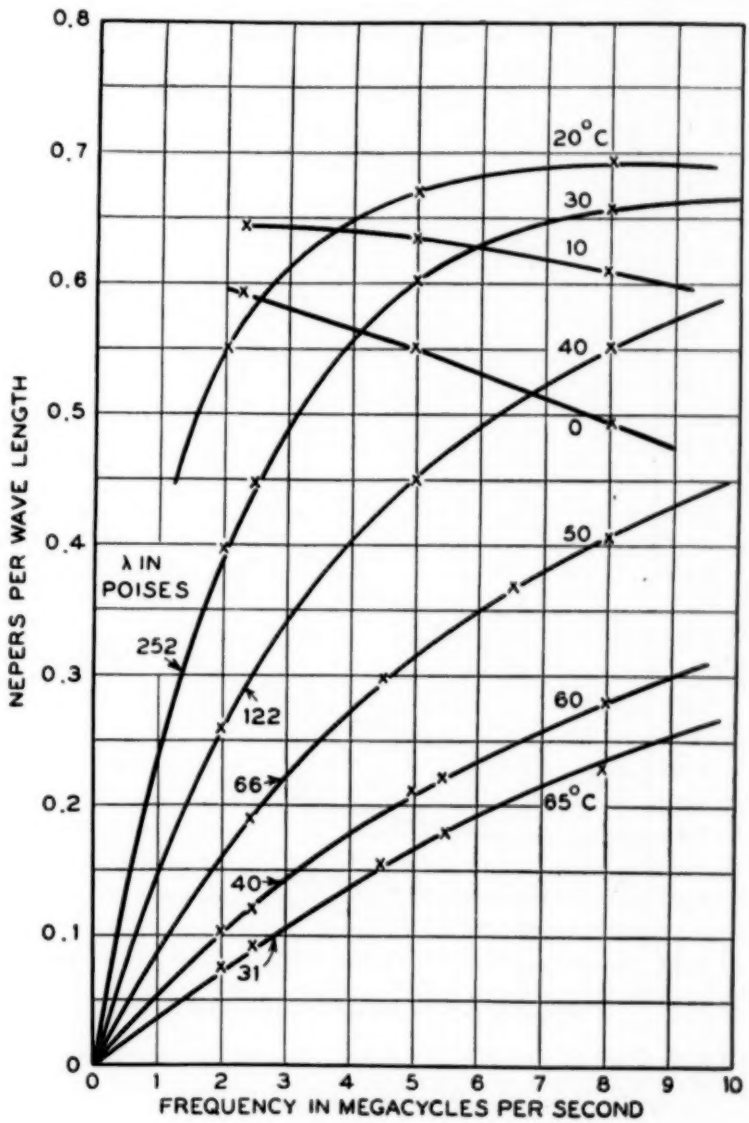

FIG. 11. Measurement of the attenuation per wave-length for polymer D plotted as a function of frequency and temperature.

viscosity. A single curve suffices for all the temperatures and for the other two polyisobutylene liquids.

IV. DISCUSSION OF LONGITUDINAL VELOCITY AND SOUND ABSORPTION IN LIQUIDS

A traditional concept of the liquid state regards a liquid as a solid substance for which the long-range order between the molecules has broken down. Alternately, if we regard a liquid as being a very dense gas as far as the interchange of energy between translational and internal vibrational modes is concerned, the natural method for accounting for the velocity dispersion and attenuation dispersion of a gas is to generalize the Herzfeld-Rice-Kneser[5] theory so that it applies for a liquid. This has recently been done by Kittel,[6] using the Tonks equation

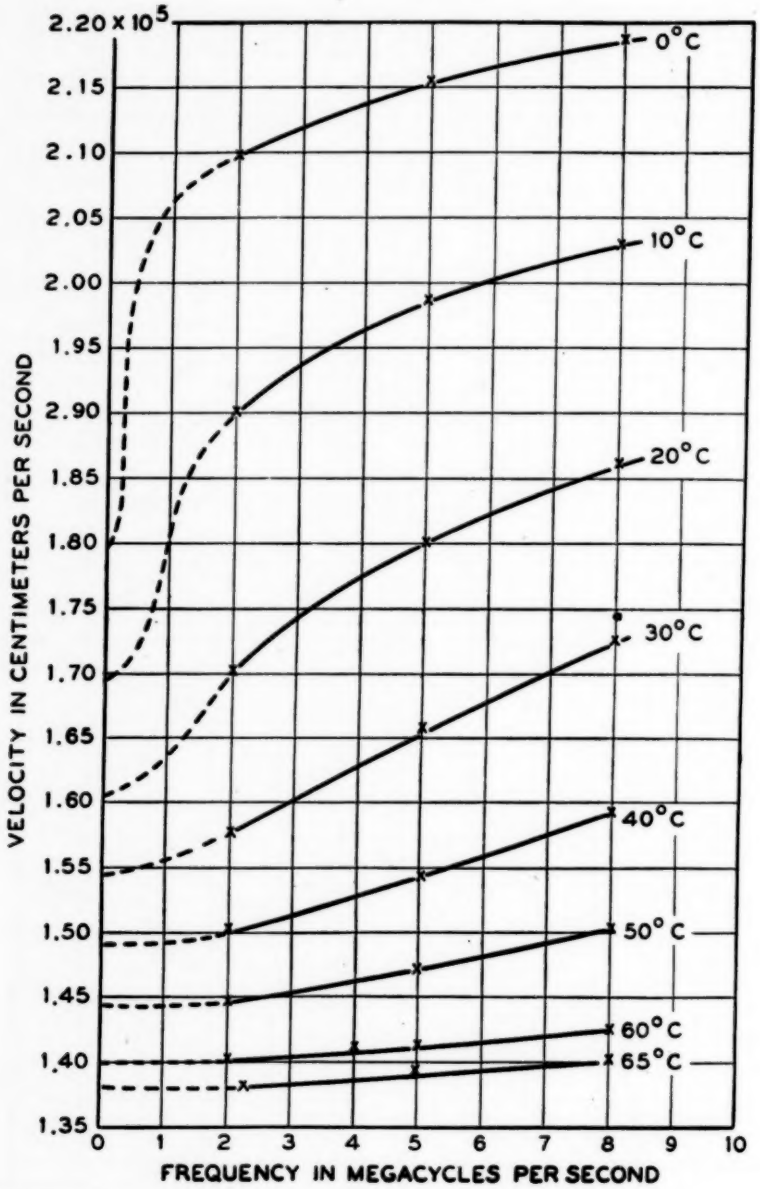

FIG. 12. Measured velocity of polymer *D* plotted as a function of frequency and temperature.

[5] K. F. Herzfeld and F. O. Rice, Phys. Rev. 31, 691 (1928); H. O. Kneser, Ann. d. Physik 11, 761, 777 (1931); 16, 347 (1933).
[6] Charles Kittel, J. Chem. Phys. 14, 614 (1946).

of state, and he finds that the attenuation A is given by

$$A=\left(\frac{\pi f^2}{v_0}\right)\left(\frac{3RC_i}{C_p^{\infty}C_v^{0}}\frac{f_0}{f_0^2+f^2}\right), \qquad (13)$$

where C_p^{∞} is the specific heat at constant pressure for an infinite frequency, i.e., with no internal modes of vibration of the molecules excited, C_v^0, the specific heat at constant volume and zero frequency, $3R=C_p-C_v$, C_i the specific heat associated with internal modes of vibration, f, the frequency, and $f_0=1/2\pi\tau$, where τ is the relaxation time which corresponds to the average lifetime of the excited vibration. On account of the larger number of collisions at higher absolute temperatures, this relaxation time is inversely proportional to the absolute temperature in degrees K. Since the attenuation per wave-length at low frequencies is

$$A_w=\frac{Av_0}{f}=\frac{2\pi^2 f\lambda}{\rho v_0^2}=2\pi^2 f\tau\left[\frac{3RC_i}{C_p^{\infty}C_v^{0}}\right] \qquad (14)$$

by Eqs. (8) and (11), a "compressional" viscosity on the gas-like theory should be

$$\lambda=\left(\frac{3RC_i}{C_p^{\infty}C_v^{0}}\right)\rho v_0^2\tau. \qquad (15)$$

When a liquid is regarded as being a solid in which the long range order between molecules has broken down, another method of explaining a compressional viscosity is the rearrangement process, after perturbation. This was first suggested by Debye[7] and has been further developed by Frenkel.[8] On this theory the compressibility is due to two components, the increase in potential energy caused by decreasing the distance between molecules, and a change in the degree of local order in the arrangement of the particles, in the sense of a more compact arrangement when the liquid is compressed, and a more open distribution when it is expanded. This change in the degree of local order must, in general, lag with respect to the variation of the pressure, since it is connected

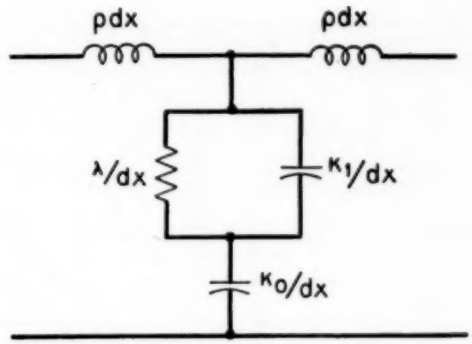

FIG. 13. Equivalent circuit for the propagation of a longitudinal wave in a liquid having an elastic compliance controlled by a relaxation mechanism.

with a rearrangement of the particles or a redistribution of their mutual orientations, i.e., with processes requiring a certain activation energy, and proceeding accordingly with a finite velocity only. This time lag of the arrangement with respect to the volume must coincide with the mean lifetime of vibrations about the same equilibrium positions which determine the shearing viscosity of the liquid. By developing this point of view Frenkel shows that the reaction of an infinitesimal volume to a compression can be represented by the network of Fig. 13, and this theory results in the variation of velocity and attenuation given by Eqs. (8) and (9). Since an activation energy U is involved in the change from one degree of order to another, the viscosity should vary with temperature according to the form

$$\lambda=Ae^{U/kT}, \qquad (16)$$

and when one plots the log of the viscosity against the inverse of the absolute temperature a straight line should result.

The longitudinal measurements, however, do not distinguish between a change in λ, which would be caused by either the H-R-K mechanism, or the Debye-Frenkel mechanism, and a change in the shear elasticity, μ, which can be caused by a secondary relaxation of the shear term. Measurements that will be described in a forthcoming paper have shown that the increase in shear elasticity with frequency is the cause of this increase in longitudinal velocity.

However, this theory does not account entirely for the measured attenuation and velocity curves

[7] See H. O. Kneser, Physik. Zeits. **39**, 800 (1938).
[8] J. Frenkel, *Kinetic Theory of Liquids* (Oxford University Press, New York, 1946), p. 208.

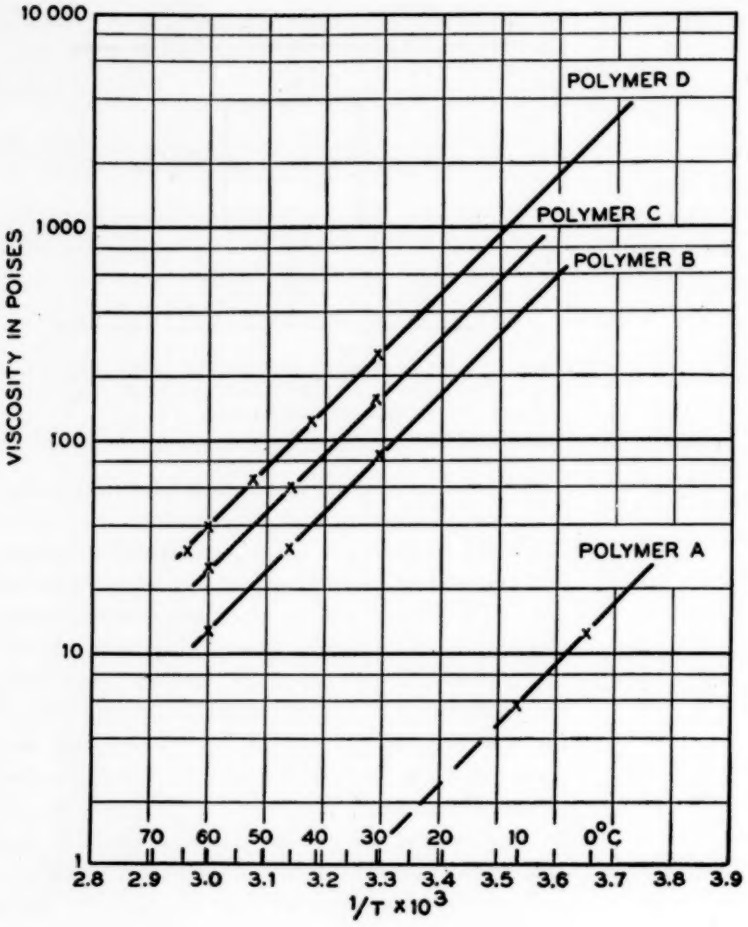

FIG. 14. Second shear viscosity of polyisobutylene liquids plotted as a function of temperature.

of Fig. 16 and Fig. 17. The calculated attenuation per wave-length for a single relaxation frequency is shown by the dot-dash line of Fig. 16. The measured value is broader on a logarithmic scale than the curve for a single relaxation frequency, and, moreover, is dissymmetrical about the maximum. We could match this curve by a dissymmetrical distribution of relaxation frequencies.

However, a simpler explanation of this effect is that a hysteresis occurs in the stress-strain relationship which introduces a constant loss per cycle. In order to get an agreement with experiment, this hysteresis loss has to be introduced in series with the elastic stiffness κ_1, giving this arm the impedance

$$(\lambda' - j\kappa_1)/\omega. \tag{17}$$

Since this arm is shunted out at very low frequencies by the second shear viscosity λ, this results in the following interpretation. At low frequencies the local order change caused by the shearing of the liquid takes place by one segment of the chain jumping from one stable potential well to another with no appreciable tangling with other chains. There is even, in this case, a small amount of hysteresis loss, as is shown by Fig. 18, which shows the measured attenuation of the lightest liquid, the polymer *A* liquid. The attenuation values measured at 2, 5, and 8 megacycles lie on straight lines that do not go through the origin at zero frequency but have intercepts of about 0.0025 neper per wave-length, indicating the presence of a slight amount of hysteresis loss. As the frequency increases, fewer and fewer of the chains accumulate enough heat energy in the time of a single cycle to rearrange to adjacent stable potential wells, and the liquid

becomes less compressible. It appears, however, that they can be displaced to intermediate potential minima. The displacement probably consists of an internal twisting. The steric restrictions imposed by the close packed methyl groups on the flexibility of individual chain then tend to hold the new twisted position. The chain segments then are not released until a later part of the cycle, and hence the strain lags behind the applied stress. It is supposed that the wave traveling through the polymer exerts such torque on certain portions of the convolved chains that an extreme biasing force for pairs twisting occurs. Thus the normally considerable activation energy for internal rotation of pairs of methyl groups past each other, in polyisobutylene, is effectively reduced to zero. Accordingly, since this potential barrier that the chains have to surmount to reach the twisted positions is so small compared, for instance, to that for proceeding to the next stable position (the latter process requires both twisting and translation), the hysteresis type of loss should continue to a very high frequency. This mechanism seems concordant with the general principles of hysteresis.

The network of Fig. 19 represents the effect of the hysteresis loss component. If we solve this network to obtain the velocity and attenuation, we have

$$Pdx=(A+jB)dx=\left(\frac{Z_1}{Z_2}\right)^{\frac{1}{2}}$$

$$=\left[\frac{j\omega\rho(dx)^2}{-\frac{j\kappa_0}{\omega}+\left[\frac{\lambda((\lambda'-j\kappa_1)/\omega)}{\lambda+((\lambda'-j\kappa_1)/\omega)}\right]}\right]^{\frac{1}{2}}, \quad (18)$$

where Z_1 the series arm is $j\omega\rho dx$, and Z_2 the shunt arm is

$$Z_2=\frac{-j\kappa_0}{\omega}+\frac{\lambda[(\lambda'-j\kappa_1)/\omega]}{\lambda+(\lambda'-j\kappa_1)/\omega}. \quad (19)$$

Solving for the attenuation A and the phase shift B, we find

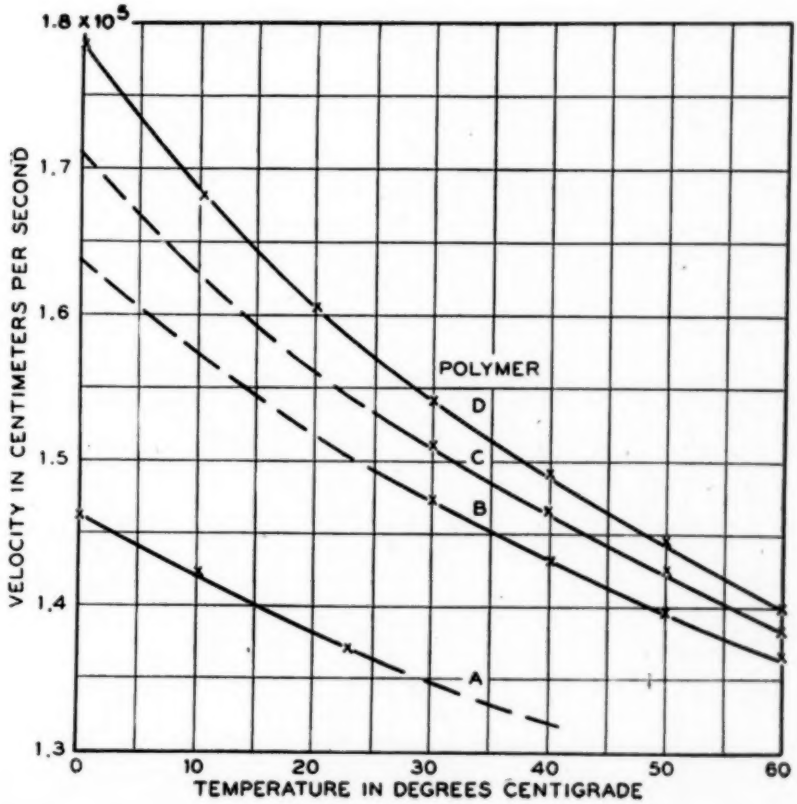

FIG. 15. Low frequency velocities for polyisobutylene liquids plotted as a function of temperature.

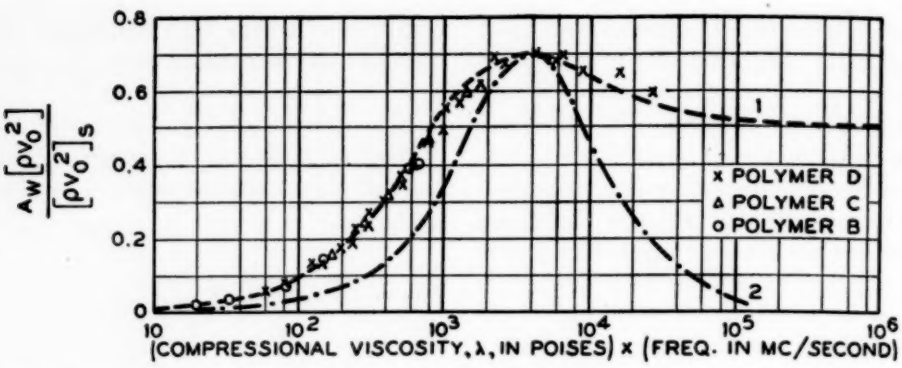

FIG. 16. Attenuation per wave-length for polyisobutylene liquids plotted as a function of secondary shear viscosity times the frequency. Dashed line calculated value assuming $\kappa_0=2.28\times10^{10}$ dyne/cm²; $\kappa^9=1.17\times10^{10}$; $\lambda'=0.53\times10^{10}$. Dashed dot line, calculated value for a single relaxation frequency. (The adjective "compressional" at the bottom of the figure should be deleted.)

$$A^2=\frac{\omega^2\rho}{2\kappa_0}\left[\frac{(\lambda'^2+\kappa_1^2)+2\omega\lambda\lambda'+\omega^2\lambda^2[(\kappa_0+\kappa_1)/\kappa_0]}{[\lambda'+\omega\lambda((\kappa_0+\kappa_1)/\kappa_0)]^2+[(\omega\lambda\lambda'/\kappa_0)-\kappa_1]^2}\right]$$
$$\times\left[-1+\left(\frac{1+(\omega^2\lambda^2/\kappa_0^2)[\lambda'^2+\kappa_1^2+\omega\lambda'\lambda]^2}{\lambda'^2+\kappa_1^2+2\omega\lambda\lambda'+\omega^2\lambda^2((\kappa_0+\kappa_1)/\kappa_0)^2}\right)^{\frac{1}{2}}\right]. \quad (20)$$

$$B^2=\frac{\omega^2\rho}{2\kappa_0}\left[\frac{(\lambda'^2+\kappa_1^2)+2\omega\lambda\lambda'+\omega^2\lambda^2[(\kappa_0+\kappa_1)/\kappa_0]}{[\lambda'+\omega\lambda((\kappa_0+\kappa_1)/\kappa_0)]^2+[(\omega\lambda\lambda'/\kappa_0)-\kappa_1]^2}\right]$$
$$\times\left[1+\left(1+\frac{(\omega^2\lambda^2/\kappa_0^2)[\lambda'^2+\kappa_1^2+\omega\lambda\lambda']^2}{\lambda'^2+\kappa_1^2+2\omega\lambda'\lambda+\omega^2\lambda^2((\kappa_0+\kappa_1)/\kappa_0)}\right)^{\frac{1}{2}}\right].$$

These can be written quite closely as

$$B=\omega\left(\frac{\rho}{\kappa_0}\right)^{\frac{1}{2}}\left(\frac{(\lambda'^2+\kappa_1^2)+4\pi\lambda'(f\lambda)+(4\pi^2/\kappa_0^2)[(\kappa_0+\kappa_1)/\kappa_0](f\lambda)^2}{(\lambda'^2+\kappa_1^2)+4\pi\lambda'(f\lambda)+4\pi^2[(\kappa_0+\kappa_1)^2+\lambda'^2/\kappa_0^2](f\lambda)^2}\right)^{\frac{1}{2}},$$
$$\frac{2\pi A}{B}=A_w=\frac{(2\pi^2/\kappa_0)(f\lambda)[\lambda'^2+\kappa_1^2+2\pi\lambda'(f\lambda)]}{[(\lambda'^2+\kappa_1^2+4\pi\lambda^2(f\lambda)+4\pi^2((\kappa_0+\kappa_1)/\kappa_0)(f\lambda)^2]}. \quad (21)$$

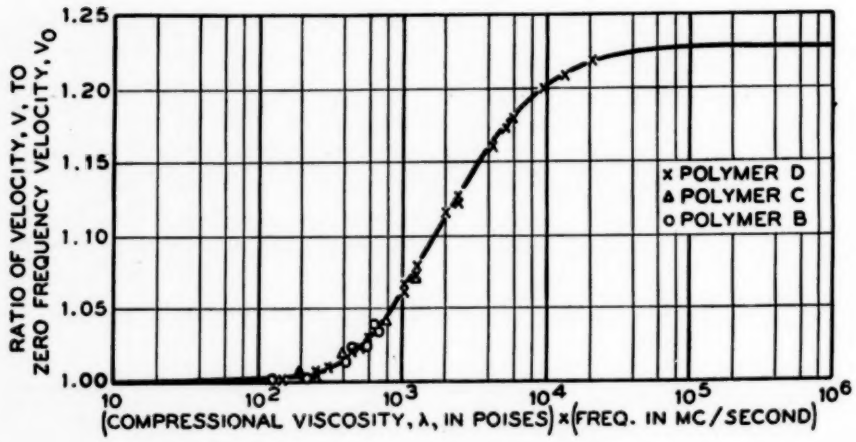

FIG. 17. Ratio of velocity to zero frequency velocity v_0 plotted as a function of secondary shear viscosity times the frequency. Solid line is calculated value assume $\kappa_0=2.28\times10^{10}$ dynes/cm²; $\kappa_1=1.17\times10^{10}$ dynes/cm²; $\lambda'=0.53\times10^{10}$ dynes/cm². (The adjective "compressional" at the bottom of the figure should be deleted.)

Several limiting cases are of interest. At low frequencies, the attenuation per wave-length and the velocity v_0 become

$$A_{w0}=\frac{2\pi^2}{\kappa_0}(f\lambda)=\frac{2\pi^2 f\lambda}{\rho v_0^2},\quad v_0=\left(\frac{\kappa_0}{\rho}\right)^{\frac{1}{2}}. \tag{22}$$

For very high frequencies the attenuation per wave-length and the velocity become

$$A_{w\infty}=\frac{\pi\lambda'}{\kappa_0+\kappa_1}\quad\frac{\pi\lambda'}{\rho v_\infty^2},$$

$$v_\infty=\left(\frac{\kappa_0+\kappa_1}{\rho}\left(1+\frac{\lambda'^2}{(\kappa_0+\kappa_1)^2}\right)\right)^{\frac{1}{2}}. \tag{23}$$

Hence with a hysteresis type of loss the attenuation per wave-length at high frequencies remains constant and independent of the frequency. This is the type of attenuation[9] found for solid bodies of the glass type, and it appears that the polyisobutylene liquids approach this condition at high frequencies.

Introducing these values in Eqs. (19), the velocity, which is ω/B, and the attenuation per wave-length can be written in the form

$$v=v_0\left(\frac{1+2A(f\lambda)+B(v_\infty^2/v_0^2)(f\lambda)^2}{1+2A(f\lambda)+B(f\lambda)^2}\right)^{\frac{1}{2}};$$
$$A_w=\frac{2\pi^2}{\kappa_0}\frac{(f\lambda)[1+C(f\lambda)]}{1+2C(f\lambda)+D(f\lambda)^2}, \tag{24}$$

where

$$C=\frac{2\pi\lambda'}{\lambda'^2+\kappa_1^2};\quad D=\frac{4\pi^2(\kappa_0+\kappa_1)}{\kappa_0(\lambda'^2+\kappa_1^2)}.$$

Hence if C, D and v_∞^2/v_0^2 are relatively constant with temperature, the velocity and attenuation per wave-length are functions of the product frequency times second shear viscosity. As indicated by the data of Fig. 16 and Fig. 17, this assumption appears to be justified.

The measured curves of Fig. 16 and Fig. 17 can be fitted quite closely by taking

$$\kappa_0=2.28\times10^{10}\text{ dynes/cm}^2;$$
$$\kappa_1=1.17\times10^{10}\text{ dynes/cm}^2; \tag{25}$$
$$\lambda'=0.53\times10^{10}\text{ dynes/cm}^2.$$

This gives a zero frequency velocity of 1.6×10^5

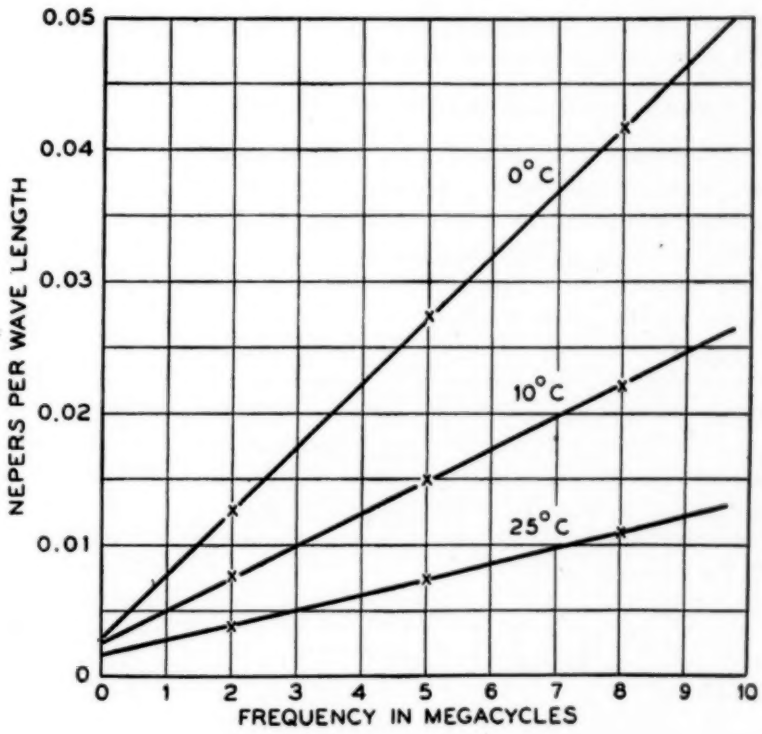

FIG. 18. Measured attenuation of polymer *A* polyisobutylene liquid plotted as a function of frequency.

[9] W. P. Mason and H. J. McSkimin, J. Acous. Soc. Am. 19, 464 (1947).

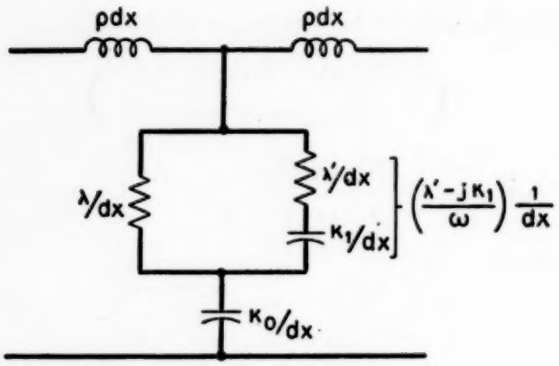

FIG. 19. Equivalent circuit for the propagation of a longitudinal wave in a liquid having an elasticity controlled by a relaxation mechanism and a hysteresis component in the rearrangement compliance.

corresponding to a temperature of 20°C, the standard condition of Fig. 16. The dashed line shows the calculated attenuation per wave-length which agrees very well with the measured points. The solid line of Fig. 17 is a plot of the ratio of velocity to zero frequency velocity, using Eq. (24) and the constants of Eq. (25). The agreement with the measured points is very good. The theoretical curve of Fig. 16 indicates that at high frequencies, polyisobutylene liquids should have an attenuation per wave-length of 0.5 neper, independent of frequency.

V. ORIGIN OF SHEAR ELASTICITY IN LIQUIDS

The present study should apply to the dynamic properties of all chain polymers, i.e., systems without cross linkage. One interesting result is that they show a shear modulus which decreases with increase in temperature contrary to that found for the "kinetic theory."

On the "kinetic theory" we have become accustomed to the unique high compliance of these substances (polymer networks held by secondary forces as well as from vulcanization), a particularly spectacular property at high amplitudes of motion. Here the "kinetic theory" of elasticity describes the elastic retractive force, F, for example as [10,11]

$$F=-T\left(\frac{\partial S}{\partial L}\right)=\left(\frac{kT\nu}{L_0}\right)\left(\alpha-\frac{1}{\alpha^2}\right),$$

where T=absolute temperature, L=length of sample, S=entropy, L_0=length of unstretched sample, ν=number of chains in a volume ∇, and $\alpha=L/L_0$. Here the theory accounts nicely for the widely observed shear modulus of 10^6 dynes/cm², and for its increase with temperature. It is, however, an equilibrium theory and requires time for equilibrium to be established before it is valid.

Most polymers show in addition to this "ideal" elasticity, several other elastic effects, portions of which have been extensively reported in earlier literature. For instance, at suitably low temperatures, ordinary supercooled organic liquids (glasses) become hard, as also do all kinds of rubbers and plastics. In this low temperature range, however, rubbery materials usually exhibit a really high shear modulus, of the order of 10^8 to 10^{10} dynes/cm². This is approximately the same whether the chains are cross linked into networks or not[12–14] and does not depend much on average length of chains or segments between cross links above a certain limit.[12] Accordingly, the displacement process here can be imagined as the biasing of the positions of small chain elements in potential wells defined by their interaction with neighboring chain elements. Thus, as expected, there is a steep decline in this modulus with increase in temperature, even for static measurements.

With increasing temperature, however, true "kinetic" theory elasticity rapidly comes into play for static or slowly varying measurements. However, the present results emphasize that all typical chain systems should also be examined for an intermediate type of elastic behavior in which the shear modulus of the order of 10^8 dynes/cm², which has the opposite temperature dependence to the kinetic theory phenomenon. This type of elasticity is markedly dependent on chain length and indeed the data are qualitatively similar to the recent conclusion[15] of the effect of average molecular weight on the *rate* of deformation of polyisobutylene, which is also notably dependent on molecular weight.

[10] F. T. Wall, J. Chem. Phys. **10**, 132 (1942); **10**, 485 (1942); **11**, 1527 (1943).
[11] P. J. Flory, Chem. Rev. **35**, 51 (1944).
[12] W. O. Baker and N. R. Pape, Report to Rubber Reserve Company May 27, 1943.
[13] J. W. Liska, Ind. Eng. Chem. **36**, 40 (1944).
[14] F. S. Conant and J. W. Liska, J. App. Phys. **15**, 767 (1944).
[15] J. Rehner, J. Polymer Sci. **2**, 225 (1946).

Hence, new causes besides kinetic theory behavior (which of course remains fundamental to rubber-like elasticity if enough time is given to establish equilibrium) must be sought to explain this intermediate type of low shear moduli in the order of 10^6 dynes/cm^2, whose presence must be regarded as well established. It may be that a composite movement, including hindered rotation *within* chains, as well as interaction of segments *between* chains, is the basis for this sort of elasticity. Such motion would be affected by chain length, through a chain articulation effect. Study of cellulose derivatives and other polymers, involving alteration of interchain forces without great changes in intrachain stiffness, will elucidate further this possibility. It is always striking that a degree of softness and high compliance may be imparted to virtually any chain system by sufficient amounts of plasticizer. Yet this does not much change the barriers to internal chain flexing, and, it is suspected, does not always directly introduce kinetic theory elasticity, but perhaps the other type of elasticity of this report.

Finally, at very high frequencies, the data on the velocity dispersion together with the shear measurements showing that the increase in longitudinal velocity is caused by an increase in shear elasticity indicate that this composite motion is relaxed and the shear elasticity is then determined by single potential wells and approaches that of a crystal. The data of Eq. (25) show that the shear elasticity equals 5.85×10^9 dynes/cm^2 and the liquid is similar to a solid having a Poisson's ratio of 0.4.

ACKNOWLEDGMENTS

The authors wish to thank Dr. J. M. Richardson for several helpful discussions on the mechanisms involved in these liquids and their effects on the loss and velocity measurements.

Quantum Theory of Localizable Dynamical Systems

P. A. M. DIRAC
Institute for Advanced Study, Princeton, New Jersey
(Received January 12, 1948)

A dynamical system is called localizable if its wave functions can be expressed in terms of variables, each referring to physical conditions at only one point in space-time. These variables may be at points on any three-dimensional space-like surface in space-time.

A general investigation is made of how the wave function varies when the surface is varied in any way. The variation of the wave function is given by equations of the Schrödinger type involving certain operators $H^{n}(u)$ which play the role of Hamiltonians. The commutation relations for these operators are obtained (Eqs. (50), (51)). The theory works entirely with relativistic concepts and it provides the general pattern which any relativistic quantum theory must conform to, provided the dynamical system is localizable.

I. INTRODUCTION

A *LOCALIZED* dynamical variable is a quantity which describes physical conditions at one point in space-time. Examples are field quantities and derivatives of field quantities to any order, also the position of a point particle at a particular time and the spin variable of a point particle at a particular time. Examples of dynamical variables that are not localized are the momentum of a point particle at a particular time in quantum theory and the spin variables of a body of finite size at a particular time, in classical or quantum theory.

A dynamical system in quantum theory will be defined as *localizable* if a representation for the wave functions can be set up in which all the dynamical variables are localized. Thus the system composed of a number of point particles interacting with fields is localizable. The representation will be called a *localized representation*.

To fix a state of motion of a dynamical system one usually specifies the wave function at a particular time. If the dynamical system is localizable and the representation is a localized one, each point in the domain of the wave function will refer to a set of points in space-time at this time. The set may be an infinite one and may be all points at this time. The wave function thus refers to points on a flat three-dimensional surface in space-time. The state of motion is then determined by physical information which refers to points on this flat three-dimensional surface.

From the general requirement of relativity that physical conditions at one point cannot influence the conditions at another point outside the light cone of the original point, one would expect the state of motion to be determinable also by physical information referring to points on any curved three-dimensional surface extending to infinity, provided this surface is everywhere space-like, i.e., the direction of the line joining any two points of it lies outside the light cone. Thus we should expect to be able to set up a wave function involving localized dynamical variables referring to points on any three-dimensional space-like surface S. This we should expect as a general characteristic of a localizable dynamical system.

The important question now presents itself. Are atomic systems in fact localizable dynamical systems in the above sense? This cannot be answered at the present time. It might very well be that states of atomic systems can be fixed only by wave functions on flat surfaces in space-time, owing to the atomic world containing some features which are not describable in terms of localized dynamical variables. It is true that all atomic models in present use that are relativistic are also localizable. But these models all lead to serious difficulties in their development. Many people think that the difficulties are directly caused by the models' being localizable and are trying to construct new theories in terms of quantities that are not accurately localizable. Heisenberg's[1] theory of the S-matrix is a general investigation on these lines.

It seems to be a very difficult and awkward

[1] W. Heisenberg, Zeits. f. Physik 120, 513, 673 (1943).

problem to set up a non-localizable dynamical system which shall be relativistic, and no work on this subject has yet progressed very far. In view of these difficulties I do not think the localizable models should be abandoned at the present time.

In most of the work that has been done on localizable dynamical systems people have confined their attention to wave functions and dynamical variables on flat surfaces in space-time, which form instants of time in some Lorentz frame. The work is thus not in relativistic form. In order to show that the theory is relativistic it would be necessary to study how the wave functions and dynamical variables transform when one changes the direction of the flat surfaces in space-time, and to show that all physical results are independent of this direction. This was done by Heisenberg and Pauli[2] for the case of electrons interacting with the electromagnetic field. But for most theories of particles in interaction (e.g., the various meson theories) it has not been done, and one does not know if these theories are relativistic.

In the following work I have investigated localizable dynamical systems on the most general lines, working only with relativistic ideas. This work provides a test for whether any theory of particles in interaction is relativistic and gives the conditions which must be satisfied for new theories.

II. THE GENERALIZED SCHRÖDINGER AND HEISENBERG EQUATIONS

Let S denote any three-dimensional space-like surface extending to infinity. We suppose a state of our dynamical system can be fixed by a wave function $\psi(q)$ involving variables q which are all localized on S. The variables q may consist of certain discrete variables, denoting positions of particles on S and their spins, if they have any, and may also consist of three-fold infinities of variables, denoting field quantities on S. If any three-fold infinities occur, then ψ is to be understood as a functional. The wave function must be capable of being normalized, according to an equation which we may write schematically

$$\int |\psi(q)|^2 dq = 1. \tag{1}$$

If the variables q contain a three-fold infinity, we must make a transformation which reduces them to an enumerable set (e.g., a transformation to particle variables) in order to be able to give a meaning to the integration in (1).

The surface S plays the role of the time in the non-relativistic theory. We have, so to speak, very many time variables in the present theory, namely all those variables needed to fix S. We must study how the wave function changes when S is changed in any way, subject to the condition that it remains space-like.

Take two surfaces S, say S_1 and S_2, and let the wave functions on these two surfaces be $\psi_1(q_1)$ and $\psi_2(q_2)$, respectively. We have to use different variables q_1 and q_2 in the two wave functions because they denote different sets of dynamical variables, localized in S_1 and S_2, respectively. From the principle of superposition of quantum mechanics, each of the functions ψ_1 and ψ_2 determins the other according to a linear law, so the two functions are connected by an equation of the form

$$\psi_2(q_2) = R\psi_1(q_1), \tag{2}$$

where R is a linear operator that can operate on a function of the q_1 variables and turns it into a function of the q_2 variables. R depends only on the dynamical system concerned and the two surfaces S_1 and S_2, and must be unitary in order to preserve the normalization of the wave function.

If the operators R connecting any two surfaces are known, then a wave function $\psi_1(q_1)$ on a particular surface S_1 determines a wave function $\psi(q)$ on an arbitrary space-like surface S. This wave function may be looked upon as a function $\psi(qS)$ of two sets of variables, the variables needed to fix S and the variables q, the latter variables being themselves dependent on S. This function $\psi(qS)$ which depends on S forms the analogue of the time-dependent wave function of non-relativistic quantum theory.

Let us consider a linear operator X_1 that can operate on a wave function $\psi_1(q_1)$ on the surface S_1 and turns it into another function of the

[2] W. Heisenberg and W. Pauli, Zeits. f. Physik 56, 1 (1929).

variables q_1, which can be looked upon as another wave function on the surface S_1. For example, X_1 may be an algebraic function of the variables q_1 and of the operators of differentiation with respect to the q_1's. Such a linear operator corresponds to a dynamical variable on the surface S_1. Of course, it need not be a localized dynamical variable, as it may involve q_1 variables localized at different points.

Suppose the linear operator X_1 changes the wave function $\psi_1(q_1)$ on S_1 into the wave function $\chi_1(q_1)$ on S_1. The wave function $\psi_1(q_1)$ on S_1 will determine an S-dependent wave function $\psi(qS)$ and, similarly, $\chi_1(q_1)$ will determine an S-dependent wave function $\chi(qS)$. We can now look upon X_1 as a linear operator which changes the S-dependent wave function $\psi(qS)$ into the S-dependent wave function $\chi(qS)$. Although X_1 refers to a particular S, namely S_1, it can in this way operate on wave functions which do not refer to any particular S, but are functions of a general S.

This way of looking upon dynamical variables on particular surfaces enables us to add and multiply dynamical variables on different surfaces. For example, the dynamical variable X_1 on the surface S_1 and the dynamical variable Y_2 on the surface S_2 can both be looked upon as linear operators operating on S-dependent wave functions $\psi(qS)$ to give other similar wave functions, and so their sum X_1+Y_2 and their products X_1Y_2, Y_2X_1 have an immediate interpretation as similar linear operators. The dynamical variables on different surfaces all form an algebra.

In order to study the consequences of the linear connection (2) between wave functions on different surfaces, let us take S_1 and S_2 to differ only by an infinitesimal of order ϵ. The surface S_2 is thus the result of applying any deformation of order ϵ to S_1. Equation (2) now gives

$$\psi_2(q_2)-\psi_1(q_1)=-i\epsilon A\psi_1(q_1), \tag{3}$$

where A is a linear operator connected with the previous R by

$$R=1-i\epsilon A. \tag{4}$$

The left-hand side of Eq. (3) is the sum of a function of the q_1's and a function of the q_2's and does not have any meaning as a single quantity. (E.g., it would have no meaning to say that the left-hand side of (3) vanishes.) For the purpose of developing the theory it is necessary to set up a connection between the domain of the function $\psi_1(q_1)$ and that of the function $\psi_2(q_2)$ so that two such functions can be added to produce another similar function. Given a function of the q_1's, we must be able to give a meaning to the *same* function of the q_2's.

The most obvious way of doing this is by introducing a general set of curvilinear coordinates u_1, u_2, u_3 on S_1, and a neighboring set of curvilinear coordinates, with the same names u_1, u_2, u_3, on S_2. This sets up a one-one correspondence between points on S_1 and points on S_2, and also between directions in S_1 at points on S_1 and directions in S_2 at points on S_2. Given a wave function on S_1 for which certain particles are at certain points with certain u-values and have certain spins, we now define the same function on S_2 as having the same particles at the points on S_2 with the same u-values, and having spins in the corresponding directions referred to the new system of coordinates. If the wave function on S_1 involves field variables, the same function on S_2 must involve in the same way the corresponding field variables with the same u-values.

In this way functions of the q_1's can be identified with functions of the q_2's, so that we can omit the suffixes and write them both as functions of the q's. The operator A becomes an operator that can be represented by a square matrix, which changes a function into another function of the same kind. The condition that R is unitary requires A to be Hermitian.

The method of identifying functions that we have introduced requires all the variables q occurring in the wave function $\psi_1(q)$ on S_1 to be defined with respect to the coordinate system u introduced on S_1. If the coordinate system is altered, the q's get altered in their meaning and so the wave function for a particular state gets altered. Equation (3) gives the law of change of the wave function $\psi_1(q)$ for any small change in the surface S_1 or in the coordinate system on it.

It becomes convenient at this stage to use the symbol S to denote a parametrized surface, i.e., a surface with a system of coordinates u_1, u_2, u_3 on it. A state of motion of a dynamical system is now fixed by a wave function $\psi_1(q)$ on any

parametrized surface S_1. It is the parametrized surface that really plays the role of the time in the non-relativistic theory—not the surface without the coordinate system.

We may take a small deformation of S_1 which does not change the surface but only changes the system of coordinates u on it. Such a deformation will cause the wave function $\psi_1(q)$ to change in a rather trivial way. Thus the operator A for such a deformation will be a trivial one and will not contain any terms corresponding to interaction between the various particles of the dynamical system. The operators A for deformations which change the surface will be the important ones and will include interaction terms.

A parametrized surface S_1 is fixed by specifying the four coordinates x_μ in space-time ($\mu=0, 1, 2, 3$) of any point on the surface as functions of the parameters $u_r (r=1, 2, 3)$, i.e., it is fixed by the four functions

$$x_\mu = x_\mu(u).$$

A small deformation of S_1 is fixed by specifying the variation δx_μ in the coordinates of a point with any given parameters u,

$$\delta x_\mu = \delta x_\mu(u). \tag{5}$$

We may resolve the displacement δx_μ into a part lying in the surface S_1 and a part normal to the surface S_1. The first part corresponds to a variation in the parameters u on the surface, say the variation, $\delta u_r = \epsilon a_r$. The second part is a displacement, of magnitude ϵa_n say, in the direction of the unit normal n_μ at each point u of the surface S_1, n_μ being defined by

$$n_\mu(\partial x^\mu/\partial u_r)=0, \quad n_\mu n^\mu=1, \quad n_0>0. \tag{6}$$

The total displacement δx_μ is thus

$$\delta x_\mu = (\partial x_\mu/\partial u_r)\epsilon a_r + n_\mu \epsilon a_n. \tag{7}$$

The deformation of S_1 may be fixed by specifying ϵa_r and ϵa_n as functions of the u's. There are two advantages in using this specification instead of that provided by (5). Firstly, one may continually apply small deformations with a_r, a_n any differentiable functions of the u's to a space-like parametrized surface S_1 and it always remains space-like. Secondly, the ϵa_r, ϵa_n specification allows one immediately to separate out those deformations for which only the coordinate system u is changed, corresponding to a trivial change in the wave function.

With the method of specifying deformations by the displacements ϵa_r, ϵa_n we are able, when we are given any deformation applied to a particular S, to give a meaning to the *same* deformation applied to any other S. We can then introduce a deformation operator $\epsilon\mathfrak{A}$ say, connected with this deformation. This deformation operator has the property that, if $F(S_1)$ is any function of S_1, i.e., any functional of the functions $x_\mu(u)$ that specify S_1, the same function $F(S_2)$ of the deformed S_2 will be given by

$$F(S_2)-F(S_1)=-i\epsilon\mathfrak{A}F(S_1) \tag{8}$$

to the first order in ϵ. If $F(S)$ and $\mathfrak{A}$ are treated as non-commutative quantities in an algebra, this equation must be replaced by

$$F(S_2)-F(S_1)=-i\epsilon\{\mathfrak{A}F(S_1)-F(S_1)\mathfrak{A}\}. \tag{9}$$

With the help of this notation, Eq. (3) becomes

$$\mathfrak{A}\psi_1(q)=A\psi_1(q).$$

If we let $\psi(qS)$ be the wave function on an arbitrary S, we get

$$\mathfrak{A}\psi(qS)=A\psi(qS), \tag{10}$$

in which $\mathfrak{A}$ is an operator which operates on the S variables and A is an operator which operates on the q variables. This equation is like the ordinary Schrödinger equation of non-relativistic quantum theory,

$$i\frac{\partial}{\partial t}\psi(qt)=\hbar^{-1}H\psi(qt), \tag{11}$$

with $\mathfrak{A}$ instead of $i\partial/\partial t$ and A instead of $\hbar^{-1}H$. There is, however, the important difference that non-relativistic quantum theory has just one Schrödinger equation (11), while the present theory has a very large number, one for each kind of deformation that can be applied to a parametrized surface S. The present theory may be compared more closely with the many-time theory of electrons in interaction with the electromagnetic field, which theory has many wave equations of the form (11), one for each electron. There is still the difference, though, that in this many-time theory all the operators $i\partial/\partial t$ commute with each other, while in the present theory

the various operators $\mathfrak{A}$ corresponding to different kinds of deformation do not in general commute.

A dynamical variable in the present theory corresponds to a linear operator which can operate on the variables q in the wave function and is independent of the variables that fix S. A linear operator which does depend on the variables that fix S is a more general thing, which is analogous to a function of dynamical variables involving the time explicitly in non-relativistic quantum theory.

The identification of functions of the variables q_1 on S_1 with functions of the variables q_2 on S_2 enables us to identify linear operators which operate on wave functions on S_1 with linear operators which operate on wave functions on S_2. This means that a dynamical variable on S_1 can be identified with a dynamical variable on S_2. Using language borrowed from non-relativistic quantum theory we may say that, if we have any dynamical variable "at the time S_1" we can give a meaning to the same dynamical variable at the time S_2.

We had previously a way of adding, and thus subtracting, dynamical variables at different times S_1 and S_2 by considering them as operators operating on the S-dependent wave function, (this process being independent of the parametrization). Let us use this to evaluate the difference between a dynamical variable at the time S_1 and the same dynamical variable at the time S_2.

Take a dynamical variable X and let X_1 be its value at the time S_1 and X_2 its value at the time S_2. X_1 changes the wave function ψ on S_1 to another wave function, which we may denote by $X\psi$, on S_1. From (2), X_1 must have the same effect on the S-dependent wave function as that operator which changes $R\psi$ on S_2 to $RX\psi$ on S_2, which is the same as changing $R\psi$ on S_2 to $RX_2\psi$ on S_2. Thus

$$X_1R\psi = RX_2\psi,$$

so that

$$X_1R = RX_2. \tag{12}$$

If S_2 differs from S_1 by an infinitesimal, we get, using (4),

$$X_2 - X_1 = -i\epsilon(X_1A - AX_1)$$

to the first order in ϵ. Introducing the commutator notation

$$XY - YX = i[X, Y],$$

we may write this result

$$X_2 - X_1 = \epsilon[X_1, A]. \tag{13}$$

It is the analogue of Heisenberg's equation of motion of non-relativistic quantum theory. It is of similar form to (9), except for a change of sign.

If we take a general quantity ξ_1 on S_1, depending on dynamical variables on S_1 and also on the variables that fix S_1, then on passing from S_1 to S_2, ξ_1 will undergo changes due to two causes, a change given by (13) arising from its involving dynamical variables and a change given by (9) arising from its explicit dependence on S. Thus the total change in ξ_1 will be

$$\xi_2 - \xi_1 = \epsilon[\xi_1, A - \mathfrak{A}]. \tag{14}$$

This corresponds to the equation

$$d\xi/dt = [\xi, H] + (\partial\xi/\partial t)$$

in non-relativistic quantum mechanics for a quantity ξ which is a function of dynamical variables and is also an explicit function of the time.

III. THE COMMUTATION RELATIONS

We shall suppose space-time is flat, as is usual in quantum theory. Embedded in this flat space we have a curved three-dimensional space-like surface S, parametrized by u_1, u_2, u_3. The square of an element of length in this surface is given by

$$-dx_\mu dx^\mu = -(\partial x_\mu/\partial u_r)(\partial x^\mu/\partial u_s)du_r du_s = \gamma^{rs}du_r du_s$$

where

$$\gamma^{rs} = -(\partial x_\mu/\partial u_r)(\partial x^\mu/\partial u_s). \tag{15}$$

Thus γ^{rs} determines the metric on the surface.

The geometrical properties of the surface (e.g., its curvature) are not completely determined by the γ^{rs}. Certain other quantities

$$\Omega^{rs} = (\partial n^\mu/\partial u_r)(\partial x_\mu/\partial u_s) = -n^\mu(\partial^2 x_\mu/\partial u_r \partial u_s) = \Omega^{sr} \tag{16}$$

are needed as well. The Ω^{rs} are not independent of the γ^{rs}, but are connected with them by cer-

tain relations due to Gauss, Mainardi, and Codazzi.[3]

When S is deformed, the γ's and Ω's get changed. This means that the γ's and Ω's do not commute with the deformation operators like $\mathfrak{A}$. We shall proceed to work out the more important commutation relations.

Take certain definite values for the parameters u, fixing a point $x_\mu(u)$ on the surface S. The deformation operator $\mathfrak{A}$ changes $x_\mu(u)$ by the amount

$$\delta x_\mu = \epsilon[\mathfrak{A}, x_\mu]$$

from (9). Equating this to the right-hand side of (7), we get

$$[\mathfrak{A}, x_\mu] = \frac{\partial x_\mu}{\partial u_r} a_r + n_\mu a_n. \tag{17}$$

Let us differentiate this equation with respect to u_s. The operator $\mathfrak{A}$ is not affected by the differentiation, since it has nothing to do with the values of u chosen above. The result is thus

$$\left[\mathfrak{A}, \frac{\partial x_\mu}{\partial u_s}\right] = \frac{\partial^2 x_\mu}{\partial u_r \partial u_s} a_r + \frac{\partial x_\mu}{\partial u_r}\frac{\partial a_r}{\partial u_s} + \frac{\partial n_\mu}{\partial u_s} a_n + n_\mu \frac{\partial a_n}{\partial u_s}. \tag{18}$$

Hence, from (15),

$$[\mathfrak{A}, \gamma^{rs}] = -\left[\mathfrak{A}, \frac{\partial x^\mu}{\partial u_r}\frac{\partial x_\mu}{\partial u_s}\right]$$

$$= -\frac{\partial x^\mu}{\partial u_r}\left\{\frac{\partial^2 x_\mu}{\partial u_t \partial u_s} a_t + \frac{\partial x_\mu}{\partial u_t}\frac{\partial a_t}{\partial u_s} + \frac{\partial n_\mu}{\partial u_s} a_n + n_\mu \frac{\partial a_n}{\partial u_s}\right\}$$

$$-\left\{\frac{\partial^2 x_\mu}{\partial u_t \partial u_r} a_t + \frac{\partial x_\mu}{\partial u_t}\frac{\partial a_t}{\partial u_r} + \frac{\partial n_\mu}{\partial u_r} a_n + n_\mu \frac{\partial a_n}{\partial u_r}\right\}\frac{\partial x^\mu}{\partial u_s}$$

$$(t = 1, 2, 3)$$

$$= \frac{\partial \gamma^{rs}}{\partial u_t} a_t + \gamma^{rt}\frac{\partial a_t}{\partial u_s} + \gamma^{ts}\frac{\partial a_t}{\partial u_r} - 2\Omega^{rs} a_n. \tag{19}$$

Let γ be the determinant formed by the γ^{rs}, and let γ_{rs} be the co-factor of the element γ^{rs} in this determinant, divided by γ. Then

$$[\mathfrak{A}, \gamma] = [\mathfrak{A}, \gamma^{rs}]\gamma_{rs}\gamma$$

$$= \frac{\partial \gamma}{\partial u_t} a_t + 2\gamma\left(\frac{\partial a_t}{\partial u_t} - \Omega_t{}^t a_n\right). \tag{20}$$

[3] See L. P. Eisenhart, *Riemannian Geometry* (Oxford University Press, 1926), p. 146.

The equation

$$\gamma^{tu}\gamma_{us} = \delta_s{}^t$$

leads to

$$[\mathfrak{A}, \gamma^{tu}\gamma_{us}] = 0$$

or

$$\gamma^{tu}[\mathfrak{A}, \gamma_{us}] + [\mathfrak{A}, \gamma^{tu}]\gamma_{us} = 0.$$

Thus

$$[\mathfrak{A}, \gamma_{rs}] = \gamma_{rt}\gamma^{tu}[\mathfrak{A}, \gamma_{us}]$$

$$= -\gamma_{rt}\gamma_{us}[\mathfrak{A}, \gamma^{tu}]. \tag{21}$$

Using (19), this gives

$$[\mathfrak{A}, \gamma_{rs}] = -\gamma_{rt}\gamma_{us}\left\{\frac{\partial \gamma^{tu}}{\partial u_v} a_v + \gamma^{tv}\frac{\partial a_v}{\partial u_u} + \gamma^{vu}\frac{\partial a_v}{\partial u_t} - 2\Omega^{tu} a_n\right\}$$

$$= \frac{\partial \gamma_{rs}}{\partial u_v} a_v - \gamma_{us}\frac{\partial a_r}{\partial u_u} - \gamma_{rt}\frac{\partial a_s}{\partial u_t} + 2\Omega_{rs} a_n \tag{22}$$

with the help of

$$\gamma_{us}\frac{\partial \gamma^{tu}}{\partial u_v} + \frac{\partial \gamma_{us}}{\partial u_v}\gamma^{tu} = 0.$$

We must now obtain the commutation relation of $\mathfrak{A}$ with n_μ. We get this by applying $\mathfrak{A}$ to Eqs. (6) which define n_μ. This gives

$$[\mathfrak{A}, n_\mu]\frac{\partial x^\mu}{\partial u_s} = -n_\mu\left[\mathfrak{A}, \frac{\partial x^\mu}{\partial u_s}\right]$$

$$= -n_\mu \frac{\partial^2 x^\mu}{\partial u_r \partial u_s} a_r - \frac{\partial a_n}{\partial u_s}$$

$$= \frac{\partial n_\mu}{\partial u_r}\frac{\partial x^\mu}{\partial u_s} a_r - \frac{\partial a_n}{\partial u_s},$$

and

$$[\mathfrak{A}, n_\mu] n^\mu = 0.$$

These four equations are sufficient to determine the four quantities $[\mathfrak{A}, n_\mu]$ and give

$$[\mathfrak{A}, n_\mu] = \frac{\partial n_\mu}{\partial u_r} a_r + \gamma_{rs}\frac{\partial x_\mu}{\partial u_r}\frac{\partial a_n}{\partial u_s}, \tag{23}$$

as is easily verified.

Let us now introduce another small deformation operator $\epsilon\mathfrak{B}$ which displaces each point

$x_\mu(u)$ on the surface S by the amount

$$\frac{\partial x_\mu}{\partial u_r}\epsilon b_r+n_\mu\epsilon b_n.$$

Thus,

$$[\mathfrak{B}, x_\mu]=\frac{\partial x_\mu}{\partial u_s}b_s+n_\mu b_n. \tag{24}$$

We shall now evaluate the commutator of $\mathfrak{A}$ and $\mathfrak{B}$.

Applying the operator $\mathfrak{A}$ to Eq. (24) and using (18) and (23), we get

$$[\mathfrak{A}, [\mathfrak{B}, x_\mu]]=\left[\mathfrak{A}, \frac{\partial x_\mu}{\partial u_s}\right]b_s+[\mathfrak{A}, n_\mu]b_n$$

$$=\left\{\frac{\partial^2 x_\mu}{\partial u_r\partial u_s}a_r+\frac{\partial x_\mu}{\partial u_r}\frac{\partial a_r}{\partial u_s}+\frac{\partial n_\mu}{\partial u_s}a_n+n_\mu\frac{\partial a_n}{\partial u_s}\right\}b_s$$

$$+\left\{\frac{\partial n_\mu}{\partial u_r}a_r+\gamma_{rs}\frac{\partial x_\mu}{\partial u_r}\frac{\partial a_n}{\partial u_s}\right\}b_n.$$

Interchanging $\mathfrak{A}$ and $\mathfrak{B}$ here and subtracting, we get

$$[[\mathfrak{A}, \mathfrak{B}], x_\mu]=[\mathfrak{A}, [\mathfrak{B}, x_\mu]]-[\mathfrak{B}, [\mathfrak{A}, x_\mu]]$$

$$=\frac{\partial x_\mu}{\partial u_r}\left(\frac{\partial a_r}{\partial u_s}b_s-\frac{\partial b_r}{\partial u_s}a_s\right)$$

$$+n_\mu\left(\frac{\partial a_n}{\partial u_s}b_s-\frac{\partial b_n}{\partial u_s}a_s\right)$$

$$+\gamma_{rs}\frac{\partial x_\mu}{\partial u_r}\left(\frac{\partial a_n}{\partial u_s}b_n-\frac{\partial b_n}{\partial u_s}a_n\right). \tag{25}$$

The commutator of the two deformation operators $\epsilon\mathfrak{A}$ and $\epsilon\mathfrak{B}$ is another deformation operator, $\epsilon^2[\mathfrak{A}, \mathfrak{B}]=\epsilon^2\mathfrak{C}$ say, which according to (25) displaces each point $x_\mu(u)$ on the surface S by the amount

$$\frac{\partial x_\mu}{\partial u_r}\epsilon^2 c_r+n_\mu\epsilon^2 c_n,$$

where

$$c_r=\frac{\partial a_r}{\partial u_s}b_s-\frac{\partial b_r}{\partial u_s}a_s+\gamma_{rs}\left(\frac{\partial a_n}{\partial u_s}b_n-\frac{\partial b_n}{\partial u_s}a_n\right), \tag{26}$$

$$c_n=\frac{\partial a_n}{\partial u_s}b_s-\frac{\partial b_n}{\partial u_s}a_s. \tag{27}$$

The deformation operator $\mathfrak{C}$ is not of quite the same nature as $\mathfrak{A}$ and $\mathfrak{B}$ since, while the displacements a_r, b_r are functions of the u's only, the c_r are functions of the γ_{rs} as well as being explicit functions of the u's. The c_r do not, in general, commute with deformation operators, as shown by Eq. (22). Thus, the set of deformation operators of the type of $\mathfrak{A}$ and $\mathfrak{B}$ do not form a Lie group. If we restrict ourselves to operators $\mathfrak{A}$, $\mathfrak{B}$, which do not change the surface S_1 but only its parametrization, so that $a_n=b_n=0$, then from (26) c_r is independent of the γ's, so that $\mathfrak{C}$ is another operator of the same nature. Thus, in this restricted case the deformation operators do form a Lie group. In the general case we can get a Lie group by taking all the deformations in which the displacements a_r, a_n are general functions of the γ's and Ω's and their derivatives, as well as being explicit functions of the u's.

The deformation operator $\mathfrak{A}$ must depend linearly on the functions $a_r(u)$, $a_n(u)$ which fix the displacement of each point $x_\mu(u)$ on the surface S. Thus $\mathfrak{A}$ must be connected with the functions $a_r(u)$, $a_n(u)$ by an equation of the form.

$$\mathfrak{A}=\int\{a_r(u)\Pi^r(u)+a_n(u)\Pi^n(u)\}d^3u,$$

$$(d^3u=du_1du_2du_3), \tag{28}$$

where $\Pi^r(u)$, $\Pi^n(u)$ are operator functions of u. The Π's are the elementary deformation operators, in terms of which any deformation operator can be linearly expressed.

We should expect an equation of the form (28) to hold also for more general deformation operators $\mathfrak{A}$ for which the displacements a_r, a_n are functions of the γ's and Ω's. The question then arises as to the order in which the two factors a and Π are to be put on the right-hand side of (28), as these two factors no longer commute. In order that one shall be able to apply these more general deformation operators to functions of S in accordance with formula (8), it is necessary that the Π's in (28) should always be to the right of their coefficients a, as this will make formula (8) follow from formula (9) together with the condition that each operator Π applied to something independent of S produces zero. It should be noticed that we get a consistent scheme when we assume that the commutator of

two of these more general operators $\mathfrak{A}$, with the Π's to the right of their coefficients, is another such operator with the Π's to the right of their coefficients, since the extra terms in the commutator arising from the Π's not commuting with the a's will all be linear functions of the Π's with their coefficients on the left. The Π's, together with the γ's and Ω's, then form an algebra with self-consistent commutation relations.

The commutation relations for the elementary deformation operators Π may easily be obtained from our previous commutation relations involving integrals of the Π's. For example, substituting

$$\mathfrak{A}=\int\{a_r(u')\Pi^r(u')+a_n(u')\Pi^n(u')\}d^3u'$$

(with a_r, a_n independent of the γ's and Ω's) in (17) and equating coefficients of $a_r(u')$, $a_n(u')$, we get

$$[\Pi^r(u'),\,x_\mu(u)]=(\partial x_\mu/\partial u_r)\delta(u-u'), \quad (29)$$

$$[\Pi^n(u'),\,x_\mu(u)]=n_\mu\delta(u-u'). \quad (30)$$

Similarly from (19) we get

$$[\Pi^t(u'),\,\gamma^{rs}(u)]=\frac{\partial\gamma^{rs}}{\partial u_t}\delta(u-u')+\gamma^{rt}(u)\frac{\partial\delta(u-u')}{\partial u_s}+\gamma^{ts}(u)\frac{\partial\delta(u-u')}{\partial u_r}, \quad (31)$$

$$[\Pi^n(u'),\,\gamma^{rs}(u)]=-2\Omega^{rs}\delta(u-u'), \quad (32)$$

and from (20) we get

$$[\Pi^t(u'),\,\gamma(u)]=\frac{\partial\gamma}{\partial u_t}\delta(u-u')+2\gamma(u)\frac{\partial\delta(u-u')}{\partial u_t}, \quad (33)$$

$$[\Pi^n(u'),\,\gamma(u)]=-2\gamma\Omega_t{}^t\delta(u-u'), \quad (34)$$

and so on.

To get the commutator of two Π's, we notice that, from (26) and (27) and the rule that coefficients must always be put to the left of the operators Π,

$$[\mathfrak{A},\,\mathfrak{B}]=\int\left\{\left(\frac{\partial a_r}{\partial u_s}b_s-\frac{\partial b_r}{\partial u_s}a_s+\gamma_{rs}\frac{\partial a_n}{\partial u_s}b_n-\gamma_{rs}\frac{\partial b_n}{\partial u_s}a_n\right)\Pi^r+\left(\frac{\partial a_n}{\partial u_s}b_s-\frac{\partial b_n}{\partial u_s}a_s\right)\Pi^n\right\}d^3u.$$

Substituting the expression given by (28) for $\mathfrak{A}$ and

$$\int\{b_r(u')\Pi^r(u')+b_n(u')\Pi^n(u')\}d^3u'$$

for $\mathfrak{B}$ and picking out coefficients of $a_r(u)b_s(u')$, $a_r(u)b_n(u')$, $a_n(u)b_n(u')$, we get

$$[\Pi^r(u),\,\Pi^s(u')]=-\frac{\partial\delta(u-u')}{\partial u_s}\Pi^r(u')-\frac{\partial\delta(u-u')}{\partial u_r}\Pi^s(u), \quad (35)$$

$$[\Pi^r(u),\,\Pi^n(u')]=-\frac{\partial\delta(u-u')}{\partial u_r}\Pi^n(u), \quad (36)$$

$$[\Pi^n(u),\,\Pi^n(u')]=-\frac{\partial\delta(u-u')}{\partial u_s}\times\{\gamma_{rs}(u)\Pi^r(u)+\gamma_{rs}(u')\Pi^r(u')\}. \quad (37)$$

In this way we obtain all the properties of the Π's.

Corresponding to the form (28) for $\mathfrak{A}$, the operator A of the Schrödinger Eq. (10) must also be expressible linearly in terms of the functions $a_r(u)$, $a_n(u)$, say

$$A=\int\{a_r(u)P^r(u)+a_n(u)P^n(u)\}d^3u, \quad (38)$$

where $P^r(u)$ and $P^n(u)$ are operators operating on the variables q of the wave function. They are, of course, Hermitian. The Schrödinger Eq. (10) for a wave function ψ now gives

$$\int\{a_r\Pi^r+a_n\Pi^n\}d^3u\psi=\int\{a_rP^r+a_nP^n\}d^3u\psi. \quad (39)$$

Since this wave equation must hold for an arbitrary small deformation, corresponding to arbitrary functions $a_r(u)$, $a_n(u)$, the wave func-

tion ψ must satisfy

$$\Pi^r(u)\psi = P^r(u)\psi, \tag{40}$$

$$\Pi^n(u)\psi = P^n(u)\psi. \tag{41}$$

These are the wave equations expressed in terms of the elementary operators Π, P.

The operators $P^n(u)$ are the Hamiltonians of the present theory and Eq. (41) is the important wave equation. There is one of these equations for each point on the surface S. Equation (40) merely states how the wave function is changed by a change in the u coordinate system, and the operators $P^r(u)$ are a kind of momentum operator, which is simple and can easily be worked out for any given dynamical system.

Let us take as an example a dynamical system composed of a number of particles without spin, the mth particle having coordinates u^m. The variables u^m may be taken as the q's in the wave function, so that it reads $\psi(u^m)$. The change in the parametrization caused by the displacements $\epsilon a_r(u)$ results in the u coordinates of a fixed point on the surface S being reduced by $\epsilon a_r(u)$, so that the coordinates of a particle u_r^m get changed to $u_r^m - \epsilon a_r(u^m)$. The operator which simply causes this change in the variables in the wave function is $-\epsilon \sum_m a_r(u^m)(\partial/\partial u_r^m)$. However, this operator is not Hermitian. It must be replaced by

$$-\tfrac{1}{2}\epsilon \sum_m \left\{ a_r(u^m)\frac{\partial}{\partial u_r^m} + \frac{\partial}{\partial u_r^m} a_r(u^m) \right\}. \tag{42}$$

This operator not only changes the variable u^m in the wave function in the required way, but also multiplies the wave function by a suitable factor, so that the normalization is preserved under the change in parametrization. We can now put

$$\int a_r(u) P^r(u) d^3u = -\tfrac{1}{2} \sum_m \left\{ a_r(u^m)\frac{\partial}{\partial u_r^m} + \frac{\partial}{\partial u_r^m} a_r(u^m) \right\},$$

from which it follows that

$$P^r(u) = -\tfrac{1}{2} \sum_m \left\{ \delta(u-u^m)\frac{\partial}{\partial u_r^m} + \frac{\partial}{\partial u_r^m}\delta(u-u^m) \right\}$$

$$= \sum_m \left\{ -\delta(u-u^m)\frac{\partial}{\partial u_r^m} + \frac{1}{2}\frac{\partial \delta(u-u^m)}{\partial u_r} \right\}. \tag{43}$$

Equations (40) and (41) can be combined into the single equation

$$\{\Pi^\alpha(u) - P^\alpha(u)\}\psi = 0 \quad (\alpha = 1, 2, 3, n)$$

From this equation and

$$\{\Pi^\beta(u') - P^\beta(u')\}\psi = 0. \quad (\beta = 1, 2, 3, n)$$

we can infer

$$[\Pi^\alpha(u) - P^\alpha(u),\ \Pi^\beta(u') - P^\beta(u')]\psi = 0. \tag{44}$$

Now the commutation relations (35), (36), (37) may be written

$$[\Pi^\alpha(u), \Pi^\beta(u')] = \int \kappa_\gamma{}^{\alpha\beta}(u, u', u'')\Pi^\gamma(u'')d^3u'', \quad (\gamma = 1, 2, 3, n) \tag{45}$$

where the κ's are certain functions of the variables u, u', u'', which may involve the γ^n at these points. From (44), (45), and the further wave equations

$$\{\Pi^\gamma(u'') - P^\gamma(u'')\}\psi = 0,$$

we get

$$\left\{ \int \kappa_\gamma{}^{\alpha\beta}(u, u', u'')P^\gamma(u'')d^3u'' - [\Pi^\alpha(u), P^\beta(u')] - [P^\alpha(u), \Pi^\beta(u')] + [P^\alpha(u), P^\beta(u')] \right\}\psi = 0. \tag{46}$$

All the four terms in the $\{\}$ here operate only on the q variables in ψ, not on the S variables. This is evident for the first and last terms, and for the others it is easily proved. Taking the second term, for example, we have

$$[[\Pi^\alpha(u), P^\beta(u')], x_\mu(u'')] = [[\Pi^\alpha(u), x_\mu(u'')], P^\beta(u')] = 0$$

from (29) and (30), showing that $[\Pi^\alpha(u), P^\beta(u')]$ commutes with all the quantities $x_\mu(u'')$ which define S, and hence it does not operate on the S variables. Thus, Eq. (46) is a condition on the wave function ψ for just one S.

Usually in quantum mechanics the wave function at one particular time is arbitrary. There are certain special dynamical systems for which it is not arbitrary, and the restrictions on the wave function at a particular time are then known as supplementary conditions. Let us sup-

pose there are no supplementary conditions in the present theory. There are then no restrictions on the wave function for one particular S, and so the operator in (46) must vanish. Thus,

$$\int \kappa_\gamma{}^{\alpha\beta}(u, u', u'')P^\gamma(u'')d^3u'' - [\Pi^\alpha(u), P^\beta(u')] - [P^\alpha(u), \Pi^\beta(u')] + [P^\alpha(u), P^\beta(u')] = 0. \quad (47)$$

This result may be written, with the help of (45),

$$[\Pi^\alpha(u) - P^\alpha(u), \Pi^\beta(u') - P^\beta(u')] = \int \kappa_\gamma{}^{\alpha\beta}(u, u', u'')\{\Pi^\gamma(u'') - P^\gamma(u'')\}d^3u''. \quad (48)$$

It can now be expressed in words, *the commutation relations between the quantities* $\Pi^\alpha(u) - P^\alpha(u)$ *are the same as those between the* $\Pi^\alpha(u)$. The argument by which this result was obtained is similar to the argument by which one infers that all the Hamiltonians must commute in the many-time theory of electrons interacting with the electromagnetic field, using the condition that all the $\partial/\partial t$ operators commute.

Equation (47) now gives, with the values of the κ's provided by (35), (36), (37),

$$[P^r(u), P^s(u')] + [\Pi^s(u'), P^r(u)] - [\Pi^r(u), P^s(u')] = \frac{\partial\delta(u-u')}{\partial u_s}P^r(u') + \frac{\partial\delta(u-u')}{\partial u_r}P^s(u), \quad (49)$$

$$[P^r(u), P^n(u')] + [\Pi^n(u'), P^r(u)] - [\Pi^r(u), P^n(u')] = \frac{\partial\delta(u-u')}{\partial u_r}P^n(u), \quad (50)$$

$$[P^n(u), P^n(u')] + [\Pi^n(u'), P^n(u)] - [\Pi^n(u), P^n(u')] = \frac{\partial\delta(u-u')}{\partial u_s}\{\gamma_{rs}(u)P^r(u) + \gamma_{rs}(u')P^r(u')\}. \quad (51)$$

Equations (49) give the commutation relations between the P^r's, and ought to be satisfied automatically if the P^r's have been correctly calculated. It may easily be checked that they are satisfied for Eq. (43). Equations (50) and (51) concern the Hamiltonians $P^n(u)$, and are *the fundamental commutation relations of the present theory.*

In non-relativistic quantum mechanics, for a dynamical system not acted on by external forces the Hamiltonian operator must not depend on the time. There must be a corresponding condition in the present theory. At first sight one would think this condition should be that the operators P^r, P^n are all independent of the S variables. This will not do, however, since it leads to a contradiction. It would make all quantities of the form $[\Pi^\alpha(u), P^\beta(u')]$ vanish, so that it would make the left-hand side of Eq. (51) independent of the S variables, while the right-hand side is not independent of them as it involves the γ_{rs}. We must take the weaker condition, that the operators P^r, P^n can involve only those functions of the S variables that describe geometrical properties of the parametrized surface S and are independent of its position and orientation in space-time. Thus they can involve the γ's and Ω's and their derivatives, but must not involve the variables $x_\mu(u)$, $\partial x_\mu(u)/\partial u_r$ except insofar as these variables are contained in the γ's and Ω's.

IV. SCALARS AND TENSORS

Let us consider a dynamical variable X on S. It varies with a variation of S according to the Heisenberg equation (13). It may be that X remains unchanged for all changes of S such that the surface and its parametrization are unchanged in the neighborhood of a particular point u'. In this case the dynamical variable X is *localized* at the point u' in S, or at the point $x_\mu(u')$ in space-time. We have here the mathematical condition for a dynamical variable to be localized at a particular point.

It may be further that X remains unchanged for all changes of S such that the point $x_\mu(u')$ remains fixed, i.e., such that S always passes through the fixed point in space-time where X is localized and the parameters u' of this point are unchanged, although the direction of S at this point may be altered. In this case X is called a *scalar*. In general, a dynamical variable X localized at a point $x_\mu(u')$ will undergo changes when S is changed subject to the condition that the point $x_\mu(u')$ remains fixed. X will then be a component

of a tensor, referred to the u's and the normal to the surface S as coordinate system, the tensor character of X being determined by its law of transformation under these changes of S.

The changes in a dynamical variable discussed above require a departure from the usual concept of a "dynamical variable at a particular time." A dynamical variable is defined in the first place as a linear operator operating on a wave function on a particular S, S_1, say. By interpreting the linear operator as an operator on the S dependent wave function, the linear operator becomes dependent on S_1 and we get Heisenberg's picture of dynamical variables. In Heisenberg's picture in non-relativistic quantum mechanics, a dynamical variable localized at a particular point P in space-time is a well-defined operator. In the present theory it is not, unless it is a scalar. In general it will depend on the direction of the surface S_1 through the point P where the dynamical variable is localized, its variation with variations in this direction being given by an equation of the form of Heisenberg's equation of motion. It may also depend on the parametrization of S_1 in the neighborhood of P, but this will involve rather trivial variations. It may also even depend on the curvature of S_1 at the point P. From the point of view of Heisenberg's picture, it would be more reasonable to count the different linear operators corresponding to a dynamical variable localized at P referred to different S's through the point P as different dynamical variables, *but this would involve a departure from the usual connection between Heisenberg's picture and Schrödinger's.*

Let

$$\mathfrak{A}^* = \int \{a_r \Pi^r + a_n \Pi^n\} d^3u,$$
$$A^* = \int \{a_r P^r + a_n P^n\} d^3u, \tag{53}$$

for functions a_r, a_n, which vanish at one particular point u in their domain. The tensor character of a dynamical variable X localized at the point $x_\mu(u)$ is determined by its commutator with A^*, in accordance with (13). Thus a scalar commutes with A^*. Any function ξ of dynamical variables and of variables which determine S, which are all localized at $x_\mu(u)$, will similarly have its tensor character determined by its commutator with $A^* - \mathfrak{A}^*$, in accordance with (14). Thus a scalar ξ commutes with $A^* - \mathfrak{A}^*$,

$$[\xi, A^* - \mathfrak{A}^*] = 0. \tag{54}$$

The four quantities $\partial x_\mu / \partial u_s$, n_μ for a particular value of μ with $s = 1, 2, 3$ form the four components of a covariant vector with respect to the u coordinate system. Their commutators with $A^* - \mathfrak{A}^*$ are, from (18) and (23)

$$\left[\frac{\partial x_\mu}{\partial u_s}, A^* - \mathfrak{A}^*\right] = \frac{\partial x_\mu}{\partial u_r}\frac{\partial a_r}{\partial u_s} + n_\mu \frac{\partial a_n}{\partial u_s},$$
$$[n_\mu, A^* - \mathfrak{A}^*] = \gamma_{rs} \frac{\partial x_\mu}{\partial u_r}\frac{\partial a_n}{\partial u_s}.$$

Any four ξ's with similar commutation relations are the four components of a covariant vector. Thus the commutation relations for a general covariant vector ξ^r, ξ^n are

$$[\xi^r, A^* - \mathfrak{A}^*] = \xi^r \frac{\partial a_r}{\partial u_s} + \xi^n \frac{\partial a_n}{\partial u_s},$$
$$[\xi^n, A^* - \mathfrak{A}^*] = \gamma_{rs}\xi^r \frac{\partial a_n}{\partial u_s}.$$

The commutation relations for other tensor characters may readily be obtained from this one.

From (20)

$$[\gamma, A^* - \mathfrak{A}^*] = 2\gamma \partial a_t / \partial u_t.$$

Thus the determinant γ is not a scalar according to the present definition. A quantity p with the same commutation relation as $\gamma^{\frac{1}{2}}$, namely

$$[p, A^* - \mathfrak{A}^*] = p \partial a_t / \partial u_t,$$

may be called a scalar density, (in a three-dimensional sense) because the integral of such a quantity over all u_1, u_2, u_3 is independent of the parametrization of S. Any scalar multiplied by $\gamma^{\frac{1}{2}}$ gives a scalar density. Similarly, a tensor multiplied by $\gamma^{\frac{1}{2}}$ may be called a tensor density.

One would be inclined to assume that the operators P^r, P^n are the components of a second-rank tensor density T, P^r being the component T^{rn} and P^n the component T^{nn}. This assumption would lead to some further simple commutation

relations between the P^r and P^n. However, I do not see any justification for this assumption in general. It leads to difficulties when there are particles with spin half a quantum present, owing to such spins not being directly describable with reference to oblique axes.

V. DISCUSSION

Any relativistic quantum theory of a localizable dynamical system will provide an example of linear operators $P^n(u)$ satisfying the commutation relations (50), (51), (provided there are no supplementary conditions). Conversely, *any example of linear operators $P^n(u)$ satisfying* (50), (51) *will provide a relativistic theory of a localizable dynamical system.* If one accepts the assumption that atomic systems are localizable, the problem of getting a relativistic theory of them becomes the problem of obtaining examples of sets of operators $P^n(u)$ satisfying (50), (51). If no suitable examples can be found, free from inconsistencies and sufficiently complicated to correspond to interaction between the elementary particles, one could infer that atomic systems are not localizable.

A field theory comparable with the present theory has been given by P. Weiss.[4] Weiss starts with a classical Lagrangian function involving field variables q, which provides an action integral bounded by any space-like surface S. Weiss then introduces momentum variables p on S, which are conjugate to the q's, also introduces Hamiltonians, and finally passes over from the classical theory to the analogous quantum theory.

Weiss' theory applies to dynamical systems which are localizable and are thus subject to the present theory, and his theory provides a method for obtaining Hamiltonians P^n satisfying the required commutation relations. The Hamiltonians obtainable in this way are not of the most general kind, but are restricted by two conditions. Firstly, the method applies only to dynamical systems describable in terms of dynamical variables satisfying the standard commutation relations of canonical q's and p's—it thus would not apply to electrons or other particles satisfying Fermi's statistics, for which the field quantities satisfy anticommutation relations. Secondly, the q's in Weiss' theory must be scalars, independent of the direction of the surface S. Only the p's may depend on this direction.[5]

Another quantum theory of fields has recently been given by Tomonaga.[6] This theory, like the present one, deals with wave functions on arbitrary space-like surfaces, but uses a different standard for identifying wave functions on different surfaces, based on the wave equations for particles without interaction. A wave function $\psi_1(q_1)$ on the surface S_1 counts as equal to a wave function $\psi_2(q_2)$ on the surface S_2 in Tomonaga's theory if the wave function $\psi_1(q_1)$ on S_1 leads to the wave function $\psi_2(q_2)$ on S_2 according to the wave equation for particles without interaction. This method of identifying wave functions avoids the need for parametrizing the surfaces S. A wave function will now change on passing from one surface S to another only on account of the interaction energy, so the Hamiltonians of Tomonaga's theory involve only the interaction energy. Tomonaga has developed his theory only for the case when all the Hamiltonians commute, but probably his method can be generalized.

[4] P. Weiss, Proc. Roy. Soc. **A169**, 102 (1938).

[5] P. Weiss, Proc. Roy. Soc. **A169**, 107 (1938), see bottom of page.

[6] S. Tomonaga, Progress of Theoretical Physics **1**, 27 (1946).

Crystal Radii of the Heavy Elements*

W. H ZACHARIASEN
Argonne National Laboratory and Department of Physics, University of Chicago, Chicago, Illinois

(Received January 21, 1948)

Crystal radii for the trivalent and tetravalent ions of the heavy elements from actinium to americium as deduced from crystal structure data are listed and briefly discussed.

THE writer has had the opportunity to carry out extensive crystal structure studies on compounds of elements 89 to 95.

Most of the compounds for which complete crystal structures have been deduced correspond to the trivalent or tetravalent states of these elements. The experimental crystal structure results show that the chemical binding is predominantly ionic for these valence states. For the purpose of crystal chemical considerations it is accordingly useful to introduce crystal radii for these ions.

The variation of lattice periods with atomic number for compounds of the heavy elements is illustrated in Tables I and II, which give the experimental results for the dioxides and the trifluorides. The dioxides have the fluorite type of structure, the trifluorides the tysonite type of structure. The lattice periods given for the trifluorides refer to the hexagonal cell containing two molecules.

TABLE I. Dioxides with fluorite type of structure.

Compound	a
ThO_2	5.5859±0.0005A
UO_2	5.4568 0.0005
NpO_2	5.425 0.001
PuO_2	5.386 0.001
AmO_2*	5.372 0.005

* Degree of purity uncertain.

TABLE II. Trifluorides with tysonite type of structure.

Compound	a_1	a_2
AcF_3	4.27 ±0.01A	7.53 ±0.02A
UF_3	4.138 0.003	7.333 0.004
NpF_3	4.108 0.001	7.273 0.004
PuF_3	4.087 0.001	7.240 0.001
AmF_3*	4.071 0.002	7.225 0.004

* See reference 1.

* The results given in this article are based on work carried out under Contract Number W-31-109-eng-38 for the Atomic Energy Project at Argonne National Laboratory.

The crystal radii given in Table III have been corrected for the effect of coordination number[1] and correspond to six coordination. The radii have been deduced from the observed interatomic distances in oxygen and fluorine compounds using crystal radii of 1.33A for F^- and 1.40A for O^{-2}. The crystal radii for the lanthanide series of ions are shown for comparison.

Many investigators have predicted that a 5*f* series of elements would begin near the end of the periodic system. The crystal structure studies of the writer provide proof of the correctness of these early predictions. In contrast to the 4*f* series of elements, there is not one but two prominent valence states for the heavy elements so far known. The trivalent state is known for actinium, uranium, neptunium, plutonium, and americium, but not for thorium and protactinium. The tetravalent state has been observed for all the elements in the series from thorium to americium.

Accordingly, one should speak of a thoride series for the tetravalent state, and of an actinide series for the trivalent state,

The slow, monotonic decrease in crystal radius with increasing atomic number, characteristic of the filling of the *f*-shell, is clearly demonstrated in Table III. A similar decrease in the size of the $(XO_2)^{+2}$ radical in going from uranyl to neptunyl to plutonyl compounds has been

TABLE III. Crystal radii.

Number of *f*-electrons	Thoride series		Actinide series		Lanthanide series	
0	Th^{+4}	0.95A	Ac^{+3}	1.11A	La^{+3}	1.04A
1	Pa^{+4}	(0.91)	$(Th^{+3}$	1.08)	Ce^{+3}	1.02
2	U^{+4}	0.89	$(Pa^{+3}$	1.06)	Pr^{+3}	1.00
3	Np^{+4}	0.88	U^{+3}	1.04	Nd^{+3}	0.99
4	Pu^{+4}	0.86	Np^{+3}	1.02	61^{+3}	(0.98)
5	Am^{+4}	0.85	Pu^{+3}	1.01	Sm^{+3}	0.97
6			Am^{+3}	1.00	Eu^{+3}	0.97

[1] W. H. Zachariasen, Zeits. f. Krist. **80**, 137 (1931).

observed. This would, of course, correspond to a uranide contraction. In the subnormal valence states the variation of crystal radius with increasing atomic number shows irregularities which are not understood at present.

The new compounds listed in Tables I and II were prepared by various chemists as follows: NpO_2 by T. J. LaChapelle and L. B. Magnussen, PuO_2 by P. Kirk; AmO_2 and AmF_3 by Sherman Fried, AcF_3 by Sherman Fried and F. Hagemann; UF_3 by J. Karle, NpF_3 by Sherman Fried, A. E. Florin, and N. R. Davidson; PuF_3 by A. E. Florin and R. E. Heath.

Detailed accounts of the various crystal structure investigations upon which the results given in this article are based will appear in Division IV of the National Nuclear Energy Series (Manhattan Project Technical Section).

PHYSICAL REVIEW VOLUME 73, NUMBER 9 MAY 1, 1948

The Question of Non-Singular Solutions in the Generalized Theory of Gravitation

A. PAPAPETROU
Dublin Institute for Advanced Studies, Dublin, Ireland

(Received November 20, 1947)

It has been already proved by Einstein and Pauli that in the relativistic theory of gravitation the field equations do not admit any non-singular static solution representing a field of non-vanishing total mass. In this paper it is shown that this theorem is also valid in the generalized theory of gravitation with non-symmetric g_{ik}.

1

IT has been proved first by Einstein[1] and then by Einstein and Pauli[2] that in the relativistic theory of gravitation (with symmetric g_{ik}) the field equations do not admit any non-singular static (i.e., with all components g_{ik} independent of t) solution which would represent a field of non-vanishing total mass. In the second paper the proof has been given for a space with a number of dimensions $n \geqslant 4$ in order to extend the validity of the theorem to the 5-dimensional theory of Kaluza.

The question arises whether this theorem is also valid in the generalized theory of gravitation with non-symmetric g_{ik}.[3] It will be shown in this paper that this question can be easily answered by using another proof of the theorem established by Einstein and Pauli. This second proof can be extended to the generalized theory, thus leading us to the result that *the same theorem is also valid in the generalized theory of gravitation.*

[1] A. Einstein, Revista (Universidad Nacional de Tucuman) **A2**, 11 (1941).
[2] A. Einstein and W. Pauli, Ann. Math. **44**, 131 (1943).
[3] A. Einstein and E. G. Straus, Ann. Mathematics **47**, 731 (1946); E. Schrödinger, Proc. Roy. I. A. **A51**, 163 (1947).

2

In this section we recapitulate the main points of the proof given by Einstein and Pauli for the theory with symmetric g_{ik}. This proof is based on the assumption that the solution is embedded in a Euclidean space, i.e., that at large distances the tensor g_{ik} tends to the metrical tensor γ_{ik} of flat space:

$$g_{ik} \to \gamma_{ik} \quad \text{for} \quad r \to \infty, \tag{1}$$

where

$$\gamma_{11}=\gamma_{22}=\gamma_{33}=-1, \quad \gamma_{44}=1, \qquad \text{all other } \gamma_{ik}=0. \tag{2}$$

Then from the field equations

$$R_{ik}=0$$

the following relation is shown to be valid in the case of static fields:[4]

$$(\mathfrak{g}^{4l}\Gamma_{4l}^{k})_{,k}=0.$$

[4] This relation has been derived in the paper of Einstein and Pauli in a rather complicated way. But it follows immediately from the field equations, and even in the stronger form

$$(\mathfrak{g}^{il}\Gamma_{il}^{k})_{,k}=0,$$

if one takes into account that

$$\mathfrak{g}^{il}{}_{;k}=\mathfrak{g}^{il}{}_{,k}+\mathfrak{g}^{sl}\Gamma_{sk}^{i}+\mathfrak{g}^{is}\Gamma_{sk}^{l}-\mathfrak{g}^{il}\Gamma_{sk}^{s}=0,$$

For a non-singular field this relation holds everywhere. Hence by integrating over the volume V inside a closed surface S one is led to the condition

$$\int_V (\mathfrak{g}^{4i}\Gamma_{4i}^{k})_{,k}dv = \oint_S \mathfrak{g}^{4i}\Gamma_{4i}^{k}n_k df = 0,$$

n_k being the components of the unit vector normal to S. On the other hand, for large values of r the field is weak and therefore one can use Einstein's equations of first approximation. It follows then that in this approximation (i.e., neglecting all terms proportional to $r^{-\alpha}$, $\alpha>1$) the field g_{ik} has the form

$$g_{11}=g_{22}=g_{33}=-[1+(2m/r)],$$
$$g_{44}=1-(2m/r); \qquad (3)$$
$$\text{all other } g_{ik}=0.$$

Inserting this in the last condition and taking as surface S a sphere $r=R$ of great radius R, one finds

$$m=0,$$

i.e., the theorem stated above.

3

Another proof of the same theorem can be based on an identity which gives the total energy of a static gravitational field in the form of an integral over the sources of the field. This identity reads:[5]

$$\int (\mathfrak{T}_4^4+\mathfrak{t}_4^4)dv = \int (\mathfrak{T}_4^4-\mathfrak{T}_1^1-\mathfrak{T}_2^2-\mathfrak{T}_3^3)dv, \qquad (4)$$

where T_k^i is the material tensor defined by

$$8\pi T_{ik} = -(R_{ik}-\tfrac{1}{2}g_{ik}R), \quad R=g^{\mu\nu}R_{\mu\nu}, \qquad (5)$$

while t_k^i is the well-known pseudotensor of the gravitational field. Indeed, if we calculate the volume integral of $\mathfrak{T}_4^4+\mathfrak{t}_4^4$ for the solution having the asymptotic form (3), we find the value m (this being one of the main justifications for the assumption that $\mathfrak{T}_4^4+\mathfrak{t}_4^4$ represents the total energy-density), and consequently the identity (4) gives

$$m=\int (\mathfrak{T}_4^4-\mathfrak{T}_1^1-\mathfrak{T}_2^2-\mathfrak{T}_3^3)dv. \qquad (6)$$

Thus we see that in the case of a non-singular field, where $T_{ik}=0$ everywhere, it is necessarily $m=0$.

4

In this and the next sections it will be shown that the identity (4) is valid also in the generalized theory of gravitation and that it can be again used for proving the non-existence of regular static solutions in this theory.

We start from two identities which have been given by Schrödinger:[6]

$$(*\mathfrak{T}_\beta^\alpha + *\mathfrak{t}_\beta^\alpha)_{,\alpha}=0,$$
$$8\pi(*\mathfrak{T}_\beta^\alpha + *\mathfrak{t}_\beta^\alpha) = \tfrac{1}{2}(*\Lambda_{\beta k}{}^{\varepsilon}\mathfrak{g}^{\alpha k} + *\Lambda_{k\beta}{}^{\varepsilon}\mathfrak{g}^{k\alpha} - \delta_\beta^\alpha *\Lambda_{ik}{}^{\varepsilon}\mathfrak{g}^{ik})_{,\varepsilon}. \qquad (7)$$

The quantity $*\mathfrak{T}_\beta^\alpha$ is related to $*R_{ik}$:

$$*\mathfrak{T}_\beta^\alpha = \tfrac{1}{2}(\mathfrak{g}^{\alpha k}\,*T_{\beta k}+\mathfrak{g}^{k\alpha}\,*T_{k\beta}),$$
$$8\pi\,*T_{ik} = -(*R_{ik}-\tfrac{1}{2}g_{ik}\,*R), \quad *R=g^{\mu\nu}\,*R_{\mu\nu}. \qquad (8)$$

The quantity $*\mathfrak{t}_\beta^\alpha$ is given by

$$8\pi\,*\mathfrak{t}_\beta^\alpha = \tfrac{1}{2}(\delta_\beta^\alpha\,*\Lambda + *\Lambda_{ik}{}^{\alpha}\mathfrak{g}^{ik}{}_{,\beta}), \qquad (9)$$

where

$$*\Lambda = \mathfrak{g}^{ik}(*\Gamma_{is}{}^{r}\,*\Gamma_{rk}{}^{s} - *\Gamma_{ik}{}^{r}\,*\Gamma_{rs}{}^{s}),$$
$$*\Lambda_{ik}{}^{\alpha} = *\Gamma_{ik}{}^{\alpha} - \delta_k^\alpha\,*\Gamma_{is}{}^{s}. \qquad (10)$$

The identities (7) are valid under the assumption that the relations

$$\overset{ik}{\mathfrak{g}\vee}_{,k}=0 \qquad (11)$$

are fulfilled everywhere. But this assumption

---

and

$$R_{ik}=-\Gamma_{ik}{}^{\alpha}{}_{,\alpha}+\Gamma_{i\alpha}{}^{\alpha}{}_{,k}+\Gamma_{i\beta}{}^{\alpha}\Gamma_{\alpha k}{}^{\beta}-\Gamma_{ik}{}^{\alpha}\Gamma_{\alpha\beta}{}^{\beta}.$$

Indeed, we find then for static fields, $(\cdots)_{,4}=0$:

$$(\mathfrak{g}^{4i}\Gamma_{4i}^{k})_{,k}+\mathfrak{g}^{4i}R_{4i} = -\mathfrak{g}^{si}\Gamma_{sk}{}^{l}\Gamma_{4i}{}^{k} = -\tfrac{1}{4}\mathfrak{g}^{si}g^{ll'}g^{kk'}(g_{l'k,s}+g_{sl',k}-g_{sk,l'})(g_{4k',i}-g_{4i,k'}),$$

and this is zero since it changes sign if we exchange the dummy indices s with k and i with k'.

[5] See R. C. Tolman, Phys. Rev. **35**, 875 (1930). A very simple derivation, showing also the limits of the validity of this identity, has been given by the present author in Proc. Roy. I. A. **A51**, 191 (1947).

[6] E. Schrödinger, Proc. Roy. I. A. **A52**, 1 (1948). We add a star to Schrödinger's $\mathfrak{T}_\beta^\alpha$ and $\mathfrak{t}_\beta^\alpha$, since these quantities have been derived from the variation of the part of the Lagrangian depending only on $*R_{ik}$. We shall use the notation $\mathfrak{T}_\beta^\alpha$ and $\mathfrak{t}_\beta^\alpha$ for the corresponding quantities derived from the total Lagrangian; see Eq. (19) below.

does not mean any restriction of the theorem we are going to prove. One sees it immediately if one remembers that in the generalized theory of gravitation Eq. (11) is a part of the field equations. Hence, for a regular solution both sets of equations, $R_{ik}=0$ *and* (11), must be fulfilled everywhere.

5

We now introduce the quantity

$$\mathfrak{T}_\beta{}^\alpha=\tfrac{1}{2}(\mathfrak{g}^{\alpha k}T_{\beta k}+\mathfrak{g}^{k\alpha}T_{k\beta}),$$
$$8\pi T_{ik}=-(R_{ik}-\tfrac{1}{2}g_{ik}R),\quad R=g^{\mu\nu}R_{\mu\nu}. \tag{12}$$

The relation between R_{ik} and ${}^*R_{ik}$ is:[7]

$$R_{ik}={}^*R_{ik}+F_{ik}, \tag{13}$$

with

$$F_{ik}=\tfrac{2}{3}(\Gamma_{k,i}-\Gamma_{i,k}). \tag{14}$$

So we find

$$8\pi\mathfrak{T}_\beta{}^\alpha=8\pi\,{}^*\mathfrak{T}_\beta{}^\alpha-\mathfrak{g}^{\alpha k}\overset{\vee}{}F_{\beta k}+\tfrac{1}{2}\delta_\beta{}^\alpha\mathfrak{g}^{\mu\nu}\overset{\vee}{}F_{\mu\nu}. \tag{15}$$

We put

$$\mathfrak{T}_\beta{}^\alpha-{}^*\mathfrak{T}_\beta{}^\alpha=\mathfrak{T}'_\beta{}^\alpha. \tag{16}$$

Computing the quantity $\mathfrak{T}'_\beta{}^\alpha{}_{,\alpha}$ we find

$$8\pi\mathfrak{T}'_\beta{}^\alpha{}_{,\alpha}=\tfrac{2}{3}\mathfrak{g}^{\mu\nu}\overset{\vee}{}{}_{,\beta}\Gamma_{\nu,\mu}=(\tfrac{2}{3}\mathfrak{g}^{\mu\nu}\overset{\vee}{}{}_{,\beta}\Gamma_\nu)_{,\mu}.$$

So if we put

$$8\pi\mathfrak{t}'_\beta{}^\alpha=-\tfrac{2}{3}\mathfrak{g}^{\alpha\nu}\overset{\vee}{}{}_{,\beta}\Gamma_\nu, \tag{17}$$

we have

$$(\mathfrak{T}'_\beta{}^\alpha+\mathfrak{t}'_\beta{}^\alpha)_{,\alpha}=0. \tag{18a}$$

Finally, we verify immediately the relation

$$8\pi(\mathfrak{T}'_\beta{}^\alpha+\mathfrak{t}'_\beta{}^\alpha)$$
$$=\tfrac{2}{3}(\mathfrak{g}^{\alpha\sigma}\overset{\vee}{}\Gamma_\beta+\delta_\beta{}^\alpha\mathfrak{g}^{\sigma\mu}\overset{\vee}{}\Gamma_\mu-\delta_\beta{}^\sigma\mathfrak{g}^{\alpha\mu}\overset{\vee}{}\Gamma_\mu)_{,\sigma}. \tag{18b}$$

Adding (7) and (18) and taking into account (10), we find

$$(\mathfrak{T}_\beta{}^\alpha+\mathfrak{t}_\beta{}^\alpha)_{,\alpha}=0,$$
$$8\pi(\mathfrak{T}_\beta{}^\alpha+\mathfrak{t}_\beta{}^\alpha)=\tfrac{1}{2}(\mathfrak{g}^{\alpha k}\,{}^*\Gamma_{\beta k}{}^\sigma+\mathfrak{g}^{k\alpha}\,{}^*\Gamma_{k\beta}{}^\sigma$$
$$-\mathfrak{g}^{\alpha\sigma}\,{}^*\Gamma_{\beta i}{}^i-\delta_\beta{}^\sigma\mathfrak{g}^{k\alpha}\,{}^*\Gamma_{ki}{}^i$$
$$-\delta_\beta{}^\alpha\mathfrak{g}^{ik}\,{}^*\Gamma_{ik}{}^\sigma+\delta_\beta{}^\alpha\mathfrak{g}^{i\sigma}\,{}^*\Gamma_{ik}{}^k$$
$$+\tfrac{4}{3}\mathfrak{g}^{\alpha\sigma}\overset{\vee}{}\Gamma_\beta+\tfrac{4}{3}\delta_\beta{}^\alpha\mathfrak{g}^{\sigma\mu}\overset{\vee}{}\Gamma_\mu$$
$$-\tfrac{4}{3}\delta_\beta{}^\sigma\mathfrak{g}^{\alpha\mu}\overset{\vee}{}\Gamma_\mu)_{,\sigma}, \tag{19}$$

where we have put

$$\mathfrak{t}_\beta{}^\alpha={}^*\mathfrak{t}_\beta{}^\alpha+\mathfrak{t}'_\beta{}^\alpha. \tag{20}$$

We mention that Eqs. (19) are the fundamental identities to which one is led by the usual variational method when starting from the Lagrangian

$$\mathfrak{L}_1=\mathfrak{g}^{ik}R_{ik}+(\mathfrak{g}^{ik}\Gamma_{ik}{}^\alpha)_{,\alpha}-(\mathfrak{g}^{ik}\Gamma_{i\alpha}{}^\alpha)_{,k},$$

which is equivalent to the usual Lagrangian

$$\mathfrak{L}=\mathfrak{g}^{ik}R_{ik}$$

insofar as it also leads to the same field equations.[8] On the contrary, Schrödinger's identities (7) are derived from the variation of ${}^*\Lambda$ which is only a part of $\mathfrak{L}_1$ and would not lead to the same field equations. But the question: Which are the identities expressing the "correct" conservation laws, cannot be easily answered, at least not by discussing the static fields represented by the few known solutions of the field equations; in the static case the volume integral of both the densities $\mathfrak{T}_4{}^4+\mathfrak{t}_4{}^4$ and ${}^*\mathfrak{T}_4{}^4+{}^*\mathfrak{t}_4{}^4$, and even of the corresponding density derived from the Lagrangian $\mathfrak{L}$, have all the same value.

6

The identity (4) can be derived in a general way[9] from the relation

$$\mathfrak{t}_i{}^i=2\mathfrak{t}_4{}^4. \tag{21}$$

We now prove that this relation is valid also in the non-symmetric theory. It follows from (17) that for static fields

$$\mathfrak{t}'_4{}^4=0,\quad \mathfrak{t}'_i{}^i=0.$$

Then from (20) and (9):

$$\mathfrak{t}_4{}^4={}^*\mathfrak{t}_4{}^4=\tfrac{1}{2}{}^*\Lambda.$$

And finally, taking into account (10) and the relation

$$\mathfrak{g}^{ik}{}_{,\alpha}+\mathfrak{g}^{sk}\,{}^*\Gamma_{s\alpha}{}^i+\mathfrak{g}^{is}\,{}^*\Gamma_{\alpha s}{}^k-\mathfrak{g}^{ik}\,{}^*\Gamma_{\alpha s}{}^s=0,$$

we find

$$\mathfrak{t}_i{}^i={}^*\mathfrak{t}_i{}^i={}^*\Lambda.$$

[7] E. Schrödinger, reference 3, relations (15) and (17).

[8] A general discussion of the identities derived from the different forms of the Lagrangian leading to the same field equations may be given in another paper.

[9] A. Papapetrou, Proc. Roy. I. A. **A51**, 191 (1947).

Thus we see that the relation (21) is holding, and consequently we have in the non-symmetric theory the identity (6):[10]

$$\int (\mathfrak{T}_4^4+\mathfrak{t}_4^4)dv=\int (\mathfrak{T}_4^4-\mathfrak{T}_1^1-\mathfrak{T}_2^2-\mathfrak{T}_3^3)dv.$$

7

We finally have to show that for a static field g_{ik} tending at infinity to γ_{ik}:

$$g_{ik}=\gamma_{ik}+g_{ik}' \quad \text{with} \quad g_{ik}'\sim 1/r, \qquad (22)$$

the volume integral of $\mathfrak{T}_4^4+\mathfrak{t}_4^4$ has the value m of the constant entering into the expressions of the diagonal components of g_{ik} according to (3). Starting from the second of Eq. (19) we find

$$\int (\mathfrak{T}_4^4+\mathfrak{t}_4^4)dv=\int \mathfrak{A}^s{}_{,s}dv=\oint \mathfrak{A}^s n_s df, \qquad (23)$$

where

$$\mathfrak{A}^s=\frac{1}{16\pi}(\mathfrak{g}^{ik}\,{}^*\Gamma_{ik}{}^s+\mathfrak{g}^{ik}\,{}^*\Gamma_{ik}{}^s-\mathfrak{g}^{ik}\,{}^*\Gamma_{ik}{}^s$$
$$+\mathfrak{g}^{is}\,{}^*\Gamma_{ik}{}^k+\frac{4}{3}\mathfrak{g}^{ks}\breve{\Gamma}_k+\frac{4}{3}\mathfrak{g}^{si}\breve{\Gamma}_i), \qquad (23a)$$

the other terms on the right-hand side of (19) vanishing in the case of static fields ($s=1, 2, 3$ only: $\delta_\beta{}^s=\delta_4{}^s=0$, and ${}^*\Gamma_{4i}{}^i=0$). On the other hand, it follows from $g_{ik}'\sim 1/r$ that all the components ${}^*\Gamma_{kl}{}^i$ will be $\sim 1/r^2$ and ${}^*R_{ik}\sim 1/r^3$. Therefore,

$${}^*\breve{R}_{ik}=-F_{ik}\sim 1/r^3,$$

and consequently.[11]

$$\Gamma_i\sim 1/r^2.$$

We see now that the two last terms in the expression of $\mathfrak{A}^s$, Eq. (23a), are $\sim 1/r^3$ and, therefore, do not contribute to the value of the total energy.[12] In the other terms of $\mathfrak{A}^s$ we must consider only the diagonal components of g_{ik} (since the other components give again terms $\sim(1/r^3)$). It follows then

$$\mathfrak{A}^s=\frac{1}{16\pi}({}^*\Gamma_{44}{}^s+{}^*\Gamma_{11}{}^s+{}^*\Gamma_{22}{}^s+{}^*\Gamma_{33}{}^s-{}^*\Gamma_{sk}{}^k).$$

And since

$${}^*\Gamma_{sk}{}^k={}^*\Gamma_{ks}{}^k={}^*\Gamma_{\underline{ks}}{}^k,$$

we see that $\mathfrak{A}^s$ depends only on symmetric components ${}^*\Gamma_{\underline{kl}}{}^i$.

Now we know that for weak fields in first approximation the symmetric part g_{ik} fulfills the same equations as in the theory of gravitation.[3] Therefore we can again make use of Einstein's equations of first approximation for the gravitational field and have then for g_{ik} exactly the same form as given by (3). Further, we notice that in this approximation the $\Gamma_{\underline{kl}}{}^i$ depend only on g_{ik}' and are given by the same expressions as in the theory of gravitation; so we see that the integral on the right-hand side of (23) has the same value as in the case of the pure gravitational field:

$$\oint \mathfrak{A}^s n_s df=m.$$

Therefore we have the relation

$$m=\int (\mathfrak{T}_4^4-\mathfrak{T}_1^1-\mathfrak{T}_2^2-\mathfrak{T}_3^3)dv,$$

which proves our theorem.[13]

The author wishes to express his thanks to Professor E. Schrödinger for valuable discussions.

[10] Since it is also

$${}^*\mathfrak{t}_i{}^i=2\,{}^*\mathfrak{t}_4{}^4,$$

we have additionally the identity

$$\int({}^*\mathfrak{T}_4{}^4+{}^*\mathfrak{t}_4{}^4)dv=\int({}^*\mathfrak{T}_4{}^4-{}^*\mathfrak{T}_1{}^1-{}^*\mathfrak{T}_2{}^2-{}^*\mathfrak{T}_3{}^3)dv.$$

But this identity cannot be used for proving our theorem, since the field equations are $R_{ik}=0$, and, generally, it will be ${}^*R_{ik}$ and ${}^*\mathfrak{T}_k{}^i\neq 0$.

[11] The vector Γ_i is determined only up to a gradient of an arbitrary scalar function. But this does not affect the value of $\mathfrak{T}_4^4+\mathfrak{t}_4^4$, since according to (15) $\mathfrak{T}_4^4$ depends only on F_{ik}, and $\mathfrak{t}_4^4={}^*\mathfrak{t}_4{}^4$ is entirely independent of Γ_i. Consequently, we can for the calculation of the total energy choose the simplest form of Γ_i which must be $\sim 1/r^2$ in order to lead to $\Gamma_{i,k}\sim 1/r^3$.

[12] These terms represent the difference between $\mathfrak{T}_4^4+\mathfrak{t}_4^4$ and ${}^*\mathfrak{T}_4{}^4+{}^*\mathfrak{t}_4{}^4$, as one can see from (18b). Hence the above conclusion means that both these densities lead to the same value of the total energy. This result has already been mentioned in Section 5.

[13] It may still be mentioned that according to the discussion given in Proc. Roy. I. A. **A51**, 191 (1947), the identity (4) holds under the condition that at great distances the quantities $\mathfrak{T}_1^1+\mathfrak{t}_1^1$, $\mathfrak{T}_2^2+\mathfrak{t}_2^2$, and $\mathfrak{T}_3^3+\mathfrak{t}_3^3$ tend to zero at least at $r^{-\alpha}$, $\alpha>3$. This condition is fulfilled in the case of a static field having the asymptotic form (22), since $\mathfrak{T}_k{}^i=0$ and $\mathfrak{t}_k{}^i\sim 1/r^4$, according to (9) and (17).

On the Hyperfine Structure of Deuterium

AAGE BOHR
*Institute for Theoretical Physics, Copenhagen, Denmark**
(Received March 15, 1948)

THE unexpected effects revealed by the very accurate measurements of the hyperfine structure of hydrogen and deuterium[1] have, as is well known, given rise to a re-examination of the consequences of quantum electrodynamics which has offered a convincing explanation of the main features of the phenomenon.[2] Still, a discrepancy so far remains between theory and experiment as regards the ratio between the HFS splittings in H and D. Assuming that the nuclei can be represented by charged mass points endowed with spin and magnetic moments, this ratio should be given by[3]

$$\kappa=\tfrac{3}{4}(\mu_D/\mu_H)\cdot(m_D/m_H)^3, \qquad (1)$$

where μ_D and μ_H are the magnetic moments of the deuteron and the proton, respectively, while m_D and m_H are the reduced electronic masses in the two atoms. The measurements, however, give a value for κ which is larger by 0.017 percent than that given by (1), whereas the estimated experimental uncertainty is only about 1:100,000.[4]

By taking the compound structure of the deuteron into account, it appears possible, however, to explain the major part of this discrepancy, at any rate. In fact, because the electron is bound by the charge of the proton, there will be an essential asymmetry between the magnetic interaction of the electron, on the one hand with the proton, and on the other hand with the neutron, of which the deuteron is composed. Thus, in the interior part of the atom, the electron "moves" very fast compared with the nucleons and in this region, therefore, the motion of the proton will only adiabatically influence the electron binding, the characteristics of which will be approximately stationary with respect to the position of the proton. Whereas the influence on the energy state of the atom of the magnetic moment of the proton will correspond with high accuracy to that of a central magnetic dipole, the effect of the neutron magnetic moment will consequently equal that of a spatial magnetization distributed with a density given by the wave function describing the motion of the neutron relative to the proton. Because of the symmetry of this distribution, the effective magnetic field of the neutron largely cancels within distances comparable to the deuteron radius. Since the magnetic moment of the neutron is negative, one should expect a relative increase in the HFS of D corresponding to

$$\epsilon=\Delta\kappa/\kappa\approx(\mu_N/\mu_D)\cdot(d/a), \qquad (2)$$

where μ_N is the magnetic moment of the neutron while d and a represent the radii of the deuteron and the deuterium atom, respectively. In fact, because of the rapid increase of the magnetic field with decreasing distance from the nucleus, the contribution to the HFS of any spherical shell of the atom, of given thickness, is approximately independent of the radius. Since $d/a \approx 10^{-4}$, the estimate (2) will be seen to give a value of ϵ which is just of the same order of magnitude as the observed effect.

The fact that, in the interior part of the atom, the proton, rather than the deuteron, responds to the electronic motion implies, of course, a certain modification of the correction factor in (1), depending on the reduced mass of the atom. The effect would, however, hardly seem to exceed the experimental uncertainty in κ, since the part of the atom in which the adiabatic adjustment holds extends only to distances from the nucleus of the order

$$\rho=d(M/m)^{\frac{1}{2}}, \qquad (3)$$

where m and M are the electron and nucleon

* Member of the Institute for Advanced Study, Princeton, New Jersey.

[1] J. E. Nafe, E. B. Nelson, and I. I. Rabi, Phys. Rev. **71**, 914 (1947); D. E. Nagle, R. S. Julian, and J. R. Zacharias, Phys. Rev. **72**, 971 (1947).

[2] Julian Schwinger, Phys. Rev. **73**, 416 (1948).

[3] G. Breit and E. R. Meyerott, Phys. Rev. **72**, 1023 (1947).

[4] J. E. Nafe and E. B. Nelson, Phys. Rev. **73**, 718 (1948). I am indebted to Professor Rabi for kindly informing me of the experimental results and for illuminating discussions regarding their theoretical interpretation.

mass, respectively. This result may be obtained from well-known arguments regarding the influence of molecular vibrations on electron binding states; and it may be noted that the distance ρ just corresponds to the atomic region where the restitutional frequency, $\hbar/m\rho^2$, of the electron configuration is comparable with the frequency, $\hbar/Md^2$, of the intrinsic nuclear motion.

Although very small compared with a, the value of ρ is still large compared with d, and in the inner atomic region where effects depending on the nuclear constitution become significant, one thus obtains a high approximation by assuming the electron binding to adjust itself to the momentary position of the proton. It may be added that this picture should not be essentially affected by exchange effects between the proton and the neutron, the frequency of which is also small compared with the local electron frequency. The contribution of the central part of the atom to the electron-neutron magnetic interaction will thus depend on the integral

$$\mathfrak{F}=\int\int \varphi^*(r)\chi^*(R) \times\{-(e/c)\boldsymbol{\alpha}\mathbf{A}\}\varphi(r)\chi(R)d\tau_r d\tau_R, \quad (4)$$

where $\varphi(r)$ and $\chi(R)$ are the wave functions representing the motion of the electron and the neutron relative to the proton. The operator $\boldsymbol{\alpha}$ is the Dirac vector, and

$$\mathbf{A}=\boldsymbol{\mu}_N\times\nabla_R\frac{1}{|\mathbf{r}-\mathbf{R}|} \quad (5)$$

is the vector potential due to the magnetic moment of the neutron. In the expression (4) the spinor parts of the wave functions have been left out since these play the same part as in usual HFS calculations where the deuteron is considered as a single particle. In fact, because of the very strong coupling between the spins of the neutron and the proton, we may, even in the region around the nucleus, with high approximation disregard combinations of the electron spin with the spins of the individual nuclear particles.

The integral (4) may be conveniently written

$$\mathfrak{F}=\int\varphi^*(r)\{(e/c)\boldsymbol{\alpha}\cdot(\boldsymbol{\mu}_N\times\nabla_r)P(r)\}\varphi(r)d\tau_r, \quad (6)$$

where

$$P(r)=\int\chi^*(R)\frac{1}{|\mathbf{r}-\mathbf{R}|}\chi(R)d\tau_R \quad (7)$$

involves the structure of the deuteron. This latter integral is easily estimated if, to a first approximation, we neglect the range of the nuclear forces compared with the deuteron radius. In fact, the deuteron wave function will then be independent of specific assumptions regarding these forces and may be written

$$\chi(R)\sim(1/R)e^{-R/d}, \quad (8)$$

with

$$d=\hbar/(MW)^{\frac{1}{2}}, \quad (9)$$

where W is binding energy of the deuteron. From (7) we thus get

$$\nabla P(r)\sim-(\mathbf{r}/r^3)(1-e^{-2r/d}), \quad (10)$$

which shows that the finite size of the deuteron simply implies an extra factor $(1-e^{-2r/d})$ in the radial part of the integral (6). In the case of the 1s state for which $\varphi(r)\sim e^{-r/a}$, the normal HFS involves the radial integral

$$\int_0^\infty e^{-2r/a}dr=a/2. \quad (11)$$

Therefore, it follows immediately that, since $a\gg\rho\gg d$, the relative decrease of the contribution of the neutron magnetic moment to the HFS is given by

$$(2/a)\int_0^\infty e^{-2r/d}dr=d/a, \quad (12)$$

corresponding to a relative correction in κ equal to

$$\epsilon=(\mu_N/\mu_D)\cdot(d/a)=1.84\cdot10^{-4}, \quad (13)$$

which conforms approximately with the observed effect.

For the estimate (13), the deuteron radius d was regarded as large compared with the range λ of the nuclear forces. Since, however, λ/d is assumed to be about $\frac{1}{3}$, it is significant, in view

of the accuracy of the measurements, to consider also the influence of the finite value of λ. In this connection it would seem necessary to take into account two different types of effects.

First, the deuteron wave function must be expected to deviate essentially from (6) at distances comparable to or smaller than λ. Since the density within such distances will be smaller than according to (8), the effect will be to increase the average distance between the nucleon and thus also the value of ϵ. Using a wave function corresponding to a rectangular potential well type of nucleon interaction of range λ, one finds, from (6) and (7), by neglecting terms of relative order $(\lambda/d)^2$,

$$\epsilon' = (\lambda/d)\epsilon \tag{14}$$

for the increase in ϵ.

A second correction to κ may result from possible deviations of the magnetic field of the nucleons from simple dipole fields, within distances comparable with the range of nuclear forces. The order of magnitude of this effect may be simply estimated by assuming a model in which the anomalous part of the nucleon magnetic moments, or approximately this part, is the result of a spatial magnetization extending over distances comparable with λ. Thus, in analogy to the estimate (12), the HFS of H would be decreased by a fraction

$$\delta_H = (\lambda'/a)[(\mu_H - 1)/\mu_H], \tag{15}$$

where λ' is some suitably chosen distance of the order of λ. Since, however, according to (4), the neutron magnetic moment is already effectively distributed over distances d, a deviation of the neutron from a point dipole within distances comparable with λ should give effects only of the relative order $(\lambda/d)^2$. One thus finds, corresponding to (15),

$$\delta_D = (\lambda'/a)[(\mu_H - 1)/\mu_D]. \tag{16}$$

This yields, by means of (13),

$$\epsilon'' = -(\delta_D - \delta_H) \approx -(\lambda'/d)\epsilon \tag{17}$$

for the resulting correction to ϵ.

It need hardly be added that such estimates of ϵ' and ϵ'' may depend considerably on the specific models chosen for the problems in question. Still, from a very general point of view it would seem that the sign of the estimates should be reliable and the close agreement of (13) with the observed value for $\Delta\kappa$ may perhaps therefore be related to the circumstance that the two corrective effects tend to cancel each other. If the estimate of ϵ' gives the right order of magnitude, it would indeed seem that the phenomenon gives a direct indication of the existence of an effect of the type corresponding to ϵ''. Together with evidence on the deuteron constitution, the hyperfine structure phenomenon might therefore offer some information regarding the nature of the anomalous magnetic moment of the proton.

The writer is indebted to Dr. Robert Oppenheimer for the opportunity of visiting the Institute for Advanced Study and benefiting from discussions with him as well as with the other members of the group working in the Institute

Letters to the Editor

PUBLICATION of brief reports of important discoveries in physics may be secured by addressing them to this department. The closing date for this department is five weeks prior to the date of issue. No proof will be sent to the authors. The Board of Editors does not hold itself responsible for the opinions expressed by the correspondents. Communications should not exceed 600 words in length.

On the Nuclear Moments of I^{127}, Ga^{69}, Ga^{71}, and P^{31}

R. V. POUND*
Lyman Laboratory of Physics, Harvard University, Cambridge, Massachusetts
March 15, 1948

BY use of a recording radiofrequency spectrometer, measurements have been made of the relative frequencies and the widths of a number of previously unreported resonance lines caused by nuclear magnetic moments in a fixed magnetic field. The absorption line resulting from the I^{127} nucleus was first found using solid NaI as a sample. The ratio of the frequency of the line to that of Na^{23} in the same sample was found, by a method previously reported,[1] to be

$$\nu(I^{127})/\nu(Na^{23}) = 0.75664 \pm 0.0002.$$

When corrected for the diamagnetic effects of the electrons in the two ions,[2] using 2.217 ± 0.002 nuclear magnetons and 3/2 for the magnetic moment and spin of Na^{23},[3] and 5/2 for the spin of I^{127}, a value of

$$\mu(I^{127}) = 2.8122 \pm 0.0030 \text{ nuclear magnetons}$$

is found for the nuclear magnetic moment of I^{127}. This is in good agreement with the value of 2.8 previously reported from hyperfine structure measurements,[4] from which the sign of the moment is taken. Evidence in support of the value 5/2 for the spin is gained from the ratio of the integrated line intensities for the Na^{23} and I^{127} lines, which was about 1:3. Under the conditions of operation of the spectrometer, the line intensity ratio should be approximately the ratio of the values of $I(I+1)$ for the two nuclei, where I is the spin.

The iodine line was also observed with an aqueous solution of NaI as the sample. The line had a breadth between points of maximum slope of 14 kc/sec., which can be compared with the widths previously reported for the lines due to Br^{79} and Br^{81} in solutions.[5] If one assumes the correlation time of the fluctuation of the grad **E** to be the same in the two cases, and that the grad **E** arises entirely from the dipolar fields of the water molecules, the spectral intensities of the components of grad **E** would be smaller for I^{127} than for Br by a factor of about 1.75, assuming the closest approach of the dipoles to be the sum of the molecular radii of the water molecules and the ionic radii. From this one is led to estimate the Br^{79} quadrupole moment as approximately 0.25×10^{-24} cm², since spectroscopic data[4,6] give -0.46×10^{-24} cm² for that of I^{127}. A check of the viscosities of the I^- and Br^- solutions showed them to be alike within 20 percent.

The lines caused by the two isotopes Ga^{69} and Ga^{71} have been observed with an aqueous solution of $GaCl_3$ as the sample. The ratio of the frequencies was

$$\nu(Ga^{71})/\nu(Ga^{69}) = 1.2701 \pm 0.0004,$$

in agreement with the ratio of the hyperfine structure $\Delta\nu$'s reported by Becker and Kusch.[7] The ratio of the frequency of the line due to Ga^{71} to that of Na^{23} was found to be

$$\nu(Ga^{71})/\nu(Ga^{69}) = 1.1529 \pm 0.0004.$$

Using this and the above values for the moment and the spin of Na^{23} and 3/2 for the spin of the gallium isotopes[8] gives

$$\mu(Ga^{69}) = 2.0165 \pm 0.0035 \text{ nuclear magnetons,}$$

and

$$\mu(Ga^{71}) = 2.5611 \pm 0.0030 \text{ nuclear magnetons.}$$

The Ga^{71} and Ga^{69} lines were about 3 and 7 kc/sec. in width, respectively, between points of maximum slope, in agreement with the ratio expected for line widths determined by a short relaxation time caused by the electric quadrupole coupling. The ratio of the squares of the quadrupole moments reported by Becker and Kusch is in good agreement with this. The broadening of the line makes the intensity observed with the modulation method proportional the fourth power of the quadrupole moment. Even though the Ga^{71} isotope is only $\frac{2}{3}$ as abundant as the Ga^{69} isotope, its line is about 4 times as intense. Comparison of the widths of these lines with those of the I^{127}, Br^{79}, and Br^{81} lines is not even so meaningful as the comparison between I^{127} and Br^{79} because the Ga^{+++} solution was rather viscous and was becoming hydrolized. The association of negative ions with water complexes is probably quite different from that of positive ions. The relative widths indicate greater similarity in the fluctuating tensors, grad **E**, than could be expected.

A spin of $\frac{1}{2}$ has been assigned to phosphorous P^{31} from observations of band spectra,[9] but no experimental data on its magnetic moment have been reported previously. The line resulting from the magnetic moment of P^{31} was found after about five days search with the automatic spectrometer. The line was found in both solid red phosphorous and in a concentrated solution of P_2O_5 in water. The spectrometer covers the range from 2 to 4 Mc/sec. in three days, and the line was found after five days continuous search with the second setting of the magnetic field, at about 2000 gauss. The frequency ratio of this line to that of Na^{23} was

$$\nu(P^{31})/\nu(Na^{23}) = 1.5310 \pm 0.0003.$$

This, together with the value $\frac{1}{2}$ for the spin of P^{31}, yields

$$\mu(P^{31}) = \pm 1.1314 \pm 0.0013 \text{ nuclear magnetons.}$$

Unfortunately, the spectrometer has not been designed to give data on the sign of the moment, but of the nuclei containing an odd number of protons and an even number

of neutrons, 39 are reported to have positive moments and only two, Ag^{107} and Ag^{109}, to have negative. If the moment of P^{31} is positive, it falls near to a curve for this class of nuclei published by Latham.[10]

Finally, it is perhaps worth reporting the detection of absorption lines believed to be due to the copper nuclei in the wire of the coil of the r-f spectrometer. These show up on several runs, including ones with no sample. With a sample of solid NaBr the copper lines are identified by their positions relative to one another and relative to the much stronger Na^{23}, Br^{79}, and Br^{81} lines.[1,8] Using 4×10^{-3} cm as the skin depth, the interior of the copper wire of the coil contains about 3 percent of the stored magnetic energy. The relaxation time of the copper nuclei must be shorter than that of the Na and Br because the lines are relatively more intense than this. Therefore, it appears likely that the relaxation time of the nuclei in the metal is less than a second but greater than 10^{-4} sec. because a relaxation time shorter than this would broaden the lines, which were about 5 kc/sec. in width.

* Society of Fellows.
[1] R. V. Pound, Phys. Rev. **73**, 523 (1948).
[2] W. E. Lamb, Phys. Rev. **60**, 817 (1941).
[3] J. B. M. Kellogg and S. Millman, Rev. Mod. Phys. **18**, 323 (1946).
[4] T. Schmidt, Zeits. f. Physik **112**, 199 (1939).
[5] R. V. Pound, Phys. Rev. **72**, 1273 (1947).
[6] K. Murakawa, Zeits. f. Physik **114**, 651 (1939).
[7] G. E. Becker and P. Kusch, Phys. Rev. **73**, 531 (1948).
[8] N. A. Renzetti, Phys. Rev. **57**, 753 (1940).
[9] M. Ashley, Phys. Rev. **44**, 919 (1933).
[10] R. Latham, Proc. Phys. Soc. **59**, 979 (1947).

Conductivity Induced in Diamond by Alpha-Particle Bombardment and Its Variation among Specimens

A. J. AHEARN
Bell Telephone Laboratories, Murray Hill, New Jersey
March 15, 1948

IN our experiments on conductivity induced in diamond by alpha-particle bombardment we obtain some response from most of the diamonds.[1] However, the magnitude of this response varies by a large factor. Moreover, in some individual specimens a large variation in response is obtained when the surface is scanned with a beam of alpha-particles.

Friedman, Birks, and Gauvin[2] report experiments in which only a small percentage of diamonds respond to bombardment by gamma-rays. In general, they find that such "counting" diamonds are transparent in the ultraviolet region, whereas their non-counting diamonds are opaque in the ultraviolet region. Following the nomenclature of Robertson, Fox, and Martin,[3] they classify their counting diamonds as type II, which is relatively rare, and their non-counting ones as the more common type I diamond.

Early in our work with diamond we investigated the ultraviolet transmission of a few specimens, some in which conductivity pulses were observed under alpha-particle bombardment and others in which no response was observed. Conductivity pulses were observed in all of the opaque diamonds. Among the transparent diamonds, conductivity pulses were observed in some but not in others.

TABLE I.

Diamond	Ultraviolet cut off in A.U.	Transmission diamond type	Diamond type from x-ray diffraction	Response to alpha-particle bombardment: positive	Response to alpha-particle bombardment: negative
2	2980	I		X	
2*E*	2900	I		X	
2*O*	2720			X	
1	2300	II	II		X
2*F*	2300	II		X	
2*H*	2250	II		X	
2*D*	2200	II			X
2M	2100	II			X
4*A*			I	X	
3*C*	2950	I	I	X	

A few diamonds were classified as to type by means of the x-ray diffraction technique of Lonsdale.[4] All specimens classified by this analysis as type I diamonds yielded conductivity pulses. The results of these ultraviolet transmission tests, x-ray diffraction tests, and alpha-particle bombardment tests are summarized in Table I.

Thus, in contrast to the gamma-ray experiments with diamond, we conclude that with alpha-particle bombardment conductivity pulses can be induced not only in diamonds that are transparent in the ultraviolet, but also in those which are opaque in the ultraviolet. There is the possibility that diamonds may be a mixture of the two types. A specimen which is a mixture could be opaque to the ultraviolet light, but the induced conductivity might be limited to the transparent parts of the diamond.

The fact that some diamonds give no response while others give a response which varies widely, not only among different specimens but also on different parts of a given specimen, might be associated with a mixture of diamond types in a given specimen. On the other hand, these variations may be associated with the degree of crystal imperfection and its variation among specimens. The trapping of electrons and positive holes that could occur at crystal imperfections is strongly indicated by the familiar space charge effects which are observed in crystal counters.

Bombarding diamond with 5-Mev alpha-particles from polonium, pulses up to 2700 microvolts have been observed with an input capacity of about 30 micromicrofarads. Friedman, Birks, and Gauvin[2] report pulses up to 50 microvolts from the few diamonds which respond to gamma-rays. Since they did not report the input capacitance of their circuit, a direct comparison of pulse magnitudes produced by alpha-particles and gamma-rays cannot be made from these data. However, the observation that more diamonds respond to alpha-particles than to gamma-rays may indicate that the alpha-particle is the more sensitive detector of the counting ability of diamond, as might be expected from energy absorption considerations.

The author is indebted to Dr. E. A. Wood for the x-ray diffraction analysis of the diamonds and to Mr. E. K. Jaycox for the ultraviolet transmission tests.

[1] Wooldridge, Ahearn, and Burton, Phys. Rev. **71**, 913 (1947).
[2] Friedman, Birks, and Gauvin, Phys. Rev. **73**, 186 (1948).
[3] Robertson, Fox, and Martin, Phil. Trans. Roy. Soc. London **463**, 232A (1934).
[4] K. Lonsdale, Proc. Roy. Soc. **A179** (1942).

Angular Distribution of n–p Scattering with 90-Mev Neutrons

J. HADLEY, E. L. KELLY, C. E. LEITH, E. SEGRÈ, C. WIEGAND, AND H. F. YORK
Radiation Laboratory, Physics Department, University of California, Berkeley, California
March 17, 1948

ONE of the important experiments that became feasible as soon as the 184-inch cyclotron started to operate was the measurement of the angular dependence of n-p scattering. As is well known, experiments of this type acquire particular significance when the de Broglie wavelength of the neutron is comparable with the range of nuclear forces.

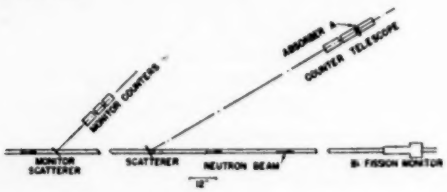

FIG. 1.

The neutron beam[1] of the cyclotron has an angular distribution well described by Serber's[2] stripping theory. We assume that the energy distribution of the neutrons is also that predicted by this theory, i.e., has a maximum at 90 Mev; the corresponding wave-length in the center of mass system is $\lambda\!\!\!^{-}=0.95\times10^{-13}$ cm.

We have used these neutrons to measure the n-p cross section as a function of the angle of scattering θ, in the CM system, between 70° and 170°. Figure 1 shows a schematic layout of the apparatus. The neutron beam produced by stripping 180-Mev deuterons on a Be target was collimated to about 2.5-cm diameter and scattered by paraffin or polyethylene targets which were larger in diameter than the neutron beam. The recoil protons used for the measurement were detected by a telescope of three proportional counters in coincidence pointing towards the scatterer. The primary neutron beam was monitored either by the protons scattered by an auxiliary hydrogenous target or by a bismuth fission chamber.

The telescope was made insensitive to protons below a certain energy by the Al absorber A. The thickness of the absorber was adjusted so that protons of energy less than $66\cos^2[(\pi-\theta)/2]$ Mev could not enter the third counter. Thus we made sure that if the recoil protons detected originated from elastic collisions of neutrons on hydrogen, the impinging neutron had an energy greater than 66 Mev. (We have neglected some small relativity correction.) By taking background measurements with a carbon scatterer and with no scatterer we distinguished the protons due to n-p scattering and those due to $(n$-$p)$ reactions on C and air.

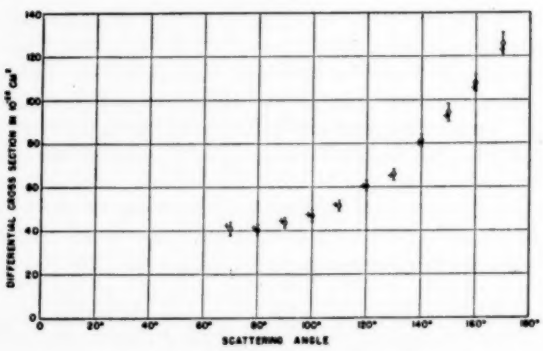

FIG. 2. Plan view of experimental arrangement.

Table I gives the cross section as a function of θ. Smaller and larger angles are being investigated but the results will not be available for some time.

From what we have said above it is apparent that our measurements give only a number proportional to $(d\sigma/d\omega)\Delta\omega$ where ω is the solid angle; however, we have normalized our figures by the following method: we have *hypothetically assumed* that $d\sigma/d\omega$ is the same for θ and $\pi-\theta$ and we have made the total scattering cross section 0.083×10^{-24} cm² as reported by Cook, McMillan, Peterson, and Sewell.[3] Our assumption on the behavior of the cross section for $\theta<90°$ is not in disagreement with some preliminary observations at $\theta<90°$ by us and with some cloud-chamber data communicated to us by Dr. W. Powell, *but is by no means established.* The data are also plotted in Fig. 2 with the relativistic corrections.

In order to avoid some sources of systematic error in these experiments, we have checked the following:

1. Plateau of the coincidence counting rate of the counter telescope *versus* voltage in the counters, bias voltage of the discriminators, duration of the opening of the coincidence gate of the counters.
2. Proportionality of the number of coincidence counts in the telescope to the intensity of the primary beam and to the thickness of the scattering target for a given primary neutron beam.
3. The influence of Rutherford scattering of the absorber A on the efficiency of the coincidence telescope.
4. Scattering by the air column traversed by the neutron beam.
5. The error introduced by the finite dimensions of the scattering target.
6. Whether the coincidence system counted only protons coming from the scatterer and all those with energy $>66\cos^2\theta$.

This list is not final and there are some important controls that should still be performed, but we feel confident enough of our results to give this preliminary account.

TABLE I. Differential cross section in 10^{-26} cm² (normalization hypothetical). The errors listed are based only on statistical standard deviations.

Scattering angle θ[a]	(b)	(c)	(d)	(e)
70	43.7±4.0	35.3± 2.8	39.0±3.7	40.8±3.1
80	42.6±3.5	32.5± 4.9	40.4±3.7	40.2±2.5
90	42.0±2.4	44.0± 4.2	45.1±4.9	43.5±2.4
100	47.0±3.0	42.4± 6.1	48.0±3.7	46.7±2.7
110	50.2±3.4	51.8± 6.1	53.0±3.5	51.4±2.5
120	59.0±2.7	59.7± 6.3	63.2±4.5	60.4±2.4
130	66.8±3.1	70.0± 7.0	61.5±3.8	65.6±2.7
140	79.5±3.1	78.5± 7.8	84.7±5.6	81.2±2.8
150	92.5±4.4	99.0± 7.0	94.0±5.4	94.1±4.1
160	105.5±3.8	127.0±10.6	107.5±7.9	107.7±3.8
170	126.0±5.8	127.5±14.0	123.2±9.4	125.7±5.0

[a] θ is the neutron scattering angle in the center of mass system.
[b] Composite of runs on apparatus 1.
[c] Run on apparatus 2, scatterer 150 mg/cm² $(CH_2)_n$.
[d] Run on apparatus 2, scatterer 283 mg/cm² $(CH_2)_n$.
[e] Weighted average of all runs with estimated error.

It must be added that these experiments were performed independently with two separate sets of equipment which were similar in principle but differed in many details. This procedure helped considerably in making us aware of unsuspected caused of trouble.

The peak of protons in the forward direction is a clear indication of the existence of exchange forces between neutron and proton. A more detailed analysis that takes into account the total scattering cross section and the angular distribution indicates that there might be comparable amounts of ordinary forces.

The authors wish to express their appreciation to Drs. E. M. McMillan, W. Powell, and R. Serber for interesting discussions. This work was done under the auspices of the Atomic Energy Commission under Contract No. W-7405-eng-48.

[1] A. C. Helmholz, E. M. McMillan, and D. Sewell, Phys. Rev. **72**, 1003 (1947).
[2] R. Serber, Phys. Rev. **72**, 1007 (1947).
[3] L. F. Cook, E. M. McMillan, J. M. Peterson, and D. C. Sewell, Phys. Rev. **72**, 1003 (1947).

The Spectrum of Locally Isotropic Turbulence

LESLIE S. G. KOVASZNAY
Johns Hopkins University, Baltimore, Maryland
March 1, 1948

RECENT theories* employ a physical picture of the fully developed turbulence at high Reynolds numbers as an "eddy-cascade" where the kinetic energy of the larger scale eddies is transferred to the smaller ones by the Reynolds stresses of the small scale motion.

Assuming similarity in this turbulent energy transport mechanism and neglecting viscosity, several authors** have succeeded in deriving a spectrum for the medium frequency range, which is a "five-thirds-power law."

It follows from Kolmogoroff's first similarity hypothesis that the spectrum of locally isotropic turbulence expressed in a non-dimensional form must be a unique function. This leaves us with only two parameters (characteristic frequency and characteristic intensity), and these can be expressed in terms of ϵ_0, the total energy dissipation per unit mass and unit time, and ν, the kinematic viscosity of the fluid. The two parameters are not independent, but may be combined into a Reynolds number which is a universal constant. We define the spectrum function $F(n)$:

$$\overline{u^2}=\int_0^\infty F(n)dn, \tag{1}$$

u = velocity fluctuation in the turbulence, n = wave number.

We make two assumptions: *first*, $S(n)$, the kinetic energy per unit mass and unit time that passes through frequency n, depends only on the values $F(n)$ and n.*** The energy transport must have dimensions of u^3l^{-1}; the only possible form is

$$S(n)=k_1F^{3/2}n^{5/2}, \tag{2}$$

where k_1 is a non-dimensional constant.

Second, the mechanism of turbulent energy transport is not affected by the viscosity; therefore k_1 is a universal constant.†

The energy that must be passed to higher frequency becomes less and less as the viscosity dissipates more and more energy into heat. We may define the viscous dissipation between frequencies zero and n as

$$\epsilon v(n)=60\pi^2\nu\int_0^n n_1^2F(n_1)dn_1. \tag{3}$$

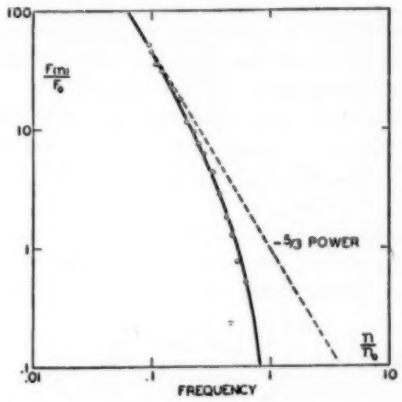

FIG. 1. Spectrum of locally isotropic turbulence.

In steady state the rate of change of energy transport is equal to the negative of the rate of dissipation

$$(dS(n)/dn)=-(d\epsilon v(n)/dn). \tag{4}$$

From (2), (3), and (4) we get an equation for $F(n)$:

$$dF/dn+(5/3)(F/n)+(40\pi^2\nu)/k_1(F/n)^{\frac{1}{2}}=0. \tag{5}$$

The solution is

$$F(n)=F_0(n/n_0)^{-5/3}[1-(n/n_0)^{4/3}], \tag{6}$$

where F_0 and n_0 are constants and

$$R_0=\frac{1}{\nu}(F_0/n_0)^{\frac{1}{2}} \tag{7}$$

is a universal constant (Reynolds number).

The spectrum function goes to zero at $n=n_0$ with a zero slope, and joins the "five-third law" for $n\ll n_0$. The only constant in the present theory is R_0, and this can be obtained from spectrum measurements. Uisng the results of L. F. G. Simons†† (3-in. grid $U_0=35$ ft./sec.), it was found that $R_0=11.5$. Using this value the measured points seem to check the theoretical curve well (Fig. 1).

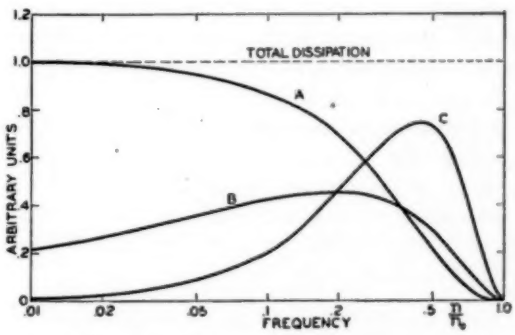

FIG. 2. Energy balance of turbulence spectrum.

The energy balance of the spectrum is shown in Fig. 2:

(a) $S(n)$ the turbulent energy transport,
(b) $d\epsilon v/dn$ the rate of viscous dissipation per frequency (wave number),
(c) $n(d\epsilon v/dn)$ the rate of viscous dissipation per turbulent "cascade-stage" (e.g., per octave).

Other formulae have been obtained connecting ϵ_0, the total dissipation of energy, with F_0, n_0 and, similarly, with R_λ, the Reynolds number of the microscale.

Disregarding the lower frequency part of the spectrum, we can compute correlation functions and other statistical properties that could be measured by cutting off the low frequency component.

A more detailed account will be published soon.

Thanks are due Drs. Francis H. Clauser and Stanley Corrsin for their kind help and stimulating discussion.

* An N. Kolmogoroff, Comptes Rendus (Doklady) U.S.S.R. **30**, No. 4, **31**, No. 6, **32**, No. 1; W. Heisenberg (unpublished, 1945); G. K. Batchelor, Proc. Camb. Phil. Soc. (October 1947).

** A. Obukhoff, Comptes Rendus (Doklady) U.S.S.R. **32**, No. 1; L. Onsager, Phys. Rev. **68**, 286 (1945); C. F. von Weizsacker (unpublished, 1945).

*** This assumption is based on the fact that the energy transport is due to the non-linear "inertia terms" in the Navier-Stokes equation. Since the product of two Fourier components of differing frequencies gives zero time average, the different stages of the cascade are uncorrelated and it is likely that no contribution is made to the energy transport by other frequencies.

† The viscous terms are linear in the Navier-Stokes equation, and the non-linear terms are not affected by viscosity. Therefore, it is natural to assume similarity in the energy transport mechanism.

†† L. F. G. Simons, Proc. Roy. Soc. **165** (1938).

On the Quantum Theory of Ferromagnetic Resonance

D. POLDER
H. H. Wills' Physical Laboratory, University of Bristol, Bristol, England
March 2, 1948

A FERROMAGNETIC material, magnetized up to its saturation value M_0 by means of a constant external field H_0, shows interesting resonance phenomena when small additional high frequency magnetic fields are applied. Kittel[1] has been able to give an explanation of the effect by using classical equations of motion for the magnetic dipoles. In the special case of a non-conducting ellipsoidal specimen, magnetized in the direction of one of its principal axes (z axis), it is easy to derive an expression for the induced alternating magnetization m when a small external alternating field $h_x \exp j\omega t$ is applied, provided that the dimensions of the ellipsoid are small in comparison with the wave-lengths of the electromagnetic waves inside the material. Neglecting damping terms and anisotropy effects one finds[2] exponential time factors being omitted):

$$[\gamma^2\{H_0+(N_x-N_z)M_0\}\{H_0+(N_y-N_z)M_0\}-\omega^2]m_x = \gamma^2 M_0\{H_0+(N_y-N_z)M_0\}h_x,$$

$$[\gamma^2\{H_0+(N_x-N_z)M_0\}\{H_0+(N_y-N_z)M_0\}-\omega^2]m_y = j\omega\gamma M_0 h_x,$$

where N_x, N_y are the demagnetization factors in the x, y directions, and so on, and where γ should be equal to the gyromagnetic ratio of the spins.

In order to justify the use of classical equations of motion, it is our aim to derive these expressions from quantum-mechanical considerations. We use as a starting point a Hamiltonian containing terms describing the interaction of the spins with the external magnetic fields, an isotropic exchange interaction between nearest neighbors, and the magnetic dipole-dipole interaction between the spins in the small ellipsoid. When the constant external field is sufficiently high and the temperature is sufficiently low only those stationary states of Schrödinger's equation will play a role for which there is nearly complete alignment of the spins. Holstein and Primakoff[3] have developed an approximate method for dealing with these states and have determined the corresponding eigenvalues of the energy in a first approximation. Their method can be considered as an improved Bloch spin-wave treatment of ferromagnetism; the improvement consists in including the dipole-dipole terms.

When we now consider the additional alternating field as a small perturbation, we can determine m_x and m_y by means of a method analogous to that used in the theory of coherent scattering. Resonance will occur at frequencies for which $\hbar\omega$ is equal to the difference of the energies of two stationary states between which the alternating magnetic field can cause transitions. We find that in H and P's approximation the energy difference between any two of these states is always equal to $2\beta[\{H_0+(N_x-N_z)M_0\}\times\{H_0+(N_y-N_z)M_0\}]^{\frac{1}{2}}$ and that the approximation eventually leads to expressions for m_x and m_y which are identical with the classical expressions if we put $\gamma=2\beta/\hbar$. Here β is the magnetic moment of the spins, and thus γ is equal to the gyromagnetic ratio in the case of free spins. By taking into account terms in the Hamiltonian, which are neglected in H and P's approximation, it should also be possible to estimate the width of the resonance line.

Our quantum-mechanical consideration suggests a possible explanation for the observed discrepancy[4] between the value of γ determined by resonance experiments and the gyromagnetic ratio. When we assume that spin-orbit interaction causes a deviation of the effective magnetic moment β of the spins from the spin only value μ_B, let us say $\beta>\mu_B$, then $\gamma>2\mu_B/\hbar$. At the same time the spin-orbit interaction will cause a still larger deviation of the effective angular momentum of the spins from the spin only value $\frac{1}{2}\hbar$. Therefore the gyromagnetic ratio may be expected to be smaller than $2\mu_B/\hbar$. It would be interesting if this connection between the deviations of the angular momentum and γ from spin only values could be verified experimentally. A fuller account of our calculations will be given shortly.

[1] C. Kittel, Phys. Rev. **71**, 270 (1947).
[2] C. Kittel, Phys. Rev. **73**, 155 (1948).
[3] T. Holstein and H. Primakoff, Phys. Rev. **58**, 1098 (1940).
[4] W. A. Yager and R. M. Bozorth, Phys. Rev. **72**, 80 (1947).

A Study of Lubricating Wax Coatings by Electron Diffraction

CHESTER RIDLON BERRY
Research Laboratories, Eastman Kodak Company, Rochester, New York
March 22, 1948

IT has been observed that certain thin coatings of carnauba wax have different lubricating qualities, although no other physical difference was apparent. Because of the sensitivity of the electron diffraction method for the investigation of thin surface films, it was applied to this problem.

Two coatings were examined, one of which was a good lubricant and the other a poor one. The good lubricant gave a diffraction pattern which showed considerably more preferred orientation than the poor lubricant. Both buffing and heat treatment of the original specimens produced poorer preferred orientation than before and corresponding poorer lubricants.

These observations confirm those of Andrew[1] and Brummage[2] on the existence of preferred orientation in good lubricants.

Since carnauba wax contains hydrocarbon residues linked by a caboxyl group, it seemed reasonable to attempt to interpret the diffraction pattern in terms of the recent work of J. Karle and L. O. Brockway[3] on the interpretation of electron diffraction patterns from hydrocarbon films. They have assumed that diffraction effects are caused only by the carbon atoms in the plane zigzag chain which have tetrahedral bond angles, the centers of the atoms being separated by 1.54A. Much of the diffraction pattern from the wax can be interpreted on the basis of their results. The preferred orientation is that in which the axis of the carbon chain is normal to the supporting surface. In this case, Karle and Brockway have shown that the intensity of the first-layer line maxima, corresponding to Bragg spacings of about 1.73A, varies from zero, when the plane of the carbon atoms is parallel to the electron beam, to a maximum when the plane of the carbon atoms is perpendicular to the electron beam. A rough comparison of the intensities of these maxima when the electron beam is at 0, 45, and 90 degrees to the direction of coating of the wax layer indicates that the plane of the carbon atoms has a preferred orientation at 90 degrees to the direction of coating.

The calculated pattern for a long carbon chain does not account for two groups of intensity maxima which occur in the pattern of the more highly oriented specimen. A single maximum having a Bragg spacing of 4.4A appears along the y axis[4] and two maxima, each having a Bragg spacing of about 2.29A, appear on or near the first-layer line at equal distances from the y axis. The origin of these maxima has not been determined.

[1] L. T. Andrew, Trans. Faraday Soc. 32, 1, 607 (1936).
[2] K. G. Brummage, Proc. Roy. Soc. 188, 414 (1947).
[3] J. Karle and L. O. Brockway, J. Chem. Phys. 15, 213 (1947).
[4] The y axis is defined by Karle and Brockway as the line in the plane of the photograph normal to the shadow edge and passing through the spot due to the undeviated beam.

The Neutron-Proton Scattering Formula: Remark on the Letter by Flügge and Hückel

TA-YOU WU AND HENRY M. FOLEY
Department of Physics, Columbia University, New York, New York
March 10, 1948

IN a recent Letter to the Editor,[1] Flügge and Hückel give the following expression for the total cross section for proton-neutron scattering for the singlet state in terms of a virtual state of positive energy $\kappa'^2\hbar^2/M$,

$$\sigma_s=4\pi/[k^2+(a^2/4)(\kappa'^2-k^2)^2]. \quad (1)$$

It appears that the virtual level is here defined by requiring the wave function to have a horizontal slope at $r=a$. To the approximation (i) $V_0\gg\kappa'^2\hbar^2/M$, where V_0 is the depth of the potential well, (ii) $|k^2-\kappa'^2|\rho^2\ll 1$, and (iii) $k\rho\ll 1$, it can be shown that, when the approximations are consistently carried out, the expression (1) should read

$$\sigma_s=4\pi/[k^2+(a^2/4)(\kappa'^2+k^2)^2]. \quad (2)$$

The vaidity of (2) can be examined immediately. Since V_0 and a are known from the analysis of Breit *et al.* to be $V_0\simeq 11.9$ Mev and $a=2.8\times10^{-13}$ cm, the definition $(d\psi/dr)_a=0$ gives $\kappa'^2\hbar^2/M\simeq 0.9$ Mev. That substituting this κ' into (2) does not give exactly the observed cross section for slow neutrons shows that (2) is not sufficiently accurate. In fact, $\kappa'^2\rho^2\simeq 0.07(\pi/2)^2=0.17$, (ii), and (iii) cannot be satisfied simultaneously. For $k^2=\kappa'^2$, the expression (2) would be somewhat more satisfactory.

It should perhaps be emphasized that different formulas are obtained by Bethe and by these authors because of the difference in the definition of the "virtual" state. The definition apparently employed by Flügge and Hückel may seem more physical in that it is in accord with the usual idea of resonance. The virtual level, however, is introduced in the formula for scattering only as an auxiliary quantity and is not essential, since the scattering is uniquely determined by the shape of the potential alone and an exact calculation of the scattering cross section is independent of any level, real or virtual. Hence, the introduction of a differently defined virtual state can hardly lead to different consequences in the problem of scattering and the theory of nuclear forces.

We may add that if the same consistent approximations are carried out (i.e., one must not simply drop ka in $\tan(ka+\delta)$), the correction factor in Bethe's formula is, in fact, $1+\kappa a$ and not $1+2\kappa a$ as claimed by these authors.

Incidently, a consistent calculation (using the exact phases) of the cross section for capture of neutron by proton from the singlet state[2] gives

$\sigma_c=0.364\times10^{-24}$ cm^2 for neutrons of (1/40) ev energy,

$\sigma_c=0.0263\times10^{-24}$ cm^2
for resonance capture, $\kappa'^2\hbar^2/M\simeq 0.9$ Mev,

as compared with the value $\sigma_c=0.5\times10^{-24}$ cm^2 for (1/40) ev as given by Bethe and Bacher. Their value is too high by a factor ~ 1.4 because they employed the approximate formula (59b) instead of the exact phases.

[1] S. Flügge and E. Hückel, Phys. Rev. 73, 520 (1948).
[2] H. A. Bethe and R. F. Bacher, Rev. Mod. Phys. 8, 138–9 (1936).

Erratum: The Microwave Spark

[Phys. Rev. 73, 496 (1948)]

D. Q. Posin
Radiation Laboratory, Massachusetts Institute of Technology, Cambridge, Massachusetts

IN the above article, the last statement in the caption under Fig. 3 should read "Average P_m lowering, 30 percent" instead of "Average P_m, 30 percent."

Microwave Resonance Absorption in Ferromagnetic Semiconductors

William H. Hewitt, Jr.
Bell Telephone Laboratories, Murray Hill, New Jersey

March 9, 1948

THE high resistivity of ferrites suggests that measurements of ferromagnetic resonance absorption in these compounds may be of particular interest. The magnitude of the absorption effect is expected to be large in comparison with that in conducting ferromagnetic materials, because in a ferrite the greater skin depth caused by its higher resistivity permits a relatively large volume of the specimen to participate in the absorption process.

On a thin plane (0.0117 in. thick) specimen of zinc-manganese-ferrite $(ZnO)(MnO)\cdot 2Fe_2O_3$ having a resistivity of 2350 ohm-cm, an initial permeability of 1700 at 1000 cycles, and a saturation magnetization M_s of 200, measurements were made at 23958 megacycles with the specimen fitted across the wave guide. The real and imaginary parts of both the permeability and the dielectric constant were separated as shown in Fig. 1.

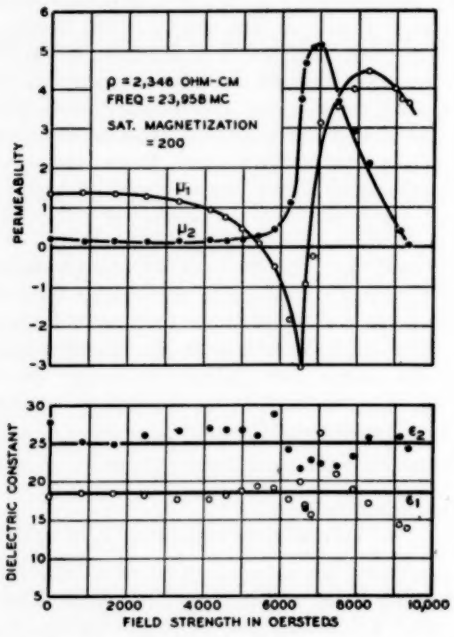

FIG. 1. Variation of real and imaginary parts of permeability and dielectric constant of $(MnO)(ZnO)\cdot 2Fe_2O_3$ as a function of applied external magnetic field (without correction for demagnetization).

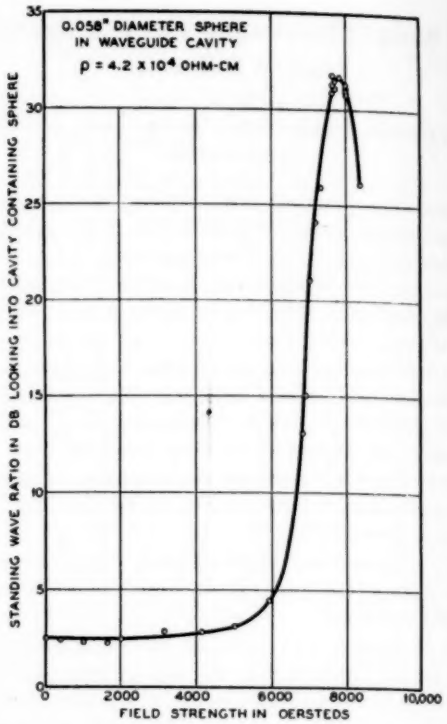
0.058" DIAMETER SPHERE IN WAVEGUIDE CAVITY
ρ = 4.2 X 10⁴ OHM-CM
STANDING WAVE RATIO IN DB LOOKING INTO CAVITY CONTAINING SPHERE
FIELD STRENGTH IN OERSTEDS

FIG. 2. Standing wave ratio of resonant cavity with $(MnO)(ZnO)\cdot 2Fe_2O_3$ sphere as a function of applied external magnetic field.

The field of an electromagnet was located parallel to the plane of the specimen and parallel to the narrow side of the wave guide. The sample was backed, in turn, by a short and by a quarter wave-length section. The input impedance looking into the specimen was determined as a function of the applied magnetic field for both circuit conditions by means of standing wave measurements. Using these data, and equations developed by W. A. Yager, the curves of Fig. 1 were obtained. The equations have more than one solution; of the possible solutions we selected that one for which $\epsilon=\epsilon_1-j\epsilon_2$ and $\mu=\mu_1-j\mu_2$ had the expected behavior as functions of H. The approximate constancy of ϵ_1 and ϵ_2 as functions of the magnetic field intensity is a check on the accuracy of the separation of the components. The high value of ϵ_2 suggests the possibility of Maxwell-Wagner losses in the sample used. Using $\omega_0=\gamma(BH)^{\frac{1}{2}}$, where $\gamma=ge/2mc$ and H (corrected for demagnetization) is the field strength at which μ_2 is maximum, we find a g value of 2.12. This is in the range of values previously observed for other materials. Yager and Bozorth[1] have reported 2.17 for Supermalloy.

It is interesting to note that using the values plotted in Fig. 1 the phase constant, β (part of the propagation constant) is negative for most of the field strength range in which μ_1 is negative. When β is negative, the direction of phase velocity of a traveling wave is opposite to the direction of attenuation.

With a small sphere (1.47-mm diam.) of a similar ferrite with a higher resistivity (4.2×10^4 ohm cm.) a g value of 2.16 is obtained using $\omega_0=\gamma H$. The sphere was located

at the $\lambda/2$ point in a cavity one wave-length long. Figure 2 shows the standing wave ratio looking into this cavity *vs.* the static field H. The frequency at maximum absorption was 23730 megacycles. The g value 2.16 for the sphere as calculated from the sphere equation $\omega_0=\gamma H$ is fairly consistent with the g value 2.12 for the plane specimen calculated from the plane equation $\omega_0=\gamma(BH)^{\frac{1}{2}}$. These equations were derived by Kittel.[2] The measurements on the sphere may therefore be considered as an approximate confirmation of the theory.

Sincere thanks are due Dr. C. Kittel and Mr. W. A. Yager for valuable suggestions and discussion, and to Mr. F. J. Schnettler who supplied the ferrite samples.

[1] W. A. Yager and R. M. Bozorth, Phys. Rev. **72**, 80 (1947).
[2] C. Kittel, Phys. Rev. **73**, 155 (1948).

Note on Zero-Zero Transitions*

MARVIN L. GOLDBERGER**
Argonne National Laboratory, Chicago, Illinois
March 19, 1948

ZERO-ZERO nuclear transitions have been suggested by Sachs[1] as an explanation of long lived isomers. He computed the energy spectra and transition probabilities for two-electron and two-quantum emissions. Stimulated by preliminary results of experiments by Goldhaber, Muehlhause, and Turkel[2] on the isomeric transition in Ir^{192} (mean life 2.16 min., energy 58 kev), which shows a continuous γ-ray spectrum in addition to conversion electrons, we have computed the γ-ray energy spectrum and lifetimes for zero-zero transitions in which one electron and one quantum are emitted. For comparison, the lifetime for the transition $og\rightarrow og$ (or $ou\rightarrow ou$) is computed by direct emission of an electron. The analogous transition in the case $og\rightarrow ou$ is strictly forbidden.

The calculation is straightforward, and most of the necessary matrix elements are given by Sachs.[1] We consider the transition $og\rightarrow og$ and $og\rightarrow ou$ with a *single* intermediate state of total angular momentum one and parity either the same or different from the ground state. The energy of the intermediate state above the ground state is taken to be either very much less than E or very much

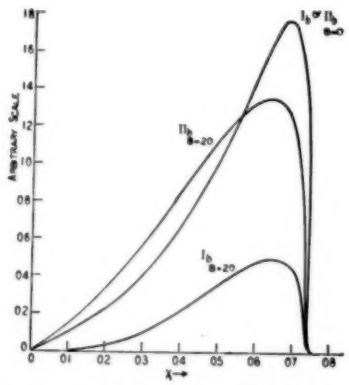

FIG. 1. Gamma-ray energy spectra; $Ib\cdots og\rightarrow 1g\rightarrow og$; $IIb\cdots ou\rightarrow 1u\rightarrow og$.

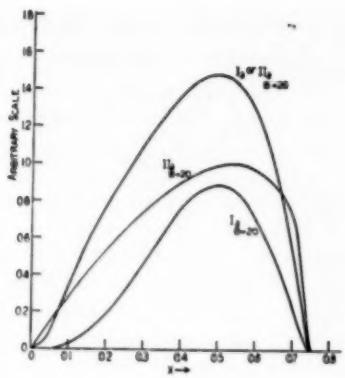

FIG. 2. Gamma-ray energy spectra; $Ia\cdots og\rightarrow 1u\rightarrow og$; $IIa\cdots ou\rightarrow 1g\rightarrow og$.

greater than (~20 times) E where E is the total energy available for the transition, namely, 58 kev. It is to be noted that this energy is insufficient to remove a K electron in Ir and, consequently, we have only L conversion.[3]

It should be emphasized that the absolute values of the lifetimes are to be regarded as merely order of magnitude estimates. The shapes of the γ-ray spectra, on the other hand, should be fairly reliable. From Figs. 1 and 2, we see that one may have a rather peaked distribution which might be confused with a sharp line.

In Table I the lifetimes calculated for the various cases are summarized. The notation and numerical data are as follows: E is the energy of the transition, I is the ionization potential in units of E, x is the γ-ray energy in units of E, β is the energy of the intermediate state above the initial state in units of E, and τ is the mean life. For our lifetime estimates we take $E=58$ kev, and $I=0.25$. (A transition from an initial state with zero angular momentum and even parity to an intermediate state of angular momentum one and odd parity and then a transition from the intermediate to the final state of zero angular momentum and even parity is symbolized by $og\rightarrow 1u\rightarrow og$, etc.

TABLE I.

	Transition	β	(sec.)
Ia	$og\rightarrow 1u\rightarrow og$	~0	5.4×10^{-2}
		~20	1.18×10^{-2}
Ib	$og\rightarrow 1g\rightarrow og$	0	2.40×10^{2}
		20	7.45×10^{4}
IIa	$ou\rightarrow 1g\rightarrow og$	0	3.22×10^{-3}
IIb	$ou\rightarrow 1u\rightarrow og$	20	8.70×10^{-3}
	$og\rightarrow og$	—	4.26×10^{-3}

The experimental evidence at the present time is insufficient to draw any definite conclusions in the case of Ir.

This work is the result of interesting discussions of the Ir problem with Professors M. Goldhaber and R. G. Sachs.

* This work has been carried out under the auspieces of the Atomic Energy Commission. It was completed and submitted for declassification on August 1, 1947.
** Also a member of the Institute for Nuclear Studies, University of Chicago, Chicago, Illinois.
[1] R. G. Sachs, Phys. Rev. **57**, 194 (1940).
[2] M. Goldhaber, C. O. Muehlhause, and S. H. Turkel, Phys. Rev. **71**, 372 (1947).

Saturation Effects in the Microwave Spectrum of Ammonia

ROBERT KARPLUS*
Mallinckrodt Chemical Laboratory, Harvard University, Cambridge, Massachusetts
March 10, 1948

ELSEWHERE in this journal a theory of saturation effects in microwave spectroscopy is presented.[1] Recently Bleaney and Penrose published the results of an experimental investigation of saturation of the ammonia (3, 3) line in a resonant cavity.[2] The semiclassical argument which was used to analyze the data led to the conclusion that the mean time between collisions effective in restoring thermal equilibrium is 75 percent greater than the mean time between collisions that interrupt the radiation and absorption processes.

Comparison of reference 1, Eq. (36) with reference 2, Eq. (7a) shows that the calculation of Bleaney and Penrose may be used, provided it is applied to each Zeeman component individually. The (saturated) absorption coefficients are then added to give the saturated absorption coefficient of the entire line.

The ammonia (3, 3) line has six active components whose intensity is equal in pairs:

$$|P^M|^2=\mu_0^2\frac{K^2M^2}{J^2(J+1)^2}=\frac{1}{16}\mu_0^2M^2 \quad M=0,\ \pm1,\ \pm2,\ \pm3.$$

In the notation of Bleaney and Penrose, therefore, there will be three saturation parameters a' that describe the behavior of the line; they may be denoted by $a'_{|M|}$ with a corresponding relative saturation $(\alpha/\alpha_0)_{|M|}$. The $a'_{|M|}$ are

$$a_1'=(1/4)a';\quad a_2'=a';\quad a_3'=(9/4)a'$$

in terms of the a' used by Bleaney and Penrose (p. 94),

$$a'=\frac{0.63}{P_{mm}^2}\left(\frac{\delta_1}{\delta_0}\right)=\frac{0.63}{P_{mm}^2}\frac{1}{(1+0.17\times10^4\alpha)^2}$$

at the higher power level studied. In Table I the calculations and comparison with experiment are summarized.

TABLE I.

p(mm)	α(cm^{-1})	a'	$(\alpha/\alpha_0)_1$*	$(\alpha/\alpha_0)_2$*	$(\alpha/\alpha_0)_3$*	$(\alpha/\alpha_0)_{\text{theory}}$	$(\alpha/\alpha_0)_{\text{exp.}}$*
0.6	7.35×10^{-4}	0.34	0.99	0.94	0.87	0.90	0.90
0.4	6.1	0.95	0.97	0.84	0.69	0.75	0.75
0.3	4.8	2.13	0.91	0.69	0.54	0.61	0.58
0.2	2.85	7.24	0.72	0.46	0.30	0.37	0.33
0.1	0.61	50.4	0.34	0.14	0.06$_4$	0.10	0.08

* The figures listed here were obtained by calculation from the graph in reference (2), Fig. 3.

Since the agreement is satisfactory, one may conclude that the same collisions interrupt the radiation process and restore thermal equilibrium.

* U. S. Rubber Company, Predoctoral Fellow.
[1] Robert Karplus and Julian Schwinger, Phys. Rev. 73, 1020 (1948).
[2] B. Bleaney and R. P. Penrose, Proc. Phys. Soc. 60, 83 (1948).

On the Fine Structure of $^4\Sigma$-States of Diatomic Molecules

A. BUDÓ AND I. KOVÁCS
Department of Theoretical Physics, University of Budapest, Budapest, Hungary
March 15, 1948

THE influence of the spin-orbit coupling on the multiplet structure of the $^4\Sigma$-states was investigated. It can be shown that this coupling gives for the four energy levels expressions identical in form with those we obtain[1] by assuming spin-spin interaction and coupling between the angular momentum $\vec{K}$ and the total spin $\vec{S}$ of the molecule.[2] This result is analogous with that found for $^3\Sigma$-states.[3] Details will be published in the Hungarica Acta Physica.

[1] A. Budó, Zeits. f. Physik 105, 73 (1937).
[2] H. A. Kramers, Zeits. f. Physik 53, 422 (1929), J. H. Van Vleck, Phys. Rev. 33, 467 (1929).
[3] M. H. Hebb, Phys. Rev. 49, 610 (1936).

On the Phenomenology of Ferromagnetic Resonance

D. POLDER
H. H. Wills' Physical Laboratory, University of Bristol, Bristol, England
March 2, 1948

A FERROMAGNETIC material, magnetized up to its saturation value M_0 by means of a constant magnetic field, shows interesting resonance phenomena when small additional high frequency magnetic fields are applied. We have found that in the case of an isotropic magnetic material a phenomenological description can be given by assuming that in Maxwell's equations those parts of the vectors B and H which are periodic in time (frequency $\omega/2\pi$) are related in the following way (exponential time factors being omitted):

$$B_x=\mu H_x-j\beta H_y,$$
$$B_y=\mu H_y+j\beta H_x,$$
$$B_z=H_z,$$

where z is the direction of the permanent magnetization and μ and β can be complex quantities. With the aid of classical equations of motion for the magnetic dipoles, such as have been used by Landau and Lifshitz[1] and Kittel,[2] it can be shown that, if we neglect damping terms, μ and β are real quantities given by:

$$\mu=(\gamma^2H_iB_i-\omega^2/\gamma^2H_i^2-\omega^2),\quad \beta=(4\pi M_0\gamma\omega/\gamma^2H_i^2-\omega^2),$$

where γ is the gyromagnetic ratio of the magnetic spins and H_i and B_i are the (constant) magnetic field strength and magnetic induction inside the material due to the constant magnetizing field. It may be emphasized that it is undoubtedly incorrect to interpret experimental results by means of a complex isotropic μ only.

With the aid of these relations, all results obtained by Kittel[3] and Snoek[4] for the behavior of ferromagnetic ellipsoids in a constant magnetic field on which small alternating fields are superposed can easily be derived.

The results are interesting since they give the dependence on the shape of the body of the frequency at which the total magnetic moment of the ellipsoids shows resonance. In the calculations the dimensions of the ellipsoids are supposed to be small in comparison with the wave-lengths of the wave-lengths of the electromagnetic waves inside the material. A further application is the calculation of the index of refraction of an electromagnetic wave propagating through a (infinitely large) specimen of non-conducting magnetized ferromagnetic material. We have found that for every direction of propagation and for every frequency there exist two different, elliptically polarized waves with different indices of refraction. The refractive index of one of these two waves shows a resonance phenomenon at a frequency given by

$$\omega^2=\gamma^2H_i(H_i+4\pi M_0\sin^2\vartheta).$$

ϑ is the angle between the direction of propagation and the z axis. The other wave does not show resonance. In the special case $\vartheta=0$ there are two circularly polarized waves, and in the case $\vartheta=\frac{1}{2}\pi$ there are two linearly polarized waves. The extension of the theory to conducting materials is simply performed by the introduction of a complex dielectric constant in Maxwell's equations. A fuller account of our calculations will be given shortly.

[1] L. Landau and E. Lifshitz, Physik. Zeits. Sowjetunion **8**, 153 (1935).
[2] C. Kittel, Phys. Rev. **71**, 270 (1947).
[3] C. Kittel, Phys. Rev. **73**, 155 (1948).
[4] J. L. Snoek, to be published in Physica.

A Low Voltage Discharge between Very Close Electrodes

L. H. GERMER AND F. E. HAWORTH
Bell Telephone Laboratories, Murray Hill, New Jersey
March 15, 1948

WHEN a condenser, charged to a potential between 15 and 60 volts, is discharged by two electrodes, a pit is formed on the positive having a volume approximately equal to the volume of metal which could be vaporized by the energy in the condenser (Fig. 1); the negative electrode shows on its surface the presence of metal spattered over from the positive. The pit can be reduced in size, or eliminated, by the addition of resistance or inductance to the circuit or by operating the contacts in vacuum. For voltages below 15 the pit is much smaller or non-existent; for voltages above 60 the discharge, which produces the pit, may be oscillatory and the difference in appearance between the two electrodes then tends to be lost. This vaporization of anode metal is one of the major factors in the erosion of telephone relay contacts.

The pit formed on the anode is the result of the melting and boiling of the metal caused by electron bombardment before the electrodes touch. Field emission from the cathode can supply the first electrons, but pure field emission would dissipate the energy over a time too long to result in marked local heating. To account for this heating, and for oscilloscopic records which have been obtained, it is necessary to assume an "avalanche" effect by which the emission is multiplied and the condenser is discharged in an enormously reduced time. For energies with which we have experimented, the total time of discharge must be less than 10^{-7} sec. Careful measurements of the separation at which the discharge occurs have shown it to be variable, from 500 to 20,000A for 50 bolts, apparently depending chiefly upon the roughness of the surface. In most of our experiments the discharge occurs at a separation less than the diameter of the anode pit which it forms, and the evaporated metal often welds the electrodes together.

FIG. 1. Photomicrograph of a pit in platinum produced by a discharge of 11 ergs. Pit diameter about 5×10^{-4} cm.

When a positive ion, formed in the air or upon the anode surface by an electron which was drawn out by the field, approaches the cathode the field is appreciably increased by its presence. Since the field was already almost strong enough to draw out electrons, this further increase at once elicits a second electron. The new electron is, in general, drawn straight across to the anode, and will not in most cases combine with the ion as it would in the absence of the applied field. While the electron is between the ion and the surface, they produce together a net field opposing further emission, but as soon as the electron passes the ion the field is again directed in the sense to draw out an electron. Thus one electron at a time escapes from the cathode until the ion is neutralized or until it reaches the cathode. The fact that the energy is dissipated almost entirely upon the anode is proof that the current is carried chiefly by electrons and that therefore each positive ion must give rise to several electrons at the cathode.*

If each of these electrons were to produce one ion, the current would increase with enormous rapidity. Now residual inductance in the circuit, even though it be as low as 10^{-8}h, limits the possible rate of rise of current and holds the voltage across the gap steady at a value which gives to an electron a probability of ionization considerably less than unity and an over-all electron multiplication factor, by the double process of production of an ion for each few electrons and of several electrons for each ion, extremely close to unity. This corresponds to a gap potential probably very near to the ionization potential of oxygen; with this fixed potential across the gap for the duration of the discharge, the circuit is quite simple and its behavior is readily understood.

* Instability of "field emission" in the presence of residual gas is well known. An explanation approximately like that given here was suggested by W. H. Bennett, Phys. Rev. **40**, 416 (1932). There seems to us little doubt that that suggestion was correct.

Ejection of Electrons by Ions at High Fields

R. R. NEWTON
Bell Telephone Laboratories, Murray Hill, New Jersey
March 15, 1948

IN the accompanying letter by Germer and Haworth, evidence is presented to show that a positive ion in a high field ($\sim 10^7$ volts/cm) must be able to eject several electrons from a metal. On the other hand, present theories of ejection by positive ions in low fields require that the ion be neutralized as the first step in the ejection process and, hence, that an ion be unable to eject more than one electron.[1] If the hypothesis of Germer and Haworth is correct, the mechanism must be qualitatively different at high fields.

A positive ion near the surface of a metal creates a deep well in the potential energy function of an electron, and, if the ion is close to the metal, an electron can readily tunnel from the metal to the ion. At low fields, the electron has no place else to go and either remains on the ion, thus neutralizing it, or returns to the metal.

At high fields the picture is different. One readily sees that the potential energy surface of the electron has a "pass" lying on the opposite side of the ion from the metal. If the field is sufficiently high, the energy at the pass is lower than the Fermi level in the metal. An electron coming from near the Fermi level can then escape to infinity. Thus an electron has become free by tunneling through the barrier between the metal and the ion, which is easier than tunneling through the barrier which exists when the field alone is present.

To get some idea of the emission caused by such a process, we have made some calculations based on a one-dimensional metal. The electrons inside the metal were assumed to occupy the energy levels of an electron in a box, with the highese energy 4.2 volts below vacuum. Letting r be the distance from the metal surface, we took the potential due to the metal to be:

$$\Phi = e/[4r + (e^2/W_0)].$$

W_0 gives the energy at the bottom of the conduction band, which was chosen to be 10 volts below vacuum. The results turn out to be independent of the length of the metal. We assumed a field of 2.5×10^7 volts/cm and made calculations for several values of r. In calculating the potential due to the ion, we included the effects of the image charge.

We then assumed that all electrons with energies above the outer maximum (which the pass becomes in one dimension), which tunnel through the inner barrier become free, and that no other tunnel through the first barrier. Following a well-known method[2] we computed a transmission coefficient through the first barrier for several energies lying above the outer maximum. This coefficient was multiplied by the number of collisions per second, with one end of the metal, made by electrons with the assumed energy and by the density of energy levels, and the product was integrated numerically over all energies from the height of the outer maximum to the Fermi level. This gives the number of electrons per second ejected from the metal, as shown by Table I.

TABLE I. Ejection of electrons by a proton. Field $=2.5\times 10^7$ volts/cm.

Distance of ion from surface, A.U.	Estimated emission, electrons per second
6	52×10^{12}
8	9×10^{12}
10	10^{12}
∞ (pure field emission)	10^{6}

The mean value of the emission rate from 10 to 6 A.U., using Simpson's rule, is 15×10^{12} electrons/sec.; if an ion travels from 10 A.U. to 6 and back to 10, with a mean velocity of 10^8 cm/sec., it would eject 1.2 electrons on the average. Since 6 A.U. is probably much too large a distance for reflection, we conclude that an ion may well be able to eject many electrons from the metal.

[1] A. Cobas and W. E. Lamb, Phys. Rev. 65, 327 (1944), (contains further references).
[2] See, for example, E. C. Kemble, *Fundamental Principles of Quantum Mechanics* (McGraw-Hill Book Company, Inc., New York, 1937), p. 109 ff.

On the Stability of the Neutral Meson

E. P. HINCKS AND B. PONTECORVO
National Research Council, Chalk River Laboratory
Chalk River, Ontario, Canada
March 17, 1948

THE discovery[1] of the disintegration of a heavy (π) meson into a light one (μ meson, most likely the particle constituting the penetrating component of the cosmic radiation) has provided strong evidence[2] in favor of the existence of neutral mesons of mass about 70 Mev.

In order to explain a photograph of a 24-Mev decay electron, observed by Anderson, Adams, Lloyd, and Rau,[3] these authors and later Marshak[4] have suggested that the μ-meson might decay into an electron and a neutral particle apparently identical with the neutral meson of Lattes, Occhialini, and Powell. Greisen[5] has recently indicated that several cosmic-ray phenomena "which have defied even qualitative explanation up to the present are made understandable in the light of the neutral meson hypothesis" provided the neutral meson decays immediately into two photons. This γ-instability has been predicted on theoretical grounds by several authors.[6]

We want to point out that we have secured experimental evidence proving an incompatibility between the hypothesis that the 2.2-μs meson decay sinto an electron and a neutral meson and the hypothesis that the neutral meson is unstable *versus* emission of two photons with a very short lifetime. The experimental arrangement has been described[7] in connection with a research—which gave a negative result—to find out whether the decay of the 2.2-μs meson consists of the emission in opposite directions of one electron and one photon, each of about 50 Mev. Clearly the same arrangement, for the details of which we refer to our previous note, is capable of deciding whether the decay of the 2.2-μs meson consists of the emission of an electron and a neutral meson unstable *versus* emission of two photons of about 35 Mev. The number of

decay electrons from mesons stopped in graphite was recorded, and at the same time electron-photon coincidences were looked for. While the net number of measured delayed coincidences (observed rate minus casual rate) is $0.01\begin{cases}+0.06\\-0.01\end{cases}$ per hour, the rate to be expected according to the hypothesis of a neutral meson unstable *versus* emission of two photons of 35 Mev with a mean life $\lesssim 10^{-10}$ sec. is about one per hour.

We conclude that either the neutral meson is not emitted in the 2.2-μs decay process, or, if it is emitted, it does not decay into two photons with a mean life $\lesssim 10^{-10}$ sec.

It seems that a similar conclusion can be reached from the experiment of Sard and Althaus,[8] who, by using a method different from ours, failed to observe a γ-radiation in the 2.2-μs decay of mesons brought to rest in brass. It should be noticed that while our experiment refers to positive and negative mesons, their experiment refers only to positive ones.[9]

There remains, of course, the possibility that there are two distinct types of neutral mesons, one of which is stable and the other unstable *versus* emission of γ-radiation.

A more complete account of this work will be submitted for publication in the near future.

[1] C. M. Lattes, H. Muirhead, G. P. S. Occhialini, and C. F. Powell, Nature **159**, 694 (1947).
[2] C. M. G. Lattes, G. P. S. Occhialini, and C. F. Powell, Nature **160**, 453 (1947); **160**, 486 (1947).
[3] C. D. Anderson, R. V. Adams, P. E. Lloyd, and R. R. Rau, Phys. Rev. **72**, 724 (1947).
[4] R. E. Marshak, Bull. Am. Phys. Soc. **22**, No. 6, p. 14.
[5] K. I. Greisen, Phys. Rev. **73**, 521 (1948).
[6] J. R. Oppenheimer, New York Meeting of American Physical Society, January, 1947; R. J. Finkelstein, Phys. Rev. **72**, 415 (1947).
[7] E. P. Hincks and B. Pontecorvo, Phys. Rev. **73**, 257 (1948).
[8] R. D. Sard and E. J. Althaus, Bull. Am. Phys. Soc. **23**, No. 2, p. 20 (1948).
[9] M. Conversi, E. Pancini, and O. Piccioni, Phys. Rev. **71**, 209 (1947).

Polarization Effects in the Ionization Loss of 1-Mev Electrons in Carbon*

FRANK L. HEREFORD
Bartol Research Foundation of the Franklin Institute, Swarthmore, Pennsylvania
March 15, 1948

THE possibility that polarization effects might reduce the energy loss by ionization of fast-charged particles was suggested by W. F. G. Swann[1] and investigated theoretically by Fermi[2] and recently by Halpern and Hall.[3] Experimental attempts to verify the effect at high energies ($\geqq 20 m_0c^2$) have proved successful in one instance,[4] inconclusive in another.[5] At lower energies the correction has not been considered effective and has been neglected in most collision problems.[6] Halpern and Hall indicate, however, that the effect at low energies is not always inappreciable; in fact, it yields an 8 percent reduction in the collision loss of 1–2-Mev electrons in carbon. By measurement of the relative stopping powers of carbon and H_2O at these energies, this prediction has been confirmed.

The success of the method depends heavily upon the discrimination between real absorption in a sample and apparent absorption due to scattering of particles out of the solid angle subtended by the counters. Fortunately, in the comparison of carbon and H_2O, this discrimination is possible. First, it may be pointed out that for the case under consideration the scattering is predominantly multiple. Williams[7] has given as the criterion for multiple scattering,

$$M=(2\pi NZ^{4/3}/\beta^2)(\hbar/mc)^2t\gg 1,$$

where N represents the electron density in a sample of thickness t cm. For the thicknesses of carbon and H_2O employed, $M=2\times 10^3$, in satisfactory accordance with the criterion. Furthermore, under these conditions, if thicknesses of different materials are measured in radiation lengths, equal thicknesses yield equal mean square scattering angles.[6] This, of course, holds only for equivalent energy distributions of particles penetrating the samples. Hence, the ideal situation would prevail if samples of equal thicknesses (in radiation lengths) would also exhibit equal stopping powers on the basis of the Halpern-Hall theory. For then the scattering loss would form the same percentage of the apparent absorption in both substances. The condition which insures this state of affairs is

$$S(H_2O)/S(C)=x(C)/x(H_2O)$$

where x denotes the radiation length, S the stopping power. In the case of carbon and H_2O this condition is satisfied to within a few percent.

In the experiment (Fig. 1) two thin-wall (0.035 g/cm^2) argon-ether counters were used. Coincidences were counted by means of a Rossi circuit, the pulses from which were fed into a scale of 64. The resolving time of the circuit as determined by the accidental coincidence rate was 0.45 10^{-6} second. Equal thicknesses (in radiation lengths) of slab carbon and H_2O were inserted alternately into a thin-wall aluminum jacket at position A. Very nearly equal counting rates were observed, the difference being evaluated by reference to an aluminum absorption curve. The stopping power ratio, $S(H_2O)/S(C)$, was taken as the ratio of the quantities $S(H_2O)/S(Al)$ and $S(C)/S(Al)$. Table I shows $S(H_2O)/S(C)$ for two sample thicknesses and the values calculated from theory.

TABLE I. Summary of results.

	Thickness of samples: Radiation lengths	g/cm^2 carbon	g/cm^2 H_2O	Effective energy range Mev	Stopping power ratio $S(H_2O)/S(C)$
Author	0.0055	0.29	0.25	$1.2<E<2.1$	1.16 ± 0.025 (exp.)
Author	0.0079	0.41	0.36	$0.8<E<2.0$	1.17 ± 0.02 (exp.)
Halpern-Hall				$1<E<2$	1.10 (calc.)
Bethe-Bloch (neglecting polarization)				$1<E<2$	1.08 (calc.)

The neglibility of scattering errors was verified by shifting each sample to position B and observing the decreased coincident rates due to the increase in the intensity scattered out of the counter train. The decreased rates for carbon and H_2O were equal to within 2 percent. In view of the dependence of the differential scattering probability upon θ^{-4}, the error in the stopping power ratio due to scattering at position A can be shown to be less than 0.2 percent.

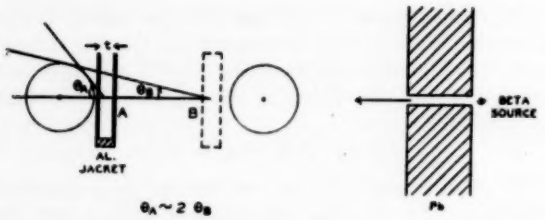

FIG. 1. Schematic diagram showing the relative positions of the counters, source, and absorber. The angle θ indicates the maximum angle at which an electron may be scattered and yet register a coincidence count.

It is planned to repeat the experiment using 10-Mev electrons from the beta-spectrum of B^{12} produced in the $B^{11}(dp)B^{12}$ reaction by the 1.75-Mev Bartol Van de Graaff generator. The radiation losses incidental at higher energies will be compensated by the choice of sample thicknesses demanded by the general scheme of the experiment.

The author is indebted to Mr. M. A. Pomerantz for many helpful discussions and to Dr. W. F. G. Swann for his frequent and helpful advice.

* Assisted by the Office of Naval Research.

[1] W. F. G. Swann, J. Frank. Inst. **226**, 598 (1938).
[2] E. Fermi, Phys. Rev. **57**, 485 (1940).
[3] O. Halpern and H. Hall, Phys. Rev. **57**, 459 (1940); **73**, 477 (1948).
[4] H. R. Crane, N. L. Oleson, and K. T. Chao, Phys. Rev. **57**, 664 (1940).
[5] E. Hayward, Phys. Rev. **72**, 937 (1947).
[6] B. Rossi and K. Greisen, Rev. Mod. Phys. **13**, 240 (1941).
[7] E. J. Williams, Proc. Roy. Soc. **169**, 531 (1939).

Neutron Deficient Isotopes of Tellurium and Antimony

M. LINDNER AND I. PERLMAN
Radiation Laboratory and Department of Chemistry, University of California, Berkeley, California
March 10, 1948

WHILE investigating the relative yields for the many reactions resulting from the irradiation of antimony with 200-Mev deuterons in the Berkeley 184-inch cyclotron, several previously unreported isotopes of tellurium and antimony were encountered. The tellurium fraction when followed on a thin mica window counter could be resolved into half-life periods of 2.5 hr., 6.0 days, and a small amount of a long-lived component. The 2.5-hour period has not been further characterized with respect to mass number or mode of decay other than to note that the radiation is predominantly electrons. The 6.0-day period is accompanied by positrons which were shown to be caused by a 3.5-minute antimony daughter which is undoubtedly the same activity assigned to Sb^{118} by Risser, Lark-Horowitz, and Smith.[1] The positron energy was found to be 3.1 ± 0.2 Mev by absorption in beryllium and from the end point of the energy distribution curve taken with a low resolution beta-ray spectrometer. Gamma-activity is also present with this period. The 6.0-day tellurium showed a high abundance of x-rays, little or no conversion electrons, and some gamma-ray activity which could be due to the 3.5-minute antimony daughter.

The tellurium fraction contained another component of 4.5-day half-life which could not be observed in the decay curve because of its low abundance but which was detected by means of its 39-hour antimony daughter. The 39-hour antimony showed x-rays of tin (critical absorption with cadmium, silver, and palladium), no detectable hard radiation or electrons, and is apparently identical with an activity recently assigned to Sb^{119} by Coleman and Pool.[2]

In order to produce a more favorable ratio of the 4.5-day tellurium to 6.0-day tellurium, antimony was bombarded with 40-Mev deuterons. Other measurements predict the production of $d,4n$ reaction in good yield and the $d,5n$ reaction in poorer yield. If the 4.5-day tellurium is Te^{119} and the 6.0-day period is Te^{118}, the desired result should be achieved. The counting rates for the x-rays of the two activities were found to be in the ratio of 40:1 in the direction anticipated. Since the activity of several days half-life is largely that of the 4.5-day tellurium (except for the positrons of the 3.5-minute Sb^{118}), the negative particles and electromagnetic radiation may be assumed to belong to this isotope. Conversion electrons of 0.2 Mev and 0.5 Mev were measured with the low resolution beta-ray spectrometer and a hard gamma-ray of about 1.5 Mev was detected through a lead absorption curve. Softer gamma-radiation could have been present. All tellurium decay curves tailed out into a longer period, probably Te^{121}.

The antimony fraction from bombardments of antimony with 200-Mev deuterons showed a number of periods which could be resolved by selectively counting the x-rays through beryllium and the electrons without absorber. There was x-ray activity of a few hours half-life which could be a mixture of the 2.8-hour and 5.1-hour periods reported by Coleman and Pool. The 2.8-day Sb^{122} showed up well in the curve taken without absorbers and the 39-hour antimony was prominent in the decay curve taken through beryllium. The yield of the 39-hour antimony was much greater than that which could have grown from its 4.5-day tellurium parent, indicating direct formation. Another antimony isotope of 6.0-day half-life was also observed. This activity is characterized by a preponderance of x-ray and gamma-ray activity with electrons in low abundance. Since the 6.0-day antimony did not appear in antimony removed from tellurium, the tellurium isobar is either stable or of half-life less than 10 minutes. Although the half-life is the same as that of the tellurium mentioned above, it could be separated chemically with antimony from tellurium and there was no positron activity accompanying it. After the decay of the 6.0-day antimony, the curve turned into the 60-day period of Sb^{124} which was identified also by its radiation characteristics. The formation of Sb^{124} presents the unanswered question as to whether this isotope is formed by the high energy deuterons or by secondary low energy neutrons.

Table I lists the isotopes of antimony and tellurium found in the bombardment of antimony with 200-Mev deuterons. The cross sections for their formation will be given in a later publication in which the yields for the large number of products of 200-Mev deuterons on antimony will be discussed.

TABLE I. Isotopes of Sb and Te formed in the irradiation of antimony with 200-Mev deuterons.

Isotope	Half-life	Decay mech.	Energy (Mev) particles	γ-rays	References
Sb	Several hours	K, e^-			2
Sb^{119}	39 hours	K	none		2
Sb	6.0 days	K, e^-, γ or IT, e^-, γ		1.1	
*Sb^{120}	2.8 days	β^-, γ, e^-			3
*Sb^{120}	60 days	β^-, γ			3
Te^{119}	6.0 days	K, no γ(?)			
Te^{119}	4.5 days	K, e^-, γ	0.2, 0.5	1.4	
*Te^{121}	140 days	IT, e^-, γ			4

* Isotope identified from properties listed in the literature but not further characterized.

The assignment of the 4.5-day tellurium—39-hour antimony isobars to mass number 119 is most reasonable in view of their production with 40-Mev deuterons on antimony, their decay characteristics, and the possibilities open. This assignment agrees with that of the 39-hour antimony by Coleman and Pool from other evidence. The most reasonable assignment of the 6.0-day tellurium—3.5-minute antimony isobars is mass number 118. They were produced with 40-Mev deuterons on antimony which would be impossible for mass number 116 and probably for mass number 117. An odd mass number (117) is also unlikely in view of observed half-life relationships. This isotopic assignment is in apparent conflict with the assignment of the 5.1-hour antimony to mass number 118.[2] However, it is possible that the 3.5-minute antimony and the 5.1-hour antimony are isomeric and that in the decay of the 6.0-day tellurium parent only the upper state (3.5-minute antimony) is formed.

If the above assignments are accepted, the 6-day antimony would have to be isomeric with a previously known activity and of these the most reasonable guess is Sb^{120}, the isomer being the 17-min. positron emitter. In order to make an assignment, a sample consisting of 95 percent isotopically pure Sn^{120} was bombarded on the Berkeley 60-inch cyclotron with 18-Mev deuterons. At this energy the cross section for the $d,3n$ reaction is known to be low as compared to the $d,2n$ reaction, so that only Sb^{120} should be formed in good yield. Three antimony activities were obtained, one the 17-minute, β^+-emitting Sb^{120}, a second the 6-day activity as anticipated, and the third the 39-hr. Sb^{119}. The K x-rays from the 6-day activity were found to be those of tin, so that the decay process is K-electron capture. The cross sections for the formation of the 6-day and 17-minute activity were roughly the same, namely 0.1×10^{-24} cm². The 6-day antimony K-capture decay is therefore assigned to Sb^{120} since the cross section is too high for any other possibilities. The Sb^{119} appeared in sixfold lower yield than the sum of the Sb^{120} isomers.

The tin fraction was found to contain a single β^--activity of 28-hour half-life. The maximum β^--energy was found from absorption in beryllium and from beta-ray spectrometer measurements to be about 0.4 Mev and no γ-radiation was present. The 26-hr. Sn of Livingood and Seaborg[5] is therefore Sn^{121}, formed in this case by the reaction $Sn^{120}(d,p)Sn^{121}$. The cross section for formation with 18-Mev deuterons is 0.02×10^{-24} cm².

The cooperation of Dr. D. C. Sewell, Mr. J. T. Vale, and all of those whose operation of the 184-inch cyclotron made these irradiations possible is gratefully acknowledged.

This paper is based on work performed under Contract Number W-7405-eng-48 with the Atomic Energy Commission in connection with the Radiation Laboratory of the University of California, Berkeley, California.

[1] Risser, Lark-Horowitz, and Smith, Phys. Rev. 57, 355 (1940).
[2] K. D. Coleman and M. L. Pool, Phys. Rev. 72, 1070 (1947).
[3] J. J. Livingood and G. T. Seaborg, Phys. Rev. 55, 414 (1939).
[4] M. L. Pool and J. E. Edwards, Phys. Rev. 69, 140 (1946).
[5] J. J. Livingood and G. T. Seaborg, Phys. Rev. 55, 667 (1939).

The Alpha-Ray Emitting Isotope in Samarium

A. J. DEMPSTER
Argonne National Laboratory, Chicago, Illinois
March 22, 1948

IT was shown by Hevesy, Pohl, and Hosemann[1,2] in 1932–34 that samarium emits slow alpha-rays with a range in air of only 1.13 cm at the rate of 89 per second per gram. The phenomenon has been confirmed by many observers. In 1938 Wilkins and Dempster[3] reported that the alpha-ray tracks from a deposit of separated isotopes laid down on a photographic plate appeared to start from the isotope of mass 148. The experiments were interrupted by the death of Professor Wilkins and only one such deposit was made. Since that time measurements of the mass of the deposits obtained with a spark source similar to that used in the 1938 experiments showed that the amount was approximately 2×10^{-10} gram. As this quantity of samarium is not enough to have produced in three and a half months the ten tracks observed, accidental contamination must have been present. This may have been caused by the spark source itself, for in experiments on the masses of beta-active isotopes it has been observed that a spark source of ions may detach from the electrodes particles of finite size consisting of many atoms, which are reflected around inside the mass spectrograph and may settle on the plate collecting the isotopic atoms. Many more rays may thus be emitted from these specks on the plate than from the separated isotopes themselves.

It is of great interest to determine the mass of the active isotope, and in the following paragraphs some preliminary observations with much larger amounts of separated isotopes are described. Several deposits were made with the hot anode ion source developed by Dr. A. E. Shaw,[4,5]

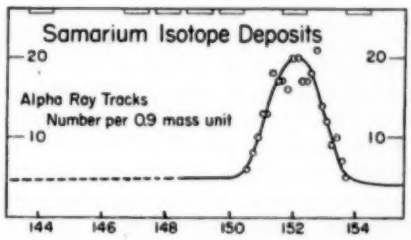

FIG. 1. Alpha-rays from separated isotopes. Ordinate points give the number of tracks within 0.45 mass unit of the abscissa mass.

where the separated isotopes are collected on metal plates coated with graphite. Alpha-ray plates were exposed for several months directly above the deposits which appeared as visible patterns of the samarium mass spectrum. One deposit which gave the distribution of tracks shown in Fig. 1 on the transfer plate was estimated from the ion current to have a total mass of 0.19 microgram. The transfer plate was exposed for 170 days, and 117 alpha-ray tracks would be expected in that time. The positions of the tracks, their lengths, and number of grains were observed, using a 95-power oil immersion objective with dark field illumination and a 10-power micrometer eyepiece. Only short tracks with lengths of 7μ or less were measured;[6] any longer tracks were ascribed to contaminations. A total of about 48 tracks that could be ascribed to samarium were found in the region between mass 150 and mass 154 as shown in Fig. 1, and no concentration was found in any other region. Each of the points through which the curve in Fig. 1 is drawn gives the number of tracks which lie in a band having its center at the mass shown and a width corresponding to 0.9 mass unit. The curve suggests that the alpha-ray emitter is the isotope at mass 152. Sputtering of part of the deposit may account for the width of the curve and the fact that the total number of tracks observed is only 40 percent of the number expected.

Other deposits were not so conclusive, and even though the unsatisfactory results with them may be attributed to loss of the deposit by sputtering, as shown by the complete removal of the graphite in some cases, the mass value 152 should be regarded as provisional for the present. Further experiments are in progress in which the isotopes are collected in small hollow chambers to avoid loss by sputtering, and more complete results may be obtained in the near future.

[1] G. v. Hevesy and M. Pohl, Nature **130**, 846 (1932).
[2] R. Hosemann, Zeits. f. Physik **99**, 405 (1936).
[3] T. R. Wilkins and A. J. Dempster, Phys. Rev. **54**, 315 (1938).
[4] A. E. Shaw, Phys. Rev. **71**, 277 (1947).
[5] A. E. Shaw, Bull. Am. Phys. Soc. **22**, No. 6, 10 (1947).
[6] P. Cuer and C. M. G. Lattes, Nature **158**, 197 (1946).

A Type of Non-Linear Random Distortion (Noise) in Pulse Communication*

ARNOLD E. ROSS
Department of Mathematics, University of Notre Dame, Notre Dame, Indiana
March 10, 1948

WHEN the information to be transmitted in pulse communication is contained in the variation of the distance between the successive pulses, one speaks of pulse position modulation without fixed reference. In the transmission of sinusoidal signals of certain frequencies by this method, there occur, at irregular time intervals, pulse precessions, each of a short duration observable either on an oscilloscope or as audio distortion (noise). These precessions "have all the earmarks of randomness"[1] with one very puzzling property, however. For some signal frequencies, this precession, when observed on the oscilloscope, always proceeds to the right and for other frequencies always to the left, thus seemingly contradicting the argument for its random origin. Developing further the mathematical theory of pulse position modulation without fixed reference introduced elsewhere,[2] we explain this lack of symmetry and show that each such precession is triggered by the (random) pulse jitter. It appears that the afore-mentioned distortion is peculiar to the modulation scheme itself and is not a property of the circuits employed to achieve this modulation.

The discussion leading to an explanation of the above-mentioned random non-symmetric distortion may be summarized as follows. First one observes that the points at which the signal is sampled are iterated images of a one-to-one continuous transformation τ (induced by the method of sampling) of the period of our signal. Then one sees that these sampling points may be distributed periodically if and only if some power (iteration) of τ has fixed points. If τ^k is the smallest power of τ with fixed points,[3] there exists a steady-state stable equilibrium distribution of exactly k distinct sampling points which form a period containing one or more periods $1/f_s$ of the signal. If the sampling does not happen to begin at one of the above equilibrium positions there occurs a transient phenomenon, *viz.*, a rapid precession of sampling points toward these "stable equilibrium" positions which are determined completely by the ratio f_s/f_p of the signal frequency f_s to the unmodulated pulse repetition rate f_p, and by the amplitude of the signal.

Besides the k stable equilibrium positions of sampling points in the case of periodic distribution there exist k fixed sampling positions which one may call "unstable equilibrium" positions. For if sampling begins at one of these positions, then the signal will be sampled only at these fixed positions in its period. However, a small deviation, say caused by pulse jitter, will lead to a rapid precession of sampling points away from these equilibrium positions and toward the k stable equilibrium positions.

In practice, the unstable chain rarely persists long enough to be observed.

The k sampling points in a stable equilibrium distribution are separated by the k points of unstable equilibrium. For certain values of the ratio f_s/f_p each stable equilibrium position of sampling has in its proximity an unstable sampling position. If, as a result of random pulse jitter, there occurs a small deviation in the direction of the unstable equilibrium position and if this deviation exceeds the distance between the stable and its neighboring unstable positions, there occurs a precession (referred to in the first paragraph) of pulses (sampling positions) toward the next and relatively distant equilibrium position. The relative positions of the adjacent stable and unstable equilibrium positions determine the direction of such a pulse precession.

* Supported by funds from ONR Contract N6ori187 and by Stromberg-Carlson Company, Rochester, New York.
[1] To quote a remark by Professor G. E. Uhlenbeck of the University of Michigan.
[2] "A theoretical study of pulse position modulation without fixed reference," Proc. I.R.E. **36**, 370A (1948).
[3] A. E. Ross, Bull. Am. Meth. Soc. **53**, 287 (1947).

Characteristics of Bismuth Fission with High Energy Particles

R. H. GOECKERMANN AND I. PERLMAN
Radiation Laboratory and Department of Chemistry, University of California, Berkeley, California
March 22, 1948

IN a previous communication[1] the fission of elements from bismuth to tantalum with high energy particles was reported and some properties of the reaction were deduced from the nature of the fission products. It is now possible to characterize further the mechanism and to show that the reaction differs considerably from the slow neutron-induced fission of uranium.

In the present studies some of the longer-lived fission products from the irradiation of bismuth with 200-Mev deuterons were examined. The most abundant fission products are those from near-symmetrical cleavage with yields falling off for lower and higher mass numbers. Although the fission yield curve appears to be a single symmetrical peak, the line of symmetry is at a mass somewhat below 100, rather than at 105–106 as would result from the fission of a compound nucleus of Bi^{209} and a deuteron. Besides the appearance of only a single peak in the fission product yield curve, another important difference from the slow neutron-induced fission of uranium was noted. Considering those cleavages in the fission of bismuth in which a light and a heavy fragment are formed, the light fragment in general has a neutron excess while the complementary heavy fragment is either neutron deficient or, by inference, stable.

These observations can be explained in terms of the following description of the process. The fission reaction competes with other reactions only after about 12 neutrons have boiled off from the compound nucleus. As will be mentioned below, the yield data can best be explained if it is assumed that bismuth or polonium of mass numbers 197–199 are the isotopes responsible for most of the fissions. The second assumption necessary to explain the observations is that the light bismuth or polonium nucleus undergoes fission preserving the same neutron/proton ratio in both fragments as in the parent nucleus. It is seen that since the postulated parent nucleus has $n/p=1.36$, the primary fission products of mass number well below 100 will be β^--emitters, those in an intermediate range will be stable, while the heaviest fission products will decay by orbital electron capture or by positron emission.

Using these assumptions (which no doubt present an oversimplification) it is possible to calculate for each mass number the most abundant primary fission product. If it is further assumed that this particular isobar is produced in almost all of the fissions producing that mass number, it should be possible to draw a smooth curve through the fission yields for these products. Furthermore, an isotope whose n/p ratio differs appreciably from 1.36 should fall well below the curve.

A fission product yield curve has been constructed on the basis of measured yields of 25 fission products. The mechanism advanced seems to give an adequate description of the fission process since the predictions and measured yields agree rather well both for isotopes that should fall on the curve and those which should lie well below it. A few of the heavy fission products depart somewhat from predictions but with these there is considerable uncertainty in estimating counting efficiencies since the decay schemes (orbital electron capture) are not known.

The following is a list of bismuth fission products which were identified in the present studies (references are given for isotopes which only recently appeared in the literature or which have been hitherto unreported): Ca^{45}, Fe^{59}, Ni^{66},[2] Cu^{67},[3] Zn^{72}, As^{74}, As^{77}, Rb^{86}, Sr^{89}, Y^{90}, Y^{91}, Zr^{95}, Mo^{99}, Ru^{103}, Ru^{106}, Ag^{111}, Pd^{112}, Cd^{115} (44 days), Te^{119},[4] Sb^{122}, I^{124}, I^{125},[5,6] I^{126}, Ba^{133}, Ce^{139}.[7] Not all of these isotopes should nor do lie on the fission yield curve. For example, the most probable representative of mass number 74 should be Ga^{74} (not measured in these studies) and the measured yield for As^{74} was below the curve by a factor of 20. Similarly, the yield for Pd^{112} was 20-fold below the curve, in line with the prediction that the most abundant isobar of mass 112 should be Cd^{112} (stable). The smooth fission yield curve drawn partly through measured yields and partly through calculated points is symmetrical about mass number 98–99, which represent maximum yields, and drops off by a factor of 100 at mass numbers $\sim$60 and $\sim$138. A rough value of 0.2×10^{-24} cm^2 for the fission cross section was obtained by integrating the smooth curve. This figure is probably uncertain by a factor of two because of uncertainties in the shape of the curve and in the deuteron beam intensity. The most abundant isotope measured, Mo^{99}, has a fission yield of 5 percent.

With respect to the mechanism for the fission of bismuth with high energy deuterons, it is probably necessary to assume that only those nuclei to which the dueteron gives up a large fraction of its energy will undergo fission. According to Serber,[8] the nucleons of a heavy element like bismuth should present, on the average, about two mean free paths between collisions by projectile nucleons in the energy range considered here and should receive about 25 Mev per collision. A moderate percentage of the projectiles should therefore give up all of their energy upon entering the bismuth nucleus and most of such events should result in fission. The observations are not in disagreement with this theory, since the measured cross section for fission is less than one-tenth of the geometric cross section and it is plausible that most of the highly excited nuclei will boil off neutrons until fission takes over as the means for further energy dissipation. The agreement of theory with the data is good here since the fissionability parameter, Z^2/A, has about the same value for a nucleus such as Po^{198} as for U^{236}.

The facts outlined above, in particular the equality of the n/p ratio in both fission fragments, suggest that the fission reaction is relatively fast and takes place with excitation energy above the threshold since the two products could be left in a lower energy state if there were a rearrangement of neutrons and protons during fission. That is, the formation of two stable nuclei would be energetically more economical than the production of one which is unstable with respect to β^--emission and one toward orbital electron capture or β^+-emission. The absence of such

marked asymmetry as is noted for the slow neutron fission of uranium may also be related to the supra-threshold energy at which the reaction occurs.

The cooperation of Dr. Duane Sewell and Mr. J. T. Vale and all those of the 184-inch cyclotron group is gratefully acknowledged. This work was performed under Contract No. W-7405-eng-48, with the Atomic Energy Commission in connection with the Radiation Laboratory of the University of California, Berkeley, California.

[1] I. Perlman, R. H. Goeckermann, D. H. Templeton, and J. J. Howland, Phys. Rev. **72**, 352 (1947).
[2] A 56-hr. β^--emitter which proved to be the parent of 5-min. Cu^{66}.
[3] A 56-hr. β^--emitter tentatively assigned to Cu^{67} on the basis of the mode of disintegration and half-life.
[4] M. Lindner and I. Perlman (submitted for publication).
[5] A. F. Reid and A. S. Keston, Phys. Rev. **70**, 987 (1946).
[6] L. E. Glendenin and R. R. Edwards, Phys. Rev. **71**, 742 (1947).
[7] D. E. Mathews and M. L. Pool, Phys. Rev. **72**, 163 (1947).
[8] R. Serber, Phys. Rev. **72**, 1114 (1947).

Theoretical Evidence for the Existence of a Light-Charged Particle of Mass Greater than That of the Electron

M. HESSABY
Institute for Nuclear Studies, University of Chicago, Chicago, Illinois*
January 29, 1948

FROM theoretical considerations developed in a previous paper,[1] it can be deduced that particles with a charge equal to that of the electron and having a mass equal to 1.444 times that of the electron may be expected to exist.

It was shown that for an elementary charge the electrostatic potential

$$U=-(1/2K)\log[1-(2Ke/r)+(2K^2e^2/r^2)],$$

where e is the charge and K is a constant, satisfies the conditions that the integral of the charge density should be convergent and equal to e, and that the integral of the energy density should also be convergent. The value of the energy integral depends on that of K, and it also depends on the sign of e; the value is equal to

$$(e/4K)[(\pi/2)+1] \quad \text{or} \quad (e/4K)[(3\pi/2)-1],$$

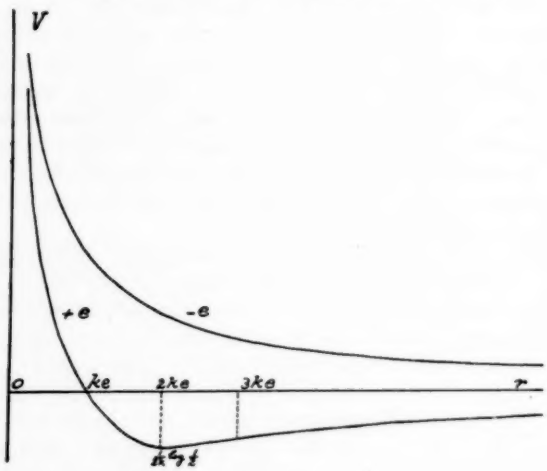

FIG. 1.

depending on whether e is negative or positive. The ratio of these two values is 1.444. Setting the value of the energy integral equal to the mass of the electron gives us the value of K, which will thus depend on the sign chosen for the charge of the electron. If this is arbitrarily taken to be negative, then we obtain $K=3.8\times10^{-4}$. There should then exist a positive particle of mass equal to 1.444 times that of the electron. A positive counterpart of the electron can also exist, but it should have a tendency to be annihilated by combining with an electron.

According to the sign of e, the potential curve takes one of the two forms shown in Fig. 1. For $e<0$, the curve has no minimum, and the force on a particle of the same sign is always repulsive. For $e>0$, there is a minimum at $r=2Ke$, and the field becomes attractive at distances smaller than $2Ke$. The force on a particle of opposite sign becomes repulsive at very small distances. With the value $K=3.8\times10^{-4}$ we find that the field changes sign for $r=3.7\times10^{-13}$.

Evidence for the existence of positive particles of mass greater than that of the electron occurring in the neighborhood of β-ray emitters has been found by Smith and Groetzinger.[2] A rough estimate of the mass, determined from the loss of momentum of the particle in a foil, has led the authors to a value approximately equal to 1.5 to 2 times the electron mass.[3]

It has also been recently reported in the press that charged particles of mass about three times that of the electron have been found by Auger in cosmic radiation.

* On leave of absence from the University of Teheran.
[1] M. Hessaby, Proc. Nat. Acad. Sci. (June 1947).
[2] L. Smith and G. Groetzinger, Phys. Rev. **70**, 96–97 (1946).
[3] Private communication by G. Groetzinger.

Production of Cosmic-Ray Mesons

GEOFFREY F. CHEW*
Institute for Nuclear Studies, University of Chicago, Chicago, Illinois
March 19, 1948

IT is currently believed that cosmic-ray mesons are produced in nuclear events induced by primary protons near the top of the atmosphere. The well-known difficulty of the absence of nuclear interaction by sea level mesons and the recent experiments with photographic emulsions[1] have led to the idea[2] that π-mesons, of mass 180 Mev, are the ones produced initially and that each π-meson quickly decays (10^{-7}–10^{-10} sec. lifetime) into an "ordinary" μ-meson of mass 100 Mev and a neutral recoil. An investigation has been undertaken to see whether these ideas are in quantitative agreement with actual observations on meson spectra and intensities.

It is found that there is indeed agreement if the mean free path for absorption of the primary protons is taken to be ~5 cm Hg and if about half the primary energy goes to charged π-mesons, the average multiplicity being around 5 at high latitudes and increasing roughly as the square root of the primary energy.

Our analysis is based on the following argument. No meson theory has as yet proved adequate, but if one uses the general picture that a field of virtual mesons surrounds

the proton and that the difference immediately after the nuclear collision between the actual and "proper" fields constitutes the meson emission, then according to Heisenberg[3] the following qualitative results are to be expected in any reasonable theory: (1) Emission is multiple and the multiplicity increases with proton energy. (2) Low energies are favored in the emitted spectrum, whose relative shape should not depend strongly on the proton energy. To put these ideas in a suitable form for computation, the following meson production spectrum, containing three arbitrary parameters, is assumed: A proton of kinetic energy E_p produces mesons whose total (kinetic+rest) energies E_m are distributed from $m_\pi c^2$ to KE_p according to a power law $E_m^{-\beta}$. The total fraction of proton kinetic energy delivered to charged π-mesons is H. The four parameters, K, β, H, and the mean free path for the nuclear process (assumed independent of E_p) are to be determined by fitting various experiments. More meaningful than the individual values of K and β is the fact that together with H they fix the multiplicity, which has an approximate energy dependence $\sim E_p^{\beta-1}$.

The altitude dependence of vertical particles penetrating 21 cm of Pb (assumed to be "fast" mesons only) at Los Angeles and at the equator[4] was used to fix β and K by the following procedure: A spectrum of primary protons was chosen by fitting the latitude effect for vertical radiation[5] to the usual high energy power law. The result was a power law $E_p^{-2.9}$ above 12 Bev, $E_p^{-1.6}$ between 12 Bev and 4 Bev, zero flux below 4 Bev. This proton spectrum produces a meson spectrum whose shape depends essentially only on β and K, and the shape of the meson spectrum at any altitude is sufficient to determine the relative intensities at all lower altitudes by the usual one-dimensional diffusion theory.[6] In this way the experimental equator meson curve and the Los Angeles-equator difference were used to fix $\beta=1.5\pm0.2$, $K=0.45\pm0.1$, independently of H and λ. This choice implies a multiplicity which increases at high energies like $E_p^{0.5\pm0.2}$ and has an average value 15H at the equator. A recent theoretical calculation[7] of the multiplicity of pseudoscalar meson production predicts an energy dependence $\sim E_p^{\frac{1}{4}}$.

The values of H and λ were fixed by experiments at higher altitudes. Schein's balloon data[8] on vertical particles penetrating 18 cm of Pb at Chicago can be extrapolated to the top of the atmosphere to obtain the total vertically incident flux, 0.10 particles cm^{-2} $sec.^{-1}$ per unit solid angle. This figure is in reasonable agreement with the bare counter rocket figure of 0.12,[9] considering that the latter may include re-entrant electrons. A calculation of the meson intensity to be expected at sea level from this incident flux and comparison with the well-known figure of 0.0074 fixes pairs of H and λ. The possible pairs are reduced by fitting the slope of the meson plus proton curve near the top, there being no maximum. The results are

$$4.5 \text{ cm Hg} < \lambda < 7 \text{ cm Hg},$$
$$0.6 \text{ cm Hg} > \kappa > 0.3 \text{ cm Hg}.$$

(A geometrical nuclear cross section corresponds to $\lambda \approx 4$ cm Hg.) The uncertainty is considerable because of the unknown number of mesons in the slow group which can penetrate 18 cm Pb (see below).

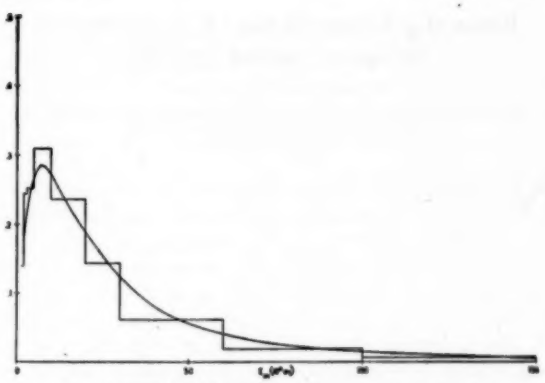

FIG. 1. Differential spectrum of mesons at sea level normalized to one particle.

As a check on the above choice of parameters, additional calculations were made of absolute latitude effect and of the meson spectrum at sea level. The results agree satisfactorily with experiment, for the latitude effect is within 20 percent and the spectrum is shown in Fig. 1, as compared to Wilson's cloud-chamber data[10] shown in blocks. The fact that the maximum occurs at a lower energy than in previous theoretical calculations[6,11] is due partly to the π-μ-decay and partly to the preference given to low energy mesons in the production process. A further test of our assumptions will come when balloon measurements of the hard component can be taken at the equator. A maximum of about seven times the sea level intensity at a pressure of 5 cm Hg is predicted.

Recent experiments [12-14] indicate that the situation is not actually as simple as assumed above. A very large number of slow mesons (kinetic energy less than 400 Mev) continues to be produced down to altitudes of about 14,000 ft. by what may be the decay of neutral particles. (All the experiments used in the above analysis fairly well exclude this slow group.) Assuming these slow mesons to be of the same variety as those observed at sea level, one finds their total energy loss throughout the atmosphere to be about equal to that of the "fast" mesons. It is therefore gratifying that our result above shows only half or less of the primary energy going immediately into fast-charged mesons.

This investigation, then, does not reveal any clear-cut inconsistencies in the proton π-μ-hypothesis, but so far rather tends to support the latter.

I am indebted to Dr. E. Fermi and Dr. M. Schein for valuable discussions of this work.

* National Research Council Predoctoral fellow.

[1] C. M. G. Lattes, G. P. S. Occhialini, and C. F. Powell, Nature 160, 453 (1947).
[2] R. E. Marshak and H. A. Bethe, Phys. Rev. 72, 506 (1947).
[3] W. Heisenberg, *Cosmic Radiation* (Dover Publications, New York, 1946), p. 126.
[4] P. Gill, M. Schein, and V. Yngve, Phys. Rev. 72, 733 (1947).
[5] R. A. Millikan, H. V. Neher, and W. H. Pickering, Phys. Rev. 63, 234 (1943).
[6] See, for example: J. Hamilton, W. Heitler, and H. W. Peng, Phys. Rev. 64, 78 (1943).
[7] H. W. Lewis, J. R. Oppenheimer, and S. A. Wouthuysen, Phys. Rev. 73, 127 (1948).
[8] M. Schein, private communication.
[9] J. Van Allen and H. Tatel, Phys. Rev. 73, 245 (1948).
[10] Wilson, Nature 158, 414 (1946).
[11] Euler and Heisenberg, Ergeb. d. exact. Naturwiss. 17 (1938).
[12] M. Schein and F. Carr, Bull. Am. Phys. Soc. 22, No. 6, 15 (1947).
[13] D. C. Moore and R. Brode, Bull. Am. Phys. Soc. (January, 1948), Los Angeles Meeting.
[14] M. Pomerantz, private communication.

Ratio of g Values of the $^2P_{1\frac{1}{2}}{}^0$ and the $^2S_{\frac{1}{2}}$ States in Ionized Calcium

J. RAND MCNALLY, JR.
George Eastman Research Laboratory, Massachusetts Institute of Technology, Cambridge, Massachusetts
March 15, 1948

NUMEROUS articles appearing in the literature point to a possible discrepancy in the value of the magnetic moment of the spinning electron.[1] Discrepancies between theory and experiment or between experiment and experiment exist in four cases, namely, (1) the fine structure of the $n=2$ state of atomic hydrogen,[2] (2) the hyperfine structure of the ground states of hydrogen and deuterium,[3] (3) the charge-mass ratio of the electron as determined from the Zeeman effect,[4] (4) the ratio of atomic g values.[5]

This note is concerned with additional evidence on the ratio of atomic g values,—in this case the ratio of the g value of the normal $^2S_{\frac{1}{2}}$ state and that of the excited $^2P_{1\frac{1}{2}}{}^0$ state of alkali-like atoms. Preliminary calculations from Zeeman data taken at fields of the order of 90,000 gauss gave ratios of g values for the elements Na, K, CaII, and Cu. Disagreements between the experimentally determined g ratios and the ratio of g values based on the Landé values were found, but the probable error of these early measurements was of the order of the effect observed. A careful selection of sharp line patterns of moderate intensity in the case of singly ionized calcium gave the value:

$$g_2/g_1=1.5013\pm0.0003,$$

where g_2 is the g value of the normal $^2S_{\frac{1}{2}}$ state and g_1 is the g value of the excited $^2P_{1\frac{1}{2}}{}^0$ state. This g ratio, which is field-independent and also independent of the value of e/m, is to be compared with the Landé g ratio of 1.5000. If one assumes that the error arises in the spin magnetic moment only then the value of the spin magnetic moment is low by 0.17 ± 0.04 percent.

[1] G. Breit, Phys. Rev. **72**, 984 (1947); J. Schwinger, Phys. Rev. **73**, 416 (1948).
[2] S. Pasternack, Phys. Rev. **54**, 1113 (1938); W. E. Lamb and R. C. Retherford, Phys. Rev. **72**, 241 (1947).
[3] J. E. Nafe, E. B. Nelson, and I. I. Rabi, Phys. Rev. **71**, 914 (1947); D. E. Nagle, R. S. Julian, and J. R. Zacharias, Phys. Rev. **72**, 971 (1947).
[4] J. A. Bearden, Phys. Rev. **55**, 584 (1939).
[5] P. Kusch and H. M. Foley, Phys. Rev. **72**, 1256 (1947); Phys. Rev. **73**, 416 (1948).

Gamma-Radiation from the Bombardment of Fluorine, Boron, and Beryllium by Protons

JAMES A. JACOBS, PHILIP R. MALMBERG, AND JOHN S. WAHL
State University of Iowa, Iowa City, Iowa
March 19, 1948

THE angular distribution of the gamma-rays has been determined for the reactions $F^{19}(p,\alpha)O^{16*}$ (gamma-ray energy 6.2 Mev), $B^{11}(p,\gamma)C^{12}$ (three gamma-rays of 16, 12, and 4 Mev), and $Be^9(p,\gamma)B^{10}$ (four gamma-rays of energies up to 6 Mev). These reactions and gamma-ray energies have been established in numerous previous papers.[1] The gamma-ray excitation curves for the first two reactions at their lowest resonances have also been measured.

All data were taken with thick targets upon a nickel backing. The fluorine target was made by painting with a suspension of CaF_2 in alcohol and water, the boron target by settling from a suspension of amorphous boron in alcohol, and the beryllium by evaporation of beryllium metal in vacuum.

The thick target excitation curves were measured by obtaining the number of counts in a Geiger tube for a given beam charge, at various bombarding energies. The accelerating voltage was measured by a resistance voltmeter (about 2700 megohms) with an estimated maximum error of 3 percent.

From the fluorine excitation curve, the resonance is at 335 kev with a half-width of 7 kev. The spread in beam energy is of the order of 5 kev, so that the true half-width is approximately 4 kev. The resonance for boron is at 165 kev with a half-width of 9 kev. Since the spread in beam energy is of the order of 3 kev at this bombarding voltage, the actual boron resonance half-width is approximately 8 kev.

In measuring the angular distribution, the detector consisted of two thin walled Geiger tubes operated in coincidence, a thin lead sheet in front of the first tube producing the secondary electrons. The tubes were enclosed in a lead box with $\frac{1}{4}$-in. thick walls, with a 1-in×4-in. opening at the front facing the target chamber. The box is mounted to rotate around the target chamber, so that at any angle the two coincidence tubes are in line with the target. The angle is measured with respect to the forward direction of the proton beam. The bombarding energy was slightly above the resonance point for fluorine and boron; for beryllium the energy was 340 kev, about at the resonance peak.

TABLE I.

Angle	Fluorine	Boron	Beryllium
45°	0.979±0.025	1.020±0.022	1.07±0.20
60°	1.015±0.025	1.034±0.022	0.64±0.15
75°	1.001±0.025	0.977±0.022	1.02±0.18
90°	1.000±0.015	0.982±0.013	1.09±0.13
105°	0.992±0.025	0.985±0.022	0.94±0.15
120°	1.011±0.026	0.996±0.022	1.03±0.19
135°	0.980±0.025	1.057±0.022	0.95±0.16

At each angle the coincidence counting rate was compared to that of a monitor Geiger tube mounted to one side. The angular distribution data obtained (normalized to unity) are given in Table I. The errors given are the statistical standard deviations.

The spherical symmetry for fluorine agrees with the result of Atchison[2] and Van Allen.[1] For boron, a 10 percent asymmetry might fit the data better than spherical symmetry, but this small effect probably is not significant compared to the standard deviation. The beryllium data, although too few counts were taken, indicate spherical symmetry, the large deviation of the 60° point probably not being significant.

[1] Typical of these are J. A. Van Allen and N. M. Smith, Phys. Rev. **59**, 501 (1941); R. G. Herb, D. W. Kerst, and J. L. McKibben, Phys. Rev. **51**, 691 (1937); N. Hole, J. Holtsmark, and R. Tangen, Zeits. f. Physik **118**, 48 (1941).
[2] F. S. Atchison, Thesis (1940) State University of Iowa.

Protective Facings on Eastman Emulsions

P. B. MAUER AND H. L. REYNOLDS
Department of Physics, University of Rochester, Rochester, New York
March 22, 1948

IN the course of investigating the range of protons in Eastman NTB emulsions certain inconsistencies appeared. These were largely explained when it was learned from Eastman Kodak Company that a thin photographically inert facing is usually applied to the emulsion for reasons of protection.

For 2.5-Mev protons entering the emulsion at an angle of four degrees and an assumed stopping power relative to air of 2000, the track length in the emulsion should be roughly 52 microns, and the depth of penetration into the emulsion would be of the order of 3 microns. With a photographically inert surface layer of one-micron thickness covering the emulsion, it is easily seen that the length of the visible track would be appreciably shorter than the true length and thus the stopping power of the emulsion would appear greater than expected. This effect would be exaggerated as the initial energy or entering angle is reduced.

This effect was verified by exposing a plate first at two degrees and then at fifteen degrees to the incident protons. Protons of 2.5 Mev entering at fifteen degrees were found to have a real (not projected) track length of the order of nine microns longer than those entering at two degrees.

Before this effect was observed many of our stopping-power determinations seemed to fall outside of the estimated limits of accuracy of the measurements. This may be explained by the fact that such a thin surface coating is difficult to apply uniformly and any variations in its thickness would alter the observed stopping power.

Rebuilding of Metal Geiger Counting Tubes

G. E. HAGEN AND D. H. LOUGHRIDGE
University of Washington, Seattle, Washington
March 19, 1948

AN investigation was made of some techniques of reviving worn-out G-M counters used on cosmic-ray measurements. These tubes were the conventional tube[1] made up of 2-in. seamless brass tubing $\frac{1}{16}$ in. thick with soldered end seams. Central electrodes were of 0.005-in. Kovar wire held rigid by a tension spring at one end and brought out through a glass seal at the other. Filling was 9 cm of argon and 1 cm of ethyl alcohol vapor. It was found that this type of tube normally has from a few months to about two years of useful life when in continuous operation at 1250 volts. Toward the end of this lifetime the plateau of stable operation shortens until proper adjustment of operating voltage becomes impossible.

Particular attention was paid to a technique suggested in conversation with S. A. Korff. One opens the tube without dismantling, rinses out with acetone, and refills with argon and alcohol. It has been shown[2] that one of the main factors in the playing-out of these tubes was the decomposition of alcohol vapor with probable deposition of a film of organic material on electrode surfaces.

A group of 59 tubes no longer operative was treated in the following manner: copper sealing tube was cut open and 50 cc of acetone poured into the tube. The tubes were then placed on a spindle and rotated end over end for an hour. During this time rotation was frequently interrupted and tubes were twisted axially to insure that all portions were thoroughly rinsed. At the end of this time the acetone was removed, and tubes were evacuated and refilled.

Seventy percent of these tubes again operated, but the rejuvenation proved to be only temporary. Tubes were set aside to age and frequently tested. After 40 days of aging (not in operation) only 50 percent of the original number of tubes remained good. Tubes were then placed in operation at 1250 volts. Although the operating voltage plateaus of some of the tubes improved with the first few days of operation, they then began to narrow. After 15 days of operation, only 20 percent of the original tubes remained serviceable, and it was concluded that this treatment is ineffective.

In another group 14 tubes were rebuilt by grinding and polishing the cathode surface with emery paper and installing a new central electrode, as suggested by Regener. After three months of operation 12 of the 14 were still in excellent working condition, and it was concluded that this procedure is effective although the grinding process is tedious.

A group of 60 tubes was then rebuilt with a new central electrode but without grinding the cathode surface. Half of these tubes had previously been rinsed with acetone. Of this entire group, 82 percent were still good after 40 days of operation, and the previous rinsing treatment apparently did not affect tube life. This suggested that the condition of the central electrode was the more important factor in the playing out of the tubes, and that the condition of the cathode surface was not critical.

To verify this last point, eight tubes were dismantled and the cathode surface thoroughly ground and polished, but the old anodes were cleaned and reinstalled. None of these tubes operated properly after refilling. In reopening tubes rebuilt with new anodes only, it was found that traces of soldering flux on cathode surface did not noticeably impair the operation of the tube, but if the same were present on the anode the tube had a tendency to go into continuous discharge. A satisfactory procedure for cleaning the anode consisted of wiping with absorbent cotton saturated with clean acetone and drying with fresh cotton. From these data it was concluded that installation of a new clean anode and refilling constitutes an effective process of rejuvenating this type of counter.

This work was supported by a grant-in-aid from the Research Corporation of New York.

[1] V. H. Regener, Rev. Sci. Inst. **18**, 267 (1947).
[2] S. S. Friedland, Phys. Rev. **71**, 377 (1947).

Neutron-Proton Scattering and Range of Nuclear Forces

TA-YOU WU
Department of Physics, Columbia University, New York, New York
March 15, 1948

CONCERNING the proton-neutron scattering at ~100 Mev, experiments at Berkeley[1] show that (i) the total cross section is $\sigma=0.83\times10^{-25}$ cm², (ii) the ratio of backward to transverse scattering (in the center of mass system) $R=\sigma(\pi)/\sigma(\pi/2)$ is ~3, and (iii) the scattering in the neighborhood of $\vartheta=\pi/2$ is almost symmetrical with respect to the directions $\pi/2$. The problem is to find the nucleon interaction that will account for these observed results. Many calculations have been made with various assumed potentials. The situation can perhaps be summarized as follows:

1. On the basis of the symmetrical theory with a rectangular potential well of range $\rho=2.8\times10^{-13}$ cm, an exact calculation gives for σ the value 0.94×10^{-25} cm² and for R a value of the order 100[2]. With a Gaussian potential e^{-r^2/a^2} where the value $1/a^2=0.266\times10^{26}$ cm^{-2} has been chosen from the analysis of Hoisington, Share, and Breit[3] and can be regarded as corresponding to the range $\rho=2.8\times10^{-13}$ cm for the rectangular well, a calculation based on the second Born approximation[2] gives $\sigma=0.96\times10^{-25}$ cm² and $R\sim57$. On the Møller-Rosenfeld theory with the Yukawa potential, a first Born approximation gives $\sigma=1.40\times10^{-25}$ cm² and $R\sim57$.[2] It is seen that in all cases the ratio R is by far too high compared with the experimental value.

2. On including tensor forces in the symmetrical theory of Rarita and Schwinger, with a rectangular well of range $\rho=2.8\times10^{-13}$ cm, an exact calculation[4] gives for σ the value 1.29×10^{-25} cm² and $R\sim10$. The asymmetry of the scattering about the directions is decreased.

3. With a rectangular well of range $\rho=2.0\times10^{-13}$ cm without tensor forces, Camac and Bethe[5] obtain, on the symmetrical theory, $\sigma=0.84\times10^{-25}$ cm² and $R=4.4$ for 80-Mev neutrons.

It is seen that the angular distribution, especially the ratio R, of the scattering is very sensitive to (i) the presence of tensor forces and (ii) the range of the nucleon interaction. To achieve better agreement with the observed R, one may have either to include tensor forces or to employ a shorter range, or to make both changes. Camac and Bethe realize, however, that the use of the smaller range $\rho=2.0\times10^{-13}$ cm will spoil the agreement with the data on proton-proton scattering at low energies.

The purpose of the present note is to suggest that, since there is really no *a priori* reason why the range of nucleon interaction should be the same for the triplet and the singlet states, one employ for the latter $\rho_s=2.80\times10^{-13}$ cm as demanded by the proton-proton scattering data at low energies, and for the former $\rho_t=1.5\times10^{-13}$ or 2.0×10^{-13} cm as indicated by the recent experiments on the scattering of neutrons by ortho- and para-hydrogen and by hydrogen in crystals.[6] In fact, one would rather expect the range to be different for the triplet and the singlet states on the symmetrical theory if the mesons involved have different masses.

TABLE I.

Gaussian, 100 Mev $1/a_s^2=0.266\times10^{26}$ cm^{-2}			Rectangular well, 80 Mev $\rho_s=2.80\times10^{-13}$ cm		
$1/a_t^2$ in cm^{-2}	σ in cm²	R	ρ in cm	σ in cm²	R
0.266×10^{26}	0.96×10^{-25}	57	2.80×10^{-13}	0.84×10^{-25}	139
0.522×10^{26}	0.95×10^{-25}	10	2.00×10^{-13}	1.01×10^{-25}	8.6
0.925×10^{26}	1.08×10^{-25}	5.7	1.50×10^{-13}	1.17×10^{-25}	5.1

Accordingly, an exact calculation of the scattering cross section at 80 Mev for a rectangular well potential of range $\rho_s=2.80\times10^{-13}$ for the singlet states and range $\rho_t=2.80$, 2.0, or 1.5×10^{-13} cm for the triplet states has been carried out on the basis of the symmetrical theory. Another calculation based on the second Born approximation[2] has also been carried out for a Gaussian potential e^{-r^2/a^2}, with $1/a_s^2=0.266\times10^{26}$ cm^{-2}, and $1/a_t^2=0.266$, $0.266\times(2.8/2.0)^2$, or $0.266(2.8/1.5)^2\times10^{26}$ cm^{-2} to correspond roughly to the ranges 2.8, 2.0, 1.5×10^{-13} cm in the case of the rectangular well. The result is shown in Table I. In general, a shorter range for the triplet states renders the triplet state scattering more isotropic. It is true that no complete agreement with the observed features concerning σ, $\sigma(\vartheta)$, and $R=\sigma(\pi)/\sigma(\pi/2)$ has yet been found for these potentials. But it is expected that the inclusion of tensor forces will further lower somewhat the ratio R in the table and increase the symmetry of $\sigma(\vartheta)$ with respect to $\pi/2$ in the neighborhood of $\pi/2$. It seems that by using two different ranges for the triplet and the singlet states and including the effect of tensor forces, it may be possible to account for the observed data on the symmetrical theory, i.e., without introducing arbitrary proportions of ordinary and exchange forces. A calculation of the deuteron problem with these shorter ranges including tensor forces would be of great interest.[7]

[1] Cook, McMillan, Peterson, and Sewell, Phys. Rev. **72**, 1264 (1947), and unpublished results.
[2] Ta-You Wu, Phys. Rev. **73**, 934 (1948).
[3] Hoisington, Share, and Breit, Phys. Rev. **56**, 886 (1939).
[4] J. Ashkin and T. Y. Wu, Phys. Rev. **73**, 973 (1948).
[5] M. Camac and H. A. Bethe, Phys. Rev. **73**, 191 (1948).
[6] Sutton, Hall, Anderson, Bridge, DeWire, Lavatelli, Long, Snyder, and Williams, Phys. Rev. **72**, 1147 (1947); Schull, Wollan, Morton, and Davidson, Phys. Rev. **73**, 262 (1948).
[7] S. Moszkowski and R. G. Sachs, Phys. Rev. **73**, 184 (1948), have calculated the deuteron problem with a Gaussian potential $\exp(-r^2/a^2)$ with $a=2.80\times10^{-13}$ cm. Comparison of this with $\exp(-0.266r^2\times10^{26})$, which fits the low energy proton-proton scattering best, shows that $a=2.80\times10^{-13}$ corresponds to too large a range for even the singlet state. For the triplet states, a must be still smaller, in view of the results of Sutton *et al.* and of Schull *et al.*, as shown in Table I.

Ultrasonic Reflections by Domains in Rochelle-Salt Single Crystals

WILLIAM J. PRICE
Rensselaer Polytechnic Institute, Troy, New York
March 22, 1948

THE propagation of 10-Mc/sec. ultrasonics in single crystals of rochelle salt has already been studied by the pulse technique.[1] In the temperature range where the crystal is ferroelectric, it has recently been observed that reflections occur from within the interior of the crystal. These reflections are a result of the domain structure and are believed to occur at the domain boundaries.

Rochelle-salt single crystals of sufficient size are known to have a domain structure in the ferroelectric temperature range.[2] Adjacent domains differ in the direction of the spontaneous polarization (either parallel or antiparallel to the x crystallographic axis). Accompanying this polarization is a shearing strain in the y–z plane, and as a result the boundaries will be regions of strain from which reflections of ultrasonic waves may occur. Studies of powder patterns on the surface of rochelle-salt crystals indicate the domains form laminae 1 to 8 mm thick in the y direction and 1 cm or more in extent in the x and z directions.

In the observations reported here, and x cut quartz transducer is cemented to one surface of a rochelle-salt single crystal cut in the shape of a rectangular parallelepiped with dimensions approximately 1 in. When the piezoelectric transducer is excited by an electrical pulse of the 10-Mc/sec. carrier frequency, an ultrasonic pulse travels through the rochelle-salt crystal and is reflected at the opposite surface. Upon returning to the transducer it is detected by the resulting electrical pulse in quartz and again reflected into the rochelle-salt specimen. The successive echoes are displayed on a cathode-ray tube.

When a compression wave is propagated along the y crystallographic axis of the rochelle-salt crystal, echoes with intensity about 40 decibels below those from the crystal surfaces are observed from the interior of the crystal. These echoes are present only in the temperature range where the crystal is ferroelectric and disappear gradually as the temperature approaches the Curie temperature (24.2°C).

When a d.c. bias field is applied in the x direction, these domain echoes are found to reduce in intensity until with a field of about 100 volts/cm, their level is at least 25 decibels below that with zero bias field. With larger fields it is found possible to reduce their level down to the noise level of the amplifier. The field necessary to reduce the domain echo intensity decreases as the upper Curie temperature is reached. The application of a sufficiently large biasing field will, of course, result in all the domains becoming polarized and sheared in the same direction; the observations of the domain echoes indicate that in this condition the strained regions at the domain boundaries are at least partially removed.

It has not been found possible to resolve the domain echoes and therefore no information has been obtained about the location or number of domains. It is felt that the best method of obtaining quantitative information is to observe the change in intensity of the echoes from the air boundaries as the domain structure is changed.

Domain echoes have also been observed when the pulse is propagated along the z direction. These echoes are about 15 decibels below those observed in the y direction. The lower intensity is accounted for by the smaller area of the domain boundaries normal to the z direction.

No indication of the Barkhausen effect has been observed in this work.

[1] H. B. Huntington, Phys. Rev. **72**, 321 (1947).
[2] Cady, *Piezoelectricity* (McGraw-Hill Book Company, Inc., New York, 1946).

The Energy Distribution of Neutrons in the Atmosphere

S. A. Korff, M. S. George, and J. W. Kerr
New York University, New York, New York
March 15, 1948

THE energy distribution of neutrons produced by the cosmic radiation in the free atmosphere has been computed by Bethe, Korff, and Placzek.[1] Experimental tests of these predictions have been made by Korff and Hamermesh[2] and by Agnew, Bright, and Froman.[3] The first of these tests was made by an instrument carried up to altitudes of about 40,000 feet (2 meters of water equivalent below the top of the atmosphere), in a free balloon flight, and the second in a B-29 at altitudes of from 20,000 to 36,000 feet. In both experiments the counting rate in a boron trifluoride counter was determined with and without boron and cadmium shields.

On September 27, 1947, we conducted a balloon flight which reached an altitude of 66,000 feet (4 cm Hg), at which altitude it remained for many hours. Our counter contained 1050 cc of ordinary BF_3 at 14-cm Hg pressure. This flight employed the same instrumentation as our previous one, in that the counting rate of a neutron counter was determined with boron and cadmium shields automatically covering and uncovering the counter at predetermined intervals. The counting rates observed with this instrument at the top altitude were as follows: 16.8 counts per minute (O) unshielded, 7.55 counts per minute (C) with 0.7-mm Cd shield, 4.48 counts per minute (B) with 7-mm powdered B_4C shield.

It will be noted that the counting rates (B:C:O) stand in the ratio of 1:1.69:3.75. At 30 cm Hg, Agnew, Bright, and Froman find ratios of approximately 1:1.7:4.2. We obtain a ratio O:C of 2.22. This is slightly greater than the ratio obtained in our previous flight; the difference is attributable to increased accuracy. There appears to be no evidence that these ratios vary with altitude in the presently observed range, i.e., from a thousand meters above ground up to 66,000 feet.

The absolute number of neutrons is not determined in a flight of this sort, for it is necessary to set the amplifier bias to such a value to exclude spurious counts that some of the neutrons are missed. The absolute counting rate will yield only a lower limit to the neutron intensity.

The flight was conducted with the aid of funds supplied by the Office of Naval Research under Contract N6onr-279. We wish to acknowledge the splendid cooperation received from Doctors Whitaker and Myers and General Sadler of Lehigh University, Dr. E. O. Salant of the Brookhaven National Laboratory, and to thank Messrs. Swetnick, Greenberg, and Collyer of the N.Y.U. staff.

[1] H. A. Bethe, S. A. Korff, and G. Placzek, Phys. Rev. **57**, 573 (1940).
[2] S. A. Korff and B. Hamermesh, Phys. Rev. **69**, 155 (1946).
[3] H. M. Agnew, W. C. Bright, and D. Froman, Phys. Rev. **72**, 203 (1947).